Lecture Notes in Electrical Engineering 648

Vijay Janyani
Ghanshyam Singh
Manish Tiwari
Tawfik Ismail *Editors*

Optical and Wireless Technologies

Proceedings of OWT 2019

Springer

Lecture Notes in Electrical Engineering

Volume 648

The book series *Lecture Notes in Electrical Engineering* (LNEE) publishes the latest developments in Electrical Engineering—quickly, informally and in high quality. While original research reported in proceedings and monographs has traditionally formed the core of LNEE, we also encourage authors to submit books devoted to supporting student education and professional training in the various fields and applications areas of electrical engineering. The series cover classical and emerging topics concerning:

- Communication Engineering, Information Theory and Networks
- Electronics Engineering and Microelectronics
- Signal, Image and Speech Processing
- Wireless and Mobile Communication
- Circuits and Systems
- Energy Systems, Power Electronics and Electrical Machines
- Electro-optical Engineering
- Instrumentation Engineering
- Avionics Engineering
- Control Systems
- Internet-of-Things and Cybersecurity
- Biomedical Devices, MEMS and NEMS

For general information about this book series, comments or suggestions, please contact leontina.dicecco@springer.com.

To submit a proposal or request further information, please contact the Publishing Editor in your country:

China

Jasmine Dou, Associate Editor (jasmine.dou@springer.com)

India, Japan, Rest of Asia

Swati Meherishi, Executive Editor (Swati.Meherishi@springer.com)

Southeast Asia, Australia, New Zealand

Ramesh Nath Premnath, Editor (ramesh.premnath@springernature.com)

USA, Canada:

Michael Luby, Senior Editor (michael.luby@springer.com)

All other Countries:

Leontina Di Cecco, Senior Editor (leontina.dicecco@springer.com)

**** Indexing: The books of this series are submitted to ISI Proceedings, EI-Compendex, SCOPUS, MetaPress, Web of Science and Springerlink ****

More information about this series at http://www.springer.com/series/7818

Vijay Janyani · Ghanshyam Singh ·
Manish Tiwari · Tawfik Ismail
Editors

Optical and Wireless Technologies

Proceedings of OWT 2019

Springer

Editors
Vijay Janyani
Department of Electronics and Communication Engineering
Malaviya National Institute of Technology
Jaipur, Rajasthan, India

Ghanshyam Singh
Department of Electronics and Communication Engineering
Malaviya National Institute of Technology
Jaipur, Rajasthan, India

Manish Tiwari
Department of Electronics and Communication Engineering
Manipal University Jaipur
Jaipur, Rajasthan, India

Tawfik Ismail
School of Engineering and Applied Sciences
Nile University
Cairo, Egypt

ISSN 1876-1100 ISSN 1876-1119 (electronic)
Lecture Notes in Electrical Engineering
ISBN 978-981-15-2925-2 ISBN 978-981-15-2926-9 (eBook)
https://doi.org/10.1007/978-981-15-2926-9

This Springer imprint is published by the registered company Springer Nature Singapore Pte Ltd.
The registered company address is: 152 Beach Road, #21-01/04 Gateway East, Singapore 189721, Singapore

Conference Committee Members

Organizing Committee

Patron

Prof. Udaykumar R. Yaragatti, Director, MNIT Jaipur

General Chairs

Prof. Vijay Janyani, MNIT Jaipur
Prof. Ghanshyam Singh, MNIT Jaipur
Prof. Manish Tiwari, Manipal University Jaipur

Conveners

Dr. Dinesh Yadav, Manipal University Jaipur
Dr. Amit Kumar Garg, IIIT Kota
Dr. Rukhsar Zafar, SKIT Jaipur
Dr. Jitendra Kumar Deegwal, GEC Ajmer

Organizing Secretaries

Dr. Ritu Sharma, MNIT Jaipur
Dr. Ashish Kumar Ghunawat, MNIT Jaipur
Dr. Monika Mathur, SKIT Jaipur
Mr. Ashok Kumar, GWEC Ajmer
Mr. Nidhish Tiwari, Jagannath University, Jaipur

IETE Oversight Committee

Prof. Deepak Bhatnagar, FIETE
Prof. S. K. Bhatnagar, FIETE
Mr. K. M. Bajaj, FIETE

Sponsorship Committee

Mr. Lokesh Sharma, Manipal University Jaipur
Mr. Sanjeev Yadav, GWEC Ajmer
Mr. Ashok Kumar, GWEC Ajmer
Mr. Narendra Kr. Godara, MNIT Jaipur
Mr. Kurra Chaithanya, MNIT Jaipur

Registration Committee

Dr. Ravi Maddila, MNIT Jaipur
Dr. Amit Garg, IIIT Kota
Dr. Monika Mathur, SKIT Jaipur
Ms. Shruti Kalra, JECRC University, Jaipur
Ms. Usha Choudhary, MNIT Jaipur

Publication Committee

Dr. Amit Garg, IIIT Kota
Dr. Vinay Kanooongo, SKIT Jaipur
Dr. Rekha Mehra, GEC Ajmer
Mr. Ashish Kumar, MNIT Jaipur
Mr. Amit Kumar Sharma, MNIT Jaipur

Hospitality Committee

Dr. Mukesh Kumar Gupta, MBM Engineering College, Jodhpur
Mr. Ankur Saharia, MNIT Jaipur
Mr. Nitesh Mudgal, MNIT Jaipur
Mr. Ankit Agrawal, SKIT Jaipur
Mr. Abhinav Bhatnagar, MNIT Jaipur

International Advisory Committee

Prof. Hiroyuki Tsuda, Keio University, Japan
Prof. Ali Gharsallah, University of Tunis El Manar, Tunisia
Prof. Buryy Oleh Anatolievyach, LPNU, Ukraine
Prof. Ajoy Kar, HW University, Edinburgh, UK
Dr. Suchandan Pal, CEERI, Pilani, India
Prof. Kolin Poul, IIT Delhi, India
Prof. Konstantin Kozadaev, BSU, Minsk, Belarus
Dr. Lotfi Osman, University of Carthage, Tunisia
Prof. Mário F. S. Ferreira, University of Aveiro, Portugal
Dr. Miklos Veres, HAS, Budapest, Hungary
Prof. Sergii Ubizskii, LPNU, Ukraine
Prof. Yuri Shpolyanskiy, University of Saint Petersburg, Russia
Dr. Yaseera Ismail, UKZN, Durban, South Africa

Technical Program Committee

Dr. Akshay Kr. Rathore, Concordia University, Canada
Prof. Takasumi Tanabe, Keio University, Japan
Prof. Toshiharu Saiki, Keio University, Japan
Dr. Bishnu Prasad Gautam, WAKHOK, Japan
Dr. Reza Abdi-Ghaleh, University of Bonab, Iran
Dr. Kalpana Dhaka, IIT Guwahati, India
Dr. Upena D. Dalal, SVNIT, Surat
Prof. Rajeev Gupta, RTU, Kota
Prof. Mithiliesh Kumar, RTU, Kota
Dr. Manish Mathew, CEERI, Pilani, India
Dr. Preetam Kumar, IIT Patna
Dr. C. Periasamy, MNIT Jaipur
Dr. Seema Verma, Banasthali University
Dr. Sanjeev Kumar Metya, NIT, Arunachal Pradesh
Dr. Narendra Kumar Yadav, JECRC University, Jaipur
Dr. Bramha P. Pandey, GLA University, Mathura
Dr. Sanyog Rawat, Manipal University Jaipur
Dr. Lokesh Tharani, RTU, Kota
Dr. Girish Parmar, RTU, Kota
Dr. Anil Yadav, Amity University, Gurgaon
Dr. Dinesh Goyal, SGVU, Jaipur
Dr. Ashok Sirohi, RCEW, Jaipur
Dr. Nagesh Janrao, Government Polytechnic, Pune

Preface

Optical and wireless technologies are advancing at an accelerating rate recently. The traditional approaches to providing high data rates to the masses are transforming and expanding in a way that is beyond our imagination. The challenges in providing uninterrupted data and broadband communications have not changed. Our mission as a technical community is to understand these challenges and find ways to mitigate them. This includes the development and management of appropriate channels, novel devices, new protocols, efficient networks, and their integration. Keeping in view the amalgamation of these issues, the proceedings of 3rd International Conference on Optical and Wireless Technologies (OWT 2019) is being presented herewith.

The conference (OWT 2019) was held in the campus of Malaviya National Institute of Technology Jaipur, during March 16–17, 2019. A total of 150 participants, including the invited speakers, contributing authors, and attendees, participated in the conference. The participants were explored to a broad range of topics critical to our society and industry in the related areas. The conference provided an opportunity to exchange ideas among global leaders and experts from academia and industry in topics like optical materials, optical signal processing and networking, photonic communication systems and networks, all-optical systems, microwave photonics, optical devices for optical communications, nonlinear optics, nanophotonics, software-defined and cognitive radio, signal processing for wireless communications, antenna systems, spectrum management and regulatory issues, vehicular communications, wireless sensor networks, machine-to-machine communications, cellular–Wi-Fi integration, etc.

Apart from high-quality contributed papers presented by delegates from all over the country and abroad, the conference participants also witnessed the informative demonstrations and technical sessions form the industry as well as invited talks from renowned experts aimed at advances in these areas. The overall response to the conference was quite encouraging. A large number of papers were received. After a rigorous editorial and review process, 72 papers were invited for presentation during the conference. Among the presented papers, 70 papers were selected

for inclusion in the conference proceedings. We are confident that the papers presented in this proceedings shall provide a platform for young as well as experienced professionals to generate new ideas and networking opportunities.

The editorial team members would like to extend gratitude and sincere thanks to all contributed authors, reviewers, panelists, local organizing committee members, and the session chair for paying attention to the quality of the publication. We are thankful to our sponsors for generously supporting this event and institutional partner (MNIT Jaipur) for providing all the necessary support, encouragement, and infrastructure in this beautiful campus. At last, we pay the highest regard to the Irisworld Science & Technology Education and Research (IRISWORLD), a "not-for-profit" society from Jaipur for extending support for financial management of the OWT 2019.

Best wishes from

Jaipur, India — Prof. Vijay Janyani
Jaipur, India — Prof. Ghanshyam Singh
Jaipur, India — Prof. Manish Tiwari
Cairo, Egypt — Dr. Tawfik Ismail

Acknowledgements

The editors wish to extend heartfelt acknowledgment to all contributing authors, esteemed reviewers for their timely response, members of various organizing committees, and production staff whose diligent work put shape to the OWT 2019 proceedings. We especially thank our dedicated reviewers for their volunteering efforts to check the manuscript thoroughly to maintain the technical quality and for useful suggestions.

We also pay our best regards to the faculty members from institutional partners (MNIT Jaipur and Manipal University Jaipur) for extending their enormous assistance during the conference-related assignments, especially to Dr. Dinesh Kumar Yadav; Dr. Lokesh Kumar, Manipal University Jaipur; Sanjeev Yadav; Dr. Ashok Kumar; Jitendra Deegwal, Government Engineering College Ajmer; Mr. Nidhish Tiwari, JNIT Jaipur; Mr. Ramesh Dewanda, Executive Member, Irisworld Society Jaipur; and Sh. Narendra Godara, MNIT Jaipur.

We also acknowledge the financial support received from our esteemed sponsors AGMATEL and OSA student chapter of MNIT Jaipur. Lastly, we extend our sincere thanks to Springer for agreeing to be our publishing partner.

Prof. Vijay Janyani
Prof. Ghanshyam Singh
Prof. Manish Tiwari
Dr. Tawfik Ismail

Our Reviewers

Dr. Surendra Agarwal, Government Women Engineering College Ajmer, skagarwal5@rediffmail.com
Dr. Ashwini Arya, College of Technology, Pantnagar, ashwiniarya.iitr@gmail.com
Dr. Ramesh Battula, Malaviya National Institute of Technology Jaipur, ramsbattula@gmail.com
Mr. Sudhir Bhaskar, Indian Institute of Technology (BHU), Varanasi, sbhaskar.rs.ece@iitbhu.ac.in
Dr. Jitendra Deegwal, Government Engineering College Ajmer, Rajasthan, jitendradeegwal@gmail.com
Dr. Tarun Dubey, Manipal University Jaipur, tarunkumar.dubey@jaipur.manipal.edu
Dr. Umesh Dwivedi, Amity University, Rajasthan, umeshkudwivedi@gmail.com
Dr. Ashish Ghunawat, MNIT Jaipur, ashishghunawat@gmail.com
Dr. Mukesh Gupta, MBM Engineering College, Jodhpur, mkgupta06@gmail.com
Dr. Nikhil Deep Gupta, Manipal University Jaipur, 2012rec9530@mnit.ac.in
Mr. Rajkumar Gupta, AUR, rkgupta1@jpr.amity.edu
Dr. Tawfik Ismail, Cairo University, tawfik@niles.cu.edu.eg
Mrs. Sheilza Jain, YMCA University of Science and Technology, sheilzajain@gmail.com
Dr. Shruti Jain, JUIT, Waknaghat, shruti.jain@juit.ac.in
Dr. Nagesh Janrao, Technical Education, janrao.nl@gmail.com
Mr. Amit Joshi, Malaviya National Institute of Technology, amjoshi.ece@mnit.ac.in
Dr. Rajesh Khanna, Thapar University, rkhanna@thapar.edu
Dr. Arjun Kumar, Intel, akdec.iitr@gmail.com
Dr. Ashok Kumar, Government Mahila Engineering College Ajmer, India, kumarashoksaini@gmail.com
Mr. Umesh Kumar, Government Mahila Engineering College Ajmer, ume2222@gmail.com
Dr. Brijesh Kumbhani, IIT Ropar, brijesh@iitrpr.ac.in
Dr. Ravi Maddila, Malaviya National Institute of Technology, rkmaddila.ece@mnit.ac.in

Mr. Saurabh Maheshwari, Government Women Engineering College Ajmer, dr.msaurabh@gmail.com
Dr. Manish Mathew, CEERI, Pilani, manish.mathew@gmail.com
Ms. Monika Mathur, Rajasthan Technical University, monikamathur16@gmail.com
Dr. Arka Prokash Mazumdar, Malaviya National Institute of Technology, apmazumdar.cse@mnit.ac.in
Mrs. Rekha Mehra, Government Engineering College Ajmer, mehrarekha710@gmail.com
Mr. Hari Mewara, Government Engineering College Ajmer, hsmewara@gmail.com
Dr. Satyasai Nanda, Malaviya National Institute of Technology Jaipur, nanda.satyasai@gmail.com
Dr. Malaya Nath, National Institute of Technology Puducherry, malaya.nath@gmail.com
Prof. Lotfi Osman, Higher School of Communication of Tunis—University of Carthage, lotfi.osman@supcom.tn
Dr. Vipin Pal, National Institute of Technology, Meghalaya, vipinrwr@yahoo.com
Dr. Trilochan Panigrahi, National Institute of Technology, Goa, tpanigrahi80@gmail.com
Dr. Girish Parmar, Rajasthan Technical University, girish_parmar2002@yahoo.com
Mr. C. Periasamy, Malaviya National Institute of Technology, cpsamy.ece@mnit.ac.in
Mr. Pravin Prajapati, Gujarat Technological University, ec.pravin.prajapati@adit.ac.in
Dr. Sanyog Rawat, Manipal University, sanyog.rawat@jaipur.manipal.edu
Dr. Chitrakant Sahu, MNIT Jaipur, chitrakant.ece@mnit.ac.in
Mr. Sourabh Sahu, Malaviya National Institute of Technology Jaipur, sourabh.ggits@gmail.com
Mr. Kapil Saraswat, Indian Institute of Technology Kanpur, kapil.iitr@hotmail.com
Dr. Preeta Sharan, The Oxford College of Engineering, Bangalore, sharanpreeta@gmail.com
Dr. Jankiballabh Sharma, Rajasthan Technical University, jbsharma@rtu.ac.in
Dr. Neeru Sharma, Jaypee University of Information Technology, neeru.sharma@juit.ac.in
Dr. Prabhat Sharma, Visvesvaraya National Institute of Technology, prabhatmadhavec1@gmail.com
Dr. Ritu Sharma, MNIT Jaipur, rsharma.ece@mnit.ac.in
Dr. Sumit Srivastava, Manipal University Jaipur, sumit.310879@gmail.com
Prof. Manisha Upadhyay, Nirma University, manisha.upadhyay@nirmauni.ac.in
Mr. Karan Verma, Universiti Teknologi PETRONAS, vermakara@gmail.com
Mr. Pankaj Verma, National Institute of Technology, Kurukshetra, pankaj@nitkkr.ac.in
Dr. Seema Verma, Banasthali Vidyapith University, seemaverma3@gmail.com
Dr. Rajesh Vishwakarma, Jaypee University of Engineering and Technology, rajesh.vishwakarma@juet.ac.in

Dr. Sandeep Vyas, Jaipur Engineering College and Research Centre, vyas.sandeep@vitej.ac.in
Dr. Ajay Yadav, Government Women Engineering College Ajmer, ajay@gweca.ac.in
Mr. Dinesh Yadav, Manipal University Jaipur, dinesh.yadav@jaipur.manipal.edu
Dr. Narendra Yadav, JECRC University, narensinghyadav@yahoo.com
Dr. Sanjeev Yadav, Government Women Engineering College Ajmer, sanjeev.yadav.in@ieee.org
Dr. Rukhsar Zafar, SKIT M&G, rukhsar.zafar@gmail.com

Invited Speakers

Prof. Philippe Gallion, Emeritus Professor, Télécom ParisTech

Title: Advanced Optical Communications and Networking

Biography: Prof. Philippe Gallion holds M.Sc., Ph.D., and "Docteur es Science" and is now Emeritus Professor at Télécom ParisTech, formerly "Ecole Nationale Supérieure des Télécommunications" where he was the chairman of Department of Communications and Electronics. He has also lectured at the Pierre and Marie Curie University (Paris VI), at several French "Grandes Ecoles" and several foreign universities. His research has brought pioneering contributions to semiconductor lasers, optical amplifiers, optoelectronic devices, coherent optical communication, and optical communication systems and networks, including quantum communications and cryptography. He is author of several textbooks and chapters and more than 300 international publications and communications. He is a Member of the Optical Society of America and a Life Member of the Institute of Electrical and Electronics Engineers (IEEE), serving as Chairman for the French Chapter of the Photonics Society.

Dr. Vinod Kumar, Dir (retd.) Wireless Research, Alcatel-Lucent Bell Labs, France

Title: 5G Standardization and Deployment: Focus on 5GNR

Biography: Dr. Vinod Kumar has 35+ years of R&D experience in mobile communications. During his 27-year tenure in Alcatel-Lucent, he initiated and contributed to research projects in 2G/5G technologies—GSM, GPRS, EDGE, UMTS, HSPA, LTE, LTE A, and IoT. He was also involved in standardization, in marketing support, and in patent management related to the above technologies. He contributed to multiple international projects (EC FP6, FP7), acted as Evaluator in EC H2020 and ANR, and Technical Auditor for CELTIC. He holds Secretary and Treasurer positions in Wireless World Research Forum (WWRF). He has been Visiting Professor for 25 years for graduate courses in mobile communications in ENST (IMT ParisTech), CentraleSupelec, ISEP, Eurecom, France, and MNIT, India. He was Associate Professor at the Université de Marne la Vallée in France for six years. He acted as a member of Industrial Advisory Board of CTIF Denmark, of Conseil Technique of Supelec, France, and of the joint INRIA-Bell Labs. He has widely lectured on 5G and IoT at IEEE and WWRF events, has been guest editor and referee for IEEE publications, and has been Ph.D. guide and examiner with CentraleSupelec and INRIA. He has 80 technical publications and 33 patents.

Prof. Ratnajit Bhattacharjee, Indian Institute of Technology, Guwahati

Title: Photoconductive Antenna: A Radiation Source for the Terahertz Band

Biography: Ratnajit Bhattacharjee is Professor in the Department of Electronics and Electrical Engineering, IIT Guwahati. His research interests include wireless communication, wireless networks, microstrip antennas, and microwave engineering and electromagnetics. He has co-authored about 140 research papers. Thirteen research students have completed their Ph.D. under his supervision. He has served as General Chair for 5th edition of IEEE Applied Electromagnetic Conference (AEMC 2015) and 22nd National Conference on Communications (NCC 2016); Chairman for the 18th NPSC 2014 and National symposium on Vacuum

Electronic Devices and Applications (VEDA 2018); and also Convener for IESC 2017. He has delivered invited talks in a number of conferences, symposia, and workshops. He has also been involved with several projects. Presently, he is Chief Coordinator for MeitY-sponsored project for setting up of an Electronics & ICT Academy at IIT Guwahati. He holds a Ph.D. (engineering) from Jadavpur University, Kolkata, and an M.Tech. (microwave engineering) from IIT Kharagpur. He did his B.E. in electronics and telecommunication engineering (first-class honors) from REC, Silchar.

Prof. V. Sinha, Chair Professor, E & ICT Academy, MNIT Jaipur

Title: A Tutorial on Error Control Coding for Mobile Communication

Biography: Professor Vishwanath Sinha received MS (Electronics) and D.Sc. Electrical Engineering from University of Ljubljana, Slovenia (erstwhile Yugoslavia). He worked as Professor at the Indian Institute of Technology Kanpur, is founder Director of LNMIT, Jaipur, is Emeritus Professor in Department of ECE, and is Chair Professor for E & ICT Academy, MNIT Jaipur, before settling down in Delhi. He has been Visiting Professor, since 1977, in a number of foreign universities/institutions in Germany, Switzerland, USA, Brazil, and Yugoslavia. The main areas of his interest are telematics, error control coding, satellite communications, and technical education. He is a fellow of Institution of Electronics and Telecommunication Engineers and Institution of Engineers, India, and a senior member of Institute of Electrical and Electronics Engineers, USA. He is also a Life Member of Indian Society for Technical Education. Several awards including S. K. Mitra and J. C. Bose Memorial Awards for best papers presented by him and published in 1976 and 1979 have recognized his rich knowledge and contribution in engineering. He has a long teaching experience at IIT Kanpur and Brazilian Space Research Institute and University of Puerto Rico and has supervised 36 Ph.D. theses. He has organized different courses for engineering colleges, working engineers and scientists, and also organized a number of large-size national/international conferences. He has to his credit more than 80 papers published/presented in national/international

journals/conferences/seminars. His research activities at IIT Kanpur and Brazilian Space Research Institute made notable contribution in various areas including development of Remote Tutor, a product which establishes a virtual university and provides online interactive teaching tool, Telematics Projects, Graphics and Indian Script Terminal Project, Military Communication Satellite Systems, Systems for Space Telecommunications and Modulation Techniques. He is endowed with rich administrative experience in various capacities within and outside the teaching institutes.

Dr. Yaseera Ismail, University of KwaZulu Natal, Durban, South Africa
Title: Quantum Communication, the Next Generation of Optical Communication
Biography: Dr. Ismail is an experimental physicist working on the development of quantum technology within the Quantum Research Group, specifically within the field of quantum communication. She holds a Ph.D. in physics and had one of her recent publication chosen as editor's pick highlighting articles of excellent scientific quality. She is a recipient of the 2016 United States TechWomen Emerging Leader Award and is a 2018 Optical Society of America Ambassador.

Dr. Rajiv Mathur CTO, Chainvine Ltd., UK
Title: Blockchain—The 'Invisible' Technology that is 'Visibly' Changing the World
Biography: Dr. Rajiv Mathur is the Chief Technology Officer and Co-founder and Director of Chainvine Limited. Chainvine is an Enterprise Blockchain and Distributed Ledger Technology Company which has received international recognition. Chainvine is headquartered in UK with offices in Basingstoke, UK; Stockholm, Sweden; and Gurugram, India. Dr. Mathur comes from a computer science R&D background with research and teaching experience at some of the world's most renowned institutions like Imperial College London. In the area of telecommunications, Dr. Mathur has held executive management positions such as being the Chief Architect at Vodafone Qatar. Dr. Mathur has been a management consultant to many retail banks and payment networks in the UK in the areas of digital transformation and fraud detection.

Contents

Compact Multi-band Octagonal-Shaped Patch Antenna with a Partial Ground for WLAN/Wi-MAX Applications 1
Ritesh Kumar Saraswat, Swasti Dubey and Kunal Jeet Singh

A Review of Techniques to Design Tunable Antenna Covered with Metamaterial 9
Suyog Vinayak Pande and R. S. Kawitkar

Long-Range Surface Plasmon Resonance-Induced Tunable Optical Bistability Using Silver Nano-layer at 1550 nm 21
Aparupa Kar, Nabamita Goswami and Ardhendu Saha

Design of Nine-Shaped MIMO Antenna Using Parasitic Elements to Reduce Mutual Coupling 31
K. Vasu Babu and B. Anuradha

Approaches of Gigabit-Class Transmission for VLC with μLED-Based WDM System 39
M. T. Rahman, Rajendran Parthiban, Masuduzzaman Bakaul and Prem Kumar

Evaluation of Performance of Is-OWC OFDM System with Spatial Diversity 49
Sunita Khichar and Pawan Kumar Inaniya

Lightweight Secure-MQTT for Internet of Things 57
Adil Bashir and Ajaz Hussain Mir

Realization of Low-Cost Field-Deployable He–Ne Laser-Based Sensor System to Check the Quality of Food from Adulteration 67
Manish Kumar and Sanjeev Kumar Raghuwanshi

Experimental Evaluation of Reliable Underwater Optical Communication in the Presence of Turbulence and Blockage 75
Ramavath Prasad Naik, Udupi Shripathi Acharya and Nitin Kumar Suyan

Performance of SM-NSTBC for Correlated HAP Fading Channels with Imperfect-CSI 85
S. Godkhindi Shrutkirthi, G. D. Goutham Simha and U. Shripathi Acharya

Impact of Core Counts and Layouts on Dispersion Behavior in Homogeneous Multicore Fiber 93
Umar Farooque, Dharmendra Kumar Singh and Rakesh Ranjan

Erbium-Doped Optical Amplifiers—Origin to Latest Trends 101
Asifiqbal Thakor and Pravin Prajapati

An Approach for Reduction of Cross-Talk in Multi-core Optical Fibers 111
Shroddha Mukhopadhyay, Samanti Das and Nikhil R. Das

Measurement of Angular Velocity and Tilt Angle of Two-Dimensional Fiber-Optic Gyroscope with Sagnac Effect 119
Somesh Mule, Arpit Rawankar, Bharati Singh and Mohit Gujar

A Simple Structural Design for Tuning of Bandgap and Window in 1D Photonic Crystal 127
Alekhya Ghosh, Arghadeep Pal and N. R. Das

Traffic Control Enhancement with Video Camera Images Using AI . . . 137
Kriti Singh and P. C. Jain

Reconfigurable Slot-Based MIMO Antenna for Cognitive Radio Application 147
Shilpi Singh and M. S. Parihar

Role of Coupling Angle on the Performance of a Ring Resonator–Waveguide Sensor 155
M. Mishra and N. R. Das

CPW-Fed Triple-Band Circularly Polarized Printed Inverted C-Shaped Monopole Antenna with Closed-Loop and Two Semi-hexagonal Notches on Ground Plane 161
Reshmi Dhara, Sanjay Kumar Jana and Monojit Mitra

Security for Mobile System: 5G 177
Naresh Kumar, Annu, Karan Verma, Ajay K. Sharma and Shashvat Sharma

Security in Wireless Sensor Network Using IPsec 189
Annu Dahiya, Naresh Kumar, Karan Verma, Ajay K. Sharma and Shashvat Sharma

Analysis of Microstrip Patch Antenna with Multiple Parasitic Patches and Shorting Vias for Bandwidth Enhancement 199
Venkata A. P. Chavali, Aarti G. Ambekar, Chinmay Kudoo, Mansi Shah, Amit A. Deshmukh and K. P. Ray

Multiband Response Investigation for Stub-Loaded Right-Angled Isosceles Triangle Microstrip Antenna 207
Aarti G. Ambekar, Venkata A. P. Chavali, Chinmay Kudoo, M. Shah, Amit A. Deshmukh and K. P. Ray

Circularly Polarized Swastik Shape Microstrip Antenna 215
Amit A. Deshmukh, Chinmay Kudoo, M. Shah, A. Doshi and A. Mhatre

Bandwidth Enhancement of E-shape and U-Slot Embedded Microstrip Antenna Using Sectoral Patches 223
A. A. Deshmukh, Mansi Shah, C. Kudoo, V. Chaudhary and A. Mhatre

Light-Fidelity (Li-Fi), a New Approach for Internet Inside Running Metro 231
Ajit Kumawat and D. Sriram Kumar

Throughput Maximization in High-Speed Train Using Hybrid RF/FSO Communication System 243
Ankita Chauhan and Pankaj Verma

A Miniaturized Printed UWB Antenna with Sextuple Stop Bands Based on U-Shaped Slot Resonators and Split Ring Resonators for IoT Applications 253
Avichal Sharma, Priyanka Agrawal, Nikhil Mishra, Saurav Kumar Sinha and Mayur S. Raut

Design of Half Adder Using Electro-Optic Effect in Mach–Zehnder Interferometer 265
Manisha Prajapat, Ankur Saharia and Ghanshyam Singh

Dual-Band Plasmonic Filter Using Nanoslit-Loaded Ring Resonator . . . 275
Yazusha Sharma, Rukhsar Zafar, Ravi Jangir, Ghanshyam Singh and Mohammad Salim

Forward Error Correction Codes—Reed–Solomon and LDPC for OFDM Over the Optical Fiber Communication Systems 281
Usha Choudhary and Vijay Janyani

Theoretical Study of Transmission Coefficient and IV Characteristic of Double Barrier GaAs/$Ga_{1-x}Al_xAs$ Heterostructure at Different Composition 'x' 289
Manish Kumar Yadav, Bramha P. Pandey and Dharmendra Kumar

Polarization Encoded Multi-logic Functions with Direct Detection 299
J. K. Saini, A. Saharia, T. Ismail, I. S. Fahim, M. Tiwari and G. Singh

Parametric Analysis of Optical Microring Resonator 307
A. Saharia, R. K. Maddila, T. Ismail, I. S. Fahim, M. Tiwari and G. Singh

Asymmetric CPW-Fed Multistubs Loaded Compact Printed Multiband Antenna for Wireless Applications 317
Ashok Kumar, Jitendra Kumar Deegwal, Arjun Kumar and Karan Verma

Nanorod Dimer-Based Optical Fiber Plasmonic Sensor 325
Manoj Kumar Falaswal, Nitesh Mudgal and Ghanshyam Singh

Optimal Pricing for RAP in Heterogeneous Wireless Railway Networks 333
Vaishali and Sandeep Santosh

Novel Design of Compact Half Equilateral Triangular MSAs Gap-coupled with Sectoral Patches 345
Amit A. Deshmukh, Vivek Chaudhary, M. Shah, C. Kudoo and A. Mhatre

Study of Approaches to Implement the Prism-Based Surface Plasmon Resonance Sensors 353
Nitesh Mudgal, Manoj Kumar Falaswal, T. Ismail, I. S. Fahim, Manish Tiwari and Ghanshyam Singh

Wideband Designs of Unequal Lengths Slot Cut Microstrip Antennas Backed by Slotted Ground Plane 363
Amit A. Deshmukh, Amita Mhatre, M. Shah, C. Kudoo and S. Pawar

Single Feed Corner Trimmed Circularly Polarized Diagonal Patch Antenna 371
Shipra Bhatia and M. V. Deepak Nair

UWB Antenna for Breast Cancer Detection Using Back Scattering 377
Praveen Kumar Rao and Rajan Mishra

Implementation of SAC-OCDMA System Using Generalized Codes Over FSO Channel 385
Sharwan Kumar Jangid and Ritu Sharma

Design and Investigation of Octagonal Patch Antenna Using Artificial Magnetic Conductor for 5G Applications 393
Ashok Kumar, Arjun Kumar, Ashok Kumar and M. V. Karthikeyan

Numerical Investigation of T-Shape Waveguide-Based Directional Coupler 401
S. Radhakrishnan, Ajit Kumawat, G. Thavasi Raja and D. Sriram Kumar

Design and Analysis of Slot Coupled Antenna on Different Dielectric Materials 409
G. Anjaneyulu and J. Siddartha Varma

The Effect of Atmosphere on FSO Communication at Two Optical Windows Under Weather Condition of Bhubaneswar City 417
Jagana Bihari Padhy, Adyasha Satarupa and Bijayananda Patnaik

Design and Analysis of SRR-Inspired Ultra Wideband Antenna 427
Ritesh Kumar Saraswat, Antriksh Raizada and Himanshu Garg

Secrecy Performance Analysis for Multi-hop and Single-Hop Relaying Model 437
Shweta Pal and Poonam Jindal

Investigation of Substrate Integrated Waveguide (SIW) Filter Using Defected Ground Structure (DGS) 449
Amrita Dixit, Ashok Kumar, Ashok Kumar and Arjun Kumar

Energy-Efficient MAC-ROUTE Cross-layer Optimal Distance Chain Protocol for Wireless Sensor Network 457
P. M. Prathibhavani and T. G. Basavaraju

Baud Rate-Based Hierarchical Multihop Routing Protocol for WSNs 469
G. V. Sowmya and M. Kiran

Performance Analysis of Underwater 2D OCDMA System 477
Ajay Yadav and Ashok Kumar

Next-Generation PON with Enhanced Spectral Efficiency: Analysis and Design 485
Mukesh Kumar Gupta, Ambrish and Ghanshyam Singh

Comparative Analysis of a Novel Shape Patch Antenna for Wi-Max Band with Genetic Algorithm Optimization 497
Priyanka Jain, Raghavendra Sharma and Vandana Vikas Thakare

Analysis of Transmission Spectra of a Metal–Liquid Crystal–Metal Waveguide Structure with Different Metallic Layers 513
Ronak Dadhich and Ritu Sharma

Studies of Various Artificial Magnetic Conductor for 5G Applications 523
Ashok Kumar, Amrita Dixit, Ashok Kumar and Arjun Kumar

A Triple Band-Reject Frequency Selective Surface with Dodecagon Patch Element 531
Jaiverdhan, Dharmveer Yadav, Sanjeev Yadav, M. M. Sharma and R. P. Yadav

Numerical Investigation of Nonlinear Parameters of Chalcogenide-Based Holey Fiber for Supercontinuum Generation in Mid-infrared Region 541
Shruti Kalra, Sandeep Vyas, Manish Tiwari and Ghanshyam Singh

Characterization of Crosstalk Under Bending and Twisting Condition in Homogeneous Multicore Fiber 551
Piyush Ranjan, Dablu Kumar and Rakesh Ranjan

Design and Crosstalk Analysis in Homogeneous Trench-Assisted Multicore Fiber under Single-Mode Condition 559
Dablu Kumar and Rakesh Ranjan

A Cavity-Backed Dual-Band SIW Antenna with Enhanced Gain and Harmonic Suppression 569
Ramesh Kumar, Chenchani Vasanthi, D. S. Chandu and Pachipala Sreekar

Multiband Antenna for Wireless Applications 577
Sachin S. Khade, Samiksha Fulzele, Akanksha Sancheti, Samiksha Gawali and Divyani Rane

Broadband Circularly Polarized CPW-Fed Inverted-L Grounded Strips and SRR Loaded Square Slot Antenna for Wi-Fi/WiMAX/5G Applications 591
Rashmi, Ashok Kumar, Jitendra Kumar Deegwal and Hari Shankar Mewara

Realization of Inter-satellite Optical Wireless Wavelength Division Multiplexed System with Polarization Interleaving for LEO, MEO, and GEO Satellites 597
Ruchi Sharma, Chetan Selwal and Ashish Kumar Ghunawat

M-Way Balanced Tree Data Aggregation Approach for Clustered Wireless Sensor Networks 607
Ikkurthi Bhanu Prasad, Biswajit Rout, Vipin Pal and Yogita

Modified Gbest-Guided ABC Algorithm Approach Applied to Various Nonlinear Problems 615
Himani and S. K. Agrawal

An UWB Antenna with Dual Notched Band Characteristics at WLAN Band and X-Band Application 625
Disha Singh, B. K. Mishra and Sanjeev Yadav

Design and Simulink Implementation of Electrical Vehicle Charging Using Wireless Power Transfer Technology 631
Manish Kumar Thukral

Hybrid Chaining Security Approach in Cloud Computing 641
Vartika Kulshrestha, Seema Verma and R. K. Challa

About the Editors

Dr. Vijay Janyani obtained his Bachelors and Masters degrees in Electronics and Communication Engineering (ECE) from Malaviya Regional Engineering College, Jaipur (now MNIT, Jaipur) and his PhD from the George Green Institute for Electromagnetics Research in Nottingham (U.K.). He has received various awards and honours, such as the University of Nottingham's Derrick Kirk Prize, the Commonwealth Scholarship UK, and the All India Council for Technical Education Career Award. He has completed various national and international government-funded research projects, and was a member of the visiting faculty at the AIT Bangkok and UoTEM Tunisia. His current research interests include optical communication, optoelectronics and photonics, numerical modelling, nonlinear optics, radio frequency (RF) and microwaves, optical networks, and solar energy.

Dr. Ghanshyam Singh received his Masters and PhD degrees in ECE from Malaviya National Institute of Technology (MNIT), Jaipur. He has been a visiting scholar/visiting professor at various universities and research centres, in the UK, Finland and Japan. Dr. Singh is engaged in joint research projects with partner researchers from Keio University (Japan), the University of Vienna (Austria), Cairo University (Egypt) and Lviv Polytechnic National University (LNPU) (Ukraine). His current research interests include antenna engineering, micro and nano-structured photonic devices, and networks and non-linear characteristics of photonic crystal fibers.

Dr. Manish Tiwari received his Ph.D. in Electronics and Communication Engineering (ECE) in the field of Photonics from Malaviya National Institute of Technology (MNIT), Jaipur. He is currently a professor at Manipal University, Jaipur. He was a visiting researcher at City University, London in 2010 and 2011 and Tsinghua University, Beijing, China in 2016. Dr. Tiwari has presented talks at a number of universities in Hong Kong, Bangkok, and London. He has also served on the panel of experts at various workshops. His current research interests include micro/nano-structured photonic devices, nonlinear optics and photonic crystal fibers.

Dr. Tawfik Ismail is an Associate professor at the School of Engineering and Applied Sciences, Nile University, Egypt. In 2015, Dr. Ismail had postdoctoral research in optical and wireless communications at the technical institute of microwave and photonic engineering, University of Graz, Austria. In 2018, he joined the optical wireless communication research group at the department of engineering and sciences, University of Oxford, UK to work in research of quantum communication in free space. His research interests are interdisciplinary which span including wireless/optical/communications, mmWave, mobile edge computing, quantum information, blockchain, healthcare, … etc. He has H-index 6 as reported by Scopus with total citations of 96, with more than 48 publications distributed between high impact journals, conferences, and book chapters.

Compact Multi-band Octagonal-Shaped Patch Antenna with a Partial Ground for WLAN/Wi-MAX Applications

Ritesh Kumar Saraswat, Swasti Dubey and Kunal Jeet Singh

Abstract A multi-band octagonal-shaped microstrip patch antenna with a compact size of $30 \times 26.5 \times 0.8$ (X, Y, Z) mm^3 is designed on FR-4 substrate, and it operates in the WLAN 2.4/5.2/5.8 GHz bands and Wi-MAX 3.5 GHz band. The compact octagonal shape (split-ring resonator)-based patch antenna with multiple bands is presented in this paper. The proposed design is implemented on FR-4 substrate fed by a 50-Ω microstrip feed line. Prototype of the proposed antenna is simulated and showed good performance across the multi-band range with respect to the return loss, omnidirectional radiation patterns, and peak antenna gains. Results are more stable over all the operating regions.

Keywords Multi-band · Octagonal split-ring radiating element · Partial ground · Patch antenna · WLAN · Wi-MAX

1 Introduction

The present scenario of wireless communication system requires compact and multiple-band antenna design. Since many systems are operating at multiple frequency range, dual- and triple-band antennas are required for various applications, such as WLAN, Wi-MAX, RFID, and satellite communication. Presently, many printed monopole antennas are proposed. Proposed design cover the wireless standards "Wireless local area network" (WLAN: 2.4–2.48, 5.15–5.35, and 5.75–5.825 GHz) and "Worldwide interoperability microwave access" (Wi-MAX: 3.4–3.69 GHz) for wireless communication applications [1].

Split-ring resonator-loaded octagonal shape encircled by circular ring antenna is proposed for Wi-MAX and WLAN. This octagonal-shaped monopole antenna represent the various characteristics such as low-power, miniaturization, low profile, optimum radiation efficiency/gain and bandwidth as compared to previously published antenna. Few of the antennas are introduced by implementing various shapes

R. K. Saraswat · S. Dubey (✉) · K. J. Singh
Manikya Lal Verma Textile & Engineering Govt. College, Bhilwara, Rajasthan, India

V. Janyani et al. (eds.), *Optical and Wireless Technologies*, Lecture Notes in Electrical Engineering 648, https://doi.org/10.1007/978-981-15-2926-9_1

of strips and slots for wireless communications [2]. Many other antennas are proposed with the compact size or simple in design geometry covering the wireless standards [3, 4].

Proposed octagonal-shaped patch antennas serve as a worthy choice to meet these aforementioned challenges. Wireless local area network (WLAN: 2.4–2.48, 5.15–5.35, and 5.75–5.825 GHz) and worldwide interoperability for microwave access (Wi-MAX: 3.4–3.69 GHz) are two among the available wireless standards which allow interconnections of devices for communication. Split-ring resonator-loaded octagonal shape encircled by circular ring antenna is proposed for Wi-MAX and WLAN.

2 Proposed Antenna's Structure

The geometrical configuration and dimension of the multi-band octagonal-shaped patch antenna is printed on an inexpensive FR-4 substrate with relative dielectric constant of 4.4 and loss tangent of 0.002 [5]. "Octagonal-shaped patch" antenna is illustrated in Fig. 1. The antenna consists of two pairs of concentric split rings facing each other.

Octagonal-shaped patch antenna is impressed on a $30 \times 26.5 \times 0.8\ mm^3$ low-cost FR-4 substrate. To create multiple bands, the radiating element is modified to form two pairs of concentric split rings, as shown in Fig. 1b. The width of the rings and the slots between the rings (g) are maintained identical for simplicity. An extensive layout of the proposed design is shown in Fig. 2, and its dimensions are cataloged in Table 1.

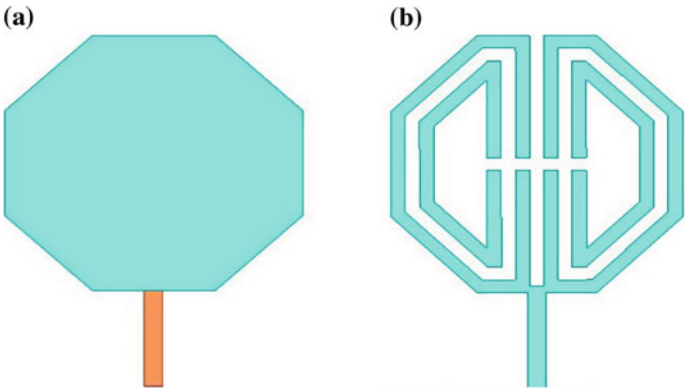

Fig. 1 Evolution of the proposed antenna; **a** octagonal-shaped antenna with feed line; **b** octagonal-shaped patch antenna with SRR

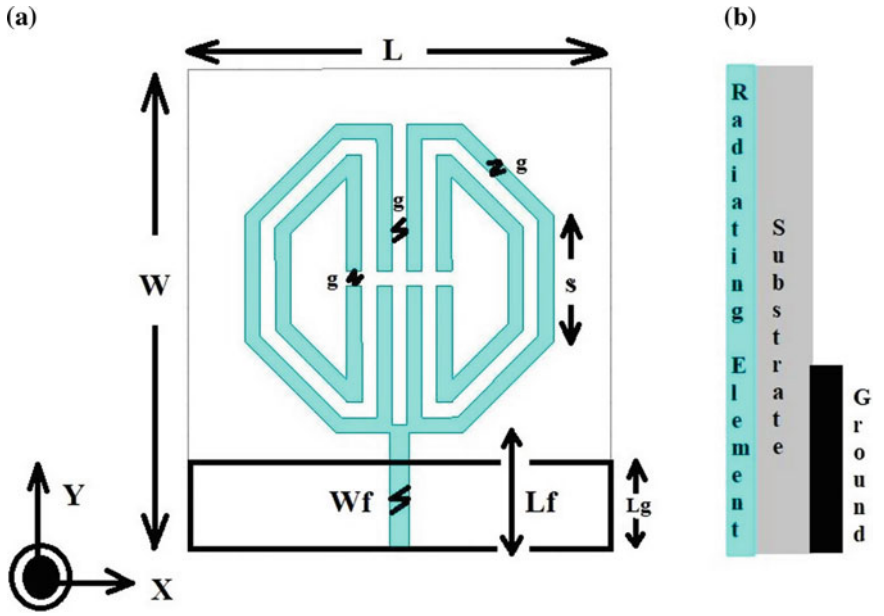

Fig. 2 Geometry of the proposed microstrip patch antenna. **a** Top view (with parameter) and **b** side view (layers of antenna)

Table 1 Dimensions of the proposed antenna

Parameter	L	W	S	g	W_f	L_f	L_g
Dimension (mm)	30	26.5	0.8	0.94	1.2	7.2	6

3 Result and Discussion

Simulations of proposed octagonal-shaped multi-band patch antenna are performed by using the HFSS. The feed width (W_f) of the simulated design plays a prime role to find the range of frequencies upon which the antenna could function.

3.1 Return Loss Characteristics

As shown in Fig. 3, the simulated impedance bandwidth for $|S_{11}| < -10$ dB. It yields an impedance bandwidth of 130 MHz centered at 2.45 GHz, 330 MHz centered at 3.5 GHz, and 1540 MHz centered at 5.2 GHz [6].

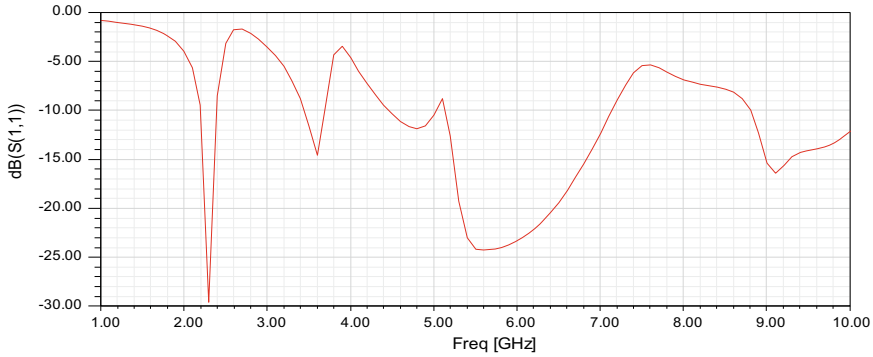

Fig. 3 Simulated return loss characteristics of the antenna

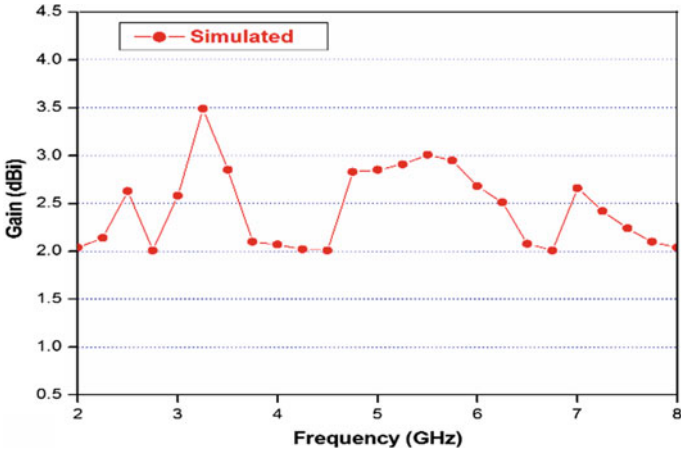

Fig. 4 Gain characteristics of the antenna

3.2 Gain Characteristics of the Antenna

Figure 4 shows the simulated gain of the proposed antenna where at lower frequencies (below 3 GHz), the gain is reduced but at higher frequencies (above 5 GHz), it is improved as compared to lower frequencies. The high-average antenna gains of 3.31 dBi are observed during simulation for WLAN and Wi-MAX standards [7, 8].

3.3 Radiation Efficiency

The radiation efficiency varies up to 89.56–60.89 and 88.78–52.34% in simulation mode at wireless standards, as shown in Fig. 5. It is also noticed that the antenna

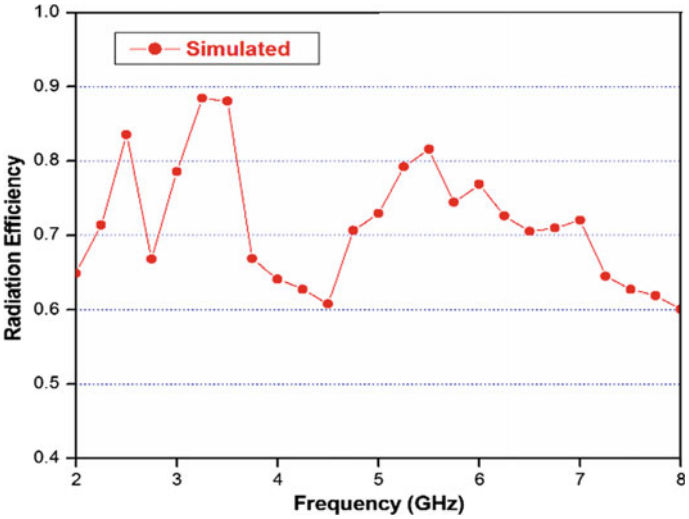

Fig. 5 Radiation efficiency of the proposed antenna

radiation efficiency stays above 70% in all the operating bands and the peak average radiation efficiency is 82.9% for the WLAN and Wi-MAX standards [9].

3.4 E-Plane and H-Plane Radiation Patterns

The simulated E-plane and H-plane radiation patterns of the proposed antenna are represented in Fig. 6. Here observed at resonant frequencies 2.51, 3.34, and 5.35 GHz for two principal planes, E-plane and H-plane, in co-polarization and cross-polarization modes. From Fig. 6, it is shown that there are dipole-like radiation patterns in E-plane and nearly stable in H-plane which makes it a good candidate for wireless communication. The cross-polarization levels less than −15 dB are achieved in both E-plane and H-plane radiation patterns for all the frequency bands of interest [10].

Figure 7 represents the 3D plot of gain of the proposed antenna structure at resonant frequencies of 2.51 GHz, 3.34 GHz, and 5.35 GHz, respectively.

4 Fabricated Antenna

The fabricated "octagonal-shaped patch antenna with partial ground" is shown in Fig. 8. By choosing the optimized dimensions of antenna ($30 \times 26.5 \times 0.8$ mm^3) and length of partial ground of 6 mm, the antenna gain is improved accordingly.

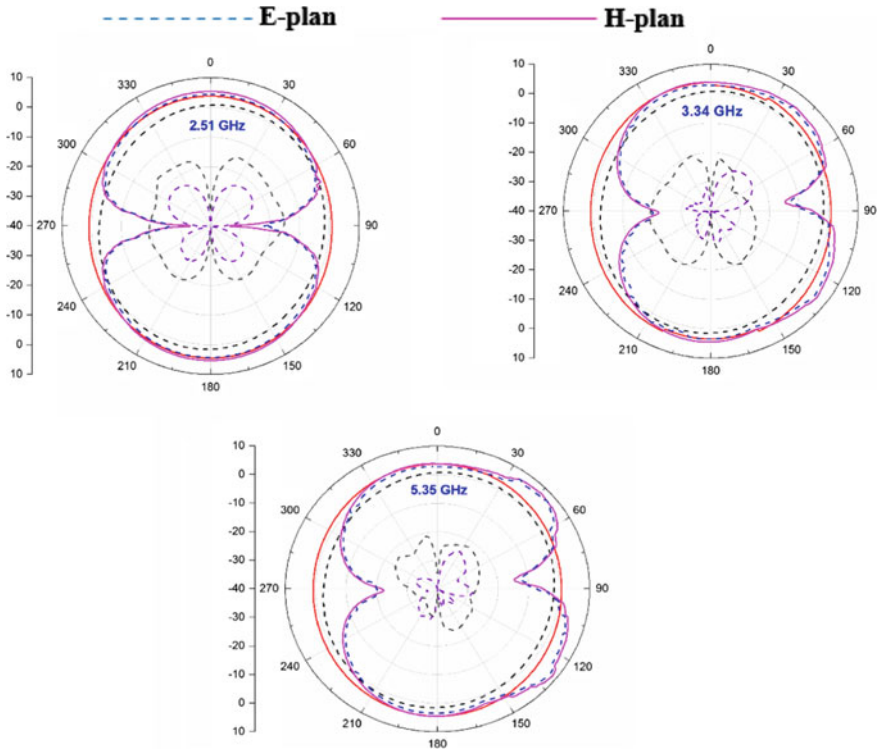

Fig. 6 E-planed and H-planed radiation patterns at different resonant frequency

This antenna fabricates using PCB prototype machine. The octagonal-shaped patch antenna is easy to fabricate, is compact in size, and is low profile.

5 Conclusion

The article presents an orthogonal-shaped patch antenna with a compact size of 30 × 26.5 × 0.8 mm^3 with feed line and a partial ground by optimizing in simulator. Triple-band octagonal-shaped patch antennas covering WLAN 2.4 GHz, Wi-MAX 3.5 GHz, and WLAN 5.5 GHz bands are evaluated with high gain and stable patterns presented in this paper. The antenna geometry is very simple and also compact making mass production easy. The proposed design consists of octagonal-shaped SRR which are used as a radiating element. The proposed antenna finds wide application in modern multiple wireless applications WLAN/Wi-MAX.

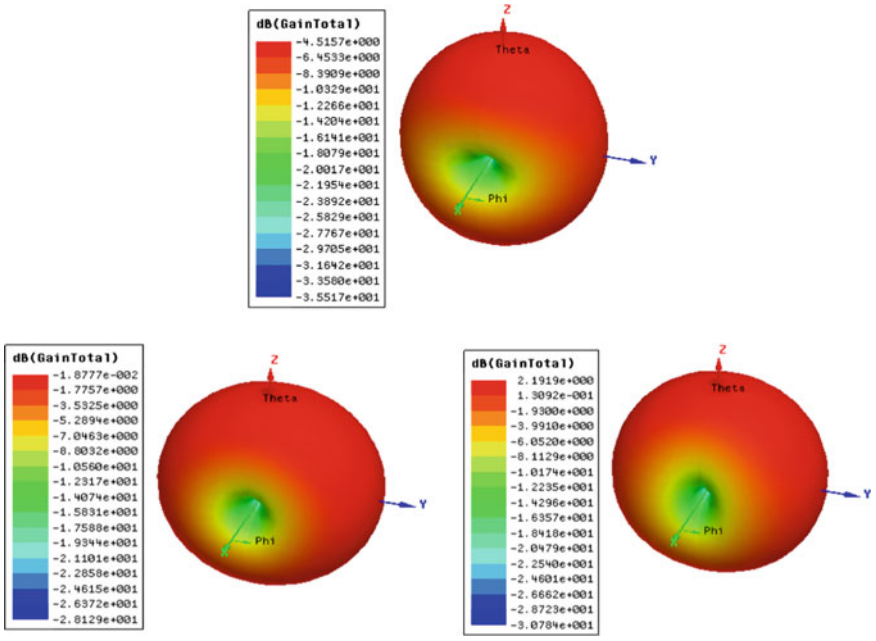

Fig. 7 3-D polar plot at different resonant frequency

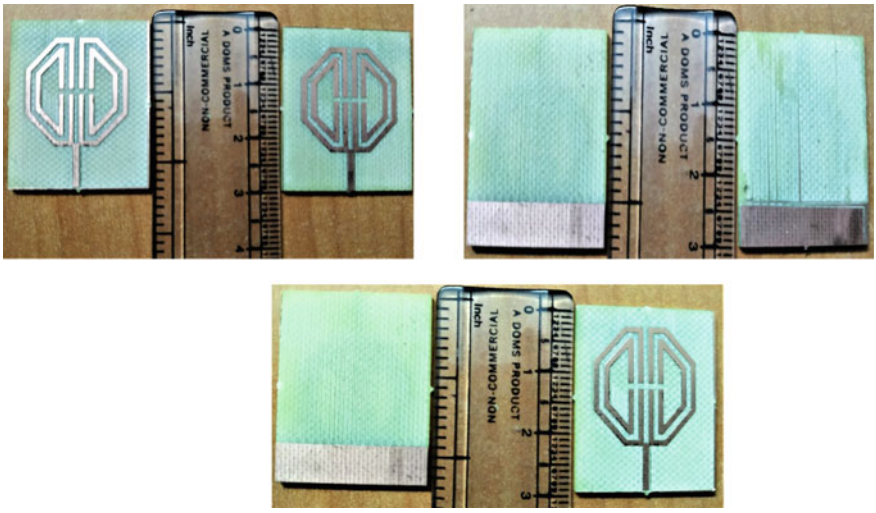

Fig. 8 Fabricated octagonal-shaped antenna with partial ground

References

1. Xu Y, Jiao YC, Luan YC (2012) Compact CPW-fed printed monopole antenna with triple-band characteristics for WLAN/Wi-MAX applications. Electron Lett 48:1519–1520
2. Li X, Shi XW, Hu W, Fei P, Yu JF (2013) Compact triband ACS-fed monopole antenna employing open-ended slots for wireless communication. IEEE Antennas Wirel Propag Lett 12:388–391
3. Basaran SC, Olgun U, Sertel K (2013) Multiband monopole antenna with complementary split-ring resonators for WLAN and Wi-MAX applications. Electron Lett 49:636–638
4. Saraswat RK, Chaturvedi AK, Sharma V, Jagmohan (2016) Slotted ground miniaturized UWB antenna metamaterial inspired for WLAN and Wi-MAX applications. In: IEEE international conference CICN, pp 23–25
5. Saraswat RK, Kumar M (2015) A frequency band reconfigurable UWB antenna for high gain applications. PIER B 64:29–45
6. Saraswat RK, Kumar M (2016) Miniaturized slotted ground UWB antenna loaded with metamaterial for WLAN and Wi-MAX applications. PIER B 65:65–80
7. Saraswat RK, Kumar M (2015) A reconfigurable patch antenna using switchable slotted structure for polarization diversity. In: IEEE international conference CSNT, 4–6th Apr
8. Saraswat RK, Kumar M, Gurjar S, Singh CP (2015) A reconfigurable polarized antenna using switchable slotted ground structure. In: IEEE international conference CSNT, 4–6th Apr
9. Saraswat RK, Kumar M (2016) Planar frequency-band reconfigurable switchable slotted ground UWB antenna. In: IEEE international conference CSNT, 5–7th Mar
10. Saraswat RK, Kumar M, Ram G, Singh A (2016) A reconfigurable microstrip bowtie patch antenna with pattern diversity. IEEE international conference CSNT, 5–7th Mar

A Review of Techniques to Design Tunable Antenna Covered with Metamaterial

Suyog Vinayak Pande and R. S. Kawitkar

Abstract Reconfigurable or tunable antennas have become the most interested topic since the demand of multi-operative antenna arises. As the requirement of more than one wireless application through a single device increases, it motivates researchers to design multiband antennas or reconfigurable antennas. This manuscript reviews the recent techniques which were used by various researches to design the tunable antennas. Various techniques were studied, viz. metamaterial, varactor diode, dielectric properties. Throughout the discussion, various issues are highlighted, and best available technique is explained.

Keywords Metamaterial · Varactor diode · Reconfigurable · Tunable

1 Introduction

In recent years, the demand of more than wireless applications to be performed through a single antenna increased. This demand leads researchers to design multiband antennas and wideband antennas. But due to limitations of such antennas, demand remains unfulfilled. As multiband antennas have limited operating frequencies, the wideband antennas allow noises and unwanted signals from operating band. These limitations motivate researchers to design such antennas which not only work on wide frequency range but have capability of having selectivity also. Here comes the introduction of reconfigurable antennas; such antennas not only cover a wide frequency band based on their operations, but they are more efficient as well. These multi-operative antennas must have better directivity and less return loss, and they must be having higher bandwidth, small size, and tunable capabilities at the desired frequency of operation.

S. V. Pande (✉) · R. S. Kawitkar
Department of Electronics and Telecommunication Engineering, Sinhgad College of Engineering, Vadgaon Pune, India

S. V. Pande
Department of Electronics and Telecomm Engineering, SVKM's NMIMS Mukesh Patel School of Technology Management and Engineering, Shirpur Campus, Shirpur, India

V. Janyani et al. (eds.), *Optical and Wireless Technologies*, Lecture Notes in Electrical Engineering 648, https://doi.org/10.1007/978-981-15-2926-9_2

Various techniques have been opted by researchers to design tunable antennas; an author designed a frequency tunable antenna using multisplit-ring-shaped metamaterial design [1] for C-band application. A waveguide-fed tunable metamaterial was designed by connecting PIN diodes in the capacitive gaps of the metamaterial structure [2]. Tunable miniaturization was achieved by placing complimentary resonators (split ring) between ground plane and patch [3]. An S-shaped metamaterial structure was proposed along with the introduction of varactor diode at different places to achieve the tunability [4].

With the help of diode, a miniaturized antenna can be designed as well as a tunable resonator or tunable metamaterial structure can also be designed. Use of mobile communication is increasing rapidly since last one decade, and use of small size and tunable antenna is also increasing due to narrowband characteristics of the antenna. As microstrip antenna has been the most favorite topic from a long time, a very vast literature is available because of various techniques; a lot of research articles have been published on the same. Numerous books were written over this topic. This research paper is prepared to explain various available techniques to design patch antenna along with the metamaterial and few recent advancements in this particular area which is one of the major factors in applications of wireless communication. These advancements include miniaturization technique, dual- and multiband designs, tunability, and effective radiation.

2 Techniques to Miniaturize and to Design Tunable Antenna

Various techniques were analyzed to see how a miniaturized as well as tunable antenna can be designed. The goal of this paper is to present insight of the research being carried out and give a brief about the techniques available to design the reconfigurable and miniaturized antenna. Rectangular patch antenna mostly preferred over other shapes of patch antennas due to its ease of calculation and good radiating results. The dimensions can be calculated from the formulas listed in [5]. Following are the techniques used so far.

2.1 Inclusion of Varactor Diode

In Figs. 1, 2, and 3, the implementation of varactor diode is represented.

Figures 1, 2, and 3 shows that varactor diodes can be implemented on ground plane, can be configured with the split-ring resonators (SRR) and may directly implemented with the feed line itself subsequently. Varactor diodes provide the tunable characteristics to antenna as well as to the metamaterial structures. Mostly, varactor diodes are configured with the split-ring resonators as this combination yields good results. This

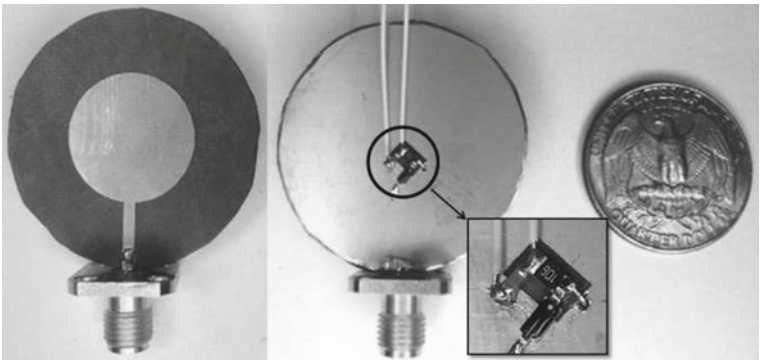

Fig. 1 Front (left) and back (right) views of the prototype antenna. Inset shows the varactor diode and biasing circuit [3]

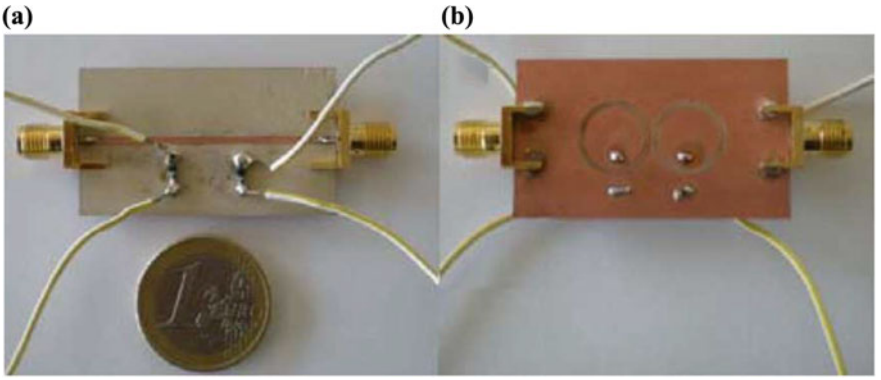

Fig. 2 Varactor diode incorporation along with the split-ring resonator [10]

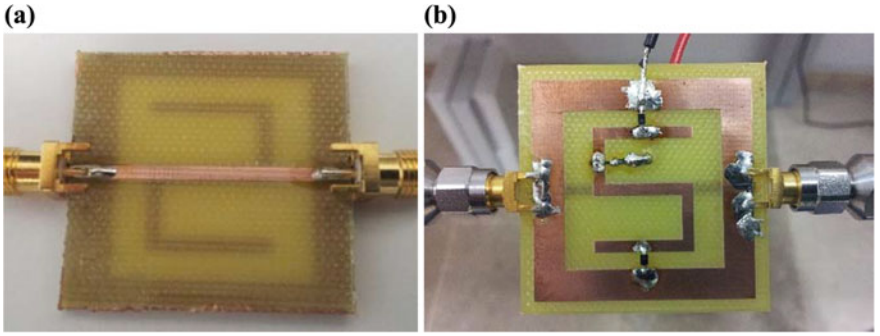

Fig. 3 Proposed tunable antenna: **a** back side and **b** front side of the fabricated antenna with varactor diode [4]

varactor diode plays the major role in designing the reconfigurable antennas. Varactor diode is basically known as variable capacitor due to its varying capacitance. When reverse bias voltage changes, the junction capacitance, the operating frequency, and the current distribution of the antenna also change. Apart from varactor diode, there are also other techniques.

2.2 *Monolithic Wall Radome*

Four T-shaped metal strips along with the two square-ring structure were used in [5] as shown in Fig. 4; this structure was placed in the monolithic radome wall and then analyzed. Radome was made by quartz epoxy. Later in the next step, varactor diodes were incorporated over the structure and again placed in the two layers of the monolithic radome, as shown in Fig. 5. Simulated results in this paper show that in frequency range of 7.65–10.21 GHz, more than 90% of the power transmission characteristic was achieved [5].

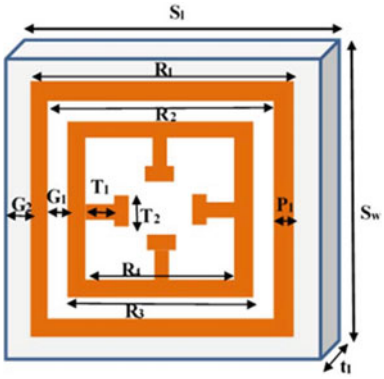

Fig. 4 Before implementing varactor diode [5]

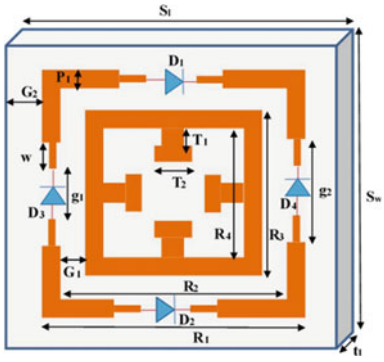

Fig. 5 After implementing varactor diodes by splitting the square rings [5]

2.3 *Effect of Substrate Properties of Metamaterial on Tunability*

It has been found that negative media structure is composite in nature. It has been analyzed that varying the substrate properties, only the overall substrate properties can be modified [6–8]. In Sheng et al. [7], it is elaborately defined the substrate properties and effect of change of substrate thickness. In [7], authors clearly defined and demonstrated the effect of thickness variation on the antenna properties.

Sudden change in the resonant frequency is observed by permittivity change and making constant the thickness of the substrate. Along with that, it was also observed that making changes in the width of substrate and not changing permittivity will result in reducing resonant frequency.

Author elaborated the concept after a deep understanding and analyzing the behavior of the substrate thickness and permittivity. It was found that when both thickness and permittivity were low at that time, the resonant frequency was very sensitive with the changes in the thickness and permittivity, which means good stability was being achieved. But when the variation of parameters were very high then sensitivity of resonant frequency decreases and subsequently response becomes smooth. To change the substrate properties, major focus could be on bias current, temperature, bias voltages, stress, etc.

The proposed structure in this research was the combination of a conventional SRR and a broadside-coupled SRR (BC-SRR) and was named as double-sided split-ring resonator (DSRR) [8]. Proposed structures of these ring resonators are shown in Fig. 6.

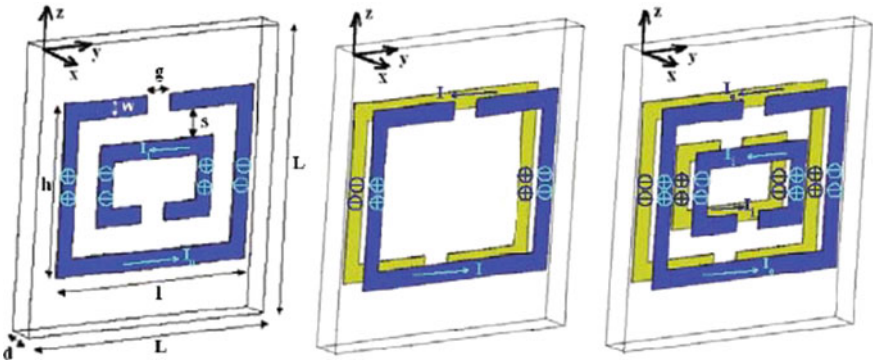

Fig. 6 Unit cell geometries for SRR-, BC-SRR-, and DSRR-type metamaterials [8]

2.4 Electromagnetic Band-Gap Substrates

Generally, a rectangular microstrip antenna is known half-wave resonator, so it is necessary to undergo a modal analysis of a microstrip line which will help in designing antenna. In this proposed design, a combination of rectangular patches with sorting pins is included. EBG structure with tunable characteristic is shown in Fig. 7. This proposed structure contains a combination of EBG units and microstrip line.

The above- and below-etched structures are combined together, i.e., they are laminated together to make out a multilayer PCB. In this proposed design, it was found that the EBG unit and the top-etched unit are not actually connected to ground; there is a very thin clearance among these two structures. Tunability was proposed among this clearance only; here the introduction of the tuning devices exists like PIN diode and varactor diode. By changing the applied voltage around the diodes, tunability can be achieved.

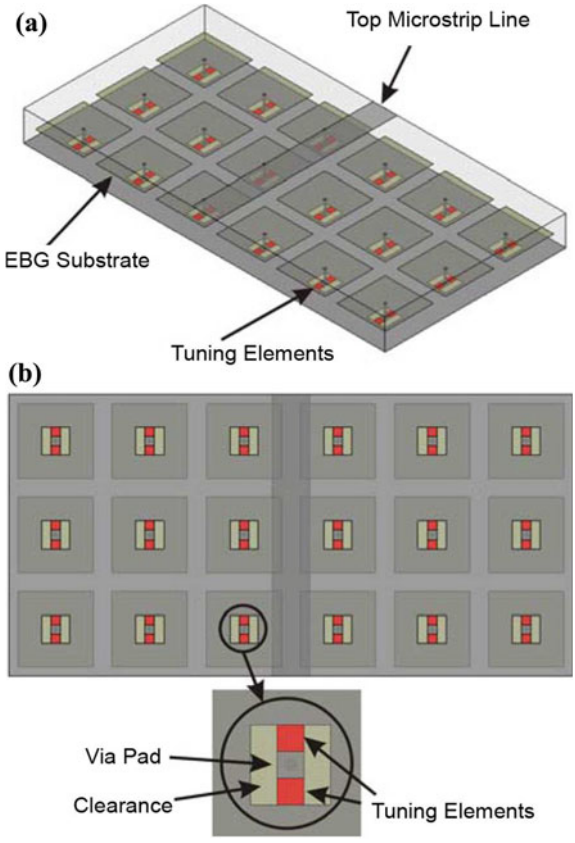

Fig. 7 **a** Prospective view and **b** bottom view of tuning element-loaded EBG [11]

2.5 Antenna with Electrically Large Property

Recently, antenna having wide bandwidth and multigigabit data rate capacity is being designed for point-to-point wireless communication and various applications of wireless local area network. The cost of designing such antenna at millimeter wave and terahertz wave is quite feasible and cheap, but designing the antenna at microwave frequency range is a tedious task. That is why antenna with electrically large properties (ELPs) is being proposed by various researchers [9].

In this proposed design, cavity coupled having only negative permeability metamaterial was used. This proposed structure with ELPs made antenna to increase resonate for more than 4.6 times after implementing metamaterial structure over the proposed antenna without affecting its radiation pattern (Fig. 8).

After comparison indicated in Table 1, it has been observed that metamaterial implementation along with the varactor diode is the best available technique to design a tunable resonator or antenna. By applying this technique, it is expected that a significant result could be achieved.

3 Conclusion

This paper has provided a tutorial on how to design a tunable antenna using metamaterial and also illustrated that how a varactor diode plays a major part when it comes to achieving tunable characteristics. Outcome of this review paper is to design a tunable microstrip antenna. The reviewed paper shows that different metamaterial structures can be implemented over the patch to provide tunable characteristics. The paper highlighted various techniques and is categorized into three parts as Table 1 is clearly indicating.

First category is for miniaturization, which can be achieved by applying metamaterial structure either on the ground plane or above of the patch. Second category is substrate change of metamaterial, in which varying thickness can modify the results. Third category is implementation of varactor diode which can provide the tunability in the designed antenna. Out of all techniques studied and presented in this paper, it was found that the varactor diode along with the metamaterial will be preferred for the designing purpose as other techniques have left few challenging problems remained unsolved. It will take researchers to do continuous efforts in this preferred method to show a better credibility than other techniques in modification of antennas as this technique yields good results.

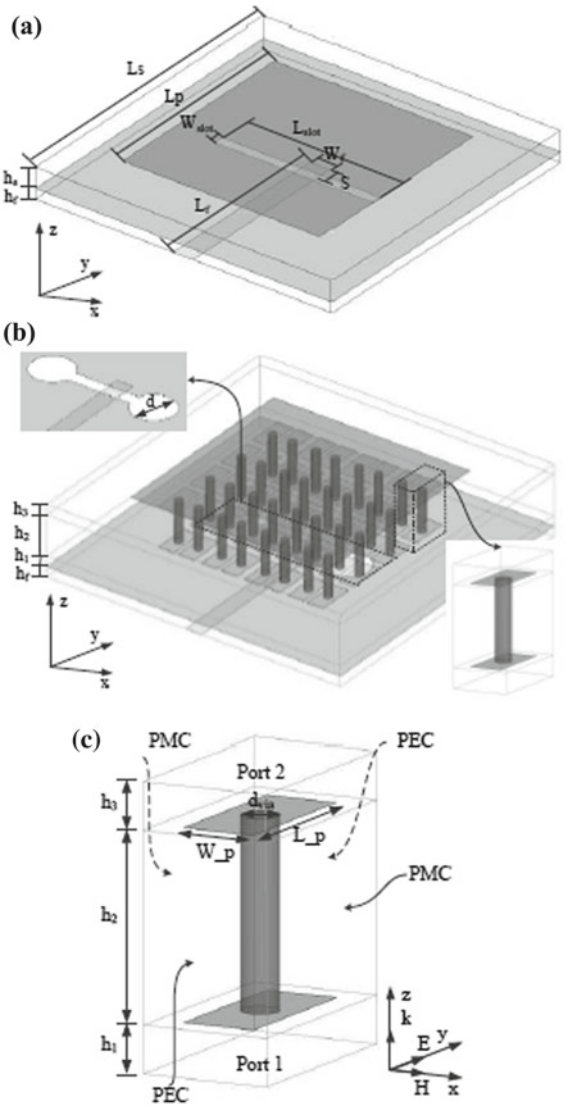

Fig. 8 Proposed antenna. **a** Microstrip antenna without metamaterial inclusion; **b** applied metamaterial structure loaded with I-shaped resonant material; **c** individual section of I-shaped structure [9]

Table 1 Comparison chart

S. No.	Tunable techniques	Configuration	Remarks
1	Metamaterial inclusion (either on ground plane or above patch)	Combination of U- and L-shaped cut on the ground plane [12]	Miniaturization up to 80% has achieved
		I-shaped slot in the ground plane [13]	Return loss improved from −27 to −46 dB
		The rectangular inset-feed microstrip patch antenna with dumbbell-shaped DGS [14]	Bandwidth increased up to 57 MHz and return loss improved to the value of −41 dB
		Aperture-coupled feed was used to modify antenna into double band [15]	Antennas modified into double-band frequency range obtained were 7.82–7.73 GHz and 8.55–9.12 GHz
		An antenna for WLAN application having L-slot DGS structure was proposed with gap coupling [16]	Single-band antenna converted to double-band, having range of frequencies 3.4–3.6 and 5.72–5.82 GHz, respectively
		A miniaturized antenna with double-band characteristics was achieved [17]	A metamaterial structure of four cells was proposed in this paper, and miniaturization of 30 and 70% for both the bands was achieved
		A different metamaterial structure was proposed in this paper [18]	This antenna works on operating frequency of 5.8 GHz, and this antenna was designed for WiMax applications
		Coaxial feed microstrip antenna with SRR metamaterial [19]	Directivity increased up to 4.5%, and gain improved up to 7.6%
		Convectional patch antenna design [20]	Miniaturization achieved till 58.2% along with 10% in return loss
		Ohm-shaped DGS implementation [21]	Dual-band antenna was designed with the help of combinational DGS, and return loss with 21% increment was achieved

(continued)

Table 1 (continued)

S. No.	Tunable techniques	Configuration	Remarks
		DGS implemented for ITS applications [22]	Eight-element patch array was proposed with defected ground structure
		A symmetrical metamaterial structure was implemented above 3.262 mm of the patch [23]	Double-band characteristic with 75% increment in the bandwidth was achieved
2	Metamaterial substrate	Metamaterial substrate having permeability range of 1–5 [11]	To miniaturize the antenna, only change in the permittivity and permeability is enough; there is no need to increase the number of substrate
		Conventional SRR and a broadside-coupled SRR (BC-SRR) [8]	It was found that by slowly increasing the substrate thickness, a quick change in resonant frequency occurred
		Varying permittivity and permeability [7]	Keeping thickness fixed and by varying the permittivity and permeability miniaturization achieved
3	Varactor diode inclusion	Varactor diode applied on S-shaped metamaterial [4]	By changing the value of input voltage across the varactor diode, tunability could be achieved
		Varactor-loaded complementary split-ring resonator [10]	Two varactor diodes were implemented along with the split ring to achieve 45% tunability
		Varactor diode with airborne radome [5]	Four varactor diodes were implemented in the split rings to enhance the tuning and can be tuned from 9 to 9.95 range

References

1. Patel SK, Argyropoulos C, Kosta YP (2018 Feb 28) Pattern controlled and frequency tunable microstrip antenna loaded with multiple split ring resonators. IET Microw Antennas Propag 12(3):390–394. doi:10.1049/iet-map.2017.0319
2. Sleasman T, Imani MF, Xu W, Hunt J, Driscoll T, Reynolds MS, Smith DR (2016) Waveguide-fed tunable metamaterial element for dynamic apertures. IEEE Antennas Wirel Propag Lett 15:606–609
3. Tang J, Ouedraogo RO, Rothwell EJ, Diaz AR, Fuchi K (2014) A continuously tunable miniaturized patch antenna. IEEE Antennas Wirel Propag Lett 13:1080–1083
4. Nesimoglu T, Sabah C (2016) A frequency tunable metamaterial resonator using varactor diodes. In: IEEE 16th mediterranean microwave symposium (MMS), pp 1–4
5. Hegde MG, Shambulingappa V, Mahima P, Athira R, Nair RU, Narayan S (2017) EM design of active metamaterial based airborne radome for electronic warfare applications. In: 2017 IEEE international conference on antenna innovations & modern technologies for ground, aircraft and satellite applications (iAIM), Bangalore, pp 1–5
6. Sheng Z, Varadan VV (2006) Effect of substrate dielectric properties and tunable metamaterials. In: IEEE antennas and propagation society international symposium, pp 4497–4500
7. Sheng Z, Varadan VV, Tuning the effective properties of metamaterials by changing the substrate properties. J Appl Phys 101(1):14909-04915
8. Ekmekci E, Turhan-Sayan G (2009) Comparative investigation of resonance characteristics and electrical size of the double-sided SRR, BC-SRR and conventional SRR type metamaterials for varying substrate parameters. Prog Electromagn Res B 12:35–62
9. Cao W, Zhang B, Jin J, Zhong W, Hong W (2017) Microstrip antenna with electrically large property (ELP) based on metamaterial inclusions. IEEE Trans Antennas Propag 65(6):2899–2905
10. Velez A, Bonache J, Martin F (2008) Varactor-loaded complementary split ring resonators (VLCSRR) and their application to tunable metamaterial transmission lines. IEEE Microw Wirel Compon Lett 18(1):28–30
11. Buell K, Mosallaei H, Sarabandi K (2006) A substrate for small patch antennas providing tunable miniaturization factors. IEEE Trans Microw Theory Tech 54(1):135–146
12. Nashaat D, Elsadek HA, Abdallah E, Elhenawy H, Iskander MF (2009) Multiband and miniaturized inset feed microstrip patch antenna using multiple spiral-shaped defect ground structure (DGS). In: IEEE antennas and propagation society international symposium, pp 1–4
13. Arya AK, Kartikeyan MV, Patnaik A (2008) Efficiency enhancement of microstrip patch antenna with defected ground structure. In: IEEE international conference on recent advances in microwave theory and applications, pp 729–731
14. Deb P, Moyra T, Bhowmik P (2015) Return loss and bandwidth enhancement of microstrip antenna using defected ground structure (DGS). In: IEEE 2nd international conference on signal processing and integrated networks (SPIN), pp 25–29
15. Aris MA, AH MT, Abd Rahman NH, Ramli N, Pasya I (2015) Frequency reconfigurable aperture coupled microstrip patch antenna using periodic defected ground structure. In: IEEE conference on antenna measurements & applications (CAMA), pp 1–4
16. Singh SK, Consul P, Sharma KK (2015) Dual band gap coupled microstrip antenna using L-slot DGS for wireless applications. In: IEEE international conference on computing, communication & automation, pp 1381–1384
17. Ramli N, Ali MT, Yusof AL, Pasya I, Alias H, Sulaiman MA (2012) A frequency reconfigurable stacked patch micro-strip antenna (FRSPMA) with aperture coupler technique. In: IEEE symposium on wireless technology and applications (ISWTA), Bandung, Indonesia
18. Ramli N, Ali MT, Yusof AL, Ya'acob N (2013) Frequency reconfigurable stacked patch microstrip antenna (FRSPMA) for LTE and WiMAX applications. In: International conference on computing, management and telecommunications (ComManTel), pp 55–59

19. Kumar A, Kumar M, Parmar G (2015) Multi band circularly polarized asymmetrical fractal boundary microstrip patch antenna using DGS for (2.58/3.02/5.58/6.44 GHz). In: 2015 IEEE international conference on communication, control and intelligent systems (CCIS) IEEE conference, pp 35–39
20. Saghanezhad SAH, Atlasbaf Z (2015) Miniaturized dual-band CPW-fed antennas loaded with U-shaped metamaterials. IEEE Antennas Wirel Propag Lett 14:658–661
21. Salamin MA, Das S, Zugari A (2018 Dec) Design and realization of low profile dual-wideband monopole antenna incorporating a novel ohm (Ω) shaped DMS and semi-circular DGS for wireless applications. AEU Int J Electron Commun 97:45–53
22. Kishore N, Upadhyay G, Tripathi VS, Prakash A (2018 Nov) Dual band rectangular patch antenna array with defected ground structure for ITS application. AEU Int J Electron Commun 96
23. Bhadoriya RPS, Nigam S (2016) Bandwidth enhancement and modification of single band patch antenna into double band. In: 3rd international conference on computing for sustainable global development (INDIACom), New Delhi, pp 1029–1032

Long-Range Surface Plasmon Resonance-Induced Tunable Optical Bistability Using Silver Nano-layer at 1550 nm

Aparupa Kar, Nabamita Goswami and Ardhendu Saha

Abstract A proposal towards analytical implementation of optical bistability in a multilayered configuration comprising a ZnSe prism, 1-μm-thick PMMA-DR1 (Polymethylmethacrylate-Disperse red) as dielectric layer, nano-Ag: polymeric composite material as a Kerr polymer and a 15-nm thin film of silver which is sandwiched between the dielectric layer and the Kerr polymer at incident light wavelength of 1550 nm with a beam waist of 0.5 mm is presented at 25 °C temperature. Here, the nonlinear Kerr medium is having quadratic dependence on the long-range surface plasmon polariton mode resonance-enhanced local electric field amplitude. Through the larger nonlinear effect of the optimized design by employing high local field effect in the nonlinear regime, a low threshold optical bistability of about 1.6 MW/cm^2 in the transmitted light intensity is achieved. The reported threshold is less compared to the previous efforts where the works were carried out with a wavelength other than the important telecommunication wavelength within the C-band. The design also provides tunability of bistable threshold by exploitation of Kerr effect-induced refractive index change through varying pump light intensity. The proposed system proffers potential applications in all-optical networks.

Keywords Bistability · Nonlinear optics at surfaces · Plasmonics · Surface plasmons

1 Introduction

During recent years, rapid development of all-optical integrated devices is observed instead of microelectronic devices to overpower the constraint on transmission rate and bandwidth that microelectronic devices suffer from. Nonlinear optical effects in all-optical devices at microscale and nanoscale proffer bright prospects in signal

A. Kar
Department of Electronics and Instrumentation Engineering, National Institute of Technology Agartala, Barjala, Jirania, Tripura (West) 799046, India

N. Goswami · A. Saha (✉)
Department of Electrical Engineering, National Institute of Technology Agartala, Barjala, Jirania, Tripura (West) 799046, India

V. Janyani et al. (eds.), *Optical and Wireless Technologies*, Lecture Notes in Electrical Engineering 648, https://doi.org/10.1007/978-981-15-2926-9_3

processing devices and high-speed communication systems [1, 2]. Optical switches employing optical bistability are among the most prominent components in all-optical devices and play a significant role in nonlinear optics [3]. The phenomenon of optical bistability is an optical effect, which is exhibited by a number of resonant optical structures whereby for a single value of the incident light intensity it is feasible to have two stable steady transmission light intensities depending upon the history of the input light intensity [3, 4]. The potential applications of bistable devices are in the design of optical storage, optotransistors, all-optical switch elements for computer memories, etc. [5–10]. In the field of optical bistability, the expected goal is to realize in a single device a set of functionalities, such as switching, modulation, memory with a fast time response, logic functions all using a low-power laser. In seeking for a solution to acquire low bistable threshold light intensities through large nonlinearity, a certain number of nanostructures utilizing high local field effect in the nonlinear regime such as photonic crystal cavities, negative-index material, sub-wavelength metallic gratings, band metamaterial, metallic gap waveguide nano-cavities have been extensively explored [11–18]. However, the desired goal can also be achieved through a resonant structure containing Kerr polymer and by employing long-range surface plasmon resonance phenomenon [19, 20]. Surface plasmons (SPs) are light-induced coherent electrons oscillations existing at metal-dielectric interfaces [21]. The surface plasmon phenomenon was first observed by "Wood" in the year 1902. When the propagation constant of the evanescent mode for total internal reflection of incident light gets equal to that of surface plasmon wave, then a resonance occurs which leads to a sharp fall in the reflected light intensity. This is known as surface plasmon resonance [21]. The two SP modes existing at the two metal-dielectric interfaces couple causing a split into two eigenmodes called short-range surface plasmon (SRSP) mode and LRSP mode with their main transverse electric field component varying either asymmetrically or symmetrically across the structure, respectively, [22]. When for a certain angle of incidence, the propagation constant of incident light and that of the LRSP mode matches, LRSP resonance takes place [22]. The influential capabilities of LRSP resonance have lead to the existence of a great deal of the literature concerning the exploration of tunable low threshold optical bistability using it [19, 20, 23]. The tunable bistable threshold is important for the all-optical devices applications [2]. Hence, the proposed configuration comprising metal and a nonlinear Kerr substrate is utilized to attain a low threshold optical bistability through the excitation of long-range surface plasmon at 1550 nm. The tunability of bistable threshold value is also realized for varying pump light intensity by exploitation of refractive index change realized through Kerr effect.

2 Proposed Scheme

This paper theoretically investigates a multilayered long-range surface plasmon configuration for the realization of optical bistability and tunability of bistable thresholds at a telecommunication wavelength of 1550 nm. The proposed multilayered

stack comprises a ZnSe prism, 1-μm-thick PMMA-DR1 (Polymethylmethacrylate-Disperse red) as dielectric layer, nano-Ag: polymeric composite material as a Kerr polymer with a 15-nm thin film of silver which is sandwiched between the PMMA-DR1 dielectric layer and the nano-Ag: polymeric composite material Kerr polymer with an incident light beam waist of 0.5 mm at 25 °C temperature, as shown in Fig. 1.

When a p-polarized monochromatic Gaussian beam is incident on the base of the dielectric prism of the proposed configuration at the resonant angle (θ_r), then the propagation constant of the evanescent mode coincides with that of the long-range surface plasmon mode. This results in resonant excitation of LRSP, which is accompanied by a sharp dip in the reflected light intensity and enhancement in local electric field amplitude. On attempting to excite LRSP mode with the increasing incident light electric field, the nonlinear dependence of the refractive index of Kerr polymer on the local electric field amplitude results in the generation of the optical bistability.

To realize optical bistability through the suggested configuration using LRSP mode, the angle of incidence (θ_0) is fixed at a value greater than the LRSP mode resonant angle (θ_r) of the configuration so as to get a large initial angle offset ($\Delta\theta = \theta_0 - \theta_r$). Under these circumstances, at very low input electric field, the system remains in the total internal reflection (TIR) mode. As the incident electric field increases, resonant angle (θ_r) advances towards the fixed incident angle (θ_0). Therefore, the LRSP mode resonance is approached and the amplitude of the resonant evanescent electric field around the nonlinear Kerr polymer is strengthened in this process which further serves to increase the transmitted electric field. When the incident light electric field attains the switching-up threshold, E_{up}, θ_r gets slightly larger than θ_0 which results in the enhancement of the LRSP mode electric field and switches the mode of the system from TIR mode to transmission mode. As we continue to increase the incident light intensity, θ_r moves farther away from the θ_0, thereby decreasing the transmittance. In contrast, when the incident light intensity decreases, θ_r decreases and begins to approach θ_0 which increases the transmittance. When the incident electric field addresses the switching-down threshold, E_{down}, transmission resonance

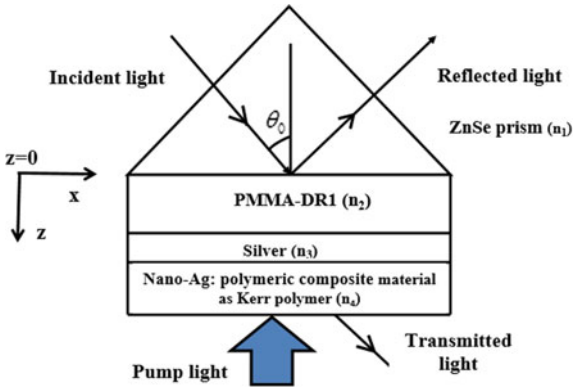

Fig. 1 Proposed configuration

occurs due to the LRSP mode resonance. Finally, on subsequently decreasing the incident light electric field, θ_r shifts away from the θ_0. Hence, the operating point of the transmittance now switches from transmission state to the TIR off-resonance state. Therefore, within a limited range of the input light electric field, referred to as hysteresis width ($\Delta E = E_{up} - E_{down}$), the system possesses two stable modes: TIR mode and transmission mode.

The tunability of the optical bistability is intrinsically important for the all-optical devices applications. The tunability of bistable threshold values has also been achieved by exploiting Kerr effect-induced refractive index change through varying pump light intensity. Now in order to compute the relation between incident electric field ($E_x^{(i)}$), reflected electric field ($E_x^{(r)}$) and transmitted electric field (E_T) of the N-layered configuration, where $B_y^{(i)}$, $E_x^{(i)}$, $E_z^{(i)}$ are the amplitudes of incident magnetic and electric fields, respectively, and $B_y^{(r)}$, $E_x^{(r)}$, $E_z^{(r)}$ are the amplitudes of reflected magnetic and electric fields having incoming wavenumber, $k = \frac{\omega}{c}\sqrt{\varepsilon_1}$, transfer matrix method has been employed after solving the boundary conditions through which the reflectance, R and transmittance, T for p-polarized light is obtained.

Considering the x-axis to be parallel to the interface and z-axis to be along the direction of propagation and based on Maxwell's equations, the magnetic field ($B_{1,y}$) and electric field ($E_{1,x}$, $E_{1,z}$) have been given below where in medium 1, p-polarized light has been incident with an incident angle, $\theta_0 >$ critical angle [1]

$$B_{1,y} = B_y^{(i)} \exp(i\,\overrightarrow{k_i}.\overrightarrow{r}) + B_y^{(r)} \exp(i\,\overrightarrow{k_r}.\overrightarrow{r}) \tag{1}$$

$$\overrightarrow{E_1} = (E_x^{(i)}, 0, E_z^{(i)}) \exp(i\,\overrightarrow{k_i}.\overrightarrow{r}) + (E_x^{(r)}, 0, E_z^{(r)}) \exp(i\,\overrightarrow{k_r}.\overrightarrow{r}) \tag{2}$$

Here, incident wavevector, $\overrightarrow{k_i} = (k \sin\theta_0, 0, k\cos\theta_0)$, reflected wavevector, $\overrightarrow{k_r} = (k \sin\theta_0, 0, -k\cos\theta_0)$, and position vector, $\overrightarrow{r} = (x, y, z)$.

Similarly, for media $m = 2, 3, \ldots, N$ with finite thickness d_m, the magnetic field ($B_{m,y}$) and electric field ($E_{m,x}$, $E_{m,z}$) are presented by

$$B_{m,y} = B_{m,y}^{(+)} \exp(i\,\overrightarrow{k}_m^{(+)}.\overrightarrow{r}) + B_{m,y}^{(-)} \exp(i\,\overrightarrow{k}_m^{(-)}.\overrightarrow{r}) \tag{3}$$

$$\overrightarrow{E_m} = (E_{m,x}^{(+)}, 0, E_{m,z}^{(+)}) \exp(i\,\overrightarrow{k}_m^{(+)}.\overrightarrow{r}) + (E_{m,x}^{(-)}, 0, E_{m,z}^{(-)}) \exp(i\,\overrightarrow{k}_m^{(-)}.\overrightarrow{r}) \tag{4}$$

where $B_{m,y}^{(+)}$, $E_{m,x}^{(+)}$, $E_{m,z}^{(+)}$ are the fields of exponentially growing waves and $B_{m,y}^{(-)}$, $E_{m,x}^{(-)}$, $E_{m,z}^{(-)}$ are the fields of evanescent waves.

Here, $\overrightarrow{k}_m^{(\pm)} = (k \sin\theta_0, 0, \mp i\kappa_m)$ with $\kappa_m = \sqrt{k^2(\sin\theta_0)^2 - \left(\frac{\omega^2}{c^2}\varepsilon_m\right)}$

ω, denotes the angular frequency of incident light, c is the light speed in vacuum, and each layer is defined by the dielectric constant, ε_m. Now analogously for medium $N + 1$,

$$B_{N+1,y} = B^{(+)}_{N+1,y} \exp(i\overrightarrow{k}^{(+)}_{N+1}.\overrightarrow{r}) + B^{(-)}_{N+1,y} \exp(i\overrightarrow{k}^{(-)}_{N+1}.\overrightarrow{r}) \tag{5}$$

$$\begin{aligned}\overrightarrow{E_{N+1}} = &\left(E^{(+)}_{N+1,x}, 0, E^{(+)}_{N+1,z}\right) \exp\left(i\vec{k}^{(+)}_{N+1}.\vec{r}\right) \\ &+ \left(E^{(-)}_{N+1,x}, 0, E^{(-)}_{N+1,z}\right) \exp\left(i\vec{k}^{(-)}_{N+1}.\vec{r}\right)\end{aligned} \tag{6}$$

$B^{(+)}_{N+1,y} = E^{(+)}_{N+1,x} = E^{(+)}_{N+1,z} = 0$ as the medium having evanescent wave only.

Here, $\overrightarrow{k}^{(\pm)}_{N+1} = (k \sin\theta_0, 0, \mp i\kappa_{N+1})$ with $\kappa_{N+1} = \sqrt{k^2(\sin\theta_0)^2 - \left(\frac{\omega^2}{c^2}\varepsilon_{N+1}\right)}$

Solving Maxwell's equation $\left(\partial_y B_z - \partial_z B_y = -ic^{-2}\varepsilon\omega E_x\right)$ for different media and applying the continuity of tangential components of the electric field and magnetic field at the interface $z = 0$ and at the interfaces $z = D_m$ where $D_m = \sum_{k=2}^{m} d_k$ with d_k being the medium thickness, we get

$$\begin{bmatrix} E^{(i)}_x \\ E^{(r)}_x \end{bmatrix} = M^{1\to 2} \begin{bmatrix} E^{(+)}_{2,x} \\ E^{(-)}_{2,x} \end{bmatrix} \tag{7}$$

with

$$M^{1\to 2} = \frac{1}{2i\varepsilon_1\kappa_2} \begin{bmatrix} i\varepsilon_1\kappa_2 - k_z\varepsilon_2 & i\varepsilon_1\kappa_2 + k_z\varepsilon_2 \\ i\varepsilon_1\kappa_2 + k_z\varepsilon_2 & i\varepsilon_1\kappa_2 - k_z\varepsilon_2 \end{bmatrix} \tag{8}$$

$$\begin{bmatrix} E^{(+)}_{m,x} \\ E^{(-)}_{m,x} \end{bmatrix} = M^{m\to m+1} \begin{bmatrix} E^{(+)}_{m+1,x} \\ E^{(-)}_{m+1,x} \end{bmatrix} \tag{9}$$

$$M^{m\to m+1} = \frac{1}{2\chi_{m+1}} \begin{bmatrix} (\chi_{m+1} + \beta^+)\exp(a) & (\chi_{m+1} - \beta^-)\exp(-b) \\ (\chi_{m+1} - \beta^+)\exp(b) & (\chi_{m+1} + \beta^-)\exp(-a) \end{bmatrix} \tag{10}$$

Here, $a = -\kappa_m D_m + \kappa_{m+1} D_m$ and $b = \kappa_m D_m + \kappa_{m+1} D_m$, $\beta^{\pm} = \omega\varepsilon_{m+1}\kappa_m$ and

$$\chi_{m+1} = \kappa_{m+1}\omega\varepsilon_m \tag{11}$$

Now,

$$\begin{bmatrix} E^{(i)}_x \\ E^{(r)}_x \end{bmatrix} = M \begin{bmatrix} E^{(+)}_{N+1,x} \\ E^{(-)}_{N+1,x} \end{bmatrix} \tag{12}$$

$$M = \prod_{u=1}^{N} M^{u\to u+1} = \begin{bmatrix} M_{11} & M_{12} \\ M_{21} & M_{22} \end{bmatrix} \tag{13}$$

For medium $N + 1$, $E^{(+)}_{N+1,x} = 0$.

Therefore, solving Eq. (12), the reflectance of the system is expressed as

$$R = \left| \frac{E_x^{(r)}}{E_x^{(i)}} \right|^2 \tag{14}$$

Now the transmitted electric field for the system can be expressed as $E_{\mathrm{T}} = E_{N+1,x}^{(-)} \exp(-\kappa_{N+1} D_N)$, and transmittance of the system is given by

$$T = \left| \frac{E_{\mathrm{T}}}{E_x^{(i)}} \right|^2, \tag{15}$$

and the incident light intensity is expressed as

$$I = \frac{c\varepsilon_0 \sqrt{\varepsilon_1} \left| E_x^{(i)} \right|^2}{2} \tag{16}$$

3 Result and Discussion

Computer-aided simulations were executed on the proposed configuration, and a number of graphs have been acquired and presented, where Fig. 2 displays the reflectance graph for incident p-polarized beam with the varying incident angle at very low incident light electric field and with zero pump light intensity. The simulated graph signifies resonant excitation of the LRSP mode by the incident light beam around the resonant angle (θ_r) of 39° which is marked by sharp dip in the of the reflected beam intensity.

The bistable behaviour of transmittance of the proposed configuration at $\theta_0 = 53°$ (which is greater than θ_{r}) and at zero pump light intensity can be clearly visualized from Fig. 3. The mentioned figure demonstrates that with the augment in incident

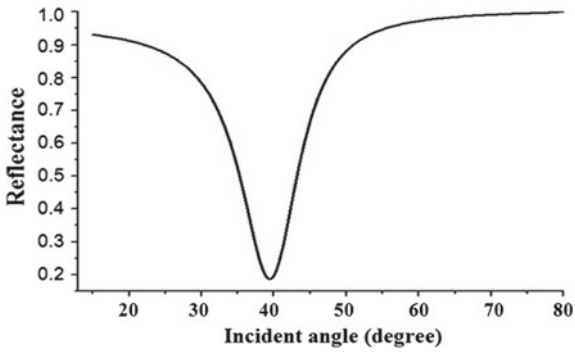

Fig. 2 Reflectance versus incident angle for incident p-polarized beam

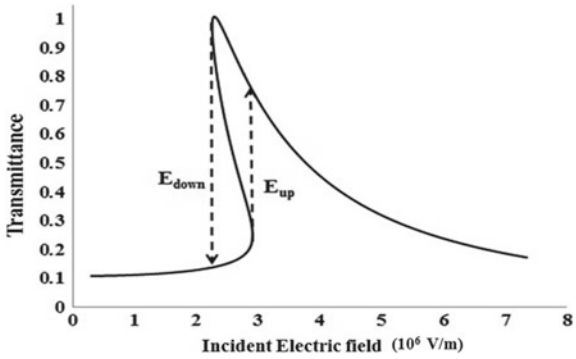

Fig. 3 Dependencies of transmittance on the incident electric field for different incident angles

light electric field, as the incident electric field reaches switching-up threshold electric field (E_{up}), a sudden switch from TIR mode to transmission mode occurs which is displayed by a dashed line pointing towards upward direction. Meanwhile, with the diminishing incident light electric field, transmittance increases till the incident light electric field reaches switching-down threshold (E_{down}) where the transmittance graph suddenly jumps from high transmission mode to TIR mode. This is represented by the dashed line pointing towards the downwards direction. In the figure, the solid line positioned between the dashed arrow lines denotes a solution of the nonlinear boundary value problem whereas the arrow in the dashed lines denotes the direction around the hysteresis loop at the threshold electric field switching points.

Compared to the existing designs, this paper presents the feasibility to obtain hysteresis with a much less switching threshold intensity of about 1.6 MW/cm^2 [19, 20, 23].

Figure 4 shows the variations of transmittance with the varying incident electric field at different pump light intensities. Generally, to attain a low switching threshold value for bistability, a large nonlinear effect plays a prominent role. This large nonlinear effect can be realized by increasing the pump light intensity applied to the kerr

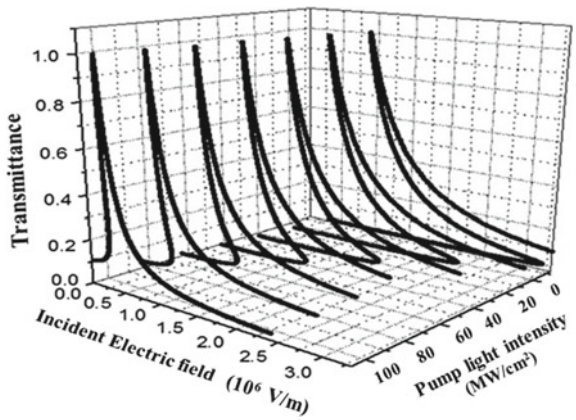

Fig. 4 Transmittance as a function of incident electric field for different Fermi energies

polymer; therefore, with the rise in pump light intensity, nonlinearity of Kerr polymer increases which reduces the threshold requirement to excite optical bistability which is also visible from the graphs.

Figure 5 shows the dependencies of transmitted electric field on the incident electric field for different pump light intensities which also portray lower bistability threshold requirement with the increase in pump light intensity.

The variation of the threshold electric fields E_{up} and E_{down} with the varying pump light intensity from 0 to 100 MW/cm^2 is shown in Fig. 6. It infers that with the increase in pump light intensity both the switch-up threshold and switch-down threshold of the bistability are lowered with the reduction of the hysteresis width, thereby indicating a tunability of threshold electric fields, E_{up} and E_{down} from 3.149 $\times$ 10^6 V/m to 0.2906 $\times$ 10^6 V/m and 2.26 $\times$ 10^6 V/m to 0.226 $\times$ 10^6 V/m, respectively.

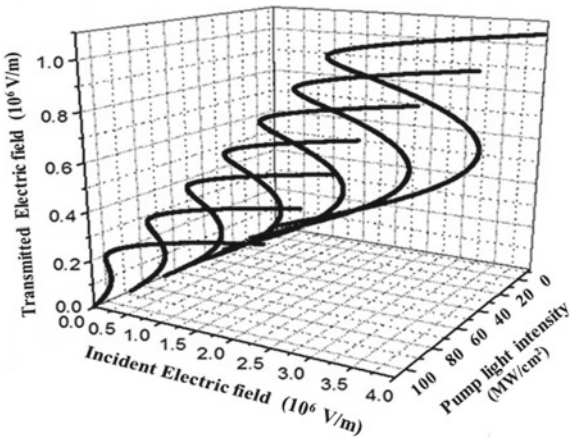

Fig. 5 Dependencies of transmittance on the incident electric for different incident frequencies at THz ranges

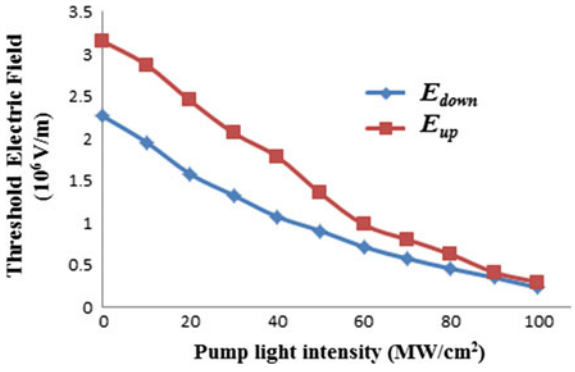

Fig. 6 Variation of the threshold electric fields for varying pump light intensity

4 Conclusion

A proposal towards the realization of optical bistability is implemented analytically in a multilayered long-range surface plasmon configuration containing nano-Ag: polymeric composite material as a Kerr polymer at a telecommunication wavelength of 1550 nm at 25 °C temperature. Here, the nonlinear Kerr medium is having quadratic dependence on the long-range surface plasmon mode resonance-enhanced local electric field amplitude. Through the larger nonlinear effect of the optimized design by employing high local field effect in the nonlinear regime, a low threshold optical bistability of about 1.6 MW/cm^2 in the transmitted light intensity is achieved which is less compared to the previous efforts where the works were carried out with a wavelength other than the important telecommunication wavelength within the C-band [19, 20, 23]. The design also provides tunability of bistable threshold by exploitation of Kerr effect-induced refractive index change through varying pump light intensity. The proposed optical bistable configuration proffers an opportunity to realize the all-optical switching, optical transistor, optical logic and optical memory with low input threshold at telecommunication wavelength and also appears to be a promising tunable optical bistable device for future applications in optical communication.

References

1. Wu C, Song G, Liu H, Cui L, Li Yu, Xiao J (2013) Optical bistability of surface plasmon polaritons in nonlinear Kretschmann configuration. J Mod Opt 60:190–196
2. Xiang Y, Dai X, Guo J, Wen S, Tang D (2014) Tunable optical bistability at the graphene-covered nonlinear interface. Appl Phys Lett 04:051108
3. Gibbs HM (1985) Optical bistability: controlling light with light. Academic Press
4. Abraham E, Smith SD (1982) Optical bistability and related devices. Rep Prog Phys 45:815–885
5. Nihei H, Okamoto A (2001) Photonic crystal systems for high-speed optical memory device on an atomic scale. Proc SPIE 4416:470–473
6. Assanto G, Wang Z, Hagan DJ, Van Stryland EW (1995) All-optical modulation via nonlinear cascading in type II second harmonic generation. Appl Phys Lett 67:2120–2122
7. Wang XL, Jiang HQ, Chen JX, Wang P, Lu YH, Ming H (2011) Optical bistability effect in plasmonic racetrack resonator with high extinction ratio. Opt Express 19:19415–19421
8. Wang GX, Lu H, Liu XM (2011) Optical bistability in metal-insulator metal plasmonic waveguide with nanodisk resonator containing Kerr nonlinear medium. Appl Opt 50:5287–5290
9. Lin XS, Yan JH, Zheng YB, Wu LJ, Lan S (2011) Bistable switching in the lossy side-coupled plasmonic waveguide-cavity structures. Opt Express 19:9594–9599
10. Lu H, Liu X, Wang L, Gong Y, Mao D (2011) Ultrafast all-optical switching in nanoplasmonic waveguide with Kerr nonlinear resonator. Opt Express 19:2910–2915
11. Dai X, Jiang L, Xiang Y (2015) Tunable optical bistability of dielectric/nonlinear graphene/dielectric heterostructures. Opt Express 23:6497–6508
12. Yanik MF, Fan SH, Soljacic M (2003) High-contrast all-optical bistable switching in photonic crystal microcavities. Appl Phys Lett 83:2739–2741
13. Min C, Wang P, Chen C, Deng Y, Yonghua L, Ming H, Ning T, Zhou Y, Yang G (2008) All optical switching in subwavelength metallic grating structure containing nonlinear optical materials. Opt Lett 33:869–871

14. Shen Y, Wang GP (2008) Optical bistability in metal gap waveguide nanocavities. Opt Express 16:8421–8426
15. Litchinitser NM, Gabitov IR, Maimistov AI, Shalaev VM (2007) Effect of an optical negative index thin film on optical bistability. Opt Lett 32:151–153
16. Litchinitser NM, Gabitov IR, Maimistov AI (2007) Optical bistability in a nonlinear optical coupler with a negative index channel. Phys Rev Lett 99:113902
17. Chen P-Y, Farhat M, Alù A (2011) Bistable and self-tunable negative-index metamaterial at optical frequencies. Phys Rev Lett 106:105503
18. Tuz VR, Prosvirnin SL, Kochetova LA (2010) Optical bistability involving planar metamaterials with broken structural symmetry. Phys Rev B 82:233402
19. Hickernell RK, Sarid D (1986) Optical bistability using prism-coupled, long-range surface plasmons. J Opt Soc Am B 3:1059
20. Montemayor VJ, Deck RT (1986) Optical bistability with the waveguide mode: the case of a finite-width incident beam. J Opt Soc Am B 3:1211
21. Nenninger GG, Tobiska P, Homola J, Yee SS (2001) Long-range surface plasmons for high-resolution surface plasmon resonance sensors. Sens Actuators B Chem 74:145–151
22. Berini P (2009) Long-range surface plasmon polaritons. Adv Opt Photonics 1:484–588
23. Wysin GM, Simon HJ, Deck RT (1981) Optical bistability with surface plasmons. Opt Lett 6:30

Design of Nine-Shaped MIMO Antenna Using Parasitic Elements to Reduce Mutual Coupling

K. Vasu Babu and B. Anuradha

Abstract This article presents a multi-band nine-shaped parasitic element which operates at wireless LAN, Wi-Fi and C-band applications. In this current design, a parasitic element is inserted between the patches having a size 60 mm × 40 mm which occupied 2400 mm^2. Due to this type, technical arrangement in the design of antenna structure greatly reduced the mutual coupling (S_{12}) around 45 dB. This reduction is obtained by inserting parasitic elements between the two microstrip patch antennas with separation between them maintained at $0.25\lambda_0$. To represent this type of arrangement the proposed design which improves the antenna parameters including the radiation patterns also.

Keywords Nine-shaped MIMO antenna · WLAN · C-band · Parasitic elements · Mutual coupling

1 Introduction

The design of MIMO antenna is one of the important issues to find the parameter of mutual coupling in between the microstrip patch antennas. To reduce those parameters, different approaches are mentioned in [1–10]. By selected the distance between the patches was $0.52\lambda_0$ in [1] using hybrid magnetic and electric fields to reducing the mutual coupling (S_{12}). In [2] design of low-pass filter with an overall size of antenna 4225 mm^2 with an isolation of 45 dB and improving the return loss 35 dB at a resonant frequency of 7.2 GHz. Defected ground structure is inserted between the two microstrip patch antennas which reduce the mutual coupling 50 dB with an antenna size 76.4 mm × 91 mm in [3]. In [4–6], different techniques are proposed to improve the parameters of S_{11} and S_{12} with a small compact size maintaining a

K. Vasu Babu (✉) · B. Anuradha
Department of ECE, Sri Venkateswara University, Tirupati, Andhra Pradesh, India

V. Janyani et al. (eds.), *Optical and Wireless Technologies*, Lecture Notes in Electrical Engineering 648, https://doi.org/10.1007/978-981-15-2926-9_4

Table 1 Distinguish between other types of techniques

References	Antenna size (mm^2)	Total area occupied (mm^2)	S_{11}(dB)/Return loss	S_{12}(dB)/Mutual coupling	f_L–f_H (GHz)	Resonant frequency (GHz)
Ahn and Park [2]	65 × 65	4225	-35	-45	7.0–7.4	7.2
Chiu and Cheng [5]	68 × 50	3400	−26	−19.7	4.10–4.18	4.17
Salehi and Tavakoli [7]	80 × 60	4800	−22	−27.91	5.8–6.2	6
Najam and Duroc [8]	54 × 45	2430	−18	−30	4.2–5.2	4.8
Suwailam [9]	60 × 80	4800	−32	−26	4.1–5.1	5
Nine-shaped MIMO with parasitic elements	60 × 40	2400	−19	−52	3.3–3.6	3.5
			−22	−32	5.0–5.7	5.3
			−55	−45	6.8–7.3	7
			−29	−40	8.5–9.0	8.8

return loss less than 10 dB and mutual coupling less than 15 dB. A very low isolation is provided by considering an antenna size of 4800 mm^2 occupied in the substrate produces a S_{11} and S_{12} are 22 and 27.91 dB is in [7]. In [8] provided the separation is $0.75\lambda_0$ between the patches using meander line a compact size maintained of 54 mm × 45 mm produced a mutual coupling 30 dB at resonant frequency of 4.8 GHz. Slotted split-ring resonators are used to reduce the mutual coupling with an isolation of 35 dB, and the separation between the two patches is maintained at $0.38\lambda_0$. Here, the proposed nine-shaped MIMO structure with parasitic elements with edge-to-edge separation is $0.25\lambda_0$ which greatly reduces the mutual coupling around 45 dB (Table 1).

2 Antenna Geometry and Analysis

The size of the antenna is 60 mm × 40 mm with an overall size of 2400 mm^2 made with dielectric substrate of FR-4 lossy and parameter of loss tangent 0.002.

This structure is designed by considering a nine-shaped dual structure on a single substrate (Fig. 1; Table 2).

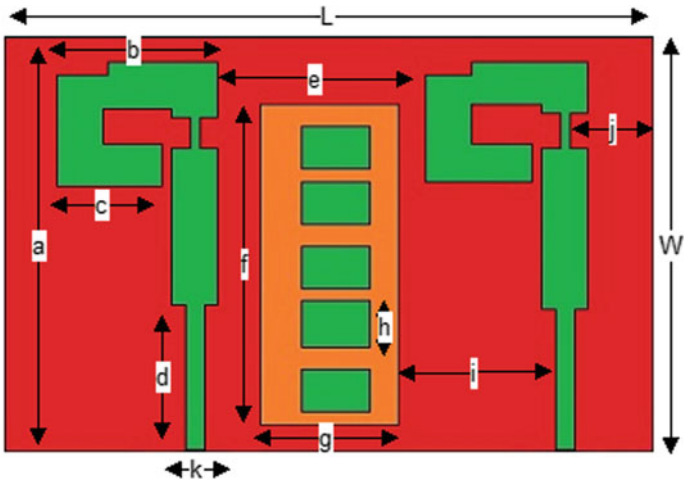

Fig. 1 Nine-shaped MIMO antenna using parasitic elements

Table 2 Nine-shaped MIMO design parameters

Design parameters	*L*	*W*	*a*	*b*	*c*	*d*	*e*	*f*	*g*	*h*	*i*	*j*	*k*
Value (mm)	60	40	30	25	4	8	7	20	7	3	5	4	3

3 Results and Discussion

The nine-shaped MIMO antenna with parasitic elements is proposed here to improve the antenna parameters of a microstrip antenna design. Figure 2 depicts the return loss of antenna resonate at four different resonant frequencies at 3.5 GHz, 5.3 GHz, 7.0 GHz and 8.8 GHz with the values of 19 dB, 22 dB, 55 dB and 29 dB, respectively. Similarly, the mutual coupling between the antennas is shown in Fig. 3 at 3.5, 5.3, 7.0

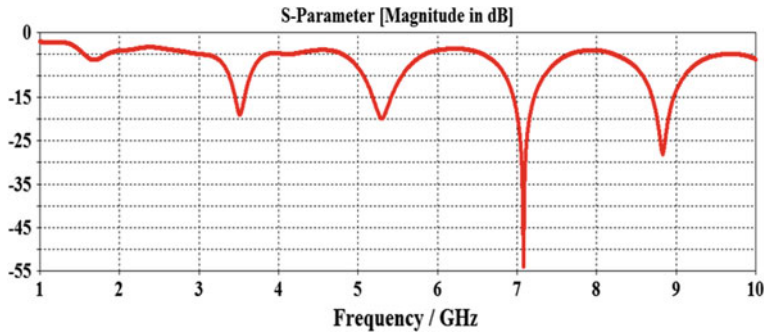

Fig. 2 S_{11} of nine-shaped parasitic elements

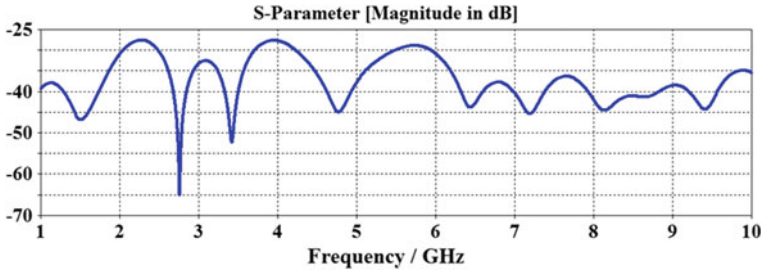

Fig. 3 S_{12} of nine-shaped parasitic elements

and 8.8 GHz with values of 40, 32, 45 and 40 dB. Figure 4 represents the comparison of S-parameters. Figure 5 depicts the surface current distribution of nine-shaped parasitic elements at (a) 3.5 GHz (b) 5.3 GHz (c) 7.0 GHz (d) 8.8 GHz, respectively.

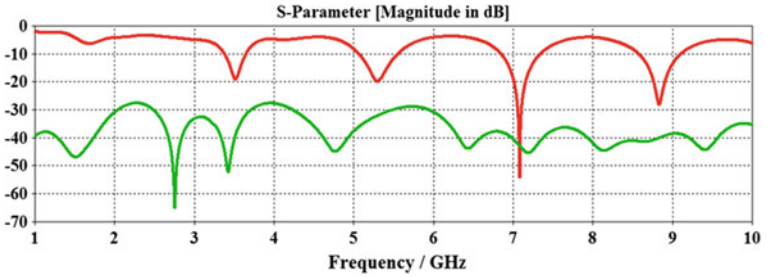

Fig. 4 S-parameters comparison of nine-shaped parasitic elements

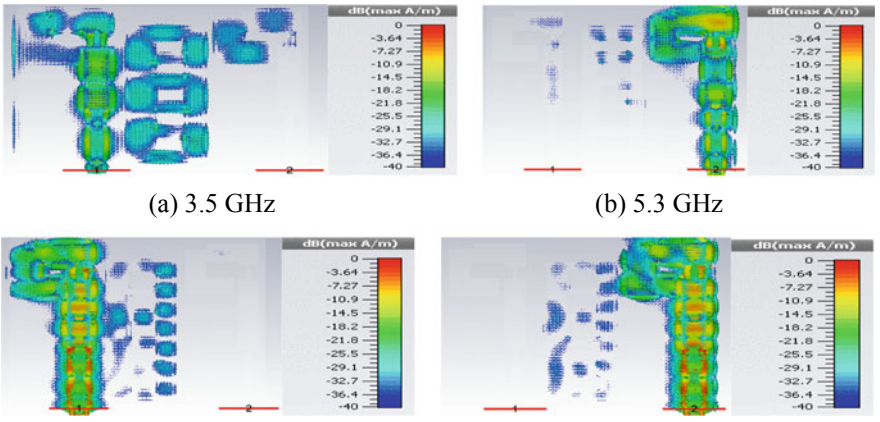

(a) 3.5 GHz (b) 5.3 GHz

(c) 7.0 GHz (d) 8.8 GHz

Fig. 5 Surface current distribution of nine-shaped parasitic elements at **a** 3.5 GHz, **b** 5.3 GHz, **c** 7.0 GHz, **d** 8.8 GHz

Figure 6 identifies that parasitic nine shape MIMO structure port #1 is excited and port #2 with characteristic impedance of 50 Ω radiation pattern. The radiation patterns of the antenna in *xz* plane are omnidirectional and in the planes of *xy* and *xz* plane are nearly have a good complementarity with separate ports are excited in the design of MIMO system. Finally, this structure improves the overall system performance as well as better radiation patters and impedance bandwidth.

4 Conclusions

In this paper, a nine-shaped MIMO antenna using parasitic elements is proposed in the applications of WLAN, Wi-Fi and C-bands. Here, a parasitic element of minimum size is considered and inserted between the two microstrip patch antennas in order to minimize the mutual coupling between the antennas with a separation distance of $0.25\lambda_0$. This type of arrangement greatly improves the mutual coupling around 52 dB at the resonant frequency. Due to this technique, the proposed antenna improves the impedance bandwidth and a good radiation pattern at the multi-band nine-shaped parasitic elements is obtained.

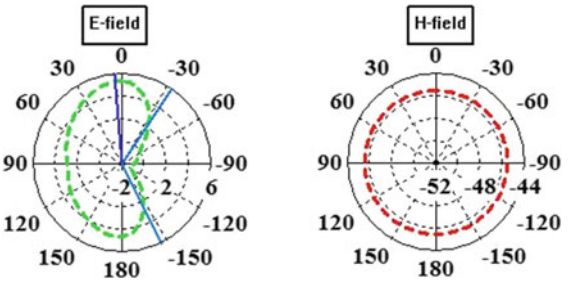

(a) Frequency at 3.5 GHz

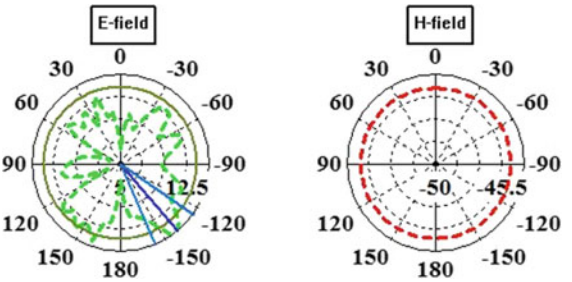

(b) Frequency at 5.3 GHz

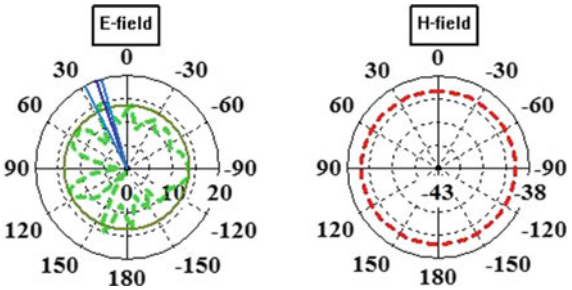

(c) Frequency at 7.0 GHz

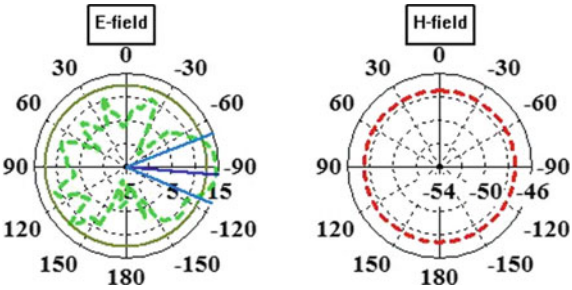

(d) Frequency at 8.8 GHz

Fig. 6 Radiation patterns of nine-shaped parasitic elements at **a** 3.5 GHz, **b** 5.3 GHz, **c** 7.0 GHz, **d** 8.8 GHz

References

1. Xue C-D, Zhang XY (2017) MIMO antenna using hybrid electric and magnetic coupling for isolation enhancement. IEEE Trans Antennas Propag 65:5162–5169
2. Ahn D, Park JS, Kim CS, Kim J, Qian Y, Itoh T (2001) A design of the low-pass filter using the novel microstrip defected ground structure. IEEE Trans Microw Theory Tech 49:86–93
3. Xiao S, Tang MC, Bai YY, Gao S, Wang BZ (2011) Mutual coupling suppression in microstrip array using defected ground structure. IET Microw Antennas Propag 5:1488–1494
4. Kumar C, Guha D (2012) Nature of cross-polarized radiations from probe-fed circular microstrip antennas and their suppression using different geometries of defected ground structure (DGS). IEEE Trans Antennas Propag 6:92–101
5. Chiu CY, Cheng CH, Murch RD, Rowell CR (2007) Reduction of mutual coupling between closely-packed antenna elements. IEEE Trans Antennas Propag 55:2341–2349
6. Shafique MF, Qamar Z, Riaz L, Saleem R, Khan SA (2015) Coupling suppression in densely packed microstrip arrays using metamaterial structure. Microw Opt Technol Lett 57:759–763
7. Salehi M, Tavakoli A (2006) A novel low mutual coupling microstrip antenna array design using defected ground structure. AEU-Int J Electron Commun 60:718–723
8. Alsath MG, Kanagasabai M, Bala Subramanian B (2013) Implementation of slotted meander line resonators for isolation enhancement in microstrip patch antenna arrays. IEEE Antennas Wirel Propag Lett 12:15–18
9. Suwailam MMB, Siddiqui OF, Ramahi OM (2010) Mutual coupling reduction between microstrip patch antennas using slotted-complementary split-ring resonators. IEEE Antennas Wirel Propag Lett 9:876–878
10. Khandelwal MK, Kanaujia BK, Dwari S, Kumar S, Gautam AK (2014) Bandwidth enhancement and cross-polarization suppression in ultra wideband microstrip antenna with defected ground plane. Microw Opt Technol Lett 56:2141–2146

Approaches of Gigabit-Class Transmission for VLC with μLED-Based WDM System

M. T. Rahman, Rajendran Parthiban, Masuduzzaman Bakaul and Prem Kumar

Abstract Visible light communication (VLC) is one of the most renowned technologies for indoor communication to compete with the upcoming 5G technology. Wavelength division multiplexing (WDM) and high-bandwidth μLEDs are the approaches to achieve gigabit-class VLC system. In this paper, we proposed a WDM-VLC model with multi-color μLED configuration using simple on–off keying (OOK) and 16 quadrature amplitude modulation (QAM) scheme. From the simulation approaches, data rate 2.7 Gb/s was achieved by OOK and 10.8 Gb/s by 16QAM after 8 m long VLC link. Therefore, BER was measured 10^{-4} and 10^{-15} when the electron lifetime and RC constant of μLED were 1 ns and 0.5 ns consequently. In addition, of the self RGBY LED was used for the experiment to get data rate 120 Mb/s by OOK and 480 Mb/s using 16QAM modulation scheme.

Keywords MicroLED · VLC · On–off keying (OOK) · High-speed communication · 16QAM · OptiSystem

1 Introduction

At present, VLC with light-emitting diodes (LEDs) has become a significant research area in optical wireless communications. Due to the high transmission capacities of VLC, it can play an important role in indoor wireless communication to drive with 5G technology [1]. There are some others techniques to increase the speed of VLC system, such as WDM, high-order modulation scheme, MIMO-OFDM, special pre- and post-equalization scheme, and μLED arrays. In WDM, individual LED transmits independent data stream with different colors (commonly used red–green–blue), considered as a different channel [2]. Therefore, GaN/InGaN-based microLED (μLEDs) is another approach to enhance the speed which can handle gigabit-class transmission easily and break the modulation bandwidth barrier 20 to

M. T. Rahman (✉) · R. Parthiban · P. Kumar
School of Engineering, Monash University Malaysia, Bandar Sunway, Malaysia
e-mail: muhammad.rahman@monash.edu

M. Bakaul
Diodar Australia, Melbourne, Australia

V. Janyani et al. (eds.), *Optical and Wireless Technologies*, Lecture Notes in Electrical Engineering 648, https://doi.org/10.1007/978-981-15-2926-9_5

>~900 MHz [3]. Spectrum slicing or WDM technology is generally used in fiber-optic communication, and it is also implemented into the high-speed VLC system. RGB LEDs are used as the optical source of VLC system, and it produces white light on the visible light spot zone. Maximum data rate of 15.73-Gb/s has been successfully achieved by the RGBY LED with Dichroic mirrors and special receiver circuit [4]. However, the bandwidth of the RGB LED is limited to 10–20s of MHz only. Therefore, InGaN-based microLED can flick 1000 times faster than commercial LEDs [5]. This means that 1000 more lights could be fitted into the same space as a typical LED. Error-free data transmission up to 1 Gbps [6] and 3 Gbps using these μLEDs was demonstrated using (OOK) and QAM [7]. Maaskant et al. reported the modulation bandwidth >450 (unit) with μLED array in [8]. A cyan μLED with a peak emission of 500 nm and approximately bandwidth 400 MHz was reported by Wun et al. [9]. The focus of this research is to show simulation and experimental approaches for achieving high-speed VLC link.

This paper is organized as follows: Section 2 describes some theories behind the modeling work. Section 3 explains the simulation approaches for high-speed VLC system using OOK and 16QAM signals with microLED. LED modulation bandwidth along with its carrier lifetime is also analyzed for the increasing bit rate along with the distance. Experimental approaches with available LEDs and its results have shown in Sect. 4. Finally, summary of the results was illustrated in the conclusion.

2 Theoretical Modeling

Non-return to zero (NRZ) pulse generator produces OOK signal using PRBS7 bit stream. In the QAM signal, the signal bit transfers as two parallel input signals, I and Q quadrature carriers. The amplitude can vary according to the source symbols. LED acts as an optical transmitter, and the received power can measure by

$$P_{\mathrm{r}} = H_{\mathrm{d}}(0)\, P_{\mathrm{t}} \tag{1}$$

where P_{r} is received power at the receiver end, P_{t} is transmitted power by LED, and $H_{\mathrm{d}}(0)$ is DC channel gain of the VLC link. If the link is direct line of sight (LOS) where no reflection from walls, the equation of DC gain in the optical channel is

$$H_{\mathrm{d}}(0) = \left\{ \begin{array}{c} \frac{(m+1)A}{2\pi d^2} \cos^m(\theta) T_{\mathrm{s}}(\Psi) g(\Psi) \cos(\Psi) \\ 0 \le \Psi \le \Psi_{\mathrm{c}}, \Psi > \Psi_{\mathrm{c}} \end{array} \right\} \tag{2}$$

where $g(\Psi)$ is the gain of FOV concentrator, Ψ_{c} is the field of view at receiver, d is the distance between LED and PD, m is the Lambertian emission which is related to LED's half power semi-angle and expressed by

$$m = -\frac{\ln 2}{\ln\left(\cos\theta_{\frac{1}{2}}\right)} \tag{3}$$

After modulating the signal, 3-dB modulation bandwidth of the LED has been measured by the equation as [4]

$$f_{3\text{dB}} = \frac{\sqrt{3}}{2\pi(\tau_n + \tau_{\text{rc}})} \tag{4}$$

where τ_n is electron lifetime and τ_{rc} is the RC constant (parasitic capacitance). VLC component range was 3–10 m [10], and the link can be described as:

$$P_{\text{Received}} = P_{\text{Transmitted}} \frac{d_{\text{R}}^2}{(d_{\text{T}} + \theta R)^2} 10^{-\alpha \frac{R}{10}} \tag{5}$$

where d_{R} is receiver aperture diameter (m), d_{T} is transmitter aperture diameter (m), θ is beam divergence (mrad), R is range (m), and α is atmospheric attenuation (dB/km). The most significant noise source in VLC systems is shot noise, arising due to striking to the photo detector. Shot noise Gaussian distribution of the detector is modeled as [11]

$$\sigma_{\text{shot}}^2 = 2 \,.\, q \,.\, \left(i_{\text{sig}} + i_{\text{noise}}\right) \,.\, \text{ENB} \tag{6}$$

where Gaussian distribution is randomly generated value between 0 and 1. Another source of significant noise which is thermal noise within the receiver front end of the PD is calculated as follows [12]

$$\sigma_{\text{thermal}}^2 = \frac{4 \,.\, k_{\text{B}} \,.\, T}{R_{\text{L}}} \,.\, \text{ENB} \tag{7}$$

where T is the absolute temperature of the device, R_{L} is the receiver load resistance, and k_{B} is the Boltzmann constant, and ENB is receiver equivalent electrical noise bandwidth. The total noise at the output up to pre-amplifier is then

$$\sigma(f) = \sigma_{\text{shot}}(f) + \sigma_{\text{thermal}}(f) \tag{8}$$

3 Simulation Approach

In the simulation model, non-return to zero (NRZ) OOK signal was used as a signal carrier modulation from Fig. 1, and microLED was configured as a light source with different electron lifetime 1 and 0.5 ns. The distance between transmitter and receiver

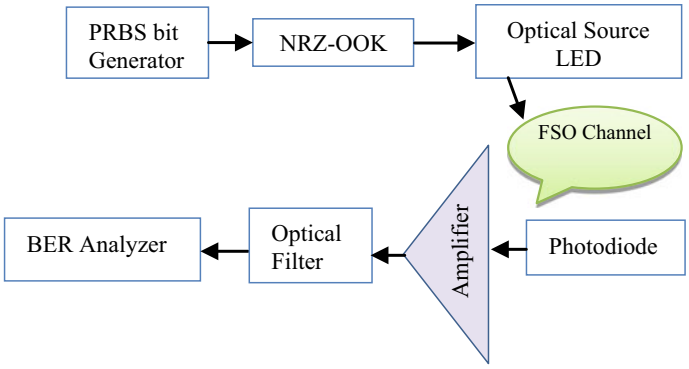

Fig. 1 Model of NRZ-OOK-based VLC system

was considered from 1m to 10m. RGBY LED was used as an optical source in the transmitter. Received signal by PD was amplified for the analyzed with BER analyzer through low-pass filter (LPF).

In this model, data transmission started from 400 Mb/s to 1 Gb/s. BER and related Q factor were shown in Table 1, and maximum 900 Mb/s data can transmit maintaining the forward error correction (FEC) limit using OOK modulation scheme. The aggregate data rate 2.7 Gb/s was achieved with the RGB WDM system. Moreover, using 16QAM, the data rate was achieved four times higher than OOK. Original transmitted signal from the transmitter and at the receiver, after filtering the received signal have shown in Fig. 2a and c. The eye diagram of the RGBY LEDs has described in Fig. 3 at the transmission rate 900 Mb/s.

Figure 4 shows the simulation model for QAM-VLC system. Using 16QAM signal, aggregate data rate can be increased four times higher than OOK which is around 10 Gb/s. The constellation diagram from 16QAM transmitter and receiver has been given in Fig. 5a and b after transmitting the data 900 Mb per single LED. In order to overcome modulation bandwidth limitation of the LEDs, we need to reduce electron lifetime and parasite capacitance constant within the active region which is more

Table 1 Data transmission rate and related BER and Q

Bit rate (Mb/s)	BER	Q
400	3.48×10^{-97}	20.62
450	1.49×10^{-73}	17.10
500	4.53×10^{-52}	15.13
600	1.06×10^{-10}	6.19
700	2.50×10^{-04}	3.47
800	1.10×10^{-03}	3.04
900	7.68×10^{-03}	2.33
1 Gb/s	1.26×10^{-02}	2.24

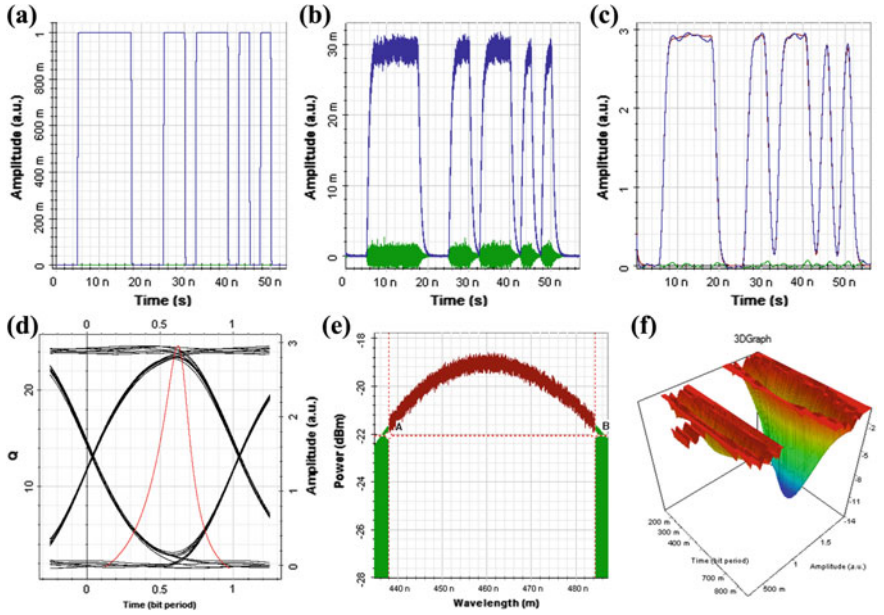

Fig. 2 **a** Original transmitted signal, **b** received signal at PD, **c** after filter the received signal, **d** eye diagram of the output signal, **e** blue LED (460 nm) spectrum is ~46.5 nm, and **f** BER of the signal

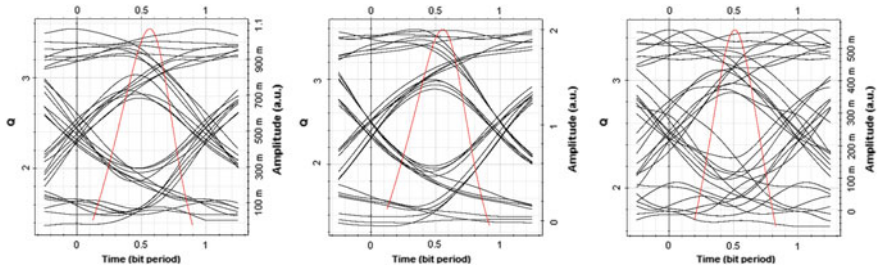

Fig. 3 Eye diagram from red–green–blue LED during data rate 900

important to achieve high-speed communication [13]. MicroLED has limited carrier lifetime only ~1 ns, and our simulation model suggests that reducing electron lifetime would be a factor to improve the efficiency of a gigabit-class transmission system. Figure 5c explains the improvement of LED transmitter performance changing its lifetime for indoor communication range.

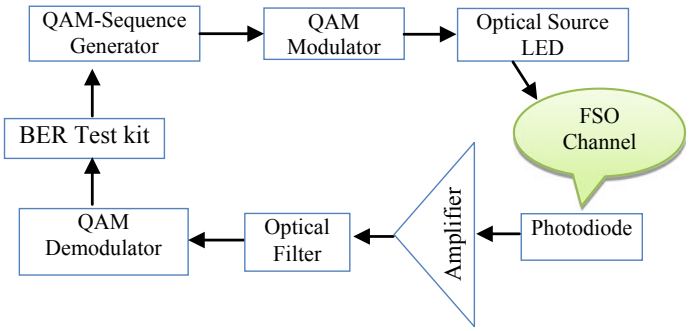

Fig. 4 Simulation model of 16QAM-VLC

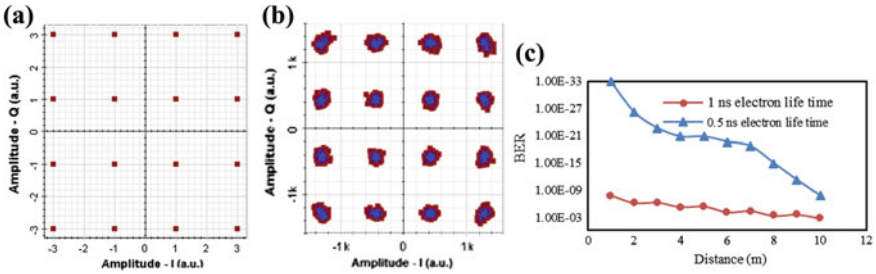

Fig. 5 Constellation diagram of **a** transmitter and **b** receiver at the receiver end. **c** BER versus distance for different LED's electron lifetime

4 Experimental Approach

For the experiment approach, single-carrier modulation technique OOK was implemented in the laboratory. It was done by available RGBY LEDs. The aggregate data rate was 120 Mb/s by OOK, and using 16QAM was around 500 Mb/s. This result is better than [14] but also suggested that it might be improved after applying advanced equalization [15]. A list of devices which was used for the experimental analysis is provided in Table 2 and experimental setup in Fig. 6.

The modulated waveforms were generated using Tektronix Arbitrary Waveform Generator (AWG) 5014c. It has four channels, each of which can sample up to 1.2 GS/s, and 500 MHz analog bandwidth. MATLAB® was used to create the required 16QAM waveforms which were uploaded to the AWG. A wideband coaxial bias tee (Mini Circuits ZFBT-4R2GW-FT) was used for basing the LED at the operating region and combine the DC component with the high-frequency modulated waveforms and it operates at 350 mA. A circular lens (15° beam angle) was fixed in front of the LED to focus the light onto the receiver. A Silicon PD (Thorlabs PDA-10A) was used as the receiver in this experiment which has an active detection area of 0.8 mm^2, wavelength sensitivity range 200–1100 nm, with a peak responsivity of

Table 2 Equipment lists for experiments

1	AWG Tektronix AWG 5014c Transmitted data bit
2	Amplifier Mini circuit ZHL-6A+
3	Bias Tee (Mini circuits) ZFBT-FT DC power supply
4	LED Oslon NUWH CCT ~4000 k LED as a Transmitter
5	Heatsink
6	Photodiode Thorlabs PDA 10A VLC Receiver
7	Oscilloscope Agilent DSO 9054H
8	Optical lens (Thorlabs C280TME-A)
9	Optical rail (stage Thorlabs)

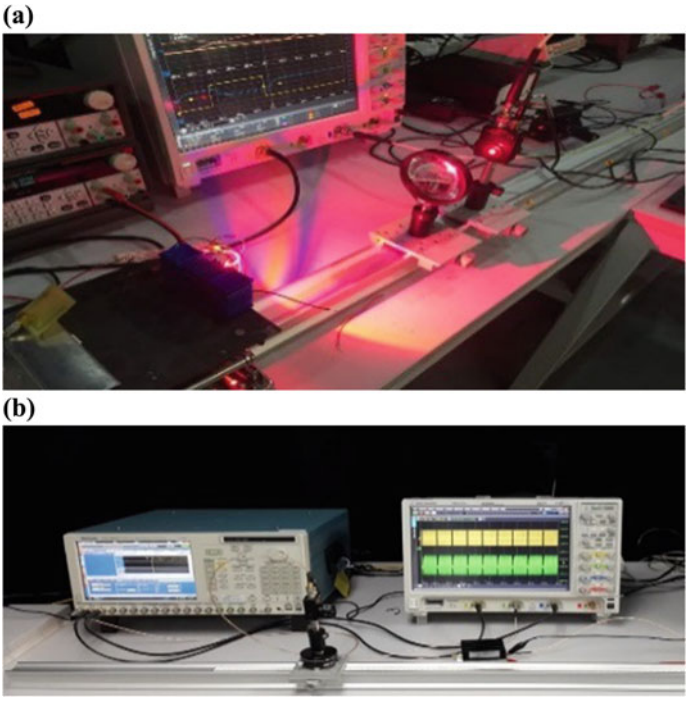

Fig. 6 VLC experimental link setup, **a** side view (top) and **b** front view (down)

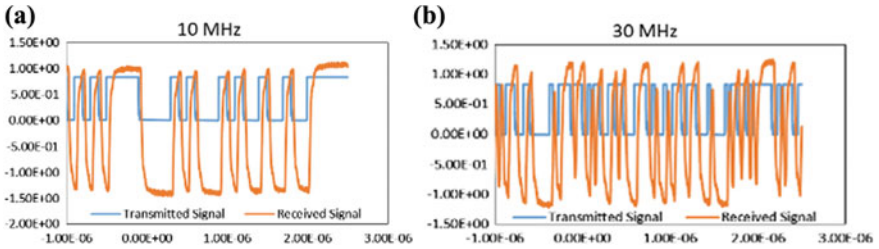

Fig. 7 **a** Received waveform at 10 MHz and **b** received waveform at 30 MHz

0.45 A/W. Power amplifier was used to amplify the signal connected after photodiode. Analog bandwidth of the AWG was set initially as 10 MHz, and it increased up to 30 MHz for both OOK and 10QAM signals. Received signal for 10 and 30 MHz has included in Fig. 7a and b.

Each sample carries one bit for the experiment, and initially, it was 10 Mb/s. It is clear from Fig. 8a and b, when the data rate exits 30 Mb/s, the signal quality was worse and eye diagram of the output was not measurable. The output signals were captured using an oscilloscope Agilent DSO 9054H.

Figure 9a shows the BER and related *Q* factor of RGBY LEDs with related data rate from 10 up to 30 Mbps. For this experiment for WDM-VLC system with OOK

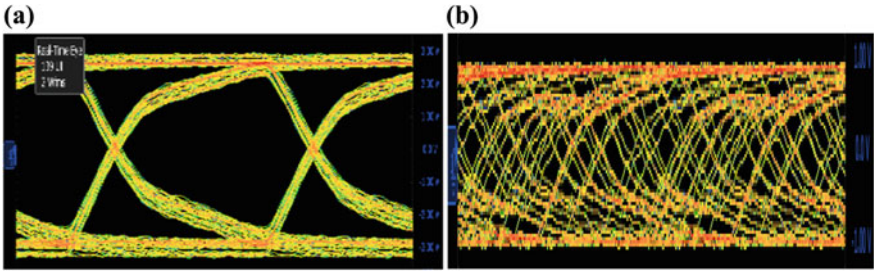

Fig. 8 **a** Related eye diagram for 10 MHz and **b** >30 MHz waveform

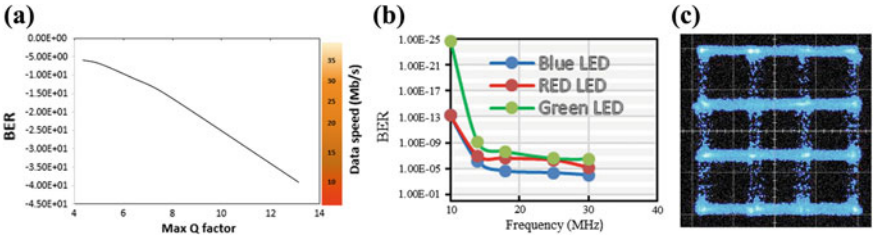

Fig. 9 **a** Experimental results for RGBY LED BER versus modulation bandwidth (MHz), and BER versus Q function, **b** BER versus maximum data rate for available RGB LED, and **c** constellation diagram of 16QAM received signal

modulation scheme and commercially available RGBY LED, max aggregate data rate was achieved as 120 Mb/s.

The overall system performance of the WDM-VLC model was analyzed by changing different data rates with OOK and QAM signals. Therefore, quality factors (Q) and BER were considered as a main parameter for checking signal quality. With the increase of sampling rate by AWG, data rate also increased and the received signal at the transmitter was distorted for the high data rate. The obtained BER is sketched in Fig. 9b with the increasing data rate up to 30 Mb/s for RGB LEDs. 16QAM signal was used to increase the data rate up to 500 Mb/s, and constellation diagram of the output has been given in Fig. 9c. To match with the simulated results in Sect. 3, we need to fabricate microLED which is not commercially available yet but future research is ongoing to make it commercially available for next-generation high-speed optical wireless communication.

5 Conclusion

In this paper, WDM-VLC model has been designed and simulated by OptiSystem v.15.1 to determine the high-speed visible light communication link for indoor environment. LED-based WDM-VLC model is configured with OOK and 16QAM modulation scheme. Maximum 2.7 Gb/s data rate was achieved by OOK and 10.8 Gb/s by 16QAM with the microLED. In addition, WDM (RGBY) LEDs are also used to achieve maximum data rate in experimental workbench. In order to use different modulation scheme, OOK and 16QAM multicarrier modulation schemes were implemented in both approaches. For the experimental approaches, 120 Mb/s data rate was achieved by OOK and around 500 Mb/s was achieved by 16QAM. MicroLED is one of the most important factors for high-speed VLC system in order to overcome modulation bandwidth limitation of the conventional of the shelf LEDs because of its shorter carrier lifetime and faster switching capability. Finally, high-speed communication link for IoT applications with high-order modulation scheme and more number of VLC channel will be included in our further research.

References

1. Haidine A, El Hassani S (2016) LTE-a pro (4.5 G) as pre-phase for 5G deployment: closing the gap between technical requirements and network performance. In: International conference on advanced communication systems and information security (ACOSIS), pp 1–7. IEEE
2. Chun H, Rajbhandari S, Faulkner G, Tsonev D, Xie E, McKendry JJD, Erdan G, Dawson MD, O'Brien DC, Haas H (2016) LED based wavelength division multiplexed 10 Gb/s visible light communications. J Lightwave Technol 34(13):3047–3052
3. Rajbhandari S, Chun H, Faulkner GE, Cameron KL, Jalajakumari AVN, Henderson RK, Tsonev D et al (2015) High-speed integrated visible light communication system: device constraints and design considerations. IEEE J Sel Areas Commun 33(9):1750–1757

4. Bian R, Tavakkolnia I, Haas H (2019) 15.73 Gb/s visible light communication with off-the-shelf LEDs. J Lightwave Technol 37:2418–2424
5. McKendry JJD, Tsonev D, Ferreira R, Videv S, Griffiths AD, Watson S, Gu E, Kelly AE, Haas H, Dawson MD (2015) Gb/s single-LED OFDM-based VLC using violet and UV gallium nitride μLEDs. In: Summer topicals meeting series (SUM), pp 175–176. IEEE
6. Herrnsdorf J, McKendry JJD, Xie E, Strain MJ, Watson IM, Gu E, Dawson MD (2016) High speed spatial encoding enabled by CMOS-controlled micro-LED arrays. In: IEEE summer topicals 2016
7. Ferreira RXG, Xie E, McKendry JJD, Rajbhandari S, Chun H, Faulkner G, Watson S et al ((2016)) High bandwidth GaN-based micro-LEDs for multi-Gb/s visible light communications. IEEE Photonics Technol Lett 28(19):2023–2026
8. Maaskant PP, Shams H, Akhter M, Henry W, Kappers MJ, Zhu D, Humphreys CJ, Corbett B (2013) High-speed substrate-emitting micro-light-emitting diodes for applications requiring high radiance. Appl Phys Express 6(2):022102
9. Wun J-M, Lin C-W, Chen W, Sheu JK, Lin C-L, Li Y-L, Bowers JE et al (2012) GaN-based miniaturized cyan light-emitting diodes on a patterned sapphire substrate with improved fiber coupling for very high-speed plastic optical fiber communication. IEEE Photonics J 4(5):1520–1529
10. Agrawal GP (2012) Fiber-optic communication systems, vol 222. Wiley
11. Kahn JM, Barry JR (1997) Wireless infrared communications. Proc IEEE 85(2):265–298
12. Keiser G (2003) Optical fiber communications. Wiley Encyclopedia of Telecommunications
13. Sukhdeo DS, Gupta S, Saraswat KC, Dutt BR, Nam D (2016) Impact of minority carrier lifetime on the performance of strained germanium light sources. Opt Commun 364:233–237
14. Li H, Chen X, Guo J, Tang D, Huang B, Chen H (2014) 200 Mb/s visible optical wireless transmission based on NRZ-OOK modulation of phosphorescent white LED and a pre-emphasis circuit. Chin Opt Lett 12(10):100604
15. Li H, Chen X, Huang B, Tang D, Chen H (2014) High bandwidth visible light communications based on a post-equalization circuit. IEEE Photonics Technol Lett 26(2):119–122

Evaluation of Performance of Is-OWC OFDM System with Spatial Diversity

Sunita Khichar and Pawan Kumar Inaniya

Abstract Inter-satellite correspondence is a free-space optical innovation which is utilized to build up communication path between satellites in space. This work is centered around the transmission of 20 Gbps information over 4500 km inter-satellite communication interface by consolidating orthogonal frequency division multiplexing plan. The 4 QAM is preferred because of its high reliability in noise than other modulation techniques. The system design includes space diversity technique with OFDM to reduce effect of fading, improve BER, and improve receiving power with increase in link distance and data rate also in comparison with previous proposed system. The simulation of proposed framework is assessed regarding signal-to-noise proportion, add up to get control or output power at receiver, RF spectrum and constellation diagram.

Keywords Inter-satellite communication · Orthogonal frequency division multiplexing (OFDM) · Quadrature amplitude modulation (QAM) · Spatial diversity

1 Introduction

In 1962, laser innovation was first created to impart among satellite and submarine [1]. It included higher transfer speed limit, bringdown electromagnetic obstruction (EMI), recurrence assets utility and lower control requirements, which brought about its application for radio-recurrence (RF) innovation [2, 3]. Besides, laser innovation was utilized as a part of optical remote correspondence (OWC) for imparting among space and satellites. Between satellite OWC (Is-OWC) frameworks regulate data motions on a light source and transmit to different satellites by means of free-space

S. Khichar (✉)
Department of Electrical Engineering, Chulalongkorn University, Bangkok, Thailand
e-mail: sunitakhichar1433@gmail.com

P. K. Inaniya
Electronics and Communication Engineering, Government Women Engineering College, Ajmer, India
e-mail: pawan.inaniya@gmail.com

V. Janyani et al. (eds.), *Optical and Wireless Technologies*, Lecture Notes in Electrical Engineering 648, https://doi.org/10.1007/978-981-15-2926-9_6

optics (FSO). The signs are then demodulated by means of optical recipients while transmitting them to the first data source. Analysts have examined FSO for various earthly applications [4–8]. Is-OWC is basically worried about satellite matching in comparative or distinctive circles while transmitting signals at the speed of light by shifting separation, time and payload insignificantly [9–11]. Space-based optical innovation is essentially utilized as a part of between satellite correspondence frameworks with the got flag control including the between satellite optical remote connection [12].

In OWC, optical OFDM is a wonderful innovation utilized for diminishing multipath blurring impacts and dealing with multipath blurring issues [11, 13–17]. This innovation can be utilized for transporting information over an extensive variety of sub-bearers with each isolated by exact frequencies of covering groups. These subtransporters utilize fast Fourier transform (FFT) for acquiring symmetry [18]. In this way, OFDM can be incorporated with Is-OWC for whole deal transmission at higher information rate. In present work, OFDM-Is-OWC communication network is used to transmit 20 Gbps information data over 4500 km distance.

One of the significant difficulties of the FSO framework is lessening of the free space, i.e., air, because of thick mist, rain, snowfall which causes the assimilation, disseminating and reflection process. The level of intensity thickness of FSO pillar is lessened because of assimilation. The bar power for longer separation [19, 20] is decreased because of scrambling. Reflection causes numerous resound impacts by striking the collector at various interims which makes trouble in recognizing the information estimations of the got flag precisely. This outcome in optical misfortune, change of the flag and turbulence in the plentifulness levels and subsequently the got influence is getting blurred. By utilizing propelled balance plans like OFDM, the impacts because of blurring can be lessened. Since, OFDM gives the diminished blurring, constrained ISI and lower multifaceted nature, it is generally embraced in the remote correspondence frameworks.

This paper has different sections. In Sect. 2, description of system is given, and Sect. 3 describes about the result obtained by the simulation using OptiSystem 12.

2 System Description

The basic structure of Is-OWC consists of satellite 1 as transmitter, satellite 2 as receiver and free space as propagation medium. Figure 1 speaks to the proposed OFDM-based between satellite correspondence framework. OptiSystem programming is utilized to show the proposed OFDM-Is-OWC framework because of its exactness. 20 Gbps information is regulated by utilizing four-quadrature plentifulness tweak (QAM) encoding group. After 4 QAM encoding, signals are forwarded or transferred to OFDM modulator for modulation. There are 512 sub carrier and 256 FFT points in OFDM modulator. These OFDM signals are additionally bolstered to quadrature modulator (QM) to tweak at 7.5 GHz recurrence. At that point,

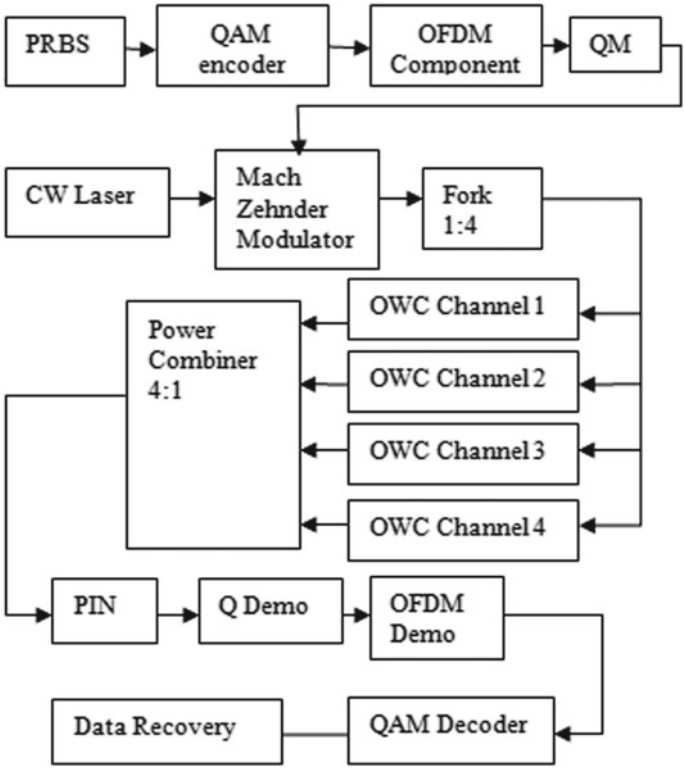

Fig. 1 Proposed inter-satellite system with OFDM and spatial diversity

these OFDM-QM signals are tweaked over optical flag by utilizing lithium niobate (LiNBO3) optical modulator and ceaseless wave (CW) laser having wavelength of 1550 nm and intensity of 0 dBm. Further, this optical flag conveying 20 Gbps OFDM signals is transported over Is-OWC interface having a traverse of 4500 km. The space turbulences are thought to be perfect in this work. The Is-OWC interface is scientifically spoken by the accompanying condition [18].

$$P_{\mathrm{R}} = P_{\mathrm{T}} G_{\mathrm{T}} G_{\mathrm{R}} L_{\mathrm{T}} L_{\mathrm{R}} (\lambda / 4\pi R)\, 2 \tag{1}$$

where

P_{T} = Power of transmitting antenna
P_{R} = Power of receiving antenna
G_{T} = Gain of transmitting antenna
G_{R} = Gain of receiving antenna
λ = Operating wavelength and
R = Distance between the two ends of the link.

The proposed framework is having assorted variety. Spatial decent variety plot is embraced here. In spatial decent variety, we will utilize numerous TX/RX with the goal that the flag quality got will be moved forward. The signal is transmitted through separate diversity branches to generate independent copies. Different fades are used for each independent signal. With '*L*' independent channels, the probability is '*PL*' where '*L*' copies of the desired signal are obtained and '*P*' be the probability of the channel gain below a critical value.

At the recipient side, p-n (PIN) photograph locator is utilized to get the optical flag. The yield of PIN photograph indicator is nourished to QM demodulator took after by OFDM demodulator and 4 QAM encoder to recover the first 20 Gbps information.

3 Result

The values are counted according to the virtual assumption of inter-satellite optical wireless communication system. Bit rate used is 10–20 Gbps. The suggesting Is-OWC setup is shown in Fig. 1. The setup is designed and tested in OptiSystem 12.

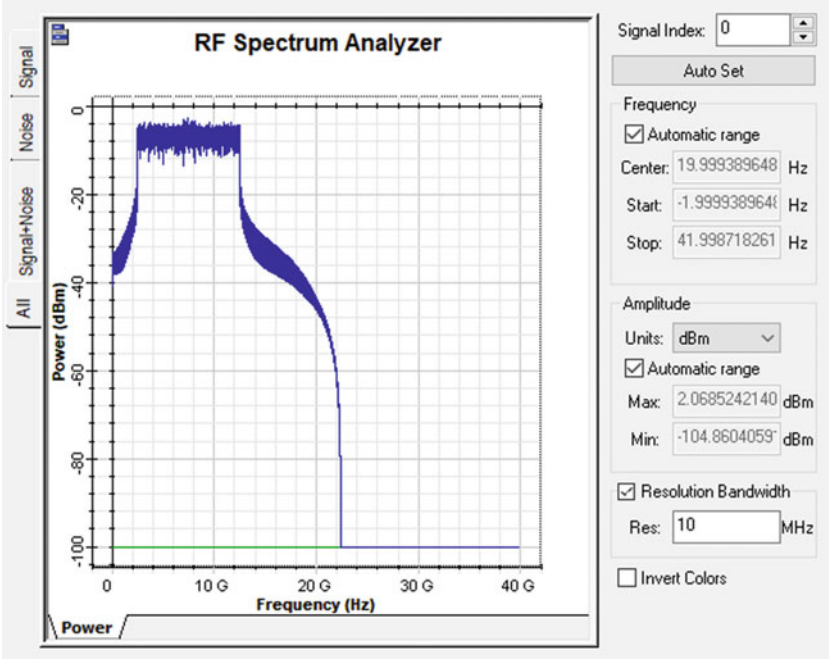

Fig. 2 RF spectrum of transmitter

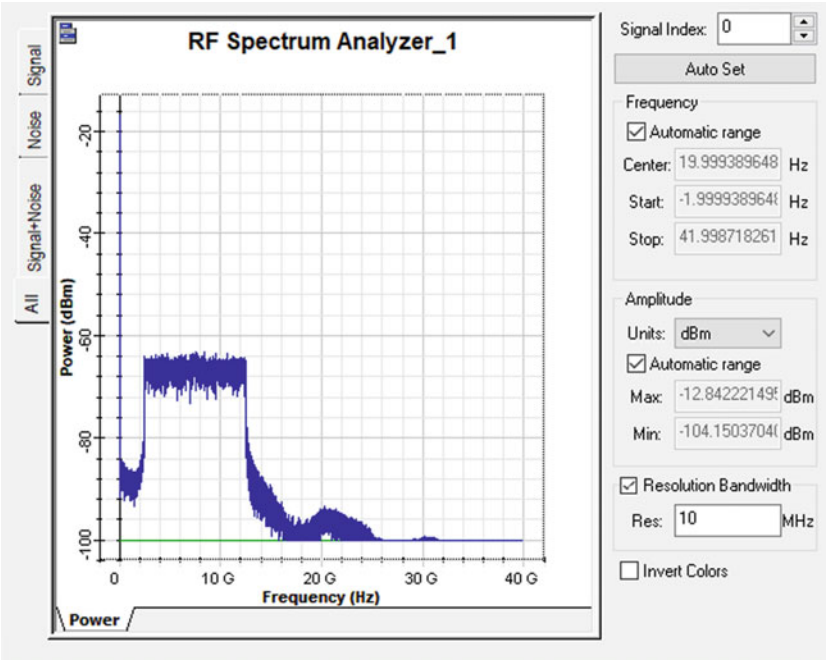

Fig. 3 RF spectrum of receiver at 1000 km

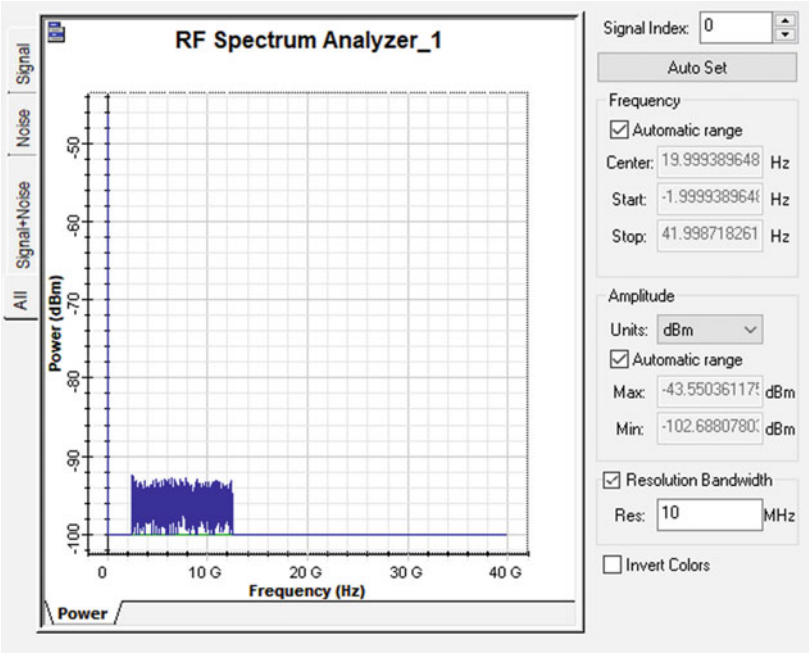

Fig. 4 RF spectrum of receiver at 4500 km

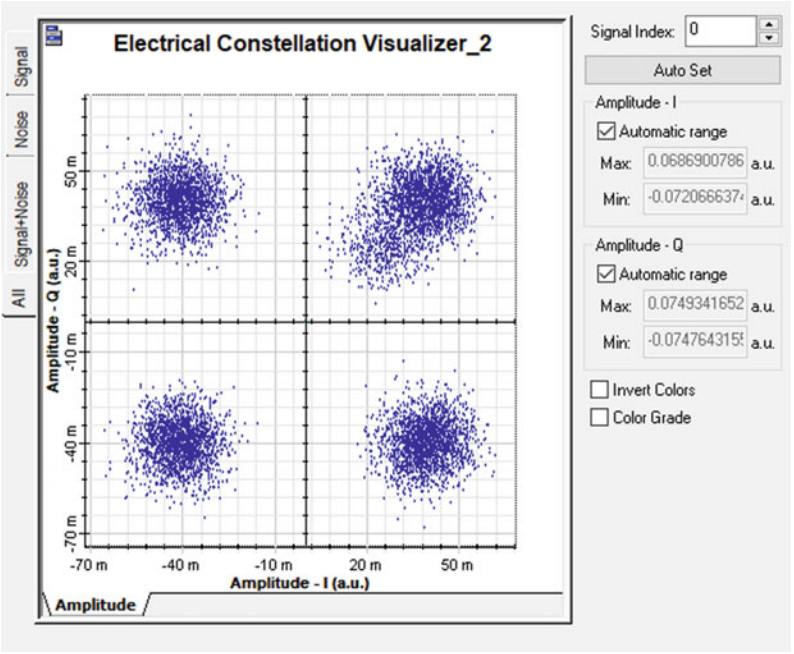

Fig. 5 Constellation diagram of receiver at 4500 km

(A) ***RF spectrum***

The flag input: Figures 2, 3 and 4 show input RF spectrum and outcome RF spectrums of transmitter and receiver, respectively.

(B) ***Constellation diagram***

It can likewise show the polar chart and gauge the likelihood of image blunder for M-ary signals.

This proposed system works for link distance 4500 km with bit rate 20 Gbps. Figure 2 shows RF spectrum of receiver at 4500 km, and Fig. 5 shows electric constellation diagram at link distance 4500 km, respectively. The value of signal-to-noise ratio for 4 QAM encoding scheme is computed as 34.67 dB, 27.23 dB and 26.09 dB for distances 1500, 3500 and 4500, respectively. This setup is analyzed for several link distances starting from 1000 km.

4 Conclusion

In this work, 20 Gbps information is transmitted over Is-OWC interface having a traverse of 4500 km by fusing 4 QAM encoding plan took after by the OFDM

system. The detailed outcome demonstrates the fruitful transmission of 20 Gbps information with satisfactory SNR and heavenly bodies.

References

1. Hecht J (2010) Short history of laser development. Opt Eng 49:091002–091002-23
2. Chaudhary S, Amphawan A (2014) The role and challenges of free-space optical systems. J Opt Commun 35:327–334
3. Lutz E, Werner M, Jahn A (2012) Satellite systems for personal and broadband communications. Springer Science & Business Media
4. Amphawan A, Chaudhary S, Neo T-K (2015) Hermite-Gaussian mode division multiplexing for free-space optical interconnects. Adv Sci Lett 21:3050–3053
5. Chaudhary S, Amphawan A, Nisar K (2014) Realization of free space optics with OFDM under atmospheric turbulence. Opt Int J Light Electron Opt 125:5196–5198
6. Chaudhary S, Bansal P, Lumb M (2014) Effect of beam divergence on WDM-FSO transmission system. Int J Comput Appl 93:28–32
7. Chaudhary S, Bansal P, Singh G (2013) Implementation of FSO network under the Impact of atmospheric turbulences. Int J Comput Appl 75:34–38
8. Sarangal H, Singh A, Malhotra J, Chaudhary S (2017) A cost effective 100 Gbps hybrid MDM–OCDMA–FSO transmission system under atmospheric turbulences. Opt Quantum Electron 49:184
9. Chaudhary S, Sharma A (2015) 6 × 20Gbps long reach WDM-PI based high altitude platform inter-satellite communication system. Int J Comput Appl 122:41–45
10. Chaudhary S, Sharma A, Chaudhary N (2016) 6 × 20 Gbps hybrid WDM–PI inter-satellite system under the influence of transmitting pointing errors. J Opt Commun 37:375–379
11. Amphawan A, Chaudhary S, Chan V (2014) 2 × 20 Gbps-40 GHz OFDM Ro-FSO transmission with mode division multiplexing. J Eur Opt Soc Rapid Publ 9
12. Vimal K, Prince S (2015) System analysis for optimizing various parameters to mitigate the effects of satellite vibration on inter-satellite optical wireless communication. In: IEEE international conference on signal processing, informatics, communication and energy systems (SPICES), 1–4
13. Amphawan A, Chaudhary S, Samad H, Ahmad J (2015) Mode division multiplexing of LG and HG modes in Ro-FSO. Poly-Tech K
14. Sharma V (2014) High speed CO-OFDM-FSO transmission system. Opt Int J Light Electron Opt 125:1761–1763
15. Sharma V, Chaudhary S (2012) Implementation of hybrid OFDM-FSO transmission system. Int J Comput Appl 58:37–40
16. Hossain F, Afroze Z (2013) Eliminating the effect of fog attenuation on FSO link by multiple TX/RX system with travelling wave semiconductor optical amplifier. In: 2013 International conference on advances in electrical engineering (ICAEE), Dhaka, pp 267–272
17. Patel P, Mishra V, Singh V (2014) Performance analysis of CO-OFDM FSO system under different weather conditions. In: 2014 2nd international conference on emerging technology trends in electronics, communication and networking (ET2ECN), Surat, pp 1–5
18. Andrews LC, Phillips RL (2005) Laser beam propagation through random media, 2nd edn. SPIE Press Book
19. Ghassemlooy Z, Popoola WO, Terrestrial free-space optical communications. In: Mobile and wireless communications: network layer and circuit level design, pp 355–391
20. Singh M, Kaur K (2013) Coherent detection WDM optical OFDM system. Int J Adv Res Comput Comm Eng
21. Chaudhary S et al (2017) 4 QAM-4PSK-OFDM inter-satellite communication system. J Opt Commun

Lightweight Secure-MQTT for Internet of Things

Adil Bashir and Ajaz Hussain Mir

Abstract In this paper, a security mechanism for MQTT-enabled Internet of things (IoT) using a simple thin cryptographic process has been proposed. The key benefits of the proposed security mechanism are the simplicity, resilience to attacks, energy efficiency, and the speed of cryptographic computations such that it can be computed quickly. The encryption of MQTT payload is performed using lightweight operations so that a smaller amount of node energy is consumed in the process. To test the effectiveness of the proposed mechanism, Contiki-based simulation setup is created, wherein the implementation of the proposed solution is performed and tested in Cooja simulator. The analysis depicts that the proposed solution consumes less energy for enciphering data, provides security against possible attacks like spoofing attack and brute-force attack, and has tiny code footprint. It is contemplated that the proposed security solution can be used in protecting message confidentiality in the Internet of things environment and other low-power wireless networks.

Keywords Message Queuing Telemetry Transport (MQTT) · Internet of things (IoT) · IoT security · Mosquito

1 Introduction

Recent developments in communication and information technology have led to the rapid growth of the Internet of things (IoT). The number of smart devices connected to the Internet is estimated to be around 20.4 billion by 2020 [1]. IoT finds its applications in immense areas that include supply chain management, smart transportation, e-health, and smart agriculture [2]. In IoT context, users are more inquisitive in the content of the message being shared rather than knowing the source of message [3]. This content-centric data sharing leads to the usage of publisher–subscriber paradigm which decouples sender and receiver sides in terms of time, space, and synchronization [4]. Among many publish–subscribe architecture-based protocols, MQTT is lightweight, simple, and easy to implement application layer protocol. However,

A. Bashir (✉) · A. H. Mir
Department of Electronics and Communication Engineering, National Institute of Technology Srinagar, Jammu and Kashmir, India

V. Janyani et al. (eds.), *Optical and Wireless Technologies*, Lecture Notes in Electrical Engineering 648, https://doi.org/10.1007/978-981-15-2926-9_7

MQTT has inadequate security and relies on the underlying transport layer for security measures; for example, it uses transport layer security (TLS) which is highly computational, therefore unsuitable for resource-constraint IoT nodes.

In this paper, a security mechanism is proposed that safeguards MQTT communications from adversaries in an energy-efficient manner. In our proposed solution, MQTT payload is encrypted using dynamically generated key at trusted system, and then, the encrypted payload is sent to the broker which later relies upon it to the right subscriber(s). The main benefit of MQTT payload enciphering is that it imparts end-to-end encryption in environments where TLS is not suitable [4]. The idea is based on using less computational cipher so that the limited available energy at IoT nodes will last for long that keeps nodes operational for a longer time. Contrasting other security approaches that use existing network security protocols, our proposed solution takes due to the consideration of constraint resources of IoT devices.

The core components and methods of the proposed security scheme include the following:

1.1 Message Queue Telemetry Transport (MQTT)

MQTT is a simple, lightweight, open publish–subscribe architecture-based application layer protocol for resource-constricted environments like Internet of things domain. Publish–subscribe architecture is based on "push" architecture where network nodes push their data to other nodes and varies from a conventional client–server architecture which is regarded as "pull" architecture where nodes (clients) have to pull information from other nodes (servers). In publish–subscribe architecture, publishing client publishes a message on a specific topic to the broker which then forwards it to all the clients (subscribers) who have subscribed for this specific topic. This architecture decouples clients in terms of space, time, and synchronization, which means that publisher and subscriber do not know about the existence of each other [4]. Figure 1 shows MQTT publish–subscribe architecture scenario where a client publishes temperature on "temp" topic to the broker which relays this topic information to the subscriber(s) of "temp" topic.

Researching about default security elements in MQTT, it is found that MQTT provides authentication of connected clients in terms of username/password authentication but does not provide encryption to communicating messages to achieve data confidentiality.

1.2 PCG-Rand

PCG-Rand is a cryptographically secure random number generator which is simple, fast, and statistically efficient. It is easy to use, having a difficult predictability rate,

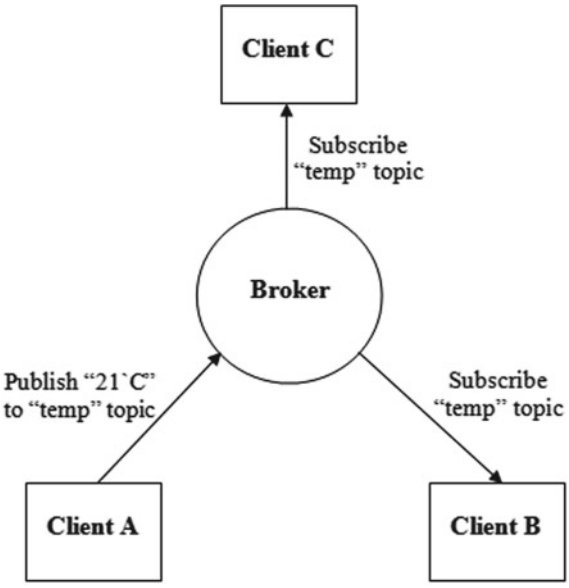

Fig. 1 MQTT publish–subscribe architecture

and has a small code size. PCG-rand algorithm is applicable to a variety of bit streams that includes 64 and 128 bits that provide 32- and 64-bit outputs [5].

2 Related Work

Researchers have proposed new cryptographic algorithms such as chaotic map, skipjack and corrected tiny encryption algorithm for low-power wireless networks like the Internet of things as given in [6]. These algorithms were evaluated against conventional encryption algorithms such as advanced encryption standard (AES) and RC5. The analysis shows that these new algorithms bring approximately a similar level of computational overhead as that of AES and RC5. For instance, AES-128 and skipjack algorithm were compared and it is found that skipjack has 26% of the computational cost of AES algorithm and provides less security than AES.

In [7], authors have used attribute-based encryption (ABE) security scheme to enable security components for publish–subscribe (Pub-Sub)-based IoT devices. Sensed messages are enciphered using the AES algorithm, and the cryptographic key is itself enciphered using ABE protocol. IoT devices, being resource constricted devices, generate fewer data bits thus enciphering fewer data bits with AES and ABE security protocols drains off the available node energy quickly, therefore making the entire network nonfunctional. Pal et al. [8] used predicate-based encryption and CP-ABE to safeguard published data and the privacy of the subscriber's topics.

Authors in [9] proposed a security scheme for IoT where a node-specific static master key is stored in network nodes. This stored fixed key is made dynamic using a challenge-based shuffling algorithm at the client and server sides. This dynamic key is used to encipher messages and is valid for a given session but is exposed for ample time in which the assailant can decrypt shared data which can bring overall network compromisation. Park and Kang [10] presented DTLS as a security protocol for IoT that is placed between the application layer and the transport layer. DTLS is based on RSA and is developed for low-power networks. The analysis of this scheme depicts that DTLS adds confidentiality, integrity, and authentication, but consumes significant device energy and induces overheads.

A lattice-based cryptosystem "NTRUEncrypt" is known to be an alternative of RSA cryptosystem. Gaubatz et al. [11] performed the comparative analysis of NTRUEncrypt, ECC, and Rabin's scheme that were candidate security protocols for resource-constraint environments like wireless sensor networks and the Internet of things. The results of comparative analysis depict that NTRUEncrypt consumes less average power in comparison to the other two protocols. However, it requires large-sized messages that might lead to packet fragmentation and increase the packet re-transmission rate due to communication errors.

It is concluded from the literature survey that most of the recently proposed security solutions for IoT are actually tiny versions of existing highly computational conventional security algorithms with a high percentage of computational cost still present in them, hence making them unacceptable for IoT applications. Therefore, new lightweight security schemes are to be designed for IoT systems which is the main focus of the work presented in this paper.

3 Methodology

In this section, we discuss the proposed security mechanism that safeguards MQTT payload of sensed data in IoT domain. Our proposed solution assumes that there is a trusted system (TS) that generate IDs and cryptographic keys for publishers and subscribers. TS, being a legitimate entity, is trusted by all nodes in a particular IoT application domain. Trusted system is responsible for managing trust associations among IoT nodes which is done by sharing a pre-shared secret (*PSS*) during an initial registration phase. PSS is shared between a trusted system and IoT nodes during the registration phase using a secure bootstrapping (for instance, a technique presented in [12]). The proposed solution uses a cryptographically secure random number generator (CSRNG) algorithm to generate cryptographic keys and asymmetric cryptosystem for encrypting MQTT payload.

Our solution uses PCG-Rand as CSRNG because of its difficult predictability rate, excellent statistical quality, and efficiency in terms of time and code space [5]. In our solution, cryptographic keys are generated and valid for each communication session. The overall flow of our proposed system is shown in Fig. 2.

Our proposed solution consists of three phases.

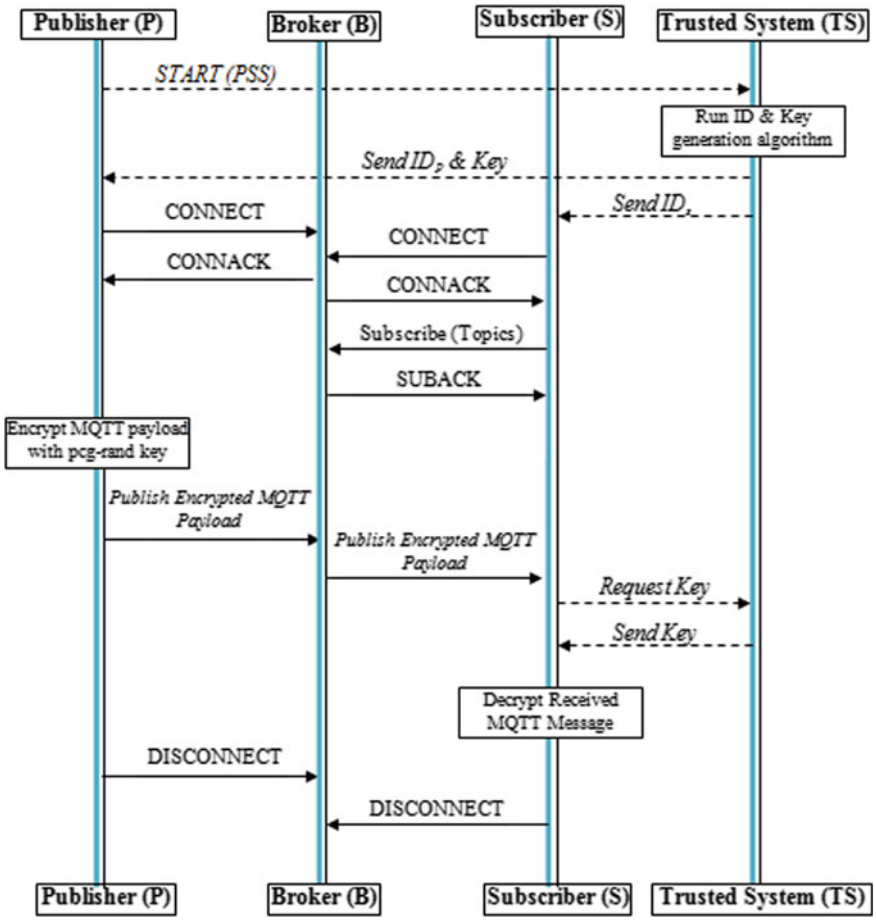

Fig. 2 Message flow diagram of the proposed system

3.1 Key Generation and Distribution Phase

- The publisher sends a "START" message encrypted with PSS to inform TS to run the ID and key generation algorithm.
- TS generates IDs and cryptographic keys for every MQTT client.
- TS sends IDs to publishing client encrypted with PSS that is shared between TS and publisher in advance.
- TS sends the encryption key to the publisher encrypted with IDs.
- Every participation client node sends CONNECT packet to the MQTT broker.

3.2 Encryption and Publish Phase

- Publisher encrypts MQTT payload using the derived key from phase 1 above.
- A simple logical invertible operation (XOR) is used as an encryption operation.
- The publisher publishes an encrypted message on a particular topic to MQTT broker. In our implementation, we have used mosquito [13] as an MQTT broker.

3.3 Decryption Phase

- Subscriber requests TS to send cryptographic key.
- Subscriber runs decryption algorithm to decipher message received from MQTT broker.

4 Implementation and Evaluation

4.1 Simulation Setup

Implementation of the proposed system is performed in the Contiki Operating System which is an open-source operating system for low-power wireless networks [14]. The simulation setup consists of a trusted system (authority node), publishers, MQTT broker (mosquito) [13], and subscribers. We have implemented MQTT-SN (sensor networks) [15] which is a lightweight library of MQTT for resource-constraint nodes. We have evaluated the proposed security scheme in terms of energy consumption, security, and performance analysis. The simulation setup is shown in Fig. 3.

4.2 Performance Analysis

Energy Consumption: Since IoT consists of resource constraint nodes which imply that IoT devices have limited resources in terms of computational power, storage capacity and often run on irreplaceable batteries. Therefore, it is important to pay attention to using the available limited energy efficiently. In order to find out the energy consumption of our security system, powertrace tool [16] of Contiki Operating System is used which computes system energy consumption E_{system} from the energy model described as in [17]

$$E_{\text{System}} = \sum_{m,n} P_{m,n} T_{m,n} \tag{1}$$

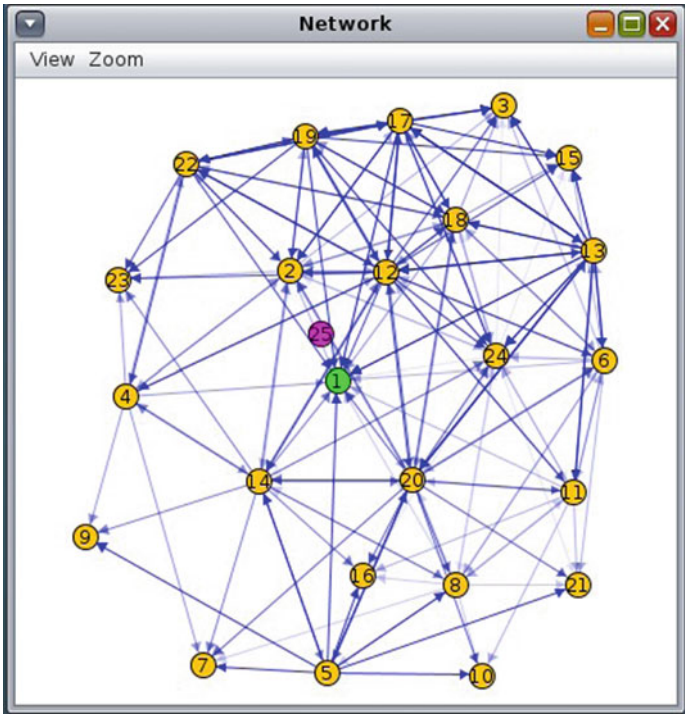

Fig. 3 Simulation network

where $P_{m,n}$ is the power consumption of component 'm' in power state 'n' and $T_{m,n}$ is the time duration of component 'm' in state 'n'. In this model, the components include CPU, flash memory, radio, and sensors, and the power states include transmitting and receiving mode for radio, active and sleep (low power mode) for CPU, memory read/write modes for flash memory. Using Eq. (1) and the values obtained from powertrace tool, we have calculated the energy consumption of our proposed system and compared that with unencrypted communications for the same simulation setup which is shown in Fig. 4.

From the plot in Fig. 4, it is analyzed that the energy consumption of the proposed security system is close enough to the system without security in place. Therefore, it can be concluded that including the proposed security system in IoT nodes will not affect their lifetime by a substantial amount.

Storage Requirements: The implementation of our method consumes approximately 26 KB which is a suitable code size for IoT devices. For instance, Zolertia z1 motes have 128 KB memory [18] which is sufficient enough for the code footprint of our implemented security mechanism.

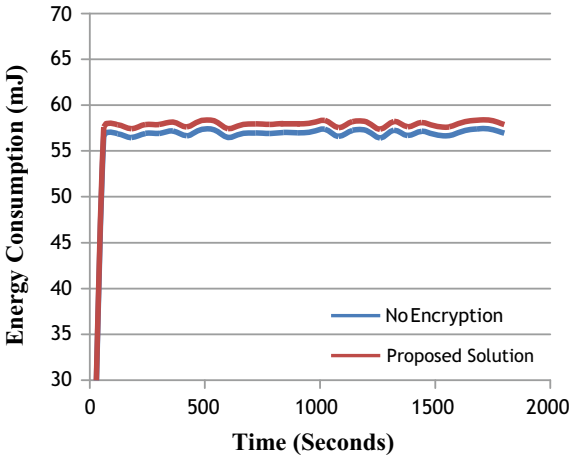

Fig. 4 Energy consumption comparison

4.3 Security Analysis

Brute-force attack: A key size of 64 bits is generated using pcg-rand which is used to encrypt data. Therefore, the number of possible values for key "k" is

$$\text{Possible values for key, } N = 2^{64} \times \left(\frac{1}{2}\right)$$

$$\text{i.e., } N = 1.84 * 10^{19} * \left(\frac{1}{2}\right)$$

The value of "N" indicates the number of conjectures an assailant has to make to find the value of cryptographic key using a brute-force algorithm. Therefore, the probability that an adversary conjectures the correct value of key is

$$\text{Probability to guess the correct key, } P = \frac{1}{N}$$

$$\text{i.e., } P = \frac{1}{1.84 * 10^{19} * \left(\frac{1}{2}\right)}$$

which is very small, therefore making the overall system resilient to brute-force attack. The method used to calculate the probability of conjecturing the value of a key by an attacker is the same as used by [19].

Spoofing Attack: A spoofing attack is a type of active attack in which unauthorized node masquerades as a legitimate node that leads to network compromisation. The proposed system is resilient to a spoofing attack. In our proposed system, if an attacker pretends to be TS, it has access to all information about session IDs and cryptographic keys by which it can decipher all communicating messages among nodes. Our proposed system counters this attack by using a pre-shared secret (PSS)

that is set up during the bootstrapping phase. Publisher that has data to be transmitted encrypts "*START*" message with PSS before forwarding it to TS for obtaining the encryption key. The illegitimate server cannot decipher "*START*" message as it does not have *PSS*, therefore unable to decipher the encrypted published messages.

5 Conclusion

Internet of things brings numerous threats because of the constraint resources of its nodes. This, in turn, hinders the growth and development of IoT at its full pace because there is no public confidence that it will not create trouble for user privacy. Most of the security protocols proposed for IoT in the literature are tiny versions of conventional complex protocols which are still complex for miniature IoT devices. Among various messaging protocols for IoT, MQTT is widely used protocol being simple, easy to implement and having small code footprint, but it lacks default security features.

In this paper, we enabled data confidentiality to MQTT payload. A lightweight cryptographic mechanism is implemented to secure confidential messages exchanged among IoT nodes. The proposed system is resilient to likely attacks such as brute-force attack and spoofing attack and requires less memory space. Comparative analysis for energy consumption shows an increase of 2.71% node energy consumption in our proposed system than in unencrypted mode which is affordable for IoT nodes. Thus, our security scheme provides strong message confidentiality and is memory and energy efficient which makes it suitable for the Internet of things nodes. The future work includes encryption using lightweight algorithms like PRESENT [20] and HIGHT [21] instead of XOR operation.

References

1. Gartner, http://www.gartner.com/newsroom/id/3598917, last accessed 2017/12/23
2. Khan R, Khan SU, Zaheer R (2012) Future internet: the internet of things architecture, possible applications and key challenges. In: Proceedings of the international conference on frontiers of information technology (FIT). IEEE, India, pp 257–260
3. Ion M (2013) Security of publish/subscribe systems. Ph.D. thesis, University of Trento. http://eprints-phd.biblio.unitn.it/993/
4. Introducing the MQTT Security Fundamentals. https://www.hivemq.com/blog/introducing-the-mqtt-security-fundamentals, last accessed 2018/03/15
5. O'Neill ME (2014) PCG: a family of simple fast space-efficient statistically good algorithm for random number generation. HMC-CS-2014-0905
6. Biswas K, Muthukkumarasamy V, Wu XW, Singh K (2016) Performance evaluation of block ciphers for wireless sensor networks. In: Choudhary R et al (eds) Advanced computing and communication technologies. Springer, Singapore, pp 443–452
7. Wang X, Zhang J, Schooler E, Ion M (2014) Performance evaluation of attribute-based encryption: toward data privacy in the IoT. In: Proceedings of international conference on communications (ICC), Sydney, NSW. IEEE, pp 725–730

8. Pal P, Lauer G, Khoury J, Hoff N, Loyall J (2012) P3S: a privacy-preserving publish-subscribe middleware. In: Springer lecture notes in computer science book series (LNCS), vol 7662
9. Mishra S (2015) Network security protocol for constrained devices in the internet of things. IEEE INDICON
10. Park J, Kang N (2014) Lightweight secure communication for CoAP-enabled internet of things using delegated DTLS handshake. In: Proceedings of international conference on information and communication technology convergence (ICTC), Busan. IEEE, pp 28–33
11. Gaubatz G, Kaps JP, Sunar B (2005) State-of-the-art in ultra-low power public key cryptography for wireless sensor networks. In: Proceedings of 3rd IEEE international conference on pervasive computing and communications workshop (PERCOMW)
12. Kang N, Oh S, Yoon S (2014) Secure initial-key reconfiguration for resource-constrained devices. IETF draft-kang-core-secure-reconfiguration 01
13. Eclipse Mosquitto Broker, https://mosquitto.org
14. Contiki Operating System, http://www.contiki-os.org/
15. Andy S-C, Hong LT (2013) MQTT for sensor networks (MQTT-SN) protocol specification version 1.2, International Business Machines Corporation (IBM). https://stanford-clark.com
16. Powertrace Tool, https://github.com/contiki-os/contiki/tree/master/apps/powertrace, (2015)
17. Dunkels A, Erikson J, Finne N, Tsiftes N (2011) Powertrace: network-level power profiling for low-power wireless networks. SICS Technical Report T2011:05, ISSN 1100-3154
18. Zolertia Mote. https://zolertia.io/product/re-mote
19. Bashir A, Mir AH (2017) Securing publish-subscribe services with dynamic security protocol in MQTT enabled internet of things. Int J Secur Its Appl 11(11):53–66
20. Bogdanov A et al (2007) PRESENT: an ultra-lightweight block cipher. In: Proceeding of workshop cryptographic hardware and embedded systems (CHES 07), LNCS 4727, Springer, pp 450–466
21. Hong D et al (2006) HIGHT: a new block cipher suitable for low resource device. In: Proceedings of CHES 2006, LNCS, vol 4249, pp 4659. Springer, Berlin

Realization of Low-Cost Field-Deployable He–Ne Laser-Based Sensor System to Check the Quality of Food from Adulteration

Manish Kumar and Sanjeev Kumar Raghuwanshi

Abstract To check the food from adulteration, it is always a challenging task for the scientist and engineers. In this paper, a relatively new method is proposed to check food from poisonous or deleterious substances which may cause injuries to health have been discussed and described. Both principles for understanding and mathematical relation are emphasized. The experimental observation with MATLAB simulation gives helium–neon laser, a powerful option for material characterization in a sensor system. We have realized the optical response of different samples (sugar, salt, mustard oil, coconut oil, almond oil) with respect to helium–neon laser power intensity. When helium–neon (He–Ne) laser light beam passes through different samples, it gives different power reading in power meter giving the relation between absorptivity of different sample concentrations. When concentrations of samples increase or added impurities, observed transmittance decreases and also finds the transmittance decrease with the increase in distance. The mathematical formula has been developed for concentration relation with solution and distance.

Keywords He–Ne laser · Food adulteration · A chemical sensor · Absorption · Food contamination

1 Introduction

The problem of food adulteration is always challenged to scientist and engineers as old as the food processing industry. The identification of food adulteration or contamination is a major issue to society. Nowadays, we are in dilemma regarding purity, thus diagnoses of every foodstuff are very essential. The modern contamination consequences degraded edible oil, milk product [1], rice pulses, meat, vegetable, fruits, and pesticide in a soft drink. The media, in 1998, give attention when petroleum product adulterates edible mustard. It results in oil poisoning in India that gives several deaths and illnesses to people. It needs advanced technology with

M. Kumar · S. K. Raghuwanshi (✉)
Department of Electronics Engineering, Indian Institute of Technology (Indian School of Mines), Dhanbad, Jharkhand, India
e-mail: sanjeevrus77@iitism.ac.in

V. Janyani et al. (eds.), *Optical and Wireless Technologies*, Lecture Notes in Electrical Engineering 648, https://doi.org/10.1007/978-981-15-2926-9_8

qualitative detection techniques for food and feedstuffs [2]. There is a different technique to characterize food products and to detect their possible adulteration. In 2002, Christophe Cordella illustrated previous existing detection technique as microscopic analysis; HPLC; GC, GC-(MS, FTIR); UV–visible spectrophotometry; AAS/AES, ICP-(AES, MS); IRMS, GC-IRMS, GC-C-IRMS; DSC; IR, mid-IR, and NMR [3]. In 2010, food characterization is done on Fourier transform infrared (FTIR) spectroscopy based on reflectance [4]. He–Ne laser has an operational wavelength of 632.8 nm and lies in the red portion of the visible spectrum. When a laser beam passes through a material with finite optical absorption, the heat generated increases temperature, which changes the index of refraction, which in turn affects the optical beam [5]. The principle of absorption and optical power-based He–Ne laser system has been analyzed with the feature of self-check and auto-calibration [6]. Different samples of sugar and salt are mixed in water of fixed quantity, and with the increase of concentration the decrease in power is observed with temperature variation [7]. Again, different samples like mustard oil, coconut oil, etc., are taken and kept them under observation. The surface plasmon resonance-based sensor has been used for high-sensitive chemical detection like pesticide in feedstuffs but it is not economical. There is a need for an economical technique that can identify the adulteration in food.

2 Mathematical Theory Related to Absorption, Transmittance, Reflectance

When a monochromatic light passed through a liquid, then some light will be absorbed (intensity decreases) by the liquid. The absorption of liquid also depends on the transparency of material as an incident angle as shown in Fig. 1. The absorption of the light beam in adjacent material can be described by Lambert and Beer's

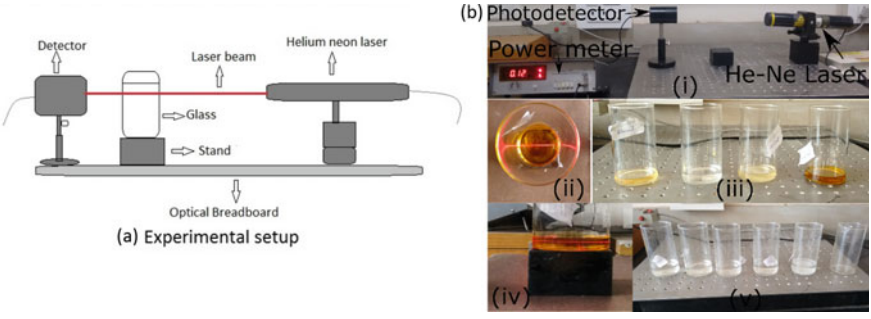

Fig. 1 **a** Layout of experimental setup detector, glass, stand, He–Ne laser, optical breadboard; **b** (i) Experimental setup to measure power transmitted through air, (ii) Laser passing through coconut oil, (iii) almond, sugar solution, coconut, mustard oil, (iv) Laser passing through coconut oil, (v) Samples containing different amount of salt solution

law, $I = I_0 \exp^{(-kct)}$ where I_0 is the incident intensity, I is the transmitted intensity, c is the concentration, t is the material thickness (light path length), and k is constant. Absorption of radiation is described by Beer's law, which states that equal thicknesses of an absorbing material absorb equal fractions of the power incident on them. The transmission of light in any medium is expressed as the ratio between the transmitted light to incident light [8]. $T = I/I_0$ shows transitivity where I_0 is the incident intensity, and I is the transmitted intensity. The light incident upon a surface or medium undergoes transmission, reflection, and absorption. $A = 2 - \log T\%$, where $T\%$ is the percent transmittance, it can be used to calculate absorbency from percentage transmittance data. Beer's law is given by $A = \alpha ct$ where α is the molar absorptivity with units of $\mathrm{L\,mol^{-1}\,cm^{-1}}$, t is the path length (centimeters) of the sample present in a container, and c is the concentration of the sample in solution, expressed in $\mathrm{mol\,L^{-1}}$. As absorption shown in $A = \alpha ct$ is directly proportional with the concentration in Beer's law, it can be possible to determine an unknown liquid concentration (Adulterated Food) after knowing the absorptivity and compare it with standard liquid absorptive known concentration.

$$A_{\mathrm{sa}}/A_{\mathrm{st}} = C_{\mathrm{sa}}/C_{\mathrm{st}} \tag{1}$$

$$C_{\mathrm{sa}} = A_{\mathrm{sa}}/(A_{\mathrm{st}} * C_{\mathrm{st}}) \tag{2}$$

A_{sa} is the absorptivity of a sample, A_{st} is the standard liquid absorptive, C_{sa} is the sample concentration, and C_{st} is the standard liquid concentration. Equations (1) and (2) show the relation of known and unknown concentration of liquid. These equations can be used to find the adulteration or contamination in foodstuff.

3 Proposed Layout and Experimental Setup

The components of the proposed experiment are shown in Fig. 1. The required components for observation are as follows: Helium-Neon Laser Source—The He–Ne laser has an operational wavelength of 632.8 nm. The maximum power is of 2 mW; Laser Power Meter (Falcon Model 147)—Laser power meter is designed to measure in the range 0.1 μW–2 mW; Photo Detector (sensor head)—The combined sensor head consisted of silicon photoelectronic sensor which converts photon to electrical unit; Optical Breadboard—It is vibration free.

4 Experimental Arrangements and Observation

The experimental setup is shown in Fig. 1. The detector head is kept in alignment with the helium–neon laser source. Helium–neon laser is rotated and adjusted to

receive power on detector so that the incident angle should be approximately zero. The sample is then placed in the glass which is kept in between the helium–neon laser and detector. Initially, the power measurement was taken in the air at a different distance. Next, the empty glass is kept in between the laser and detector. The power is detected and recorded. Let the power recorded in the air at 50 cm distance be P_a and power recorded with glass in the air be P_1. So, when the power recorded by putting glass in between is subtracted from the power recorded in air, the actual power absorbed by the glass can be found out. Thus, the power absorbed by glass be P_g,

$$P_g = P_a - P_1 \tag{3}$$

Similarly, when the glass is filled with a particular amount of water and at 50 cm distance, the power recorded be P_2, then the power absorbed by water is given by

$$P_w = P_a - P_g - P_2 \tag{4}$$

After this, some amount of salt is added to the water, and again the helium–neon laser is adjusted to record the power at 50 cm distance. The output power recorded is P_3. Then, the power absorbed by the salt of added quantity be given by

$$P_s = P_a - P_g - P_w - P_3 \tag{5}$$

The reading was recorded with different samples also like almond oil, coconut oil, and mustard oil. A graph is plotted with the power and distance to analyze their behavior with increasing distance. Equations (3–5) show the different relationships that are useful to calculate the number of feedstuffs in the proposed experiment.

Figure 2 shows the power variation with the concentration of sugar solution. The corresponding polynomial equation has been observed through experimental observation. Polynomial obtained at $d = 60$ cm, $F(x) = p_1x^2 + p_2x + p_3$ where

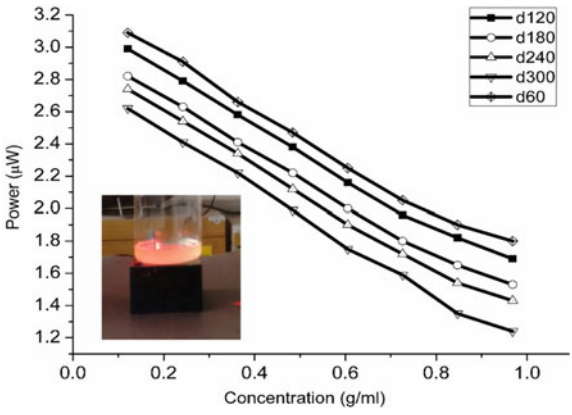

Fig. 2 Sugar solution in water at a different concentration at a different distance

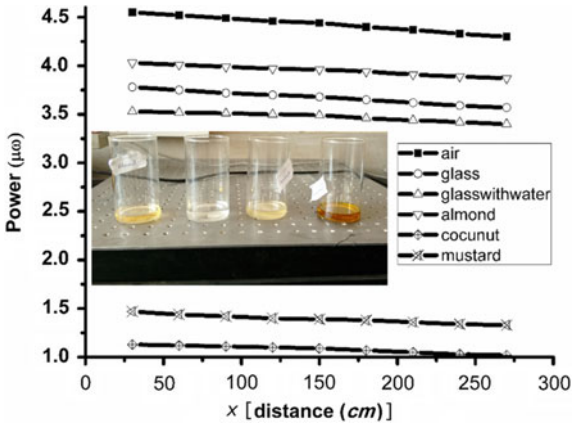

Fig. 3 Phenomena on material almond oil with a distance of 30 cm

$p_1 = 0.1262(0.03521, 0.2171)$, $p_2 = -1.055(-1.261, -0.8486)$,$p_3 = 2.314(2.215, 2.414)$.

Figure 3 shows the salt solution in water power measurement where g= glass, w = water, p_1 = power of the solution of water and 3.86 g of salt, p_2 = power of solution of water and 7.72 g of salt, p_3 = power of the solution of water and 11.58 g of salt, p_4 = power of solution for water and 15.44 g of salt, and p_5 = power of the solution of water and 19.3 g of salt.

5 Data Analysis for Adulterated Food

Following specifications of apparatus have been used in this experimental work (a) distance travelled in a sample by laser light = 5.68 cm; (b) thickness of glass (total length travelled in glass) = 0.4 cm; (c) volume of water taken for making a sugar solution and salt solution = 49.02 and 70.04 ml. The power absorbed in the glass is more than the power absorbed in air. When water is put into the glass, then power received by the detector decreases showing power is absorbed by water. The power obtained in coconut oil is least, or we can say that its molecule content scatters lighter than water molecules. Mustard oil increases the power received in the detector because mustard oil helps in focusing the beam and thus giving more power in the output. Almond oil transmits more power than coconut oil and mustard oil.

Figure 4 shows that the power observed in the power meter decreases with an increase in distance as well as an increase in salt concentration. In experimental observation, when the solution becomes saturated and no more salt is able to get dissolved in the solution and transmission has no noticeable change, if further salt is added after saturation.

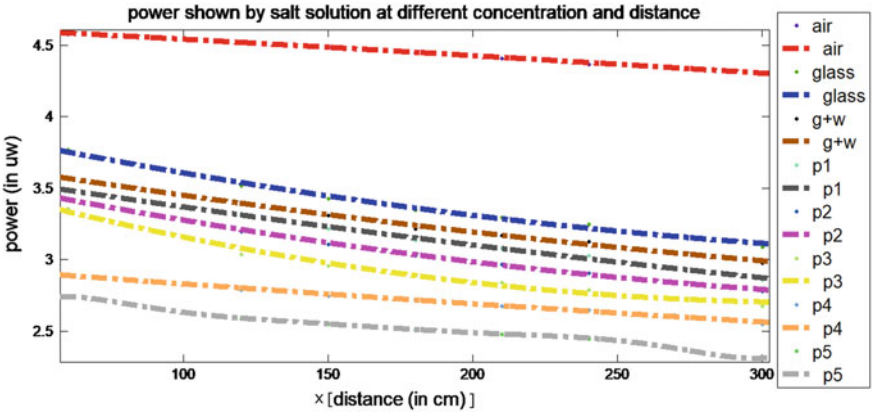

Fig. 4 Salt solution in water power measurement at a different distance

Figure 5 shows a relationship between the concentration and power at a fixed distance. Air has the highest power transmission; the glass has lower power transmission than air but greater than the salt solution. The polynomial obtained is a two degree which can be used to get the power reading of the salt solution at a particular distance with different concentration. Using all these, data graphs are plotted and polynomials are at distance = 30 cm, $F(x) = p_1x^2 + p_2x + p_3$, where $p_1 = -12.66(-62.58, 37.25)$, $p_2 = 0.2957(-16.26, 16.85)$, $p_3 = 2.526(1.335, 3.717)$. The response of sensors has been mathematically expressed by higher-order polynomials. The absorption coefficient can be correlated with respect to the substance under consideration.

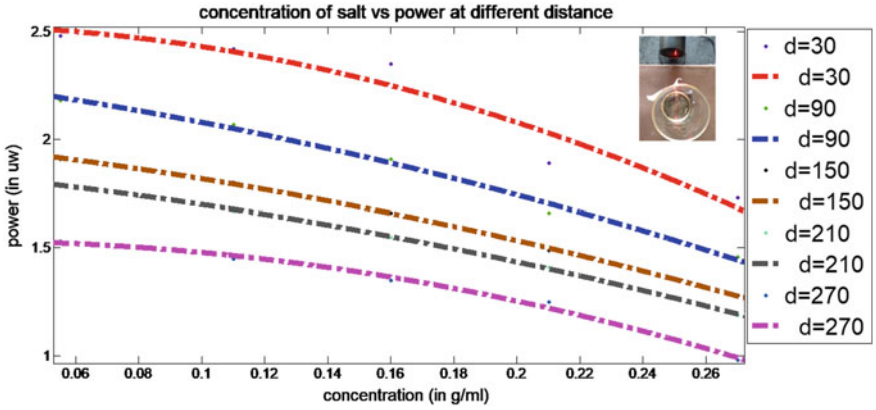

Fig. 5 Power obtained when the distance of 30 cm

6 Conclusion

Paper provides a very simple method which is based on working of He–Ne laser at a wavelength of 633 nm to check the quality of food from adulteration. Various edible oils have been analyzed by using the proposed technique to estimate the relationship of absorbed power by different samples. The rule of thumb has been set up by deriving absorption/transmittance of light polynomial expression for different samples. Almond oil shows more transmittance than coconut oil and mustard oil. Hence, the transmittance relationship between these oils can be given as almond oil > mustard oil > coconut oil. The power transmitted by sugar solution and salt solution decreases with increase in the distance and concentration. The result matches with the obtained mathematical formula given in the paper for salt and sugar solution. The concentration can be obtained from using polynomials of unknown samples. Thus, a sensor can be made using these polynomial equation relations. Similarly, the sensors would be able to detect the sugar concentration, salt concentration, and edible oil impurities. Using all of these data and analyzing, a standard has been formed which can be useful for the detection of the particular food sample at unknown concentration and adulteration.

Acknowledgements This work was financially supported by the project title "Design and Development of Deployable Thin Film based Evanescent Field Sensor to Check the Quality of food from Adulteration" funded by Council of Scientific and Industrial Research (CSIR) India with Sanction No. 70(0077)/19/EMR-II - dated: 17/07/2019 and IIT(ISM) Project No. CSIR (32)/2019-2020/663/ECE. This project is sponsored by Council of Scientific and Industrial Research (CSIR)-Central Scientific Instruments Organisation (CSIO) Chandigarh-160030. The authors would like to thank Dr. Umesh Kumar Tiwari, Principal Scientist CSIR-CSIO Sector 30, Chandigarh-160030 and Dr. Sudipta Sarkar pal, Principal Scientist, Advanced Material and Sensors, CSIR-CSIO Sector 30, Chandigarh-160030 for providing necessary technical and experimental support to develop the HE-NE laser based sensor system to Check the Quality of food from Adulteration.

Conflict of Interest Authors do not have any conflict of interest to this work.

References

1. de Souza Ribeiro L, Gentilin FA, de Franca JA, de Souza Madureira Felicio AL, de M. Franca MB (2016 July) Development of a hardware platform for detection of milk adulteration based on near-infrared diffuse reflection. IEEE Trans Instrum Meas 65(7):1698–1706
2. Mosig JR, Besson J-CE, Gex-Fabry M, Gardiol FE (1981 Mar) Reflection of an open-ended coaxial line and application to nondestructive measurement of materials. IEEE Trans Instrument Meas IM-30(1):46–51
3. Cordella C, Moussa I, Martel A-C, Sbirrazzuoli N, Lizzani-Cuvelier L (2002 Mar) Recent developments in food characterization and adulteration detection: technique-oriented perspectives. J Agric Food Chem 50(7):1751–1764
4. Rodriguez-Saona L, Allendorf M (2011) Use of FTIR for rapid authentication and detection of adulteration of food. Ann Rev Food Sci Technol 2(1):467–483

5. Whinnery JR (1974) Laser measurement of optical absorption in liquids. Acc Chem Res 7(7):225–231
6. Varpula T, Seppa H, Saari J-M (1989) Optical power calibrator based on a stabilized green he-ne laser and a cryogenic absolute radiometer. IEEE Trans Instrum Meas 38(2):558–564
7. Firestone D (2013) Physical and chemical characteristics of oils, fats, and waxes. AOCS Press, Urbana, Illinois
8. Tissue BM (2013 July) Basics of analytical chemistry and chemical equilibria. Wiley

Experimental Evaluation of Reliable Underwater Optical Communication in the Presence of Turbulence and Blockage

Ramavath Prasad Naik, Udupi Shripathi Acharya and Nitin Kumar Suyan

Abstract In this paper, we have evaluated the performance of underwater wireless optical communication (UWOC) link in the presence of turbulence, air bubbles and blockage of 2.5-m-length channel. To mitigate the effects of turbulence and air bubbles, we have employed channel coding and receiver diversity combining techniques. Blocking causes the burst errors, and to mitigate the effect of blocking, we have employed interleaved channel-coded receiver diversity combining technique. Bit error rate (BER) performance of UWOC system evolved, and improvement in BER is achieved by employing channel codes, receiver diversity combining and interleaved channel codes.

Keywords Underwater wireless optical communication (UWOC) · Turbulence · Blockage · Channel coding · Receiver diversity combining

1 Introduction

In recent years, interest in UWOC system and its possible applications has grown enormously for strategic and commercial use. Communication through underwater channels has more challenges than free-space channels. If these challenges are suitably addressed, UWOC has the potential to provide high speed as well reliable data transmission between underwater platforms for short-distance links. While acoustic signals are well suited for data transmission over long links, the data rate is limited. By employing optical transmission, we can exceed a data rate of one Gbps (gigabits per second) over short-distance links. Main challenges of the UWOC system are absorption and scattering of the optical signal, which can cause loss of data. Absorption and scattering are caused due to the presence of turbidity and salinity in the water channel. By use of wavelengths in the range of 450–520 nm (blue and green) LED/LASER sources, absorption and scattering in the water medium can be

R. Prasad Naik (✉) · U. Shripathi Acharya
National Institute of Technology Karnataka, Surathkal, Karnataka 575025, India

N. K. Suyan
Govt. Engineering College, Jhalawar, Rajasthan 326023, India

V. Janyani et al. (eds.), *Optical and Wireless Technologies*, Lecture Notes in Electrical Engineering 648, https://doi.org/10.1007/978-981-15-2926-9_9

minimised and the reliability of communication can be enhanced [1, 2]. Turbulence, air bubbles and signal blockage in the water medium can degrade the system performance. To mitigate the effects of turbulence and blockage, we have employed channel coding, interleaved coding and receiver diversity combining techniques.

The research work on UWOC has been growing enormously due to its higher transmission speeds and vast availability of electromagnetic spectrum. Most of the research works are focused on the enhancement of UWOC system performance in the presence of turbulence by employing channel coding and receiver diversity combining techniques. In [2], UWOC system with BCH (Bose–Chaudhuri–Hocquenghem) (31, 11) code and 31×31 interleaved length (31, 11) BCH code was employed to mitigate the effects of turbulence and blockage. Optical communication through the turbid underwater channels and various receiver diversity combining techniques to enhance the UWOC system performance in different turbid and turbulent environments is demonstrated [3]. Underwater optical channel properties in the presence of varying water characteristics like turbidity, salinity and temperature are presented in [4]. In [5], the performance of UWOC with clear and harbour water in the presence of different populations of air bubble presented.

This paper describes the performance of an UWOC system through a channel incorporating turbulence and blockage at turbidity of 10 NTU (Nephelometric turbidity units) and salinity of 14.28 ppt (parts per thousand). In addition, a BCH (63, 30) and 63×63 length block interleaver followed by receiver diversity combining (equal gain combining (EGC)) technique have been employed to mitigate the effects of turbulence and burst errors (created by blockage) in the underwater channel. The UWOC set-up is designed to work at a speed of 120 Kbps. To best of our knowledge, a BCH code with interleaver and diversity reception has not been employed in experimental UWOC studies so far.

The remaining part of the paper is organised as follows: Sect. 2 represents the system model, the experimental set-up is presented in Sect. 3. Section 4 describes channel coding, interleaved coding and receiver diversity combining techniques. Experimental BER results and description are given in Sect. 5, and then conclusion is given in Sect. 6.

2 System Model

Stream of text data is converted into American Standard Code for Information Interchange (ASCII) and then into binary data. This binary data is On-Off Keying (OOK), modulated with the 470 nm blue light-emitting diode (LED) and then transmitted through the turbulent and blockage water channel. At the receiver, photo-detector detects the changes in the intensity falls on them and delivers current, and using transimpedance amplifier, equivalent voltages of current are obtained. These voltages are converted into a binary using a comparator with a suitable threshold. Finally, binary data is converted back into text data.

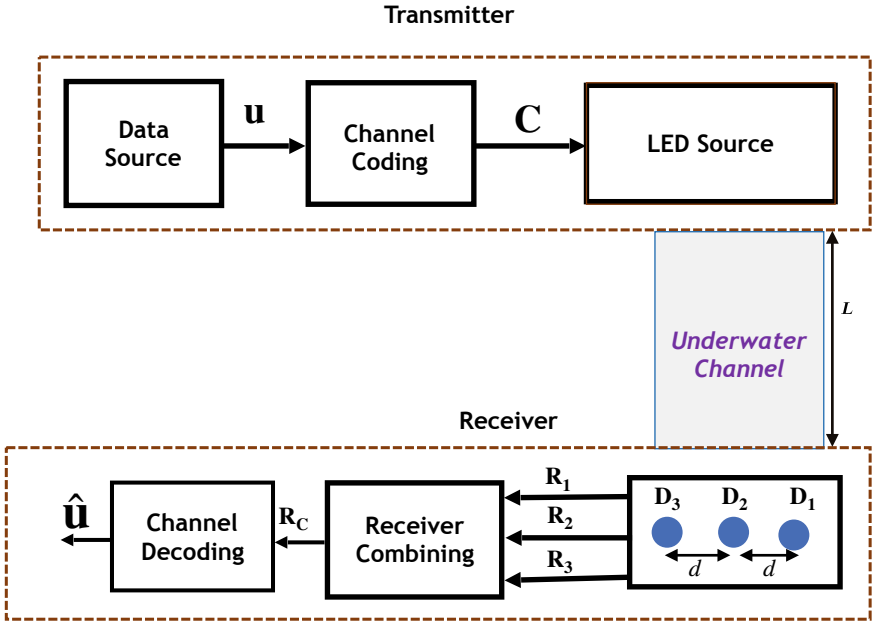

Fig. 1 Block diagram of UWOC system

Figure 1 shows the block diagram of UWOC system channel coding and receiver diversity combining. Here, binary data **u** is channel coded as **C** and then On-Off Keying modulated with 470 nm LED source. This optical data transmitted through the underwater channel of length $L = 2.5$ m, and a bunch of photo-detectors D_1, D_2, D_3 are used at the receiver; these detectors are separated by $d = 3$ cm from each other photo-detector and then followed by channel decoding $\hat{\mathbf{u}}$.

From Fig. 1, we have differentiated UWOC system into three different blocks which are as follows.

2.1 Transmitter

Here we have converted text data into binary as **u**, and then sent to channel coding and then modulated with LED source. We have used $LXML\text{-}PB01\text{-}0040$ blue LED of 500 mW power capacity operating at $\lambda = 470$ nm for transmitting binary data. The Arduino board can drive a maximum current of 400 mA in an external load. We have driven the LED directly from the Arduino board and have not employed any additional driver circuits.

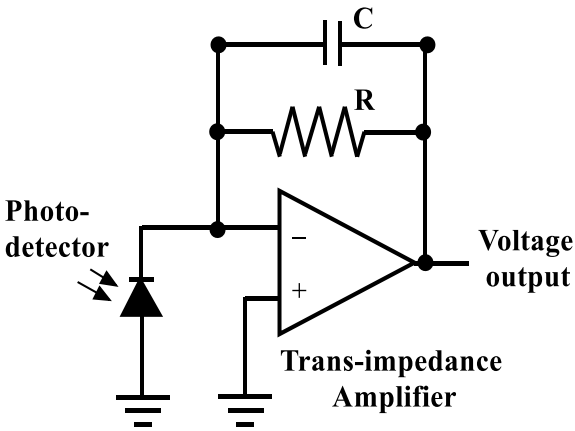

Fig. 2 TSL 254R photo-detector

2.2 Receiver

$TSL\ 254R$ light-to-voltage optical sensor (photo-detector) is placed at the receiver to detect changes in the transmitted irradiance. The response of photo-detector is

$$R = \eta\,(I_0 + I_b)\,u + n \tag{1}$$

Here, photo-detector responsivity $\eta = 0.7$ A/W at $\lambda = 470$ nm, I_0 is incident irradiance, I_b is background noise and n is AWGN with zero mean and $\frac{N_0}{2}$ variance, N_0 is power spectral density of noise. $TSL\ 254R$ circuit diagram is shown in Fig. 2; here the feedback resistor $R = 1\,\mathrm{M}\Omega$. Detector output voltage is directly proportional to the irradiance on the photo-detector. The transmitter and receiver functions have been implemented on the same processing platform (Arduino board), and hence, synchronisation is maintained without difficulty.

2.3 Underwater Channel

For evaluation of UWOC system performance, we have taken water-filled PVC pipes and aquarium. Using PVC pipes will yield better UWOC system performance as ambient light (which constitutes background noise for the detector) will not be present. However, it is not possible to use PVC pipes in all underwater optical links. Hence, performance evaluation with aquarium set-up in the presence of ambient light affecting will allow a more realistic test of the UWOC link. Further, creating conditions of turbulence will not be easily possible in a closed PVC pipe environment. For this reason, we have conducted all of our experimental work with glass aquarium tanks. The aquarium is filled with approximately 300 l of water. In the water channel, we have created turbulence, air bubbles and blockage to degrade the system performance,

with the help of Aqua Wave Maker WM-3000 having 5 l/min flow rate, jets having airflow rate 5.5 l/min and 0.15 MPa pressure and a rotating plate driven by DC motor with nearly 120 rpm speed, respectively.

3 Experimental Set-Up

Optical signal experiences absorption and scattering in water due to the presence of turbidity and salinity. We have added a calculated amount of suspended particles for turbidity and salts for salinity. We have measured absorption of light in water sample for different wavelength sources and plotted as shown in Fig. 3; it is observed that 470–530 nm (blue and green) and 650–700 nm (red) wavelength sources have less absorption. This result is obtained with the help of AU-2701 model UV-VIS double-beam spectrophotometer. Turbidity, conductivity, absorption and scattering of freshwater and sample water collected from the channel are measured and shown in Table 1. For generating turbulence, air bubbles and blockage, we have used four jets of each having 5.5 l/min airflow rate for air bubbles generation, wave maker for generating turbulences having flow rate of 5 l/min and a paddle driven by motor to create blockage with 120 rpm speed. An incandescent lamp is placed at the aquarium to create background noise. Figure 4 shows the underwater channel with turbulence, air bubbles and background noise due to the incandescent lamp. An optical bandpass filter BP 470/35 of central wavelength 470 nm with ± 35 bandwidth is used to pass optical signal within the wavelength range of (470 ± 35) nm and eliminates other wavelength signals.

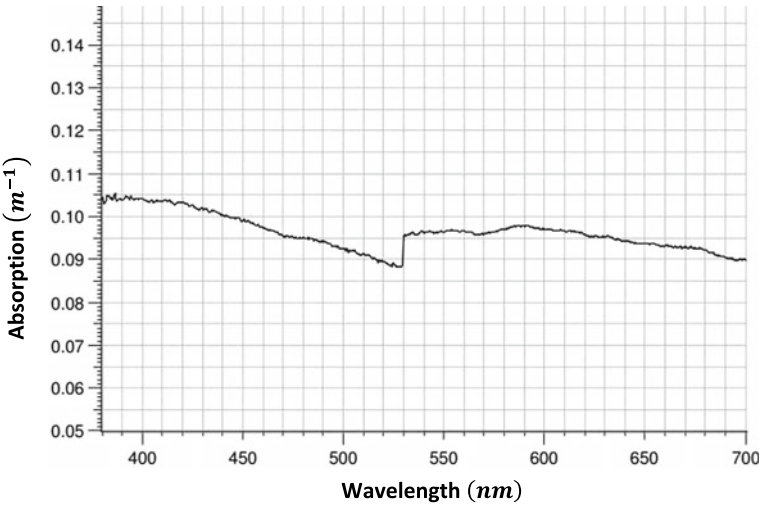

Fig. 3 Absorption with respect to various source wavelengths

Table 1 Freshwater and sample water characteristics

Water type	Turbidity (NTU)	Conductivity (mS/cm)	Absorption at 470 nm (m^{-1})	Scattering at 470 nm (m^{-1})
Freshwater	3	0.18	0.01	0.047
Sample water	10	22.5	0.0957	0.5495

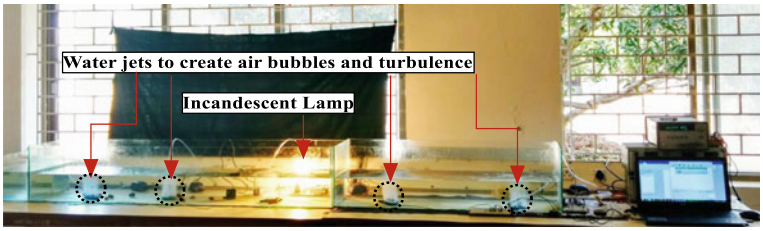

Fig. 4 Experimental set-up

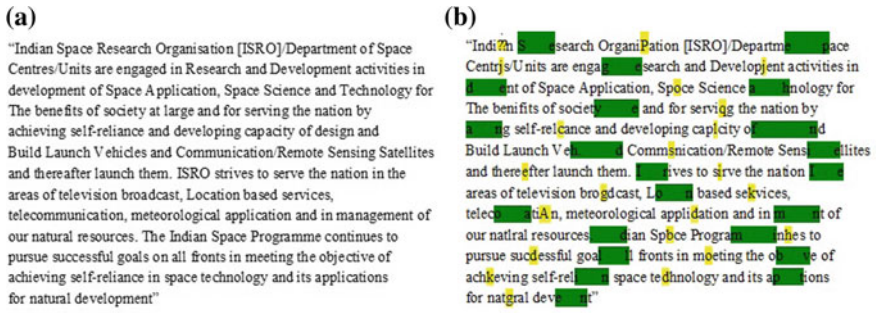

Fig. 5 Data samples: **a** transmitted data and **b** received data in the presence of turbulence and blockage

We have sent data shown in Fig. 5a in the presence of turbulence and blockage for uncoded SISO case at a transmit power of 25.5 dBm and the received data shown in Fig. 5b. In Fig. 5b, we have marked received data with yellow and green colours to identify the errors occurred due to turbulences and blockage. Yellow-coloured data occurs due to random fluctuation of irradiance from high to low, so the corresponding text character will be received as some other text character, while the data will be lost due to blockage will be zeros in the received data, which are marked with green colour.

4 Channel Coding and Receiver Diversity Combining

To mitigate the effect of turbulence, air bubble and blockage in the underwater channel, we have employed channel coding, receiver diversity combining and interleaved channel-coded receiver diversity techniques.

4.1 Channel Coding

For correcting t-bit errors, we have used BCH code of length $n = q^m - 1$ over $GF\,(q^m)$ (Galois field), where $q = 2$ for binary codes. For $m = 6$ and $t = 6$, this leads to construction of (63, 30) BCH code [6]. Group elements are $\{1, \alpha, \alpha^2, \ldots, \alpha^{62}\}$ partitioned into conjugacy classes with conjugate roots, using these roots calculating the minimal polynomials with the help of primitive polynomial in $GF\left(2^6\right)$ is $p(x) = x^6 + x + 1$. Generator polynomial $g(x)$ is least common multiple of minimal polynomials and is given as

$$\begin{aligned} g(x) = {} & x^{33} + x^{32} + x^{30} + x^{29} + x^{28} + x^{27} + x^{26} + x^{23} + x^{22} + x^{20} \\ & + x^{15} + x^{14} + x^{13} + x^{11} + x^9 + x^8 + x^6 + x^5 + x^2 + x + 1 \end{aligned} \tag{2}$$

Generator matrix $\mathbf{G_{30\times 63}}$ is obtained from generator polynomial $g(x)$. Encoded data is $\mathbf{C_{1\times 63}} = \mathbf{u_{1\times 30}} \,.\, \mathbf{G_{30\times 63}}$, where $\mathbf{u_{1\times 30}}$ is transmitted binary data and $\mathbf{C_{1\times 63}}$ is codeword. Berlekamp–Massey decoding algorithm is used for decoding the received data through channel [7].

4.2 Receiver Diversity Combining

Employing multiple photo-detectors at the receiver has performance improvement compared to single photo-detector [8]. Received data R_C for multiple photo-detectors is

$$R_C = \frac{1}{M} \sum_{i=1}^{M} \left(\sqrt{P_t} u \eta_i I_i + n_i \right), \quad 1 \le i \le M \tag{3}$$

where $u \in \{0, 1\}$ represents the input bit sequence, P_t is transmit power, M is number of photo-detectors, η is photo-detectors responsivity, I is irradiance received from the underwater channel and n is additive white Gaussian noise (AWGN). For equal gain combining (EGC), received data R_C is,

$$R_C = \frac{\eta \sqrt{P_t} u}{M} \sum_{i=1}^{M} I_i + n \tag{4}$$

here, $\eta_1 = \eta_2 = \cdots = \eta_M = \eta$ for same photo-detectors. We have employed three photo-detector EGC as receiver diversity combining.

4.3 Interleaved BCH Code

Due to blockage burst errors determined in the received code-word, using 63×63 length interleaver with (63, 30) BCH code can correct 378 length burst error among 3969 transmitted bits.

5 Experimental BER Results

In this section, we present experimental BER results with respect to transmit power in terms of decibel-milliwatts (dBm). Figure 6 shows the experimental BER results of UWOC with uncoded single-input single-output (SISO), channel coding (BCH), receiver diversity combining (EGC) and 63×63 length interleaved channel coding techniques.

From Fig. 6, it can be inferred that a power gain of more than 2.5 dBm can be saved to achieve a BER of 3×10^{-4} from without receiver diversity to with receiver diversity combining. Channel-coded SISO can save 3 dBm of transmit power compared with channel-coded receiver diversity technique and same for interleaved BCH with and without receiver diversity combining. From uncoded SISO to interleaved channel-coded receiver diversity can gain nearly 5 dBm of transmit power at BER of 3×10^{-4}.

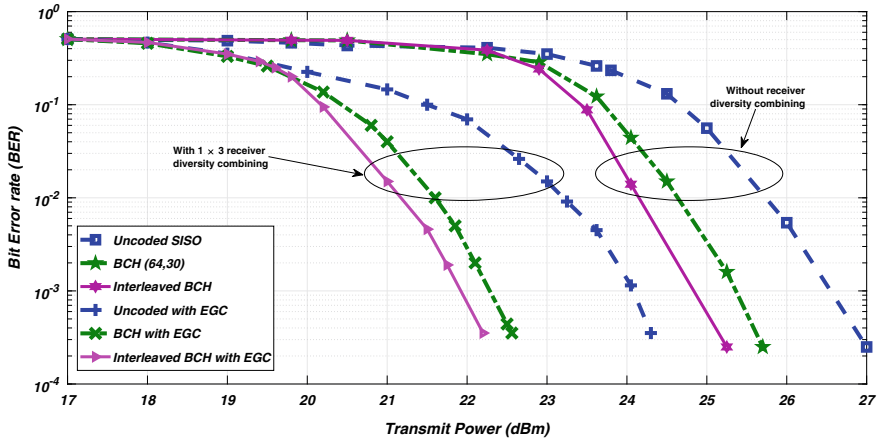

Fig. 6 Experimental BER results of UWOC links

6 Conclusion

We have established an UWOC link with 2.5-m-length underwater channel working in the presence of turbulence, air bubbles and blockage conditions at 120 Kbps transmission speed. By employing suitable channel codes and receiver diversity combining techniques, we can enhance the performance of UWOC in the presence of turbulence, air bubbles and blockage. We have achieved a transmit power gain of 5 dBm from uncoded SISO to (63, 30) BCH-coded 63×63 length interleaver with 1×3 EGC.

In our future work on this topic, we will design and implement high-speed UWOC links (500 Kbps), with channel coding, interleaving and diversity reception to enhance the integrity of data transfer.

References

1. Smart JH (2005) Underwater optical communications systems, part 1: variability of water optical parameters. In: Military communications conference, 2005. MILCOM 2005. IEEE, pp 1140–1146
2. Ramavath PN, Kumar A, Godkhindi SS, Acharya US (2018) Experimental studies on the performance of underwater optical communication link with channel coding and interleaving. CSI Trans ICT 6(1):65
3. Ramavath PN, Acharya US Reliable optical communication through turbid and turbulent seawater channels. Opt Laser Technol (unpublished)
4. Jamali MV, Khorramshahi P, Tashakori A, Chizari A, Shahsavari S, AbdollahRamezani S, Fazelian M, Bahrani S, Salehi JA (2016) Statistical distribution of intensity fluctuations for underwater wireless optical channels in the presence of air bubbles. In: Iran workshop on communication and information theory (IWCIT), 2016. IEEE, pp 1–6
5. Oubei HM, ElAfandy RT, Park KH, Ng TK, Alouini MS, Ooi BS (2017) Performance evaluation of underwater wireless optical communications links in the presence of different air bubble populations. IEEE Photonics J 9(2):1
6. Lin S, Costello DJ (2001) Error control coding. Pearson Education India, New Delhi
7. Blahut RE (1983) Theory and practice of error control codes. Addison-Wesley, Reading, MA
8. Ghassemlooy Z, Popoola W, Rajbhandari S (2012) Optical wireless communications: system and channel modelling with Matlab®. CRC Press, Boca Raton

Performance of SM-NSTBC for Correlated HAP Fading Channels with Imperfect-CSI

S. Godkhindi Shrutkirthi, G. D. Goutham Simha and U. Shripathi Acharya

Abstract This paper analyzes the performance of Spatially Modulated Non-orthogonal Space Time Block Code (SM-NSTBC) scheme for a correlated high altitude platform (HAP) MIMO system in the presence of imperfect channel state information (Imp-CSI). The proposed SM-NSTBC employs cyclic codewords derived over Galois Field, which satisfies full rank property. The performance of SM-NSTBC is compared with traditional STBCs such as SM-OSTBC and STBC-SM schemes. It is observed through simulations that SM-NSTBC outperforms SM-OSTBC and STBC-SM schemes by a minimum of 2 dB in HAP correlated environments. Monte-Carlo simulations have been performed to validate the claims.

Keywords High Altitude Platform (HAP) · Imperfect Channel State Information (Imp-CSI) · Spatially Modulated Non-orthogonal Space Time Block Code (SM-NSTBC)

1 Introduction

HAP-MIMO system has gained a huge attention recently as it overcomes the limitation of existing terrestrial communication system in terms of capacity and cost. Its applications have unfolded a new perspective for satisfying the unquenchable demand of connectivity and data. It can be viewed as an unmanned, solar-powered standalone architecture with varied applications in Internet of Things, emergency communication, remote system connectivity, navigation system, real-time monitoring, disaster management, quality Internet service for fast-moving vehicles [1, 2]. The HAP-MIMO has benefits such as a replacement infrastructure, quick restoration, large coverage, high capacity, data rate, lesser local scattering, etc. Due to these advantages, HAP-MIMO is considered to be one of the competitive technologies for the deployments as a part of the 5G connectivity.

S. Godkhindi Shrutkirthi (✉) · G. D. Goutham Simha · U. Shripathi Acharya
National Institute of Technology Karnataka, Surathkal, Mangalore, India
e-mail: ec15f01.ssg@nitk.edu.in

V. Janyani et al. (eds.), *Optical and Wireless Technologies*, Lecture Notes in Electrical Engineering 648, https://doi.org/10.1007/978-981-15-2926-9_10

Over the past decade, there have been many literatures which have analyzed the capacity and channel behaviors of HAP-MIMO system [2, 3]. In HAP-MIMO communication, a signal undergoes effects of diffraction, scattering and reflection causing the arrival of multipath components at the receiving end, thus leading to fading environment [4–6]. Incorporating multiple-input multiple-output system provides visible increment in diversity as well as coding gain of communication system. Spatial correlation (SC) places a crucial role for any system with multiple antennas elements. Spatial correlation is mainly caused due to less spacing between the antenna elements in a single antenna array and physical channel conditions. There exist restriction for achieving sufficient spacing between antenna elements at the transmitter and at the receiver. Thus, the effect of SC amongst channel must be considered while designing the elemental space between antenna array elements [7]. It becomes very important to consider the effect of SC to design a robust system, which could provide a reliable communication even in highly spatially correlated HAP fading environment.

This paper analyzes the performance of SM-NSTBC over a spatially correlated HAP-MIMO environment with the Imperfect-CSI. The performance of the proposed SM-NSTBC has been compared with existing SM-OSTBC and STBC-SM schemes for spatially correlated HAP-MIMO system.

The paper organization is as follows: Sect. 2 gives a brief description of HAP-MIMO channel model under spatially correlated fading scenario. In Sect. 3, we have discussed the design of SM-NSTBC scheme proposed for HAP-MIMO communication system. Section 4 presents the simulation results followed by the conclusions in Sect. 5.

2 System and Channel Model

2.1 Signal and Channel Model

A HAP-MIMO communication system is considered with N_t number of transmit antennas, N_r number of receiver antennas and N_a number of active antennas. At the receiver, signal is received over T symbol durations, the received signal is given in Eq. (1).

$$\mathbf{Y} = \mathbf{HX} + \mathbf{n} \tag{1}$$

here, $\mathbf{Y} \in \mathcal{C}^{N_r \times T}$ is the received signal, $\mathbf{H}$ is a $N_r \times N_t$ channel matrix, $\mathbf{X} \in \mathcal{C}^{N_t \times T}$ is the transmitted vector, and $\mathbf{n}$ is circularly symmetric complex independent and identically distributed (i.i.d.) Gaussian noise with zero mean and unit variance ($\mathcal{CN}(0, 1)$). The channel matrix $\mathbf{H}$ is the combination of both line of sight (LoS) and non-line of sight (NLoS) components. HAP channel is estimated by approximating its CDF and PDF as shown in [8], which shows a resemblance to Rician distribution. The channel matrix of HAP is given in Eq. (2).

$$\mathbf{H} = \sqrt{\frac{K}{1+K}}\mathbf{H}_{LoS} + \sqrt{\frac{1}{1+K}}\mathbf{H}_{NLoS} \tag{2}$$

here, $\mathbf{H}_{LoS}$ is the LoS component, $\mathbf{H}_{NLoS}$ represents the NLoS components, and $K = \frac{\sigma^2_{LoS}}{\sigma^2_{NLoS}}$ is the Rician factor, where σ^2_{LoS} is the power of LoS and σ^2_{NLoS} is the power of NLoS components, respectively.

The $\mathbf{H}_{NLoS}$ follows Rayleigh distribution, and $\mathbf{H}_{LoS}$ is obtained as shown in [9] and is given by Eq. (3).

$$\mathbf{H}_{LoS} = \begin{bmatrix} 1 \\ e^{j2\pi \frac{d_R}{\lambda} \sin(\theta_A)} \\ \vdots \\ e^{j2\pi \frac{d_R}{\lambda}(N_r-1) \sin(\theta_A)} \end{bmatrix} \begin{bmatrix} 1 \\ e^{j2\pi \frac{d_T}{\lambda} \sin(\theta_D)} \\ \vdots \\ e^{j2\pi \frac{d_T}{\lambda}(N_t-1) \sin(\theta_D)} \end{bmatrix}^T \tag{3}$$

where λ is the signal wavelength, d_R is the separation between antenna elements of receiver array, d_T is the separation between antenna elements of transmit array, θ_A represents the angle of arrival, and θ_D represents the angle of departure [10].

2.2 Spatial Correlation

The mathematical analysis of spatial correlation can be given by Kronecker channel model [11]. The spatially correlated channel matrix $\mathbf{H}_c$ is given below.

$$\mathbf{H}_c = \sqrt{R_{Rx}}\mathbf{H}\sqrt{R_{Tx}} \tag{4}$$

here, R_{Tx} and R_{Rx} are transmitter correlation matrix and receiver correlation matrix, $\mathbf{H}$ represents the HAP uncorrelated channel matrix. This correlated channel matrix can also be obtained as $\mathbf{H}_c = \text{vec}(\mathbf{H})R_s^{1/2}$, here vec($\mathbf{H}$) is vectorization of $\mathbf{H}$ and $Rs = R_{Rx} \bigotimes R_{Tx}$, where $\bigotimes$ Kronecker product.

The spatial correlation between any two distinct antenna pairs depends on the product of corresponding transmit and receive correlation elements. The following subsection gives a brief description of conventional system models.

2.3 STBC-SM

Basar et al. in [12] proposed a novel technique known as Space Time Block Coded Spatial Modulation (STBC-SM). This technique would incorporate benefits of both STBC and spatial modulation (SM). In STBC-SM, Alamouti STBC is transmitted through spatial domain. STBC-SM retains the diversity advantage of STBC, and spectral efficiency is increased by the use of additional information bits which are conveyed by antenna selection bits.

2.4 SM-OSTBC

In Spatially Modulated Orthogonal Space Time Block Codes (SM-OSTBC), the codewords are designed to retain the non-vanishing determinant property. In SM-OSTBC, spatial constellation matrix is multiplied with the existing codeword, and this leads to a transmit diversity of order 2 [13].

3 SM-NSTBC Design

This paper describes the novel concept called Spatially Modulated Non-Orthogonal Space Time Block Code (SM-NSTBC) [10]. SM-NSTBC is designed using cyclic codes over $GF(q^m)$, here q is a prime and m is the order of an extension field. The codewords are designed to achieve the full rank property.

Codeword Design: The cyclic codewords are of length n such that $(n|q^m - 1, m \leq n)$ are obtained over $GF(q^m)$. These constructions can be viewed as $m \times n$ matrix over $GF(q)$, which has rank equal to m. These code vectors can be punctured to obtain codewords of length m, which can be expressed as $m \times m$ matrix over $GF(q)$ with rank m, inturn eliminating the redundant $(n - m)$ columns. Let $a(i, j) \in GF(q)$, and then, obtained codeword is as follows.

$$\mathbf{a}_{(i,j)} \in GF(q) = \begin{bmatrix} a_{0,0} & a_{0,1} & \cdots & a_{0,m-1} \\ a_{1,0} & a_{1,1} & \cdots & a_{1,m-1} \\ \vdots & \vdots & \cdots & \vdots \\ a_{m-1,0} & a_{m-1,1} & \cdots & a_{m-1,m-1} \end{bmatrix} \tag{5}$$

Mapping Technique for SM-NSTBC: The codewords designed for SM-NSTBC have full rank, so it becomes important to retain the full rank property after mapping. Gaussian Map and Eisenstein Maps are the rank preserving maps employed in SM-NSTBC. Incorporating these mapping techniques ensures that the full rank property of the designed SM-NSTBC is retained. The mapping values of q for $GF(q)$ are given in Table 1. Both Gaussian and Eisenstein mapping techniques satisfy the property of rank preserving and are bijective [14, 15].

Table 1 Gaussian and Eisenstein Mapping Values [15]

q	π	**u**	**v**
5	2 + i	−1	1 + i
13	3 + 2i	−2	1 + 2i
17	4 + i	−2	2 + i

q	Π	α	β
7	3+2ρ	2	1
13	3+4ρ	1	2
19	5+2ρ	4	1

SM-NSTBC Construction: The information bits are first encoded to $m \times m$ full rank codeword matrices. The codeword matrices are obtained over $GF(5^4)$, $GF(7^4)$,

$GF(13^4)$ and $GF(17^4)$, i.e., $m = 4$. Thus, 4×4 full rank codeword matrix is obtained. This designed matrix is then divided into two sub-matrices, one is used for antenna selection, and the other sub-matrix is conveyed through the activated antennas [10].

Let N_t be the number of transmit antennas, $N_t > 2$, N_a be the number of active antennas. Consider $N_t = 4$ and $N_a = 2$, then the transmission of codeword given in Eq. (5) is deduced to (6).

$$\mathbf{X}_{SM} = \begin{bmatrix} 0 & \Im\{a_{3,1}\} & \Im\{a_{3,2}\} & 0 \\ \Im\{a_{2,0}\} & \Im\{a_{2,1}\} & 0 & 0 \\ 0 & 0 & 0 & \Im\{a_{2,3}\} \\ \Im\{a_{3,0}\} & 0 & \Im\{a_{2,2}\} & \Im\{a_{3,3}\} \end{bmatrix} \tag{6}$$

Here, $\Im\{\cdot\}$ is the rank preserving map, the **0**s in the matrix of Eq. (6) indicate the inactive state of the antennas. This scheme can further be extended to $N_a = 4$ and for any number of transmit antennas $N_t > 3$ as devised [10]. At the receiver, full codeword is obtained, and then, maximum likelihood decoding technique is employed to obtain the antenna selection bits and the transmission bits. A brief description of SM-NSTBC scheme is given in Algorithm 1.

Algorithm 1: SM-NSTBC scheme algorithm

Input: Incoming data stream
Start
Consider $2^{\lfloor \log_2 (q^m) \rfloor}$ bits
Step 1: Encode the data stream into codeword matrix $\mathbf{M}$ such that $\mathbf{M} \in \mathcal{C}_{m \times m}$.
Step 2: Obtain antenna selection bits $[\mathbf{M}_1]$ and information bits $[\mathbf{M}_2]$ from the punctured codeword.
Step 3: Activating Antennas
  $[\mathbf{M}_1] \rightarrow \mathcal{C}_1[a(1)a(2)\cdots a(m)]$
Step 4: Mapping of Information bits: $C_2[i(1)i(2)\cdots i(m)]$
Step 5: Define a suitable map for transmission of codewords
$\varphi : [\mathbf{M}_2] \rightarrow \Im(\mathcal{C}_2)$
Obtain suitable rank preserving maps: $\mathbf{X} = \varphi(C_2)$
Step 6: Obtain $\mathbf{X}_{SM}$ by combining $\mathcal{C}_1$ and $\mathcal{C}_2$.
Step 7: At the receiver end, ML decoding is performed to estimate the transmitted bits from $\mathbf{X}_{SM}$. $\hat{\mathbf{X}}_{SM} = \text{argmin} \|\mathbf{Y} - \mathbf{H}\mathbf{X}_{SM}\|_F^2 \; \forall \mathbf{X}_{SM} \in \mathbf{C}$
end
Output: Final decoded bits

In the following section, Monte-Carlo simulations for SM-NSTBC, SM-OSTBC and STBC-SM over spatially correlated HAP-MIMO environment have been analyzed.

4 Simulation Results

For simulations, we have used σ_e^2 values such that $0 \leq \sigma_e^2 \leq 0.99$. In order to understand and obtain the complete effect of Imp-CSI, the value of σ_e^2 is kept fixed for all values of SNR. For spatial correlated scenario, the transmit antenna spacing of 0.1Λ and receiver antenna spacing of 0.5Λ are considered. Here, SM-NSTBC system is denoted as $C(N_t, N_r, N_a)$ where N_t, N_r, N_a are number of transmit, receiver and active antennas, respectively.

Figure 1a shows the performance of SM-NSTBC derived over $GF(5)$ with $C(N_t = 6, N_r = 4, N_a = 4)$ yielding a spectral efficiency of 4.643 bpcu over correlated HAP-MIMO environment for $\sigma_e^2 = 0, 0.5, 0.9$. Figure 1b gives the performance comparison of SM-NSTBC and STBC-SM [12] for spectral efficiency of $(\eta = 4)$ bpcu. It is shown that SM-NSTBC outperforms STBC-SM by $\sim$3 and $\sim$2 dB over correlated HAP-MIMO environment.

In Fig. 2, it is observed that SM-NSTBC gives a performance improvement over SM-OSTBC [13] by approximately 5dB and approximately 3 dB over highly correlated HAP-MIMO scenario. In Fig. 2a, SM-OSTBC attains $\eta = 6$bpcu for $N_t = 16$ which is very large when compared to proposed SM-NSTBC which utilizes only $N_t = 6$ to achieve $\eta = 5.6$ bpcu, and a performance improvement of about $\sim$3 dB is observed. In Fig. 2b, SM-OSTBC achieves $\eta = 7.5$, SM-NSTBC yields $\eta = 7.4$ bpcu, and the proposed SM-NSTBC outperforms SM-OSTBC by approximately 4 dB.

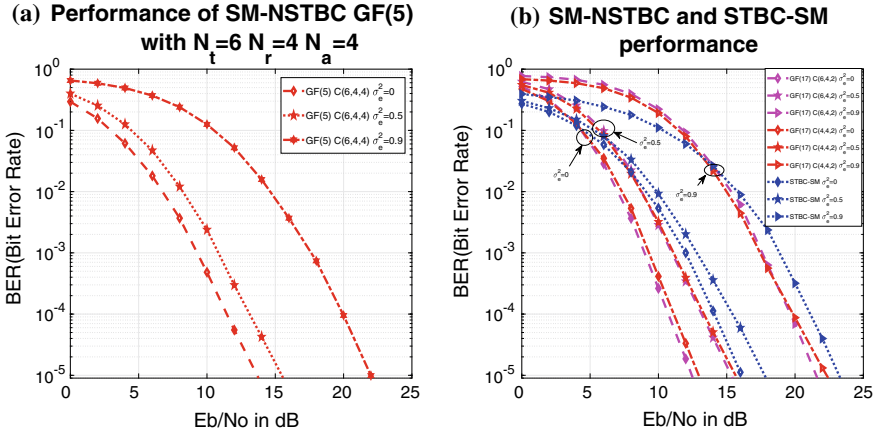

Fig. 1 **a** Performance of SM-NSTBC with $C(6, 4, 4)$ over GF(5). **b** Performance of SM-NSTBC and STBC-SM for $\eta = 4$ bpcu

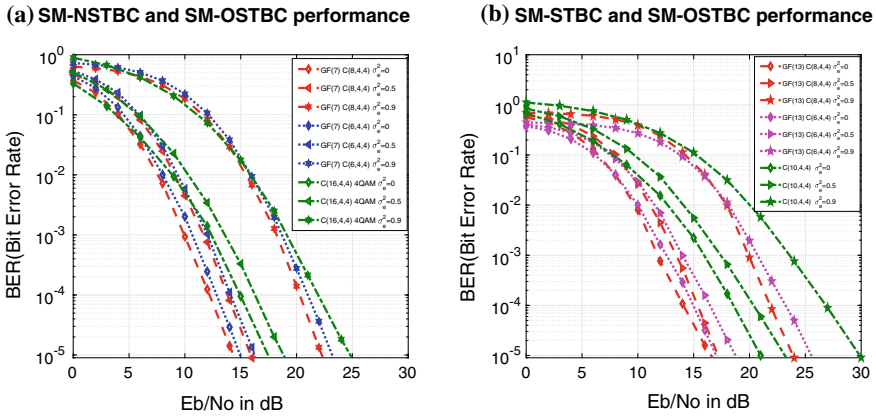

Fig. 2 **a** BER performance of SM-NSTBC for $\eta = 5.5$ and SM-OSTBC for $\eta = 6$ bpcu. **b** Performance of SM-NSTBC and SM-OSTBC for $\eta = 7.5$ bpcu

5 Conclusion

A newly constructed design of SM-NSTBC is proposed in this paper to provide reliable communication over a correlated HAP-MIMO channel. SM-NSTBC has been devised from full rank cyclic codes over Galois Field. A performance improvement of approximately 2–5 dB is observed as compared to SM-OSTBC and STBC-SM for varying spectral efficiencies and Imperfect-CSI. Monte-Carlo simulations are performed over correlated HAP-MIMO channel to validate the results. By observing the above advantages, we conclude that SM-NSTBCs can be employed in HAP-MIMO as a substitute architecture to existing MIMO techniques.

References

1. Mozaffari M, Saad W, Bennis M, Nam YH, Debbah M (2018) A tutorial on UAVs for wireless networks: applications, challenges, and open problems (online). Available from: https://arxiv.org/abs/1803.00680. 2 Mar 2018
2. Feng W, Wang J, Chen Y, Wang X, Ge N, Lu J (2018) UAV-aided MIMO communications for 5G Internet of Things. IEEE Internet Things J
3. Mohammed A, Mehmood A, Pavlidou F-N, Mohorcic M (2011) The role of high-altitude platforms (HAPs) in the global wireless connectivity. Proc IEEE 99(11):1939–1493
4. Michailidis ET, Kanatas AG (2010) Three-dimensional HAP-MIMO channels: modeling and analysis of space-time correlation. IEEE Trans Veh Technol 59(5):2232–2242
5. Shimamoto S (2006) Prediction of propagation path loss for stratospheric platforms mobile communications in urban site LOS/NLOS environment. In: IEEE international conference on communications, 2006. ICC'06, vol 12. IEEE
6. Sudheesh PG, Sharma N, Magarini M, Muthuchidambaranathan P (2018) Effect of imperfect CSI on interference alignment in multiple-High Altitude Platforms based communication. Phys Commun 29:336–42

7. Nabar RU, Bolcskei H, Paulraj AJ (2005) Diversity and outage performance in space-time block coded Ricean MIMO channels. IEEE Trans Wirel Commun 4(5):2519–2532
8. Zaji A (2012) Mobile-to-mobile wireless channels. Artech House, Norwood, MA
9. Cho YS, Kim J, Yang WY, Kang CG (2010) MIMO-OFDM wireless communications with MATLAB. Wiley, Hoboken, NJ
10. Shrutkirthi G, Goutham SGD, Acharya US (2019) A MIMO SM-NSTBC scheme for High Altitude Platform communication systems: study and analysis. In: 2019, 6th international conference on signal processing and integrated networks (SPIN-2019). IEEE (in press)
11. Mesleh RY, Haas H, Sinanovic S, Ahn CW, Yun S (2008) Spatial modulation. IEEE Trans Veh Technol 57(4):2228–2241
12. Basar E, Aygolu U, Panayirci E, Poor HV (2011) Space-time block coded spatial modulation. IEEE Trans Commun 59(3):823–32
13. Le M-T, Ngo V-D, Mai H-A, Tran XN, Di Renzo M (2014) Spatially modulated orthogonal space-time block codes with non-vanishing determinants. IEEE Trans Commun 62(1):85–99
14. Goutham SGD, Raghavendra M, Shriharsha K, Acharya US (2017) Signal constellations employing multiplicative groups of Gaussian and Eisenstein integers for enhanced spatial modulation. Phys Commun 25:546–554
15. Lusina P, Gabidulin E, Bossert M (2003) Maximum rank distance codes as space-time codes. IEEE Trans Inf Theory 49(10):2757–2760

Impact of Core Counts and Layouts on Dispersion Behavior in Homogeneous Multicore Fiber

Umar Farooque, Dharmendra Kumar Singh and Rakesh Ranjan

Abstract Dispersion behaviors in homogeneous multicore fiber (MCF) with different core layouts and core counts have been investigated numerically using the FemSIM simulation software and MATLAB. It is noted that with the decrease in core pitch dispersion level decrease. The SLS core layout has the lowest value of dispersion compared to the other core layouts for a fixed core count. Core pitch in MCF decreases with the increase in core count in different core layouts and hence the level of dispersion decreases. However, the number of surrounding cores at different core pitch also affects the dispersion behavior. The investigations presented in the paper will help in low dispersion homogeneous MCF design.

Keywords Multicore fiber · Homogeneous · Dispersion · Core layout · Core count

1 Introduction

The information carrying capacity of the single-core single-mode fiber (SC-SMF) approaches toward the limit of 100 Tb/s due to different fiber phenomenon and it is anticipated that it may no longer satisfy the future rapidly increasing capacity demand [1]. Therefore, the multicore fiber (MCF) based space-division multiplexing (SDM) having multiple cores in a common cladding region is an emerging technique to overcome the capacity issue of the SC-SMF [2]. In contrast to the single degree of freedom in terms of core parameters in SC-SMF, the MCF exhibits degree of

U. Farooque (✉) · D. K. Singh · R. Ranjan
Optical Fiber Communication and Photonics Laboratory, Department of Electronics and Communication Engineering, National Institute of Technology Patna, Patna, Bihar 800005, India

D. K. Singh
e-mail: dksingh@nitp.ac.in

R. Ranjan
e-mail: rr@nitp.ac.in

U. Farooque
Department of Electronics and Communication Engineering, Muzaffarpur Institute of Technology Muzaffarpur, Muzaffarpur, Bihar 842003, India

V. Janyani et al. (eds.), *Optical and Wireless Technologies*, Lecture Notes in Electrical Engineering 648, https://doi.org/10.1007/978-981-15-2926-9_11

freedom in terms of core pitch (D), core count, core arrangement or layout, outer cladding thickness (OCT), the cladding diameter (CD), etc. [3]. In MCF, the multiple cores may have the same core radius as well as same refractive index (R.I.), known as homogeneous MCF or it may have cores with either different core radius or R.I. or both, called as heterogeneous MCF [4]. Further, depending upon the core pitch, MCFs are classified as uncoupled MCF (U-MCF) in which core pitch is sufficiently large such that individual core is used as a separate waveguide with adequately low crosstalk between adjacent cores, while in coupled MCF (C-MCF), cores are placed sufficiently close to each other to increase the core density at the cost of increased crosstalk level [5].

Recently, uncoupled homogeneous MCFs (U-HMCF) with different core counts have been utilized in transmission experiments to achieve capacities one Pb/s and beyond [6, 7] under the single-mode conditions. The main issues in the transmission of optical signals over long distance with high transmission capacity in MCF are the dispersion and crosstalk phenomenon. However, there is extensive study on the crosstalk estimation and suppression in homogeneous and heterogeneous MCF [8–12]. Arrangements of cores, i.e., core layouts in the fixed cladding region of the fiber have significant impact on the crosstalk level and have been studied [13]. However, to the best of the author's knowledge impact of core layouts on the dispersion behavior in homogeneous MCFs have not been studied in detail.

Therefore, in the present analysis, first of all we have studied the impact of core pitch on the dispersion behavior in a two-core homogeneous MCF. Then, we have investigated the impact of different core layouts on the dispersion behavior in homogeneous MCF for the same number of cores within the fixed cladding diameter and with the same core parameters. Further, the impact of core counts on the dispersion behavior for different core layouts has also been studied numerically using FemSIM simulation software and MATLAB. The different core layouts utilized are the circular one-ring structure (C-ORS), hexagonal ORS (H-ORS), circular dual ring structure (C-DRS), hexagonal DRS (H-DRS), and square lattice structure (SLS) [13]. While, the core counts considered here are 12 Core, 16 or 18 Core. It is observed from the analysis that for a fixed core count, core layouts have significant effect on the dispersion behavior in homogeneous MCFs, which is mainly due to the fact that different core layouts have different core pitch and with the variation in core pitch, the mode coupling behavior changes and hence, this changes the value of the mode effective refractive index. Further, with the increase in the core counts in different core layouts, the core pitch changes differently and hence, the effective refractive index values and dispersion level changes differently in different core layouts. Therefore, this analysis will be beneficial in the design of low dispersion homogeneous MCF structure.

The organization of the paper is as follows: the design parameters and the schematic designs of the homogeneous MCFs with different core counts and layouts have been shown in Sect. 2. Section 3 presents the results and discussion. Lastly, conclusion of the present work has been presented in Sect. 4.

2 Design Parameters and the Schematic Designs of the Homogeneous MCF

The schematic design of the two-core MCF has been shown in Fig. 1. The cores are similar in nature, i.e., homogeneous cores with core radius 4.5 μm and the relative refractive index difference between the core and the cladding 0.35%. The R.I. of the cladding is taken as 1.45. The core pitch is represented by D, the cladding diameter is taken as 125 μm. The values of core parameters have been chosen to support only single mode to propagate in the usual optical communication wavelength region (1530–1630 nm).

In Figs. 2 and 3, different core layouts of homogeneous MCF have been shown for the 12 Core count and the 16 or 18 Core count, respectively. The cladding diameter is fixed for both the cases and is equal to 225 μm. The core parameters are same for all the core layouts and the cladding index is also same in all cases and equal to 1.45. The core pitches in different layouts are shown by D_1, D_2, and D_3.

The expressions for the core pitch in different core layouts with different core counts have been derived and expressed in (1)–(4).

Circular ORS

$$D_1 = \left(\frac{\text{CD} - 2 \times \text{OCT}}{2}\right)\sqrt{2 \times (1 - \cos(2\pi/N))}, \tag{1}$$

where, N = total number of cores.

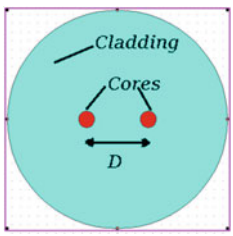

Fig. 1 Schematic design of homogeneous two-core MCF

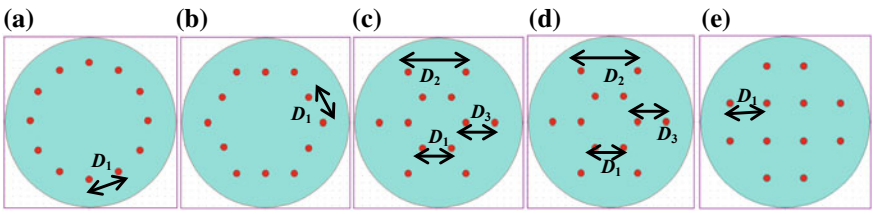

Fig. 2 Schematic designs of 12 Core homogeneous MCFs in different layouts: **a** circular ORS; **b** hexagonal ORS; **c** circular DRS; **d** hexagonal DRS; **e** SLS

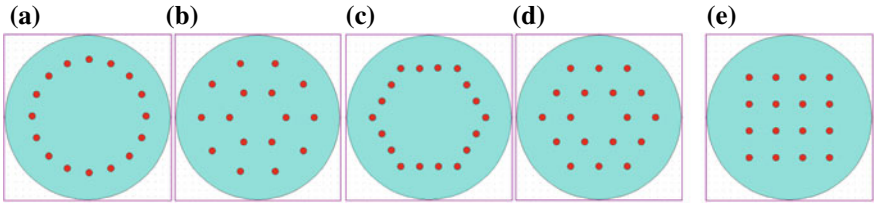

Fig. 3 Schematic designs of 16 or 18 Core homogeneous MCFs in different layouts: **a** circular ORS; **b** hexagonal ORS; **c** circular DRS; **d** hexagonal DRS; **e** SLS

Hexagonal ORS

$$D_1 = \frac{\left(\frac{\text{CD}-2\times\text{OCT}}{2}\right)\sqrt{2\times(1-\cos(2\pi/6))}}{n+1}, \tag{2}$$

where n = number of cores in any one side of the hexagon and have values 1 and 2 for 12 Core and 18 Core, respectively.

Circular DRS

$$D_1 = \frac{\left(\frac{\text{CD}-2\times\text{OCT}}{2}\right)\sqrt{2\times(1-\cos(2\pi/n))}}{2},$$
$$D_2 = \left(\frac{\text{CD}-2\times\text{OCT}}{2}\right)\sqrt{2\times(1-\cos(2\pi/m))}, \quad D_3 = \left(\frac{\text{CD}-2\times\text{OCT}}{2}\right), \tag{3}$$

where n and m represent the core counts in the inner and the outer circles, respectively. While, D_1, D_2, and D_3 are the core pitch for inner circle, outer circle, and the core pitch between the two circles.

Hexagonal DRS

$$D_1 = \frac{\frac{1}{2}\left(\frac{\text{CD}-2\times\text{OCT}}{2}\right)\sqrt{2\times(1-\cos(2\pi/6))}}{n+1},$$
$$D_2 = \frac{\left(\frac{\text{CD}-2\times\text{OCT}}{2}\right)\sqrt{2\times(1-\cos(2\pi/6))}}{m+1}, \quad D_3 = \left(\frac{\text{CD}-2\times\text{OCT}}{2}\right), \tag{4}$$

where n and m represent the core counts in one side of the inner and the outer hexagon, and have values 1 and 2 for 12 Core and 18 Core, respectively. While, D_1, D_2, and D_3 are the core pitch for inner hexagon, outer hexagon, and the core pitch between the two hexagons.

3 Results and Discussion

The dispersion behavior in homogeneous MCF can be obtained by using (5):

$$D(\lambda) = -\frac{\lambda}{c}\frac{\mathrm{d}^2 n_{\mathrm{eff}}(\lambda)}{\mathrm{d}\lambda^2} \tag{5}$$

For the analysis of dispersion behavior in different core layouts of MCFs, wavelength-dependent variation in mode effective refractive index (n_{eff}) in different core layouts of MCFs have been obtained numerically using FemSIM software and is utilized in (5).

From Fig. 4, it is observed that in a homogeneous two-core MCF, $|D(\lambda)|_{\max}$, i.e., maximum value of the dispersion for the core pitch 20 μm, 30 μm, and 40 μm are 6.27 ps/km nm, 7.7 ps/km nm, and 9 ps/km nm, respectively, i.e., with the increase in core pitch dispersion values increases.

Further, from Fig. 5a, it is observed that for the same core count, different core layouts have different core pitch, which can be obtained from (1)–(4). Therefore, the different core layouts have different dispersion behaviors. The values of $|D(\lambda)|_{\max}$ for the circular ORS, circular DRS, hexagonal ORS, hexagonal DRS, and SLS layouts are 28.93 ps/km nm, 13.03 ps/km nm, 38 ps/km nm, 13.03 ps/km nm, and 9.06 ps/km nm, respectively. Due to same core pitch in circular DRS and hexagonal DRS, their dispersion behaviors are same and coincide to each other. Since the core pitch in SLS structure is largest, with the largest number of surrounding cores, which makes the maximum dispersion value least as compared to other layouts.

In order to observe the impact of core count, we have extended the analysis to observe the dispersion behavior for 16 or 18 Core MCFs with different core

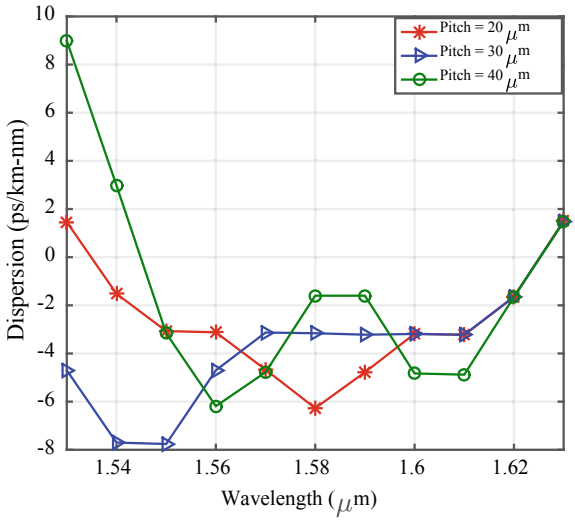

Fig. 4 Core pitch dependent dispersion variations in two-core homogeneous MCF

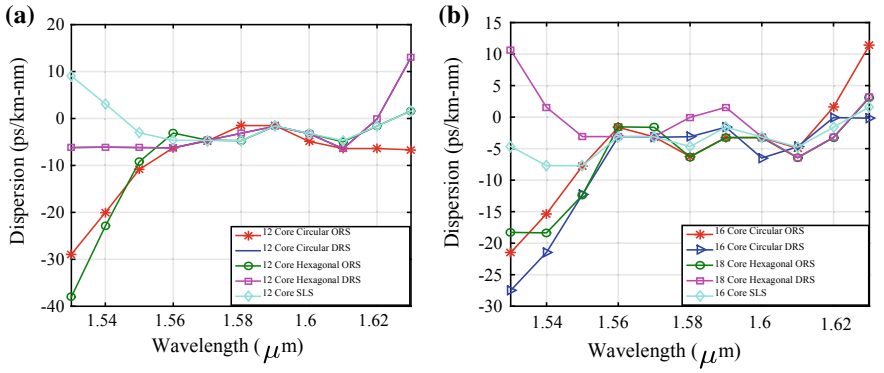

Fig. 5 Core layout dependent dispersion variations in **a** 12 Core; **b** 16 or 18 Core homogeneous MCF

layouts which are shown in Fig. 5b. It is observed that the values of $|D(\lambda)|_{\max}$ for the circular ORS, circular DRS, hexagonal ORS, hexagonal DRS, and SLS layouts are 21.49 ps/km nm, 27.5 ps/km nm, 18.29 ps/km nm, 10.63 ps/km nm, and 7.7 ps/km nm, respectively.

In circular ORS, hexagonal ORS, and SLS structures, the decrease in $|D(\lambda)|_{\max}$ with the decrease in core pitch shows the common trend, while the increase in $|D(\lambda)|_{\max}$ with the decrease in core pitch in circular and hexagonal DRS is mainly due to the fact that the values of mode effective refractive index in homogeneous MCF depend not only on the core pitch but also on the number of surrounding cores at different core pitch. From the above analysis, it is observed that SLS layout has the lowest level of dispersion, and with the increase in the core count, this value of dispersion decreases due to decrease in core pitch. Therefore, core counts and layouts have significant impact on the dispersion behavior in homogenous MCF.

4 Conclusion

Within the fixed cladding region, the impact of core layouts, i.e., the arrangement of cores and core counts on the dispersion behaviors of homogeneous MCFs have been investigated numerically using the FemSIM software and MATLAB. It is observed from the analysis that with the decrease in core pitch, the value of dispersion decreases. As the different core layouts with the same core count may have different core pitch, and the SLS layout among them has the highest core pitch along with highest number of surrounding cores and hence, the lowest dispersion level. Further, with the increase in core counts, this level of dispersion decreases due to decrease in core pitch. The investigations presented in the paper will help in low dispersion homogeneous MCF design.

Acknowledgements This research work is a part of Early Carrier Research Award project sponsored by Science and Engineering Research Board, Department of Science and Technology, Govt. of India. We also thank National Institute of Technology Patna, Bihar, India, and Muzaffarpur Institute of Technology Muzaffarpur, Bihar, India, and Visvesvaraya Ph.D. Scheme, MeitY, Govt. of India for providing the immense support and encouragement.

References

1. Saitoh K, Matsuo S (2016) Multicore fiber technology. J Lightwave Technol 34:55–66
2. Koshiba M (2014) Design aspects of multicore optical fibers for high-capacity long haul transmission. In: Proceeding of microwave photonics and the 9th Asia-Pacific microwave photonics conference, Sendai, pp 318–323
3. Hayashi T (2016) Multi-core optical fibers realizing high density/capacity transmission. In: Proceeding of IEEE CPMT symposium, Japan, pp 169–172
4. Tu J, Long K, Saitoh K (2016) An efficient core selection method for heterogeneous trench assisted multicore fiber. IEEE Photonics Technol Lett 28:810–813
5. Saitoh K, Fujisawa T, Sato T (2017) Coiling size dependence of group delay spread in coupled multicore fibers without intentional twisting. J Lightwave Technol 35:4559–4566
6. Takara H, Sano A, Kobayashi T, Kubota H, Kawakami H, Matsuura A, Miyamoto Y, Abe Y, Ono H, Shikama K, Goto Y, Tsujikawa K, Sasaki Y, Ishida I, Takenaga K, Matsuo S, Saitoh K, Koshiba M, Morioka T (2012) 1.01-Pb/s (12 SDM/222 WDM/456 Gb/s) crosstalk-managed transmission with 91.4-b/s/Hz aggregate spectral efficiency. In: Proceeding of European conference and exhibition on optical communication, Amsterdam, Netherlands (Paper Th.3.C.1)
7. Puttnam BJ, Luís RS, Klaus W, Sakaguchi J, Deigado Mendinueta JM, Awaji Y, Wada N, Tamura Y, Hayashi T, Hirano M, Marciante J (2015) 2.15 Pb/s transmission using a 22 core homogeneous single-mode multicore fiber and wideband optical comb. In: Proceeding of European conference on optical communication, Valencia, pp 1–3
8. Ye F, Tu J, Saitoh K, Morioka T (2014) Simple analytical expression for crosstalk estimation in homogeneous trench assisted multicore fibers. Opt Express 22:23007–23018
9. Koshiba M, Saitoh K, Kokubun Y (2009) Heterogeneous multicore fibers: proposal and design principle. IEICE Electron Express 6:98–103
10. Saitoh K, Matsui T, Sakamoto T, Koshiba M, Tomita S (2010) Multicore hole assisted fibers for high core density space division multiplexing. In: Proceeding of optoelectronics and communications conference, Sapporo, pp 164–165
11. Xie X, Tu J, Zhou X, Long K, Saitoh K (2017) Design and optimization of 32-core rod/trench assisted square-lattice structured single mode multicore fiber. Opt Express 25:5119–5132
12. Tu J, Saitoh K, Koshiba M, Takenaga K, Matsuo S (2012) Design and analysis of large-effective area heterogeneous trench-assisted multicore fiber. Opt Express 20:15157–15170
13. Ye F, Tu J, Saitoh K, Takenaga K, Matsuo S, Takara H, Morioka T (2016) Design of homogeneous trench assisted multicore fibers based on analytical model. J Lightwave Technol 34:4406–4416

Erbium-Doped Optical Amplifiers—Origin to Latest Trends

Asifiqbal Thakor and Pravin Prajapati

Abstract In today's era of high data transmission, the communication system employs optical fiber as a main transmission path for data transmission. To compensate losses along the transmission path, there is a requirement of optical amplifiers. Erbium-doped optical amplifier (EDFA) is one of the most popular optical amplifiers available in the market. In this paper, starting from the basic operating principle to the latest trends in the design and development of the optical communication system with EDFA has been discussed. The important EDFA configurations, the chronological development of EDFA and design issue of the EDFA design also have been addressed. Finally, the future scopes in the design of EDFA with possible solutions are also discussed.

Keywords EDFA · DWDM · RAMAN · HOA · ASE · BER

1 Introductions

In optical communication when the signal is transmitted through the optical fiber for long distance (>100 km), the signal gets attenuated. To compensate for the loss, the signal should be restored. Restoring of the signal can be done by repeaters or optical amplifiers (OA). Whenever electrical repeaters are used, it requires optical to electrical conversion before amplification and electrical to optical conversion after amplification. This will increase the complexity and cost of the system. In contrast to that if OA are used, it will amplify the signal in the optical domain without optical to electrical and electrical to optical conversion. OA are used to provide optical amplification of the signal by stimulated emission of photons using rare earth ions which are implanted in the silica fiber core. The most popular OA available in the market are EDFA, Raman amplifier, semiconductor optical amplifier (SOA), optical parametric amplifiers (OPA), etc. Among these amplifiers, EDFA is made up by

A. Thakor (✉) · P. Prajapati
A. D. Patel Institute of Technology, V.V. Nagar, Gujarat, India
e-mail: ec.asifiqbal@adit.ac.in

P. Prajapati
e-mail: ec.pravin.prajapati@adit.ac.in

V. Janyani et al. (eds.), *Optical and Wireless Technologies*, Lecture Notes in Electrical Engineering 648, https://doi.org/10.1007/978-981-15-2926-9_12

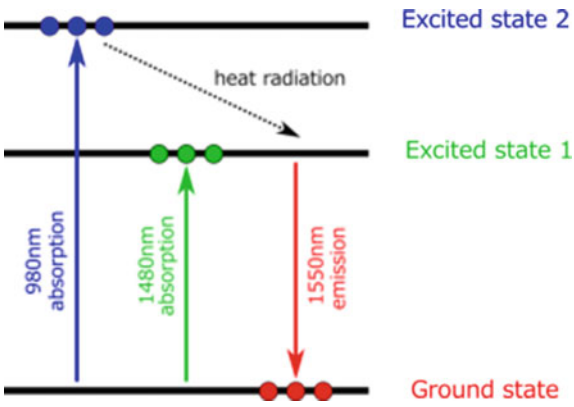

Fig. 1 Energy diagram of Er ions [2]

doping of erbium ions with the silica fiber, which can operate in 1550 nm window at which the loss of silica fiber is minimum [1].

The main part of the EDFA is an erbium-doped fiber which is made up of silica fiber doped with erbium ions. Figure 1 shows the energy diagram of erbium (Er), showing how amplification takes place at 1550 nm with a pump frequency of either 980 nm or 1480 nm.

When the pumping wavelength is 1480 nm, Er ions absorb the light and excite to the excited state 1. When the pump power is sufficient and population inversion occurs, then stimulate inversion takes place and amplification occurs. When the pumping wavelength is 980 nm, the Er ions absorb the light and excite to the excited state 2 as shown in Fig. 1, where it remains for the short duration and Er ions relaxed to excited state 1 by photon emission. This creates a population inversion between ground state and excited state 1, and amplification takes place at 1550 nm. Since the invention of the EDFA, optical communication system has changed in terms of speed and high data rates. With the use of EDFA, the wavelength division multiplexing (WDM) technology has emerged to fulfill the increasing demands of data traffic [3].

In this paper, Sect. 2 describes the configuration of EDFA. Section 3 includes the literature survey to improve the performance of EDFA. In Sect. 4, a hybrid optical amplifier using EDFA is described. The last section is having the future scope of the EDFA and hybrid OA.

2 EDFA Configuration

Figure 2 shows the EDFA configuration. It consists of erbium-doped fiber (EDF), pump laser and wavelength selective couplers.

The input signal enters through the input port. Pump combiner combines the input optical signal and pump signal, and then the combined signal will pass through the EDF where amplification occurs. The amplified signal is available at the output.

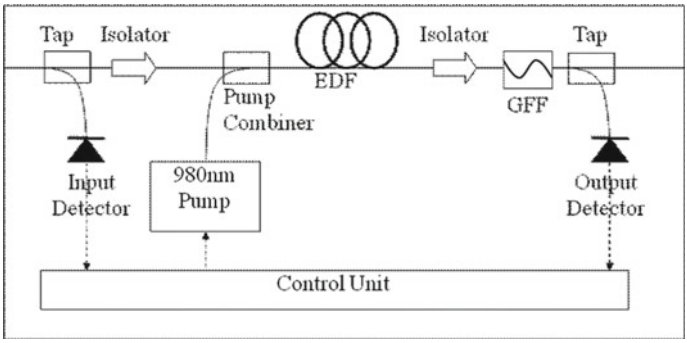

Fig. 2 EDFA configuration [4]

The purpose of the isolator is to prevent the back reflection. In multichannel WDM amplifiers, gain flattening filter (GFF) can be used to provide a flat gain.

In EDFA, the energy of the pumping photon is used to raise the electron into the excited state. There are three methods of pumping in EDFA: forward pumping, backward pumping and bidirectional pumping. In forward pumping, the input optical signal and pump signal have the same direction and are combined using coupler or wavelength division multiplexer, the input signal is amplified by taking the energy from the pump signal and the amplified signal then coupled to the fiber and travel through the optical fiber. In backward pumping, the input signal and pump signal have opposite direction. In bidirectional pumping for optimum performance of the EDFA, both forward pumping and backward pumping are combined, two pump sources are used and input signal propagated in the forward direction [5].

In the design of EDFA, the gain and noise figure (NF) are very important parameters to be considered. For a given pump power, EDFA gain depends upon the wavelength of the signal and the length of EDFA in the fiber. The gain of EDFA is maximum for a particular value of length for given pump power and after that for higher length, the gain will decrease. So to achieve maximum gain, one has to optimize pumping power and fiber length. NF also depends upon the pump power and EDFA length. Various researches have been carried out to improve the performance of the EDFA. The next section describes the literature survey about EDFA.

3 EDFA: Chronological Development

For the achievement of the flat gain, bit error rate (BER) and NF of EDFA, for the optimized value of pump power and fiber length, Ismail et al. [6] have designed simulation based WDM optical network system using OptiSystem software. For 16 input signal channels and 8 m length of the fiber, they have measured gain and NF for different pump power. They have achieved a flat gain of 38 ± 0.5 dbm 1546–1558 nm wavelength with BER $<10^{-4}$ and NF of <9 dB. They have also proved that for the

higher pump power, the gain flatness will be reduced, which will also increase the NF and BER.

Raghuwanshi and Sharma [7] have developed MATLAB-based Simulink model using forward pump EDFA for the study of amplifier gain, NF, etc. Here, the input signal of 1550 nm and pump source of 1480 nm is chosen. The result of this simulation for the gain v/s length of the fiber is shown in Fig. 3. From Fig. 3, it is clear that up to certain limits, the gain is increasing and then after the saturation point, the gain is decreasing. The reason for this is an insufficient population inversion due to higher pump depletion.

Similarly, Fig. 4 shows the variation of NF with respect to fiber length for different value of pump power. Figure 4 shows that NF is decreasing as the pump power increases. This is because high pump power results in a strong population inversion before the gain saturates.

By using multi-parameter optimization tools, Pradhan et al. [8] have done the optimization of fiber length, pump power and frequency spacing of input signal in order to achieve maximum gain and minimum NF of EDFA. For the simulation purpose, they have used Giles and Disurvire model of EDFA to find out various parameters of EDFA amplifier performance. For the improvement of the OSNR,

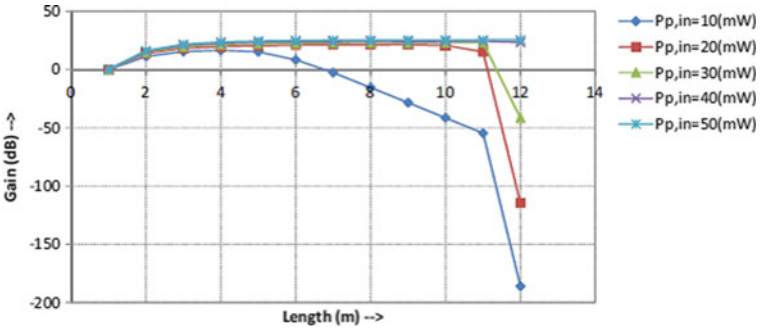

Fig. 3 Gain variation with length of fiber for different pump power [7]

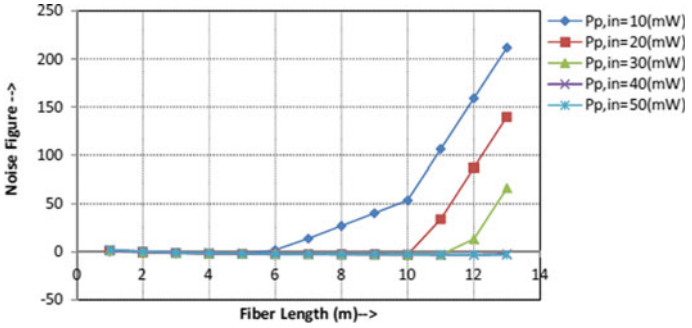

Fig. 4 NF variation with length of fiber for different pump power [7]

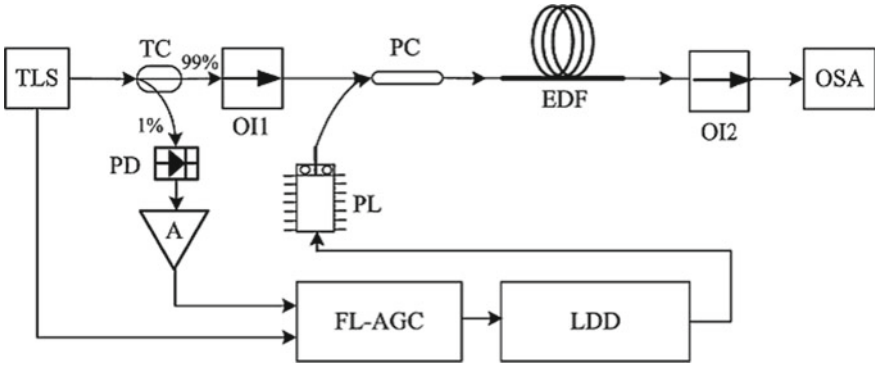

Fig. 5 Fuzzy logic-based AGC EDFA [9]

pump power of 980 nm is used, and WDM analyzer is used for the measurement of the maximum gain and minimum NF. They have suggested that compared to counter pumping and bidirectional pumping, co-pump EDFA is better. They have also observed that by decreasing the channel spacing, the effect of four wave mixing and self phase modulation (SPM) increases, which will degrade the performance of EDFA and also BER increases by distance.

Yucel et al. [9] have developed the AGC card based on fuzzy logic for controlling the pump current for particular values signal power and signal wavelength as shown in Fig. 5.

In this scheme, the input signal is launched from the tunable laser source (TLS). This input signal is separated by tap coupler (TC). 1% of the input is used by the fuzzy logic AGC (FL-AGC) card to control the current of pump laser (PL), and 99% of the signal is given to pump coupler (PC). This 1% of the optical signal is converted to the electrical signal by photo diode (PD), and then it is converted to a digital value by ADC and given to fuzzy algorithm. The output of the fuzzy algorithm is converted to the analog values needed by pump laser current driver (LDD). This value of the pump current is used to keep gain constant. Wavelength and power of the signal corresponding to the optimum value of the pump current are measured using the fuzzy logic. Optical isolators (OI1, OI2) are used to prevent the back reflections. They have recommended this approach for photonic engineering applications.

In addition to that, in the optical link whether it is single amplifier or multiple amplifiers if there are failures in the single optical amplifier, the entire system will get failure which leads to a loss of information rate of the optical link. In that situation, the optical data should pass through the alternate path to bypass the faulty amplifier, and if optical power sent to link can be optimized, then it is possible to recover part of the information rate, and the failure of the link can be avoided. Silva et al. [10] showed that optical path can be added to avoid the damaged amplifier to prevent link failure. They suggested different methods for the compensation of the amplifier failure. They have proved that by optimizing the signal power given to fiber, by setting the gain of amplifiers and by extra passive optical amplifier in the link, it

is possible to recover 74% of information rate for the 500 km link length, 69% of information rate for 1000 km and 64% of information rate for 2000 km link.

In dense wavelength division multiplexing (DWDM) system, EDFA should be operated in the long wavelength band. The performance of the DWDM is degraded due to input channel power/wavelength variation or numbers of channel used for amplification. In that case wide, band EDFA having a flat gain should be used. Durak et al. [11] have proposed gain-flattened and gain-clamped L-band EDFA design based on Fabry–Perot (F-P) configuration-based lasing cavity model. In that configuration, they have placed symmetrical fiber Bragg gratings at both the input and output side of EDFA. Due to the lasing, they have achieved a constant population inversion in EDF, which leads to the gain clamping in the system.

They have done the simulation using Optiwave software of lasing controlled L-EDFA using 20 m EDF length, forward pump laser wavelength 974 nm and backward pump laser wavelength 976 nm, and power for both the pump laser was 120 mW. They have also performed the experiment to check gain flatness, and they have obtained the result as shown in Fig. 6 which shows that higher gain was measured at higher wavelength and at 1558 nm the gain is almost constant and also the noise performance is better.

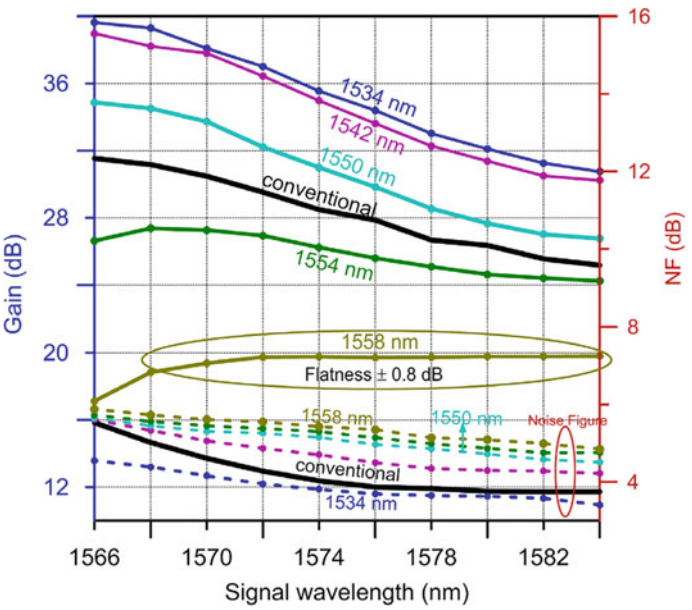

Fig. 6 Variation of gain with wavelength [11]

4 Hybrid Amplifier Using EDFA

Due the requirement of high speed and high data rate, there is an increasing demand for higher bandwidth DWDM system. In order to use optical fiber amplifiers for the maximum available fiber bandwidth, different combination of amplifiers should be connected, which is known as hybrid amplifiers. Hybrid OA can be connected either in series or in parallel combination of two or more OA for different wavelength. In parallel combination, DWDM signals are demultiplexed in different wavelength, then they are amplified by the amplifiers, and then the signals are multiplexed with the coupler. This system is simple, but the disadvantage of this system is the unusual wavelength exists between each gain and also due to the coupler losses the NF increases. While in series combination the gain spectrum is wide, signal gain is large, high pump efficiency and do not require the couplers [12].

Various researches have been done to improve the performance of the hybrid OA. Singh et al. [13] have developed the analytical model for hybrid amplifiers, using EDFA-RAMAN for the optimization of various parameters like Raman length, EDFA length and pump power to obtain the higher gain using genetic algorithm. They have also done the simulation using 100 DWDM channels having the bandwidth range from 187 to 189.5 THz. This system is giving the flat gain >18 dB in this range.

In order to increase the transmission capacity of the system, one has to increase the bit rate, the bandwidth of the signal or channel density. Assuming the bandwidth of the signal is limited by the bandwidth of the OA, gain bandwidth product can be increased by the flat gain and amplification of more than one optical fiber bands.

Singh and Kaler [14] have simulated two stages OA (EDFA-Raman) for DWDM system with gain equalization techniques in order to achieve a higher flat gain and low NF. The result in Fig. 7 shows that the gain is increasing after the second stage and also the gain is considerably flat. The disadvantage of this system is that optical signal to noise ratio (OSNR) and NF are degraded.

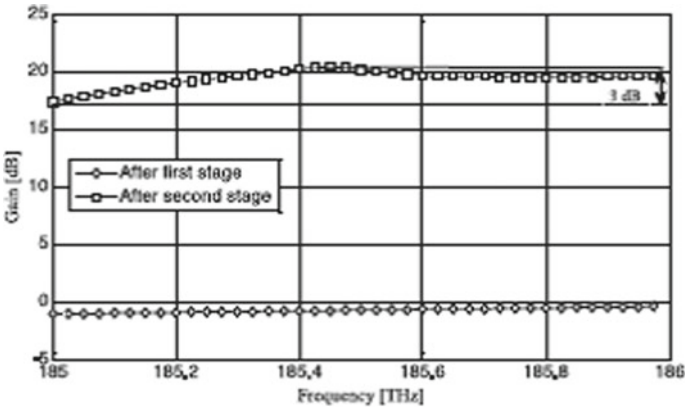

Fig. 7 Gain flatness versus frequency [14]

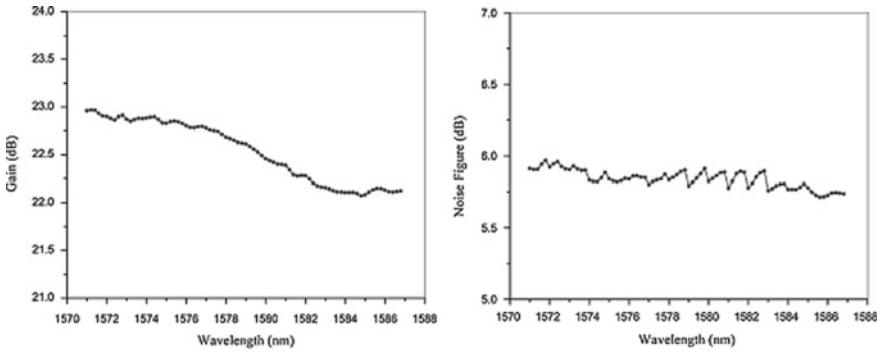

Fig. 8 Variation of gain and NF versus wavelength [17]

Malik et al. [15] have done the comparison of the different combination of the hybrid OA for long-distance combination. The parameters for the comparison they have checked are eye diagram, output power, *Q*-factor and BER. After the comparison, they have observed that hybrid amplifier SOA-EDFA provides higher output power, best eye diagram and lowest BER at a distance of 100 km

EDFA is used for obtaining the larger gain and low NF, but Er–Yb co-doped fiber amplifiers are also giving the higher gain with the smaller fiber length. In EYDFA, highly doped Yb ions are available around the Er ions. These Yb ions are acting as an ionic buffer and reduce the effect of clustering and transmission efficiency from pump to Er ions increases. Harun et al. [16] presented an efficient EYDFA (single and double stage) using a single pump. They have achieved the gain of around 38 dB and NF of around 5 dB using forward pumping at a wavelength of 1536 nm.

For 80 × 100 GB/s DWDM system, Obaid and Shahid [17] have simulated Raman–EYDFA hybrid amplifier in the wavelength range of 1571–1587 nm with a channel spacing of 0.2 nm using OptiSystem and MATLAB. They obtained a higher flat gain, without any costly gain clamping component. The result of this simulation is shown in Fig. 8. The nonlinearity in the gain and NF is due to ASE produced by each amplifier. The gain is >22 dB at each wavelength.

5 Future Scope of Research in EDFA

System performance depends upon the OSNR of the individual optical channels. OSNR can be increased by the high amplifier output and low NF or by reducing the span loss. Gain flatness is also a critical parameter in DWDM systems. It is a critical parameter for maintaining system performance under varied channel loading conditions caused by either network reconfiguration or partial failure. For the achievement of the flat gain pump power, length of the fiber and frequency spacing of the input signal should be optimized. Placement of the EDFA at particular

interval and with the spare EDFA can also be used in order to avoid the loss of information. In order to compensate the overall losses and also the nonlinearity in the OA, hybrid amplifiers can be used. Various combinations of hybrid OA like SOA-EDFA, EDFA-EDFA, RAMAN-EDFA, RAMAN-SOA and EDFA-RAMAN-EDFA for varying transmission distance and various data formats can be analyzed to get large flat gain, low NF and larger bandwidth. Alternatively, fluoride and telluride-based fibers can also have good gain and bandwidth characteristics. Similarly, other components like praseodymium and indium fluoride (I_nf), etc., -based fiber will be analyzed and simulated, and new designs can be proposed. More numbers of channels can be transmitted with reduced channel spacing by incorporating different co-doping concentration, multiple pumping schemes, where the pump wavelengths and pump powers can be chosen carefully to ensure a good performance.

6 Conclusion

The main design issues of EDFA design such as flat gain, low NF, high gain, high saturation level and effect of nonlinearities have been discussed. The research work reported regarding the reduction of noise, utility of channel density, enhancement in bandwidth, etc., has been presented and discussed for better understanding. The future scope of research in the design of EDFA and its possible methodology have been presented, which gives insight into the researchers of the optical domain for their research work. This paper will help beginners who have started the research work in the optical amplifier domain.

References

1. Becker PC, Olsson NA, Simpson JR (1999) Erbium doped fiber amplifiers. Academic Press, San Diego, CA
2. https://www.fiberlabs-inc.com/glossary/erbium-doped-fiber-amplifier/
3. Masataka N (2014) Evolution of EDFA from single-core to multi-core and related recent progress in optical communication. Opt Rev 21(6):862–874
4. Finisar White Paper: introduction to EDFA technology. http://www.finisar.com
5. Anthonya R, Lahiri R, Biswas S (2014) Gain clamped L-band EDFA with forward-backward pumping scheme using fiber Bragg grating. Optik 125:2463–2465
6. Ismail MM, Othman MA, Zakaria Z, Misran MH, Meor Said MA, Sulaiman HA, Shah Zainudin MN, Mutalib MA (2013) EDFA WDM optical network design system. Procedia Eng 53:294–302
7. Raghuwanshi SK, Sharma R (2015) Modeling of forward pump EDFA under pump power through MATLAB. Int Nano Lett 5:155–160
8. Pradhan D, Mandloil A (2018) Design optimization of EDFA for 16 × 10 Gbps data rate DWDM system using different pumping configurations. Wirel Pers Commun 106:2079–2086
9. Yucel M, Goktas HH, Celebi FV (2014) Design and implementation of fuzzy logic based automatic gain controller for EDFAs. Optik 125:5450–5453

10. Silva NA, Pinto AN (2018) Optimizing the placement of spare amplifier cards to increase the achievable information rate resilience. Opt Fiber Technol 45:40–46
11. Durak FE, Altuncu A (2018) All-optical gain clamping and flattening in L-band EDFAs using lasing controlled structure with FBG. Opt Fiber Technol 45:217–222
12. Zyskind J, Bolshtyansky M (2011) *EDFAs*, Raman amplifiers and hybrid Raman/EDFAs. Optically amplified WDM networks. Elsevier Inc., San Diego, pp 83–116
13. Singh S, Kaler RS (2015) Performance optimization of EDFA–Raman hybrid optical amplifier using genetic algorithm. Opt Laser Technol 68:89–95
14. Singh S, Kaler RS (2014) Multistage gain-flattened hybrid optical amplifier at reduced wavelength spacing. Optik 125:5357–5359
15. Malik D, Pahwa K, Wason A (2016) Performance optimization of SOA, EDFA, Raman and hybrid optical amplifiers in WDM network with reduced channel spacing of 50 GHz. Optik 127:11131–11137
16. Harun SW, Abdul-Rashid HA, Muhd-Yassin SZ, Abd-Rahman MK, Jayapalan KK, Ahmad H (2008) 37.2 dB small-signal gain from Er/Yb co-doped fiber amplifier with 20 mW pump power. Opt Laser Technol 40:88–91
17. Obaid HM, Shahid H (2018) Novel flat-gain L-band Raman/Er-Yb co-doped fiber hybrid optical amplifier for high capacity DWDM system. Optik 175:284–289

An Approach for Reduction of Cross-Talk in Multi-core Optical Fibers

Shroddha Mukhopadhyay, Samanti Das and Nikhil R. Das

Abstract Multi-core fiber (MCF) is a practical approach to realize space division multiplexing for high-capacity transmission in optical communication system. However, a major impairment toward increasing core density to enhance the capacity is inter-core cross-talk. In this paper, a design to reduce the cross-talk is discussed, by placing air holes between the cores and taking heterogeneous cores. Cross-talk is computed from the mode field values obtained using finite difference method. The results show improved performance with respect to the reduction of cross-talk through increased modal confinement and decrease of higher-order modes. A detailed study on the effect of radii of the cores and air holes on the cross-talk has also been presented.

Keywords Optical fibers · Multi-core · Cross-talk · Air holes · Modes · Heterogenous cores

1 Introduction

With the increase in data traffic, there have been developments in the field of optical communication to expand the transmission capacities of optical fibers [1]. With the advent of various multiplexing techniques, namely time-division multiplexing (TDM), wavelength division multiplexing (WDM) and other modern digital technologies, the maximum transmission capacity through a single-mode fiber has increased [2]. However, the capacity has an upper limit of approximately 100 Tbit/s because of the fiber fuse phenomenon and Shannon limit [3]. Space division multiplexing (SDM) will accelerate and realize high-capacity transmission exceeding

S. Mukhopadhyay (✉) · S. Das · N. R. Das (✉)
Institute of Radio Physics and Electronics, University of Calcutta, 92, Acharya Prafulla Chandra Road, Kolkata 700009, India
e-mail: mshroddha@gmail.com

N. R. Das
e-mail: nrd@ieee.org; nrd.rpe@caluniv.ac.in

S. Das
e-mail: samantituna96@gmail.com

V. Janyani et al. (eds.), *Optical and Wireless Technologies*, Lecture Notes in Electrical Engineering 648, https://doi.org/10.1007/978-981-15-2926-9_13

petabit/s, and a high-capacity distance product of over 1 exabit s^{-1} km^{-1} [4]. SDM realized by multi-core fibers (MCFs) and few-mode fibers (FMFs), is expected to overcome the transmission capacity limitations of conventional single-mode fiber (SMF). In order to enable simultaneous transmission of different signals, multi-core fiber (MCF) incorporates multiple cores within a single cladding. Its wide range of benefits extends from reduced space requirement to significantly high data rates [5].

In principle, each of the cores in an MCF acts as a separate dielectric waveguide, allowing independent propagation of light through them. However, if the distance between two cores within the fiber is very small, there might be a chance of undesirable spatial overlap of the corresponding mode fields, which, in turn, results in power coupling between cores. These circumstances pave way for cross-talk in MCFs. Super-modes are created when the light which is initially coupled into one core, can eventually couple over to other cores within the fiber [6, 7]. This coupling can be minimized by using large enough spacing between the cores, but this will lead to low core density. To avoid substantial cross-talk in optical communication systems, often, the fiber cores diameters are made in the order of a few micrometers, to obtain single-mode propagation in a particular wavelength range. An inter-core distance of about 30–40 μm may be sufficient to avoid cross-coupling even within kilometers along the length of the optical fiber. In such weakly coupled fibers, the cladding diameter of 125 μm allows only a few number of cores, thereby reducing the core density [6]. The strong modal confinement has been proposed by using air holes around the multiple cores [8–10] or with heterogeneous designs where the different cores have different refractive indices. In principle, the fiber diameter can also be increased, but that is impractical, because it increases the bending loss [9]. Keeping these factors in mind, in this paper, a hole-assisted MCF structure with fewer number of air holes is proposed.

2 Design Aspects

The schematic cross-section of a hole-assisted MCF structure proposed in this study is shown in Fig. 1. It consists of seven cores arranged in a hexagonal array with equal

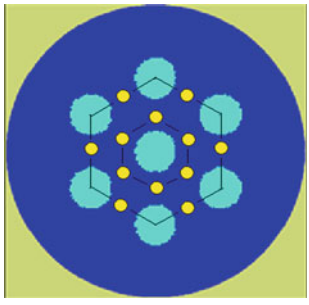

Fig. 1 Schematic cross-section of the proposed hole-assisted MCF

spacing between any two cores. Air hole is present at the mid-point of the straight line joining the centers of two adjacent cores. Previous studies in hole-assisted multi-core fibers for reducing inter-core cross-talk have been implemented by surrounding each core with air holes [11]. The proposed design is expected to achieve nearly similar improvements in cross-talk but with less complexity and easier manufacturability. The proposed structure has the nominal specifications: radius of core is 6 μm, radius of air holes is 4 μm, radius of cladding is 50 μm, inter-core distance is 20 μm; core-to-air hole distance is 10 μm, refractive indices of core and cladding are 1.46 and 1.45, respectively.

The analysis is done using 2D finite difference method (FDM). The fiber cross-section is discretized into the finite number of points and the discretized Helmholtz equation (for dielectric media) is converted into the matrix form of eigenvalue equation, as shown below.

$$\mathbf{AU} = \mathbf{bU}, \tag{1}$$

where **U** represents the E-field and **b** the eigenvalue. The matrix **A** is solved for eigenvectors to find the electric field intensity pattern (modes). Cross-talk occurs due to the overlap of transmitted modes between adjacent cores. Theoretically, cross-talk is calculated by the amount of signal power that leaks from the main channel into the adjacent channel compared to the original signal power at the main channel. However, in this paper, the modal distribution is studied taking only the 2-D cross-section of a particular core, which gives an idea of the cross-talk pattern occurring due to modal overlap The measure of cross-talk can be obtained as the ratio of the electric field at the middle of the line joining the two cores to that at the neighboring core center, as shown below:

$$\text{Measure of Cross-talk (dB)} = 10 \log \frac{E_{\text{clad}}}{E_{\text{core}}}, \tag{2}$$

where E_{clad} = electric field intensity in the cladding; E_{core} = electric field intensity in the center of a core. It has been shown that cross-talk can be improved using heterogeneous cores within the fiber [12]. The present study is extended using heterogeneous cores in the proposed MCF structure.

3 Results and Discussion

Using the techniques mentioned in the previous section, the computations are done writing codes in MATLAB. To verify the computational approach, the results for LP01 mode and an LP11 mode of a single-mode fiber are compared with those obtained using COMSOL simulation in Fig. 2, and a very good agreement has been found.

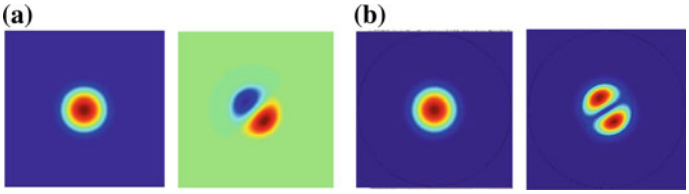

Fig. 2 LP01 and LP11 using **a** MATLAB codes and **b** COMSOL simulation

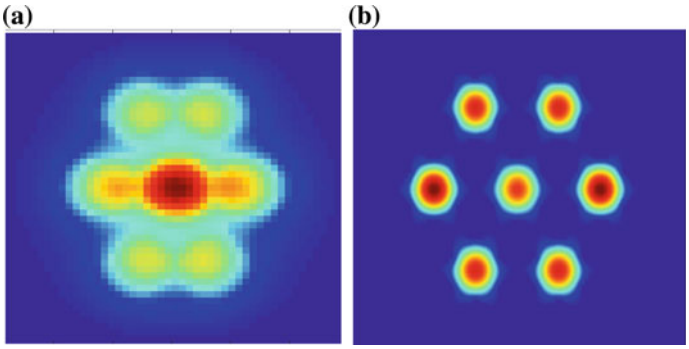

Fig. 3 Mode plots for MCF structure **a** without air holes and **b** with air holes. **a** Without air holes, measure of cross-talk = −8.63 dB, **b** with air holes, measure of cross-talk = −65.29 dB

In Fig. 3, the computed modes are plotted for a seven core MCF structure (a) without and (b) with air holes. The nominal values of different material and structural parameters are taken as mentioned earlier.

In Fig. 3a, it is observed that there is a huge amount of modal overlap resulting in considerable cross-talk. Clearly, on putting air holes (Fig. 3b) around the cores, cross-talk decreases significantly. Using Eq. (2), it is seen that the measure of cross-talk improves drastically from −8.63 to −65.29 dB using the proposed structure. The mode field diameter also decreases from 20.05 (Fig. 3a) to 13.1426 μm (Fig. 3b). The placement of air holes in the proposed structure creates a larger refractive index contrast between the core and the air holes and as a result the overlap of various modes is successfully prevented. Thus, there is further scope of increasing the core density within the MCF which will lead to higher channel capacity.

Figure 4 shows the variation of the cross-talk pattern with respect to varying (a) core radius and (b) air hole radius, respectively. In Fig. 4a, it is seen that the decrease in core radius decreases the cross-talk. This is because the spacing between cores increases reducing the chances of overlap of modes. Good results (in our refractive indices combination) are obtained when R_core $\leq$ 10 μm. Again, when the air hole radius is varied from 0 to 6 μm, the cross-talk varies from 0 to −248 dB, keeping core radius constant. It is known that with the increase in the radius of air holes, the effective modal area reduces. Hence, from Fig. 4b, it is observed that there is an improvement in cross-talk with the increase in the radius of air holes.

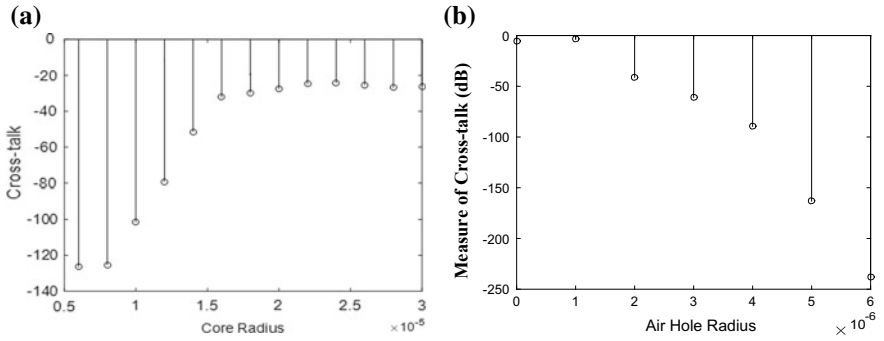

Fig. 4 Variation of cross-talk with **a** core radius (μm) keeping air hole radius constant at nominal value and **b** air hole radius keeping core radius at nominal value

The effect of core radius and air hole radius is shown in compact form in Fig. 5. This suggests the choice of the combination of core radius and air hole radius to design the MCF for target maximum cross-talk.

In Fig. 6, cross-talk is plotted as a function of delta ($\Delta = \frac{n_2^2 - n_1^2}{n_2^2}$) with core refractive index as parameter. From the figure, it is seen that as the delta value is being changed from 0 to 0.04, the measure of cross-talk [as calculated from Eq. (2)] is found to decrease from -54 to -62 dB. Thus, it is concluded that cross-talk decreases with increase in delta. But we need to keep the delta value within the industrial limit otherwise designing of such fibers will be impractical.

The maxima of the modes obtained from the analysis of the MCF with air holes are shown in Fig. 7. From the figure, it is observed that effectively only six modes (with

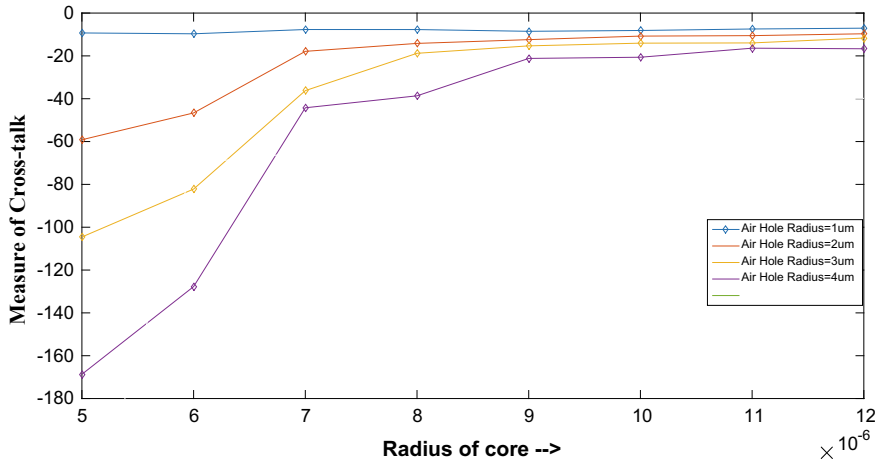

Fig. 5 Plot for measure of cross-talk with core radius for different values of air hole radius

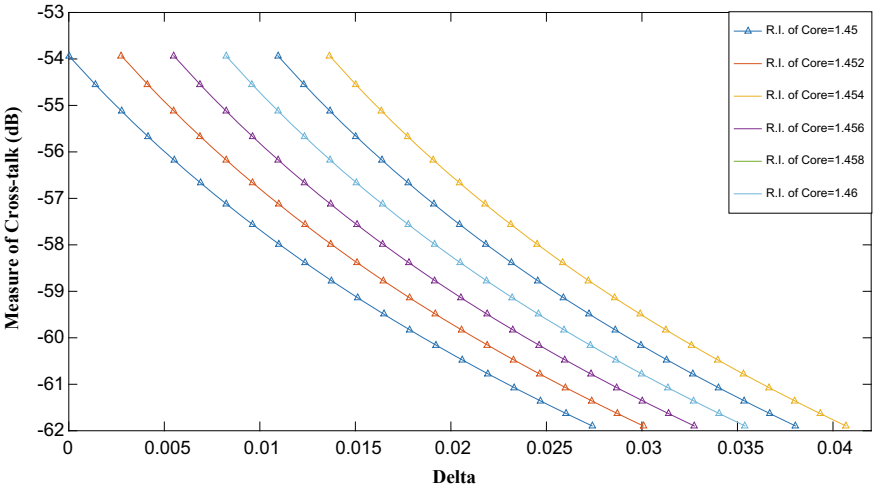

Fig. 6 Variation of cross-talk with delta for different core R.I. keeping core radius and air hole radius fixed at nominal values

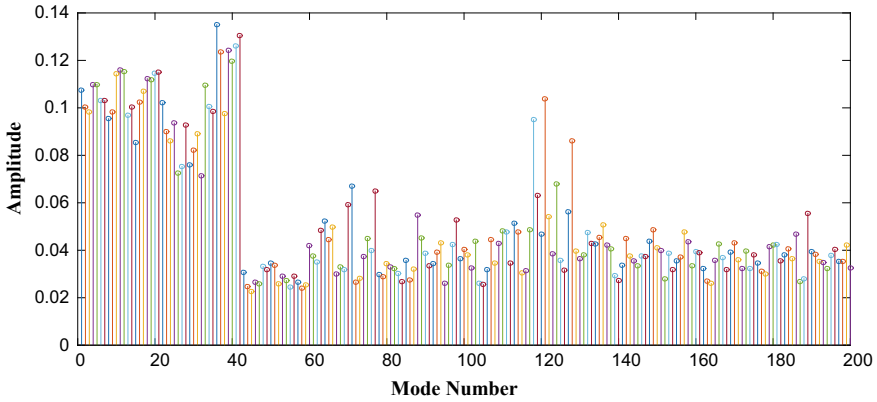

Fig. 7 Plot of modal maxima with mode number for proposed MCF structure

their degenerates) propagate through the fiber and, hence, intermodal dispersion gets reduced upon placing air holes around the cores.

Table 1 is given to compare the performance of the proposed structure with that of some structures reported earlier in literature (mentioned in Refs. [8–10]). It is concluded from the table that considering both simplicity of the structure and improvement in cross-talk performance, the proposed structure is the best alternate. Cross-talk is disadvantageous when the channels are carrying separate signals. However, if the structure is used as a coupler, the same modal overlap will be beneficial in coupling signal from one core to another.

Table 1 Comparative study of performance of different homogeneous structures (R_Core = 6 μm, R_airhole = 4 μm)

Work	Structure	Measure of cross-talk (dB)	Remarks
Reference [8]	Seven core structure with 12 air holes surrounding each core	−66.2452	Improvement in cross-talk performance at the cost of more numbers of air holes
Reference [9]	Seven core structure with six air holes surrounding each core with inter-core distance four times the core radius	−89.6244	Improvement in cross-talk performance at the price of significant reduction in core density
Reference [10]	Trench-assisted seven core fiber (R.I. of Trench = 1.3, W_Trench = 4 μm)	−45.3016	Relatively higher cross-talk, also difficult from the point of manufacturing
Proposed design	Seven core structure with an air hole placed at the bisection point of the straight line joining two cores	−65.29	Fairly low cross-talk with a very simple structure

The study is extended for the proposed MCF structure using cores as heterogeneous. The mode plot is shown in Fig. 8. Introduction of heterogeneous core improves the measure of cross-talk even more. Here, the measure of cross-talk is −110.91 dB, which is even better than that in Fig. 2b using homogeneous cores. Also, the mode field diameter reduces to 10 μm. Thus, cores can be placed closer, resulting in higher core density and, hence, higher fiber capacity.

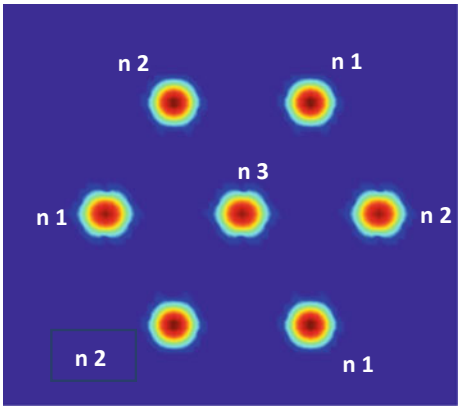

Fig. 8 Modes of the proposed MCF structure with heterogeneous cores. Radius of core = 6 μm, radius of cladding = 50 μm and radius of air hole = 4 μm. The structure comprises of three different refractive index combinations in the seven cores as shown; namely $n_1 = 1.457$, $n_2 = 1.454$, $n_3 = 1.46$, and the refractive index of cladding is taken as 1.45. Measure of cross-talk is obtained as −110.91 dB

4 Conclusion

In this paper, a compact hole-assisted multi-core fiber has been proposed. The proposed structure is simple to design, yet it overcomes the disadvantages that are present in a traditional multi-core fiber without air holes. This compact structure ensures minimization due to bending losses and reduced manufacturing cost compared to the other air hole structures reported in literature. Moreover, the study has been done by changing other fiber parameters like core radius, air hole radius, relative refractive index between core and cladding. We have shown how the cross-talk reduces significantly by varying all of these parameters. This implies that core density can be increased within the fiber. Thus, the parameters can be suitably chosen to keep cross-talk within the specified limit. The study is extended for the proposed design by incorporating heterogeneous cores. The study has shown that overlapping between modes decreases thus further reducing the cross-talk. Hence, the core density of the MCF can be significantly increased for high-capacity optical transmission.

References

1. Snyder AW, Love J (1983) Optical waveguide theory. Chapman and Hall, London
2. Mizuno T, Miyamoto Y (2016) High-capacity dense space division multiplexing transmission. NTT Network Innovation Laboratories, Japan
3. Sasaki Y et al (2017) Few mode multicore fibers for long haul transmission line. Opt Fiber Technol 35:19
4. Inao S et al (1979) Multicore optical fiber. In: Optical fiber communication conference, Washington, DC, USA, Paper WB1
5. Saitoh K (2016) Multicore fiber technology (tutorial review). J Lightwave Technol 34:55
6. Hayashi T et al (2013) Physical interpretation of intercore crosstalk in multicore fiber: effects of macrobend, structure fluctuation, and microbend. Opt Express 21:5401
7. Xia C et al (2012) Hole-assisted few-mode multicore fiber for high-density space-division multiplexing. IEEE Photonics Technol Lett 24:1914
8. Ziolowicz et al (2014) Hole-assisted multicore optical fiber for next generation telecom transmission systems. Appl Phys Lett 105:81106
9. Saitoh K et al (2010) In: OECC 2010, 7C2-1
10. Takenga K et al (2011) In: OFC 2011, OWJ4
11. Van Uden RGH et al (2014) Ultra-high-density spatial division multiplexing with a few mode multicore fibre. Nat Photonics 8:865
12. Imamura K et al (2011) Investigation on multi-core fibers with large Aeff and low micro bending loss. Opt Express 19:10595

Measurement of Angular Velocity and Tilt Angle of Two-Dimensional Fiber-Optic Gyroscope with Sagnac Effect

Somesh Mule, Arpit Rawankar, Bharati Singh and Mohit Gujar

Abstract Fiber-optic gyroscope comes under the category of optical gyroscopes which works on the principle of Sagnac effect. This paper provides a crux of fiber-optic gyroscope and its working principle. Fiber-optic gyroscopes work on the principle of the Sagnac effect. In Sagnac effect, the light beam is split into two separate beams. These beams then propagate in opposite directions with respect to each other. When the setup is stationary, the beams travel in same path and reach the output without any delay, if the setup is rotating, then one beam travels less distance than the other beam, and at output these beams arrive at different time and undergo interference to produce a fringe pattern which is sensitive to the phase difference between the beams. Fiber-optic gyroscope works on the similar basis, with a difference that the beams are made to travel within an optical fiber. These beams are obtained by passing light through a coupler and launched into the fiber using a collimator. Fiber-optic gyroscope is majorly used in military and aeronautical-based applications.

Keywords Sagnac effect · Fiber-optic gyroscope (FOG) · LabVIEW · Interferometer · Angular rotation

1 Sagnac Interferometer

Sagnac interferometer was the first optical experiment which successfully demonstrated the precise measurement of changes in orientation of an object. By calculating the phase difference produced by two beams of light that are propagating in opposite direction, their time difference can be evaluated. As shown in Fig. 1, the counter-propagating light beams were obtained by splitting a single beam of light, using a beam splitter. Both the emerging beams are then allowed to interfere with each other, and they produce a fringe pattern as shown in Fig. 2. The fringe pattern obtained is sensitive to any phase difference present between the two counter-propagating beams [1, 2].

S. Mule (✉) · A. Rawankar · B. Singh · M. Gujar
Department of Electronics and Telecommunication, University of Mumbai, Mumbai, India

V. Janyani et al. (eds.), *Optical and Wireless Technologies*, Lecture Notes in Electrical Engineering 648, https://doi.org/10.1007/978-981-15-2926-9_14

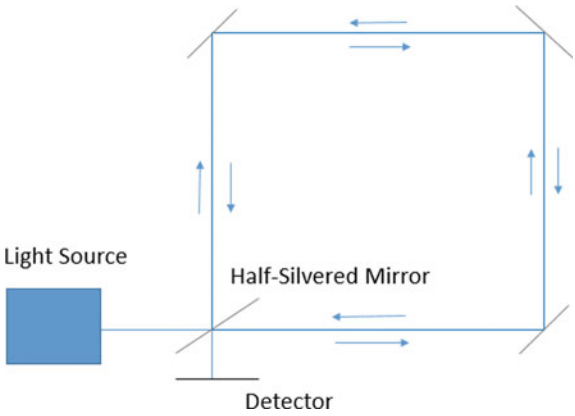

Fig. 1 Free-space Sagnac interferometer

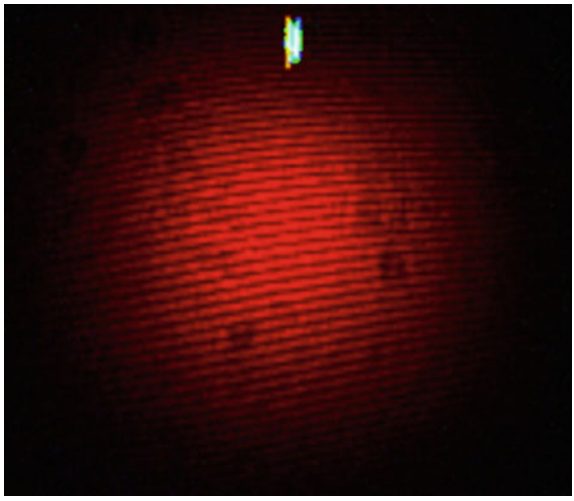

Fig. 2 Fringe pattern obtained with Sagnac interferometer

Assume the radius of interferometer as r. Then, the time taken by the two beams is given by [3]:

$$t_{\pm} = \frac{(2\pi r \pm r\Omega_{\text{rot}} t_{\pm})}{v} \tag{1}$$

where $t+$ is time taken by the beam moving along the direction of rotation, $t-$ is time taken by the beam moving against the direction of rotation. v is the velocity of propagation of the beam around the loop. Ω is angular frequency of rotation of the interferometer. The time difference between the two beams can be calculated as:

$$\delta t = \frac{(4\pi r^2 \Omega_{\text{rot}})}{(v^2 - (r\Omega_{\text{rot}}))} \tag{2}$$

The phase difference between two beams is given as:

$$\Delta\phi = \frac{v\delta t}{\lambda_0} \tag{3}$$

where λ_0 is wavelength of laser.

2 Fiber-Optic Gyroscope

Fiber-optic gyroscope is a type of optical Sagnac interferometer. It works by sending a beam of light using laser. The CW laser with input power 30 mW and wavelength 730 nm is used for this experiment. To improve the coupling of laser beam into a single-mode fiber, collimators are used. The coupler used is a 3-dB coupler for wavelength 700–850 nm, and this coupler splits the beam from laser into two beams. Both the beams return back to the coupler where they are detected by the photodiode after traveling a closed loop of 100 m fiber in opposite direction. The fiber-optic gyroscope is prepared in the laboratory with diameter of 80 cm, and total number of fiber turns up to 40. The time taken by each beam to return is recorded. If the fiber-optic gyroscope is stationary, the beams will reach the starting point at same time. If it is rotating, then the beams travel different distances and so return at different times. In this case, the beam which is moving in the direction of rotation will get delayed as it should travel greater distance while the other beam which is moving in direction opposite to rotation travels less distance and reaches earlier [4, 5]. This time difference of the two beams can be calculated by LabVIEW software, and using curve fitting software, the angular rotation can be calibrated.

The second setup is also fiber-optic gyroscope setup, where it uses same principle of Sagnac interferometer such that couplers one end is connected to laser of 850 nm and the other end to optical power meter's output port. Thus, the light splits in two parts, and at the other end of this coupler it is connected to the two ends of single-mode fiber. Using this setup as shown in Fig. 3, we calculate power w.r.t speed in RPM (Fig. 4).

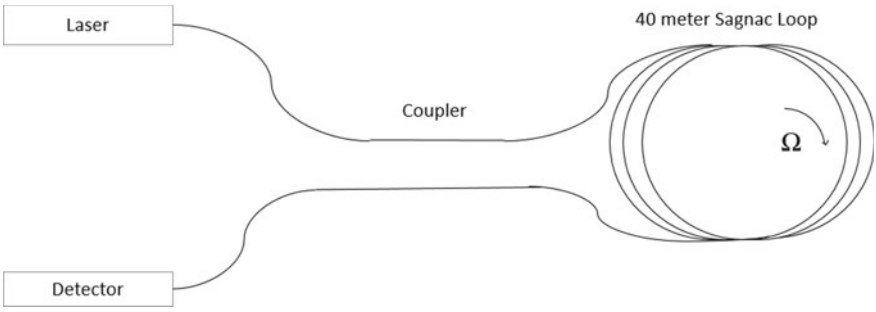

Fig. 3 Structure of fiber-optic gyroscope

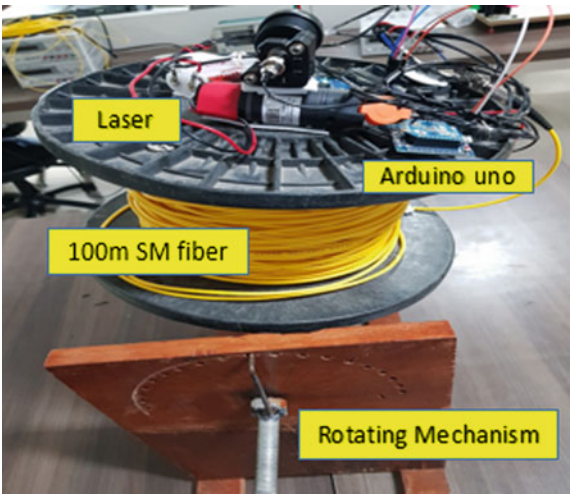

Fig. 4 Rotating mechanism with data acquisition system

The setup shown in Fig. 5 is fiber-optic gyroscope in which single-mode 100 m optical fiber is used and is winded around the rotating table. The laser source of 850 nm wavelength used is coupled into fiber using 50:50 beam splitter. The other end of splitter is connected to collimator which focuses light onto photodiode and from photodiode, it is given to microcontroller to convert analog signal to digital signal, and thus, using LabVIEW, we plot the graph. Tilt angle can be measured from the mechanism as shown in Fig. 6 by directly using markings on the board. We can also determine the tilt angle by calculating path difference between the two beams because of bending in the fiber. Fringes consist of alternate dark and bright bands, and by shifting the maxima of bright band, we can change the path difference.

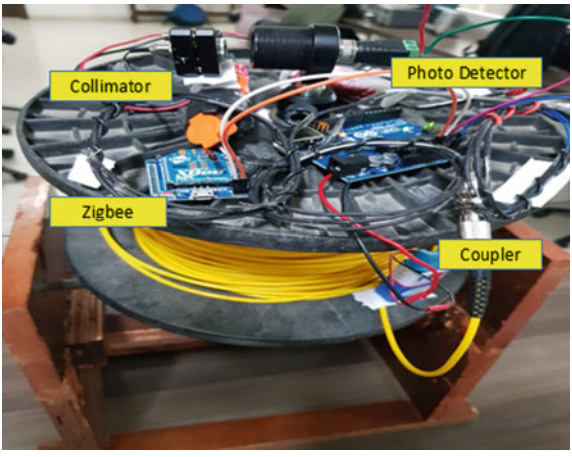

Fig. 5 Fiber-optic gyroscope setup

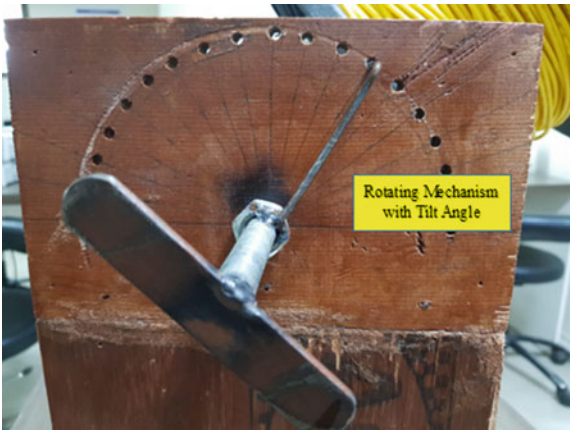

Fig. 6 Mechanism for manual measurement of tilt angle

Condition for constructive interference:

$$\text{Path Difference, } \Delta d = n\lambda \quad \text{where } n = 0, 1, 2, \ldots \tag{4}$$

Condition for destructive interference:

$$\text{Path Difference, } \Delta d = (n + 1/2)\lambda \quad \text{where } n = 0, 1, 2, \ldots \tag{5}$$

3 Result

As we rotate the setup once in clockwise direction and other in anticlockwise direction, we get the different values of voltages for that particular instance of rpm. The both beams take same amount of time to reach photodiode; thus, total path difference is zero which is observed in case of no rotation, mentioned in Table 1. In this case, there is no voltage difference observed at photodetector. But as soon as we rotate the table, it is observed that there is voltage difference at photodiode corresponding to

Table 1 Average voltage value detected at photodiode for different RPM of optical cable

Speed in RPM	Photodiode voltage (mV)
3.3	420
3.0	410
2.2	400
2.0	390
1.5	375
1.2	360

path difference of both counter-clockwise and clockwise propagating beams. This change is due to rotation, and hence, one beam reaches prior compared to other. Thus, this voltage difference obtained depends on the speed of rotation, i.e., more is the speed of rotation (RPM) larger is the voltage difference obtained and vice versa [6], thus giving high precision in detection of minute change in rotation.

This graph in Fig. 7 provides the information of voltage difference for corresponding rpm. When whole system is rotated, there is no voltage difference as the system is stationary. Hence, we use these results and plot a graph by curve fitting using LABFIT.

From Fig. 8, we get plot of straight line.

Thus, equation for straight line,

$$Y = AX + B \tag{4}$$

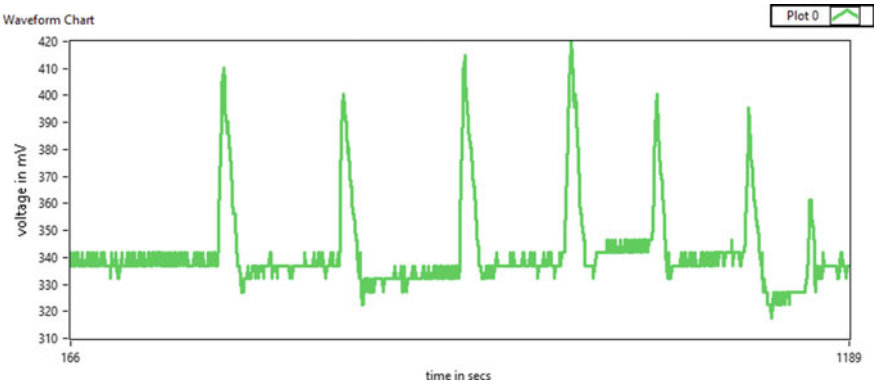

Fig. 7 Photodiode voltage variation with rotation in RPM

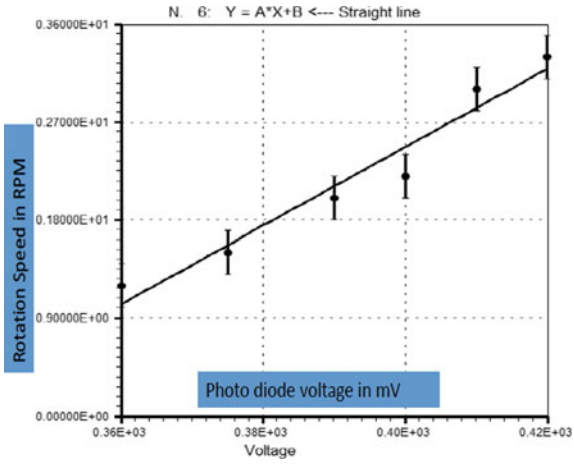

Fig. 8 Curve fitting plot of voltage versus RPM

where

Y is the RPM
X is the voltage in mV
A and B are constants.

From this graph, we get value for A and B with a error margin (ΔA and ΔB) of $\pm 5\%$

$A = 0.036$
$B = -11.9$
$\Delta A = 0.0018$
$\Delta B = 0.595.$

Therefore, Eq. (4) is written as,

$$\text{RPM} = 0.036 * V + (-11.9) \tag{5}$$

4 Conclusion

Fiber-optic gyroscope can be proven to be best alternative to free-space-based Sagnac interferometer due to its disadvantage of providing less precision and stability in measurement of angular rotation. In case of free-space setup, laser beam completes only one loop while in case of fiber gyroscope laser travels in 40 loops. Therefore, fiber-optic gyroscope can overcome this issue of stability and precision by using the principle of Sagnac interferometer. Here, free-space optics is replaced with fiber cable in which the light from laser is coupled in cable using coupler, and thus, by observing the path difference we calculate the angular rotation. Hence, high precision value of angular rotation is obtained which detects even the minute change.

References

1. Eason G, Noble B, Sneddon IN (1955) On certain integra of Lipschitz-Hankel type involving. Philos Trans R Soc Lond: Ser A: Math Phys Sci 247:529–551
2. Siegman AE (1986) Lasers. University Science Books, Mill Valley, CA
3. Yariv A, Yeh P (2007) Photonics—optical electronics in modern communication, 6th edn. Oxford University Press, New York
4. Hodgson N, Weber H (1997) Optical resonators. Springer, New York, pp 41–42
5. Bergh RA, Lefevre MC, Shaw HJ (1981) All single-mode fiber-optic gyroscope. Opt Lett 6:198–200
6. Ferrar CM (1989) Progress in fiber optic gyro development. ISA Trans 28(2):41–49

A Simple Structural Design for Tuning of Bandgap and Window in 1D Photonic Crystal

Alekhya Ghosh, Arghadeep Pal and N. R. Das

Abstract Tuning of bandgap in a photonic crystal is of immense importance for applications in various optical devices, such as optical filters and cavities. In this paper, a simple structural design is proposed to control both the bandgap and the bandgap window using a 1D photonic crystal. The method aims to change the bandgap by inserting a third intermediate layer of different refractive index between two layers of two fixed refractive indices in one period of the structure. The analysis is done using scattering matrix method (SMM) for a finite number of periods of the structure. The results show that there exists an optimum choice of the refractive index of the intermediate layer for which the bandgap reaches a minimum. In addition, it is also seen that refractive index of the intermediate layer can be chosen to tune the position of the bandgap window.

Keywords Photonic crystal · Tuning · Bandgap · Window · PBG

1 Introduction

Photonic crystals are structures having artificial modulation of refractive index. These show an attractive characteristic of manipulating the electronic wave propagation through the structures. The periodic lattice structures that create bandgaps for electrons which is one of the pillars of solid-state electronics are mirrored in photonics by these fabricated structures. The photonic bandgap that is an inherent property of these crystals makes it capable of guiding light or inhibiting the flow depending upon the wavelength of the concerned light. The scientific community was allured by the works of Yablonovitch [1] in this field. Controlling light also includes spontaneous emission controlling, which is achievable using photonic crystals [2]. The concept was extended and was used in the fabrication of 2D photonic crystals [3, 4]. Three-dimensional photonic crystals have been studied for both optical wavelength region [5] and near-infrared wavelength [6]. Tuning of bandgap is one of the most interesting

A. Ghosh · A. Pal (✉) · N. R. Das (✉)
Institute of Radio Physics and Electronics, University of Calcutta, 92,
Acharya Prafulla Chandra Road, Kolkata 700009, India
e-mail: nrd@ieee.org; nrd.rpe@caluniv.ac.in

V. Janyani et al. (eds.), *Optical and Wireless Technologies*, Lecture Notes
in Electrical Engineering 648, https://doi.org/10.1007/978-981-15-2926-9_15

features of photonic crystals. Over the decades, various efforts have been done to get a control over this forbidden gap. A mechanically tunable structure photonic crystal was suggested using coupled photonic slabs [7] having high sensitive nature. Liquid crystals have been widely implemented in this regard as several external fields may be varied to tune their properties. In [8], it was found that by altering the orientation of the nematic director, 2% photonic bandgap may be opened or closed which can be further be tuned by variation of temperature. This temperature-dependent refractive index of liquid crystal helps to tune the photonic crystal [9] resulting in a shift of 70 nm, while the predicted shift was 113 nm.

Bandgap enhancement has also gathered much attention. A simple structural way to get a large bandgap is by increasing the dielectric constant between the successive layers of photonic crystal [10]. A locally increasing or decreasing period length can also yield wider reflection range [10], with the fundamental aim of exploiting the Bloch oscillations of photonic carriers. Such structures are referred to as chirped photonic crystals which have been further investigated. The chirp parameter controls the shift of band edges which directly affects the broadening of photonic bandgap done in [11]. Moreover, the photonic bandgap can further be incremented by a chirped distributed Bragg reflector (DBR) under oblique incidence. In [12], the sub-DBRs are stacked successively with varying values of thickness of two constituent dielectric layers. It was concluded that the chirped structure does not influence the fundamental reflection band but stimulates the higher-order reflection band. Application of hetero-structure photonic crystal or quantum well-like structure (cascaded form of two or more photonic crystals) also results in enlargement of photonic bandgap [13, 14]. The total reflection frequency range is incremented to a great extent for all incident angles in [13] for both TM and TE modes. Reference [14] highlights the study of 1D structure at different angles using transfer matrix method and Bloch theorem yielding the reflection range of the hetero-structure to be higher than that of individual photonic crystals. Methods including disordered one-dimensional photonic crystal have also been studied in the same perspective. Reference [15] portrays that the high reflection range in case of a disordered multilayer with average thickness of 4 is much wider than that of similar stack reflectors. Studies on disordered photonic have been made by using numerical techniques in [16]. In [17], extension in bandgap in binary dielectric–dielectric PCs is achieved through introducing disorder. In photonic biosensors, such enhancement in stopband is achieved by implementing cascaded grating waveguides [18]. This optical grated waveguides are also used for chemical concentration sensor and direct label-free protein biosensors [19].

In the present paper, we propose a simple structure of 1D photonic crystal to tune the bandgap and window position. The theoretical background is described in Sect. 2. In Sects. 3 and 4, the proposed structure is described and the results are presented, respectively. Section 5 concludes the paper.

2 Theoretical Background

In this work, we have analysed the structures of 1D photonic crystals using SMM. This method is preferred over the conventional transfer matrix method due to reasons of numerical instability inherent in the process. On the other hand, SMM is both stable and memory efficient. It has some advantages over the plane wave expansion method (PWEM) also. PWEM considers the structure to be infinite in length, which is also unattainable and an approximation of the real case. However, SMM deals with only finite number of layers to correctly calculate the transmittance and reflectance of a given structure.

In SMM, each of the concerned layers is considered to be surrounded by layers of zero thickness which are known as gap mediums. This would not have any effect electromagnetically, since the width of the gap mediums is zero.

At the end, the reflectance $\boldsymbol{R}$ and transmittance $\boldsymbol{T}$ are calculated by using the formula

$$\boldsymbol{R} = \frac{\left|\vec{\boldsymbol{E}}_{\boldsymbol{ref}}\right|^2}{\left|\vec{\boldsymbol{E}}_{\boldsymbol{inc}}\right|^2} \quad \text{and} \quad \boldsymbol{T} = \frac{\left|\vec{\boldsymbol{E}}_{\boldsymbol{ref}}\right|^2}{\left|\vec{\boldsymbol{E}}_{\boldsymbol{inc}}\right|^2} \times \frac{\boldsymbol{Re}\left[\boldsymbol{k}_z^{\boldsymbol{trn}}/\boldsymbol{\mu}_{\boldsymbol{r,trn}}\right]}{\boldsymbol{Re}\left[\boldsymbol{k}_z^{\boldsymbol{inc}}/\boldsymbol{\mu}_{\boldsymbol{r,inc}}\right]} \tag{1}$$

where $\vec{\boldsymbol{E}}_{\boldsymbol{ref}}$ is the reflected electric field from the structure, $\vec{\boldsymbol{E}}_{\boldsymbol{inc}}$ is the electric field incident to the structure, $\boldsymbol{\mu}_{\boldsymbol{r,trn}}$ is the permeability of the transmission region, $\boldsymbol{\mu}_{\boldsymbol{r,inc}}$ is the permeability of the incidence region, $\boldsymbol{k}_z^{\boldsymbol{trn}}$ is the wave vector along z-direction in transmission region and $\boldsymbol{k}_z^{\boldsymbol{inc}}$ is the wave vector along z-direction in incidence region. Here, z-direction is considered to be the direction of propagation or the direction along which the dielectric constant is varied.

3 Proposed Structure

In the structure shown in Fig. 1, we have considered a 1D photonic crystal with the two extreme layers having the highest refractive index and least refractive index. The refractive index of the intermediate layers gradually decreases as we move from the layer of highest refractive index to the layer of lowest refractive index. Here, the aim is to achieve a linearly graded photonic crystal.

Let the value of the dielectric medium layer having highest refractive index be ε_2 and that of lowest dielectric layer be ε_1. So, ε_2 and ε_1 are the two extreme layers. Let there be N intermediate layers between these two extreme layers having dielectric values to be $\varepsilon_1', \varepsilon_2', \ldots, \varepsilon_N'$. From the above structural configuration, we get $\varepsilon_1 < \varepsilon_1' < \varepsilon_2' < \cdots < \varepsilon_N' < \varepsilon_2$. Moreover, each of these layers has a thickness d. A period of the structure consists of a total of $N + 2$ number of layers. The thickness of each periodic part of 1D photonic crystal is considered to be L where $L = (N + 2) \times d$. This periodic structure is repeated to form the entire crystal.

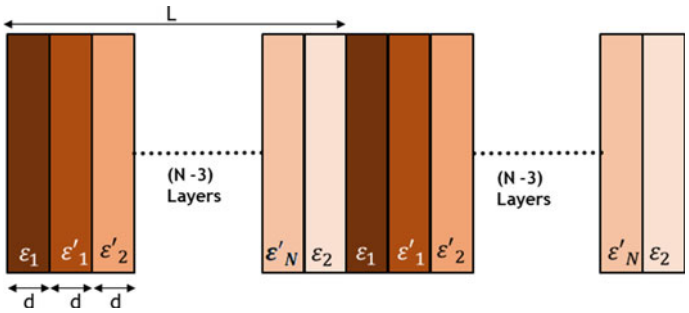

Fig. 1 A 1D photonic crystal structure is made where a N number of layers have been introduced between two fixed layers

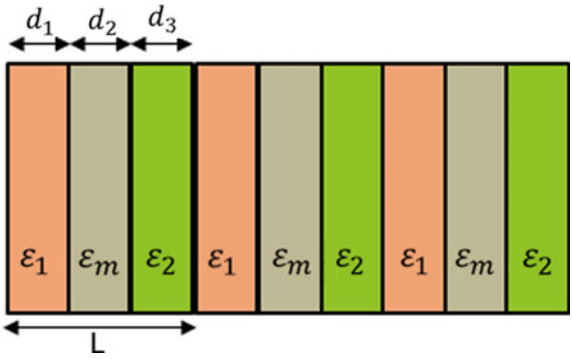

Fig. 2 A layer is introduced between two fixed layers for tuning the bandgap

We have considered a modified structure of 1D photonic crystal shown in Fig. 2. Here, the photonic crystal of form ABAB is converted to ACBACB. In other words, an extra layer is inserted in between two end layers. Let the first layer be a dielectric ε_1 followed by a middle layer with dielectric ε_m and the last layer of a period with dielectric ε_2. The thickness of the first, middle and last layers in a periodic part is d_1, d_2, d_3. The overall period has a thickness of L, where $L = d_1 + d_2 + d_3$. In this study, we have studied the variation of central frequency of PBG and the width of PBG with the changing dielectric constant of the intermediate layer. The width of the layer is kept constant. The value of ε_1, ε_3 is kept constant. In one case, d_1 and d_2 are kept constant, and in another case, d_1 and d_2 are varied.

4 Results

An extra layer is added in between two fixed layers whose dielectric constant is varied and accordingly width of the layer is also varied, as in Fig. 2.

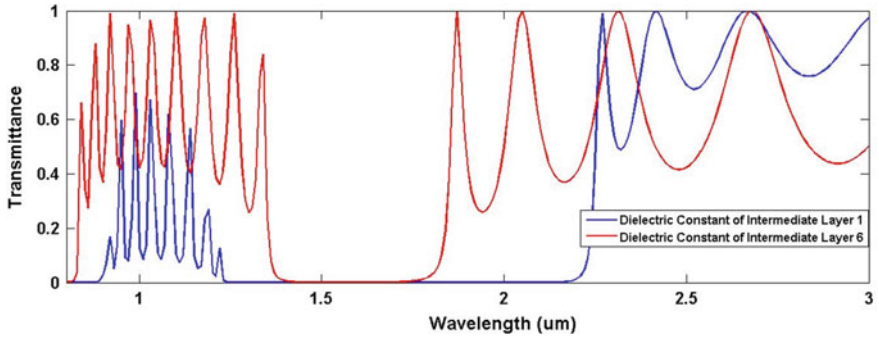

Fig. 3 Bandgap for intermediate layer having dielectrics 1 and 6

From Fig. 3, it can be observed that the central wavelength of the PBG is almost same for the intermediate layer having two different ε_m (here 1 and 6), but the width of the PBG is different significantly in the two cases.

From Fig. 4, it is clearly seen that the PBG varies with the change in the dielectric constant of the middle layer although the dielectric constant of the two end layers is fixed. For this study, the dielectric constant of the middle layer is varied from 1 to 20.

It can be easily seen from Fig. 4 that the PBG first decreases with the increase in the dielectric constant of the intermediate layer, and it is minimum for a certain value of ε_m, say $\varepsilon_{m,\min}$. After the minimum, it rises with a lesser slope compared to its fall before $\varepsilon_{m,\min}$. It may also be seen that the PBG can be of higher value or lesser value compared to the PBG of structure having no intermediate layers, which is depicted by the red line. However, as the optical length is fixed for all the cases here, the central wavelength of the PBG remains almost constant having a very close value to the central wavelength for the structure having no intermediate layer. This is represented in Fig. 5.

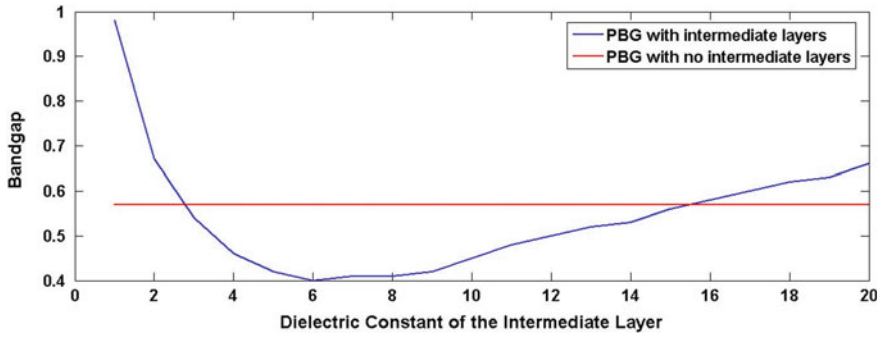

Fig. 4 Bandgap variation in response to varying intermediate layer dielectric

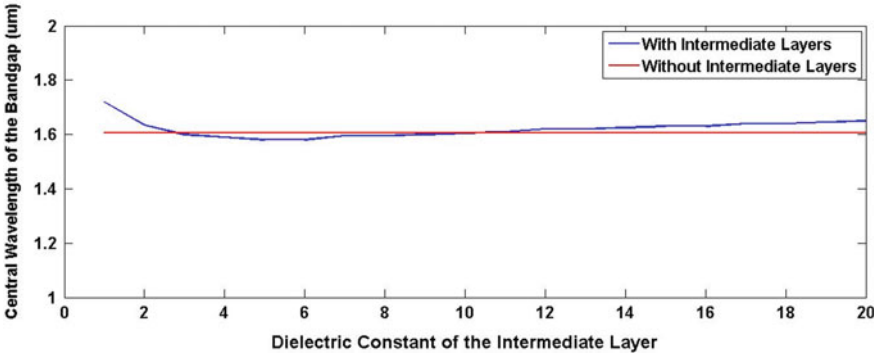

Fig. 5 Variation of bandgap with dielectric keeping optical length fixed

Dielectric constant of the intermediate layer is varied from keeping the thickness of each of the layers fixed to a predetermined value.

Here, the width of the intermediate layer is kept constant to a particular value. The dielectric constant of the layer is varied from 1 to 20. Here also, the dielectric constant of the two end layers is kept constant.

From Fig. 6, it is seen that both the central wavelength of the PBG and the width of the PBG have changed if ε_m of the intermediate layer is changed keeping the width of the layer fixed.

In Fig. 6, we can see that the width and the position of the bandgap and its harmonics differ significantly if the dielectric constant of the intermediate layer is changed.

Figure 8 depicts that the central wavelength of the PBG for the structure shown in Fig. 1 gradually increases with increase in dielectric constant of the intermediate layer. This may be attributed to the fact that as width of the layer is constant, and the dielectric constant is increasing, the refractive index would also increase, resulting

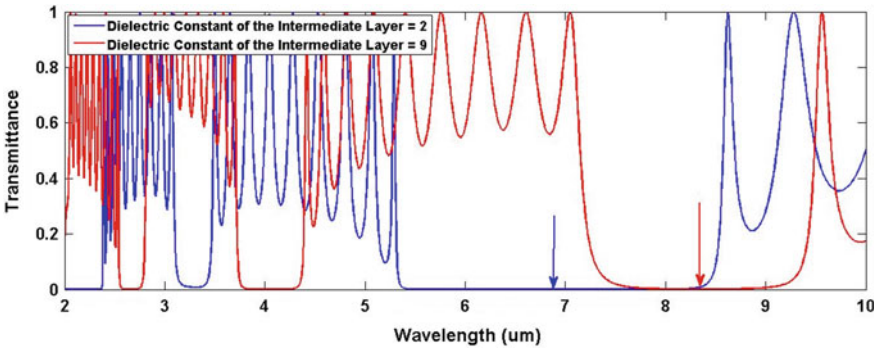

Fig. 6 Variation of transmittance with change in intermediate layer dielectric keeping width of the layers fixed

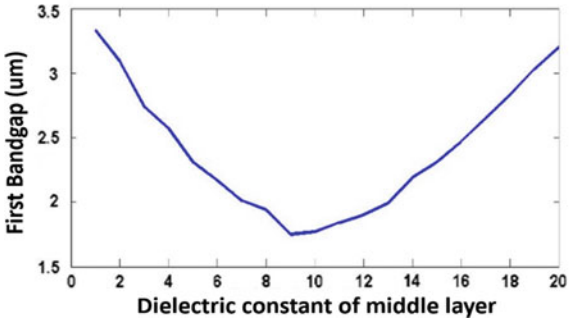

Fig. 7 Variation of width of bandgap with change in intermediate layer dielectric

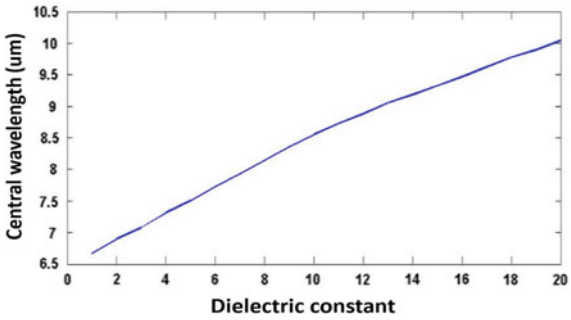

Fig. 8 Change in central wavelength with increase in intermediate layer permittivity

in an overall increment in the optical path length. On the other hand, the bandgap shows a similar effect as in Fig. 9.

The position of the minima of the PBG depends upon the refractive indices of the two end layers. The table represents the variation in the position of the minima with the dielectric constants of the two end layers.

The position of the minima of the PBG depends upon the dielectric constants of the two end layers. Table 1 represents the variation in the dielectric constant of the intermediate layer ($\varepsilon_{\min}$) for minimum PBG with the dielectric constants of the two end layers. It can be observed that $\varepsilon_{\min}$ is closer to ε_2 and also is more sensitive to ε_2.

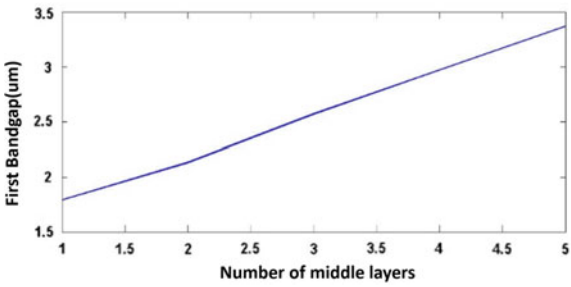

Fig. 9 Change in width of bandgap with increase in number of intermediate layers

Table 1 Variation of intermediate layer permittivity for minimum bandgap for different values of dielectric constants of end layers

Width of the layers (μm)	Dielectric constant of the left end layer (ε_1)	Dielectric constant of the right end layer (ε_1)	Dielectric constant of the intermediate layer for minimum bandgap (ε_{min})
0.48	3.8	11.7	9
0.48	7	11.7	10
0.48	1	11.7	8
0.48	3.8	15	13.5
0.48	3.8	7	6

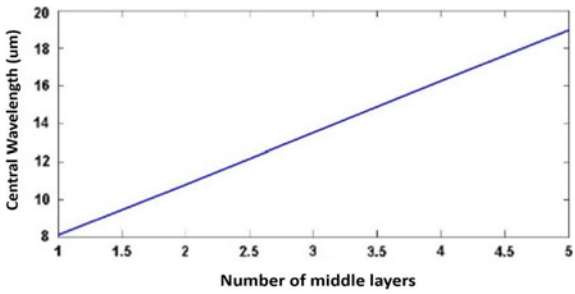

Fig. 10 Variation of central wavelength with increase in number of intermediate layers

Increasing the number of intermediate layers of fixed width having dielectric constant in between the two end layers:
From Fig. 10, it can be seen that the central wavelength of the PBG and the PBG itself is increasing if more number of layers of fixed width are introduced in between two fixed layers shown in Fig. 9. Here also, the optical path length is increasing (as width is fixed and refractive index is increasing). On the other hand, it suggests that a more gradual change in dielectric constant increases the PBG if the width of the layers is fixed. So, a graded index PC has wider bandgap than a step index PC if all the layer widths are fixed and not changed.

However, if the structure is made such that, irrespective of the number of intermediate layers introduced in between two end layers the total length of the unit cell is fixed and this characteristics is not maintained.

5 Conclusion

A simple method to control the bandgap of one-dimensional photonic crystal is proposed by introducing a layer between two fixed layers of a period of the crystal. The minimum value of bandgap implies a narrow stopband optical filter. Also, the position of the minimum can be tuned with suitable choice of parameters for material

and structure. The dielectric constant of the intermediate layer corresponding to the minimum bandgap depends on the dielectric constants of the layers on its both sides. The minimum position is sensible to the higher of the dielectric constants of the two side layers. Increasing the number of intermediate layers with gradual change in dielectric constants, the photonic bandgap and the position (central wavelength) of the bandgap window can be increased. The promising results for tuning the bandgap by the proposed simple methods are encouraging for future study and applications in components for optical signal processing.

References

1. Yablonovitch E (1987) Inhibited spontaneous emission in solid-state physics and electronics. Phys Rev Lett 58(20):2059–2062
2. Joannopoulos JD, Meade RD, Winn JN (1995) Photonic crystals: molding the flow of light. Princeton University Press, Princeton, NJ
3. Grüning U, Lehmann V, Ottow S, Busch K (1996) Macroporous silicon with a complete two-dimensional photonic band gap centered at 5 μm. Appl Phys Lett 68:747
4. Qiu M, He S (2000) Optimal design of a two-dimensional photonic crystal of square lattice with a large complete two-dimensional bandgap. J Opt Soc Am B 17(6):1027–1030
5. Noda S, Yamamoto N, Sasaki A (1996) New realization method of 3D photonic crystal in optical wavelength region. Jpn J Appl Phys 35(7B):L909–L912
6. Noda S, Tomoda K, Yamamoto N, Chutinan A (2000) Full three-dimensional photonic bandgap crystals at near-infrared wavelengths. Science 289(5479):604
7. Suh W, Yanik MF, Solgaard O, Fan S (2003) Displacement-sensitive photonic crystal structures based on guided resonance in photonic crystal slabs. Appl Phys Lett 82:1999
8. Busch K, John S (1999) Liquid-crystal photonic-band-gap materials: the tunable electromagnetic vacuum. Phys Rev Lett 83(5):967
9. Leonard SW, Mondia JP, van Driel HM, Toader O, John S, Busch K, Birner A, Gösele U, Lehmann V (2000) Tunable two-dimensional photonic crystals using liquid-crystal infiltration. Phys Rev B 61(4):R2389–R2392
10. Lousse V, Fan S (2005) Tunable terahertz Bloch oscillations in chirped photonic crystals. Phys Rev B 72:075119
11. Wu C-J, Chu B-H, Weng M-T, Lee H-L (2009) Enhancement of bandwidth in a chirped quarter-wave dielectric mirror. J Electromagn Waves Appl 23:437–447
12. Wu C-J, Chu B-H, Weng M-T (2009) Analysis of optical reflection in a chirped distributed Bragg reflector. J Electromagn Waves Appl 23:129–138
13. Wang X, Hu X, Li Y, Jia W, Xu C, Liu X, Zi J (2002) Enlargement of omnidirectional total reflection frequency range in one-dimensional photonic crystals by using photonic heterostructures. Appl Phys Lett 80:4291
14. Srivastava R, Pati S, Ojha SP (2008) Enhancement of omnidirectional reflection in photonic crystal heterostructures. Prog Electromagn Res B 1:197–208
15. Zhang D, Li Z, Hu W, Cheng B (1995) Broadband optical reflector—an application of light localization in one dimension. Appl Phys Lett 67:2431
16. Guida G (2003) Numerical studies of disordered photonic crystals. Prog Electromagn Res 41:107–131
17. Wu C-J, Rau Y-N, Han W-H (2010) Enhancement of photonic bandgap in a disordered quarter-wave dielectric photonic crystal. Prog Electromagn Res 100:27–36
18. Sahu S, Ali J, Yupapin PP, Singh G, Grattan KTV (2018) High-Q and temperature stable photonic biosensor based on grating waveguides. Opt Quantum Electron 50:307

19. Pham SV, Dijkstra M, Hollink AJF, Kauppinen LJ, de Ridder RM, Pollnau M, Lambeck PV, Hoekstra HJWM (2012) On-chip bulk-index concentration and direct, label-free protein sensing utilizing an optical grated-waveguide cavity. Sens Actuators B 174:602–608

Traffic Control Enhancement with Video Camera Images Using AI

Kriti Singh and P. C. Jain

Abstract Traffic congestion has been an emerging issue when it comes to problems faced by commuters on road on a daily basis. It leads to loss of time, money, and fuel when one is stuck in a traffic jam. This has led to the need of more path-breaking technologies in the field of intelligent transport systems (ITS). Today, a lot of data are available which can be used to extract important information and perform the desired analysis. With CCTV surveillance cameras at almost every traffic pole, information like count of vehicles can be used to analyze the traffic patterns at a particular location. In this paper, different methods have been used to get the accurate count of vehicles and their performances have been analyzed. Popular image processing method background subtraction and deep learning algorithms: R-CNN, Fast R-CNN and Faster R-CNN have been implemented.

Keywords Count vehicles · Deep learning · Neural networks · CNN · Background subtraction

1 Introduction

With increasing number of vehicles on roads, traffic congestion has become a major problem. To manage the traffic smartly, intelligent traffic systems (ITS) have been developed which increases security and helps users find the most suitable route and provides them with many options during their travel. For monitoring traffic conditions in real time, concerned departments have put many traffic surveillance cameras on highway toll stations, main traffic poles, tunnel entrances, and exits [1]. Existing technologies are using sensors. The present generation of ITS relies on sensors for vehicle detection and classification. While they are the most researched and widely used technology, they have several drawbacks: They are exposed to stress

K. Singh (✉) · P. C. Jain
Electrical Engineering Department, School of Engineering, Shiv Nadar University, Greater Noida, India
e-mail: ks395@snu.edu.in

P. C. Jain
e-mail: premchand.jain@snu.edu.in

V. Janyani et al. (eds.), *Optical and Wireless Technologies*, Lecture Notes in Electrical Engineering 648, https://doi.org/10.1007/978-981-15-2926-9_16

as traffic drives over them reducing sensor and road surface lifespan; their repair and replacement require closure of lanes, resulting in traffic disruptions; and most sensors only provide basic vehicle detection and counting information. Sensors like inductive loops get affected by water, snow, or other external accumulations on the road surface. Most sensors are not able to detect and classify vehicles accurately, that is why now smart technologies like cameras are used for getting the required data. With cameras present almost at every traffic poles, acquiring data has become easy and hassle free. There is no extra cost and labor required for maintenance of the setup. Cameras, especially high-performance machine vision cameras, are becoming popular in intelligent traffic systems. Also, real-time monitoring produces a huge amount of data every hour which can be accessed and used easily. With the available data information, one can obtain the count of vehicles. The count of vehicles can give us the information regarding the amount of traffic in a region, or an idea when the road gets busiest, so that the concerned authorities can choose the time for repair work. This information can be helpful in knowing which route commuters take the most and hence can help the authorities to accordingly take appropriate steps to improve the transport and other facilities.

The main aim of this paper is to provide an assessment of traffic through vehicle counting using video and image processing methods. Any device such as a cell phone or GPS can receive the result of the processed traffic information and use it to decide the best route to take and can thus avoid traffic busy paths. The fact that every traffic pole has CCTV cameras installed can provide us a cost-effective way to get data which can be sent to the processor where it can be processed further to get the required information.

2 Related Work

Surveillance systems have been commonly used for various purposes, for example, traffic and airport monitoring. An object detection system is necessary to monitor the object of interest in the environment continuously. There are several issues that are needed to be considered when developing such intelligent monitoring system, such as object detection, recognition, and tracking [1]. Background subtraction is one method that can be used for pre-processing of object detection. Background subtraction procedure is usually comprised of two steps: building background statistically and detecting the foreground by subtracting the background from the scene [2]. In other words, background subtraction process segments the image into foreground and background. The problem of background subtraction has been researched in the past 10 years. Wren et al. [3] used a single Gaussian function to represent the intensity of background pixel. However, a complex environment cannot be easily represented with only one Gaussian function. Therefore, a mixture of Gaussian is used [4]. Stauffer and Grimson [5] have used combinations of several Gaussian distributions to model the object and environment. But due to limitations of this image processing method, like its dependence on various external factors, there is rise of other deep

learning techniques. There are a large number of approaches in the literature related to vehicle classification using computer vision. In the past 10 years, deep convolution neural networks [6, 7] have significantly improved image classification [7] and object detection [8, 9] accuracy. In comparison with image classification, object detection is a more challenging task as it requires more complex methods to solve the problem. Due to this complexity, present approaches train models in multi-stage pipelines that are slow and inefficient.

3 Methodology

Recent years have seen an explosion of deep learning approaches in object detection. These approaches have leveraged significantly larger datasets than ever before and often achieve excellent results on datasets with large number of classifications or multiple tasks. Among the top contenders for algorithms on object detection, one is Faster R-CNN proposed by Ren et al. [10]. Girshick et al. [11] proposed the method of region proposals in CNN which lead to the algorithms like R-CNN, Fast R-CNN, and Faster R-CNN. He further used bounding box regressors for bounding box. These methods have shown good results with different datasets and are now widely used for detection problems. In this paper, analysis of these algorithms is done to get the desired result.

3.1 Background Subtraction

The Gaussian distribution can be of two types, univariate and multivariate, in which their probability density function (PDF) includes parameters like mean, variance, or covariance. The parameters are calculated using expectation maximization technique. By Baye's rule, a latent variable is defined as

$$\tau(z_k) = p(z_k = 1|x) = \frac{p(z_k = 1)p(x|z_k = 1)}{\sum_{j=1}^{K} p(z_j = 1)p(x|z_j = 1)} = \frac{\pi_k N(x|\mu_k, \Sigma_k)}{\sum_{j=1}^{K} \pi_j N(x|\mu_j, \Sigma_j)} \quad (1)$$

We initialize parameters like means, covariance, and mixing coefficients and evaluate the initial value of log likelihood. Our goal is to maximize the log likelihood function. Then, latent variable is calculated with these parameters. With this value of latent variable, again the parameters are calculated, and log likelihood is calculated to check if it is converging. As explained [12] in Gaussian mixture model, every pixel in a frame is modeled into Gaussian distribution. First, every pixel is divided by its intensity in RGB color space. Every pixel is computed for its probability whether it

is included in the FG or BG with

$$P(X_t) = \sum_{i=1}^{K} \omega_{i,t} \cdot \eta(X_t, \mu_{i,t}, \Sigma_{i,t}) \tag{2}$$

where $\eta(X_t, \mu_{i,t}, \Sigma_{i,t})$ is probability density function, and

$$\eta(X_t, \mu, \Sigma) = \frac{1}{(2\pi)^{\frac{n}{2}} |\Sigma|^{\frac{1}{2}}} \exp^{-\frac{1}{2}(X_t-\mu)\Sigma^{-1}(X_t-\mu)} \tag{3}$$

In Stauffer and Grimson method [5], every RGB is uncorrelated with each other. Therefore, the difference in intensity can be assumed to possess uniform standard deviation. The covariance matrix then can be formulated as:

$$\Sigma_{i,t} = \sigma_{i,t}^2 I. \tag{4}$$

For every Gaussian that is bigger than the designated threshold, it is classified as background. The other distribution that is not included in the previous category is classified as foreground.

$$B = \arg\min_{b} \left(\sum_{i=1}^{b} \omega_{i,t} > T \right) \tag{5}$$

If a pixel matches with one of the K Gaussian, then the value of ω, μ, and σ is updated.

$$\omega_{i,t+1} = (1 - \alpha)\omega_{i,t} + \alpha \tag{6}$$

$$\mu_{i,t+1} = (1 - \rho)\mu_{i,t} + \rho \cdot X_{t+1} \tag{7}$$

$$\sigma_{2i,t+1} = (1 - \rho)\sigma_{2i,t} + \rho(X_{t+1} - \mu_{i,t+1}) \cdot (X_{t+1} - \mu_{i,t+1})T \tag{8}$$

where:

$$\rho = \alpha \times \eta(X_{t+1}, \mu_i, \Sigma_i) \tag{9}$$

Meanwhile, if there is a case where all K of Gaussian do not match, then only the ω is updated

$$\omega_{j,t+1} = (1 - \alpha)\omega_{j,t} \tag{10}$$

If every parameter has been found, then the foreground detection can be performed.

This was implemented on MATLAB. Foreground detector, which computes and returns a foreground mask using the Gaussian mixture model (GMM) in MATLAB, was used. A traffic surveillance video was used, its first few frames were used to learn and fix the background, and then, the background subtraction was used to detect the moving objects. The blob analysis function was used to analyze and get the area and centroid of the bounding boxes which was further used to count the vehicles.

3.2 R-CNN, Fast R-CNN, and Faster R-CNN

CNN is a good classifier, but when it comes to detection problems, the time taken by CNN network to process each image by convolutions and pooling layers is not appropriate for real-time applications. To reduce the time complexity of the problem, Ross Girshick and team came [10] up with the algorithm R-CNN where R stands for regions. The main idea was to do convolutions over a set of regions rather than the whole image. For this, region proposals were to be formed for each image. Selective search algorithm [13] is used which gives nearly 2000 region proposals, and these 2000 regions act as input to the convolution layer. As given in [13], the selective search algorithm works in the following steps:

1. Initially segmentation on input image to generate many candidate regions.
2. Using an iterative greedy algorithm to recursively combine similar regions into larger ones.
3. Using the generated regions to produce the final candidate region proposals.

In R-CNN, input from the convolution layer further goes to the pooling layer where it is dimensionally reduced for further processing. The layers of CNN act as feature extractors, and as we go deeper in the network, the complexity of features learned increases. The first convolution layer extracts low-level features like edges, lines, and corners, and as we go deeper in the network the complexity of features learned increases. The input of size $N \times N \times D$ is convolved with H kernels, each of size $k \times k \times D$ separately. Convolution of an input with one kernel produces one output feature, and with H kernels it independently produces H features which then form a feature map. Later, the same group of researchers came up with Fast R-CNN [14] and Faster R-CNN [10]. The proposed Fast R-CNN takes the input through the convolution layer, and the region proposals are formed from the output of the convolution layer which is further processed by the next layers of the network. In Faster R-CNN, the difference was in terms of the algorithm used for region proposals. In this case, a network is used to propose the region proposals instead of an algorithm.

The network was trained with labeled data (Fig. 1) of car images which had coordinates of the bounding boxes for the object to be detected. The dataset contained 295 images with at least 1–2 labeled instances. The data were divided into training and testing data with 60% being training and the rest being testing data. The input image was resized to $32 \times 32 \times 3$ dimension, and the convolution layer had filters of 3×3 dimension. Zeros were padded to the input before convolution, so that the

Fig. 1 Example of data given for training

corner pixels were not left out while moving the filter window through the image. For pooling, max pooling was used. In total, there were 11 layers which included two convolutions, three ReLu, two fully connected, one softmax, and the final classification layer. After the classification layer, a bounding box regressor was used. As the image goes through the convolutions and pooling layers, a feature map is produced. Then, for each region proposals, a fixed-length feature vector is extracted from the feature map which is the ROI (region of interest). The ROIs are then fed as input to the fully connected classification layers which branches into two sublayers giving softmax probability estimates over different classes and a set of coordinates for bounding boxes as output.

4 Results

Figure 2a shows CCTV's original video. The background subtraction method was able to give segmented image as shown in Fig. 2b, and the detections were made,

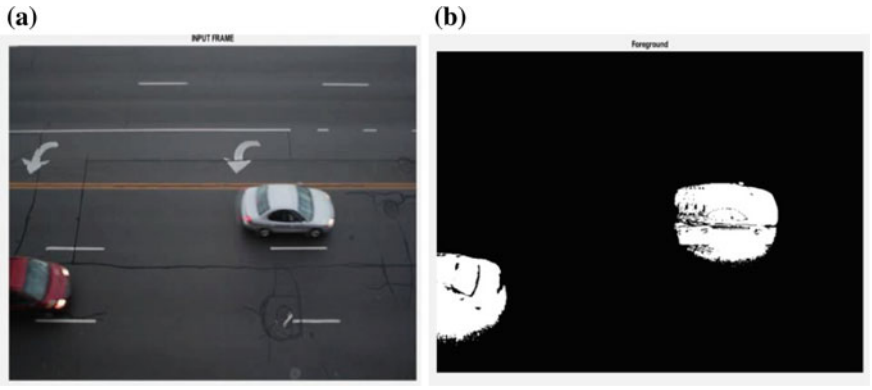

Fig. 2 **a** CCTV video; **b** after background subtraction

but the accuracy was not appreciable. The accuracy of detection was around 40%. With the deep learning algorithm, the accuracy increased to around 70%. Detection in foggy condition was very poor as compared to R-CNN algorithms.

Results obtained from R-CNN detections in foggy and clear images with overlapping cars are shown in Fig. 3a and b. Bounding boxes (yellow color) with confidence scores can be seen in Fig. 3a and b. A comparison in terms of accurate detections on a test image is given in Table 1. In case of deep learning, tuning of parameters was required to get the desired result. Learning rates for the three different R-CNNs were tuned, and to measure the performance, average precision-recall score was calculated as shown in Fig. 4a–c.

A comparison between the three different R-CNNs on the basis of important parameters is given in Table 2. The training time is the parameter obtained on training the model on 177 images out of the dataset of 295 images.

Fig. 3 **a** Detection in foggy weather; **b** detection in case of overlapping cars

Table 1 Comparison of algorithms for accurate detection on test images

Algorithm	No. of cars (original)	No. of cars (predicted)
Background subtraction	4	7
R-CNN	4	3

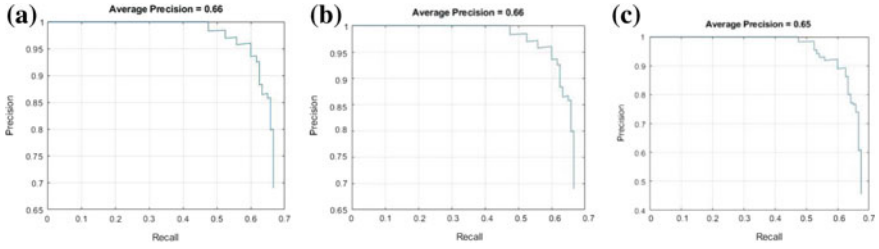

Fig. 4 **a** R-CNN; **b** Fast R-CNN; **c** Faster R-CNN

Table 2 Comparison of algorithms for different parameters

Algorithm	Training time (s)	Average precision-recall score	Tuned learning rate
R-CNN	700	0.66	1.000e−06
Fast R-CNN	420	0.66	1.000e−06
Faster R-CNN	1324	0.65	1.000e−04

5 Conclusions

In background subtraction, the detection of cars was not accurate which lead to inaccurate count of cars. The method of background subtraction is not adaptive because the background is learned on first few images after which it is fixed. This may not work for real-life scenarios as the environment and lighting keep changing throughout the day. Also, the moving shadows of the car were detected in some cases which lead to inaccuracy. To combat these problems, we moved to deep learning algorithms. It was observed that the algorithms were able to detect cars in low light and foggy environment. Even the overlapping cars were detected with good accuracy. In deep learning, we focused on three algorithms R-CNN, Fast R-CNN and Faster R-CNN. It was observed that the time taken to test and train these models was least in Fast R-CNN and maximum in Faster R-CNN. This can be possibly due to the fact that the region proposals were predicted in case of Faster R-CNN. Accuracy-wise, the accuracies of Fast R-CNN and R-CNN were same and the accuracy of Faster R-CNN was more. Higher learning rates lead to less accuracy in predictions. The proposed algorithm of R-CNN works well in severe weather conditions as compared to the background subtraction method.

References

1. Lee W, Lee M (2010) A multi-class object classifier using boosted gaussian mixture model. Neural information processing. Theory and algorithms. Lecture notes in computer science, vol 6443. Springer, Berlin, Heidelberg, pp 430–437
2. Xue G, Sun J, Song L (2012) Background subtraction based on phase feature and distance transform. J Pattern Recognit Lett 33:1601–1613
3. Wren C, Azarbayejani A, Darrell T, Pentland A (1996) Pfinder: real-time tracking of the human body. In: Proceedings of the second international conference on automatic face and gesture recognition, pp 51–56
4. Friedman N, Russell S (1997) Image segmentation in video sequences: a probabilistic approach. In: Proceeding UAI'97: proceedings of the thirteenth conference on uncertainty in artificial intelligence, pp 175–181
5. Stauffer C, Grimson WEL (1999) Adaptive background mixture models for real-time tracking. In: 1999 conference on computer vision and pattern recognition (CVPR '99), pp 23–25
6. Krizhevsky A, Sutskever I, Hinton G (2012) ImageNet classification with deep convolutional neural networks. NIPS
7. LeCun Y, Boser B, Denker J, Henderson D, Howard R, Hubbard W, Jackel L (1989) Back propagation applied to handwritten zip code recognition. Neural Comput 1:541–551

8. Girshick R, Donahue J, Darrell T, Malik J (2014) Rich feature hierarchies for accurate object detection and semantic segmentation. In: CVPR
9. Sermanet P, Eigen D, Zhang X, Mathieu M, Fergus R, LeCun Y (2014) OverFeat: integrated recognition localization and detection using convolutional networks. In: ICLR
10. Ren S, He K, Girshick R, Sun J, Cortes C, Lawrence N, Lee D, Sugiyama M, Garnett R (2015) Faster R-CNN: towards real time object detection with region proposal networks. Advances in neural information processing systems, vol 28. Curran Associates, Inc., New York, pp 91–99
11. Girshick R, Donahue J, Darrell T, Malik J (2014) Rich feature hierarchies for accurate object detection and semantic segmentation. In: CVPR, UC Berkeley
12. Nurhadiyatna A, Jatmiko W, Hardjono B (2013) Background subtraction using Gaussian mixture model enhanced by hole filling algorithm (GMMHF). In: 2013 IEEE international conference on systems, man, and cybernetics
13. Uijlings JRR, van de Sande KEA, Gevers T, Smeulders AWM (2012) Selective search for object recognition. Technical report, University of Trento, Italy/University of Amsterdam, the Netherlands
14. Girshick R (2015) Fast R-CNN. In: 2015 IEEE international conference on computer vision

Reconfigurable Slot-Based MIMO Antenna for Cognitive Radio Application

Shilpi Singh and M. S. Parihar

Abstract A multiband *C* shape slot reconfigurable MIMO antenna integrated with wideband sensing antenna is proposed for cognitive radio (CR) application. The wideband sensing antenna designed for CR is offering an impedance bandwidth of 5.15 GHz (0.85–6 GHz). The frequency-reconfigurable *C* slot-based MIMO antenna referred as communicating antenna in CR is capable to switch between multiple frequency sub-bands, i.e., 1.8, 2.1, 2.5 and 3.6 GHz, assigned for various communication applications. A two-element reconfigurability MIMO antenna is acknowledged by utilizing the PIN diode. The proposed MIMO antenna for CR could improve data throughput and channel capacity of the system. Both antennas share the same substrate/platform could be used to sense electromagnetic spectrum in a wide range and to communicate using GSM, LTE, UMTS, 3G, Wi-Fi, Bluetooth, WiMAX and WLAN frequency bands, respectively.

Keywords Ultra-wideband (UWB) antenna · Multiple-input multiple-output (MIMO) · Reconfigurable antennas · Cognitive radio (CR)

1 Introduction

In the course of recent years, cognitive radio framework is getting lot of consideration and reshaping the future of wireless communications through enhanced spectrum efficiency, information reliability and high data rate. Today research in cognitive radio is focused to realize effective wireless communication systems to make optimal utilization of under-utilized spectral resources. The thought behind cognitive radio is to make an intelligent remote gadget that can monitor the surrounding RF environment condition continuously and recognize an unused or idle frequency spectrum.

S. Singh (✉) · M. S. Parihar
Indian Institute of Information Technology Design and Manufacturing, Jabalpur, Madhya Pradesh, India
e-mail: 1712108@iiitdmj.ac.in

M. S. Parihar
e-mail: mparihar@iiitdmj.ac.in

V. Janyani et al. (eds.), *Optical and Wireless Technologies*, Lecture Notes in Electrical Engineering 648, https://doi.org/10.1007/978-981-15-2926-9_17

That way more remote gadgets can work in the similar recurrence bands, empowering them for proficient utilization of the available spectrum. Thus, it is alluring to develop gadgets or devices that can learn from the perceptions and make choices about when and how to transmit the information using idle frequency band without disturbing its primary user [1, 2]. In recent years, CR system has been examined broadly due to their electronically dynamic characteristics. In [3–5], various types of frequency-reconfigurable antennas were discussed for CR system and different applications. [3] Proposed a frequency-reconfigurable antenna to cover frequency sub-band from 2.3 to 3.6 GHz spectrum for non-uniform WiMAX applications in wireless communication. A continuous frequency tuning from 1.64 to 2.12 GHz was achieved in [4] by circular monopolar patch antenna. A frequency-reconfigurable, high-isolation multiple-input multiple-output antenna was presented in [5] for *S*- and *C*-bands applications, i.e., 2.45, 3.4 and 5.3 GHz. Since CR require extensive band sensing antenna and narrowband reconfigurable antenna, in [6–8], distinctive antenna was proposed to realize such antennas [6]. Proposed a CR application-based reconfigurable antenna which was controlled optically. Presented antenna covers 2.65–10.3 GHz UWB band and three narrowbands. In [7], inverted *U*-shaped antenna is proposed for sensing which covers 2.63–3.7 GHz frequency bands and four sub-frequency bands are achieved by horizontal slots in ground plane. In [8], a rotational patch antenna is proposed to introduce reconfigurability in antenna which covers multiple frequency bands from 2.1 to 10 GHz. In [9–11], various antennas for cognitive radio platform are presented. Different design techniques for integration of communicating antenna and ultra-wideband sensing antenna are presented for various wireless communication applications. Most of the reported literature was on CR systems which could sense the spectrum beyond 2 GHz, not covering GSM spectrum.

In this chapter, a wideband sensing antenna incorporated with reconfigurable MIMO antenna is proposed for various wireless applications. Sensing antenna covers 0.85–6 GHz of spectrum, covering the frequency spectrum below 1 GHz. The proposed CR system with reconfigurable MIMO antenna could be used to sense and communicate with GSM1800/Bluetooth/WLAN/WiMAX and other adjacent bands. Another feature of this antenna is GND plane is utilized for reconfigurable MIMO antenna. Proposed antenna provides high isolation between ports (>15 dB) and ECC below 0.01 which is prerequisite for communicating antenna (Fig. 1).

2 Details of the Antenna Layout

Design of *C* slot-based reconfigurable MIMO antenna with wideband sensing antenna is shown in Fig. 2a, b. The complete system for CR is designed on single board of dimension $110 \times 110 \times 1.5$ mm^3. Both antennas are designed using Rogers substrate with relative permeability $\varepsilon = 3.55$, loss tangent of 0.0027 and thickness 1.5 mm.

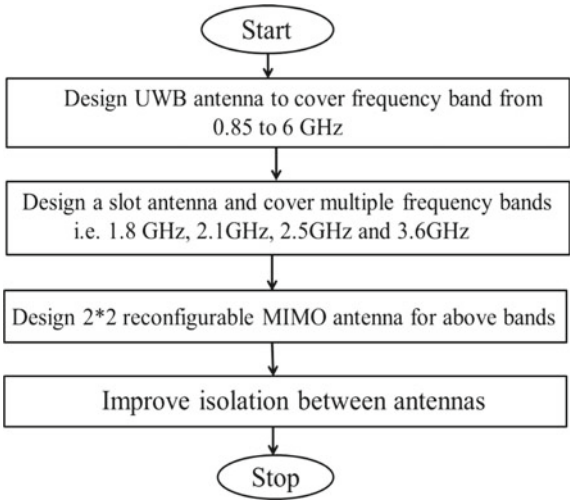

Fig. 1 Flowchart of proposed work

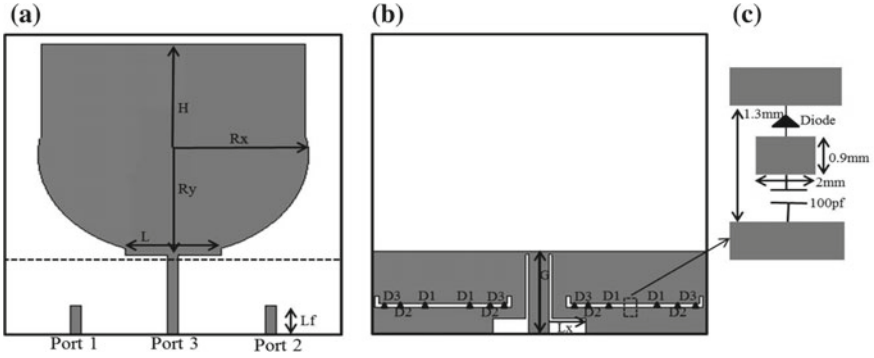

Fig. 2 **a** Top view (sensing antenna), **b** bottom view (MIMO antenna), **c** biasing circuit

2.1 Detail of the Wideband Sensing Antenna Layout

The UWB design procedure was started with an ellipse-shaped antenna with certain length and this structure operate over 2 GHz. To bring down the frequency an additional block of certain length and width was added. The length L is used to control the upper cutoff frequency while length H is used to control the lower cutoff frequency. The performance of wideband sensing antenna with and without block is shown in Fig. 3. It is shown that the proposed wideband antenna covers a frequency spectrum from 0.85 to 6 GHz is below −10 dB in the entire spectrum.

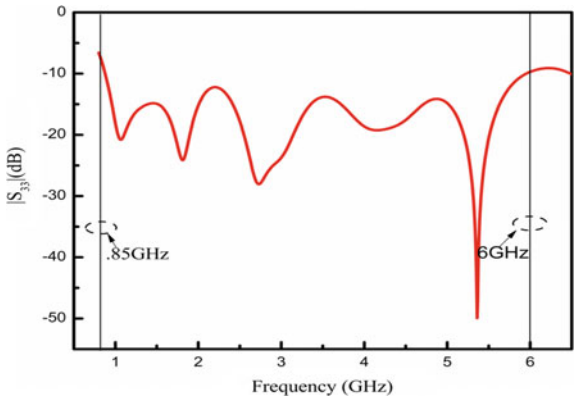

Fig. 3 Simulated reflection coefficients of wideband sensing antenna

2.2 *Detail of the Frequency-Reconfigurable MIMO Antenna Layout*

Two *C*-shaped slots of width 1.3 mm were etched from the ground plane and excited with microstrip feed line. These slots are used to realize 2 × 2 reconfigurable MIMO antenna. Reconfigurability in MIMO antenna is obtained by incorporating PIN diodes at proper position as appeared in Fig. 2 and biased them appropriately to select desired frequency band. The length of each slot is $\lambda g/2$, where λg is the guided wavelength at their corresponding resonance frequency. Beam lead PIN diodes HPND 4005 are used which have very low capacitance in OFF states. It provides 4.7 Ω resistance in forward bias (ON state) and 0.017 pF capacitance in reverse bias (OFF state). The complete biasing network to activate the PIN diodes is also shown in Fig. 2c. A100 pF capacitor is used for blocking the RF signal from DC supply voltage. To increase the isolation between sensing and communicating reconfigurable MIMO antenna, an *L*-shaped slot is etched between them. The *L*-shape slot suppresses the surface current which results in less mutual coupling. The optimum dimensions of the proposed antenna system are: $Rx = 42$ mm, $Ry = 25$ mm, $H = 34$ mm, $L = 27.81$ mm, $Lf = 13.3$ mm, $G = 30$ mm and $Lx = 12$ mm.

3 Simulation Results and Discussion

Reconfigurable *C*-shaped slot-based multiband frequency-reconfigurable MIMO antenna combined with wideband sensing antenna is modeled and simulated using CST, a 3D finite integral technique (FIT) based electromagnetic. Simulated reflection coefficient S_{33} of wideband sensing antenna is below −10 dB throughout the band and having bandwidth of 6.5 GHz from 0.85 to 6 GHz. In this way, bandwidth required for UWB applications is fulfilled. It is clear that the sensing antenna can be

used to sense the electromagnetic spectrum including lower GSM frequency band. The simulated UWB sensing antenna reflection coefficient is shown in Fig. 3.

Figure 4 depicts the 2D gain pattern in *XZ* plane at 1.8, 2.1, 2.5 and 3.6 GHz when antenna (port 3) is excited. It is noticeable that the pattern of this antenna is omnidirectional which is prerequisite for sensing antenna.

Figure 5a depicts the simulated *S*-parameter (S_{11}/S_{22}) result of the frequency-reconfigurable slot-based MIMO antenna. Because of the symmetry property of the reconfigurable MIMO antenna, the results for differential ports 1 and 2 are theoretically identical. The reconfigurable MIMO antenna can operate at 1.8 GHz, 2.1 GHz, 2.5 GHz and 3.6 GHz frequencies by activating different PIN diodes. The four biasing states to obtain four frequency bands are shown in Table 1. The slot antenna resonates at their respective frequency when the slot length is $\lambda g/2$ which is controlled using PIN diode.

To increase the isolation between reconfigurable MIMO antenna ports, two *L*-shaped slots are etched between them. In Fig. 5b, we can see that isolation gets increase with the introduction of slot in reconfigurable antenna. Isolation between MIMO antenna ports at 1.8 GHz is 15 dB without slot and with *L* slot isolation it is increased to better than 27 dB.

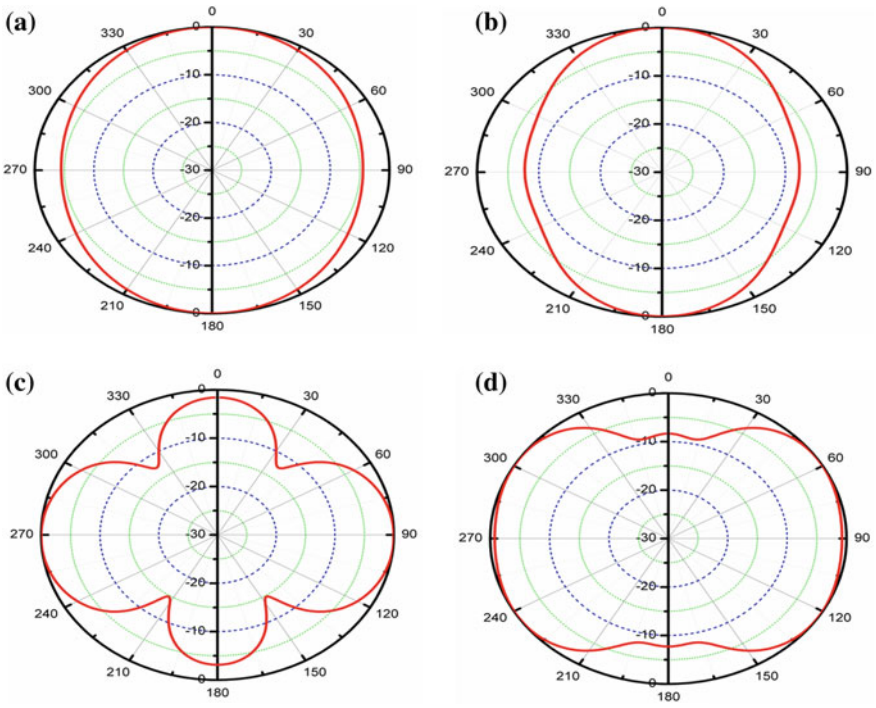

Fig. 4 Simulated 2D pattern at **a** 1.8 GHz, **b** 2.1 GHz, **c** 2.5 GHz and **d** 3.6 GHz

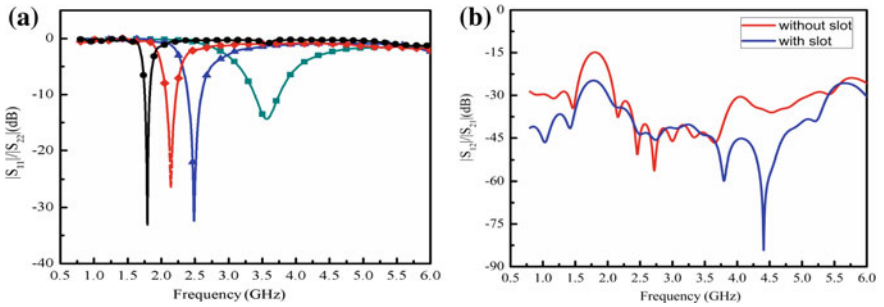

Fig. 5 Simulated result of **a** frequency-reconfigurable MIMO antenna, **b** isolation between MIMO antenna ports with or without slot at f = 1.8 GHz

Table 1 MIMO antenna operation modes

Frequency (GHz)	Diodes ON	Diodes OFF
3.6	D1	D2, D3
2.5	D2	D1, D3
2.1	D3	D1, D2
1.8		D1, D2, D3

Figure 6 shows the 2D gain pattern of MIMO antenna when reconfigurable MIMO antenna port 1 or port 2 is excited with 1.8, 2.1, 2.5 and 3.6 GHz RF signals. It is noticeable from Fig. 6 that the radiation pattern of antenna is omnidirectional which is desirable for slot based MIMO antenna. Figure 7 shows port isolation between MIMO antenna and wideband sensing antenna ($S_{31}/S_{13}/S_{32}/S_{23}$) is greater than 15 dB at all four frequencies while isolation between reconfigurable MIMO antenna (S_{12}/S_{21}) is better than 25 dB which is quite worthy for practical application. ECC of proposed antenna is below 0.01 which is prerequisite for MIMO antenna to operate independently (Table 2).

4 Conclusion

A planar *C*-shaped slot-based reconfigurable antenna incorporated with spectrum sensing antenna is presented for CR application. PIN diode is used for reconfigurable communication bands at frequencies 1.8, 2.1, 2.5 and 3.6 GHz. Isolation between ports is >25 dB for reconfigurable ports while >15 dB for UWB and MIMO for all operating frequencies. Wideband antenna covers 0.85–6 GHz frequency band below 10 dB in the whole spectrum. The ports isolation is increased using *L*-shaped slot between antennas. The 2D gain pattern of sensing as well as MIMO antenna is omnidirectional which is prerequisite for CR application. The proposed structure

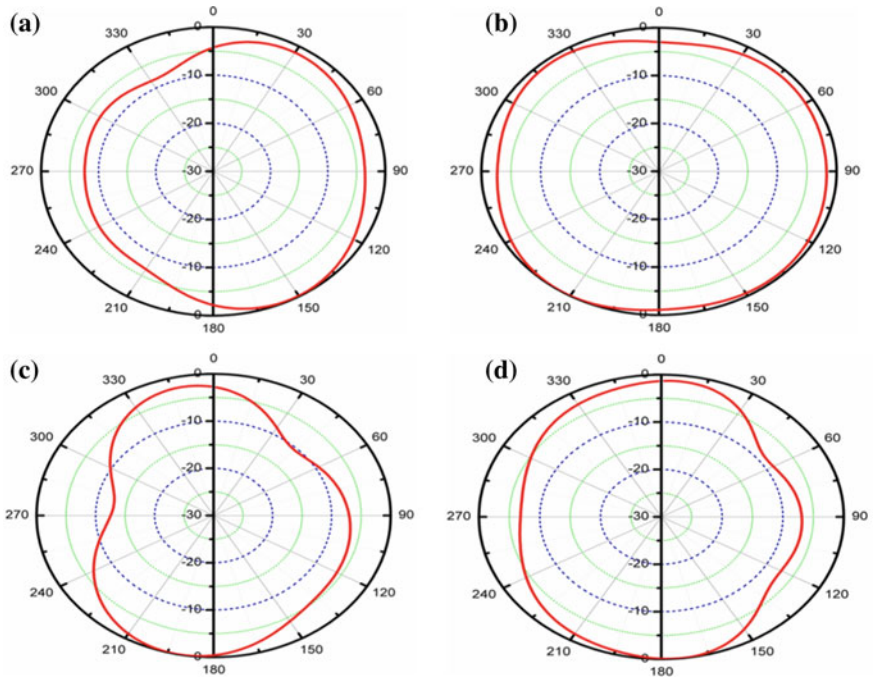

Fig. 6 Simulated 2D gain pattern at **a** 1.8 GHz, **b** 2.1 GHz, **c** 2.4 GHz and **d** 3.6 GHz

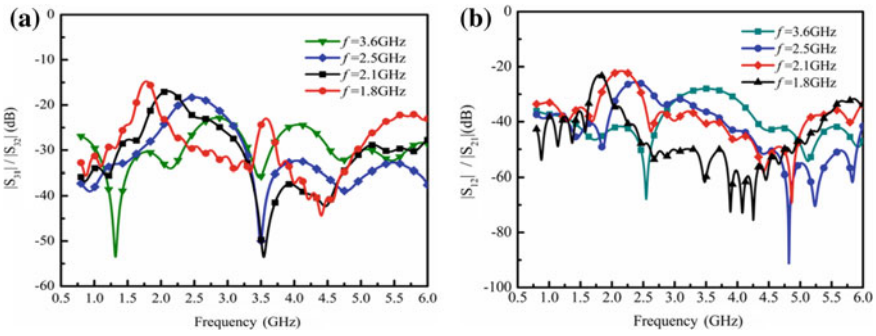

Fig. 7 Simulated result of **a** mutual coupling between sensing antenna and MIMO antenna $|S_{31}|/|S_{32}|$, **b** isolation between MIMO antenna ports $|S_{21}|/|S_{12}|$

Table 2 Comparison of work

References	f = 1.8 GHz	f = 2.1 GHz	f = 2.5 GHz	f = 3.6 GHz	UWB
[5]	✗	✗	✓	✓	✗
[11]	✗	✗	✓	✗	✓
[12]	✗	✗	✓	✓	✗
Work	✓	✓	✓	✓	✓

is compact (in view of covering GSM band) and can be used for applications like WiMAX (3.6 GHz), WLAN band (2.4 GHz), GSM (1.8 GHz) and 4G applications.

References

1. Bernhard J, Bonek E, Christodoulou CG, Kunkef D, Melde KL (2014) Guest editorial for the special section on antenna systems and propagation for cognitive radio. IEEE Trans Antennas Propag 62(3):1015–1018
2. Mitola J (2009) Cognitive radio architecture evolution. Proc IEEE 97(4):626–641
3. Lim JH, Song CW, Jin ZJ, Yun T-Y (2013) Frequency reconfigurable planar inverted-F antenna using switchable radiator and capacitive load. IET Microw Antennas Propag 7(6):430–435
4. Ge L, Luk KM (2014) Frequency-reconfigurable low-profile circular monopolar patch antenna. IEEE Trans Antennas Propag 62(7):3443–3449
5. Pandit S, Mohan A, Ray P (2018) Compact frequency-reconfigurable MIMO antenna for microwave sensing applications in WLAN and WiMAX frequency bands. IEEE Sens Lett 2(2)
6. Jin G, Zhang D, Li R (2011) Optically controlled reconfigurable antenna for cognitive radio applications. Electron Lett 47(17):948–950
7. Mansoul A, Ghanem F, Hamid MR, Trabelsi M (2014) A selective frequency-reconfigurable antenna for cognitive radio applications. IEEE Antennas Wirel Propag Lett 13:515–518
8. Tawk Y, Costantine J, Avery K, Christodoulou C (2011) Implementation of a cognitive radio front-end using rotatable controlled reconfigurable antennas. IEEE Trans Antennas Propag 59(5):1773–1778
9. Tawk Y, Costantine J, Christodoulou C (2014) Reconfigurable filtennas and MIMO in cognitive radio applications. IEEE Trans Antennas Propag 62(3):1074–1084
10. Hussain R, Sharawi MS (2015) Integrated reconfigurable multiple-input–multiple-output antenna system with an ultra-wideband sensing antenna for cognitive radio platforms. IET Microw Antennas Propag 9(9):940–947
11. Hussain R, Sharawi MS (2015) A cognitive radio reconfigurable MIMO and sensing antenna system. IEEE Antennas Wirel Propag Lett 14:257–260
12. Lim JH, Jin ZJ, Song CW, Yun TY (2012) Simultaneous frequency and isolation reconfigurable MIMO PIFA using PIN diodes. IEEE Trans Antennas Propag 60(12):5939–5946

Role of Coupling Angle on the Performance of a Ring Resonator–Waveguide Sensor

M. Mishra and N. R. Das

Abstract In the present work, the effect of coupling angle on the coupling of light from a ring resonator to a bent-waveguide has been studied. It has been shown that by bending the waveguide along the ring, the percentage of first trip light coupling from the resonator into the waveguide can be increased up to a particular value of coupling angle named as θ_m. It has been seen that beyond θ_m, the light coupling percentage starts decaying and ends up with a zero coupled light in the bus waveguide. For getting more light coupled to the waveguide, the value of θ_m should increase and it has been done by reducing the waveguide core width. Suitable choice of the coupling angle helps achieve a very high FSR and Q of the ring resonator.

Keywords Coupling · Angle · Bend · Ring · Waveguide

1 Introduction

Optical ring resonator is one of the basic components required for designing of photonic integrated circuits (PICs). It is of different types having different characteristics which make it eligible for applications like communication and biosensors [1–6]. Though it is a well-known and well-established photonic component, however, it has some almost unavoidable limitations which drastically reduce its performance in certain specific applications. To enhance the efficiency of optical ring resonator-based components, two vital properties of optical ring resonators need to be improved. One is its free spectral range (FSR) which varies inversely with the ring circumference, and another one is its quality factor (Q-factor) which varies directly on the coupling percentage. Unfortunately, both these properties contradict each other resulting difficulty in achieving better Q-factor for higher FSR values. For high FSR applications, the ultra-small circumference of ring reduces the coupling length between the ring

M. Mishra (✉) · N. R. Das
Institute of Radio Physics and Electronics, University College of Science and Technology, University of Calcutta, 92, APC Road, Kolkata 700009, India
e-mail: madhusudanmishra@ieee.org

N. R. Das
e-mail: nrd@ieee.org

V. Janyani et al. (eds.), *Optical and Wireless Technologies*, Lecture Notes in Electrical Engineering 648, https://doi.org/10.1007/978-981-15-2926-9_18

and the straight bus waveguide and hence stands against the efficient coupling of light from ring to waveguide and vice versa. Due to small size, the ring cannot be made elliptical in order to increase the coupling length keeping the bending loss in mind. In such cases, though we are able to achieve quite a good amount of FSR value, we have to satisfy ourself with a poor Q-factor of the ring resonator. In such cases, it is quite essential to enhance the coupling of ring–waveguide coupler for better Q-factor in a high FSR application [7]. This is the demand of today's communication and medical applications for getting more error free, accurate and reliable performance of PIC-based components.

The coupling length of the ring–waveguide coupler can be increased by bending the waveguide along the ring by maintaining the minimum coupling gap between the ring and the bus waveguide up to a certain angle (θ). This is a good idea and also works well. However, this design has to be done below certain bending angle of the waveguide known as maximum coupling angle θ_m. Beyond that angle, the coupled power in the waveguide decreases with the increasing value of coupling angle. The value of θ_m mainly depends upon the structure of the ring and the waveguide. In this work, we have studied the percentage of light coupling (single trip) between the ring and waveguide with respect to different coupling angles of the waveguide for a given structure. The study has been done on various dimensions of the waveguide core, and the best one among them has been reported.

2 Device Structure

Figure 1 shows the schematic structure of the considered ring–waveguide coupler. The core of the ring and waveguide made of silicon using SiO_2 as their cladding. The width and height of the core are 490 × 220 nm for the ring and 430 × 220 nm for the waveguide, respectively. The inner radius of the ring is of 11.11 um, and the coupling gap between the ring and the waveguide is set to 200 nm, which is a reasonable value for fabrication. During the study, maintaining the same coupling gap, the waveguide width has been varied as 490, 470, 450 and 430 nm, reporting 430 nm as the optimized one among them.

3 Results and Discussion

Finite-element-method-based simulations have been carried out using COMSOL for various coupling angles to find out the light coupling from ring to waveguide. At first, the bus waveguide core has been used as 430 × 220 nm (Fig. 1) to observe the role of coupling angle, and results have been discussed. Later, a comparative study has been done using various waveguide core widths, and the role of device dimension on the coupling angle has been discussed. Figure 2 shows the TE mode pictures for ring and waveguide. Figure 3 shows the pictures of coupled light in the waveguide from the

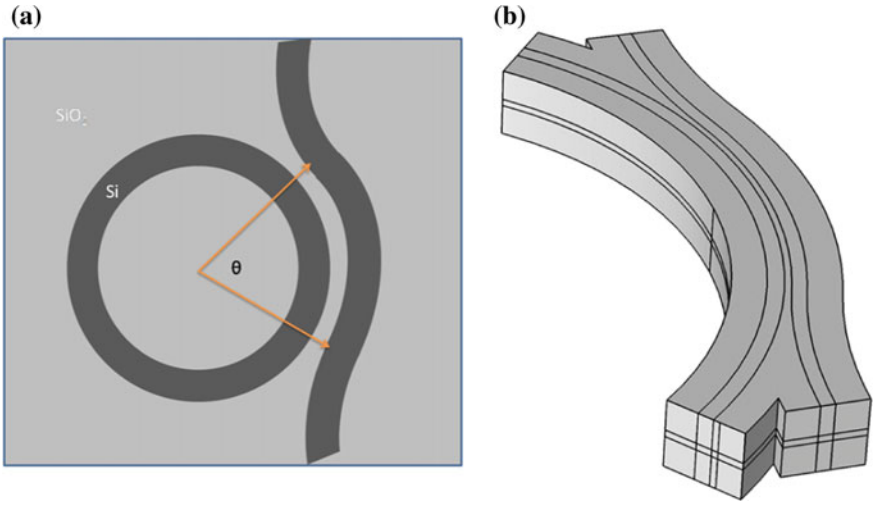

Fig. 1 **a** Schematic of device structure and **b** simulated structure

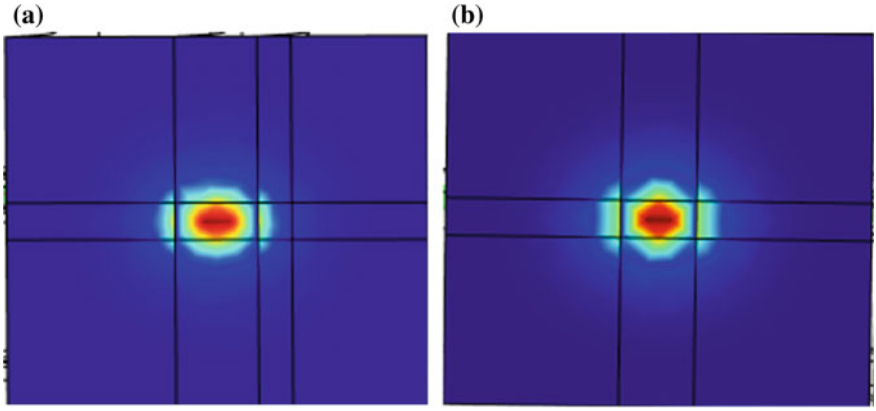

Fig. 2 **a** TE mode of the ring and **b** TE mode of the waveguide structure

ring resonator for 20°, 40° and 50° of coupling angles. Comparing the pictures, we see that as the angle of coupling increases, the light output of the waveguide increases by decreasing the light in the ring showing an efficient coupling characteristic.

A close observation to Fig. 3 can give us another vital information regarding the waveform of propagating light within the ring as well as in the bent bus waveguide. Both of them have the red peaks and blue peaks side by side, and the light is getting coupled more and more with the increased coupling angle. The plot for coupled light with respect to different coupling angles is given in Fig. 4a. It can be clearly noticed that, as θ increases, the amount of light coupling to the waveguide also increases. A maximum coupling percentage up to 64% has been achieved for $\theta = 50°$ for this

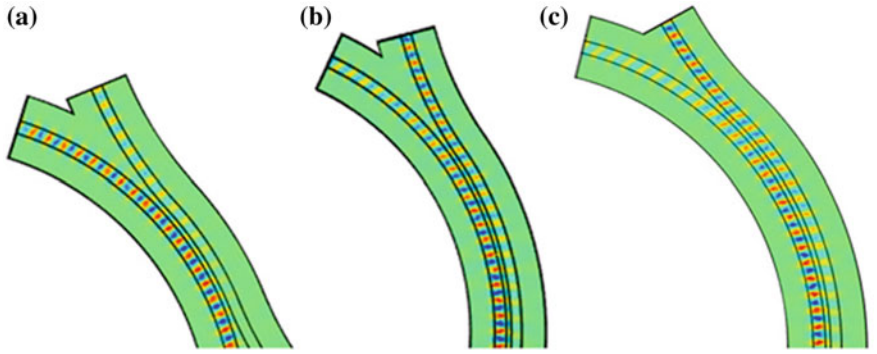

Fig. 3 Light coupled for **a** $\theta = 20°$, **b** $\theta = 40°$ and **c** $\theta = 50°$ in the ring–waveguide coupler structure with waveguide core width of 430 nm

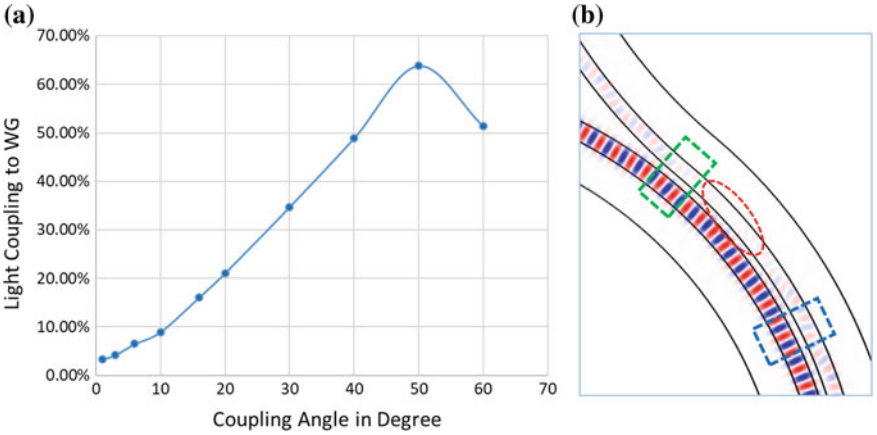

Fig. 4 **a** Percentage of light coupled into the waveguide for different value of coupling angle; **b** decrease in coupled light in waveguide (red-dash circled) for θ much higher than θ_m

structure. However, after 50°, the light coupling decreases for higher values of θ. Thus, here 50° is the optimum coupling angle (θ_m) for maximum coupling of light from resonator to the waveguide.

As θ increases more and more beyond θ_m, this effect becomes more and more dominant and for a particular range of θ, the waveguide has almost no light for its output as shown within red-dashed ellipse in Fig. 4b. The reason for this is clearly there in Fig. 4b itself. Looking at Fig. 4b, if we deeply observe the area enclosed by the blue-dashed rectangle (below the red-dashed ellipse) we can see that the blue peaks and the red peaks of bent bus waveguide are placed adjacent to their opposite colour peaks of the ring, showing almost 180° phase shift between them. This phase difference gets even closer to 180° as the coupling angle increases further. Then for a particular value of θ, this effect reaches to its peak and there is no light left in the

bus waveguide (red-dashed circle). This happens due to appearance of the optical path difference between the ring and the waveguide along with the back-coupling starts reducing the coupled light present in the waveguide (WG).

It can also be seen from Fig. 4b that if we increase θ even greater than that, the phase matching occurs (can be seen from area enclosed under green-dashed rectangle) and then the light starts coupling into the waveguide again, and the whole process gets repeated. Figure 5 shows a comparison plot between light coupled from ring to waveguides of different core widths maintaining the same coupling gap of 200 nm. It can be clearly noticed that, as the width of waveguide core increases, the structure becomes more and more sensitive to θ. For the waveguide core widths of 450, 470 and 490 nm, the values of θ_m are about 30°, 25° and 17°, respectively. This happens due to the increment in optical path of guided light within the waveguide as its effective index is increasing due to better confinement of light in bigger size of core. This also leads to decrease in percentage of first trip light coupling from ring to waveguide drastically as shown in Fig. 5. The waveguide with minimum core width gets more coupled light with a greater θ_m. Similarly, if the ring core dimension can be reduced further by suitably adjusting its other parameter for the same FSR, the performance of light coupling versus coupling angle can also be further increased to make the structure more efficient.

Hence, to achieve a better performance in our photonic components, we should choose a suitable core dimension for both ring and waveguide. This will give rise to a better θ_m, and hence, better Q-factor for higher FSR values can be achieved.

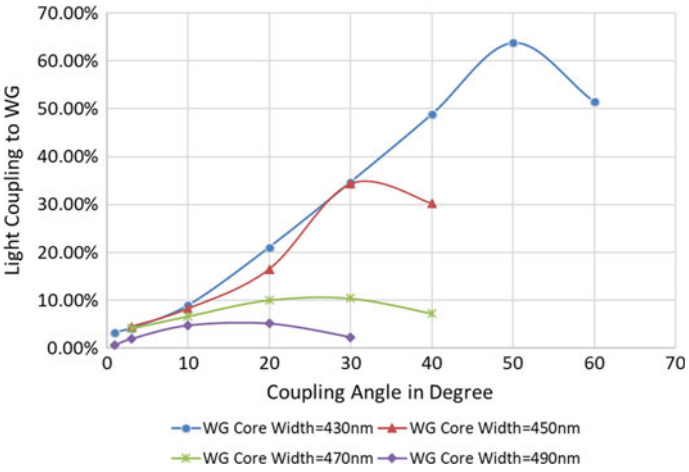

Fig. 5 Percentage of light coupled into the waveguides of different core widths for different value of coupling angle with coupling gap of 200 nm

4 Conclusion

Light coupling from ring to waveguide can be enhanced by bending the waveguide along the ring up to an angle θ_m. However, after θ_m, further increment in θ leads to optical path difference and back-coupling, thereby decreasing the single trip percentage of light coupling from ring to waveguide. Further increment in θ_m can be done by proper choice of ring (keeping the FSR unchanged) and waveguide core dimensions. Hence, it is essential to choose a suitable coupling angle (within θ_m) for a particular set of core dimensions while designing such type of structures. This study can also be helpful for designing of bent optical couplers.

Acknowledgements This work is financially supported by INSPIRE Fellowship programme (IF 150280) of Department of Science and Technology (DST), India.

References

1. Sarkaleh AK et al (2017) Optical ring resonators: a platform for biological sensing application. J Med Signals Sens 7(3):185–191
2. Girault P et al (2015) Integrated polymer micro-ring resonators for optical sensing applications. J Appl Phys 117:104504
3. Afroozeh A et al (2011) Simulation of soliton amplification in micro ring resonator for optical communication. J Teknol 271–277
4. Yariv A (2002) Critical coupling and its control in optical waveguide-ring resonator systems. IEEE Photonics Technol Lett 14:483
5. Vahala KJ (2003) Optical microcavities. Nature 424:839
6. Chao CY, Guo LJ (2003) Biochemical sensors based on polymer microrings with sharp asymmetric resonance. Appl Phys Lett 83:1527
7. Bogaerts W et al (2012) Silicon microring resonators. Laser Photonics Rev 6(1):47–73

CPW-Fed Triple-Band Circularly Polarized Printed Inverted C-Shaped Monopole Antenna with Closed-Loop and Two Semi-hexagonal Notches on Ground Plane

Reshmi Dhara, Sanjay Kumar Jana and Monojit Mitra

Abstract This paper is related to a triple-band circularly polarized (CP) printed antenna with coplanar waveguide feeding. The antenna is composed of an inverted C-shaped monopole, a CPW-fed ground plane with two semi-hexagonal notches and a square ring. By utilizing the inverted C-shaped monopole, CP radiation could be achieved at the lower band first. Then, two semi-hexagonal notches are etched from the ground plane, to obtain wide impedance bandwidth and a CP characteristic at upper band. A square closed loop is introduced at the left side of the patch which gives second wide CP band. The structure leads to simulated impedance bandwidth (IBW < -10 dB) of 8 GHz (1.31–9.31 GHz) with simulated center frequencies of 5.31 GHz, 150.63%. The simulated triple CP and ARBW are 270 MHz ($f_c =$ 4.01 GHz, 6.75%), 407 MHz ($f_c = 6.45$ GHz, 6.29%) and 368 MHz ($f_c = 8.57$ GHz, 4.29%), within the range of simulated impedance bandwidth curve. The maximum simulated peak gain is 2.16 dBi at 8.8 GHz. Proposed antenna happens to be suitable for 'S' and 'C' band wireless communication applications.

Keywords Circular polarization (CP) · Coplanar waveguide (CPW) · Square ring · Impedance bandwidth (IBW) · 'S' and 'C' band

1 Introduction

Recently, single-feed circularly polarized microstrip antenna has been developed to make the system more compact. But by using single-feed mechanism, CP band is very

R. Dhara (✉) · S. K. Jana
Department of Electronics and Communication Engineering, National Institute of Technology Sikkim, Ravangla, South Sikkim, India
e-mail: reshmidhara@yahoo.co.in

S. K. Jana
e-mail: skjiit@gmail.com

M. Mitra
Department of Electronics and Telecommunication Engineering, Indian Institute of Engineering Science and Technology, Shivpur, West Bengal, India
e-mail: monojit_m1@yahoo.co.in

V. Janyani et al. (eds.), *Optical and Wireless Technologies*, Lecture Notes in Electrical Engineering 648, https://doi.org/10.1007/978-981-15-2926-9_19

small. In order to increase CP band, perturbation technique has to be used. So that, two orthogonal degenerates' modes with equal amplitude with a 90° phase difference have to be generated and give wide CP. In some mobile satellite communication and most of the wireless communication, CP has been used. Antenna miniaturization and multiband are essential for a modern rapidly developing communication system.

A novel single-feed planar cross-monopole antenna has been reported in Ref. [1]. Designed antenna size is very large 50 × 50 × 1.5 mm^3. Obtained IBW is 70% ranging from 2.18 to 4.78 GHz. A wideband circularly polarized printed monopole antenna with coplanar waveguide feeding is designed in Ref. [2]. By using the asymmetric ground plane, at the upper band first CP radiation could be achieved. Then, to obtain wide impedance bandwidth and broadband CP characteristic a rectangular open loop is used. The measured IBW is 96.5% ranging from 1.48 to 4.24 GHz, and the 3 dB axial ratio bandwidth is 63.3% ranging from 1.9 GHz and 2.05 GHz to 3.95 GHz, dimension 55 × 50 × 1 mm^3. Another compact dual-band rectangular microstrip antenna (RMSA) is designed in Ref. [3] by a single-band rectangular microstrip antenna with two different single-slotted planes and a slotted ground plane. The antenna is linearly polarized (LP), and obtained IBW is 5.15–5.35 GHz and 5.725–5.825 GHz, size 12 × 8 × 1.5875 mm^3 which can be used for IEEE 802.11 a WLAN application. Another novel antenna has been designed [4] by using a microstrip-line feeding technique. The measured IBW is 6.56 GHz which covers the range from 2.32 to 8.88 GHz, whereas ARBW is 1.2 GHz ranging from 3.2 to 4.4 GHz, size 45 × 40 × 1.6 mm^3. A tetra-band circularly polarized CPW-fed monopole antenna is designed in Ref. [5], size 55 × 55 × 1.6 mm^3. The measured IBW ranging from 2.58 to 12.49 GHz and the simulated AR tetra-band are 633.9 MHz, 152.8 MHz, 433.4 MHz and 172 MHz resonating at 6.75 GHz, 8.29 GHz, 9.35 GHz and 11.53 GHz, respectively.

As mentioned above, the size of the antenna is very large compared to the proposed designed antenna and also got three wide CP bands to compare to earlier research. In this paper, a triple-band circular polarized and wide impedance band antenna is designed. An inverted C-shaped printed antenna primarily has been used here for a CP at lower band frequency region. Two semi-hexagonal notches on the ground plane for a CP at upper band and one square closed loop are designed to achieve a broad impedance match and wideband CP operation bandwidth at middle band. The presented antenna shows three 3 dB AR bands 270 MHz ($f_c = 4.01$ GHz), 407 MHz ($f_c = 6.29$ GHz) and 368 MHz ($f_c = 8.57$ GHz) can be used for 'S' and 'C' band wireless communication applications.

2 Antenna Design

A. Antenna Configuration

The geometry of the proposed antenna has been depicted in Fig. 1. The dimension of the antenna is 25 × 25 × 1.6 mm^3. On the top of a substrate FR4 epoxy (dielectric

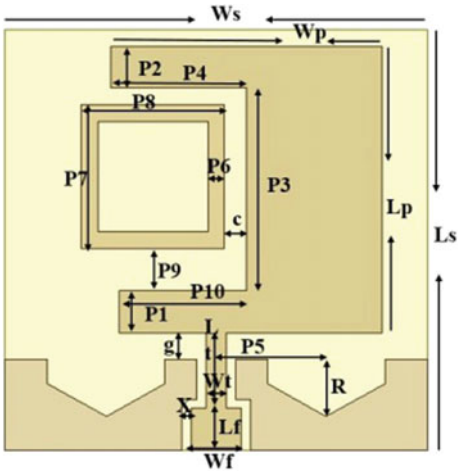

Fig. 1 Dimension of the simulated proposed antenna top view

constant $\varepsilon_r = 4.4$ and $\tan\delta = 0.02$), the antenna is fabricated. On the backside of the substrate, no metal is printed. A 50 Ω CPW feeding line with a width of W_f and two identical gaps of width 'x' are produced to feed the inverted C-shaped monopole. A proper gap between CPW-fed ground and patch is used here to create coupling between them which gives CP at lower band. Two semi-hexagonal notches with a proper position from feed line and a proper diameter are etched from the ground plane in order to get wide impedance band at upper band. A square closed loop is added on the left side of the patch with a gap 'g' from patch and a proper length '$P7$' which one creates CP at middle band. By tuning the gap size and the height of the closed loop, triple CP modes could be obtained. According to the simulation studies from ANSYS HFSS version 13, the optimized parameters are listed in Table 1.

B. **Operating Principle**

To realize the operating principle of the designed antenna, three paradigms (Ant. 1–Ant. 3) are illustrated in Fig. 2. The return loss (S_{11}) and AR performances of Ant.

Table 1 Optimal dimension of the proposed antenna

Parameter	Value (mm)	Parameter	Value (mm)	Parameter	Value (mm)
L_s	25	W_t	1.2	$P8$	8.5
W_s	25	$P1$	2.5	$P9$	2.5
L_p	17	$P2$	2.5	$P10$	7.5
W_p	16	$P3$	12	c	1.3
h_{sub}	1.6	$P4$	8	X	0.55
L_f	2.5	$P5$	6.5	g	1.6
W_f	3	$P6$	1.0	R	4.0
L_t	4.5	$P7$	8.5		

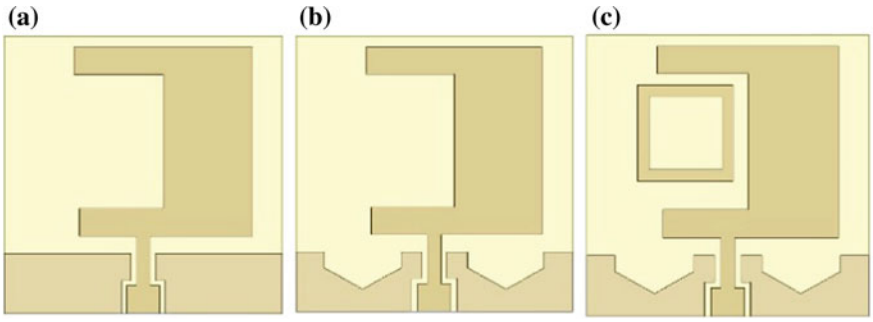

Fig. 2 Three improvement processes of proposed antenna: **a** Ant. 1, **b** Ant. 2 and **c** Ant. 3

1–3 are also compared in Figs. 3 and 4. First, a conventional CPW-fed monopole Ant. 1 is proposed to generate the fundamental resonant CP mode at 4.2 GHz, which is controlled by the feed gap between monopole and ground plane. Ant. 1 is first designed using a rectangular patch and a CPW-fed ground at a resonant frequency 4.2 GHz, as it comes in C band allocation which is useful in radars, mobile phones and commercial wireless LAN. But to get CP radiation at this designed frequency, we need to create two orthogonal degenerates' modes with equal amplitude with a

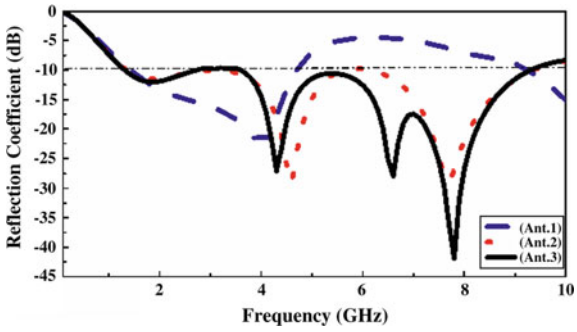

Fig. 3 Simulated reflection coefficient for the proposed antenna improvement process

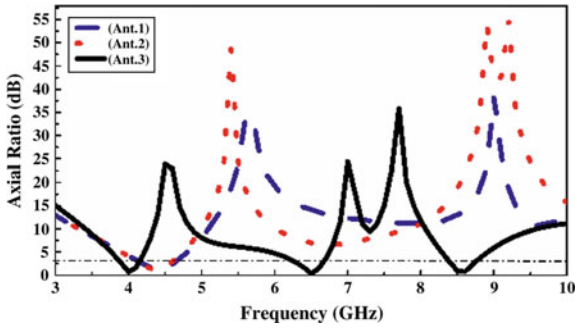

Fig. 4 Simulated reflection axial ratio bandwidth for the proposed antenna improvement process

90° phase difference. So first, the rectangular patch is shifted to the right from the center of the feed line, and then a rectangular slot has been etched from the left side of the radiating patch. As a result, *y*-directed horizontal current has increased which generates a CP mode at 4.4 GHz resonating frequency and we got Ant. 1 as shown in above shape. In order to increase IBW and create CP radiation at other resonant frequencies, two semi-hexagonal notches are etched from ground in Ant. 2. From Fig. 3, it is clear that this notch increases capacitive impedance and as a result gives wide impedance bandwidth. From Fig. 4, we can see that CP radiation has been improved compared to earlier at higher frequency region but still that does not satisfy 3 dB band. So to improve CP radiation at higher region and to create another CP resonance at middle band, a closed loop is added with a particular gap and length from patch, so that the resonance can occur at middle zone frequency region and also improve CP radiation at higher frequency region due to coupling between patch and loop in Ant. 3. In Fig. 4, it is clear that another two CP modes can be obtained as mentioned in above criterion. Finally by using Ant. 3, we have got wide IBW and three wide CP bands.

As we know, it is difficult to generate CP radiation for a traditional monopole antenna because of the weak radiation in horizontal direction. This can be explained by the surface current distributions at 6.5 GHz in Fig. 5. From Fig. 5a, we can see that the current distributions of the two ground planes in horizontal direction are in the opposite direction. Therefore, the horizontal current is counteracted, and vertically polarized radiation could be produced due to the small horizontal components. Hence, at 6.5 GHz we get LP and the value of AR in the whole band is large, which is shown in Fig. 4. The CP operation could be achieved by the excitation of two orthogonal modes with a 90° phase difference. In order to generate a horizontal component, a closed loop to left of the monopole is adopted with a gap from patch. Figure 5b shows that horizontal currents are yielded at the closed loop in Ant. 3. By employing the coupled effect between the closed-loop square ring and the monopole, CP radiation can be generated at 6.5 GHz. The square ring is capacitively coupled by the monopole radiator, which transmits energy on the square ring streaming like a traveling-wave

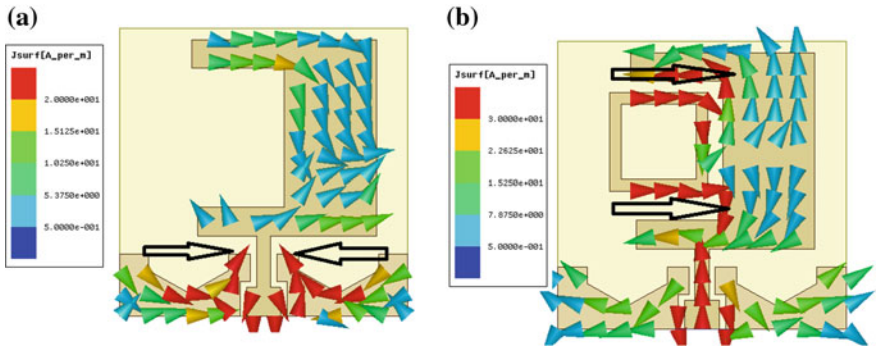

Fig. 5 Simulated surface current distribution at frequency 6.5 GHz for **a** Ant. 2 and **b** Ant. 3

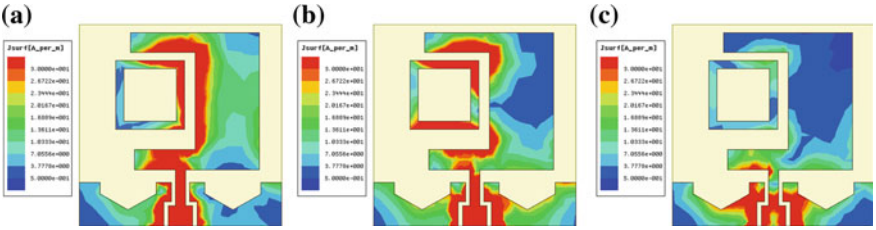

Fig. 6 Simulated surface current distributions for Ant. 3 at frequency **a** 4.0 GHz, **b** 6.5 GHz, **c** 8.6 GHz

mode, and therefore the CP operation in middle band is introduced. As it is revealed from Fig. 4, the middle CP band is yielded by the square ring, with the upper CP mode performance by tuning the position and radius of the semi-hexagonal notches. In addition, the impedance matching in CP band is also improved to cover the whole 3 dB AR bandwidth. From the comparison results between the three antennas, Ant. 3 has both good impedance matching and three wide CP bands.

For the purpose of illustrating the CP principle, distributions of surface current at 4.0, 6.5 and 8.6 GHz are analyzed in Fig. 6 for proposed antenna. From current distribution in Fig. 6a, it is clear that inverted C-shaped monopole dominates CP radiation at lower frequency band, whereas closed-loop square ring dominates the middle band CP radiation. This can be prove from Fig. 6(b) that the maximum surface current density are around the ring which is accountable for generating CP radiation at the middle band frequency region. Figure 6c depicts that higher CP radiation can be dominated by semi-hexagonal notches on the ground plane.

Figure 7 shows the simulated surface current distribution at 4 GHz for phases of (a) 0°, (b) 90°, (c) 180° and (d) 270°. From Fig. 7, it can be seen that the predominant surface current turns in an anticlockwise direction as time increases; thus, the polarization sense is right-hand circularly polarization (RHCP) for the frequency at 4 GHz. Similarly, from Figs. 8 and 9 it can be seen that the predominant surface current turns in an clockwise direction as time increases; thus, the polarization sense is left-hand circularly polarization (LHCP) for the frequencies 6.5 GHz and 8.6 GHz, respectively.

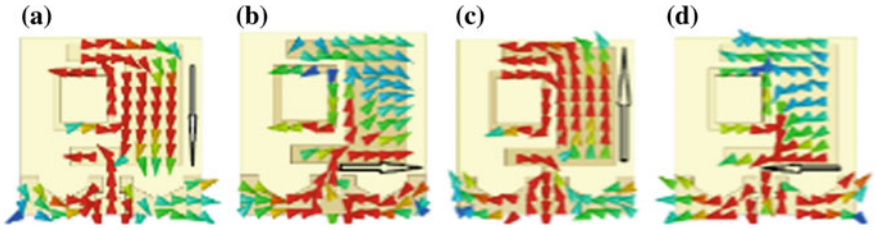

Fig. 7 Simulated surface current distribution for phases of **a** 0°, **b** 90°, **c** 180° and **d** 270° at 4.0 GHz

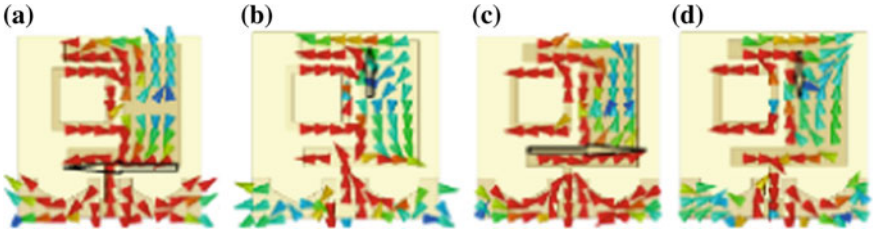

Fig. 8 Simulated surface current distribution for phases of **a** 0°, **b** 90°, **c** 180° and **d** 270° at 6.5 GHz

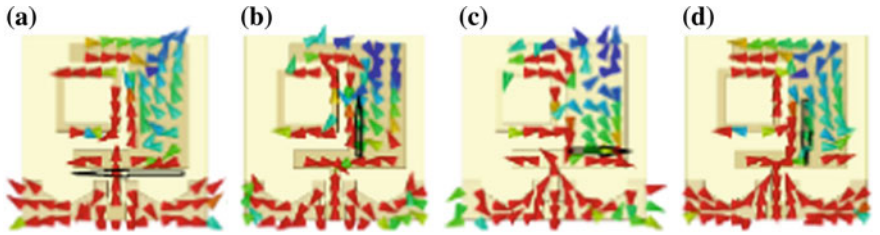

Fig. 9 Simulated surface current distribution for phases of **a** 0°, **b** 90°, **c** 180° and **d** 270° at 8.6 GHz

C. **Parametric Study**

To get the optimized dimensions of the monopole antenna, a different parameter study is analyzed. The feed gap height '*g*' between CPW-fed grounds of the patch is studied and presented in Fig. 10.

In addition, an important feature of the proposed antenna is the effect of impedance matching produced from the coupling effects between the CPW-fed ground plane and the feed point. For this, the effects of the feed gap height $g = 0.6$, 1.6, 2.6, 3.6 and 4.6 mm on the performance of the proposed inverted C-shaped monopole antenna are also studied and presented in Fig. 10. The obtained results clearly show that the lowest resonant frequency of the proposed design moves toward higher frequency band and forms by increasing the feed gap height '*g*'. The higher resonant frequency

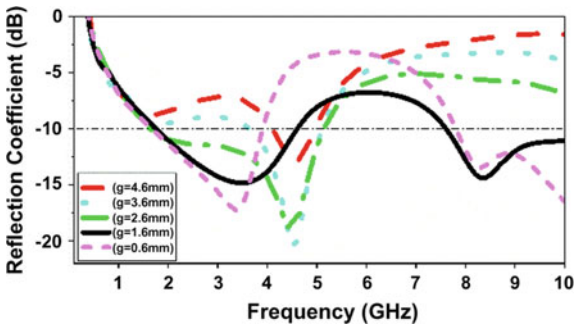

Fig. 10 Simulated return loss against frequency for the proposed planar inverted C-shaped monopole antenna with various *g* lengths

of the proposed design also moves toward higher frequency band and disappears gradually. This is because increasing the feed gap height significantly increases the total parallel capacitive effect, lowering quality factor and increasing the resonance frequency. The impedance bandwidth changes significantly by varying the feed gap. This is due to the sensitivity of the impedance matching to the feed gap. The ground plane, acting as an impedance matching circuit, tunes the input impedance and the operating bandwidth, while the feed gap is varied [5]. To summarize, the optimized feed gap (g) is observed to be at $g = 1.6$ mm.

Figure 11 shows the effect for position of hexagonal notches on the ground plane from the center of the feed line to the center of semi-hexagonal notch. From Fig. 11, it is clear that when position is $P5 = 6.5$ mm it gives wider IBW due to greatly increased capacitive effect.

Figure 12 shows the effect for radius of semi-hexagonal notches. When the radius $R = 4$ mm gives wider IBW as along notches current path length increases and best matching occurrence is compared to other.

Figure 13 shows the effect of feed gap between CPW-fed ground and quarter-wave transmission line. From Fig. 13, it can be seen that when the feed gap length x is 0.55 mm antenna gives wider bandwidth due to impedance matching between feed and ground.

Figure 14 illustrates the S_{11} curves by varying the value of the length of closed-loop square ring $P8$. As expected, the S_{11} at lower band has shifted to the lower

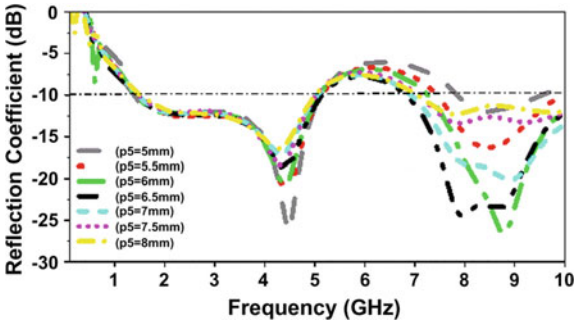

Fig. 11 Simulated return loss against frequency for the proposed planar inverted C-shaped monopole antenna with various $P5$ lengths

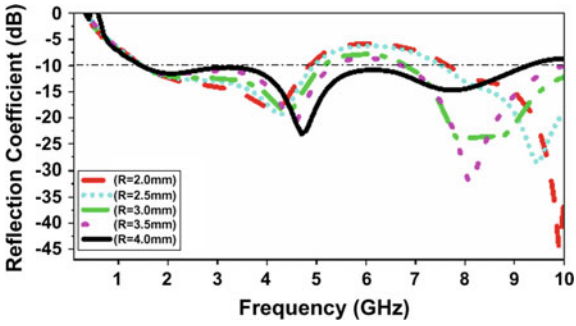

Fig. 12 Simulated return loss against frequency for the proposed planar inverted C-shaped monopole antenna with various R radii

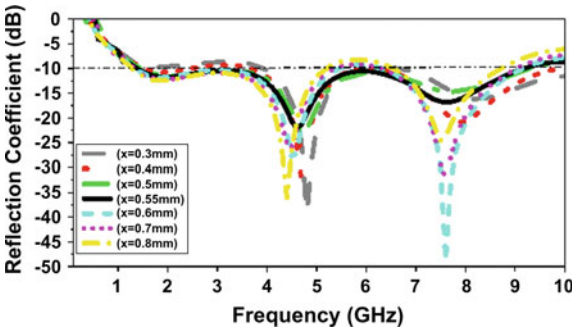

Fig. 13 Simulated return loss against frequency for the proposed planar inverted C-shaped monopole antenna with various *X* lengths

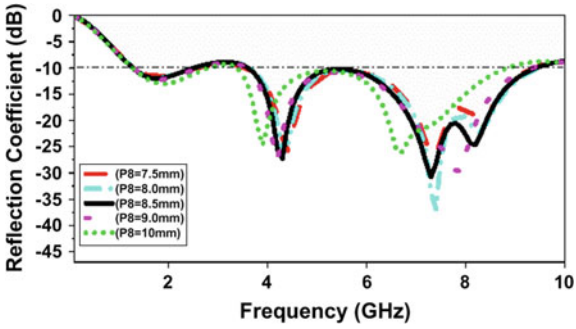

Fig. 14 Simulated return loss against frequency for the proposed planar inverted C-shaped monopole antenna with various *P*8 lengths of loop

resonating frequency, as well as higher resonance frequency also shifts toward the lower region as we increase the length. This is reasonable because the length can control the current distributions on the loop. By increasing the length of the square ring, the current path length increases; as a result, inductive impedance of the antenna has increased, so the slow-wave factor has been increased; as a result, group velocity has decreased, and resonant frequency moves toward the lower value. Finally, the optimal value is $P8 = 8.5$ mm.

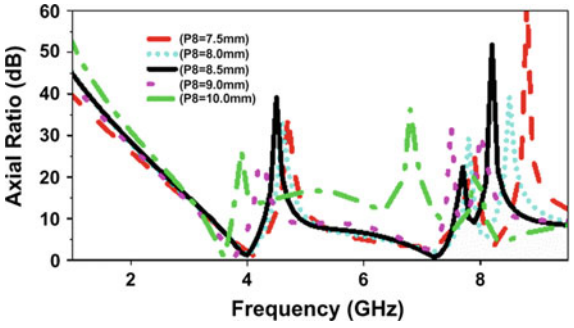

Fig. 15 Simulated ARBW against frequency for the proposed planar inverted C-shaped monopole antenna with various *P*8 lengths of loop

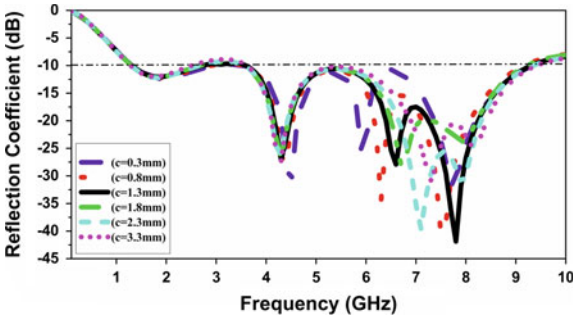

Fig. 16 Simulated return loss against frequency for the proposed planar inverted C-shaped monopole antenna with various length gaps *C*

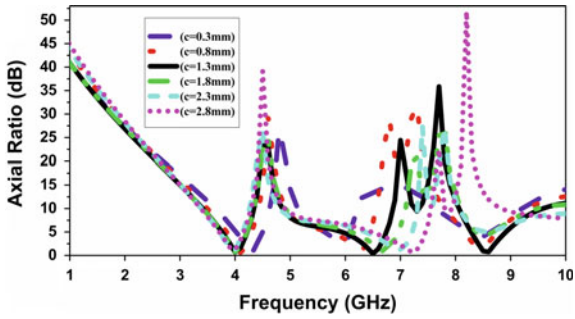

Fig. 17 Simulated ARBW against frequency for the proposed planar inverted C-shaped monopole antenna with various length gaps *C*

Figure 15 shows the AR curves by varying the value of the length *P*8 of closed-loop square ring. By varying the length, the CP bandwidth can be changed as horizontal current distributions are changed when $P8 = 8.5$ mm gives wider optimal bandwidth compared to other length.

Figure 16 shows the S_{11} by varying the gap '*c*' between square loop and monopole antenna. By the varying gap $c = 0.3, 0.8, 1.3, 1.8, 2.3$ and 3.3 mm employing the coupled effect between the closed-loop square ring and the monopole, as a result current distribution also changes. From Fig. 16, it is clearly shown that with increasing gap, the lower resonating frequency shifting is negligible where the higher resonating frequency shifted toward the higher frequency region. The current path length decreases due to decreasing coupling with increasing gap; as a result, inductive impedance of the antenna has decreased, so the slow-wave factor has been decreased; as a result, group velocity has increased, and resonant frequency moves toward the higher value. Finally, the optimal value is $c = 8$ mm.

Figure 17 illustrates the AR curves by varying the gap length '*c*'. By employing the coupled effect between the closed-loop square ring and the monopole, CP radiation can be generated. The optimal value is $c = 8$ mm as in this position large horizontal current can be generated due to coupling as compared to other position.

3 Result and Discussion

The simulation was performed using ANSYS HFSS. From Fig. 3, it is clear that proposed antenna has the −10 dB impedance bandwidth (IBW) of the simulated reflection coefficient to cover the range from 1.31 to 9.31 GHz, IBW is 8 GHz, and center frequency is 5.31 GHz, 150.63%.

As shown in Fig. 4, the simulated ARBW of the proposed antenna is 270 MHz (f_c 4.01 GHz, 3.88–4.15 GHz, 6.75%), 407 MHz (f_c 6.47 GHz, 6.26–6.67 GHz, 6.29%) and 368 MHz (f_c 8.57 GHz, 8.39–8.75 GHz, 4.29%) which are within the range of simulated IBW curve. Obtained three circular polarized bands can be used for S and C band applications.

Figure 18a shows the simulated radiation pattern for the *XZ* plane ($\varphi = 0°$) and *YZ* plane ($\varphi = 90°$) at 4.0 GHz. The simulated radiation pattern in Fig. 18a, b has shown that the cross-polarization levels are 29 dB lower than co-polarization levels in the broadside direction.

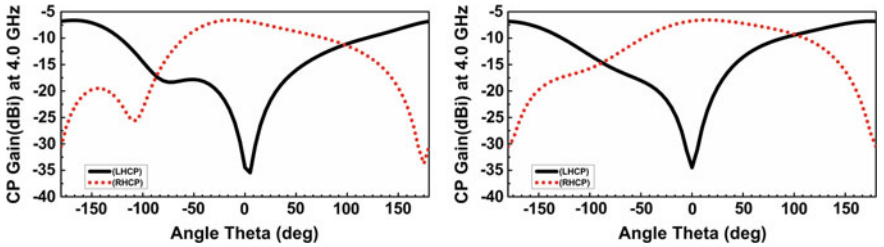

Frequency = 4.0 GHz

(a) XZ plane (b) YZ plane

Fig. 18 Simulated radiation pattern for the proposed antenna in the **a** *XZ* ($\varphi = 0°$) plane and **b** *YZ* ($\varphi = 90°$) plane

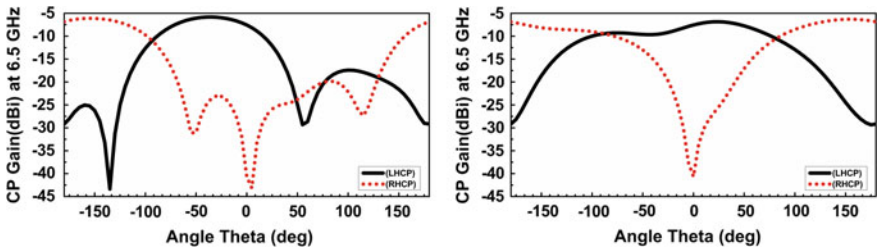

Frequency = 6.5 GHz

(a) XZ plane (b) YZ plane

Fig. 19 Simulated radiation pattern for the proposed antenna in the **a** *XZ* ($\varphi = 0°$) plane and **b** *YZ* ($\varphi = 90°$) plane

Figure 19a shows the simulated radiation pattern for the *XZ* plane ($\varphi = 0°$) and *YZ* plane ($\varphi = 90°$) at 6.5 GHz. The simulated radiation pattern in Fig. 19a, b has shown that the cross-polarization levels are 35 dB lower than co-polarization levels in the broadside direction.

Figure 20a shows the simulated radiation pattern for the *XZ* plane ($\varphi = 0°$) and *YZ* plane ($\varphi = 90°$) at 8.6 GHz. The simulated radiation pattern in Fig. 20a, b has shown that the cross-polarization levels are 27 dB lower than co-polarization levels in the broadside direction.

Figure 21 shows the real (resistance) and imaginary (reactance) parts of the simulated input impedance at 50 Ω quarter-wave microstrip feed line. Within the CP operating bands 3.88–4.15 GHz, 6.26–6.67 GHz and 8.39–8.75 GHz, impedance matching is well maintained as the resistance is close to 50 Ω and the reactance is small close to 0 Ω.

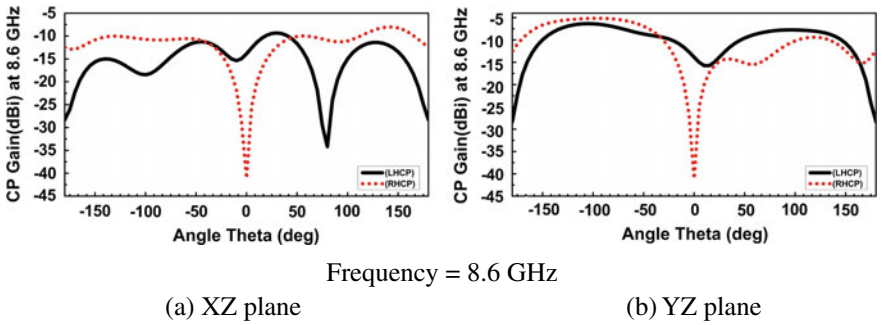

Fig. 20 Simulated radiation pattern for the proposed antenna in the **a** *XZ* ($\varphi = 0°$) plane and **b** *YZ* ($\varphi = 90°$) plane

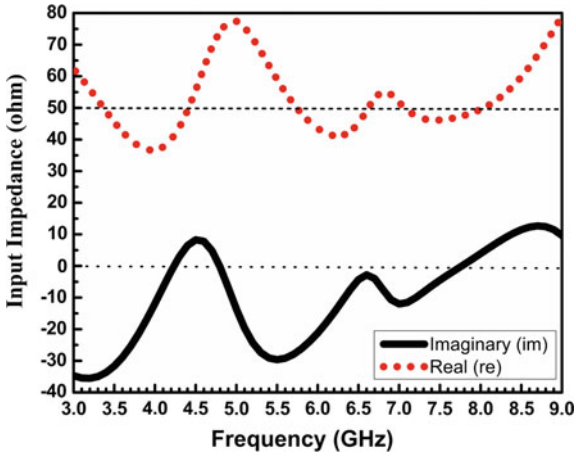

Fig. 21 Simulated impedance [resistance (real) and reactance (imaginary)] plot for proposed antenna

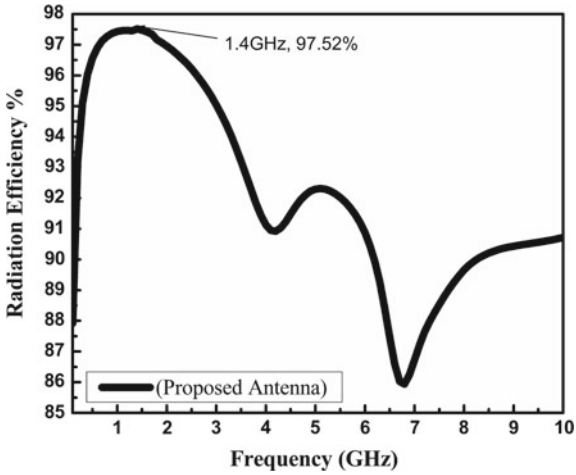

Fig. 22 Simulated radiation efficiency for proposed antenna

Figure 22 shows the simulated radiation efficiency for proposed antenna versus frequency. For entire circular polarized band, simulation efficiency is within 85–98%, the maximum efficiency is 97.52% at 1.4 GHz and the efficiency at the center frequency of CP band is 91.13% at 4.0 GHz, 87.96% at 6.5 GHz and 90.27% at 8.6 GHz, respectively.

Figure 23 shows the radiation pattern for the proposed antenna at $\varphi = 0°$ (XZ plane) and $\varphi = 90°$ (YZ plane) for LHCP and RHCP at frequencies 4.0 GHz, 6.5 GHz and 8.6 GHz, respectively. A good LHCP and RHCP can be observed from those figures.

The simulated peak gain of this proposed antenna is 2.16 dBi at a frequency of 8.8 GHz as depicted in Fig. 24, and the peak gain at the center frequency of CP band is −3.18 dBi at 4.0 GHz, 0.71 dBi at 6.5 GHz and 2.12 dBi at 8.6 GHz, respectively.

4 Conclusion

A triple-band circularly polarized inverted C-shaped patch antenna has been proposed in this paper. The proposed antenna uses an inverted C-shaped radiating patch that gives the perturbation of electric field of equal magnitude but in phase quadrature. These E-fields are the cause of wide CP band at lower resonating frequency. Two semi-hexagonal notches on the ground plane give wider IBW and CP radiation at higher resonating frequency. A square closed loop is added on the left side of the radiating patch. Tuning the loop gives another CP band at middle band frequency. The proposed antenna can provide three circular polarized bands over wide frequency bands within the range of simulated result. The ARBW is 270 MHz ($f_c = 4.01$ GHz, 6.75%), 407 MHz ($f_c = 6.45$ GHz, 6.29%) and 368 MHz ($f_c = 8.57$ GHz, 4.29%).

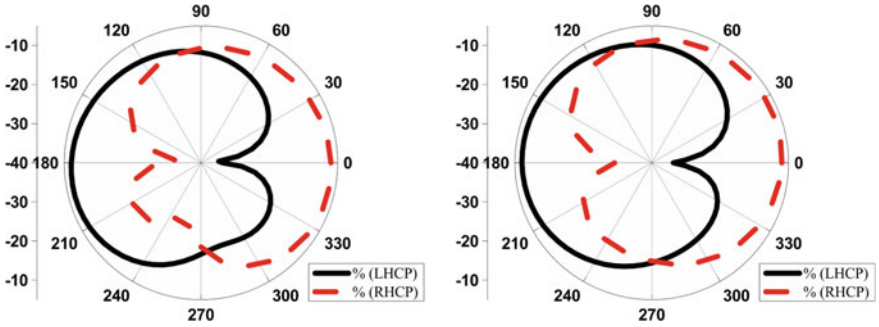

Frequency = 4.0 GHz

(a) XZ plane (b) YZ plane

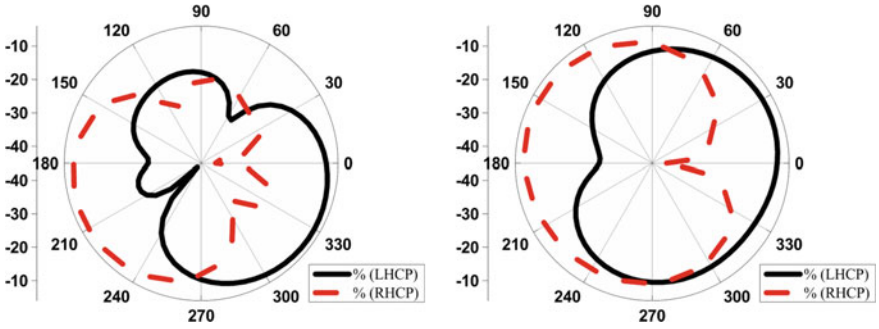

Frequency = 6.5 GHz

(c) XZ plane (d) YZ plane

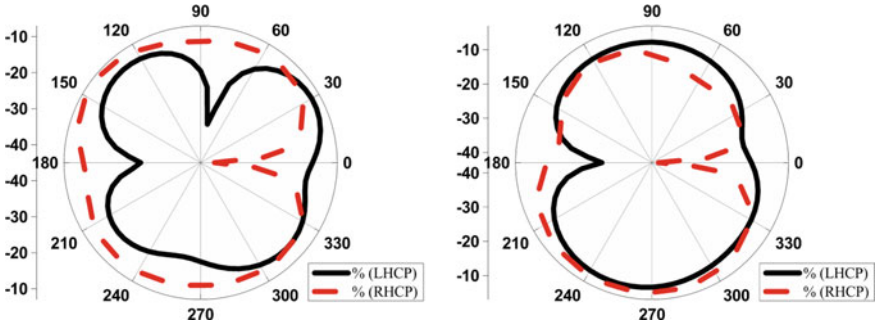

Frequency = 8.6 GHz

(e) XZ plane (f) YZ plane

Fig. 23 Simulated radiation patterns (LHCP and RHCP) in the **a**, **c**, **e** for *XZ* ($\varphi = 0°$) and **b**, **d**, **f** for *YZ* ($\varphi = 90°$) planes

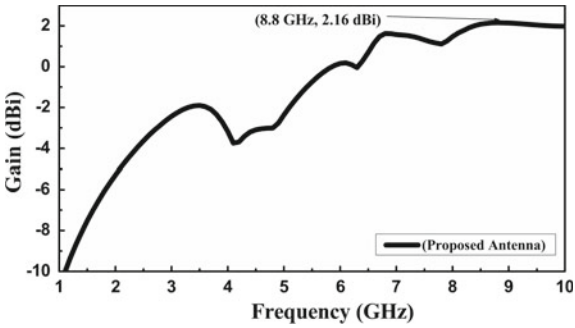

Fig. 24 Simulated peak gain for the proposed antenna

References

1. Tseng CF, Huang CL (2009) A wideband cross monopole antenna. IEEE Trans Antennas Propag 57(8):2464–2468
2. Ding K, Guo YX, Gao C (2017) CPW-fed wideband circularly polarized printed monopole antenna with open loop and asymmetric ground plane. IEEE Antennas Wirel Propag Lett 16:833–836
3. Chakraborty U, Kundu A, Chowdhury SK, Bhattacharjee AK (2014) Compact dual-band microstrip antenna for IEEE 802.11 a WLAN application. IEEE Antennas Wirel Propag Lett 13:407–410
4. Wu JW, Ke JY, Jou CF, Wang CJ (2010) Microstrip-fed broadband circularly polarised monopole antenna. IET Microw Antennas Propag 4(4):518–525
5. Dhara R, Midya M, Mitra M, Jana SK (2017) CPW-fed tetra band circular polarized antenna for wireless communication applications. In: Applied electromagnetics conference (AEMC), 2017 IEEE, pp 1–2

Security for Mobile System: 5G

Naresh Kumar, Annu, Karan Verma, Ajay K. Sharma and Shashvat Sharma

Abstract There have been numerous advancements in mobile wireless communication since the last few decades. This innovation consists of a number of generations and is still in progress. The journey of mobile wireless communication started with 1G followed by 2G, 3G, 4G, and under research upcoming generation 5G. In this paper, an attempt has been made to contribute to the upcoming mobile generation (5G) by uncovering security risks in the upcoming 5G network and finding vulnerabilities in the 5G network. We have also thrown some light on the new emerging technology 5G, its concept, requirements, features, benefits, and hardware and software requirements.

Keywords Mobile network architecture · 5G · AKA mechanisms · MAC

1 Introduction

In all mobile generations [1], security is one of the most important requirements. AAA (Authentication, Authorization, and Accounting) is very much needed between user and mobile network. The mobile wireless generation (G) generally means a change in speed, frequency, technology, latency, etc. Each generation has some advanced features which are better than the previous one.

1G is used only for voice calls and is analog in nature, while 2G includes voice as well as data transmission and is based on digital technology. 3G, however, overcomes limitations of both the generations and is having enhanced features like increased data rate, multimedia conferencing, etc. 4G is mainly responsible for the drastic change in mobile communication system. High voice quality, very low latency, video calling,

N. Kumar (✉) · Annu · K. Verma · S. Sharma
Department of Computer Science and Engineering, National Institute of Technology Delhi, New Delhi 110040, India

K. Verma
e-mail: karanverma@nitdelhi.ac.in

A. K. Sharma
NIT Jalandhar, Jalandhar, India

V. Janyani et al. (eds.), *Optical and Wireless Technologies*, Lecture Notes in Electrical Engineering 648, https://doi.org/10.1007/978-981-15-2926-9_20

and strong security are the remarkable features of this generation. It is totally IP based. There were many loopholes in each generation that were solved in successive generations. The next generation is 5G that will incorporate very high speed for transferring gigabits of data within a fraction of second, HD video calling, and stronger security than all the previous ones. There are various features like handling the mobility management, IoT devices, network function virtualization and software-defined networking, etc. As in each generation of mobile communication system, there are always some loopholes that existed in it whether it is speed, synchronization, security issues, etc. Keeping these factors in our mind, one may find flaws in every generation of mobile system and can contribute to the system in order to make changes in upcoming generations. After a rigorous survey of various research papers, we have found various shortcomings whose solutions can play a major role in the proper advancement of next generation. So our major objective is to uncover security risks in the upcoming 5G network and contribute to the 5G system by learning more about the flaws pertaining to 5G. This paper is organized as follows. In Sect. 2, we explain the summary of generalized advanced mobile communication architecture and the procedure how authentication and various mechanisms work. In Sect. 3, we have briefly given a general summary of 5G architecture. In Sect. 4, vulnerabilities in protocols used in all preexisting mobile generations are discussed. Finally, we have proposed architecture for overcoming weakness and then concluded after showing results.

2 Basic Concepts of Advanced Mobile Generation Architecture

2.1 Architecture

Generally in all advanced generations of mobile communications, we see the architecture [2] shown in Fig. 1:

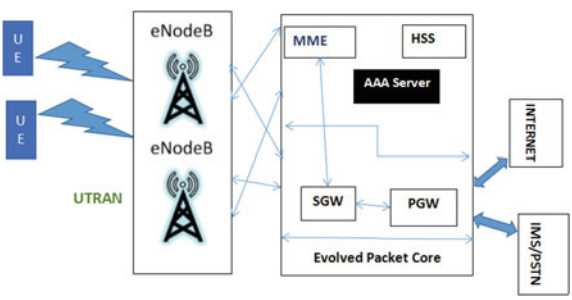

Fig. 1 Generalized architecture of advanced mobile generations

- User equipment (UE) is the mobile device in which SIM (subscriber identity module) is inserted and that is capable of sending and receiving wireless radio waves.
- Evolved Packet Core unites voice and data on an Internet Protocol (IP) service architecture, and voice is treated as just another IP application. It also acts as a framework for providing converged data and voice on the network.
- eNodeB (evolved NodeB): major part of mobile network UTRAN (Universal Terrestrial Radio Access Network). Mobile devices connect with the network through this eNodeB that acts as the base station. They provide connectivity between mobile station and the radio network.
- MME (Mobility Management Entity) is responsible for controlling the core network. Authentication is basically handled by this unit. It manages session states and tracks a user across the network. It tracks UE's location and decides the route of data packets.
- HSS (Home subscriber server) is basically a database that is capable of storing the user data and the secret keys. It includes all the needed information regarding users' authentication and confidentiality keys.
- P-GW (Packet Data Network Gateway) plays a major role in the interaction of mobile network with Internet and allocates IP addresses mobile systems. Billing and policy charging are also maintained by this unit.
- S-GW (Serving Gateway) routes data packets through the access network.
- AAA server takes care of authentication and authorization of user equipment as well as network.
- PSTN (public switched telephone network) combination of all telephone networks for public telecommunication.

2.2 Authentication Procedure

For authentication and other security measures, AKA [3, 4] (authentication and key agreement) protocol is used.

Figure 2 shows the authentication and key agreement mechanism [2]. It involves authentication from both the sides, i.e., both the mobile station as well as base station will be authenticated. Initially, UE sends IMSI (international mobile subscriber identity) to base station which is sent to HSS for connecting through the core network. Home subscriber server randomly produces a RAND number and generates authentication tokens after passing the RAND and user's key (specific to UE corresponding to that IMSI) through a function (applying some cryptography) generally a result of it is called as XRES (response by network). These tokens include a lot of details about the results obtained after applying a cryptographic algorithm for RAND number and many details like sequence number (SQN). After this, MME stores those result and sends the RAND challenge and various tokens like SQN, etc. to UE so that it can check for the authenticity of network. After this, it will send its RES (response), and

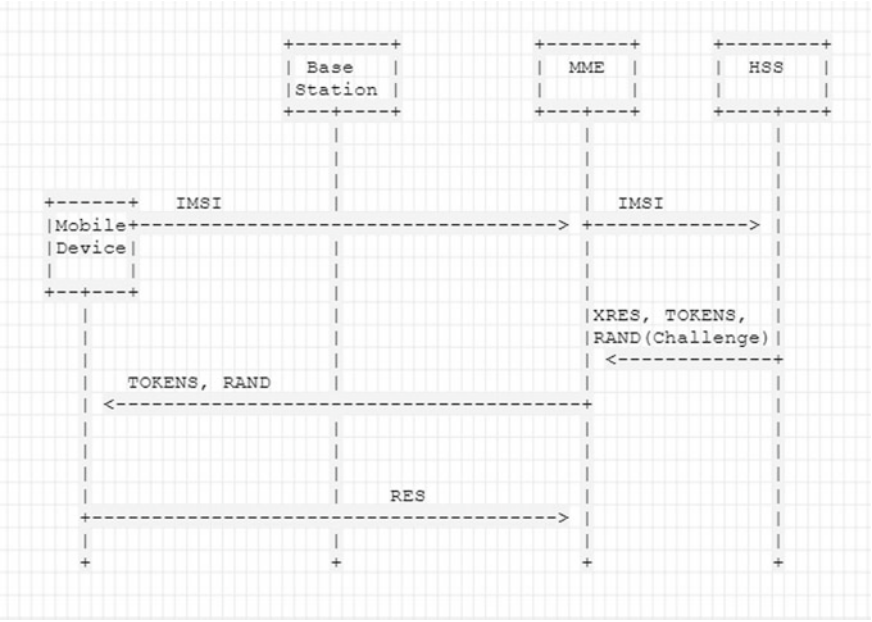

Fig. 2 Authentication procedure

SQN is a sequence number that is required for prevention of replay attacks. Then after getting response, MME compares the result (RES ==XRES?) and authenticates them. Now the other keys like IK (integrity key), CK (confidentiality key), etc. using which the data to be sent is encrypted and decrypted between mobile device and the core network. IMSI is a unique number usually fifteen digits, associated with GSM and Universal Mobile Telecommunications System (UMTS) network mobile phone users. The IMSI is a unique number identifying a subscriber.

3 Overview of 5G Architecture

A brief overview of 5G architecture [5] is shown in Fig. 3. The advanced base station for this generation is called gNodeB.

The access and mobility management function (AMF)	The session management function (SMF)	User plane function (UPF)	Policy control function (PCF)	Unified data management (UDM)
• Registration management • Connection management • Mobility management • Authentication • Authorization	• Session allocation, release or modify • IP address allocation • Route traffic to destination • Stoppage of interfaces	• Packet routing and forwarding • Packet inspection of policy rule • Lawful intercept • Reporting traffic usage	• Govern network behavior • Charging of data usage • Gives rules to control plane	• Repository for security keys used in authentication • Stores various information of user

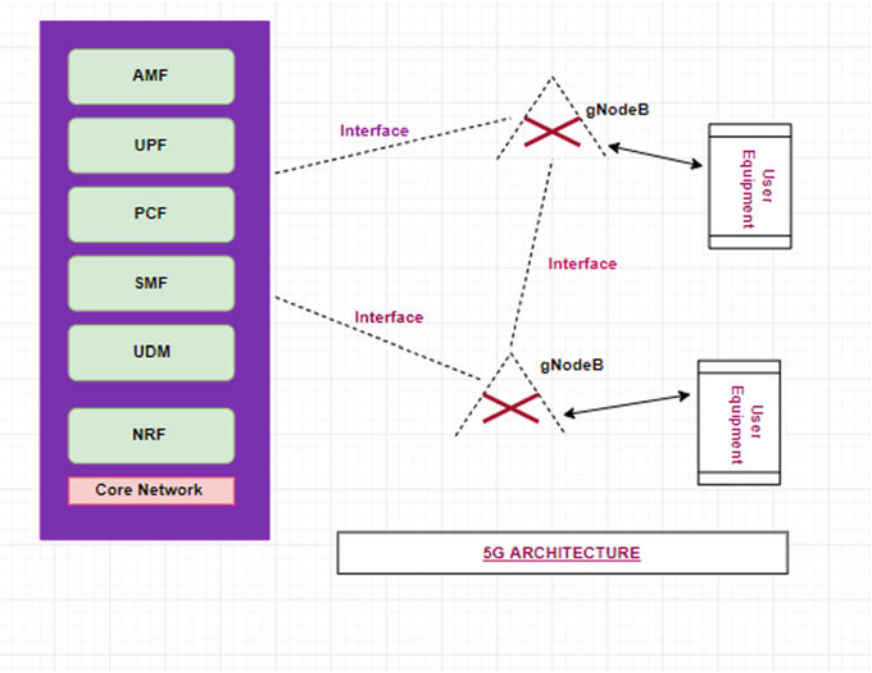

Fig. 3 Simplified architecture of 5G. *Note* This is a proposed architecture in meeting #119 January 16–20, 2017, Dubrovnik, Croatia

Similar functions as described in Fig. 1 can be assumed for this architecture too.

4 Vulnerabilities in Preexisting Mobile Generations

Many research works have been suggested in the literature for security flaws and various contributing factors regarding upcoming generation of mobile communication.

Numerous researchers have proposed new methods to increase the performance. In [6] paper, it includes various techniques about 1G system that was based on analog system. It supports data speed of up to 2.4 kbps. At that time, there were cordless telephones. The major weakness was that it supports only voice. It has low capacity, poor handoff, less secure, and poor voice link. So, an enhanced security, high speed, and data services were very much required. Then came second generation where data rate of up to 64 kbps, roaming facility, voice and data services, enhanced security (A5/A8) was there as described in [7]. But it had some weaknesses too like it does not support high data rates, had weaker digital signal, and many more security issues.

Thus, major advancements described in [8] that came was because of 3rd Gen Systems that played a major role in raising the living standard of mobile System

that involved faster data rates, supports multimedia applications such as video and photography. Value-added services like GPS, video call and video conferencing, and high-speed mobile Internet access. But due to expensive hardware cost, requirement of 3G compatible handsets, high power consumption, and the major problem of "Fake Station Problem," a new proposal was very much required that leads service provider to switch to another need of generation, i.e., "4G." It is still the most successful and smooth generation of mobile system as it provides various features like: high voice quality, streaming media, video calling, very low latency, strongest security, and IP based. Abdrabou et al. [9] discusses 4G in a very manageable way. But still due to the fast growth of advancements and modern lifestyle, the aim is to be smarter and smarter, and it was not enough as due to development of more secure algorithms, hackers are also becoming more smarter day by day. So there are lots of things that are needed to be updated like the major vulnerabilities found in [9–11] are: No End-to-End Security, Mobility Management (signals in bullet trains), and Fake Station Problem still exist in this generation too. Finally, the proposed solution for these shortcomings was reflected in [12], and it gave some key points about increasing performance for fifth generation of mobile system. Key features are: IP based, very low latency, mobility management, simpler hardware, jamming solutions, and MITM attack solutions.

But still some major problems or to be precise, major vulnerabilities still exist. Attackers with a transceiver can be able to hinder wireless transmission, insert unwanted messages, or jam messages of high importance.

Major vulnerabilities/challenges in any mobile communication system:

- **Jamming**: a signal that introduces interference into a communication channel blocking the incoming and outgoing flow between mobile station and base station.
- **IMSI Catching**: Initially, whenever UE attaches for the first time/resynchronization, it sends the IMSI to MME in clear text that can be captured by attacker.
- **Mobility Management**: When the call connection is in progress while the mobile is moving, the network has to follow the mobile users and allocate enough resource to provide continuing service without user's awareness.

The first challenge is jamming which involves destructive interference of signals in order to jam the mobile radio signals. Here, a particular range of frequency is distorted to block the radio waves of mobile station, thereby jamming the incoming as well as outgoing signals. Generally, we can use techniques like FHSS (frequency hopping spread spectrum) and DSSS (direct sequence spread spectrum) where the frequency is constantly changed after an interval of time, and in former technique, we amplify the frequency with reference to a seed value. In this way, intruder will be unable to track the operating frequency, and thus, we can prevent it. But it requires usage of high-frequency band (Fig. 4).

The major vulnerability which we will be discussing here is of IMSI catching, which compromises user's authenticity as well as confidentiality. Initially whenever UE attaches for the first time, it sends the IMSI to MME in clear text which is sent from MME to eNodeBs and from eNodeBs to UEs. An attacker can request

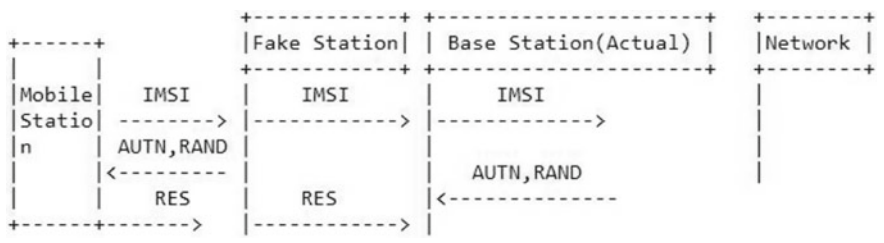

Fig. 4 IMSI catching (IMSI sent in plaintext for first attachment)

without awareness of the user by using various social engineering tools and then trace messages between eNodeB and UE to decode them and fetch the IMSI. There is also another fault that occurs whenever resynchronization occurs at the time of handover because at that time also, IMSI is sent in plaintext that can easily be sniffed by attacker. If at any time synchronization fails, then at that time too, it becomes an opportunity for an intruder to trace the necessary details.

Clearly, here an intruder, after using any social engineering tool, may be using a fake base station like SDR (software-defined radios), or Airprobe can make UE to connect to itself and then that fake station will pretend to be the actual mobile station for the subsequent station or for the core network.

Another challenge is of handling mobility of UE. In this fast-growing world, transportation means are also working over various needs like speed, etc. Due to fast running vehicles, it will be quite challenging to maintain the quality of service (QoS), meaning that switching of networks so as to let the service continue without any distortion.

5 Proposed Methodology

There can be two methods to achieve protection against the attack regarding IMSI catching:

- "Public key cryptography" can be used in order to encrypt IMSI to reduce the problem of IMSI catching and that particular algorithm which has been used to encrypt various details can be confidential only to the UE and gNodeB (mobile station for 5G).
- Every time a mobile SIM try to connect to base station, it can use a temporary name (pseudonym) of IMSI that will be updated in both the station (home server as well as mobile SIM), and there will be checking for all updation that will lead to provide both authenticity and confidentiality. So each time, user will get the new updated IMSI and will be identified by this identity only.

Although updating every time, that pseudonym will cost more effort in managing all the stuffs. So, we have proposed architecture for ensuring security which is shown below:

Here as shown in Fig. 5, sender and receiver can be considered as that of mobile station and base station or vice versa. We are assuming that the keys corresponding to each UE and the base station are already stored in databases. Now whatever the message sender is sending will be encrypted by applying an algorithm using keys and will be sent by appending it with its MAC (message authentication code, i.e., a digest or one-way hash value of message that is unique for a particular message).

Since digest or MAC [13] of a particular message is unique for a particular message, thus, if anyone tries to change the message, its MAC will also be changed. Thus, we are appending it to ensure the integrity of data so that data tampering can also be traced. After this, we have used another encryption using key 2 and generated cipher 2 which will be transferred to the channel which will be decoded at the receiving end using reverse process and after separating the two, that is, cipher and MAC, we can again generate this message (with XMAC) and check for the integrity of it by

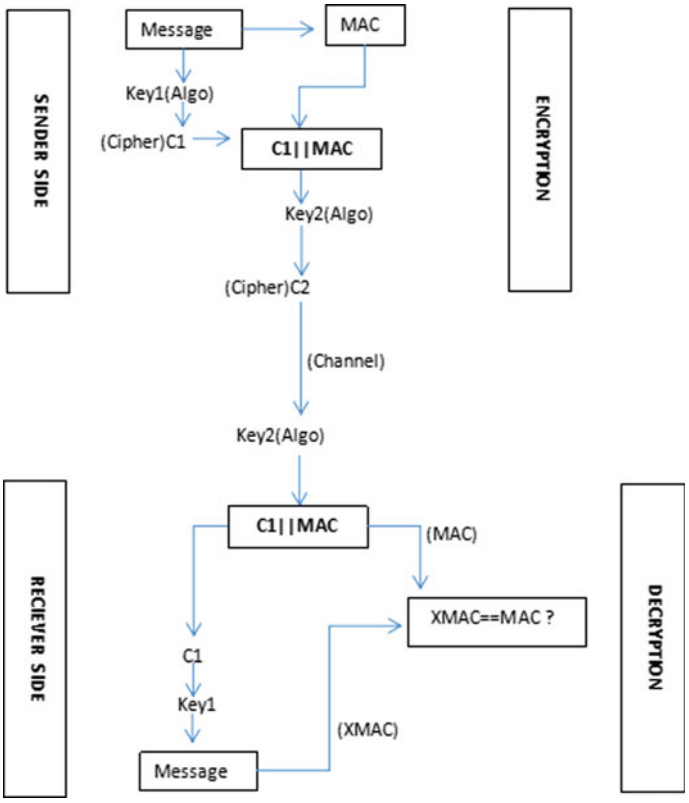

Fig. 5 Proposed architecture to overcome security issues

Table 1 Proposed analysis of algorithm

Algorithm	Size of data (MB) and corresponding time (s)						
Size	0.13	0.65	1.30	2.61	5.23	10.4	20.9
AES	0.14	0.41	0.73	1.45	3.10	7.59	22.70
DES	0.16	0.48	0.88	2.01	3.62	7.35	16.28
Blowfish	0.14	0.40	0.70	1.58	3.18	6.17	12.37
RC4	0.11	0.45	0.83	1.66	4.75	6.76	14.9
Twofish	0.10	0.28	0.51	1.39	2.86	5.32	13.27

comparing it with the previous one. In this way, authenticity and integrity of data are ensured. IMSI can also be secured using this method. Using this approach, confidentiality, integrity, and authenticity are achieved. Now it will be less efficient if we use weaker encryption algorithm, so it is very much required that the algorithm used to encrypt the data should be very much stronger to break it. But another challenge is of time an encryption algorithm takes to encrypt or decrypt the data. Because a stronger algorithm will take more time, thus will increase the latency. So an attempt has been made to find the middle point of that trade-off between the time of encryption and the level of security an algorithm provides. In this way, security as well as reduced latency can be achieved.

6 Results

According to the proposed solution given here, various algorithms have been implemented to test various parameters over this architecture. In Fig. 5, different algorithms can be substituted at the place of variable "Algo." Then, time spent in encryption and decryptions of an algorithm are compared with various algorithms used here (Table 1).

All algorithms are coded in Python and ran on Intel Core i7 @3.4 GHz processor under Windows 8.1. It can be verified from the graph in Fig. 6 that Blowfish and Twofish have the best performance among others. And both of them are known to have better encryption (i.e., stronger against data attacks) than the other ones. Various factors that indirectly affect the results have not been taken into the consideration. These readings are taken by keeping link delay/capacity and other factors constant.

7 Conclusion

Protocols used in all the mobile generations were not capable of fulfilling various demands of security like integrity, confidentiality, etc. due to disclosure of important identities like IMSI and various entities. Because of these vulnerabilities, an

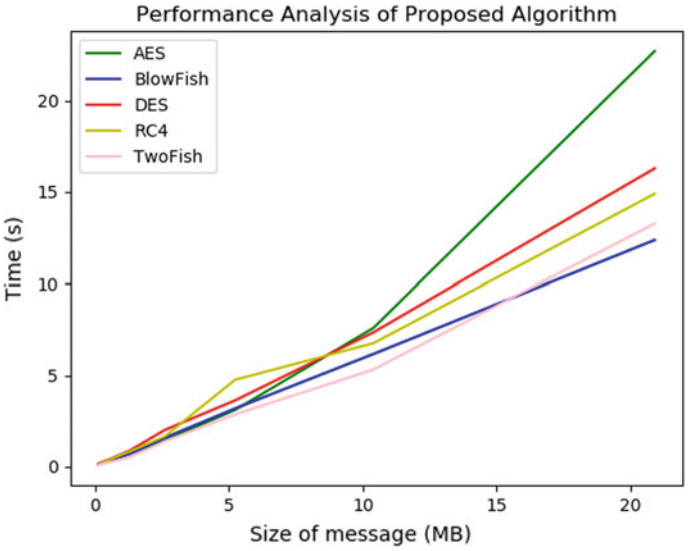

Fig. 6 Comparison results of various algorithms

attempt is made to create authentication mechanism to overcome weaknesses. The method proposed is more efficient. Analysis is done using CrypTool and Simulation using Python programming language. According to results, it can be concluded that Blowfish is better than other ones. It is efficient algorithm in terms of encrypting time and strength of security. Thus, the issue for IMSI catching can easily be solved using symmetric key cryptography. Hopefully, this will contribute to solve integrity, confidentiality, etc. issues in near future.

References

1. Vora LJ (2015) Evolution of mobile generation technology: 1G to 5G and review of upcoming wireless technology 5G. Int J Mod Trends Eng Res 2(10):281–290
2. Behrad S, Bertin E, Crespi N (2018) Securing authentication for mobile networks, a survey on 4G issues and 5G answers. In: 2018 21st conference on innovation in clouds, internet and networks and workshops (ICIN), pp 1–8
3. GPP (2017) Network architecture. TS 23.002, Tech. Spec. 14.1.0
4. Purkhiabani M et al (2011) Enhanced authentication and key agreement procedure of next generation evolved mobile networks. IEEE J
5. Alliance N (2015) 5G white paper. Next Gener Mob Netw Whitepaper
6. Nitesh GS, Kakkar A (2016) Generations of mobile communication. Int J Adv Res Comput Sci Softw Eng 6(3)
7. Barkan E, Biham E, Keller N (2003) Instant ciphertext-only cryptanalysis of GSM encrypted communication. In: Annual international cryptology conference, Springer, Heidelberg, pp 600–616

8. General Report on the Design and Evaluation of 3GPP Standard Confidentiality and Integrity Algorithms (3G TR 33.908 version 3.0.0 Release 1999)
9. Abdrabou MA, Elbayoumy ADE, El-Wanis EA (2015) LTE authentication protocol (EPS-AKA) weaknesses solution. In: 2015 IEEE seventh international conference on intelligent computing and information systems (ICICIS), pp 434–441
10. GPP (2017) Security architecture. TS 33.401, Tech. Spec. 15.1.0
11. Bikos AN, Sklavos N LTE/SAE security Issues on 4G wireless networks. IEEE Secur Priv 11(2):55–62
12. Fang D, Qian Y, Hu RQ (2018) Security for 5G mobile wireless networks. IEEE Access 6:4850–4874
13. Ferguson N, Schneier B, Kohno T (2015) Message authentication codes. In: Cryptography engineering: design principles and practical applications, pp 89–98

Security in Wireless Sensor Network Using IPsec

Annu Dahiya, Naresh Kumar, Karan Verma, Ajay K. Sharma and Shashvat Sharma

Abstract As applications of the wireless sensor network (WSN) continuously increasing, the communications of wireless sensor technologies have become the most emerging fields of wireless communication technologies. When we use sensor networks in a remote environment, health monitoring, and machine automation, security of these networks will become the main concern. The main focus of this work is to make sensor networks secure by ensuring authentication, integrity, and confidentiality. The proposed approach used IPsec with sensor network protocols. In this work, IPsec has been used to provide security and integrity for the sensor network. IPsec, the protocol of the network layer, provides connectionless integrity, data origin authentication, protection against replay attacks, and confidentiality. In this chapter, some changes will be made in the IPsec protocol suite for using it with WSN.

Keywords IPsec (Internet Protocol Security) · SA (Security Association) · SAD (Security Association Database) · SPD (Security Policy Database) · ESP (Encapsulating Security Payload) · AH (Authentication Header)

1 Introduction

Wireless sensor networks usually interact with sensitive data or these networks may be deployed in unattended environments, so it is necessary to ensure these networks' security [1]. Research work is based mostly on the security of the wireless network. This research work aims to develop a system which ensures an end-to-end security and also ensures source and destination authentication. When data is transmitted between sensor nodes, an attacker can spoof data or attackers capture the legitimate

A. Dahiya (✉) · N. Kumar · K. Verma · S. Sharma
NIT Delhi, Delhi, India

K. Verma
e-mail: karanverma@nitdelhi.ac.in

A. K. Sharma
NIT Jalandhar, Jalandhar, India

V. Janyani et al. (eds.), *Optical and Wireless Technologies*, Lecture Notes in Electrical Engineering 648, https://doi.org/10.1007/978-981-15-2926-9_21

nodes and replace them with the vulnerable nodes. The proposed approach provides a secure tunnel between the sender and the receiver through which data will be transmitted securely. The tunnel also provides security for data spoofing and vulnerable node attack.

In this chapter, we use the IP datagram security protocol IPsec. Protocols in IPsec suite interact with one another to maintain secure private communications across networks. IPsec is a protocol of network layer [2]. The network layer is the lowest layer of the layered architecture which provides the end-to-end security [1]. Network layer also provides security for the data of the upper layers. IPsec protocol suite consists of many protocols [2]. The protocols in the IPsec suite are Authentication Header (AH), Encapsulating Security Payload (ESP), Internet Security Association and Key Management Protocol (ISAKMP), and Internet Key Exchange (IKE) [3]. ESP provides confidentiality, authentication, and integrity. And AH provides authentication and integrity. ISAKMP sets up Security Association (SA) automatically and maintains cryptographic keys. IKE is a protocol which is used for exchanging security keys; it is not necessary that we can use IKE within IPsec. Recently, two versions of IKE are present—IKEv1 and IKEv2—in research work, we are considering IKEv2. The main difference between IKEv1 and IKEv2 is that two exchange modes—main mode and aggressive mode—are used in IKEv1 and in IKEv2; we have only one exchange mode. The implementation requires little modification in used protocols for working efficiently within WSN. We will use sensor network protocols with IPsec.

The remaining work is as follows: Section 2 is related work, and it gives the main objective of our work. Section 3 provides an overview of IPsec protocol. Section 4 provides comparative study between various protocols. Section 5 is result section. Section 6 will be dedicated to the conclusion.

2 Related Work

In [3], the author discussed various security flaws in a wireless sensor network. The author discussed the attacks on various layers of the network like application layer, transport layer, network layer, and data link layer and also discussed the security requirement. Security requirements in the network are confidential, the integrity of data, authentication of the node, authentication of broadcast, freshness, etc.

In [4] also, the author discussed various security threats. Only attacks on the network layer and data link layer were discussed, whereas other layer attacks were not discussed. Some of the attacks like Sybil attack, wormhole attack, selective forwarding, etc., were discussed, and we also got to know about the problem created by these attacks. And for preventing these attacks, some of the security protocols like SPINS, LEAP, and TinySec were explained by the author.

In [5], the author proposed a secure key management scheme. In the proposed scheme, author used elliptic curve cryptography and Diffie–Hellman algorithm.

The proposed scheme used hierarchical WSN architecture. And at last, author analyzes security provided by the proposed approach with three main issues of secure communication—these are confidentiality, integrity, and authentication.

In [6], the author did an extensive survey on security protocols of WSN and discussed various aspects of protocols. At last, we got to know about the services provided by these protocols. But it is not clear with the survey which protocol is better than others like on the basis of energy which one is good and on the basis of security which one is most secured protocol.

In [1], the author proposed a new approach to enhancing the security of IPsec. IPsec provides security to the IP packet. So the author proposed a new secure key exchange mechanism. The key exchange mechanism is based on Diffie–Hellman protocol. The main benefit from this work is one phase and optimize transmission time.

In [7], the author discussed the implementation of the Minisec on Telos platform. TinySec and Zigbee are link layer protocols. But the limitation with Zigbee and TinySec is that Zigbee provides high-level security while the energy consumption is also high, and TinySec offers lower energy consumption while the level of security provided by this is low. The author implemented Minisec which is a network layer protocol, and Minisec offers high-level security with lower energy consumption.

3 IPsec Overview

As explained in Sect. 1, IPsec [13] is used for protecting IP datagram. IPsec is not a single protocol, but it is a suite of protocols which contain many protocols for ensuring end-to-end security.

3.1 Architecture Used

As shown in Fig. 1, IPsec protocols work as follows:

Firstly, sender will send its security association to receiver. And receiver replied back with own SA. IKE is used for maintaining SA. Then, phase two SA will be negotiated between sender and receiver. During phase two, general-purpose SA negotiated. After completion of both the phases, data transmission will take place. ESP [11, 12] and AH are used for integrity and confidentiality.

Protocols explanation:

- **ESP**: ESP is one of the protocols of the IPsec suite which is used for providing authentication, confidentiality, and integrity.
- **AH**: AH is also used by IPsec for integrity, but the main difference between AH and ESP is that confidentiality is not provided by AH. So for confidentiality, we have to use ESP.

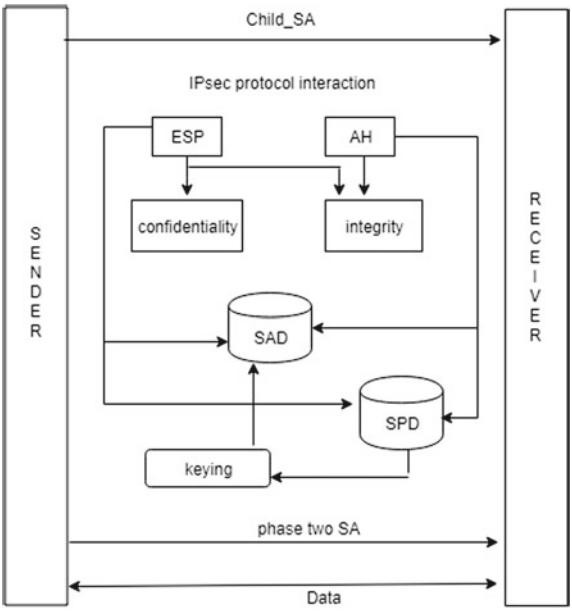

Fig. 1 Security Association and protocol interaction

- **SAD**: Security Association Database contains information about the protocol used like ESP or AH, the algorithm used for exchanging key like Diffie–Hellman, for encryption used RSA, source and destination addresses.
- **SPD**: Security Policy Database is used to store information about modes of the protocols and the lifetime of the Security Association.

3.2 IKEv2 Security Association Establishment

In this chapter, we used one of the IPSEC protocols, IKEv2. For ensuring end-to-end security, IKEv2 maintains Security Association (SA) between sender and receivers. Each sender and receiver exchanges six messages at the time of SA. They will exchange their keys, hashing algorithms, and encryption algorithms used. IKEv2 uses two databases Security Association Database (SAD) and the Security Policy Database (SPD). All the information about security association and security policies will be stored in these databases. For more information about IKEV2, read RFC 4306 (Fig. 2).

SPI (Security Parameter Index): We may have multiple sessions with a node. So to map the IKE packet with the correct IKE_SA, we use SPI.
Next payload: It contains the information about what we have after the header. It is some data or SA.

Fig. 2 IKE header format [10]

IKE_SA sender SPI				
IKE_SA receiver SPI				
Next Payload	Major Version	Minor Version	Exchange Type	Flags
Message ID				
Length				

Exchange type: It indicates that what we are exchanging. Either it is IKE_AUTH or IKE_SA_SENDER or IKE_SA_RECEIVER.
Flags: Flag bits are used to indicate specific options for a message. Some of these bits are X, V, and R.
'X': Sender sets that bit to 0 and receiver ignores it when sending the message.
'V': This bit clears during sending and ignored at the time of the incoming message.
'R': When a message in a response to some previous message, then this bit is set and ignored in the request message.

3.3 IKEv2 Architecture

IKEv2 works in two phases:

1. Phase one
2. Phase two (Fig. 3).

1. **Phase One**

In phase one, the two IKE peers sender and receiver establish a secure and authenticated channel between each other with which they will be communicated further. For establishing a secure tunnel, some information will be exchanged between peers, and this is called the IKE Security Association (SA).
Algorithm SA establishment

Fig. 3 IKEv2 architecture [10]

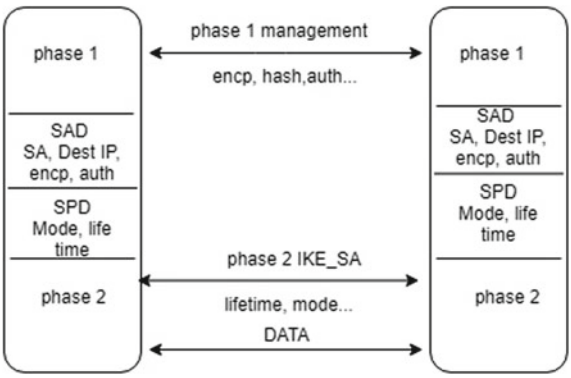

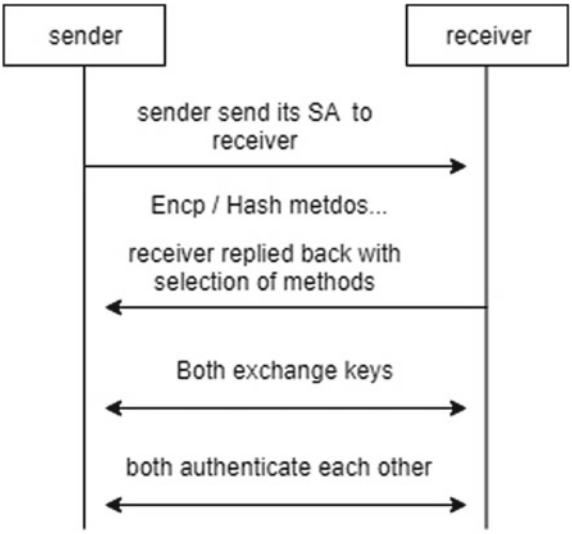

Fig. 4 IKE phase one message flow [8, 9]

Step 1: SENDER → IKE_SA_SENDER (sender sends own SA to receiver) [SA comprised of information like RSA, DES, AES, Diffie–Hellman, MAC, MODES]
Step 2: RECEIVER → IKE_SA_RECEI. (receiver replied back to sender) [selection of methods from sender SA like RSA, Diffie–Hellman, aggressive mode, MAC]
Step 3: After exchanging Security Association between sender and receiver, all the information will be stored in SAD and SPD.
IKE_SA → SAD, SPD.
Step 4: Keys exchanged and peers authenticated now nodes are ready for data exchange (Fig. 4).

2. **Phase Two**

The phase two request or response pair transmits identities IKE_AUTH, proves confidentiality corresponding to the two identities, and sets up an SA for the first IKE_SA which was established during phase one (Fig. 5).

4 Comparison of Security Protocols of Wireless Sensor Network (WSN)

In order to choose the appropriate security protocol for sensor network, this section gives a comparative study between the different security protocols that can be used. Because sensor nodes have limited resources like low processing power, small memory, and limited battery life, our aim is to find wireless sensor network protocol which would help us to provide authentication encryption, integrity, and also compatibility with resource constraints sensor nodes. From all the security protocols,

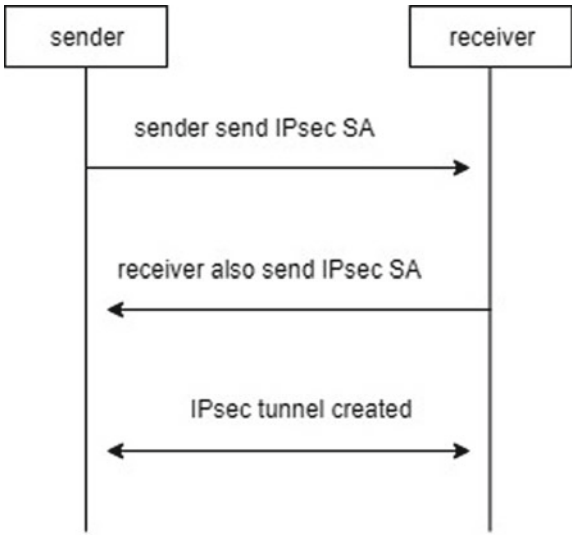

Fig. 5 IKE phase two exchange [8, 9]

we will choose security protocol based upon two criteria. The first criterion is the energy consumption, and the second criterion is the security. The security protocols for sensor network are LEAP, SPINS, Minisec, and TinySec. The author of [6, 2] compares all these security protocols and come to a solution that Minisec is better among all these protocols in terms of energy consumption and security.
Some of these protocols are:

LEAP (Localized Encryption and Authentication Protocol): It is a key management protocol which supports secure communication. It also provides authentication and confidentiality.
SPINS (Security Protocol for Sensor Network): The Encryption mode used by SPINS is counter mode (CTR). It works with two protocols:

(1) SNEP
(2) μTESLA

SNEP provides data authentication, confidentiality, and data freshness.
μTESLA provides authenticated broadcast.
TinySec: The services provided by TinySec is also similar to SPINS, but the main difference between TinySec and SPINS is that counter is not used by TinySec. For encrypting data, TinySec uses Cipher Book Chaining (CBC).
Minisec: It is also a security protocol. But the energy requirement of Minisec is much lesser than TinySec, and the security provided by Minisec is high. Minisec uses offset codebook (OCB) mode for data encryption (Table 1).

Table 1 Protocols' comparison [2, 6]

Protocol	Encryption	Freshness	MAC used	Key agreement	Overhead
LEAP	Yes	No	Yes	Pre-deployed variable	Variable
TinySec	Yes	No	Yes	Any	4 byte
Minisec	Yes	Yes	Yes	Any	4 + 3 byte
SPINS	Yes	Yes	Yes	Symmetric delayed	8 byte

5 Variation in Protocol

IPsec protocol suite comprises ISAKMP (IKE), AH, and ESP for security association, confidentiality, integrity, and authentication. Instead of using ESP and AH in sensor network, we will use sensor network security protocols because sensor network security protocols can also provide authentication, integrity, freshness, MAC, and confidentiality. Sensor nodes are very small, and processing power and battery power are not present in a huge amount in these nodes. So sensor nodes cannot withstand heavy algorithms.

6 Results

In this subsection, we evaluate the performances of our security protocols with regard to the security and energy consumption. We compare the results to find more secure and energy-efficient protocols for providing security in sensor network.

Figure 6 shows the energy consumption of various security protocols. We analyzed energy consumption of security protocols. From the analysis, we got to know that energy consumption of Minisec is lowest and energy consumption of LEAP is highest.

Figure 7 shows encryption mode comparison between time and message size. In Sect. 6, encryption mode used by protocols is explained. Minisec uses OCB mode, and the time required for OCB encryption is lesser than other encryption modes.

7 Conclusion

The main issues associated with security are ensuring confidentiality, integrity, and authenticity. This chapter's aim is to solve these issues in sensor network by using IPsec. In this work, we used IPsec with sensor network protocols and solved the issues of confidentiality, integrity, and authentication. In result section, we analyzed energy consumption and security provided by various protocols. From the analysis, it can be concluded that Minisec is better than other protocols in terms of security

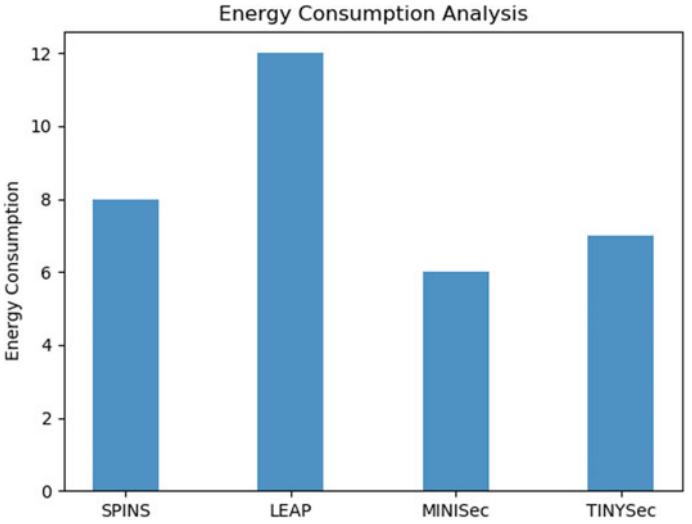

Fig. 6 Energy consumption analysis

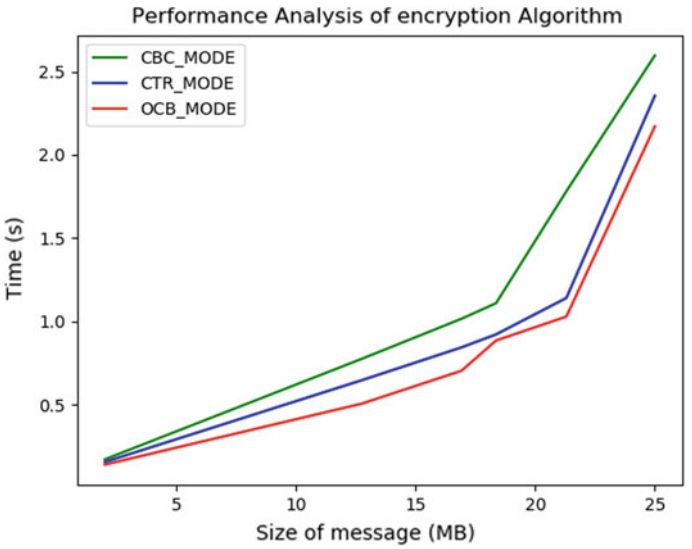

Fig. 7 Encryption modes

and energy consumption. By using Minisec with our proposed scheme, we can easily solve the issues of confidentiality and authentication.

References

1. Marwa A, Malika B, Nacira G (2013) Contribution to enhance IPSec security by a safe and efficient internet key exchange protocol. In: 2013 world congress on computer and information technology (WCCIT)
2. Bhalla M, Pandey N, Kumar B (2015) Security protocols for wireless sensor networks. In: 2015 international conference on green computing and internet of things (ICGCIoT)
3. Yi L, Zhongyong F (2015) The research of security threat and corresponding defense strategy for wsn. In: 2015 seventh international conference on measuring technology and mechatronics automation (ICMTMA)
4. Karakaya A, Akleylek S (2018) A survey on security threats and authentication approaches in wireless sensor networks. In: 2018 6th international symposium on digital forensic and security (ISDFS)
5. Hayouni H, Hamdi M (2015) Energy efficient key management scheme for clustered hierarchical wireless sensor networks. In: 2015 IEEE 12th international conference on networking, sensing and control (ICNSC)
6. Boyle D, Newe T (2007) Security protocols for use with wireless sensor networks: a survey of security architectures. In: 2007 third international conference on wireless and mobile communications ICWMC'07
7. Luk M et al (2007) MiniSec: a secure sensor network communication architecture. In: 2007. 6th international symposium on information processing in sensor networks, IPSN
8. Haddad H, Berenjkoub M, Gazor S (2004) A proposed protocol for internet key exchange (IKE). In: Canadian conference on electrical and computer engineering, 2004, vol 4
9. Kaufman C (2005) Internet key exchange (IKE V2) protocol. RFC 4306 IETF
10. Kasraoui M, Cabani A, Chafouk H (2014) IKEv2 authentication exchange model in NS-2. In: 2014 international symposium on computer, consumer and control (IS3C)
11. Atkinson R (1995) RFC1827-IP encapsulating security payload (ESP)
12. http://www.ietf.org/rfc/rfc1827.txt
13. Doraswamy N, Harkins D (1999) IPsec—the new security standard for the internet, intranets, and virtual private networks. Prentice Hall Inc, Upper Saddle River, NJ

Analysis of Microstrip Patch Antenna with Multiple Parasitic Patches and Shorting Vias for Bandwidth Enhancement

Venkata A. P. Chavali, Aarti G. Ambekar, Chinmay Kudoo, Mansi Shah, Amit A. Deshmukh and K. P. Ray

Abstract Analysis of a microstrip patch antenna with multiple parasitic patches and shorting vias for bandwidth enhancement is carried out in order to identify modes on the fed triangular patch and parasitic patches to put forth a clear explanation about the same. Fed and parasitic patches are simulated individually, and then, combined structure is studied and mode identification is done by comparing overall modal frequencies with that of the frequencies of individual patches. Also, modified configuration of shorted antenna is proposed which resulted in a simulated bandwidth of 1056 MHz and measured bandwidth of 1130 MHz.

Keywords Multiple parasitic patches · Shorting vias · Bandwidth enhancement · Microstrip patch antenna · Trapezoidal patch

1 Introduction

Microstrip antennas (MSA) are popular due to their low profile, lightweight and compatible nature. However, conventional microstrip antennas suffer from drawbacks such as narrow bandwidth and less gain. Several methods have been reported to enhance the bandwidth of MSAs such as increasing substrate thickness in which surface wave propagation is observed [1], lowering the dielectric constant using suspended dielectric configurations, using slot cut techniques in which a resonant slot is cut on the MSA which optimizes the spacing between fundamental mode and

V. A. P. Chavali · A. G. Ambekar · C. Kudoo (✉) · M. Shah · A. A. Deshmukh
Department of EXTC, SVKM's DJSCE, UOM, Vile–Parle, Mumbai, India

V. A. P. Chavali
e-mail: venkata.chavali@djsce.ac.in

A. G. Ambekar
e-mail: aarti.ambekar@djsce.ac.in

A. A. Deshmukh
e-mail: amit.deshmukh@djsce.ac.in

K. P. Ray
Department of Electronics, DIAT, Pune, India

V. Janyani et al. (eds.), *Optical and Wireless Technologies*, Lecture Notes in Electrical Engineering 648, https://doi.org/10.1007/978-981-15-2926-9_22

higher-order modes of MSA enhancing its bandwidth [2–4] and using multi-layer configurations where parasitic patches are stacked above or below the fed patch to enhance the bandwidth of MSA, but the overall height of the antenna is increased [5]. One more prominent technique to realize wider bandwidth is using gap-coupled techniques where parasitic patches are placed close to the fed patch on the same layer as that of the fed patch, and by optimizing the space between fed and parasitic patches, bandwidth can be increased [6–9]. For example, a gap-coupled sectoral MSA has been reported in [9], enhancing its bandwidth from 1.6 to 12.3% by optimizing the space between fed and parasitic sectoral patches. In addition to the above techniques, shorting posts can also be inserted in the MSA which enhances the impedance bandwidth of the antenna as shorting posts affect the impedance characteristics of the antennas, while simultaneously making the antenna compact as shorting achieves same resonant frequency with reduced antenna size [10, 11]. In [10], a triangular patch with V-shaped slot and shorting posts is reported, where bandwidth enhancement is achieved using shorting posts. In [11], two variations of an equicrural triangular patch with multiple parasitic patches are reported. In the first antenna, wider bandwidth (13.8%) is due to the addition of a trapezoidal patch and two triangular patches, and in the second antenna, the bandwidth enhancement (17.4%) is achieved by inserting two shorting posts symmetrically in the trapezoidal patch of the first antenna where feed position is modified. The mathematical expressions for resonant frequencies of the fed and parasitic patches also have been provided. However, the clear explanation about the modes of the triangular patches and modified modes of the trapezoidal patch after inserting the shorting posts is not mentioned in the reported paper. To put forth a clear explanation about the same, analysis of the reported microstrip patch antenna with multiple parasitic patches and shorting vias for bandwidth enhancement is carried out. Further, a modified configuration of the same antenna with enhanced bandwidth has been proposed and experimentally verified by fabricating the patch. A close agreement between simulated and measured values is observed.

2 Reported Microstrip Patch Antenna with Multiple Parasitic Patches and Shorting Vias for Bandwidth Enhancement

Reported microstrip patch antenna with multiple parasitic patches and shorting vias for bandwidth enhancement is as shown in Fig. 1a. However, the dotted non-truncated portion represents antenna 1 with $\theta = 71°$, truncated antenna structure is antenna 2 with $\theta = 47°$, and antenna 2 with shorting vias is considered as antenna 3.

The common parameters of antenna 1, antenna 2 and antenna 3 are $h = 1.6$ mm, $\varepsilon_r = 4.4$, feed radius $r = 0.65$ mm, $L = 36$ mm, $W = 39$ mm, $L_1 = 18.8$ mm, $W_1 = 1.2$ mm and $W_2 = 0.6$ mm. For antennas 1 and 2, feed position is considered at $(-1.3, 0)$, whereas for antenna 3 feed position is at $(-0.8, 0)$. The truncation length $L_5 = 5.4$ mm.

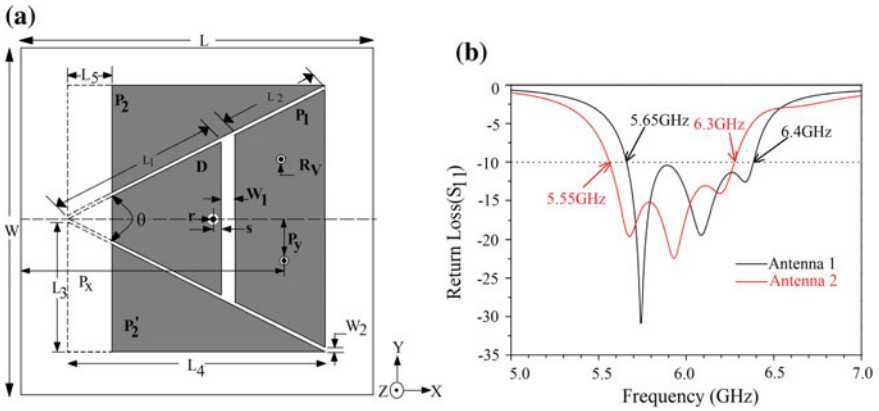

Fig. 1 **a** Geometry of reported antenna; **b** return loss plots of antennas 1 and 2 [11]

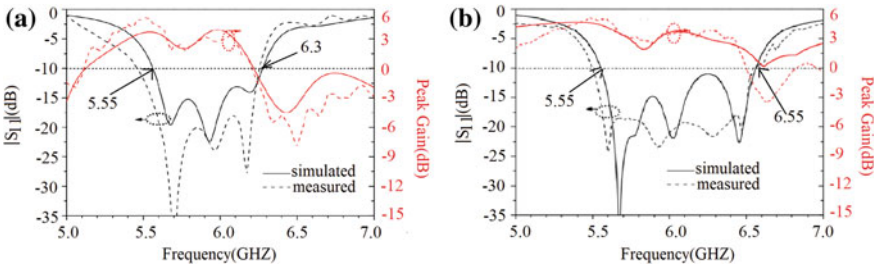

Fig. 2 **a** Return loss plot and peak gain plot of antenna 2; **b** return loss plot and peak gain plot of antenna 3 [11]

The return loss (S_{11}) plots of antennas 1 and 2 are shown in Fig. 1b, and Fig. 2a shows return loss and peak gain plots of antenna 3. From Fig. 1b, it is understood that to reduce the operating frequency, antenna 1 is truncated, and no significant difference in the bandwidth is observed between antennas 1 and 2 which is approximately 750 MHz. Also, it is reported that 3 resonances are observed in both the antennas corresponding to fed patch, parasitic trapezoidal and right-angled triangular patches. The bandwidth obtained after inserting shorting posts is approximately 1000 MHz as shown in Fig. 2b.

3 Analysis of MSA with Multiple Parasitic Patches

To understand the modal behavior of the antenna initially, all patches are simulated individually using IE3D software. The individual resonant frequencies are analogized with the frequencies of the peaks observed in the resonance frequency plot

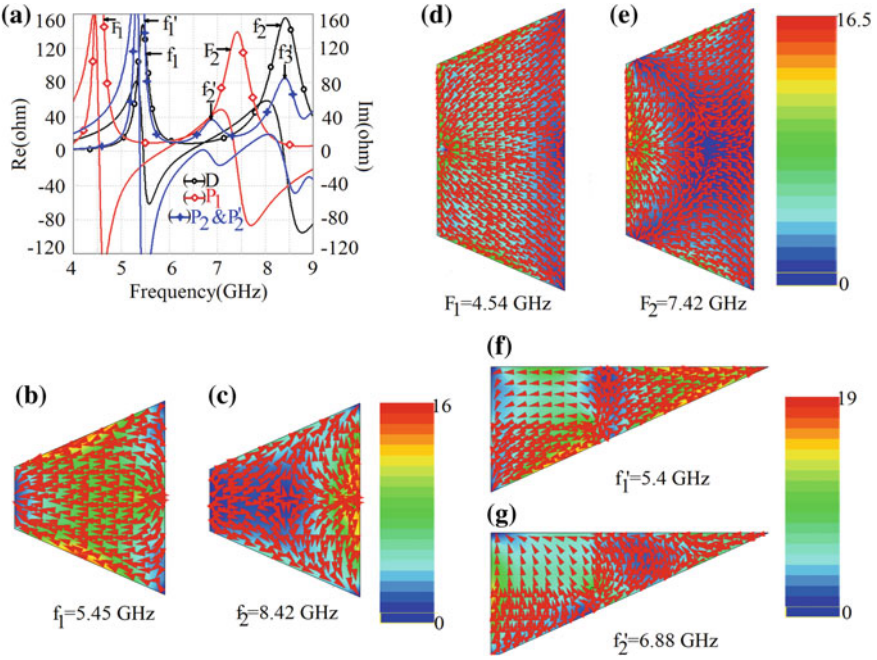

Fig. 3 **a** Resonance frequency plots of individual patches; **b–g** surface current distribution of individual patches

of combined structure, and by comparing the corresponding surface current distributions, the modes which are responsible for broadband behavior are identified. Figure 3 shows the resonance frequency plots and surface current distributions of individual patches at the frequency values observed in resonance frequency plots. The modes observed within the simulated frequency range are on truncated triangular patch TM_{10} at 5.45 GHz and TM_{12} at 8.42 GHz, on trapezoidal patch TM_{10} at 4.55 GHz and TM_{20} at 7.42 GHz and on right-angled triangular patches TM_{02} at 5.4 GHz and TM_{11} at 6.88 GHz. These modal frequencies are compared with that of the resonant peak frequencies and its corresponding surface current distributions obtained for the complete reported structure as shown in Fig. 4. The first peak of the complete structure corresponds to TM_{02} mode of parasitic right-angled triangular patch, and second peak corresponds to the TM_{02} mode of parasitic trapezoidal patch. The simulated result of return loss is shown in Fig. 4a. A bandwidth of about 11% is achieved, whereas reported bandwidth is 12.6% as shown in Fig. 2b for antenna 2. By comparing resonance modes and return loss plot in Fig. 4a, it is clear that the modes which are responsible for broader bandwidth are TM_{02} mode of parasitic right-angled triangular patch and TM_{02} mode of parasitic trapezoidal patch as their frequency values lie within the frequency range of return loss less than −10 dB.

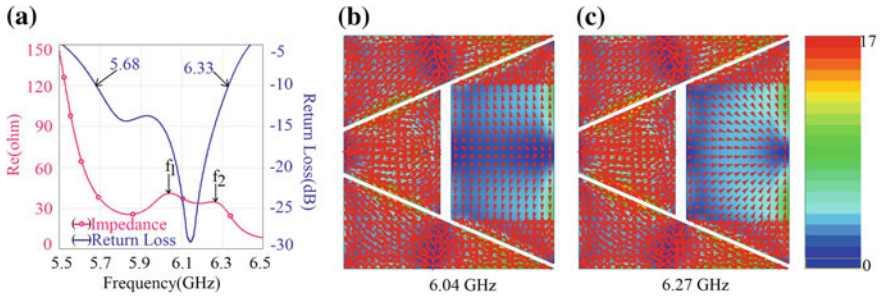

Fig. 4 **a** Resonance frequency plot and return loss plot of reported antenna without shorting posts; **b**, **c** surface current distributions of reported antenna at different frequencies

4 Analysis of MSA with Multiple Parasitic Patches and Shorting Vias

Microstrip antenna with multiple parasitic patches and shorting vias is also analyzed following the same procedure as mentioned in Sect. 3. The resonance frequency plots of individual patches are shown in Fig. 5a. The surface current distribution of trapezoidal patch (A_2) only is shown in Fig. 5b–d representing TM_{10}, $TM_{1/2,\,2}$ and $TM_{3/2,\,0}$ modes, respectively. The modes on the remaining patches (A_1-fed patch and A_3-right-angled triangular patch) observed to be same as that of the modes are identified in Sect. 3.

From Fig. 6, it is clear that the modes responsible for wider bandwidth in microstrip patch antenna with multiple parasitic patches and shorting vias are TM_{02} mode of parasitic right-angled triangular patch and TM_{10} mode of parasitic trapezoidal patch whose impedance is reduced and frequency is increased because of the shorting. A bandwidth of 544 MHz is noticed from return loss plot as shown in Fig. 6a.

Further, bandwidth is observed to be increased further by modifying the gap between the fed and trapezoidal parasitic patch to 0.5 mm and shorting probe radius

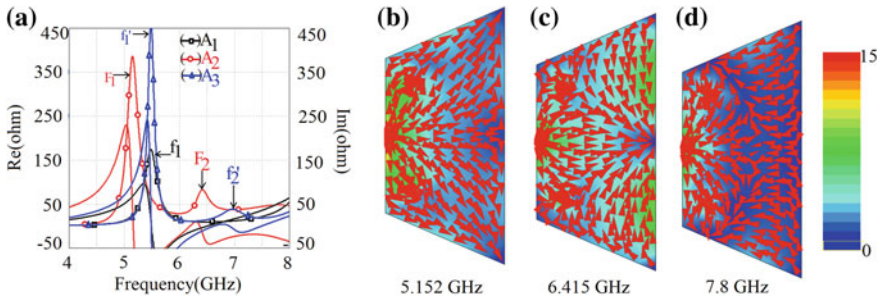

Fig. 5 **a** Resonance frequency plot of individual patches; **b–d** surface current distributions of shorted trapezoidal patch at different frequencies

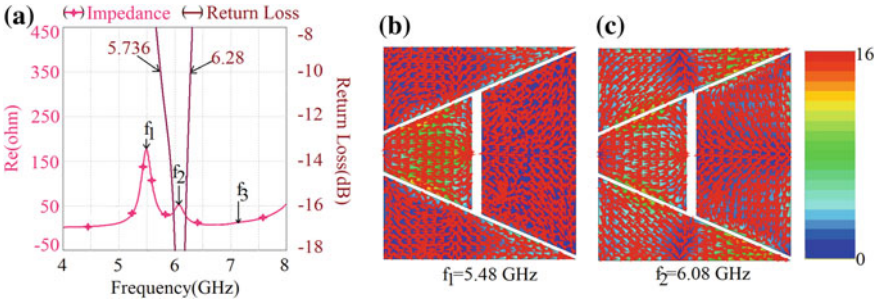

Fig. 6 **a** Resonance frequency and return loss plot of MPA with multiple parasitic patches and shorting vias; **b**, **c** surface current distributions

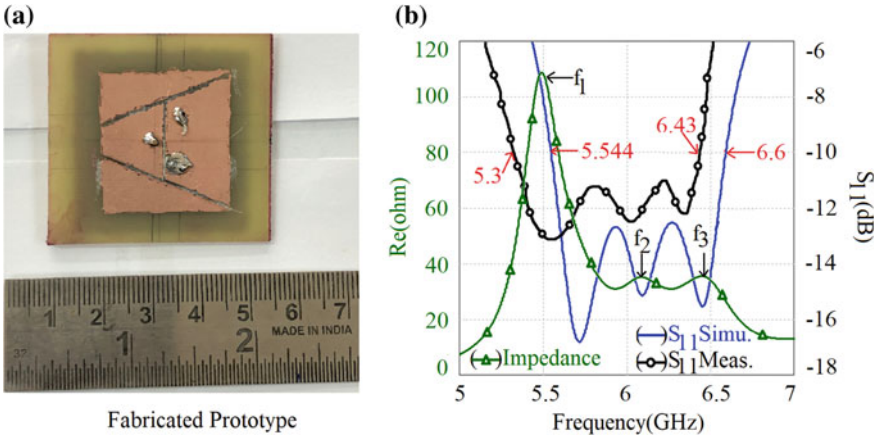

Fig. 7 **a** Fabricated prototype of proposed antenna; **b** resonance frequency and return loss plot

to 0.6 mm. Fabricated prototype of modified antenna, resonant frequency plot, simulated and measured return loss plots are shown in Fig. 7a, b. Resonant frequency shift toward lower range of frequency is observed. A simulated bandwidth of 1056 MHz and measured bandwidth of 1130 MHz are realized.

5 Conclusions

Analysis of a microstrip patch antenna with multiple parasitic patches and shorting vias is presented where modes responsible for wider bandwidth in un-shorted MPA and shorted MPA are explained in detail. A modified configuration is also proposed

by varying the spacing between fed and parasitic patches and shorting post radius. Simulated and experimental results are tallied by fabricating the patch where a close matching between simulated and measured results is observed.

References

1. Wong KL (2002) Compact and broadband microstrip antennas, 1st edn. Wiley, New York
2. Kumar G, Ray KP (2003) Broadband microstrip antennas, 1st edn. Artech House, USA
3. Weigand S, Huff GH, Pan KH, Bernhard JT (2003) Analysis and design of broad-band single-layer rectangular U-slot microstrip patch antennas. IEEE Trans Antennas Propag 51(3):457–468
4. Deshmukh AA, Ray KP (2017) Analysis and design of broadband U-slot cut rectangular microstrip antennas. Sādhanā. 42(10):1671–1684
5. Egashira S, Nishiyama E (1996) Stacked microstrip antenna with wide bandwidth and high gain. IEEE Trans Antennas Propag 44(11):1533–1534
6. Abraham J, Mathew T, Aanandan CK (2016) A novel proximity fed gap coupled microstrip patch array for wireless applications. Prog Electromagn Res 61:171–178
7. Deshmukh AA, Kamble P, Doshi A, Venkata APC (2018) Multi-resonator variations of 120° sectoral microstrip antennas for wider bandwidth. In: Proceedings of international conference on wireless communication, pp 169–175
8. Deshmukh AA, Pawar S (2018) Gap-coupled designs of compact F-shape microstrip antennas for wider bandwidth. In: Proceedings of international conference on wireless communication 2018, pp 85–93
9. Kandwal A, Khah SK (2013) A novel design of gap-coupled sectoral patch antenna. IEEE Antennas Wirel Propag Lett 12:674–677
10. Wong H, So KK, Gao X (2016) Bandwidth enhancement of a monopolar patch antenna with V-shaped slot for car-to-car and WLAN communications. IEEE Trans Veh Technol 65(3):1130–1136
11. Da Xu K, Xu H, Liu Y, Li J, Liu QH (2018) Microstrip patch antennas with multiple parasitic patches and shorting vias for bandwidth enhancement. IEEE Access 6:11624–11633

Multiband Response Investigation for Stub-Loaded Right-Angled Isosceles Triangle Microstrip Antenna

Aarti G. Ambekar, Venkata A. P. Chavali, Chinmay Kudoo, M. Shah, Amit A. Deshmukh and K. P. Ray

Abstract Two multiband configurations, one using right-angled isosceles triangle patch included with stubs and another using semicircular patch embedded with a slot along with stubs fabricated on a thicker substrate of glass epoxy, were reported. The first configuration gave triple-band operation at 3.5 GHz, 2.45 GHz and 1.96 GHz with respective gains of 7.5, 7.9 and 5.8 dBi, while the second also gave triple-band operation at 5.5 GHz, 3.5 GHz and 2.45 GHz with respective gains of 1.8, 1.5 and 1.2 dBi. Conversely, an explanation of resonant modes that results in multiband operation was not given for any of the configurations. In this paper, a detailed investigation explaining the triple-band response of one of the reported works, right-angled isosceles triangle patch, is presented using resonance curve plots, return loss plots and its surface current distributions. It is observed that length variations of stubs integrated with patch antenna modify the various frequencies modes in such a way that yields multiband response. The position and dimensions of stubs with given feed result in matched input impedances at TM_{10}, TM_{21} and TM_{30} modes of the triangular patch those results into triple-band response.

A. G. Ambekar · V. A. P. Chavali · C. Kudoo · M. Shah (✉) · A. A. Deshmukh
Department of Electronics and Telecommunication, SVKM's DJ Sanghvi COE, UOM, Vile-Parle, Mumbai, India
e-mail: shahmansi385@gmail.com

A. G. Ambekar
e-mail: Aarti.Ambekar@djsce.ac.in

V. A. P. Chavali
e-mail: Venkata.Chavali@djsce.ac.in

C. Kudoo
e-mail: ckudoo4@gmail.com

A. A. Deshmukh
e-mail: Amit.Deshmukh@djsce.ac.in

K. P. Ray
Department of Electronics, DIAT, Pune, India
e-mail: kpray@rediffmail.com

V. Janyani et al. (eds.), *Optical and Wireless Technologies*, Lecture Notes in Electrical Engineering 648, https://doi.org/10.1007/978-981-15-2926-9_23

Keywords Right-angled isosceles triangle · Stubs · Multiband response · Microstrip · Higher-order modes

1 Introduction

Because of various advantages, microstrip antennas are preferably used nowadays in most of the wireless communication applications. Different shapes like rectangular, circular and triangular and their variations are used for various configurations of microstrip antennas [1–3]. For triangular microstrip antennas, resonance frequency equations can be derived by equating their area with either rectangular or circular microstrip antennas combinations [4, 5]. A single mobile handset is required to handle various applications like GSM, Bluetooth, WiFi, etc., which require different bands of frequencies. Hence, a multiband antenna is required in such type of applications. By embedding a slot or by connecting a stub at proper position, multiband response can be realized in a microstrip in various antennas [6–12]. In this paper, an intensive analysis of multiband response of reported right-angled isosceles triangle patch antenna (RAITMSA) loaded with a pair of stubs is presented using resonance curve, return loss plots and surface current distributions [13]. The present analysis explains about the effect of variations in stub lengths on various resonant modes like TM_{01}, TM_{10}, TM_{11}, TM_{21} and TM_{30} of RAITMSA. For verification of the same, reported antenna is simulated in IE3D and also fabricated and tested. The antenna measurements were carried, vector network analyzer (ZVH–8), spectrum analyzer (SMB 100A) and frequency generator (FSC 6), inside an antenna laboratory.

2 Stub-Loaded Right-Angled Isosceles Triangle Microstrip Antenna (RAITMSA) for Multiband Response

A right-angled isosceles triangle microstrip antenna connected with a pair of monopoles at the patch edges reported in [13] is as shown in Fig. 1a. The basic RAITMSA is fabricated on dielectric substrate of glass epoxy with relative permittivity of 4.4. Patch is separated by height of 1.586 mm from the main ground plane.

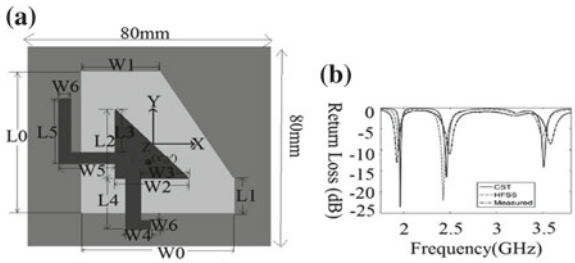

Fig. 1 **a** Geometry of RAITMSA loaded with stubs; **b** measured return loss plot for RAITMSA loaded with stubs [13]

Two monopoles are connected, respectively, at the edge of base and height of patch. For getting the compactness, these monopoles are slightly bent at their edges. Patch resonates at 3.5 GHz, monopole connected at bottom resonates at 2.45 GHz, the one connected to height resonates at 1.96 GHz, and the same can be revealed from return loss plot as shown in Fig. 1b. Main problem with the reported configuration is radiation direction of monopoles, and main patch is in opposite direction. So, the overall gain of antenna reduces. To overcome this, a reflected ground plane is added below the main ground plane separated by a height of 5 mm. So, just for increasing, the gain reflector ground plane is needed. Now, only with main ground plane, both the monopoles are partly in air without any backing ground plane. But with any backing ground plane, those finite or infinite monopoles can be treated as simply two stubs connected to the patch edges. Variations of length of these stubs are responsible for getting triple-band operation.

For reducing time required for simulation, the reported configuration is simulated on infinite ground plane using IE3D, and corresponding resonance curve plot is as shown in Fig. 2a. Three peaks are observed, respectively, at $f_1 = 1.28$ GHz, $f_2 = 2.19$ GHz and $f_3 = 3.24$ GHz corresponding to three bands. As the simulation is done on infinite, ground plane and stubs are coming out of ground plane which increases effective dielectric constant, and hence, corresponding frequencies reduce compared to the reported values [13]. The mode explanation at respective peaks is not given in reported work. For getting information of excited modes at three peaks, surface vector current distributions are observed as shown in Fig. 2b–d. From the surface current distribution, it is clear that lengths of stub affect the current path length and hence the frequencies of corresponding modes. However, detailed explanation of the same is not given in reported work [13]. Hence, a detailed investigation is done with respect to various slit dimensions of the reported antenna giving the explanation of its effect on modes those result into dual-band response. The same is explained in the next section.

3 Analysis of Stub-Loaded RAITMSA for Multiband Response

Analysis of actual reported structure in [13] is started with basic RAITMSA as shown in Fig. 3a. The configuration is simulated for different feed positions as 'A to D', and corresponding overlapped resonance curve is observed in Fig. 3b.

The feed position affects the excitations of number of modes and their impedances. The corresponding current distributions for one of the feed positions are as shown in Fig. 4a–c. A half-wavelength variation is observed along hypotenuse of patch that corresponds to TM_{01} mode while half-wavelength variation is observed along base and height of patch which corresponds to TM_{10} mode. For third peak, two half-wavelength variations are observed along height and base while one half-wavelength variation is observed along hypotenuse that corresponds to TM_{21} mode. Proper

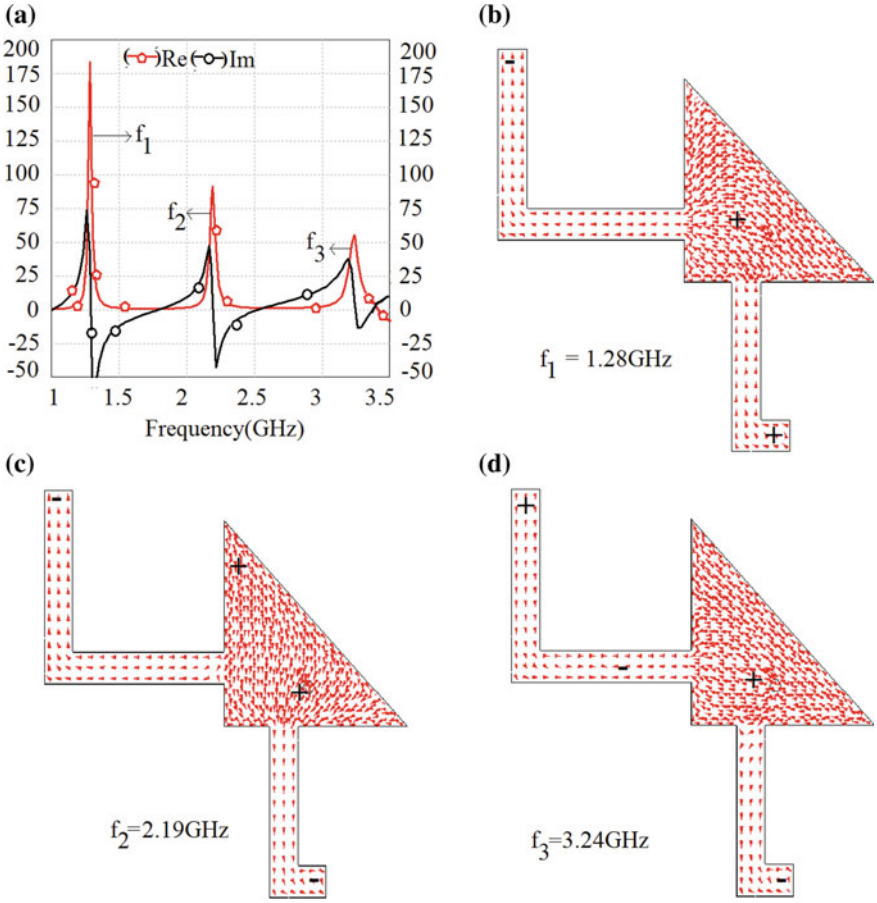

Fig. 2 **a** Simulated resonance curve; **b–d** simulated surface current distribution for stub-loaded RAITMSA

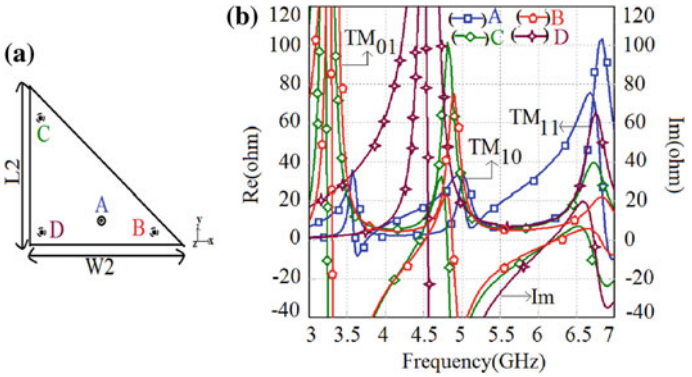

Fig. 3 **a** RAITMSA; **b** resonance plots for varying feed positions for RAITMSA

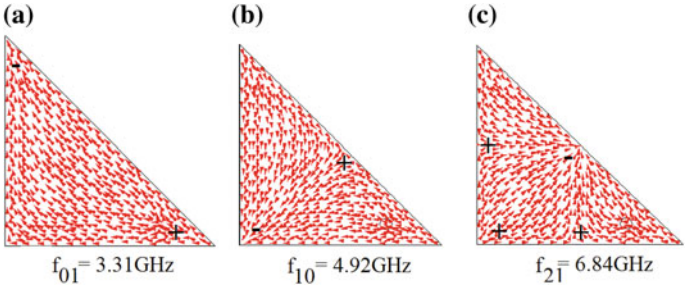

Fig. 4 **a–c** Surface current distributions at feed position 'B' for RAITMSA

impedance matching can be observed at feed position '*A*' which is optimized feed position. The overlapped resonance curves for different stub lengths 'SL' are as shown in Fig. 5a, b. Analogous to each peak, surface current distributions are also observed for each length variations. For one of the stub length variations, corresponding surface current distributions are as shown in Fig. 6a–d.

For only RAITMSA without stubs, only three resonant modes are observed, namely TM_{01}, TM_{10} and TM_{21}. On introduction of stubs at the edges, patch excitation

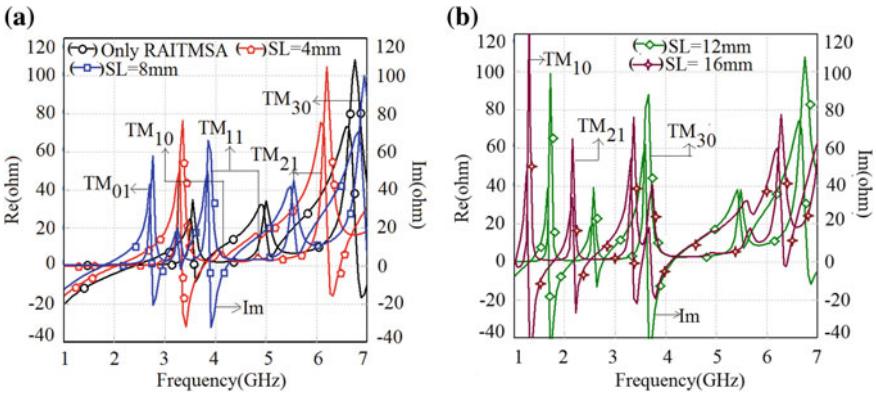

Fig. 5 **a**, **b** Resonance plots for stub length variations for stub-loaded RAITMSA (SL = stub length)

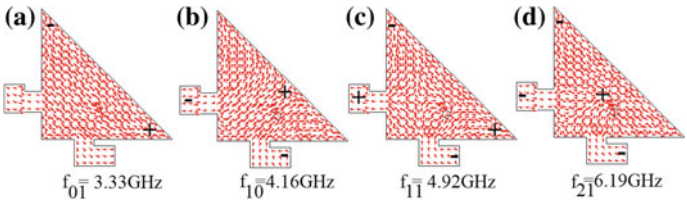

Fig. 6 **a–d** Surface current distribution at SL = 4 mm

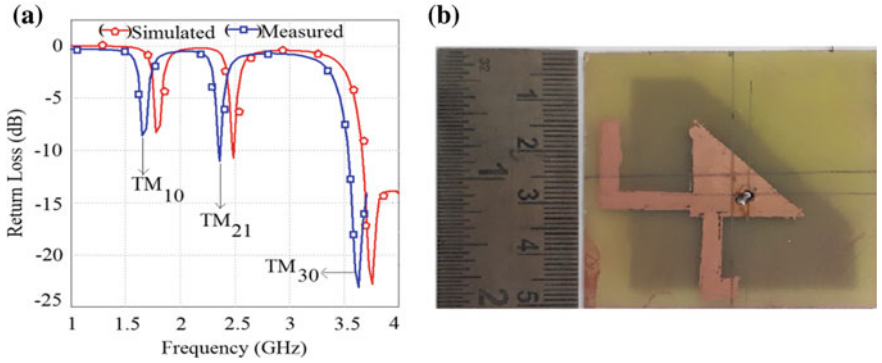

Fig. 7 **a** Return loss plot; **b** fabricated prototype for stub-loaded RAITMSA

of TM_{11} and TM_{30} modes is observed. As the length of stubs increases corresponding area of patch increases, ultimately current path length increases which reduces the corresponding mode frequency. Excitation of TM_{11} mode is not observed for stub length equal to 12 mm and 16 mm as corresponding patch length does not provide proper impedance matching for the respective mode. For the optimized configuration at stub length equal to 16 mm, corresponding to three bands mentioned in reported work [13], three resonant modes are observed, namely TM_{10}, TM_{21} and TM_{30}.

The same configuration is fabricated on glass epoxy substrate as per the given dimensions in [13]. The simulated as well as measured return loss plot and fabricated prototype are as shown in Fig. 7a, b. Variations in measured and simulated results are observed because of errors occurring during fabrication of the patch. As the patch is fabricated on glass epoxy, losses are more; hence, gain is less than 0 dB. Polarization of the given configuration is remaining linear as the difference between co-polar and cross-polar levels observed is less than 10 dB.

4 Conclusions

An extensive analysis of a stub-loaded right-angled isosceles triangle antenna loaded with a pair of stubs designed for triple-band operation is carried out in the present work. The exploration is carried out using simulated resonance curve and surface vector current distributions. Basic excited modes are TM_{10}, TM_{01}, TM_{11}, TM_{21} and TM_{30}. Integration of stubs affects the current path length and effective area of patch which reduces the corresponding mode frequencies and separates out them that yields multiband response. Same configuration is fabricated on glass epoxy, and return plots are verified. This type of study provides insight into functioning of antennas with stubs. This will also help in designing of similar types of antennas at different frequency ranges.

References

1. Wang KL, Yang KP (1997) Small dual frequency microstrip antenna with cross slot. Electron Lett 33(23):1916–1917
2. Bahal IJ, Bhatia B (1980) Microstrip antenna. 1st edn. Artec House
3. Kumar G, Ray KP (2003) Broadband microstrip antennas, 1st edn. Artech House, USA
4. Garg R, Long SA (1988) An improved formula for the resonant frequencies of the triangular microstrip patch antenna. IEEE Trans Antennas Propag 36(4):570
5. Ray KP, Kumar G (1999) Determination of the resonant frequency of microstrip antennas. Microw Opt Technol Lett 23(2):114–117
6. Deshmukh A, Ray KP (2009) Stub loaded multi-band slotted rectangular microstrip antennas. IET Microw Antennas Propag 3(3):529–535
7. Hu X, Li Y, Chen W, Tan H, Long Y (2013) Novel dual frequency microstrip antenna with narrow half-ring and half-circular patch. IEEE Antennas Wirel Propag Lett 12:3–6
8. Wong KL, Fang ST (1998) Reduced size circular microstrip antenna with dual-frequency operation. Microw Opt Technol Lett 18(1):54–56
9. Lu JH, Tang CL, Wong KL (2000) Novel dual frequency and broadband designs of slot loaded equilateral triangular microstrip antennas. IEEE Trans Antennas Propag 48(7):1048–1054
10. Chen J, Wang J, Tong KF, Armaghany A (2017) A dual band dual polarization slot patch antenna. In: International proceedings on IEEE international conference on computational electromagnetics (ICCEM), IEEE, Kumamoto Japan, pp 34–35
11. Deshmukh A, Mishra A, Shah F, Patil P, Ambekar A (2018) Variations of slot cut multi-band isosceles antennas for dual polarized response. Lecture notes on data engineering and communications technologies, vol 19. Springer, Singapore, pp 103–110
12. Deshmukh A, Ray K (2010) Resonant length formulations for dual band slot cut equilateral triangular microstrip antenna. Wirel Eng Technol 1(2):55–63
13. Jhamb K, Li L, Rambabu K (2011) Novel integrated patch antennas with multi-band characteristics. IET Microw Antennas Propag 5(12):1393–1398

Circularly Polarized Swastik Shape Microstrip Antenna

Amit A. Deshmukh, Chinmay Kudoo, M. Shah, A. Doshi and A. Mhatre

Abstract Novel design of Swastik shape patch antenna is proposed for realizing circular polarized response. Two pairs of orthogonal rectangular slots, which realize swastika shape configuration, yield tuning in between the TM_{01} and TM_{10} mode frequencies of equivalent square patch that along with modified TM_{11} mode yields impedance and axial ratio bandwidth of 565 MHz (47.18%) and 43 MHz (4%), respectively. Proposed antenna yields broadside gain of above 6 dBi over most of the impedance bandwidth with peak gain close to 7 dBi. Proposed configuration with given bandwidth and gain characteristics can find applications in mobile base station communication antennas as well as in personal communication systems.

Keywords Circular polarized microstrip antenna · Axial ratio bandwidth · Resonant mode tuning · Swastik shape patch

1 Introduction

In wireless communication systems, antenna forms an integral part of the design and it is used for signal trans-reception. In practical scenario, signal that arrives at receiver undergoes multiple paths and due to which as per the ray theory of electromagnetic propagation, it travels through the different path lengths [1]. Due to this phase and polarization of the signal arriving at the receiver antenna varies [1].

A. A. Deshmukh · C. Kudoo (✉) · M. Shah · A. Doshi · A. Mhatre
EXTC, SVKM's DJ Sanghvi COE, Vile–Parle, Mumbai, India
e-mail: ckudoo4@gmail.com

A. A. Deshmukh
e-mail: amitdeshmukh76@gmail.com

M. Shah
e-mail: shahmansi385@gmail.com

A. Doshi
e-mail: doshiakshay4192@gmail.com

A. Mhatre
e-mail: amhatre.89@gmail.com

V. Janyani et al. (eds.), *Optical and Wireless Technologies*, Lecture Notes in Electrical Engineering 648, https://doi.org/10.1007/978-981-15-2926-9_24

Here, the polarization of wave may not remain the same as that of the polarization of the radiating wave at the transmitter. Due to this varying polarization, circular polarized (CP) antennas are preferred at the receiver that minimizes the signal loss [2]. The CP response in antennas is obtained by using two radiators operating at nearly the same frequency and amplitude but with space and phase quadrature [2]. Microstrip antenna (MSA) offers a better low-cost solution here as a single radiating patch with suitable modifications can realize CP response [3, 4]. While using MSAs, CP response is realized by using various techniques, to name a few, a use of power divider network along with dual feeds in single patch, a coaxial feed design used in narrow slit cut MSA, use of modified radiating patch shapes or use of widely reported resonant slots like, U-slot or pair of rectangular slot which yields design of the E-shape MSA [4–10]. With any kind of modifications realized in the radiating patch to create three conditions for CP response, frequency and impedance variations at various resonant modes take place. Therefore, correct knowledge about the modifications imposed in the patch on patch resonant modes is needed, as this can lead to design guideline. In this paper, novel configuration of proximity fed air suspended Swastik shape MSA realized by placing four rectangular slots on radiating and non-radiating edges of square MSA (SMSA) is presented. The four-slot positions are selected such that it realizes optimum spacing between SMSA's TM_{10} and TM_{01} resonant modes which realize CP response. The axial ratio (AR) bandwidth (BW) of 43 MHz (4%) is obtained that completely lies inside impedance BW of 565 MHz (47.18%). Here, the impedance BW consists of three resonant modes, namely TM_{10}, TM_{01} and TM_{11}. The four slots reduce the frequency of TM_{11} mode such that it is occupied inside the impedance BW. Slots also modify the surface current vectors at above-mentioned resonant modes that yield broadside radiation pattern across impedance BW and yield gain of above 6 dBi across the same. Across AR BW, the peak gain of above 7 dBi is offered by the proposed antenna. In the proposed design, suspended thicker substrate is used for overall gain and BW enhancement as well as a systematic study is presented for highlighting the effects of slots that achieve appropriate mode frequency inter-spacing to achieve CP response. Simpler parametric formulations for realizing similar configuration at different frequency are presented. Antenna designed using the same yields similar CP response. Thus, novelty in the present work is in a simpler configuration for CP response supported with a detailed study based on patch resonant modes and parametric formulation for redesigning of a similar antenna. Antenna discussed here is studied using IE3D, and measurements were carried out using ZVH—8, FSC 6 and SMB 100A.

2 Swastik Shape MSA

Design of Swastik shape MSA fed using proximity strip is shown in Fig. 1a, b. The patch is etched on FR4 substrate with parameters, $\varepsilon_r = 4.3$, $h = 1.6$ mm, and further, it is suspended above the ground plane using an air gap 'h_a'. The SMSA length (L_p) is calculated such that on total substrate thickness of 29.6 mm (~$0.115\lambda_g$), its

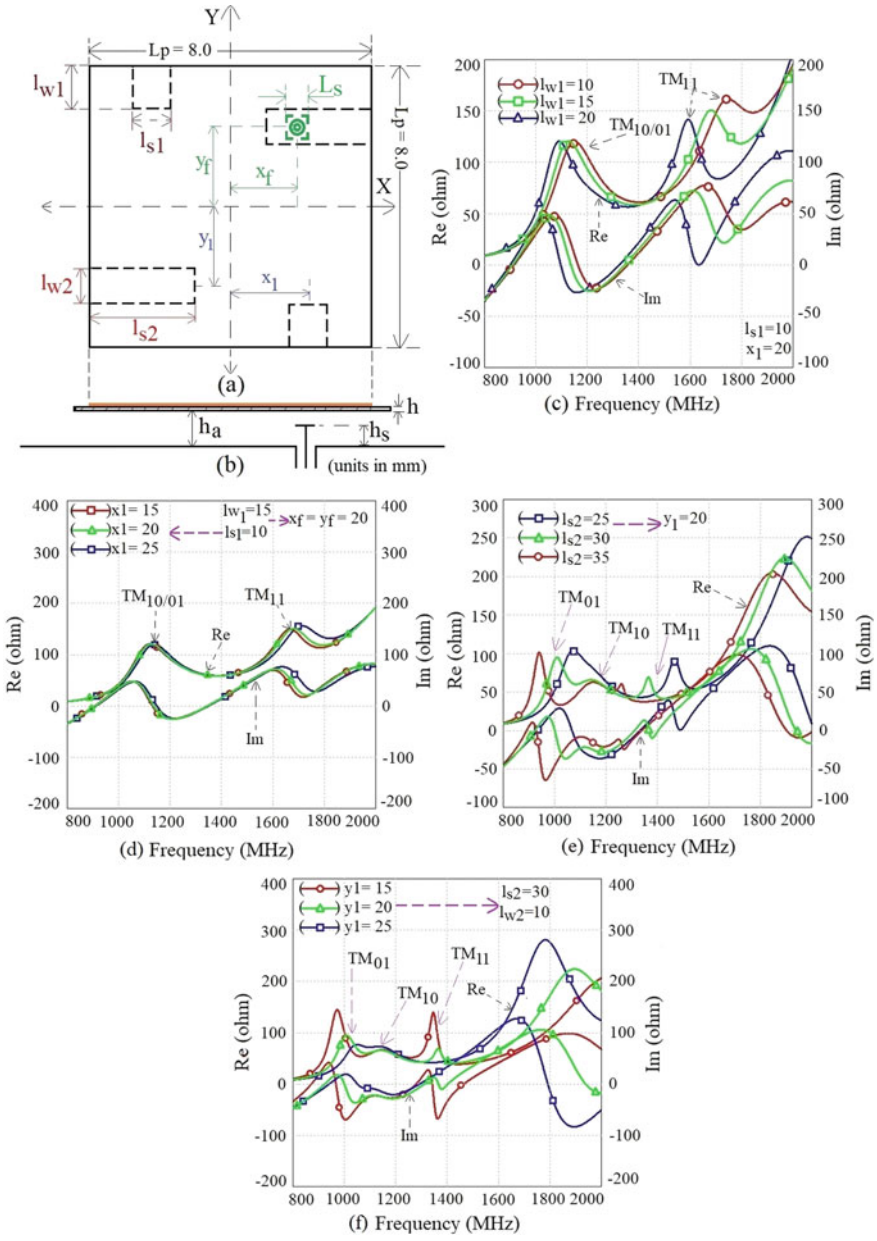

Fig. 1 **a**, **b** Swastik shape MSA and its resonance graphs for variation in **c** l_{w1}, **d** x_1, **e** l_{s2} and **f** y_1

fundamental TM_{10} and TM_{01} mode frequencies are around 1200 MHz. To realize Swastik shape MSA, two pairs of orthogonal slots are introduced on to the four edges of SMSA as shown in Fig. 1a. The slots' position is selected in such a way that they will realize tuning in between TM_{10} and TM_{01} modes of SMSA and also will modify surface current vector directions at next higher-order TM_{11} mode. The parametric study is carried out for variations in slot dimensions, and their impedance graphs are shown in Fig. 1c–e. For 'x_f' = 'y_f' = 20 mm, increment in slot length 'l_{w1}', which is embedded at an offset position of 'x_1' = 20 mm, does not largely reduce TM_{10} and TM_{01} mode frequencies. Surface current distributions at observed peaks are shown in Fig. 2a, b. Since SMSA is taken, TM_{10} and TM_{01} mode frequencies are nearly equal and currents exhibit half wavelength variation along patch diagonal length. Due to TM_{11} mode, next resonant peak shows half wavelength variation along square patch side lengths. Variations in slot position 'x_1' also do not separate out the TM_{10} and TM_{01} resonant modes. To degenerate two orthogonal modes, another pair of slots of length 'l_{s2}' x 'l_{w2}' is introduced.

The slots along the horizontal direction reduce TM_{01} mode frequency, and thus, two isolated peaks because of TM_{10} and TM_{01} modes are observed. The spacing between them increases with the slot length 'l_{s2}'. The surface current distribution with these additional rectangular slots is shown in Fig. 2c–e. At first mode, i.e. TM_{01}, surface currents on Swastik shape patch are along *Y*-axis whereas over TM_{10} and TM_{11} modes, current are along *X*-axis. Thus, CP response will be realized nearer to TM_{01} and TM_{10} mode frequencies. The optimum results for Swastik shape MSA are shown in Figs. 2f, g and 3a–d. Respective simulated and measured impedance BW is 565 MHz (47.18%) and 591 MHz (49.27%). The air suspended fabricated design is provided in Fig. 2g

Antenna gain is above 6 dBi over most of the impedance BW. Across AR BW of 43 MHz (4%), gain is larger than 7 dBi. At higher frequencies of BW, gain is reduced and same is attributed to orthogonal current vectors present at modified TM_{11} resonant mode. Radiation pattern exhibits maxima in the plane which is orthogonal to plane of the antenna. The co- and cross-polarization components are within 3 dB difference. For feed position shown in Fig. 1a, right-hand CP response is offered by Swastik shape MSA. Based upon the optimum design discussed, a simpler parametric formulation for redesigning of Swastik shape MSA is realized. Various antenna parameters are expressed in terms of TM_{10} mode guide wavelength (λ_g) in the optimized design and they are, $l_{w1} = 0.0586\lambda_g$, $l_{s1} = l_{w2} = 0.039\lambda_g$, $l_{s2} = 0.1173\lambda_g$, $L_s = 0.063\lambda_g$, $h_s = 0.098\lambda_g$, $x_f = y_f = 0.0782\lambda_g$. For total substrate thickness ($h + h_a$) of $0.115\lambda_g$, resonance frequency equation for RMSA is used for calculating side length of SMSA as reported in [3]. Here, edge extension length of twice the 0.7 ($h + h_a$) is taken. Using above parametric equations, the Swastik shape MSA is designed for $f_{TM10} =$ 950 MHz. Its return loss (S_{11}), gain and AR BW plots are shown in Fig. 3e, f.

Respective values of impedance BW using simulation and experiment are 440 MHz (45.03%) and 444 MHz (46.06%). The AR BW is from 844 to 886 MHz (42 MHz, 4.86%). Across AR and impedance BW, redesigned antenna offers gain of above 6 dBi. For substrate thickness ($h + h_a$) of $0.115\lambda_g$, Swastik shape MSA is also redesigned for $f_{TM10} = 1500$ MHz where it offered impedance BW of 664 MHz

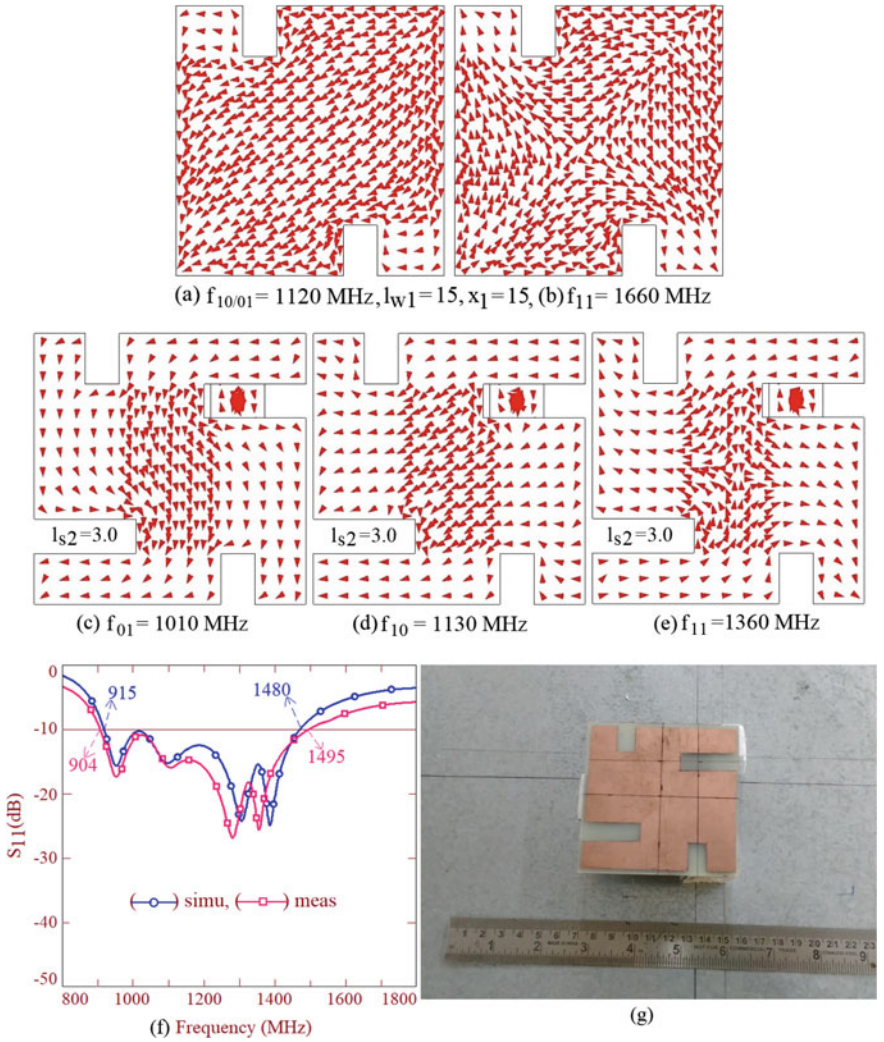

Fig. 2 **a**–**e** Surface current distributions of observed resonant modes for Swastik shape MSA, its **f** optimum return loss (S_{11}) plot and **g** fabricated antenna

(45.3%) with AR BW of 58 MHz (4.41%). To prove the above parametric formulation for 1500 MHz, Swastik shape MSA is also redesigned for total substrate thickness of $0.1\lambda_g$. Here, the feeding strip is placed at a height of $0.08\lambda_g$. With above antenna dimensions, antenna yields AR and impedance BW of 42 MHz (3.15%) and 648 MHz (44.1%), respectively. Thus, proposed parametric equations can be used to design CP antenna at given frequency and on thicker air suspended substrate.

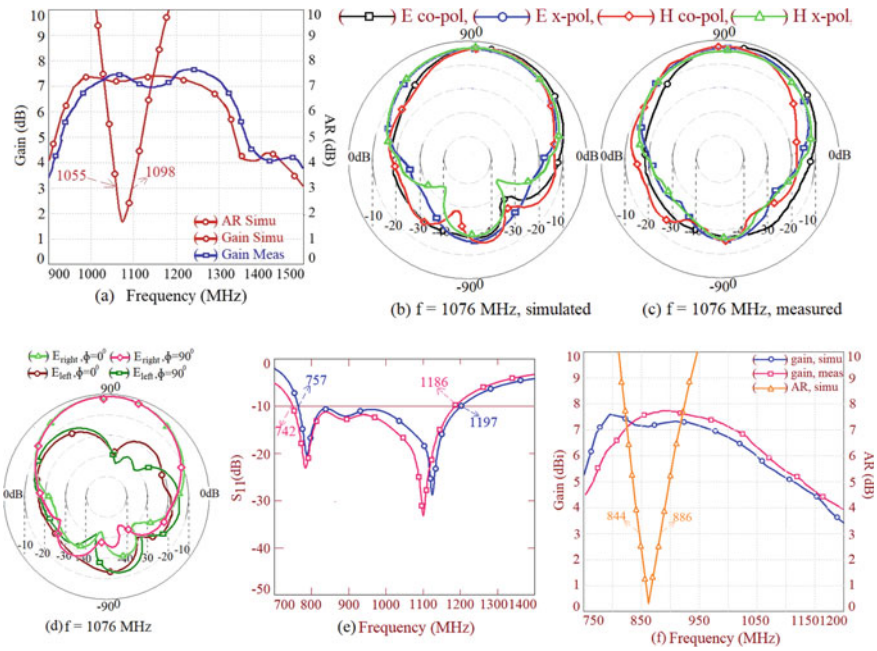

Fig. 3 **a** Gain and AR BW plots, **b**, **c** polar radiation and **d** polarization plots for Swastik shape MSA, **e** return loss plots and **f** gain and AR BW plots for Swastik shape MSA for $f_{TM10} = 950$ MHz

3 Conclusions

Design of Swastik shape MSA is presented for CP response. An orthogonal pairs of rectangular slots, tune the spacing between TM_{01} and TM_{10} modes on square patch and along with reduced frequency TM_{11} mode, yield AR and impedance BW of 43 MHz (4%) and 565 MHz (47.18%), respectively. The antenna offers peak gain of above 7 dBi. The parametric formulation for redesigning of CP antenna is presented, which is useful for realizing similar antenna at different frequencies on air suspended substrate. Thus, novel configuration of Swastik shape MSA with detailed explanation about antenna functioning backed by the design guidelines is the new contribution in the present study.

References

1. Pozar DM (1989) Microwave engineering, 3rd edn. Wiley, New York
2. Balanis CA (1997) Antenna theory analysis and design. Wiley, New York
3. Kumar G, Ray KP (2003) Broadband microstrip antennas, 1st edn. Artech House, USA
4. Lee HF, Chen W (1997) Advances in microstrip and printed antennas. Wiley, New York

5. Yang Z-J, Zhu L, Xiao S (2018) An Implantable circularly polarized patch antenna design for pacemaker monitoring based on quality factor analysis. IEEE Trans Antennas Propag 66(10):5180–5191
6. Wu Q-S, Zhang X, Zhu L (2018) A wideband circularly polarized patch antenna with enhanced axial ratio bandwidth via co-design of feeding network. IEEE Trans Antennas Propag 66(10):4996–5003
7. Guo Y-X, Bian L, Shi XQ (2018) Broadband circularly polarized annular-ring microstrip antenna. IEEE Trans Antennas Propag 57(8):2474–2477
8. Yang SLS, Lee KF, Kishk AA (2008) Design and study of wideband single feed circularly polarized microstrip antennas. Prog Electromagn Res 80:45–61
9. Baudha S, Dinesh Kumar V (2015) Corner truncated broadband patch antenna with circular slots. Microw Opt Technol Lett 57(4):845–849
10. Khidre A, Lee KF, Yang F, Eisherbeni A (2010) Wideband circularly polarized E-shaped patch antenna for wireless applications. IEEE Antennas Propag Mag 52(5)

Bandwidth Enhancement of E-shape and U-Slot Embedded Microstrip Antenna Using Sectoral Patches

A. A. Deshmukh, Mansi Shah, C. Kudoo, V. Chaudhary and A. Mhatre

Abstract A tapered width designs of E-shape and U-slot embedded rectangular microstrip antenna is discussed which yields 3–5% increment in impedance bandwidth. Further, without increasing the overall patch area, gap-coupled designs of E-shape and U-slot embedded rectangular microstrip antennas along with narrow sectoral patches are proposed. The proposed configuration of E-shape patch and U-slot cut patch yields bandwidth of 272 MHz (31%) and 230 MHz (25.13%), respectively. These bandwidths are 5 and 3% higher as compared with their respective tapered width E-shape and U-slot embedded designs. Proposed configurations yield pattern maximum in the bore-sight direction with peak gain of around 9 dBi. With the realized bandwidth and pattern characteristics, proposed configurations can be useful in personal as well as mobile communication systems in 800–1000 MHz spectrum.

Keywords Rectangular microstrip antenna · Broadband microstrip antenna · Gap-coupled design · U-slot · E-shape microstrip antenna · Sectoral shape patch

1 Introduction

In the designs of wireless communication, microstrip antenna (MSA) finds wide applications because of their numerous advantages [1]. The MSAs were regarded as narrow bandwidth (BW) antennas since in earlier designs, cavity formed between the radiation patch and the ground plane possesses higher value of quality factor [2]. However, over last few decades, many techniques have been evolved that enhances the antenna BW. To name a few, use of parasitic patches in the same layer as that of fed patch or placed above the fed patch, use of thicker substrate along with modified feeds, and use of resonant slots which are embedded inside the MSA [2–7]. Out of these techniques, slot cut method has been widely preferred ahead of gap-coupled stacked configurations since patch area is not increased. It was believed that slot introduces second resonant modes nearer to the fundamental mode that increases BW. But detailed study on slot antenna showed that increase in BW is result of

A. A. Deshmukh · M. Shah (✉) · C. Kudoo · V. Chaudhary · A. Mhatre
EXTC, SVKM's DJ Sanghvi COE, Vile Parle, Mumbai, India

V. Janyani et al. (eds.), *Optical and Wireless Technologies*, Lecture Notes in Electrical Engineering 648, https://doi.org/10.1007/978-981-15-2926-9_25

modifications in frequency and impedance at orthogonal higher-order modes rather than a new resonant mode being introduced [8]. The E-shape MSA has been realized by embedding pair of slots on rectangular MSA (RMSA) radiating edge [7]. Increase in BW of E-shape MSA as well as U-slot cut RMSA has been realized by tapering the patch width [9]. With minimal increment in patch area, increase in BW by nearly 3% as well as higher broadside peak gain has been achieved [9]. With tapering of the width, an empty space is observed around the E-shape modified non-radiating edge which can be used to increase the BW further.

This paper discusses novel gap-coupled configurations of tapered width E-shape MSA and U-slot embedded RMSA along with narrow sectoral shape gap-coupled patches. As sectoral patch occupies the vacant area adjoining the non-radiating edge of modified E-shape and U-slot embedded RMSA, an increase in overall patch size is not significant. The BW realized in these designs is a function of sectoral patch radius as well as its position nearer to the patch non-radiating as well as the radiating edge. The detailed parametric study is presented for optimizing the configurations. The design of tapered patch width E-shape MSA with two sectoral patches yields BW of 272 MHz (31%) which is nearly 5% higher as compared with design of tapered width E-shape MSA. A design of tapered patch width U-slot cut RMSA with two sectoral patches yields BW of 230 MHz (25.13%). This BW is around 3% additional to that design with tapered width U-slot cut RMSA design. As observed amongst the two slot cut variations, E-shape design with sectoral patches gives higher BW. Two antennas offer radiation pattern which exhibit maximum in the plane which is orthogonal to the plane of the antenna showing linear polarization. The E-shape MSA design yields co-polar broadside peak gain of around 9.3 dBi, whereas U-slot cut design yields nearly 8.8 dBi of peak co-polar gain. Thus in comparison with E-shape MSA, U-slot embedded RMSA and their tapered width variation, proposed gap-coupled designs yields better characteristics in terms of the BW and gain. Thus, novelty in the present study is in providing simpler gap-coupled configurations with enhanced antenna characteristics. Configurations in the present paper have been optimized by using simulation software 'IE3D,' followed by the experimental validations. The N-type connector having 0.32 cm inner wire diameter has been used to feed the antennas while using square ground plane with side length 35 cm. Antenna testing using RF instruments like, ZVH—8, FSC 6, and SMB 100A have been carried out.

2 Wideband Gap-Coupled Tapered Width E-Shape MSAs

A gap-coupled design of E-shape MSA using tapered patch width (W & w_1) is provided in Fig. 1a. Dimensions of antenna and frequencies refereed in this paper are in 'cm' and 'MHz,' respectively. The E-shape geometry and sectoral patches are etched on FR4 with substrate parameters as, $\varepsilon_r = 4.3$, $\tan\delta = 0.02$, and $h = 0.16$ cm. The etched patch is further suspended above the ground plane using air gap of 'h_a' cm. Thus, here total substrate thickness is '$h + h_a$.' In this paper, dimensions of E-shape MSA and substrate are taken to be same as that used in optimum design

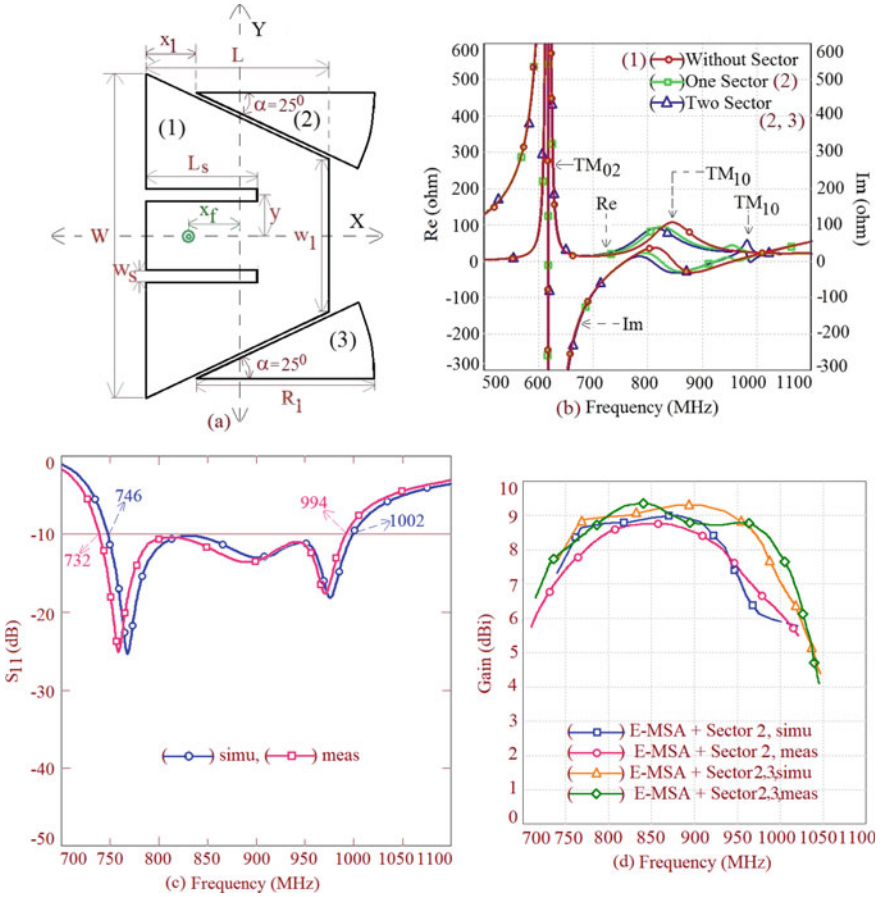

Fig. 1 **a** Coaxially fed tapered width E-shape MSA along with sectoral patches, their **b** impedance graphs, **c** return loss (S_{11}) plot for tapered width E-shape MSA gap-coupled with single sectoral patch and their **d** gain variation over BW for gap-coupled sectoral designs

in [9]. Thus, various antenna parameters in tapered width E-shape MSA are, 'h_a' = 2.0, 'L' = 13, 'W' = 23, 'w_1' = 11, 'L_s' = 7.8, 'w_s' = 0.8, and 'y' = 5.8 cm which yields BW of 224 MHz (25.8%). Here, first sectoral patch '2' is gap-coupled with E-shape MSA. The impedance graph for the same is shown in Fig. 1b. In the sectoral patch, radius (R_1) nearly equals half wavelength, i.e., TM_{10} mode, at the desired parasitic frequency. Optimum BW depends on 'R_1' as well as the patch position 'x_1' along non-radiating edge. The position 'x_1' changes the coupling as parasitic patch is being placed nearer to the radiating edge of E-shape MSA where field polarity is maximum. An optimum response with single sectoral patch is obtained for 'R_1' = 12.8, 'x_1' = 4.15, and 'x_f' = 3.8 cm which is shown in Fig. 1c. Simulated BW is 256 MHz (29.3%), whereas measured BW is 262 MHz (30.36%). The gap-coupled

design offers peak gain of around 8.8 dBi as given in Fig. 1d, which same as that is offered by tapered E-shape patch [9]. Hence to enhance the gain another sectoral patch is gap-coupled as given below.

The radius of second patch is taken same as that of the first patch. Addition of second sectoral patch (marked as '3' in Fig. 1a), changes the impedance levels at TM_{10} mode of sectoral patch which increases the BW. For 'x_1' = 3.45 cm, an optimum response is realized as shown in Fig. 2a. Using simulation, BW is 272 MHz (31.05%) and that using experiment, BW is 275 MHz (31.88%). With same sectoral patch radius, this BW is slightly higher as compared to single sectoral patch design.

Polar radiation pattern shown in Fig. 2d–g nearer to the band edge frequencies and across the BW is in broadside direction. Antenna offers peak gain of 9.3 dBi which is higher than tapered E-shape MSA as well as its gap-coupled design with single sectoral patch. Similarly, tapered width U-slot cut RMSA is optimized for wide band response as shown in Fig. 2h. Return loss plots with single and two gap-coupled sectoral patch designs, fabricated antenna, pattern at band start and stop frequencies for two sectoral patch design and gain variation in two variations is shown in Figs. 2i and 3a–h. Simulated and measured BW's in single sectoral patch design with U-slot cut RMSA are, 224 MHz (24.45%) and 228 MHz (25%), respectively.

Using single sectoral patch, antenna offers gain of around 7 dBi over complete VSWR BW with peak gain close to 9 dBi. Using second sectoral patch, BW and gain improve marginally. Here, simulated and measured BW's are 230 MHz (25.13%) and 234 MHz (25.97%), respectively. Antenna exhibits broadside pattern. In E-shape and U-slot embedded gap-coupled designs, E-plane and H-plane are along $\phi = 0°$ and 90°, respectively, and they offer linear polarization. The maximum of antenna gain is above 9 dBi due to marginal improvement in aperture area. In comparison with E-shape and U-slot embedded RMSA designs as well as their tapered width variation, proposed configurations offer 3–5% increment in impedance BW with increment in peak gain as well. Thus, simpler wideband gap-coupled designs of slot cut MSAs without large overall increment in patch size are the novelty in this proposed study. For realized antenna characteristics, proposed designs will be useful in applications of mobile communication.

3 Conclusions

Simpler wideband gap-coupled designs of E-shape and U-slot embedded RMSAs with sectoral patches are proposed. As sectoral patch occupies vacant area adjoining the coaxially fed MSA, overall increment in size is smaller. In E-shape MSA combination with two sectoral patches yields BW of above 270 MHz (>30%), whereas similar U-slot cut design offers BW of above 230 MHz (>25%). These BW's are 3–5% higher as compared with their tapered width variation. Due to increase in aperture area, gap-coupled designs offer maximum gain of above 9 dBi.

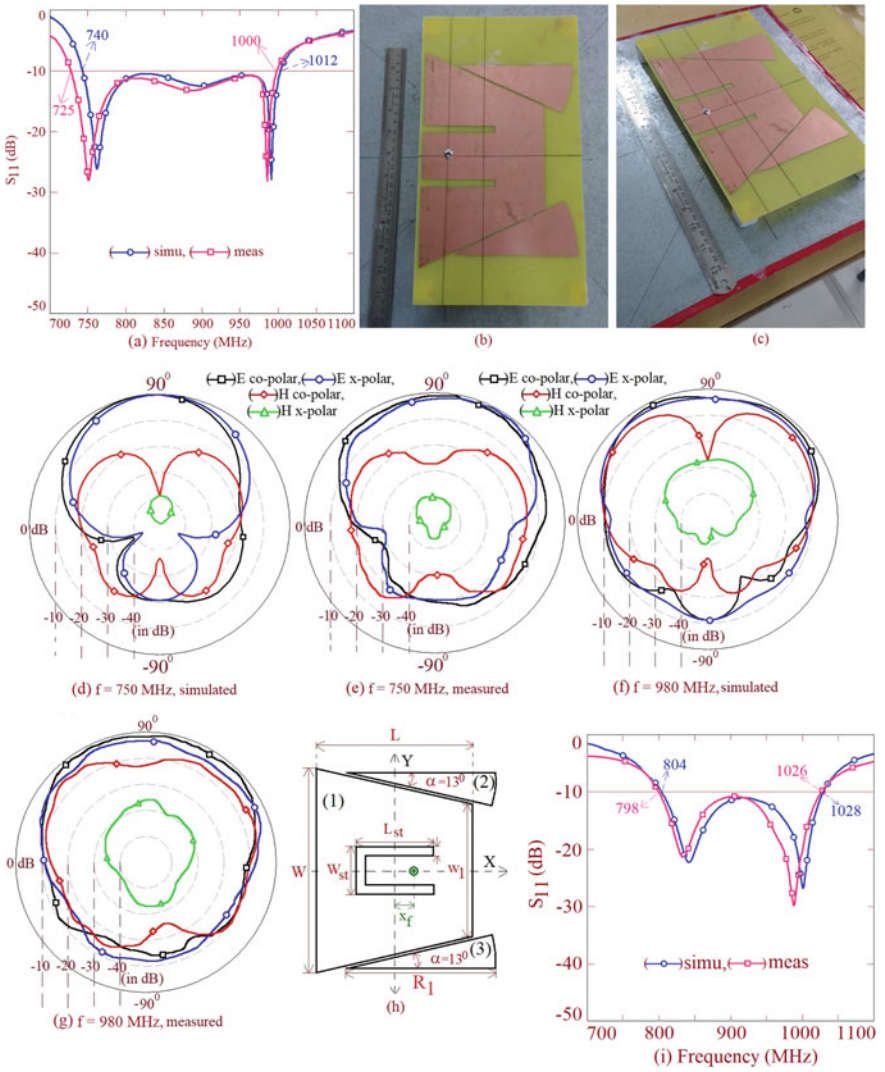

Fig. 2 **a** Return loss plot, **b**, **c** fabricated antenna, **d**–**g** radiation pattern at band start and stop frequency for sectoral patches gap-coupled with E-shape MSA, **h** sectoral MSAs gap-coupled with U-slot cut RMSA and its **i** return loss plot for single sectoral patch gap-coupled design

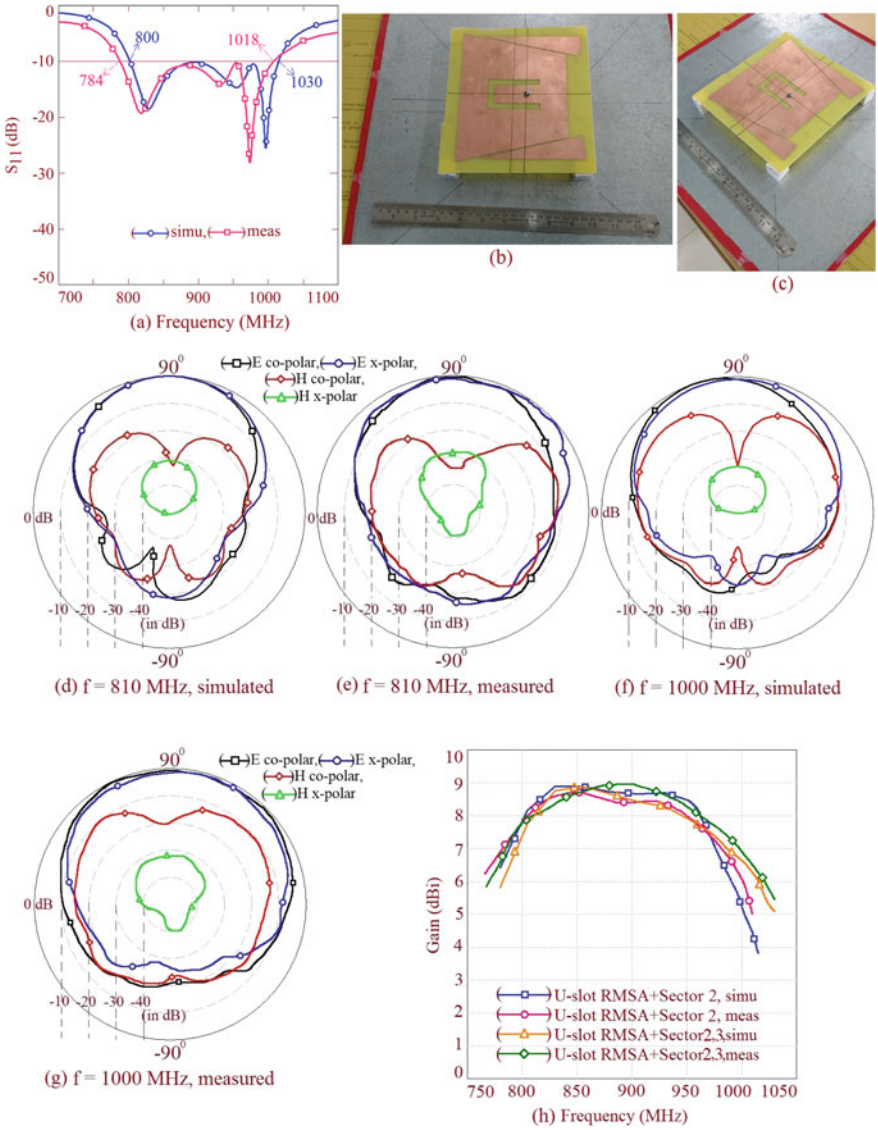

Fig. 3 **a** Return loss plot, **b**, **c** fabricated design, **d**–**g** radiation pattern at band edge frequency and **h** gain variation over the BW for U-slot cut RMSA gap-coupled with sectoral patches

References

1. Balanis CA (1997) Antenna theory: analysis and design. Wiley, New York
2. Lee HF, Chen W (1997) Advances in microstrip and printed antennas. Wiley, New York
3. Abbaspour M, Hassani HR (2008) Wideband star-shaped microstrip patch antenna. Prog Electromagn Res Lett 1:61–68
4. Rafi Gh, Shafai L (2004) Broadband microstrip patch antenna with V-slot. IEE Proc Microw Antennas Propag 151(5):435–440
5. Baudha S, Dinesh Kumar V (2015) Corner truncated broadband patch antenna with circular slots. Microw Opt Technol Lett 57(4):845–849
6. Tiwari RN, Singh P, Kanaujia BK (2017) Butter fly shape compact microstrip antenna for wideband applications. Prog Electromag Res Lett 69:45–50
7. Wong KL (1997) Compact and broadband microstrip antenna. Wiley, New York
8. Deshmukh AA, Ray KP, Kadam A (2013) Analysis of slot cut broadband and dual band rectangular microstrip antennas. IETE J Res 59(3):193–200
9. Deshmukh AA, Shah M, Kudoo C, Mhatre A (2018) Variations of wide band E-shape and U-slot cut rectangular microstrip antennas. Proc ICACC, Kochi, India

Light-Fidelity (Li-Fi), a New Approach for Internet Inside Running Metro

Ajit Kumawat and D. Sriram Kumar

Abstract Light-Fidelity (Li-Fi) is an emerging technology which would essentially move the Internet out of your router, and into your light fixtures. In mobility scenario, high mobility and limited bandwidth in wireless communication lead to poor quality. So in running metro trains, it is difficult to give the facility of fast Internet. A cost-effective solution is light-fidelity (Li-Fi) communication. Visible light will provide the communication and illumination, both in metro. Which consume less power compare to the existing fluorescent light sources in metro. We propose the idea of Li-Fi as a new Wi-Fi for metro and give the designing of metro saloon with minimum number of LEDs. We analyze interference and illumination with passenger position inside metro saloon and we consider the dimensions and required illumination level used by Delhi Metro Rail Corporation (DMRC) for metro train for fixing the light-emitting diode(LED) inside the metro saloon.

Keywords Li-Fi · DMRC · VLC · Light-emitting diode · High mobility · Wi-Fi · Interference · Illumination

1 Introduction

Visible light communication (VLC) is well-known technology for indoor communication in optical wireless. It uses LEDs lights for communication between the transmitter and receiver. Recent advances in technology have made it possible to integrate the transmitter and receiver to form a transceiver. For Li-Fi application, the high-power LEDs can be used to achieve a bandwidth similar to low power LEDs. High-power LEDs enable data transmission to an increased distance [1]. Li-Fi does have its limitations. Most notably, VLC has a much shorter range than the radio spectrum. The visible light spectrum also cannot transmit through walls or other barriers.

A. Kumawat (✉) · D. Sriram Kumar
Department of Electronics and Communication Engineering, National Institute of Technology, Trichy 620015, India
e-mail: kumawatajit93@gmail.com

D. Sriram Kumar
e-mail: srk@nitt.edu

V. Janyani et al. (eds.), *Optical and Wireless Technologies*, Lecture Notes in Electrical Engineering 648, https://doi.org/10.1007/978-981-15-2926-9_26

These disadvantages, however, can be turned into advantages. In a confined space such as metro, passengers do not have to worry about range limitations or Wi-Fi dead spots. The signal will be available wherever visible light can reach. The space limitations of Li-Fi can also enhance user security because hackers are not able to access the signal from remote places. Li-Fi offers relief to RF communication through its huge bandwidth provision and Li-Fi will replace the existing power-consuming light sources inside metro train and provide illumination as well as Internet inside running metro. VLC provides frequency range from 430 to 790 THz for communication. So we get more data rate (Gbps) in visible light communication compare to RF communication.

1.1 Related Works

A lot of research has been carried on wireless communication in high-speed trains. In [2], architecture, design, and deployment of Wi-Fi service inside running metro trains have been given. Wi-Fi devices, operating in non-licensed spectrum, were used and improvement is achieved in signal strength by −20 dB and handover timeout by 2 s. In [3], instead of ISM band at 2.4 GHz, the frequency of 2.6 GHz has been selected in order to obtain interference-free measurements with similar propagation properties and the 2.6 GHz 021 wireless link characterized for three metro environments (tunnel, station, and open field) and attenuation have been discussed. In [4], for high-speed trains (more than 200 km/h), the novel architecture for Seamless Wireless Internet is given and obtained that the average packet loss during the handoff time is very small. But in these researches, Wi-Fi is bandwidth limited and less Internet speed. So the new effective approach to overcome the problems is light-fidelity (Li-Fi) communication in metro trains. That will provide Internet as well as illumination. In [4], the applications of visible light communication in railways were discussed. There was brief explanation of use of Internet in running train by using visible light communication (VLC). But there was no explanation and criteria for installation of LEDs for communication and illumination inside the train.

1.2 Our Approach and Contribution

We notice, the metro saloon dimensions used by Delhi Metro Rail Corporation (DMRC) in designing of M/T car, for our arrangement of LEDs in metro saloon. To arrange the LEDs inside metro saloon, the concept of finding and fixing of LEDs inside indoor application were used. The illumination required by DMRC in metro saloon taken under consideration to find the minimum number of LEDs. In [5], the general analysis of co-channel interference in Li-Fi attocell network has been shown. We noticed and analyzed the co-channel interference for a particular application of metro. We analyze the interference due to changing height between transmitter and

receiver, when a passenger is seating and in standing position. We also analyzed the vertical illumination distribution in metro saloon. We calculate the minimum number of LED inside metro saloon that can provide the required illumination with lower interference. The latest work for metro environment is going for train to ground communication through VLC [6] and the use of VLC in metro application [4]. So here, after analyzing these work, we come with the proposal of Li-Fi installation inside metro.

The arrangement of the paper is as follows. In Sect. 2, we show the current lighting system in metro saloon with their specification. In Sect. 3, we present the dimensions of metro saloon as par DMRC data sheets. In Sect. 4, installation of LEDs is given. In Sect. 5, the analysis of interference is shown. In Sect. 6 the vertical illumination distribution in metro saloon is shown. In Sect. 7 the challenges faced by Li-Fi installation in metro are discussed. The paper concludes with Sect. 8.

2 Existing Lighting System

In Delhi Metro Rail Corporation (DMRC)metro trains, light sources used for illumination is fluorescent lights. The power consumption of fluorescent lamp is more and the lifetime is less than LED [7]. So the effective solution is use of LEDs for illumination in metro saloon. The specification of the lights such as ratings, average intensity level, and number of fixtures is given in Table 1. And the component required to operate the light system with their failure rate given in Table 2. These specifications are required to install the LED lights inside the metro saloon. While installation, we need to maintain the illumination level as per specification, inside the saloon (Fig. 1).

Table 1 Light specification

Component	Rating	Average intensity	Quantity
Fluorescent light	36 W & 230 v ac	300 lux at 1500 mm above floor level	13
Fluorescent light	36 W & 110 v dc	50 lux at 1200 mm above floor level	13

Table 2 Light component specification

Component	Failure rate	Dimensions	Quantity (kg)
Inverter for fluorescent light	50,000 h & 230 v ac	280 × 25 × 21	13 & 0.20
Inverter for fluorescent light	50,000 h & 110 v dc	270 × 65 × 40	13 & 0.44

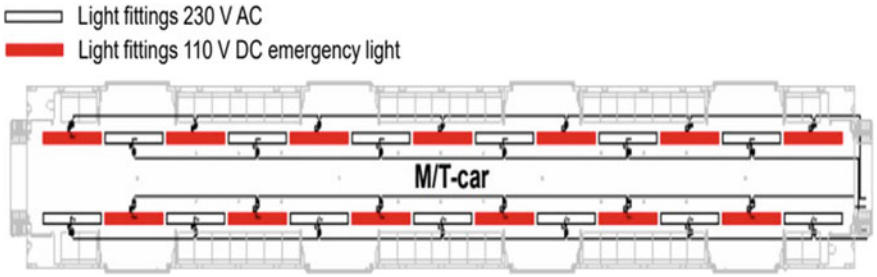

Fig. 1 Shown the light fitting in metro saloon of M/T car, there is total 26 light, In the top view, white color shows ac supply light and red color shows dc supply light

3 Dimensions of Metro Saloon

In this section, we show the dimensions of metro saloon, used by Delhi Metro Rail Corporation (DMRC)for metro train in Table 1. And the structure of M/T car with these dimensions also shows in Fig. 2. We need the area of metro saloon to calculate the LEDs. So Further we consider these values (Table 3).

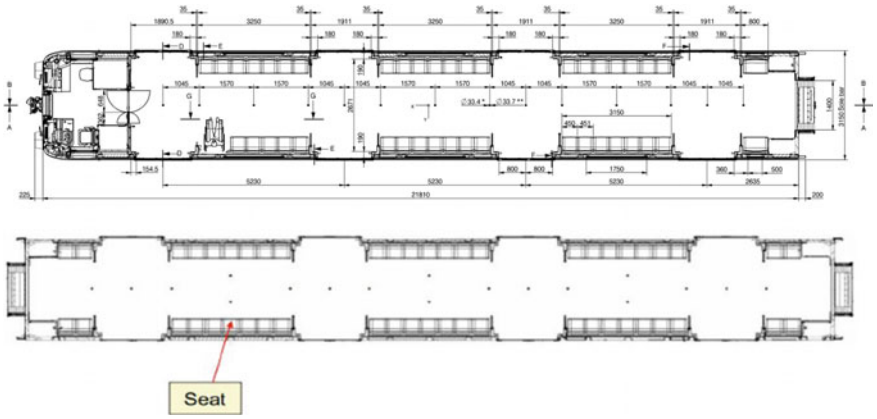

Fig. 2 Shown dimensions of metro saloon of M/T car, the top view of metro saloon is represented

Table 3 Dimensions of metro saloon

Parameter	Dimensions
Length of saloon	19,340 mm
Height of saloon	2050 mm
Width of saloon	2950

4 Installation of LEDs

In this section, we calculate the number of LEDs needed to fix in metro saloon according to the given dimension and required illumination level. For fixing the LEDs, we consider the concept of finding and fixing of LEDs inside indoor rooms or offices. The calculation of LEDs is following as:

4.1 Total Wattage of Fixture

The wattage in total fixture given by, Number of LEDs in one fixture * each LED watt. Here, we are considering 1 LED of 12 w in every fixture.

4.2 Lumen Per Fixture

The practical LED has luminous efficacy as 90–130 lumens per watt. Here, we are considering 130 lumens per watt for finding the lumen per fixture which is given by Luminous efficacy * each fixture's watt.

4.3 Number of Fixtures

The number of fixture is found by given formula. Here, the required lux (300 lx), we are considering according to DMRC existing light system. And for maintenance factor (M.F), we are taking standard value 0.9 and utilization factor (U.F) as 0.85. The area is calculated by given above metro structure dimensions.

$$N = \frac{\text{Required lux} * \text{Area}}{\text{M.F.} * \text{U.F.} * \text{Lumen per fixture}}$$

The number of LEDs and the distance between LEDs are given in Table 4 and the final metro saloon model after fixing is shown in Fig. 3.

Table 4 Led lighting fixing

Parameter	Values
Total number of LED	17
Number of row of fixture	1
Axial and transverse spacing between LEDs	1.16 m

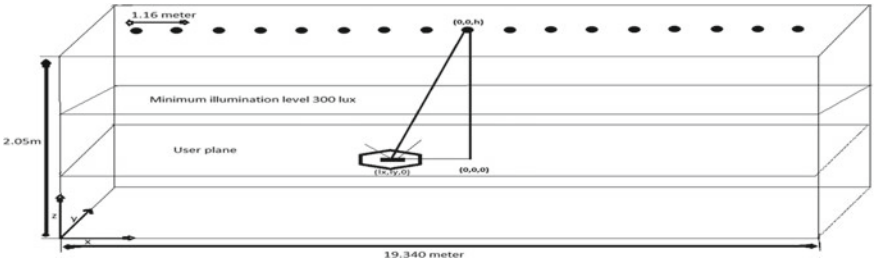

Fig. 3 Figure showing metro saloon model after fixing LEDs

5 Illumination Analysis

LEDs are used for dual propose of illumination and communication. So in this section, the distribution of illuminance in metro saloon surface will be discussed. The illuminance expresses the brightness of an illuminated surface. The luminous intensity in angle Ø it is given as

$$I(\emptyset) = I(0)\cos^m(\emptyset) \tag{1}$$

where Ø is the angle of irradiance with respect to the axis normal to the transmitter surface, $I(0)$ is the center luminous intensity and m is the order of Lambertian emission defined as

$$m = \frac{\ln 2}{\ln(\cos \emptyset_{1/2})}$$

where $\emptyset_{1/2}$ is the semi angle at half illuminance of a LED. The horizontal illuminance/intensity at a point (x, y) and the received power at the receiver are given (Fig. 4).

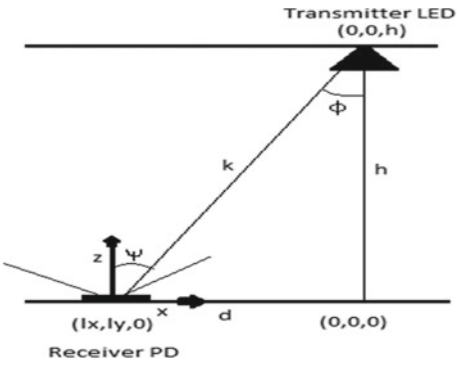

Fig. 4 Figure showing line-of-sight (LOS) propagation geometry. The ϕ and φ are the transmission angle at LED and incident angle at PD, respectively

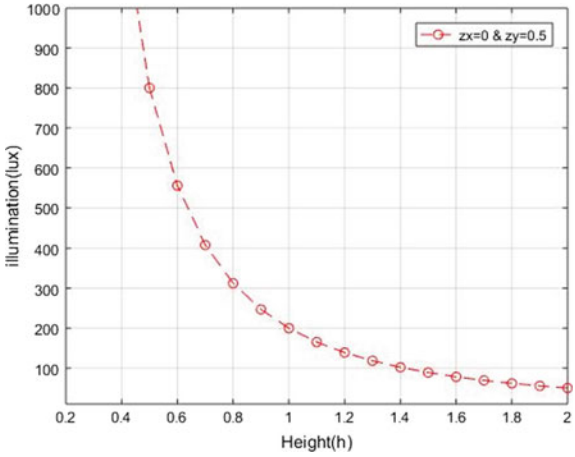

Fig. 5 Graph showing the illumination level, for two different position of passenger, ($l_x = 0$, $h = 2.05$) and ($l_x = 0.5$, $h = 0.58$) passenger moving in l_y direction

$$E_{\text{hor}} = I(0)\cos^m(\emptyset)/k^2 \,.\, \cos(\varphi) \tag{2}$$

We assume that PD has no orientation toward the LED and surface is parallel to the ground. So, we have incident angle and irradiance angle same. $d = \sqrt{l_x^2 + l_y^2}$ denotes the location of user PD from origin and k is the distance between the LED and a detector surface. Equation 2 can be modified as

$$E_{\text{hor}} = I(0)\cos^{(m+1)}(\emptyset)/k^2 \tag{3}$$

By using the above illumination Eq. (3) and the geometry of the link in Fig. 3, the illumination equation can be modifying as

$$I = I(0)h^{(m+1)}(l_x^2 + l_y^2 + h^2)^{-(m+3)/2} \tag{4}$$

where h is the height from LED access point to floor, $I(0)$ is the center luminous intensity, and l_x, l_y positions of passenger.

The consideration for illuminance of LED lighting is required. Generally, illuminance of 250–300 l_x 1.5 mm above the floor is required in metro saloon. Further, we show the illumination variation with movement of passenger or photo detector (Figs. 5 and 6).

6 Interference Analysis

In this section, we show the interference variation for passenger seating and standing position. For Li-Fi installation in metro saloon, Li-Fi attocell network is form because of regular geometry of LED access points. In [5], such a network, the LEDs

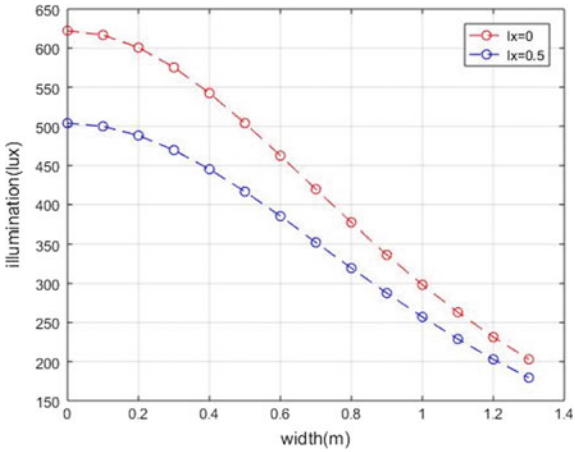

Fig. 6 Graph showing the illumination level, for two different position of passenger, ($l_x = 0$, $h = 2.05$) and ($l_x = 0.5$, $h = 0.58$) passenger moving in l_y direction

simultaneously transmit on modulated intensities of different colors or light wavelength, the LEDs transmitting on the same optical wavelength can be considered as co-channel interference. In the paper, we assume an optical wireless channel, in an optical link, the channel DC gain is given [8] as:

$$G(0) = \frac{(m+1)}{2\pi D_d^2} A_{\text{pd}} \cos^m(\emptyset) T_s(\Psi) g(\Psi) \cos(\Psi) \quad 0 \le \Psi \le \Psi_c \tag{5}$$

where D_d is the distance between a transmitter and a receiver, A_{pd} is the physical area of the detector in a PD, φ is the angle of irradiance, ψ is the angle of incidence, T_s (ψ) is the gain of an optical filter, and $g(\psi)$ is the gain of an optical concentrator. Here, we considered T_s (ψ) and $g(\psi)$ is 1. Ψ_c denotes the width of the field of vision at a receiver. By using the gain Eq. (5) and the geometry of the link in Fig. 2, the gain equation can be modifying as

$$G_{\text{ia}}(z) = \frac{(m+1)}{2\pi} A_{\text{pd}} h^{(m+1)} \left((l_x + \text{ia})^2 + l_y^2 + h^2\right)^{\frac{-(m+3)}{2}} \tag{6}$$

In [5], by using the gain equation, the signal to interference plus noise ratio, when height is constant and PD moves in x and y direction is given by,

$$\gamma(z) = \frac{\left(z^2 + h^2\right)^{-m-3} \rho(D_0)}{\sum_{-\infty \backslash 0}^{+\infty} \left((z_x + \text{ia})^2 + z_y^2 + h^2\right)^{-m-3} \rho(D_{\text{ia}}) + \Omega} \tag{7}$$

where Ω is given as:

$$\Omega = \frac{4\pi^2 N_0 W}{P_0^2 (m+1)^2 A_{\text{pd}}^2 R_{\text{pd}}^2 h^{2m+2}}$$

Table 5 Simulation parameter

Parameter	Seating position (m)	Standing position (m)
l_x, l_y	0.25	0.25
h	2.050	2.050
l_z	0.69	1.28
n	0.75	0.75

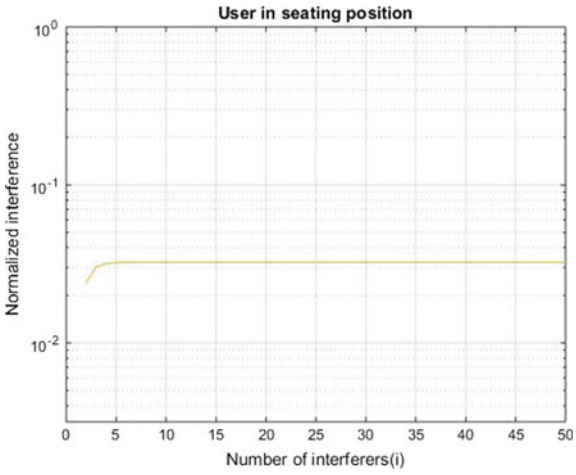

Fig. 7 Graph showing the normalized interference variation with interfering LED when $h = 2.075$ and $zz = 0.69$

In metro, the passenger can move in x and y directions and the height (z-direction), also different for different passenger. And passenger can be in seating and standing positions in metro. So the normalized interference term $I_\infty(z)$ from Eq. 7 after consideration of above situation is given as

$$I_\infty(z) = \sum_{-\infty\backslash 0}^{+\infty} \left((l_x + \text{in})^2 + l_y^2 + (h - l_z)^2\right)^{-m-3} \tag{8}$$

where h is the height from LED access point to floor and l_z is the variation in height according to the position of passenger. Further, we show the graphical analysis of interference by using MATLAB. The simulation parameter for analysis is given (Table 5 and Figs. 7 and 8).

7 Challenges

The installation of Li-Fi in metro does face some challenges. Some of them are discussed in this section.

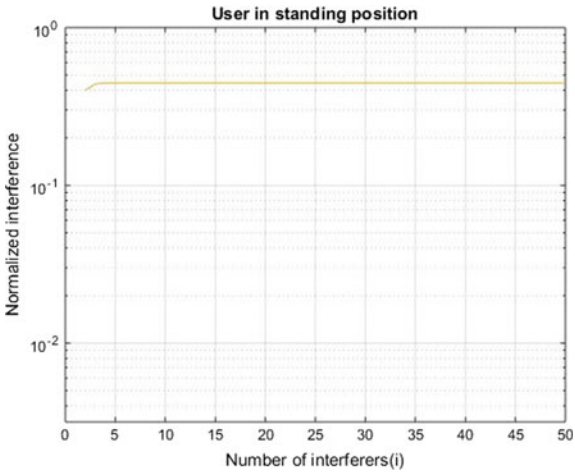

Fig. 8 Graph showing the normalized interference variation with interfering LED when $h = 2.075$ and $zz = 1.28$

Noise sources including sunlight and ambient light which is not capable for VLC is the challenges faced by Li-Fi technology. The ground-to-metro communication in higher mobility is also a big challenge in Li-Fi. A lot of research has been carried on that. In [9], a free-space optical ground-to-train communications system is proposed which consists of optical transceivers placed on the train and along the railway track. The complexity and the cost involved in integrating this technology in an existing infrastructure of metro trains is another challenge. These some challenges are to be overcome before this technology can be fully employed.

8 Conclusion

The results are analyzed in terms of interference analysis with different positions of user and illumination analysis inside metro saloon. The illumination level is more just below the LED, as height is increased, means the user in seating or standing position, illumination will change. Passenger in standing position gets more illumination than passenger in seating position. The illumination level will decrease with respect to distance. If a passenger moves toward LED, he will get more illumination and if he goes beyond, the illumination will get decrease. The interference value will become constant as the interfering LEDs will increase due to the limited field of view of detector. The effect of the last LEDs on the PD below the first LED will be negligible.

The significance of Li-Fi in metro is that it will provide huge bandwidth (300 THz), power consumption will be less due to LED, there is no electro–magnetic interference in VLC like RF communication, and passengers do not have to worry about Wi-Fi dead spots. They will get signal wherever visible light can reach.

References

1. Ahfayd MH, Farhat ZA, Sibley MJN, Mather PJ, Lazaridis PI (2018) Selection of high power LEDs for Li-Fi applications. Consum Electr, IEEE Trans 51:1950–1958
2. Prajapati A, Rawal D, Patel PN, MishraV (2014) Design and deployment of Wi-Fi service inside running metro trains. In: 2014 2nd international conference on emerging technology trends in electronics, communication and networking
3. Arriola A, Briso C, Moreno J, Echeverria E (2017) Characterization of an outdoor-to-indoor wireless link in metro environments at 2.6 GHz. In: 2017 15th international conference on ITS telecommunications (ITST)
4. Ahamed BS (2016) Visible light communication in railways. In: The international conference on railway engineering (ICRE)
5. Surampudi A, Ganti RK (2018) Interference characterization in downlink Li-Fi optical attocell networks. J Lightwave Technol 36(16)
6. Fathi-Kazerooni S, Kaymak Y, Rojas-Cessa R, Feng J, Ansari N, Zhou M, Zhang T (2018) Optimal positioning of ground base stations in free-space optical communications for high-speed trains. IEEE Trans Intell Transport Syst 19(6)
7. Sinnadurai R, Ahamed Khan MKAA, Azri M, Vikneswaran (2012) Development of white LED down light for indoor lighting. In: 2012 IEEE conference on sustainable utilization and development in engineering and technology
8. Komine T, Nakagawa M (2004) Fundamental analysis of visible light communication using LED lights. IEEE Trans Consum Electr 50(1)
9. Paudel R, Minh HL, Ghassemlooy Z, Rajbhandari S (2010) High speed short range optical wireless ground-to-train communications. In: The 11th annual postgraduate symposium on the convergence of telecommunications, networking and broadcasting (PGNet), Optical Communications Research Group, Northumbria University, pp 1–5

Throughput Maximization in High-Speed Train Using Hybrid RF/FSO Communication System

Ankita Chauhan and Pankaj Verma

Abstract The increasing demand of high-speed Internet in railway communication is not fully accomplished by radio frequency (RF) technology and free-space optical (FSO) technology when considered independently. Hence, a hybrid RF/FSO scheme in high-speed trains is proposed, where RF link can be used as a backup link in case of poor visibility. The throughput of integrated RF/FSO system is compared with the free-space optical and RF system individually. The performance of the system is analyzed through analytical results. In results, the performance of the integrated RF/FSO system is five times better when compared to RF system or FSO system independently.

Keywords High-speed trains · Free-space optical communication · Hybrid RF/FSO network · Switching system

1 Introduction

High-speed trains (HSTs) have become global choice of transportation (HSTs) for a large number of long-distance travelers. Currently, the HST has attained the highest speed of 500 km/h [1]. The increase in the use of Internet-connected digital devices poses a large demand for reliable and fast Internet access in high-speed trains. To support these demands of wireless communication applications, there is perpetual need of higher bit rates to drive the developing technologies in the field of wireless optical communication (WOC) and millimeter wavelength radio frequency (MMW-RF). The WOC can be further categorized as free-space optical (FSO) communications, visible light communications (VLC), and ultra-violet (UV) communications. The FSO technology is widely used for symbol transference due to higher bit rate, higher transmission reliability, large unlicensed spectrum, cheaper and speedy deployment [2, 3]. Due to high velocity of the train, the system capacity or throughput of free-space

A. Chauhan (✉) · P. Verma
Department of Electronics and Communication Engineering, National Institute of Technology Kurukshetra, Haryana, India

P. Verma
e-mail: pankaj@nitkkr.ac.in

V. Janyani et al. (eds.), *Optical and Wireless Technologies*, Lecture Notes in Electrical Engineering 648, https://doi.org/10.1007/978-981-15-2926-9_27

optical systems for high-speed trains may be much lower than stationary point-to-point (P2P) free-space optical communication system [4]. However, FSO technology cannot replace current RF communication systems. The requirement of line of sight limits the implementation of FSO links [5, 6]. An attractive solution is to build a wireless system including both FSO and reliable lower-rate RF links, forming hybrid FSO/RF communication systems. This paper discusses the hybrid FSO/RF system in HSTs using FSO and MMW-RF communication technologies. Both the technologies FSO and MMW-RF offer huge capacity (up to a few Gbps) by operating in the unlicensed free-space optical band and 70 GHz frequencies, at very small cost [7–9]. Although both links have many common features, they are not affected in the same way in case of weather and meteorological conditions [10]. For FSO link, fog is the main attenuation factor and rain does not cause much effects, similarly RF links (70 GHz) can withstand with heavy rain condition and fog does not cause any particular effect [8, 10]. The adjunct nature of MMW-RF and FSO links led to various approaches in hybrid RF/FSO information transmission systems. Such type of system maintains the high data rate transmissions as well as shows excellent data link reliability and performance in all weather condition. To analyze the performance of this system, two types of switching have been used; first individual switching and second integrated switching. Individual switching schemes are defined by, when to switch between the two links for different visibility condition to obtain maximum capacity. In this scheme, total available power is utilized by one link (either FSO or RF) [11–15]. Authors in [11] obtain the error probability and throughput expression for the hybrid RF/FSO scheme with two levels of threshold. In a time-varying fading channel, for hybrid RF/FSO link, the authors in [12] present a closed-form throughput expression. In [13], the feasibility of RF/FSO is investigated and hybrid link with the different decoders and encoders is considered. In [14], data rate and link reliability of hybrid FSO/RF scheme are considered. Hybrid RF/FSO communication system can also be established by multiplexing the data over both the links (FSO and RF) for high-speed trains (HSTs). But, in above case, the power is equally divided between both FSO and RF link. This is also called integrated switching [16–18].

In this paper, we have analyzed the performance of hybrid RF/FSO communication system in HST. The system contains rotating transceiver to minimize the impact of handover and to combat the effect of atmospheric conditions. Our contribution in this work is as follows:

1. In this paper, rotational transceivers installed on the ground base stations and on top of the train to increase the effective coverage area of every ground base station.
2. Different switching methods for the high-speed train hybrid RF/FSO communications system have been used. Three transceivers are installed on the train (one is rotating and two are fixed). During handover, fixed transceiver (FSO system) is used to switch from source to target base station and rotating transceiver (FSO/RF link) is used to make continuous link between ground and train. Thus,

the users sitting inside the train do not face handover problem. On the other side, visibility which is less then RF link on the train is used to communicate with the ground base station.

3. Performance of integrated RF/FSO scheme with RF and FSO link is compared.
4. The MATLAB simulator is used to justify the result.

Further, the manuscript is categorized as follows. In Sect. 2, network architecture of HSTs is introduced. The system model for the hybrid RF/FSO scheme is introduced in Sect. 3. Section 4 presents the simulation results, followed by the conclusion in Sect. 5.

2 Network Architecture of High-Speed Train

Figure 1 shows stratified two-hop network architecture, consisting of radio frequency/free-space optical transceivers and used to provide high-speed data connection for high-speed train. Inside the train, the handheld devices are connected to access point and access points are further connected to mobile router by fiber optic link. Mobile router and three transceivers (rotating RF/FSO transceiver and fixed transceiver) are connected to the central controller (CC) of the rail via fiber link. CC is liable for controlling the system to maximize the performance of the network. The three transceivers (two fixed and one rotating) are fixed at the same place and position on the train. So, ME, MR, APs, CC, and three transceivers create a mobile

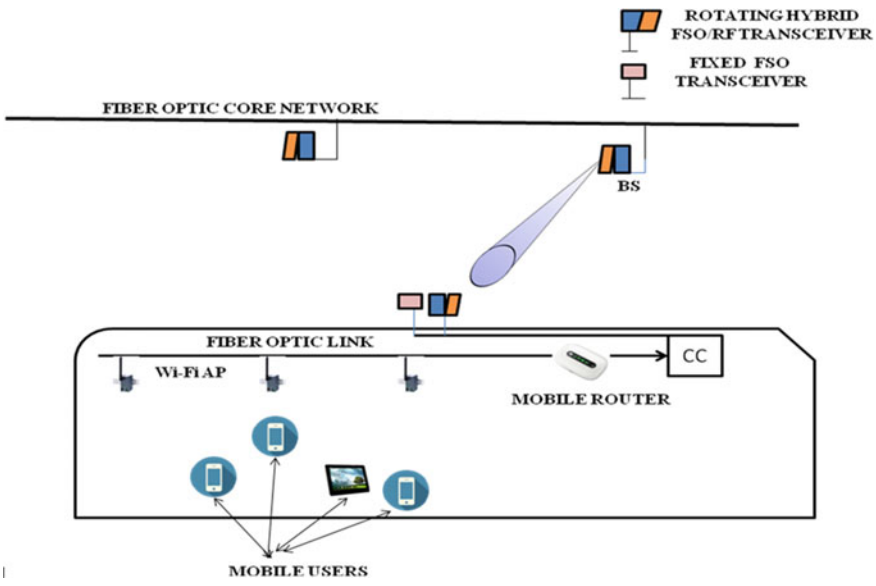

Fig. 1 Network designing of HST

network. Every base station located near the railway track is connected to a rotating transceiver (one FSO and one RF). When HST moves along the railway track and weather is clear then FSO is used to connect to the base station otherwise RF is used.

3 System Model for Hybrid RF/FSO System

3.1 Power Allocation for the Individual Switching Scheme

In this case, the power is fully drained either on the radio frequency (RF) link or on free-space optical (FSO) link (Fig. 2).

3.1.1 Power Allocation for FSO System

We first develop the system model in which radio frequency link used as a backup link when the quality of the free-space optical link degrades. In the individual scheme, at any given time instant, only one link (either FSO or RF) is in on mode and the other one is in idle mode. Received signal for the FSO link can be written as [11]

$$\psi_0 = RX_0J + N_0 \tag{1}$$

Here, J denotes the information symbol having average power V_t^0, N_0 is additive white Gaussian noise (AWGN) with mean zero and standard deviation Δ_{n0}, and responsivity of the receiver is represented by R which is assumed to be 1. X_0 is the intensity gain and it is defined as

$$X_0 = X_{f0}X_{l0} \tag{2}$$

where X_{f0} and X_{l0} are the atmospheric turbulence and path loss-induced fading coefficients. The path loss-induced fading coefficient can be written as

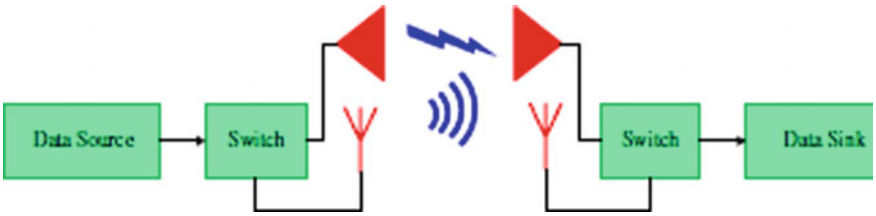

Fig. 2 Individual FSO/RF switching system

$$X_{l0} = \left(\text{erf}\left(\frac{\sqrt{F}}{\psi Z}v\right)\right)^2 \text{e}^{-\mu_0 Z} \tag{3}$$

where $F = \frac{\pi D^2}{4}$ is the aperture area of the receiver having the diameter denoted by D, velocity of the train denoted by v, divergence angle of the beam is denoted by ψ (in radian), link distance is denoted by Z in km, and weather-dependent coefficient is denoted by μ_0 in km^{-1} given by

$$\mu_0 = \frac{3.91}{L}\left(\frac{\gamma_1}{\gamma_0}\right)^{-q} \tag{4}$$

Here, L denotes the detectable or visibility distance (in km), optical wavelength is represented by γ_1 (in nm), γ_0 is reference wavelength whose value is 550 nm, and q is a function which depends upon visibility range and obtained by

$$\begin{array}{c} q = L - 0.5 \quad 0.5 \le L \le 1 \\ 0.16L + 0:34 \quad 1 \le L \le 6 \end{array} \tag{5}$$

Parameter X_{f0} is a random variable having gamma distribution, i.e.,

$$y_{X_{fo}}(X_{fo}) = \frac{2cd^{\frac{c+d}{2}}}{\Gamma(c)\Gamma(d)} X_{fo}^{\frac{c+d}{2}-1} k_{c-d}\left(2\sqrt{cdX_{fo}}\right) \tag{6}$$

$k_p(.)$ is modified second-order Bessel function of order '*p,*' gamma function is denoted by $\Gamma(.)$, and parameter c and d are atmospheric-dependent random variable [19]

$$c = \left[\exp\left(\frac{0.49\Delta_d^2}{1 + 1.11\Delta_d^{12/5}}\right) - 1\right]^{-1} \tag{7}$$

$$d = \left[\exp\left(\frac{0.51\Delta_d^2}{\left(1 + 0.69\Delta_d^{12/5}\right)^{5/6}}\right) - 1\right]^{-1} \tag{8}$$

where Δ_d^2 is the Raytov variance and the SNR of the FSO link received at the receiver can be written as

$$\text{SNR} = \frac{R^2 V_t^0 X_0^2}{\Delta_{n0}^2} \tag{9}$$

3.1.2 Power Allocation for RF System

Received signal for the RF scheme is written as

$$\Psi_0 = X_R J + N_R \tag{10}$$

Here, J denotes the information symbol having average power V_t^R and N_R is AWGN with mean zero and variance Δ_{nR}^2. X_R is the channel coefficient which can be written as

$$X_R = \sqrt{X_{lR} X_{fR}} \tag{11}$$

In which X_{lR} and X_{fR} are the path loss coefficient and channel fading coefficient having Rayleigh distribution, respectively, and X_{lR} can be written as

$$X_{lR} = S_t + S_R - 20\log_{10}\left(\frac{4\pi Z v}{\gamma_R}\right) \tag{12}$$

S_R and S_t are the receiver and transmitter antennas gain, respectively, and Z is the separation between receiver and transmitter (km), v is the velocity of the train, and wavelength of RF channel is represented by γ_R.

3.2 *Power Allocation for the Integrated FSO/RF Switching Scheme*

Overall bit rate of the integrated RF/FSO scheme is defined by [20] (Fig. 3)

$$C = \rho_0 C_0 + \rho_R C_R \tag{13}$$

in which C_R and C_0 are the bit rates of RF and FSO channels defined as

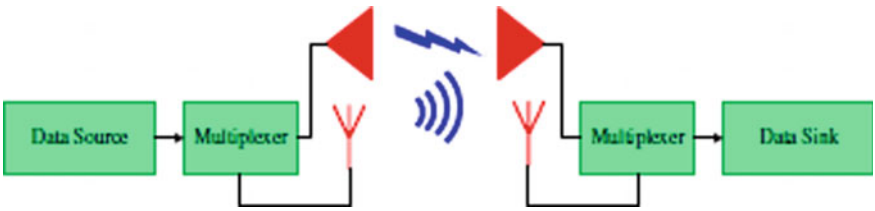

Fig. 3 Integrated FSO/RF switching system

$$C_0 = B_0 \log_2\left(1 + \frac{V_t^0 X_0^2}{\Delta_{n0}^2}\right) \tag{14}$$

$$C_R = B_R \log_2\left(1 + \frac{V_t^R X_R^2}{\Delta_{nR}^2}\right) \tag{15}$$

ρ_0 and ρ_R can be 0 or 1 depending upon which link is active at that time instant.

4 Simulation Result

This section aims to present analytical and numerical results of the system described in Sect. 3. We developed a MATLAB code to study the performance evaluation of the defined network. In Table 1, we discuss the necessary relevant parameters for RF and FSO systems [13].

Results are obtained for all links FSO, RF, and integrated FSO/RF individually. We consider a point-to-point (P2P) integrated RF/FSO system, and the separation between the receiver and the transmitter is denoted by Z and bandwidth of FSO system is assumed to be 1 Gbps and for RF channel it is 100 Mbps and velocity of the train is assumed to be 350 km/hr.

Table 1 Parameters of RF and FSO subsystems

FSO subsystem		
Parameter	Symbol	Value
Wavelength	γ_1	1550 nm
Beam divergence angle	Ψ	2 mrad
Noise variance	Δ_{n0}^2	10^{-14} A^2
Receiver aperture diameter	D	20 cm
Refractive index structure parameter	C_n^2	10^{-15} m$^{\frac{3}{2}}$
Responsivity	R	1 A/W
RF subsystem		
Noise PSD	Δ_{nR}^2	−114 dB/MHz
Receiver antenna gain	S_R	44 dBi
Bandwidth	B_R	100 MHz
Transmitter antenna gain	S_t	44 dBi
Carrier frequency	f_c	60 GHz

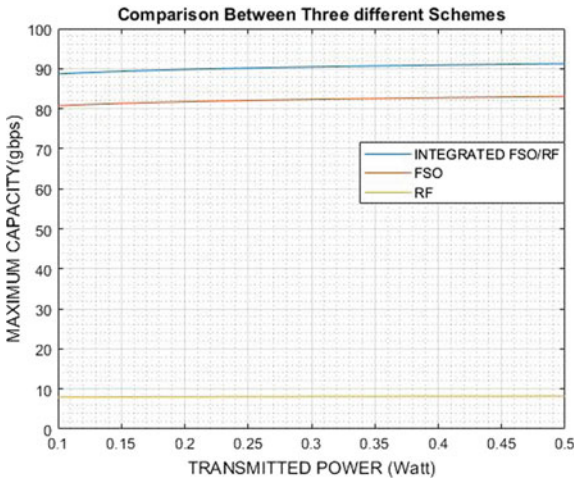

Fig. 4 Maximum capacity versus transmitted power for different schemes (for $Z =$ 3 km and visibility $= 5$ km)

4.1 Comparison Between Three Different Schemes for Same Distance

As shown by the graph, the maximum capacity for the integrated RF/FSO system is greater than that of individual case. This graph is plotted for fairly good visibility and the value for 'L' is assumed to be 5 km. For a given visibility condition, integrated FSO/RF system always outperforms the individual system (Fig. 4).

4.2 Comparison Between Three Different Schemes for Same Transmitted Power

As shown by the graph, when the value of Z (distance between receiver and transmitter) increases, the maximum capacity for all schemes decreases. The maximum capacity of the integrated RF/FSO system is greater than other two schemes. For a fairly good visibility condition ($L = 5$ km), there is a little difference between integrated RF/FSO system and FSO system.

5 Conclusion

The complementary nature of millimeter wavelength radio frequency link and free-space optical link led to various ways in developing the hybrid RF/FSO system for transmission of data. Power allotment problem for both the cases (for individual link and for integrated FSO/RF link) is discussed in this paper. Mathematical results tell

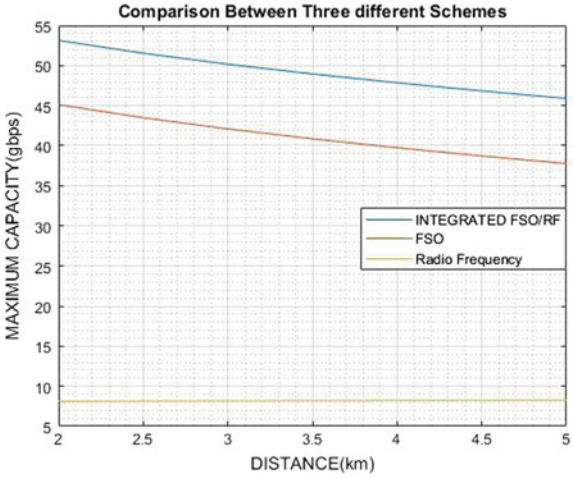

Fig. 5 Maximum capacity versus distance for different schemes (for $V_t = 0.5$ W and visibility = 5 km)

that the supremacy of the integrated RF/FSO system over the individual system is so remarkable such that the integrated FSO/RF scheme always defeats individual system for visibility as poor as five times lower than individual system (Fig. 5).

References

1. Top ten fastest trains in the world, http://www.railwaytechnology.com/features/feature-top-ten-fastest-trains-in-the-world/. Accessed 01 May 2016
2. Jagadeesh VK, Ansari IS, Palliyembil V, Nathan PM, Qaraqe KA (2016) Channel capacity analysis of a mixed dual-hop RF-FSO transmission system with Málaga distribution. IET Commun 10(16):2119–2124
3. Rakia T, Yang H-C, Alouini M-S, Gebali F (2015) Outage analysis of practical FSO/RF hybrid system with adaptive combining. IEEE Commun Lett 19(8):1366–1369
4. Urabe H et al (2012) High data rate ground-to-train free-space optical communication system. Opt Eng 51(3):031204
5. Ansari IS, Yilmaz F, Alouini M-S (2016) Performance analysis of free-space optical links over Málaga (M) turbulence channels with pointing errors. IEEE Trans Wireless Commun 15(1):91–102
6. Tang Y (2013) Hybrid free space optical and RF wireless communication. University of Virginia, Ph.D. dissertation, Department of Electrical Engineering
7. Giannetti F, Luise M, Reggiannini R (1999) Mobile and personal communications in the 60 GHz band: a survey. Wirel Pers Commun 10:207–243
8. Andrews L, Philips RL, Hopen CY (2001) Laser beam scintillation with applications. SPIE Press
9. Farid AA, Hranilovic S (2007) Outage capacity optimization for free-space optical links with pointing errors. J Lightwave Technol 25(7):1702–1710
10. Wu H, Kavehrad M (2007) Availability evaluation of ground-to-air hybrid FSO/RF links. Int J Wir Inf Netw 14(1):33–45
11. Li J, Uysal M (2003) Optical wireless communications: system model, capacity and coding. In: IEEE vehicular technology conference, pp 168–172

12. Chatzidiamantis ND, Karagiannidis GK, Kriezis EE, Matthaiou M (2011) Diversity combining in hybrid RF/FSO systems with PSK modulation. In: International conference on communication (ICC), pp 1–6
13. Kazemi H, Uysal M, Touati F (2014) Outage analysis of hybrid FSO/RF systems based on finite-state markov chain modeling. In: 3rd international workshop in optical wireless communications (IWOW), IEEE, pp 11–15
14. Abadi MM, Ghassemlooy Z, Zvanovec S, Bhatnagar MR, Wu Y (2017) Hard switching in hybrid FSO/RF link: investigating data rate and link availability. In: IEEE, ICC workshops, pp 463–468
15. Sharma S, Madhukumar AS, Swaminathan R (2018) Switching-based hybrid FSO/RF transmission for DF relaying system. In: IEEE wireless communications and networking conference (WCNC), pp 1–6
16. Eslami A, Vangala S, Pishro-Nik H (2010) Hybrid channel codes for efficient FSO/RF communication systems. IEEE Trans Commun 58(10):2926–2938
17. Wu Y, Yang Q, Park D, Kwak KS (2017) Dynamic link selection and power allocation with reliability guarantees for hybrid FSO/RF systems. IEEE Access 13654–13664
18. Khan MN, Gilani SO, Jamil M, Rafay A, Awais Q (2018) Maximizing throughput of hybrid FSO-RF communication system: an algorithm. IEEE Access 30039–30048
19. Karimi M, Uysal M (2012) Novel adaptive transmission algorithms for free-space optical links. IEEE Trans Commun 1808–3815
20. Moradi H, Falahpour M, Refai HH, LoPresti PG, Atiquzzaman M (2010) On the capacity of hybrid FSO/RF links. In: Global telecommunications conference (GLOBECOM), pp 1–5

A Miniaturized Printed UWB Antenna with Sextuple Stop Bands Based on U-Shaped Slot Resonators and Split Ring Resonators for IoT Applications

Avichal Sharma, Priyanka Agrawal, Nikhil Mishra, Saurav Kumar Sinha and Mayur S. Raut

Abstract In this paper, a miniaturized modified UWB antenna operating at sextuple rejection bands for use in Device-to-Device communication, wireless sensor networks, microwave imaging sensing applications, and Internet of things (IoT) is presented. This paper proposes a design inseminating four U-shaped rectangular slot resonators on the radiating patch and placing two split-ring resonators (SRR) near the 50 Ω. Crostrip feed line-patch junction of the traditional stair-cased ultra-wideband (UWB) antenna. The proposed antenna is printed on a low profile substrate Rogers RO5880 with dielectric constant 2.2. The simulated and measured results show that the traditional ultra-wideband (UWB) antenna specimen delivers a wide impedance bandwidth from 3 to 10 GHz. The presented antenna design possesses eminent return loss performance (-15 dB < S11 < -35 dB) for all operating frequencies and high rejection characteristics across all stop bands with an omnidirectional farfield radiation pattern (6.22 & 7.75 GHz) and good radiation efficiency (80% Typ.) over the entire frequency band except at the stop bands due to SRR & CSRR technique implementation in reference antenna; Furthermore, radiation patterns, surface current distributions, reflection coefficient and VSWR (1 < VSWR < 2) of the proposed antenna at the corresponding center frequencies of the operating bands are delineated in the paper.

Keywords Sextuple rejection bands · Slot resonator · Split ring resonator (RSRR) · Omnidirectional · Frequency notching · Internet of things (IoT) · UWB

A. Sharma · P. Agrawal
ZinZout Teletech, Pune, India
e-mail: avichal.sharma@zinzouteletech.com

P. Agrawal
e-mail: priyanka.agrawal@zinzouteletech.com

N. Mishra (✉) · S. K. Sinha · M. S. Raut
Sinhgad Institute of Technology, Lonavala, India

M. S. Raut
e-mail: mraut.sit@sinhgad.edu

V. Janyani et al. (eds.), *Optical and Wireless Technologies*, Lecture Notes in Electrical Engineering 648, https://doi.org/10.1007/978-981-15-2926-9_28

1 Introduction

With the advent of UWB technology, new doors have been unlatched for exponentially growing wireless communication systems. In 2002, U.S. Federal Communication Commission (FCC) authorized 7.5 GHz bandwidth ranging from 3.1 to 10.6 GHz. Since then ultra-wideband (UWB) systems has been commercially deployed in fields of wireless communication systems, imaging radar and localized systems because of wide impedance bandwidth, high gain radiation characteristics, high channel capacity, low power spectral density with high data rates [1, 2]. Wideband antennas has become an appealing challenge in research and development of wireless communication systems [3]. Among the UWB Antenna systems in the recent literature survey, experiments has been conducted using a low-profile small microstrip monopole [4] planar antenna technology along with defected or partial ground structures to extend bandwidth and performance making it usable for device to device (D2D) communication, IoT based applications, microwave image sensing applications and bio-medical applications (early-stage cancer detection) [5] and WBAN systems etc. [6, 7]. Several miniaturized CSRR to CSRR coupled quad-notch band based UWB antenna was proposed to obtain rejection bands [8] at multiple wireless applications including WiMAX, WLAN, 4G/LTE and ITU 8 GHz frequency bands.

In this work, a highly compact 50 Ω microstrip-line fed printed sextuple ultra-wideband (UWB) antenna using a combination of the U-shaped slot resonators evolved from complementary split ring resonators and the split-ring resonator (SRR) [9] for rejecting the WiMAX, INSAT, lower WLAN, upper WLAN, and ITU 8 GHz wireless communication frequency bands [10, 11]. For the initial design, a traditional stair cased design reference UWB antenna is designed and fabricated to operate within the desired 3.1–10.6 GHz UWB frequency band. Then, the reference UWB antenna is modified for the proposed sextuple band-notched UWB antenna to reject the 3.55, 4.55, 5.25, 5.75, and 8.25 GHz bands for WiMAX, INSAT, lower & upper WLAN, and ITU Telecommunication 8 GHz frequency bands, respectively. To optimize the dimensions of the SRR and RCSRR based U-shaped slot resonators, a commercially available 3D-EM software, CST Microwave Studio is used. The proposed antenna design with sextuple stop bands is fabricated, and the measurements are presented for the verification. Finally, the design process in relation to the return loss, VSWR, antenna farfield gain, farfield directivity, surface current density and radiation pattern are described in detail. Sextuple frequency stop band operation at 3.50, 5.25, 5.75, 7.55, and 8.25 GHz frequency bands of the proposed antenna design has been achieved by amending the UWB characteristics achieved in the proposed system because of introducing U-shaped slot resonators and Rectangular Complementary Single Split Ring Resonators on the top side of the substrate plane, the proposed antenna size is quite miniaturized ($29 \times 30 \times 0.8$ mm^3) for use in portable IoT applications.

The remaining of this paper is organized as follows. In Sect. 2, the geometrical analysis and design approach for designing proposed antenna is presented and

discussed in detail. Also, performance and discussion of simulated results are discussed in detail. Section 3 reviews measurement setup and experimental results of the proposed and the reference UWB antenna, with conclusions is drawn in Sect. 4.

2 Antenna Design

The structural design of the proposed UWB antenna starts with the use of traditional stair cased structured reference UWB antenna as the radiating element to operate within the desired UWB frequency band. The structure of proposed antenna design is fabricated on Rogers RO5880 substrate with thickness 0.8 mm, relative permittivity of 2.2 and loss tangent tanδ of 0.0009 as shown in Fig. 1. A modification has been done to the traditional UWB antenna to efficiently notch the interfering frequency bands that fall within the operating UWB frequency band.

The objective is to obtain rejection bands at 3.55, 4.55, 5.25, 5.75, and 8.25 GHz bands for a conventional UWB antenna with U shaped slots and rectangular split-ring resonator (RSRR) for rejecting the WiMAX, INSAT, lower WLAN, upper WLAN, and ITU 8 GHz frequency bands.

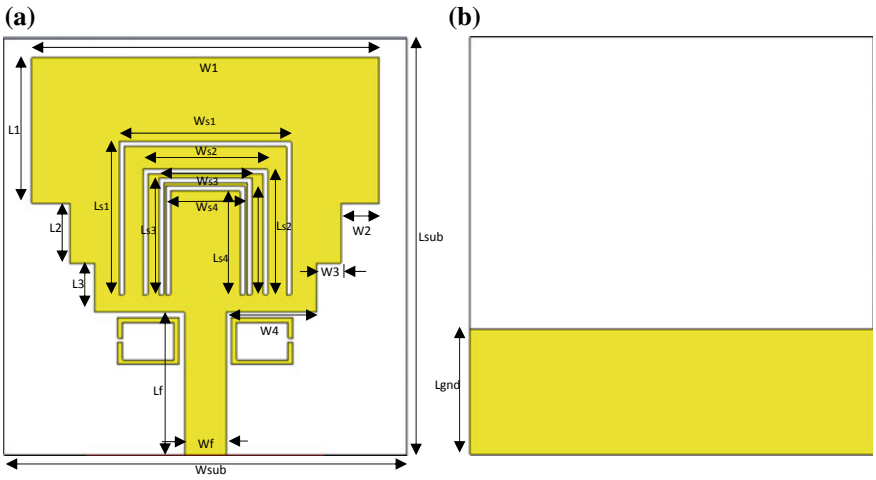

Fig. 1 Proposed antenna geometry layout **a** front view, **b** rear view

2.1 Design Equations for the U-Shaped Slot Resonator and Ring Resonator

For the initial design of the Rectangular CSRR on patch plane, the length *La* and width *Wa* in Fig. 1a [4, 12], the desired notched band frequency (f_{notch}) design equations are given by Eq. (1):

$$La + 2Wa = \frac{\lambda g}{2} + \frac{c}{2f_{\text{notch}}\sqrt{\varepsilon_{\text{eff}}}} \tag{1}$$

$$\varepsilon_{\text{eff}} = \frac{\varepsilon r + 1}{2} + \frac{\varepsilon r - 1}{2}\left(1 + \frac{12h}{wf}\right)^{-0.5} \tag{2}$$

where, λg is the guided wavelength at the desired frequency, εr is the relative dielectric constant of the substrate, f_{notch} is the desired stop band frequency, and c is the speed of light. The effective dielectric constant can be calculated from Eq. (2), where *Wf* is width of Microstrip feedline and *h* is the height of the substrate. Parametric simulations have been performed to obtain the optimal width of the Rectangular U-Shaped Slots. *Ws* equals 0.3 mm.

For the initial design of the Rectangular Single Ring SRR of horizontal axis length *Lx*, vertical axis length *Ly* and width of the SRR *Ws* in Fig. 1b, Eq. (3) has been used to calculate the desired notch frequency for the resonators:

$$2(Lx + Ly - 2Ws) = \frac{\lambda g}{2} = \frac{c}{2f_{\text{notch}}(2)\sqrt{\varepsilon_{\text{eff}}}} \tag{3}$$

where f_{notch} (2) is the desired resonant notched band frequency for the Rectangular U-shaped Slot Resonators, and λg is the guided wavelength at the desired frequency.

The dimensions of both reference and proposed antenna with description is listed in Table 1.

The prototype of the proposed antenna is also fabricated as shown in Fig. 2e.

2.2 Parametric Study

See Fig. 3(a–f).

Table 1 Antenna design specifications (according to Fig. 2)

Parameter	Value (mm)	Description	Parameter	Value (mm)	Description
*L*sub	30.00	Length of substrate	*Ws*1	12.40	Width of slot 1
*L*gnd	9.00	Length of ground	*Ws*2	9.00	Width of slot 2
*W*sub	29.00	Width of substrate	*Ws*3	6.70	Width of slot 3
Wf	3.00	Width of feed line	*Ws*4	5.90	Width of slot 4
Lf	10.30	Length of feed line	*Ls*1	11.00	Length of slot 1
*W*1	25.00	Width of patch 1	*Ls*2	9.00	Length of slot 2
*W*2	2.75	Width of patch 2	*Ls*3	8.40	Length of slot 3
*W*3	1.75	Width of patch 3	*Ls*4	7.80	Length of slot 4
*W*4	6.50	Width of patch 4	*Ws*	0.30	Slot thickness
*L*1	10.50	Length of patch 1	*Lx*	3.40	Width of CSRR
*L*2	4.30	Length of patch 2	*Ly*	4.40	Length of CSRR
*L*3	3.50	Length of patch 3	*g*1	0.30	Gap of CSRR

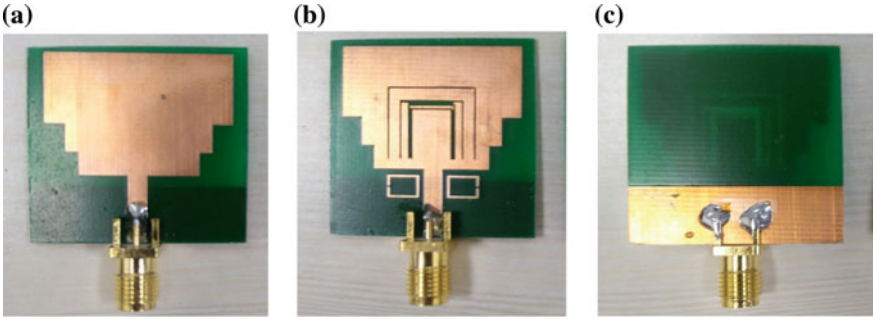

Fig. 2 Prototype of the reference and proposed antenna. **a** Traditional UWB antenna (front view); **b** Proposed antenna (front view); and **c** the reference and proposed antenna (rear view)

2.3 Experimental Results

2.3.1 Simulated Input Voltage Standing Wave Ratio (VSWR)

We have used commercially available EM solver Computer Simulation Technology MWS to optimize and characterize SRR and CSRR dimensions for better performance. The proposed sextuple band-notched UWB antenna is simulated using CST MWS simulator. VSWR (Voltage Standing Wave Ratio) of the presented antenna design is 1:2 for all operating frequencies at 3.0, 3.95, 4.90, 5.25, 6.22 and 7.75 GHz as depicted in Fig. 4a which reports minimum reflection coefficient and exceptional

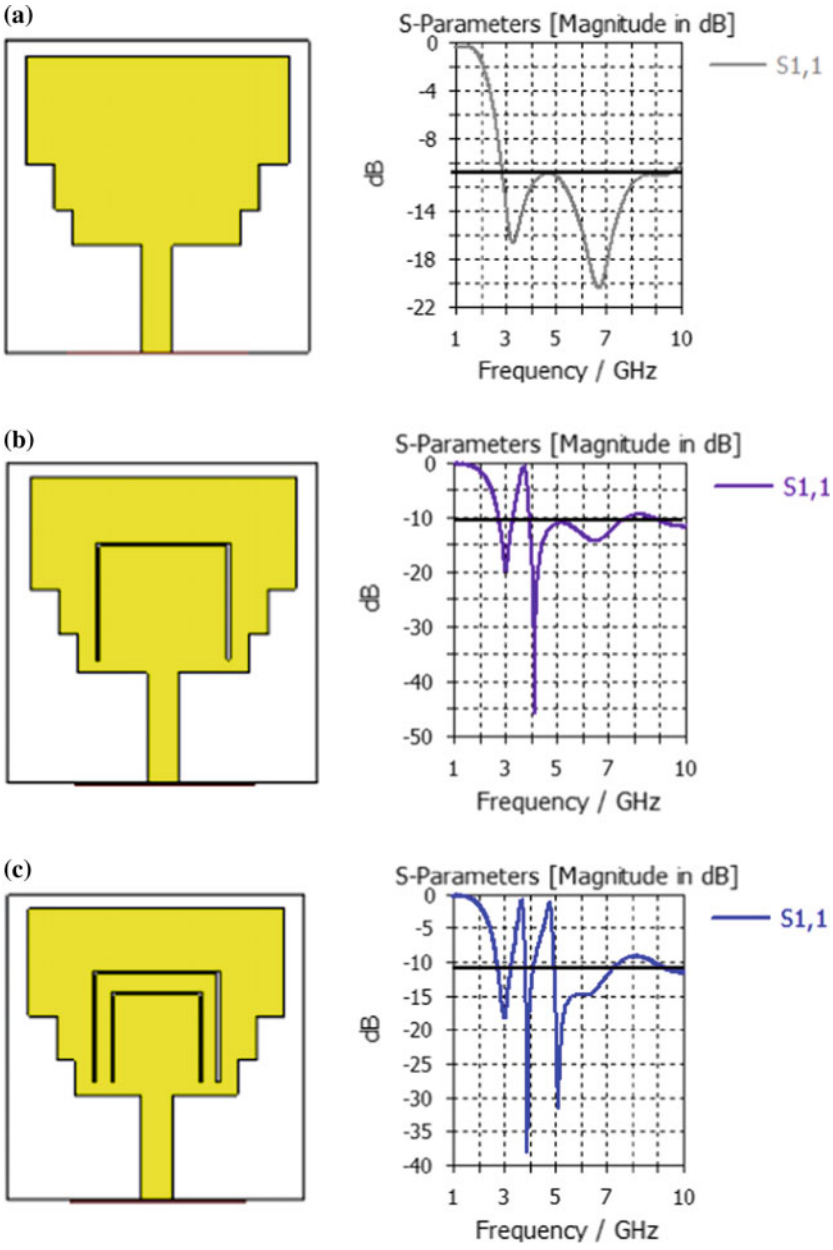

Fig. 3 Design steps of the proposed antenna with the corresponding reflection coefficient results at each stage. The left column shows the antenna structure under design at different stages **b** Step 1: adding notch at worldwide-interoperability for microwave-access (WiMAX; 3.50 GHz); **c** Step 2: adding notch at Indian National Satellite (INSAT; 4.55 GHz); **d** Step 3: adding notch at the lower wireless local area network (WLAN; 5.25 GHz); **e** Step 4: adding notch at upper WLAN (5.75 GHz); **f** Step 5: adding notch at ITU 8 GHz (8.25 GHz)

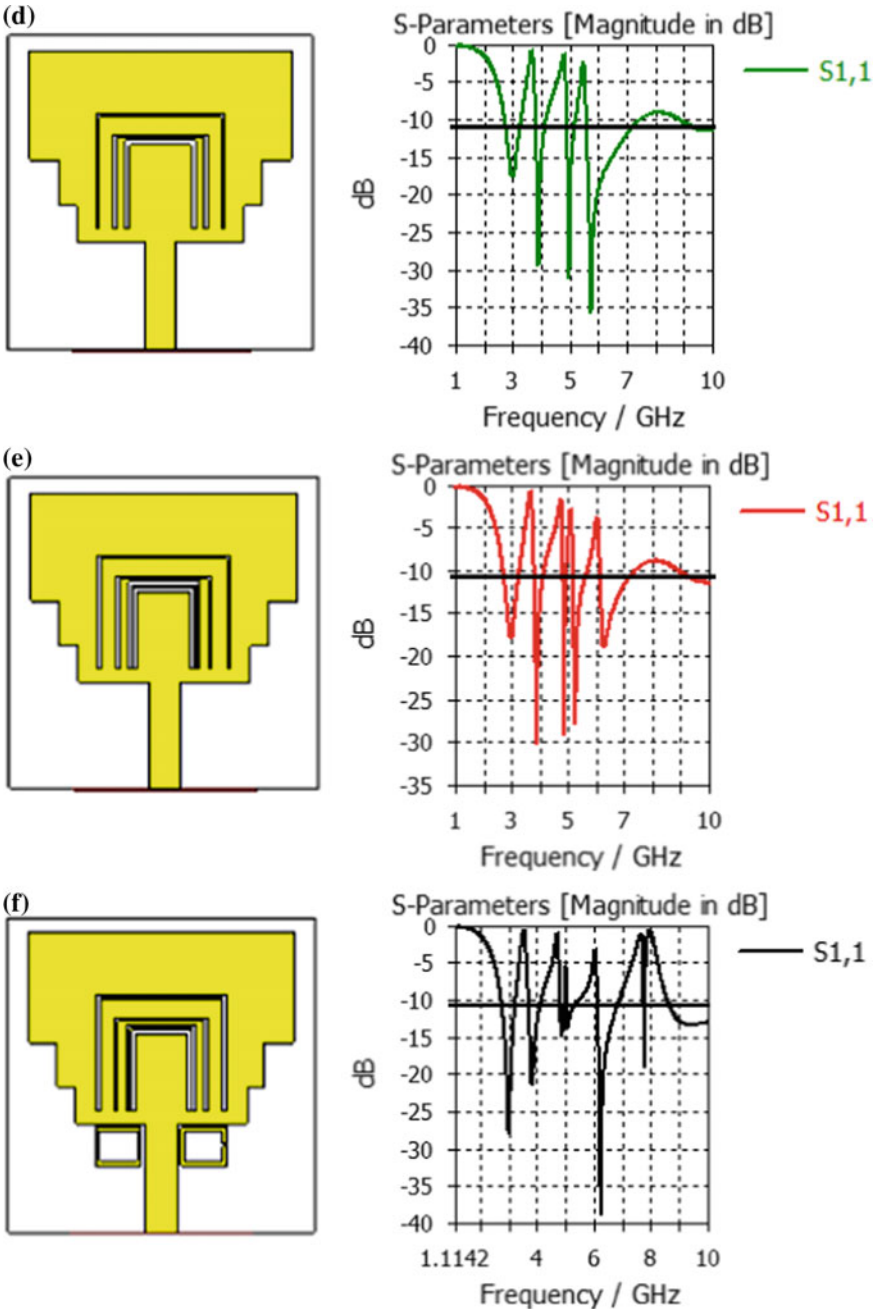

Fig. 3 (continued)

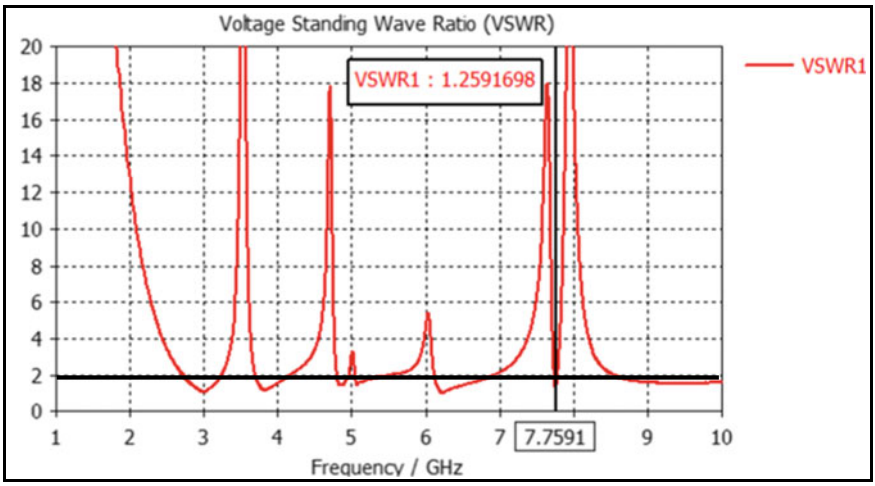

Fig. 4 Simulated VSWR of the presented sextuple band-notched UWB antenna

filtering characteristics for wireless applications including WiMAX, INSAT, lower & upper WLAN, and ITU 8 GHz frequency bands, respectively.

2.3.2 Antenna Farfield Gain & Directivity (Radiation Efficiency)

The simulated antenna farfield gain radiation efficiency and realized antenna gain are presented in Fig. 5c at 6.22 and 7.75 GHz frequency, which shows proper suppression occurs in the primary radiator represented by the antenna gain as well as at the antenna input in the form of the impedance mismatch at the notched bands. Also, simulated farfield directivity has been illustrated in 6d for the reference and proposed antenna at 6.22 and 7.75 GHz frequency.

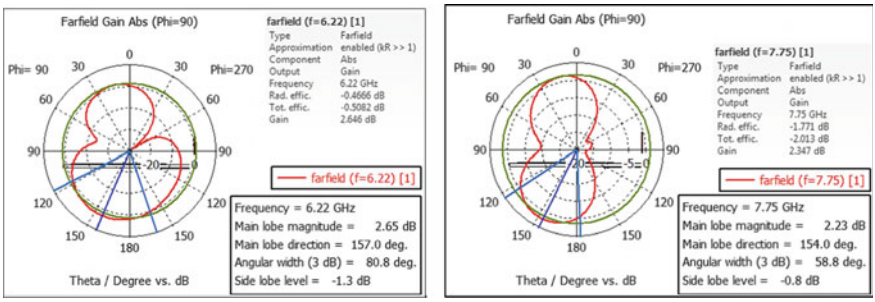

Fig. 5 Farfield radiation pattern & farfield gain measurement setup for the reference and proposed antenna at 6.22 and 7.75 GHz frequency

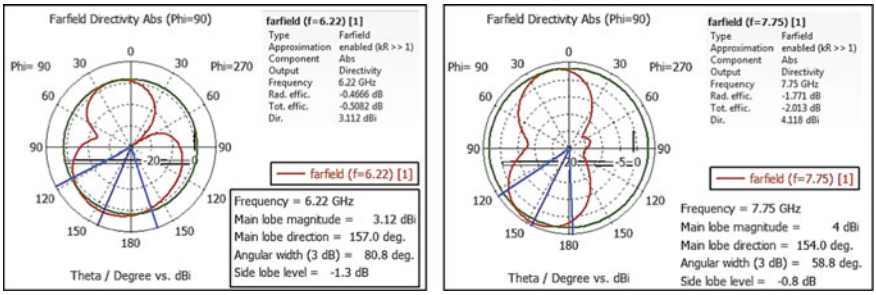

Fig. 6 Farfield radiation pattern & farfield directivity measurement setup for the reference and proposed antenna at 6.22 and 7.75 GHz frequency

2.3.3 Surface Current Distributions

To further evaluate the sextuple band-notching function resulting from R-CSRR based U-shaped slot resonators and RSRR, the surface current distributions for the proposed antenna have been simulated at 3.55, 4.55, 5.25, 5.75, and 8.25 GHz. As shown in Fig. 7b, notch band current density is more strenuous at slot

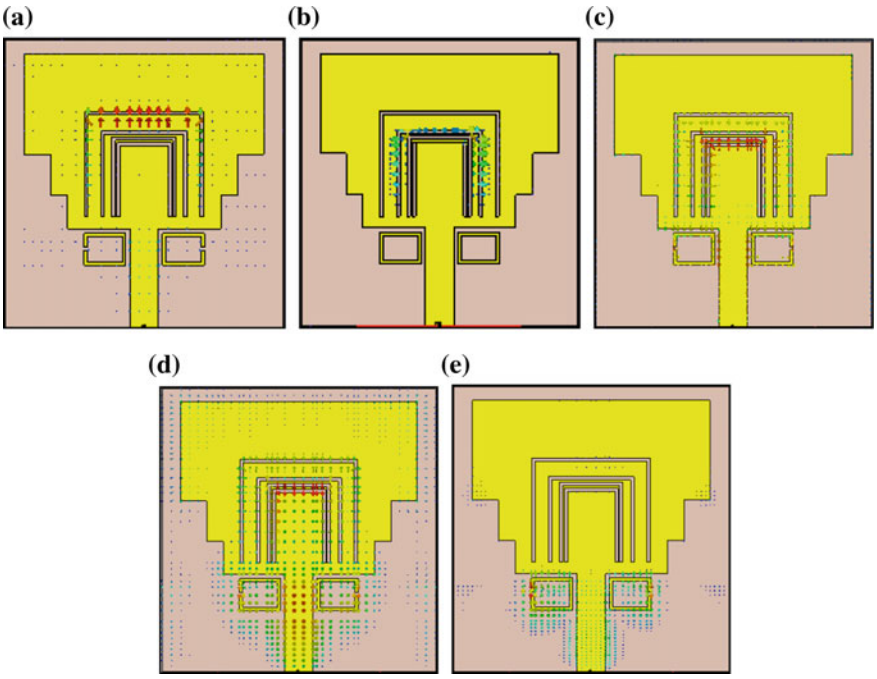

Fig. 7 Surface current distribution pattern of the proposed antenna at the corresponding center frequencies of the notched bands **a** 3.55 GHz; **b** 4.55 GHz; **c** 5.25 GHz; **d** 5.75 GHz; **e** 8.25 GHz

resonators which emanates drastic impedance mismatch around the resonant frequencies producing sextuple rejection bands in the spectrum.

3 Conclusion

In this work, a novel miniaturized sextuple-mode 50 Ω. crostrip-fed ultra-wideband (UWB) antenna with high rejection performances across all notch bands is proposed using four U-shaped rectangular slot resonators and two rectangular split-ring resonators (RSRR). By simply adjusting dimensions of U-shaped slots and RSRR, the six rejection bands have been allocated in the conventional UWB antenna at 3.50, 4.55, 5.25, 5.75, and 8.25 GHz with notched bands showing high rejection characteristics were measured using vector network analyzer (VNA) (Model No. VNA Master MS2025B, make Anritsu). The simulation results of the proposed antenna specimen from CST MWS were verified practically using Vector network analyzer. There is a slight frequency shift in the rejection bands of proposed antenna. The dimensions of the slots have been found to be a key tuning knob to achieve the desired notching frequencies. With such compact size, the simulated results of the proposed antenna correspond well with the measurements. The antenna possesses a roughly omnidirectional radiation pattern with a desired gain elimination at the notched-bands over the entire operating band. Hence, the proposed antenna will be the most suitable candidate to be used in Device to Device (D2D) communication, wireless sensor networks, and IoT applications.

Acknowledgements This work was supported by a grant-in-aid of ZinZout Teletech, Pune and Sinhgad Institute of Technology, Lonavala.

Conflicts of Interest: The authors declare no conflict of interest.

References

1. The Federal Communications Commission (2002) Revision of part 15 of the commission's rules regarding ultra-wideband transmission systems. The Federal Communications Commission, Washington, DC, USA
2. Chóliz J, Hernández Á, Valdovinos A (2011) A framework for UWB-based Communication and location tracking systems for wireless sensor networks. Sensors 11(9):9045–9068
3. Zhang J, Orlik PV, Sahinoglu Z, Molisch AF, Kinney P (2009) UWB systems for wireless sensor networks. Proc IEEE 97(2):313–331
4. Balanis C (2016) Antenna theory: analysis and design, 4th edn. Wiley, New Jersey, NJ, USA
5. Li X, Bond EJ, Van Veen B, Hagness S (2005) An overview of ultra-wideband microwave imaging via space-time beamforming for early-stage breast-cancer detection. IEEE Antennas Propag Mag 47(1):19–34
6. Valderas D, Sancho JI, Puente D, Ling C, Chen X (2010) Ultrawideband antennas: design and applications, 1st edn. Imperial College Press, London, UK

7. Lizzi L, Ferrero F, Monin P, Danchesi C, Boudaud S (2016) Design of miniature antennas for IoT applications. In: 2016 IEEE sixth international conference on communication
8. Rahman M, Ko D-S, Park J-D (2017) A compact multiple notched ultra-wide band antenna with an analysis of the CSRR-TO-CSRR coupling for portable UWB applications. Sensors 17(10):2174
9. Islam MT, Islam MM, Samsuzzaman M, Faruque MRI, Misran N (2015) A negative index metamaterial-inspired UWB antenna with an integration of complementary SRR and CLS unit cells for microwave imaging sensor applications. Sensors 15(5):11601–11627
10. Ali Z, Singh V, Singh A, Ayub S (2011) E-shaped microstrip antenna on Rogers substrate for WLAN applications. In: 2011 international conference on computational intelligence and communication networks
11. Zhu F, Gao S, Ho AT, Abd-Alhameed RA, See CH, Brown YW, Li J, Wei G, Xu J (2013) Multiple band-notched UWB antenna with band-rejected elements integrated in the feed line. IEEE Trans Antennas Propag 61(8)
12. Balanis C (2008) Modern antenna handbook. Wiley, New Jersey, NJ, USA
13. Abbas SM, Ranga Y, Verma AK, Esselle KP (2014) A simple ultra-wideband printed monopole antenna with high band rejection and wide radiation patterns. IEEE Trans Antennas Propag 62(9):4816–4820
14. Dumoulin A, John M, Ammann M, McEvoy P (2012) Optimized monopole and dipole antennas for UWB asset tag location systems. IEEE Trans Antennas Propag 60(6):2896–2904
15. Liu H, Cheng Y, Yan M (2011) Electrically small loop antenna standing on compact ground in wireless sensor package. IEEE Antennas Wirel Propag Lett 10:438–441
16. Ban YL, Yang YL, Li MY, Zhang LW, Wang H (2015) Printed monopole slot antenna for WWAN metal-rimmed smartphone applications. In: 2015 international symposium on antennas and propagation (ISAP), Hobart, TAS, pp 1–4
17. Elfergani TE, Hussaini AS, Rodriguez J, Abd-Alhameed RA (2016) Dual-band printed folded dipole balanced antenna for 700/2600 MHz LTE bands. In: 2016 10th European conference on antennas and propagation (EuCAP), Davos, pp 1–5
18. Caytan O, Lemey S, Agneessens S, Ginste DV, Demeester P, Loss C, Salvado R, Rogier H (2015) Half-mode substrate-integrated waveguide cavity-backed slot antenna on cork substrate. Antennas Wirel Propag Lett 99
19. Kim D-O, Jo N-I, Jang H-A, Kim C-Y (2011) Design of the ultrawideband antenna with a quadruple band rejection characteristic using a combination of the complementary split ring resonators. Prog Electromagn Res 112:93–107
20. Ma T-G, Hua R-C, Chou C-F (2008) Design of a multiresonator loaded band-rejected ultrawideband planar monopole antenna with controllable notched bandwidth. IEEE Trans Antennas Propag 56(9):2875–2883
21. Dong YD, Hong W, Kuai ZQ, Chen JX (2009) Analysis of planar ultrawideband antennas with on-ground slot band-notched structures. IEEE Trans Antennas Propag 57(7):1886–1893
22. Zhu F, Gao S, Ho ATS, See CH, Abd-Alhameed RA, Li J, Xu J (2012) Dual band-notched tapered slot antenna using λ/4 band-stop filters. IET Microw Antennas Propag 6(15):1665–1673
23. Tang M-C, Wang H, Deng T, Ziolkowski RW (2016) Compact planar ultrawideband antennas with continuously tunable, independent band-notched filters. IEEE Trans Antennas Propag 64(8):3292–3301

Design of Half Adder Using Electro-Optic Effect in Mach–Zehnder Interferometer

Manisha Prajapat, Ankur Saharia and Ghanshyam Singh

Abstract This paper demonstrates the effective applicability of electro-optic effect for the implementation of half adder using Mach–Zehnder interferometers (MZIs). Performance enhancement using electro-optic switch implemented using MZIs based on titanium-diffused lithium niobate (Ti:$LiNbO_3$) functioning as waveguide medium at 1.33 μm wavelength is detailed in the work. The design implemented consists of three MZIs giving optimized operation in terms of low insertion losses, high extinction ratio and low switching voltage. Further, the titanium strip thickness and the arm gap between waveguides of the electrode regions were varied and analysis of the device performance has been done. Mathematical description of the device operation is also included, and the obtained results of MATLAB simulations and beam propagation method applied were compared and verified.

Keywords Mach–Zehnder interferometer (MZI) · Electro-optic effect · Beam propagation method (BPM)

1 Introduction

Electro-optic MZI has been widely used in optical systems recently due to high-speed operation requirements. They find wide applicability due to their inherent advantages of reliability and high-speed switching capabilities which makes them competent candidates in next-generation optical networks [1]. In the field of opto-electronics, high-speed communication has been achieved by virtue of low complexity offered by these devices where optimization plays a major role in the fast processing of optical data [2, 3]. For high-speed telecommunication systems, optical logic gates require significant elements as they have to achieve various functionalities in optical signal processing like switching, regeneration, addressing, multiplexing/demultiplexing, decision making, computation, coding/decoding and so on [4]. MZI switch is designed using titanium-diffused lithium niobate because of which

M. Prajapat (✉) · A. Saharia · G. Singh
Department of Electronics and Communication Engineering, Malaviya National Institute of Technology, Jaipur, Rajasthan 302017, India
e-mail: 2017PWC5407@mnit.ac.in

V. Janyani et al. (eds.), *Optical and Wireless Technologies*, Lecture Notes in Electrical Engineering 648, https://doi.org/10.1007/978-981-15-2926-9_29

high speed of operation above the 40 Gb/s at long-haul optical transmission system [5, 6], large capacity, transverse electric field in the direction of propagation, zero residual birefringence, less complexity and high EO coefficient for less switching time can be attained [7].

Different types of materials and their configurations have been examined in this work to get the desired all-optical switches. For this purpose, the materials should possess high nonlinearity characteristics, low operating voltage to ensure quick response times and low switching losses in switching operation [8, 9]. Further, thermo-optic effect and electro-optic effect can also be employed. To put it in a nutshell, half adder using MZI based on titanium-diffused lithium niobate is a novel design and by varying the thickness of Ti strip and arm gap insertion loss and ER are calculated, respectively. In this paper, a half adder is being simulated using the beam propagation method. In Sect. 2, an electro-optic effect of MZI switch is discussed. Section 3 describes the mathematical equations of the sum and carry outputs of half adder. In Sect. 4, implementation of half adder is described and results are verified by MATLAB simulation. Furthermore, in Sect. 5, the experimental results demonstrating insertion losses (ILs) involved and extinction ratio (ER) for varying thicknesses of Ti strip and interferometer arm gap have been discussed, and Sect. 6 concludes the work done.

2 MZI Schematic and Principle of Operation

The refractive index of the light propagating through the arms of the interferometer faces a change on application of an electrical voltage. This variation in refractive index introduces phase shifts in the lights propagating through them which lead to a resultant output port switching. This transduction phenomenon is widely named as electro-optic effect where the light at the output port switches with application of an input bias. The schematic layout of 2×2 MZI switch used in simulation analysis is shown in Fig. 1.

When the phase change is π, then the corresponding applied voltage is denoted by V_π which is given as [3]

$$V_\pi = \frac{\lambda}{n^3} \frac{1}{r} \frac{d}{L} \tag{1}$$

The device performance can be modeled by the IL and ER involved, where IL is the ratio of output power with respect to the input given by [3]

$$\text{IL(dB)} = 10 \log_{10} \left(\frac{P_{\text{out}}}{P_{\text{in}}} \right) \tag{2}$$

The ratio of circuit ON state power to OFF state output power gives the ER and is given by [3]

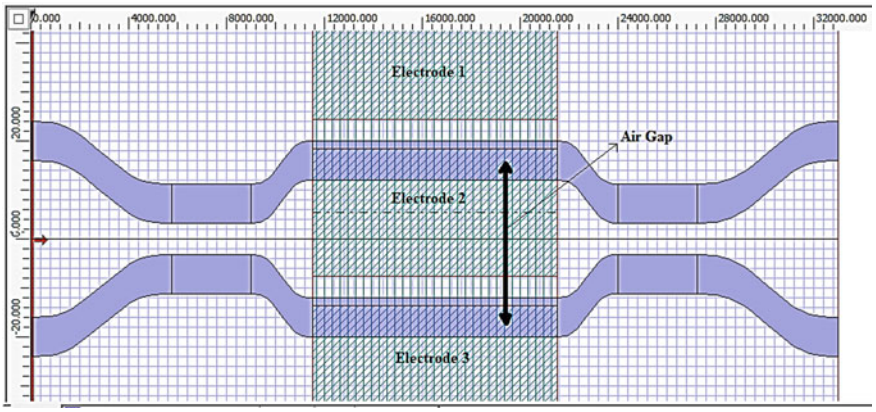

Fig. 1 Structure of MZI

$$\mathrm{ER(dB)} = 10\log_{10}\left(\frac{P_{\mathrm{on}}}{P_{\mathrm{off}}}\right) \tag{3}$$

3 Mathematical Equations of Half Adder Output

Figure 2 depicts the layout used to structure the proposed half adder. Half adder is a combinational circuit in digital electronics which adds two 1-bit binary digits and generates two bits where one bit is sum, obtained by XOR operation, and the other is carry bit generated by AND operation.

Mathematical equation for normalized power of MZI single-staged circuit can be effectively used for normalized power evaluation at the output ports of MZI-2 and MZI-3 [3, 4]. In this work as shown in the figure, output ports 3 and 1 (Fig. 2), respectively, have been used for evaluation. The output power at both the output ports can be evaluated utilizing the following equations:

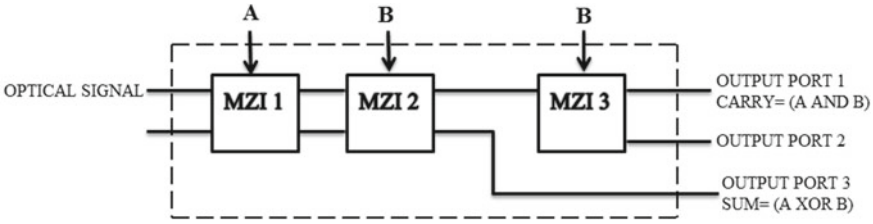

Fig. 2 Block diagram of half adder

$$m_1 = \left|\frac{\mathrm{OUT2_{MZI2_1}}}{\mathrm{E_{in}}}\right|^2 = \cos^2\left(\frac{\Delta\varphi_{\mathrm{MZI1}}}{2}\right)\sin^2\left(\frac{\Delta\varphi_{\mathrm{MZI2}}}{2}\right) \tag{4}$$

$$m_2 = \left|\frac{\mathrm{OUT2_{MZI2_2}}}{\mathrm{E_{in}}}\right|^2 = \sin^2\left(\frac{\Delta\varphi_{\mathrm{MZI1}}}{2}\right)\cos^2\left(\frac{\Delta\varphi_{\mathrm{MZI2}}}{2}\right) \tag{5}$$

$$m_3 = \left|\frac{\mathrm{OUT1_{MZI3}}}{\mathrm{E_{in}}}\right|^2 = \sin^2\left(\frac{\Delta\varphi_{\mathrm{MZI1}}}{2}\right)\sin^2\left(\frac{\Delta\varphi_{\mathrm{MZI2}}}{2}\right)\sin^2\left(\frac{\Delta\varphi_{\mathrm{MZI3}}}{2}\right) \tag{6}$$

Equations (4)–(6) are solved using the assumptions given below

$$\left.\begin{aligned}\Delta\varphi_{\mathrm{MZI1}} &= \tfrac{\pi}{\mathrm{V}_\pi}\mathrm{A}\\ \Delta\varphi_{\mathrm{MZI1}} &= \tfrac{\pi}{\mathrm{V}_\pi}\mathrm{B}\\ \Delta\varphi_{\mathrm{MZI1}} &= \tfrac{\pi}{\mathrm{V}_\pi}\mathrm{B}\end{aligned}\right\} \tag{7}$$

Signal A is controlling MZI-1, and Signal B is controlling MZI-2 and MZI-3. At second electrode, each MZI 0.00 V voltage represents logic 0 and 6.75 V voltage represents logic 1. Hence, the following expressions for sum and carry of the proposed half adder can be obtained as:

Output port 3 (XOR logic for sum of half adder) $= \left|\frac{\mathrm{OUT1_{MZI2}}}{\mathrm{E_{in}}}\right|^2 = m_1 + m_2$

$$= \cos^2\left(\frac{\Delta\varphi_{\mathrm{MZI1}}}{2}\right)\sin^2\left(\frac{\Delta\varphi_{\mathrm{MZI2}}}{2}\right) + \sin^2\left(\frac{\Delta\varphi_{\mathrm{MZI1}}}{2}\right)\cos^2\left(\frac{\Delta\varphi_{\mathrm{MZI2}}}{2}\right) \tag{8}$$

Output port 1 (AND logic for carry of half adder) $= \left|\frac{\mathrm{OUT1_{MZI3}}}{\mathrm{E_{in}}}\right|^2 = m_3$

$$= \sin^2\left(\frac{\Delta\varphi_{\mathrm{MZI1}}}{2}\right)\sin^2\left(\frac{\Delta\varphi_{\mathrm{MZI2}}}{2}\right)\sin^2\left(\frac{\Delta\varphi_{\mathrm{MZI3}}}{2}\right) \tag{9}$$

4 Implementation of Half Adder

4.1 Implementation of Half Adder Using MATLAB

To implement the half adder, three MZIs were used, as represented in Fig. 2. At the input of MZI-1, the optical signal is applied and its both output ports as shown in the figure are connected directly to MZI-2 input ports. In MZI-2, one of the output ports, the bar port is connected to the first input port of MZI-3 and other, and the cross-port is taken as the output port of the circuit giving the resultant sum of the half adder circuit implemented (XOR operation). The carry generated by the circuit can be obtained at bar port as shown in the figure which is the first output port of

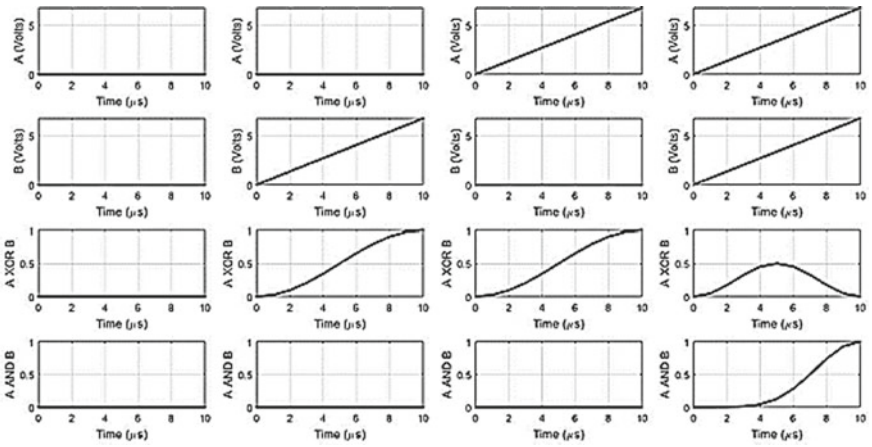

Fig. 3 Simulation results of implemented half adder using MZIs

MZI-3. Figure 3 shows the results of MATLAB analysis of the implemented half adder. The first and second rows in Fig. 3 represent the input control signals A and B, respectively, used in the simulation. The third and fourth rows denote the outputs obtained which are the sum and carry obtained through XOR and AND operations.

4.2 Implementation of Half Adder Using BPM

Proposed half adder structure can be analyzed using the beam propagation method. Ti:$LiNbO_3$ channel waveguides are used to define the optical propagation implementing the half adder operation. The design and simulation parameters used are given in Table 1.

In simulation analysis, transparent boundary conditions (TBCs) have been employed with 1000 mesh points involved. Transverse magnetic field polarization has been used in the simulation analysis, and 0.5 and 1.3 are the scheme parameter and propagation steps used. The results of simulation using BPM are shown in Fig. 4, where the half adder is seen to give acceptable results through proper selection of

Table 1 Parameters used in design of proposed device

Parameters	Value or modal of parameter
Wavelength (λ)	1.33 μm
Electrode separation (d)	6 μm
Substrate refractive index (n)	1.47
Electro-optic coefficients (r)	3.66×10^{-10} m/V
Interferometer arm length (L)	10,000 μm

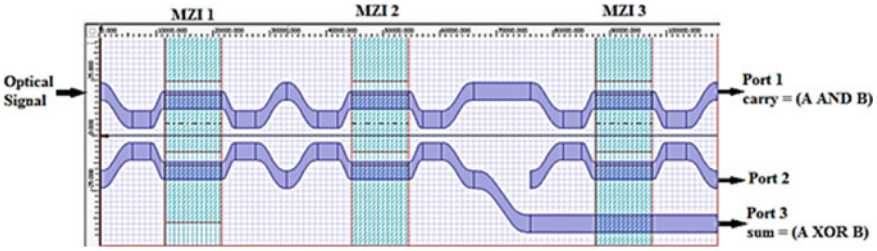

Fig. 4 Layout of proposed half adder

control signals. The operating principle of the proposed structure can be well monitored using the truth table, Table 2. The results of simulation-based analysis have been compared with the BPM results for its validation and verification as shown in Figs. 4 and 5.

Table 2 Inputs and outputs at port ends of MZIs

Control/input signals		Outputs		
A	B	Port 1 (C = A AND B)	Port 2	Port 3 (S = A XOR B)
0	0	0	1	0
0	1	0	0	1
1	0	0	0	1
1	1	1	0	0

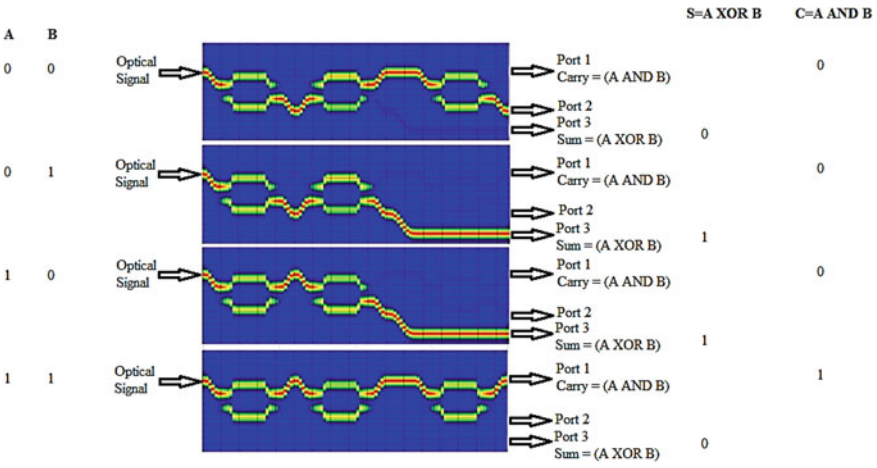

Fig. 5 Results of the half adder using beam propagation method

5 Study of Different Parameters Influencing the Performance of Half Adder

5.1 Impact of Ti Strip Thickness on IL and ER

Impact of Ti strip thickness on power performance of the half adder has been investigated by varying the thickness of Ti strip from 0.05 to 0.09 μm and graphs are plotted between the extinction ratio vs the thickness of titanium strip and insertion loss vs thickness of titanium strip. And we obtain the highest value 28.68 dB of extinction ratio and lowest value of insertion loss 0.024 dB at the 0.05 μm thickness, we increase or decrease the titanium thickness, the extinction ratio will be low, and insertion ratio will be high.

5.2 Impact of Arm Gap on ER

In this, the arm gap, i.e., gap between the waveguides in the electrode region, is varied from 31 to 35 μm and variation in the output power of the half adder has been studied. Figure 6 depicts the results obtained in this analysis, where the variation of ER with increase in arm gap is plotted. The highest value of ER attained is 29.97 dB when arm gap of 32 μm is considered and ER is found to decrease as we increase or decrease the arm gap (Fig. 7).

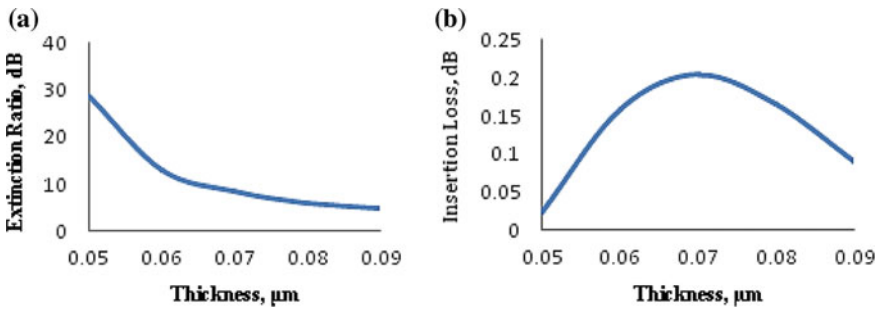

Fig. 6 **a** Variation of ER with increase in thickness of Ti strip and **b** variation of IL with increase in thickness of Ti strip

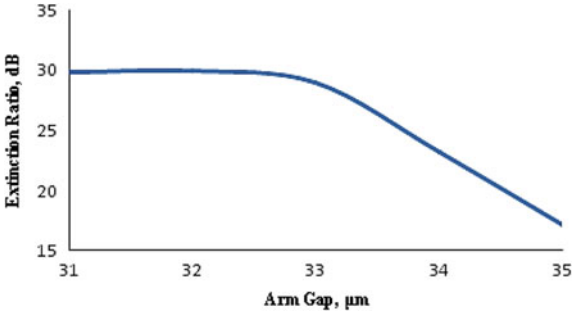

Fig. 7 Variation of extinction ratio with arm gap

6 Conclusion

In this paper, electro-optic effect has been used in realization of half adder circuit using MZIs and beam propagation method has been used for simulation. The advantage of the proposed design is that it requires less number of components than those implemented using SOA-MZI [10]. The results have been compared and verified using MATLAB simulations. The impact of Ti strip thickness variation and arm gap between the waveguides on the device performance has also been analyzed via evaluation of IL and ER. It can be concluded from the analysis that optimum performance of the device can be ensured when an arm gap of 32 μm and Ti strip thickness of 0.05 μm are chosen. The values of ER and IL are obtained theoretically; the lowest value of IL obtained in this work is 0.024 dB, and the maximum value of ER obtained is 26.86 dB.

Acknowledgements The authors are grateful for laboratory facilities made available by the Department of Electronics and Communication Engineering of Malaviya National Institute of Technology to carry out this work.

References

1. Singh G, Yadav RP, Janyani V (2012) High performance mach-zehnder optical switch. Opt Appl XLII(3). https://doi.org/10.5277/oa1203. ISSN: 1899-7015
2. Singh G, Yadav RP, Janyani V (2010) Ti:$LiNbO_3$ based mach-zehnder interferometric all optical switches: a review. A chapter with new advanced technologies, INTECH Publication, Austria, pp 311–322. https://doi.org/10.5772/9422. ISBN: 978-953-307-067-4
3. Khatun R, Ahmmed KT, Chowdhury AZ Hossen R (2015) Optimization of 2 × 2 MZI electro-optic switch and its application as logic gate. In: 18th international conference on computer and information technology (ICCIT), 2015, pp 294–299
4. Kumar S, Singh G, Bisht A, Sharma S, Amphawan A (2015) Proposed new approach to the design of universal logic gates using the electro-optic effect in mach-zehnder interferometers. Appl Opt 54(28):8479–8484

5. Kumar H, Kumar L, Janyani V, Oleh B, Serhij U, Singh G (2017) Gray to binary code converter using Ti-indiffused lithium niobate based mach-zehnder interferometer. In: Advances in Optical Science and Engineering, Springer proceedings in Physics, Optronix-2016, vol 194. © Springer Nature Singapore Pte Ltd., Kolkata, pp 257–262. https://doi.org/10.1007/978-981-10-3908-9_31. ISBN: 987-981-10-3907-2
6. Singh G, Yadav RP, Janyani V (2011) Modeling of a 2 × 2 electro-optic mach-zehnder interferometer optical switch with s-bend arms. Photonic Lett Pol 3(3):119–121. https://doi.org/10.4302/plp.2011.3.10. ISSN: 094
7. Mohammed Nazmi A, Abo Elnasr HS, Aly MH (2012) Performance evaluation and enhancement of 2 × 2 Ti: $LiNbO_3$ mach zehnder interferometer switch at 1.3 and 1.55 μm. Open Electr Electron Eng J 6(1)
8. Wooten EL, Kissa KM, Yi-Yan A, Murphy EJ, Lafaw DA, Hallemeier PF, Maack D et al (2000) A review of lithium niobate modulators for fiber-optic communications systems. IEEE J Sel Top Quantum Electron 6(1):69–82
9. Li GL, Yu PKL (2003) Optical intensity modulators for digital and analog applications. J Lightwave Technol 21(9):2010
10. Mehra R, Jaiswal S, Dixit HK (2013) All optical half adder design based on semiconductor optical amplifier. In: 2013 tenth international conference on wireless and optical communications networks (WOCN), pp 1–5

Dual-Band Plasmonic Filter Using Nanoslit-Loaded Ring Resonator

Yazusha Sharma, Rukhsar Zafar, Ravi Jangir, Ghanshyam Singh and Mohammad Salim

Abstract Plasmonics plays a key role in dealing with the demerit of the diffraction limit which is offered by traditional optical-based devices. Here, we have investigated a simple plasmonic dual-band optical filter that operates on desired optical band. The filter is based on metal-dielectric-metal (MDM) waveguide in order to facilitate sub-wavelength confinement. The MDM waveguide is coupled to nanoslit-loaded ring resonator. The presence of nanoslit excites the special mode in the resonance spectrum, known to be Fano modes, and by varying the position of slit, resonance can be tuned accordingly.

Keywords Plasmonics · Dual-band filter · Metal-dielectric-metal (MDM) · Sub-wavelength confinement

1 Introduction

In optical communication system, several transmission bands are defined and standardized by IEEE or ITU to support different applications. The E band is typically avoided to curtail the effect of large transmission losses. E band shows high absorption peak for water content. Wavelength-division multiplexing technique is being used by several applications to carry multiple wavelengths in order to enhance the bandwidth. In the current era of optical network, S, C and L bands are being used thoroughly due to their properties of inhabiting low optical losses in glass fiber [1]. Therefore, most of the optical devices or networks are designed to operate in this desired band. The optical fiber possesses the tremendous advantage of transferring the signal worldwide with extreme speed, but the transmitter and receiver end of optical communication unit is prone to O-E-O conversion [2, 3]. This conversion is the stumbling block in high-speed optical communication system because data

Y. Sharma (✉) · R. Zafar · R. Jangir
Department of Electronics and Communication Engineering, Swami Keshvanand Institute of Technology, Management and Gramothan, Jaipur, India

G. Singh · M. Salim
Department of Electronics and Communication Engineering, Malaviya National Institute of Technology, Jaipur, India

V. Janyani et al. (eds.), *Optical and Wireless Technologies*, Lecture Notes in Electrical Engineering 648, https://doi.org/10.1007/978-981-15-2926-9_30

needs to be converted before (after) transmission (reception). The high latency during conversion is directly related to complexity. This latency can combat if all-optical devices are designed [4]. In this regard, photonics and its devices have emerged as a key technology to felicitate the optical/photonics on-chip integrated circuits [5]. Recently, several optical devices and components based on Plasmonics is the area of the current research [6]. Plasmonics is an approach that studies the interaction phenomenon of optical signal with dielectric/metal interface. Plasmonics deals with two sub-branches: propagating plasmons and non-propagating plasmons [6, 7]. Plasmonics has the inherent advantage of combining the merits of high-speed photonics with electronics at chip-scale [7]. This fascinating feature of Plasmonics helps to utilize special optical features that deal with the signal confinement far beyond the diffraction law [6–9]. The MDM (metal-dielectric-metal) waveguide of multiple interfaces-based propagating plasmon is considered as the best candidate to design many optical waveguides to be applicable in on-chip designing such as filters, demultiplexers, buffers and sensors. [10–14]. A wideband optical buffer with ultra-large delay bandwidth product is reported recently which uses MDM plasmonic waveguide [15]. Mirnaziry et al. investigated stubs-based plasmonic filter and also gave its theoretical analysis [16]. Therefore, MDM-based plasmonic waveguide shows potential in realizing optical/photonic-based ICs [12–16]. In this paper, we have utilized a similar MDM waveguide and simulated a dual-band optical filter that operates on desired optical band. The geometrical parameters are adjusted so that the device can be designed to operate at desired band (S, C and L). Waveguide geometry and result analysis are discussed in the next sections.

2 Geometry and Design Parameters

The cross-sectional view and refractive index distribution of the proposed structure are depicted in Fig. 1a, b. The structure comprises a resonating ring waveguide which is coupled with a metallic nanoslit. The resonator is excited through a Gaussian-modulated field centered at 1550 nm.

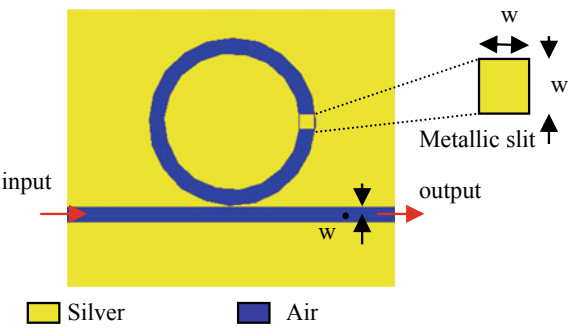

Fig. 1 **a** Cross-sectional view of the proposed geometry with following assumed parameters: w (width of MDM waveguide) = 50 nm, r (radius of ring waveguide) = 150 nm and slot dimension 50 nm × 50 nm

MDM waveguide is coupled to a ring resonator and the width of MDM waveguide, and the ring is kept same for transferring maximum power from MDM waveguide to resonator. The structural parameters are as: width of the MDM waveguide and ring resonator ($w = 50$ nm) and radius of ring resonator $r = 150$ nm (average of radius of outer circle and inner circle). The dielectric material of MDM waveguide and the resonator is chosen to be air medium ($n = 1$), and the metallic portion is opted to be silver. Its frequency-dependent relative permittivity is characterized by Drude model [17]:

$$\varepsilon_m(\omega) = \varepsilon_\infty - \frac{\omega_p^2}{\omega^2 + i\tau\omega} \tag{1}$$

where $\varepsilon_\infty (= 3.7)$ is the dielectric permittivity, $\omega_p (= 9.1\,\text{ev})$ is the bulk plasma frequency, $\tau (= 0.018\text{ev})$ is the electron collision frequency and ω. the angular frequency of the incident wave in vacuum. However, silver suffers from a serious limitation of being rapidly deteriorated, but the ohmic losses associated with the silver are smaller as compared to other metals.

3 Simulation, Result and Discussion

The structure is simulated using 2D finite difference in time domain (FDTD) method. The grid sizes in the x and z directions are chosen to be $\Delta x = \Delta z = 2$ nm, and the time step is set as Courant condition. When a p-polarized wave is given as input to MDM waveguide, SP mode is excited which propagates tightly along the dielectric/metal interface [18]. The transmission spectrum for proposed structure is shown in Fig. 2. The transmission spectrum spans over a broad frequency band giving two peaks ($\approx$ 1550 and 1650 nm) and one notch near 1600 nm.

The nanoslit available in the ring resonator is responsible for notch frequency. The resonance pattern shown in Fig. 2 is generally known to be Fano resonance which arises due to the introduction of asymmetry in the perfect structure. Figure 3 explains the magnetic field distribution for the simulated structure. It is depicted that an extra mode is excited by placing a metallic slit. This mode interferes with the existing modes and suppresses the transmission to a minimum value as shown in transmission spectrum. It is the interesting phenomenon of Fano resonance that it can be tuned by changing the structural parameters [2, 19, 20]. The phenomena of resonance tuning by changing the structural parameter of MDM plasmonic waveguide are reported recently [20]. The notch or band-stop frequency can be shifted to the desired frequency by shifting the position of nano metallic slit. Mode profile and transmission spectrum for different positions of nanoslit are shown in Figs. 3 and 4, respectively.

It is clear from transmission spectrum that notch frequency experiences blueshift by changing position of metallic slit (in the order $270° - 180° - 90° - 0°$). One more

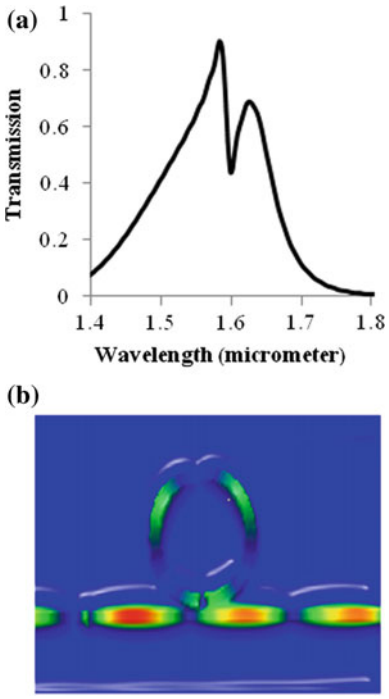

Fig. 2 **a** Transmission spectrum. **b** Magnetic field distribution for the proposed structure

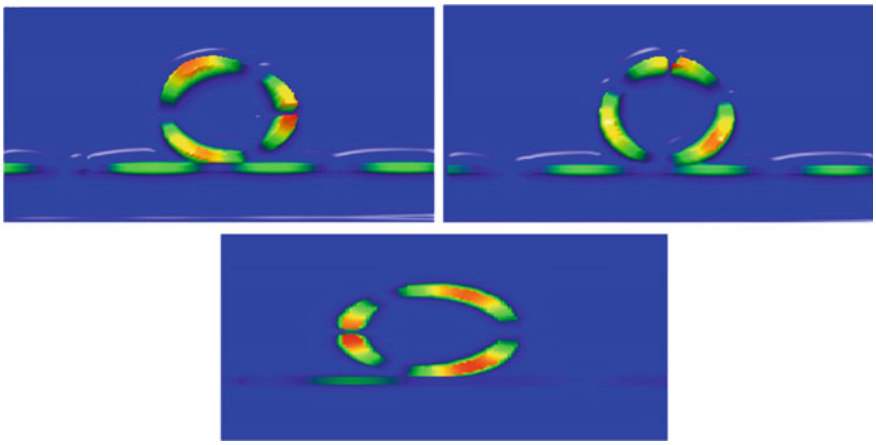

Fig. 3 Magnetic field distribution for variation in position of metallic slit ($\theta = 0°, 90°, 180°$)

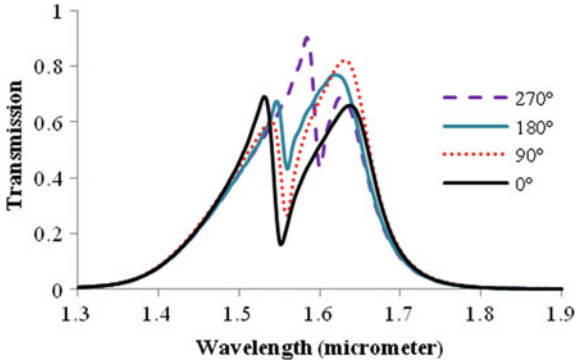

Fig. 4 Transmission spectrum of proposed structure for different positions of metallic slit calculated using FDTD method

important feature of Fano resonance is the asymmetry associated with the resonance spectrum [21]. Therefore, asymmetric nature of resonance can also be tailored along with the tuning of resonance wavelength.

Thus, the proposed structure of ring waveguide with metallic slit proves to be quite helpful in tuning the operating frequency band or notch frequency to the desired operating frequency. This opens the wide application area that includes plasmonic filter, de-multiplexer, sensor, etc.

4 Conclusion

A dual-band optical filter has been simulated that operates on desired optical band. The optical fiber possesses the tremendous advantage of transferring the signal world-wide with extreme speed, but the transmitter and receiver end of optical communication unit is prone to O-E-O conversion. This conversion is the stumbling block in high-speed optical communication system because data needs to be converted before (after) transmission (reception). The high latency during conversion is directly related to complexity. This latency can combat if all-optical devices are designed. Plasmonics plays an important role in realizing all-optical devices. Therefore, a MDM waveguide-based optical filter is proposed. The resonator used in the structure is ring waveguide which is coupled with metallic slit. The presence of the metallic slit in the waveguide excites the special modes known as Fano modes. These modes show quite asymmetric behavior, and the value of transmission coefficient drops to zero at the vicinity of resonance. The resonance frequency of Fano mode can be tuned by controlling the position of metallic slit. The desired operating band and notch frequency can be selected by rotating the position of metallic slit. This unique feature opens the avenue in desired application area which includes plasmonic filter, de-multiplexer, sensor, etc.

References

1. Bands O, Laurent B, Draka G (2008) From O to L: the future of optical-wavelength bands. Broadband Prop. Retrieved online from http://www.fs.com/blog/from-o-to-l-the-evolution-of-optical-wavelength-bands-2.html
2. Piao X, Yu S, Park N (2012) Control of Fano asymmetry in plasmon induced transparency and its application to plasmonic waveguide modulator. Opt Express 20(17):18994–18999
3. Inoue KYO (1996) Noise translation characteristics in OE/EO conversion with a Mach-Zender modulator. IEEE Photonics Technol Lett 8(10):1322–1324
4. Winzer PJ, Fludger C, Miyamto Y (2006) Introduction to the issue on optical communications. IEEE J Sel Top Quantum Electr 12(4):467–468
5. Shibata Y, Kikuchi N, Tohmori Y (2003) Photonic integrated devices for high speed signal processing and switching. In: IEEE conference on optical fiber communications, vol 2, pp 667–669
6. Maier SA (2006) Plasmonics: the promise of highly integrated optical devices. IEEE J Sel Top Quantum Electron 12(6):1671–1677
7. Ozbay E (2006) Plasmonics: merging photonics and electronics at nanoscale dimensions. Science 311: 189–193
8. Maier SA (2007) Plasmonics: fundamentals and applications. Springer, Berlin
9. Gramotnev DK, Bozhevolnyi SI (2010) Plasmonics beyond the diffraction limit. Nat Photon 4(2):83–91
10. Zia R, Selker MD, Catrysse PB, Brongersma ML (2004) Geometries and materials for subwavelength surface plasmon modes. J Opt Soc Am 21(12):2442–2446
11. Han Z, Forsberg E, He S (2007) Surface plasmon Bragg gratings formed in metal-insulator-metal waveguides. IEEE Photon Technol Lett 19(2):91–93
12. Zhou Y, Yang B (2014) A 4-way wavelength demultiplexer based on the plasmonic broadband slow wave system. Opt Exp 22(18):21589–21599
13. Xu L, Wang S, Wu L (2014) Refractive index sensing based on plasmonic waveguide side coupled with bilaterally located double cavities. IEEE Trans Nanotechnol 13(5):875–880
14. Jin X-P, Huang X-G, Tao J, Lin X-S, Zhang Q (2010) A novel nanometeric plasmonic refractive index sensor. IEEE Trans Nanotechnol 9(2):134–137
15. Zafar R, Salim M (2015) Achievement of large normalized delay bandwidth product by exciting electromagnetic-induced transparency in plasmonic waveguide. IEEE J Quantum Electron 51(10):134–137
16. Mirnaziry SR, Setayesh A, Abrishamian MS (2011) Design and analysis of plasmonic filters based on stubs. J Opt Soc Am B 28(5):1300–1307
17. Johnson JB, Christy R-W (1972) Optical constants of the noble metals. Phys Rev B 6:4370–4379
18. Sulliran DM (1996) Exceeding the Courant condition with the FDTD method. IEEE Microw Guided Wave Lett 6(8):289–291
19. Singh R, Al-Naib I, Cao W, Rockstuhl C, Koch M, Zhang W (2013) The Fano resonance in symmetry broken terahertz metamaterials. IEEE Trans Terahertz Sci Technol 3(6)
20. Zafar R, Salim M (2014) Wideband slow light achievement in MDM plasmonic waveguide by controlling Fano resonance. Infr Phys Technol 67:25–29
21. Zafar R, Salim M (2017) Analysis of asymmetry of Fano resonance in plasmonic metal-insulator-metal waveguide. Photonics and nanostructures-fundamentals and applications, vol. 23. Elsevier

Forward Error Correction Codes—Reed–Solomon and LDPC for OFDM Over the Optical Fiber Communication Systems

Usha Choudhary and Vijay Janyani

Abstract In this paper, authors have compared the performance of two popular optical FEC codes, Reed–Solomon (RS) and low-density parity-check (LDPC), to improve the performance of an OFDM over the optical fiber communication system. Both RS and LDPC codes improve the BER performance at receiver with different laser power levels. For received optical power 3 dBm, RS coded OFDM shows BER ($2.32 * 10^{-14}$), LDPC coded OFDM shows ($1.39 * 10^{-15}$), whereas BER recorded for uncoded OFDM for this laser power range is ($9.17 * 10^{-12}$). Data array size in LDPC is almost two times compared to RS code and uncoded OFDM. Required optical power at receiver (receiver sensitivity) for laser power 0 dBm for uncoded OFDM (18.89 dBm), RS coded OFDM (13.88 dBm) and LDPC coded OFDM (12.69 dBm). LDPC outperforms in almost every aspect like decoder complexity, processing delay, BER and can be selected for improvement in nonlinearity and dispersion issues for closely spaced subcarriers in ODFM for optical fiber.

Keywords OFDM · LDPC · Reed–Solomon · BER

1 Introduction

Orthogonal frequency-division multiplexing (OFDM) over the optical fiber is capable to reduce the dispersion (chromatic, polarization mode and intermodal) in the medium, very similar to the mitigation of ISI in wireless channel [1–3], if sufficient guard length or cyclic prefix length is provided. In case of optical fiber channel, most important challenge for transmission of OFDM is high peak-to-average power ratio (PAPR). High input power raises the nonlinear effects in fiber material that is basically a dielectric material and the effective refractive index changes with input power level [4]. Nonlinearity in optical fiber results in spreading of the frequency

U. Choudhary (✉) · V. Janyani
ECE Department, MNIT, Jaipur, India

V. Janyani
e-mail: Vjanyani.ece@mnit.ac.in

V. Janyani et al. (eds.), *Optical and Wireless Technologies*, Lecture Notes in Electrical Engineering 648, https://doi.org/10.1007/978-981-15-2926-9_31

spectrum of optical pulse resulting in four-wave mixing (FWM), inelastic scattering (SBS, SRS) and these have a interrelation with chromatic dispersion (CD) and polarization mode dispersion (PMD) [5]. Closely spaced orthogonal subcarriers are affected differently so the overall bit error rate (BER) will be influenced by the worst affected subcarriers. Forward error correction (FEC) codes will help to improve the error performance as well as larger code length permits the use of slower speed opto-electrical components [6]. Two very popular FEC codes Reed–Solomon (RS) and low-density parity-check (LDPC) codes with OFDM for optical fiber systems are compared in this paper regarding total power transmitted and BER performance. Paper is organized as follows: Sect. 2 covers the optical OFDM, Sect. 3 is about different FEC schemes, Sect. 4 is for simulation and results, and finally the conclusion is presented in Sect. 5.

2 Optical OFDM

An overlapped spectrum of orthogonal subcarriers makes the OFDM one of the most bandwidth efficient multi-carrier schemes. N orthogonal subcarriers can be generated with single digital signal processor (DSP) unit that calculates the N point IFFT of mapped symbols [7] and this DSP provides a range of flexibility in network parameters without any major change in existing hardware and network setup. Incoming bitstream is first mapped with PSK or QAM modulation and then converted in parallel form to calculate N point IFFT. N point IFFT $x(n)$ of any sequence $x(k)$ can be written as

$$\text{IFFT}\{x(n)\} = \frac{1}{N}\sum_{n=0}^{N-1} x(k)e^{\frac{j2\pi kn}{N}}, n = 0, 1, \ldots N-1 \tag{1}$$

Here, $k = \log_2 M$, for M-ary modulation scheme. Similarly, FFT is calculated at receiver side to demodulate the OFDM signal. OFDM gives best spectral efficiency, eliminates the ISI because of multipath as well as it makes PAPR very high and it is very sensitive for phase and frequency offset because it may cause the loss of orthogonality among the carriers and reception is highly erroneous. OFDM in optical domain was first demonstrated more than 30 years later to its first study in RF channel [8] because of two major obstacles: first, OFDM signal is bipolar in nature, whereas optical signal should be unipolar, and second, OFDM is basically coherent detection scheme, whereas most of the optical fiber networks were direct-detection type. Addition of sufficient DC bias to OFDM signal to make it unipolar and clipping the negative polarity of OFDM signal are two basic methods to resolve the first issue, whereas coherent OFDM in optical domain is a complex system but it helps to mitigate the dispersion very effectively and makes the dispersion management simpler that can be included in DSP section without need of extra optical components like DCF, FBG and OPC [9]. If guard interval or cyclic prefix interval

in OFDM symbol is larger than total possible dispersion or temporal broadening of optical pulse, inter symbol interference (ISI) can be avoided almost completely [6]. So OFDM in optical fiber domain comes with some extra challenges and provides a future possibility for flexible, very high speed and adaptive data link setup.

3 Forward Error Correction Codes

Message bits (k) are converted into code word (n) bits to add the redundancy that helps to recover the message after attenuation and distortion throughout the transmission channel, code rate is defined as $R = k/n$ [10]. In optical domain, first-generation codes were mainly BCH/RS codes, whereas RS (255, 239) was more popular for long haul communication systems. Combination of different codes was experimented in second generation and third generation mainly includes turbo codes and LDPC codes [6]. In case of OFDM, we would like to select the FEC scheme that can improve the BER performance in presence of nonlinearity in optical fiber channel. RS code is basically a concatenated code and it may be classified in burst error-correcting codes. These codes can be applied to high speed transmission up to 40 Gbps. RS codes RS (255, 239) were first choice for optical fiber communication as it transmits at Gbps range that suffers with intra channel nonlinearity and is quite prone to burst error [11, 12]. LDPC code first proposed by Gallager in 1960 has become a favorite FEC for real-time high speed transmission. LDPC has a large size generator matrix that has very low density of 1's; with number of 1's per column and per row constant. This is a soft iteratively decodable code that performs much better regarding BER, decoder complexity and maximum possible channel capacity [13–15]. In this paper, the performance of both RS (255, 239) and LDPC (64800, 32400) is compared with an OFDM transmitted signal over optical fiber. It is demonstrated how inclusion of a particular FEC affects the BER performance and required power for given reference BER. Figure 1 shows a direct-detection OFDM with FEC for optical fiber communication system.

4 Simulation and Results

Performance analysis for uncoded OFDM and OFDM with FEC as RS (255, 239) and LDPC (64800, 32400) is observed with simulation tool Optsim 2017.03 and MATLAB. OFDM generation with 100 point IFFT, QPSK symbol mapping, with and without FEC encoder is done with MATLAB and final data is sent over the electrical input of MZM optical modulator for transmission over the fiber. Data stream with length (32400,1) is generated for initial input to LDPC encoder as we would like to make a similar base for all three schemes so same data length is used for uncoded OFDM and RS encoder, although for completing the message symbol in RS encoder padding of some zero bits is done as last bits. After generation of coded

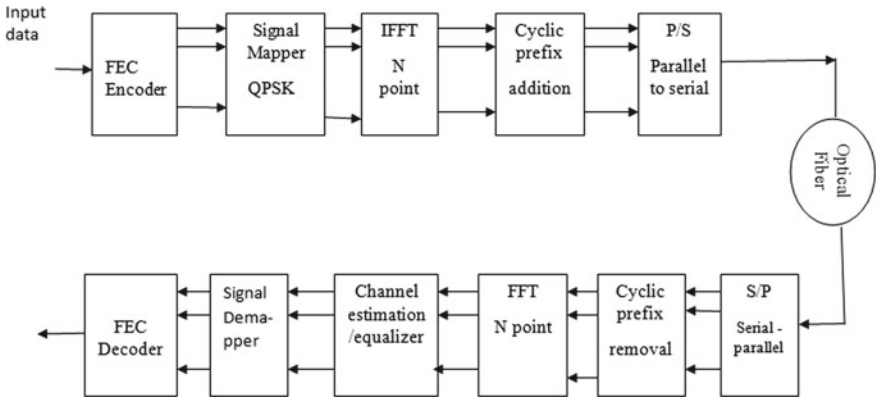

Fig. 1 Block diagram for an OFDM system with FEC over the optical fiber channel

and uncoded OFDM signal, the size of data array that finally feeds the electrical recorder in Optsim is observed and normalized electrical power transmitted to optical modulator is calculated. Electrical power is calculated by squaring and summing the each data element. Unipolar OFDM is generated by adding the bias. Figure 2 shows the schematic setup for simulation and Fig. 3 is electrical signal that comes from recorder to optical modulator.

Fiber span is a combination of two fiber sections as D^- and D^+ with dispersion coefficient −40 and 20 ps/nm/km and length of 2 km and 4 km, respectively [13]. Optical signal is received at sensitivity receiver with PIN photodetector, bit rate 10 Gbps, −3 dB two sided bandwidth 300 GHz, reference BER $1 * 10^{-12}$ and receiver sensitivity under test conditions −23.93 dBm. Simulation results show BER at received optical power that is recorded for laser power as variable (−3 dBm to + 3 dBm). Electrical recorder at receiver sends the data to MATLAB for demodulation and decoder. For comparison of all three types of OFDM uncoded, RS code and LDPC code, we also observed the required optical power at sensitivity receiver for pre-decided reference BER. Table 1 shows the simulation parameters.

Simple OFDM sends data array size (20250,1) for electrical input to optical modulator, RS-OFDM sends (21750,1) and LDPC-OFDM sends (40500,1). Normalized power calculated by squaring and summing the data array (Electrical power = sum(x^2)) and it comes $1.5 * 10^{+3}$, $2.02 * 10^{+4}$, $1.072 * 10^{+4}$, respectively, for uncoded OFDM, RS-OFDM and LDPC-OFDM. FEC code increases the total transmitted data length ($n > k$) as well as total transmission power is also increased. In second case, if we keep the total optical power transmission constant than the inclusion of FEC decrease the energy per bit that results very low value of E_b/N_o per bit [10].

Figure 4 compares the total optical power required at sensitivity receiver with respect to laser power varying from −1 dBm to +3 dBm for all three types of OFDM and Fig. 5 is comparison of BER at received optical power at receiver.

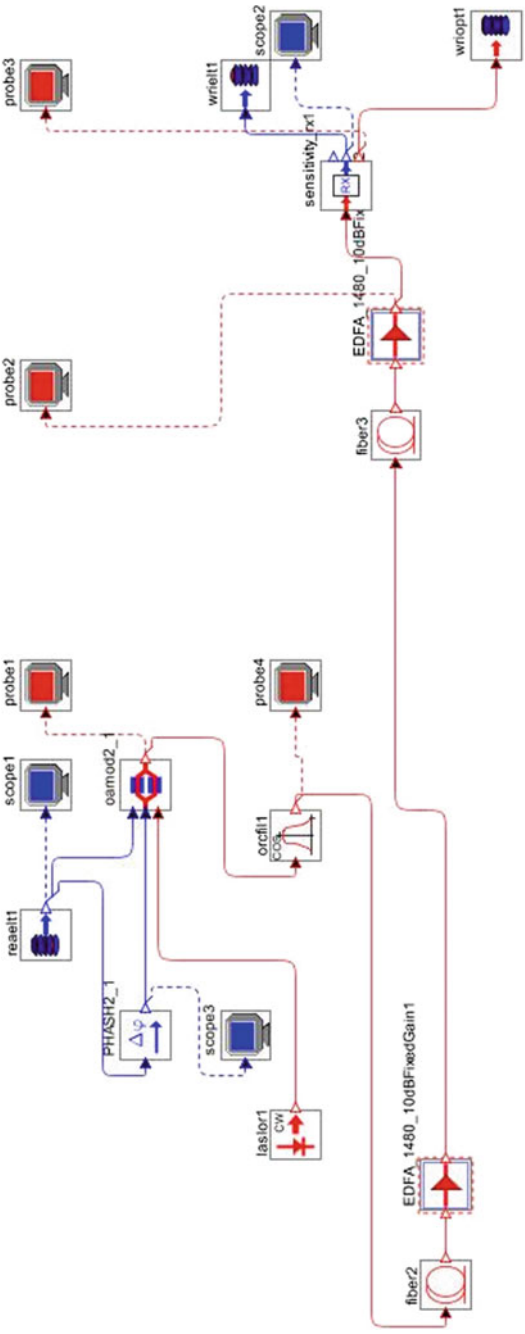

Fig. 2 Schematic setup for simulation of coded and uncoded OFDM over the optical fiber

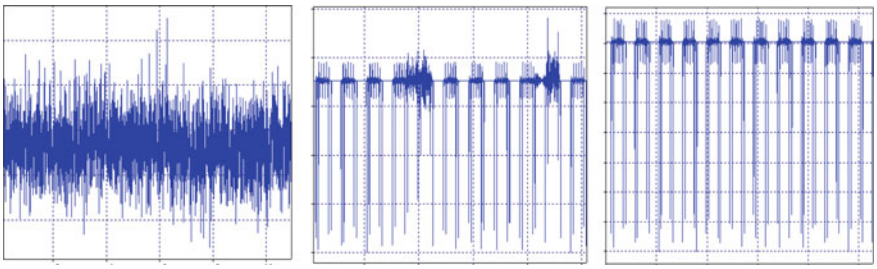

(a) Uncoded OFDM (b) RS coded OFDM (c) LDPC coded OFDM

Fig. 3 Electrical signal for different OFDM signals; *X*-axis: time scale: 2 nsec per unit; *Y*-axis: 0.1 a.u. per unit

Table 1 Simulation parameters

No. of IFFT points	100
Cyclic prefix	25
Symbol mapper	QPSK
LDPC encoder (*n, k*)	64800, 32400
RS encoder (*n, k*)	255, 239
Fiber length	4 km D^+, 2 km D^-
Laser power	−3 to +3 dBm
Reference bit rate	10 Gbps
−3 dB two sided bandwidth	300 GHz
Reference BER	$1 * 10^{-12}$

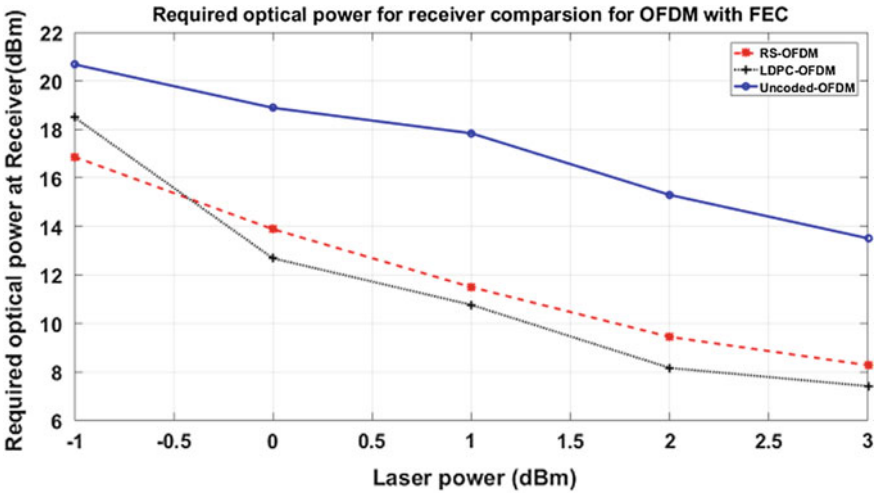

Fig. 4 Optical power required at receiver for reference BER $1 * 10^{-12}$

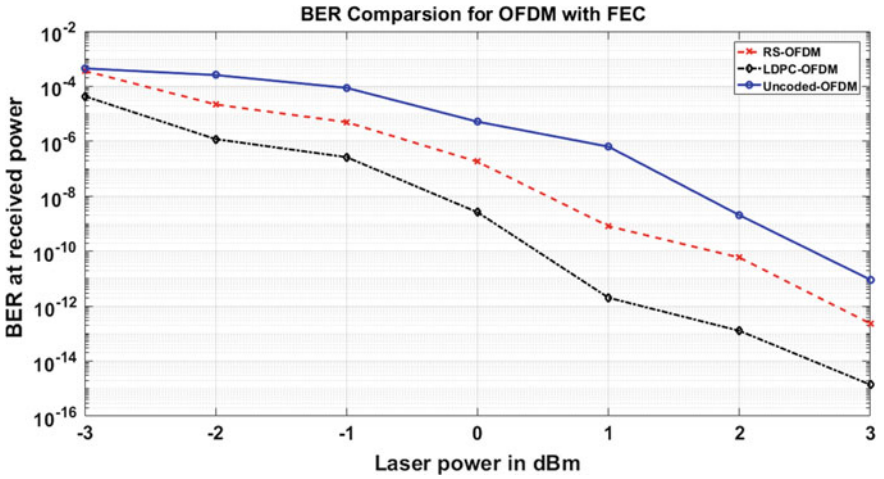

Fig. 5 BER for received optical power at receiver

5 Conclusion

Transmission of OFDM over optical fiber comes with many challenges and doubts about the accommodation of new technology with existing resources and chances for commercial success. Advancement in DSP units can handle the scope of flexibility and adaptive system requirements. OFDM with FEC can resolve the issue of nonlinearity and dispersion much efficiently so we compared two very popular FEC schemes for optical domain with OFDM. Simulation results show that FEC both RS and LDPC increase the required optical power at receiver front end still BER is decreased. LDPC needs almost twice data array size still BER performance is better when compared to RS code. We can further study the LDPC code for clipped OFDM also that is quite favorable for low power, slow speed data transmission in an adaptive data rate channel conditions.

References

1. Cho YS, Kim J, Yang WY, Kang CG (2010) MIMO-OFDM wireless communications with MATLAB, Wiley-IEEE Press
2. Armstrong J (2009) OFDM for optical communications. J Lightw Technol
3. Armstrong J (2008) OFDM: from copper and wireless to optical. In OFC/NFOEC 2008–2008 conference on optical fiber communication/national fiber optic engineers conference
4. Agrwal G (2007) Nonlinear fiber optics. Academic press
5. Agrawal GP (2015) Fiber-optic communication systems. Wiley
6. Shieh W, Djordjevic I (2009) OFDM for optical communications. Academic Press
7. Weinstein SB, Ebert PM (1971) Data transmission by frequency-division multiplexing using the discrete fourier transform. IEEE Trans Commun Technol 19(5):628–634

8. Yang Q, Al Amin A, Shieh W (2011) Impact of nonlinearities on fiber optic communications. Springe, New York
9. Shieh W, Chen W, Tucker RS (2006) Polarisation mode dispersion mitigation in coherent optical orthogonal frequency division multiplexed systems. Electron Lett 42(17):996
10. Haykin SS (2013) Digital communication systems, vol. 2, no. 2, pp 110–111
11. Anderson JB, Mohan S (1991) Source and channel coding. Springer, US, Boston, MA
12. MacWilliams FJ, Sloane NJ (1977) The theory of error-correcting codes, Part 2. Elsevier
13. Djordjevic IB, Vasic B, Neifeld MA (2007) LDPC-coded OFDM for optical communication systems with direct detection. IEEE J Sel Top Quantum Electron 13(5):1446–1454
14. Futaki H, Ohtsuki T (2002) Performance of low-density parity-check (LDPC) coded OFDM systems. IEEE Int Conf Commun 3:1696–1700
15. Djordjevic IB, Arabaci M, Minkov LL (2009) Next generation FEC for high-capacity communication in optical transport networks. J Light Technol

Theoretical Study of Transmission Coefficient and IV Characteristic of Double Barrier GaAs/$Ga_{1-x}Al_xAs$ Heterostructure at Different Composition 'x'

Manish Kumar Yadav, Bramha P. Pandey and Dharmendra Kumar

Abstract In this paper, we have theoretically investigated the impact of different composition 'x' of the barrier height on transmission coefficient and IV characteristics of GaAs/$Ga_{1-x}Al_xAs$ double barrier heterostructure. In this study, GaAs/$Ga_{1-x}Al_xAs$ based double barrier heterostructure is selected at operating temperature 10 K. The calculated results show that IV characteristic and transmission coefficient are the crucial measurable quantity to anticipate the double barrier heterostructure property. When the height of barrier is less, then the transmission coefficient and IV characteristics of GaAs/$Ga_{1-x}Al_xAs$ double barrier heterostructure are high. The calculated results are in good agreement with the available reported results from the other workers.

Keywords Transmission coefficient · Resonant tunneling · IV characteristics · Alloy composition · Fermi-dirac distribution

1 Introduction

Recently, the challenges of silicon technology are the quantum mechanical tunneling effect, whereas bandgap engineering devices excel in quantum mechanical effects, thus produces faster switching property of devices [1]. The single layer of semiconductor is required in silicon technology, whereas a bundle of numerous nanometer-scale thin films of layer semiconductors having dissimilar bandgap are incorporated in bandgap engineering devices [2]. Shockley had patented of the BJT describing the advantages of using junction having multiple semiconductors, while Kroemer [3] investigated the use of semiconductor heterostructure and Capasso [4, 5] inspected dubbed 'bandgap engineering'. The reported previous work has been done on heterostructure, laid the base for the development of modulation-doped technique by Dingle [6] and this development is followed by the discovery of high electron mobility transistor (HEMT) [7].

M. K. Yadav (✉) · B. P. Pandey · D. Kumar
Department of Electronics & Communication Engineering, Madan Mohan Malaviya University of Technology, Gorakhpur, India

V. Janyani et al. (eds.), *Optical and Wireless Technologies*, Lecture Notes in Electrical Engineering 648, https://doi.org/10.1007/978-981-15-2926-9_32

A double heterostructure can be formed by introducing a thin layer having narrow bandgap of a material 'A' between two layers of a material 'B' with wider bandgap. When the thickness of the layer 'A' is sufficiently thin compared to the de-Broglie wavelength, it pertains the quantum confinement effect and is known as single quantum well (QW). The appropriate doping in quantum well results thermally generated intrinsic or extrinsic charge carriers which tried to degrade energy level of the system and charge carriers accumulated in quantum well [8, 9]. The heterostructure is generally two forms asymmetric or stepped quantum well [10]. Both types of quantum well formed through inserting an alloy layer between well and barrier. The simple double heterostructure is used to form various potential structures such as superlattices, asymmetric or symmetric and double/multiple quantum wells for light source. The chirped superlattice active region of a mid-infrared laser is most complicated layer structure till the date [11]. Type-I system possesses the wider bandgap and nestled within the material; therefore, holes or electrons drop into quantum well within the same layer of material. Type-I system is useful for fast recombination because charge carriers (electrons and holes) are confined in the same layer of semiconductor materials. Type-II system in which bandgap of the materials is arranged in such a manner that the quantum well formed in the active region is in distinct layer of semiconductor materials. This results that the hole and electron are confined in different layers of the semiconductor materials. Type-II system leads to longer recombination times of hole and electron [12]. The quantum well is made of peculiar layers of materials having the narrow and wide bandgap semiconductors. The band offset ratio is the difference in energies of conduction band to the difference in energies of valence band. The band offset is the most useful experimental values. In earlier work, growing of thick layers of Al-GaAs [13] or GaAs [14] and broad analysis of their optical properties of heterostructure quantum well was done. The quantum well heterostructure has wider area of applications including modern electronic devices such as heterojunction bipolar transistors (HBT), resonant tunneling devices (RTD) and modulation-doped field-effect transistors (MODFET) and also in optoelectronic devices and structures such as quantum well, superlattice optical laser diodes [15–17] and photodetectors [18].

In this paper, we have theoretically investigated the impact of different composition 'x' of the barrier height on IV characteristics and transmission coefficient of GaAs/$Ga_{1-x}Al_xAs$ double barrier heterostructure. The QWWAD simulation tool is used and the material properties of this investigation are given in Table 1 [19]. In this

Table 1 Properties of material used in simulation setup are bandgap E_g (eV), electron effective mass (m^*), material density ρ (kgm^{-3}), lattice constant A_0 (Å) and band alignment

Properties	Values
Bandgap E_g (eV)	$1.426 + 1.247x$
Electron effective mass (m^*)	$(0.067 + 0.083x)\, m_0$
Material density ρ (kgm^{-3})	5317.5
Lattice constant A_0 (Å)	$5.65(1–x) + 5.66x$
Band alignment	$\Delta V_{VB} = 0.33\Delta E_g$, $\Delta V_{CB} = 0.67\Delta E_g$

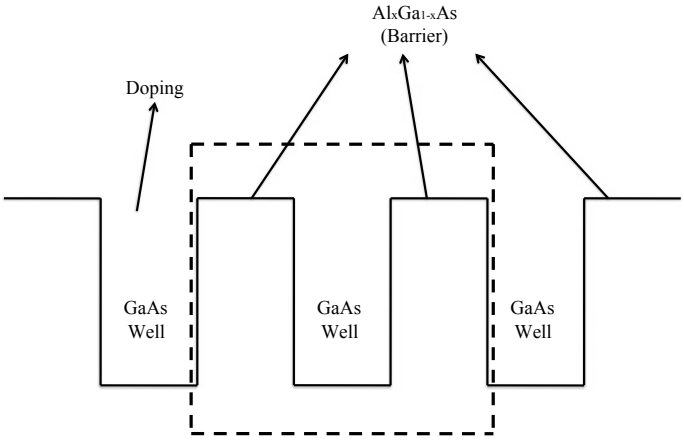

Fig. 1 Structure of GaAs/$Ga_{1-x}Al_xAs$ double barrier heterostructure

study, GaAs/$Ga_{1-x}Al_xAs$ based double barrier heterostructure is selected at operating temperatures of 10 K. The calculated results reveal that when the height of barrier is less, transmission coefficient and IV characteristics of GaAs/$Ga_{1-x}Al_xAs$ double barrier heterostructure are high. The calculated results are in good agreement with the available reported results from the other workers.

2 Structure Specification

Figure 1 shows GaAs/$Ga_{1-x}Al_xAs$ multiple barrier heterostructure. For our calculation, we have studied double barrier heterostructure as shown in box of above structure. The design has single well (active region) surrounded by two barriers of $Ga_{1-x}Al_xAs$. The active regions act as an injector. The design has been theoretically investigated including three different double barrier structure including 30 Å $Ga_{1-x}Al_xAs$ (barrier)/20 Å GaAs (well)/30 Å $Ga_{1-x}Al_xAs$ (barrier), 30 Å $Ga_{1-x}Al_xAs$ (barrier)/30 Å GaAs (well)/30 Å $Ga_{1-x}Al_xAs$ (barrier), 30 Å $Ga_{1-x}Al_xAs$ (barrier)/40 Å GaAs (well)/30 Å $Ga_{1-x}Al_xAs$ (barrier) based on different alloy composition such as ($x = 0.2, 0.4, 0.6, 0.8$) [20].

3 Results and Discussion

In this paper, we have theoretically investigated the impact of different composition 'x' of the barrier height on transmission coefficient and IV characteristics of GaAs/$Ga_{1-x}Al_xAs$ double barrier heterostructure. In this study, GaAs/$Ga_{1-x}Al_xAs$ based double barrier heterostructure is selected at operating temperature $T = 10$ K.

3.1 Transmission Coefficient

Transmission coefficient defined as the possibilities of any one electron (when striking on a barrier structure) will tunnel through structure and contributes current flow [19]. According to Ferry's concept [21], transmission coefficient is given by

$$T(E) = \begin{cases} \frac{1}{1+\left(\frac{K^2+k^2}{2Kk}\right)^2 \sinh^2(kL)}; E < V \\ \frac{1}{1+\left(\frac{K^2-K'^2}{2KK'}\right)^2 \sin^2(K'L)}; E > V \end{cases} \quad (1)$$

where $K = \frac{\sqrt{2m*E}}{\hbar}$, $k = \frac{\sqrt{2m*(V-E)}}{\hbar}$
where E stands for carrier energy, L stands for barrier width, k and K stand for wave vector.

If $E > V$, then $k = iK'$, where $K' = \frac{\sqrt{2m*(E-V)}}{\hbar}$; where m^* stands for effective mass through barrier structure, $\hbar$ stands for plank's constant.

Figure 2 shows transmission coefficient versus energy of GaAs/$Ga_{1-x}Al_xAs$ double barrier heterostructure for different composition ($x = 0.2, 0.4, 0.6, 0.8$) at well width 20 Å, 30 Å and 40 Å, respectively. Figure 2a shows highest transmission coefficient (~1) as well width 20 Å, at electron energy 139.011, 201.696, 246.219 and 277.842 meV for composition 0.2, 0.4, 0.6 and 0.8, respectively. It is inspected that by keeping barrier thickness fixed, maximum value of transmission coefficient exists at 'x' = 0.2, and also, we have observed when we have changed the composition of the material, height of the barrier is also changed accordingly, and due to this, the peak value of the transmission coefficient is also changed. If we increase the composition 'x,' height of the barrier is also increased, and because of this, peak of transmission coefficient becomes lower and move toward higher resonant energy. This is because electron tunneling is difficult through barrier having high height and confinement effect results in increased resonance energies when the barrier height increase as per Eq. (1) [19]. We have compared the calculated results with the reported results from other workers which show a good agreement with the reported work [22–25]. Figure 2b shows highest transmission coefficient (~1) as well width 30 Å, at electron energy 103.948, 144.081, 168.493 and 184.424 meV for composition 0.2, 0.4, 0.6 and 0.8, respectively. Figure 2c shows highest transmission coefficient (~1) as well width 40 Å, at electron energy 80.596, 107.468, 122.209 and 131.400 meV for composition 0.2, 0.4, 0.6 and 0.8, respectively. And, it is also examine that for composition 0.6 and 0.8 transmission coefficient coefficient becomes high 2nd time due to the existence of 2nd quasi-bound state. This is because when the thickness of the well is large, then the electron deep penetrates into the well [19].

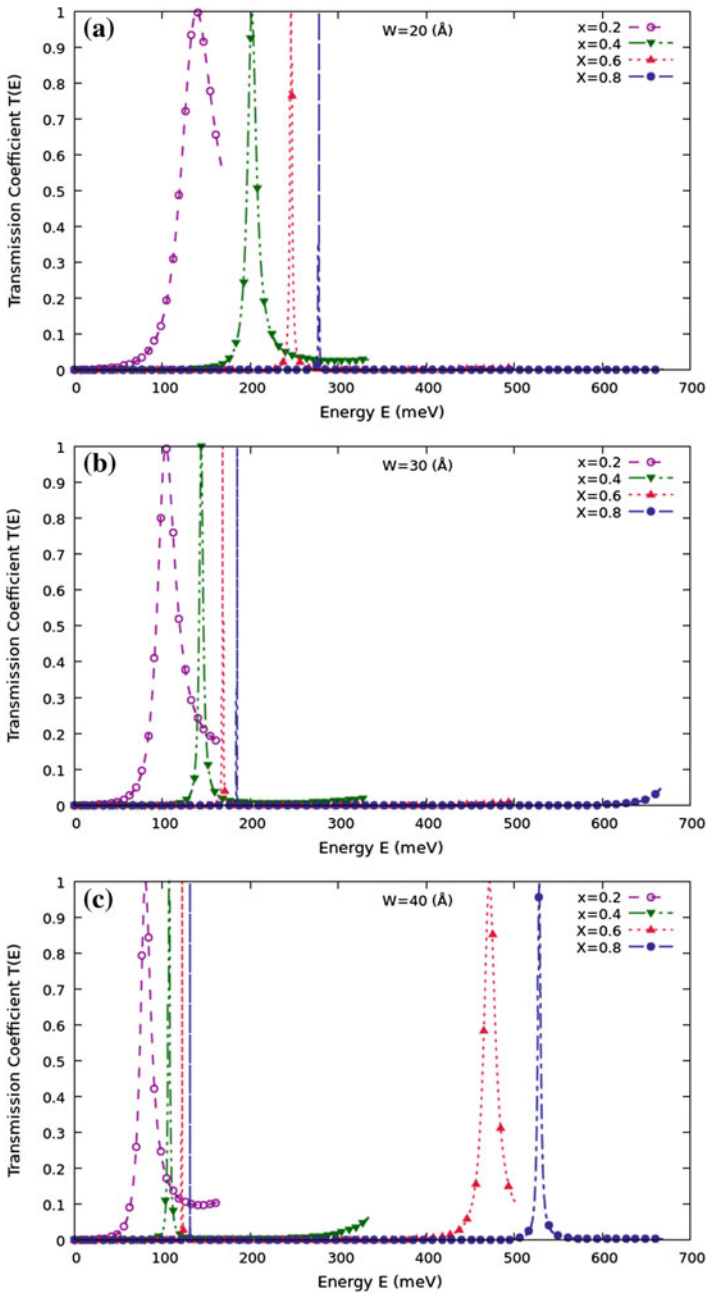

Fig. 2 **a** Transmission coefficient versus energy for 30 Å $Ga_{1-x}Al_xAs$/20 Å GaAs/30 Å $Ga_{1-x}Al_xAs$ double barrier heterostructure at different composition ($x = 0.2, 0.4, 0.6, 0.8$). **b** Transmission coefficient versus energy for 30 Å $Ga_{1-x}Al_xAs$/30 Å GaAs/30 Å $Ga_{1-x}Al_xAs$ double barrier heterostructure at different composition ($x = 0.2, 0.4, 0.6, 0.8$). **c** Transmission coefficient versus energy for 30 Å $Ga_{1-x}Al_xAs$/40 Å GaAs/30 Å $Ga_{1-x}Al_xAs$ double barrier heterostructure at different composition ($x = 0.2, 0.4, 0.6, 0.8$)

3.2 IV Characteristics

The number of carriers that tunnel through the double barrier structure at any field is equal to the current. It is described by multiplying number of carriers with the probability of specific carriers tunneling at any particular energy [19].

$$I \propto \int_{\text{band}} T(E) f^{\text{FD}}(E) \rho^{\text{3D}}(E) \mathrm{d}E \tag{2}$$

Integral is done over the density of state having three-dimensional or bulk form, and energy of carriers and Fermi–Dirac distribution function when the carriers approaching the structure of barrier which are lies in bulk band.

where f^{FD} stand for Fermi–Dirac distribution function, $\rho^{\text{3D}}(E)$ stands for density of state in (3D) bulk forms, $T(E)$ stands for transmission coefficient [19].

$$\rho(E) = \frac{1}{2\pi^2}\left(\frac{2m_{\text{eff}}}{\hbar^2}\right)^{3/2} (E - \Delta E)^{1/2} \ominus (\mathrm{E} - \Delta \mathrm{E}) \tag{3}$$

$$f^{FD} = \frac{1}{\exp([E - (E_F + \Delta E)]/KT) + 1} \tag{4}$$

where ΔE stands for gain in energy with respect to the double barrier center, T stands for temperature, m_{eff} stands for effective mass of structure and $\hbar$ stands for plank's constant .

Figure 3a–c shows IV characteristic of GaAs/$Ga_{1-x}Al_x$As double barrier heterostructure for different composition ($x = 0.2, 0.4, 0.6, 0.8$) at well width 20 Å, 30 Å and 40 Å, respectively. It is observed that when the height of the barrier is less, then the feasibility of electron tunneling is high, and because of this, transmission coefficient becomes high, and hence, current and modulation efficiency also becomes high. When the barrier height is increased, then transmission coefficient is decreased, and hence, it is observed that current and modulation efficiency is also decreased. This is because feasibility of electron tunneling is less due to the barrier having high value of height as per Eq. (2) [19].

4 Conclusion

In this present investigation, it is concluded that transmission coefficient and IV characteristic are the crucial measurable quantity to estimate the double barrier heterostructure property. This study predicts that at temperature ($T = 10$ K), the less barrier height makes feasible to high electron tunneling. Therefore, transmission coefficient becomes high which results current and modulation efficiency also becomes higher. When the barrier height increases, transmission coefficient decreases, and hence, current and modulation efficiency also decreases.

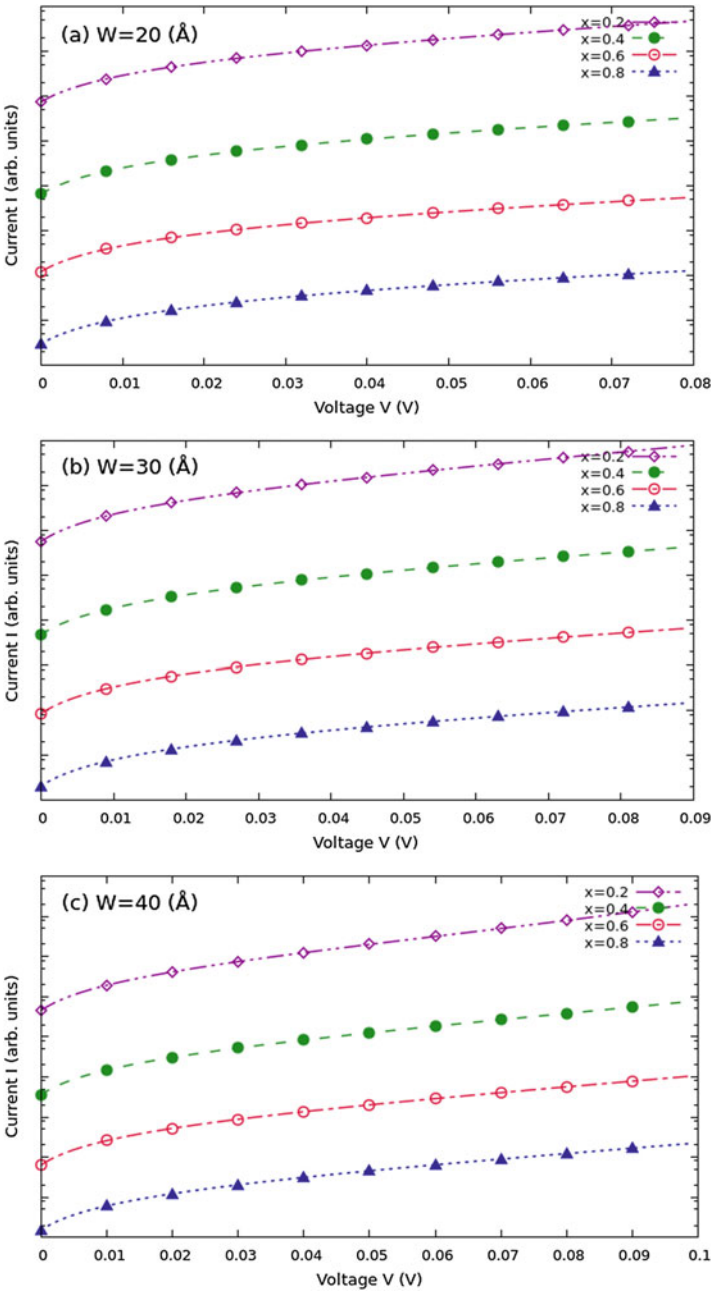

Fig. 3 **a** IV characteristic curve for 30 Å $Ga_{1-x}Al_xAs$/20 Å GaAs/30 Å $Ga_{1-x}Al_xAs$ double barrier heterostructure at different composition ($x = 0.2, 0.4, 0.6, 0.8$). **b** IV characteristic curve for 30 Å $Ga_{1-x}Al_xAs$/30 Å GaAs/30 Å $Ga_{1-x}Al_xAs$ double barrier heterostructure at different composition ($x = 0.2, 0.4, 0.6, 0.8$). **c** IV characteristic curve for 30 Å $Ga_{1-x}Al_xAs$/20 Å GaAs/40 Å $Ga_{1-x}Al_xAs$ double barrier heterostructure at different composition ($x = 0.2, 0.4, 0.6, 0.8$)

References

1. Alamo JA (2011) Nanometre-scale electronics with III–V compound semi-conductors. Nature 479:317–323. https://doi.org/10.1038/nature10677
2. Sun L, Haight R, Sinsermsuksakul P, Kim SB, Park HH, Gordon RG (2013) Band alignment of SnS/Zn(O, S) heterojunctions in SnS thin film solar cells. J Appl Phys Lett 103:181904–181905. https://doi.org/10.1063/1.4821433
3. Kroemer H (2001) Nobel lecture: quasielectric fields and band offsets: teaching electrons new tricks. Rev Mod Phys 73:783–793. https://doi.org/10.1103/revmodphys.73.783
4. Capasso F (1987) Band-gap engineering: from physics and materials to new semiconductor devices. Science 235:172–176. https://doi.org/10.1126/science.235.4785.172
5. Heber J (2010) The staircase to flexibility (An interview with Federico Capasso). Nat Mater 9:374–375. https://doi.org/10.1038/nmat2758
6. Dingle R, Stormer HL, Gossard AC, Wiegmann W (1978) Electron mobilities in modulation doped semiconductor heterojunction super-lattices. J Appl Phys Lett 33:665
7. Mimura T (2002) The early history of the high electron mobility transistor (HEMT). IEEE Trans Microw Theor Tech 50(3):780–782. https://doi.org/10.1109/22.989961
8. Turkulets Y, Shalish I (2018) Probing dynamic behavior of electric fields and band diagrams in complex semiconductor heterostructures. J App Phys 123:024301–024306. https://doi.org/10.1063/1.5013274
9. Ferreira R, Balkan N, Xavier M (2012) Semiconductor modeling techniques. In: Springer series in materials science, vol 159. Springer, Berlin
10. Kinsler P, Kelsall RW, Harrison P (1999) Interface phonons in asymmetric quantum well structures. Superlatt Microstruct 25:163–166. https://doi.org/10.1006/spmi.1998.0631
11. Tredicucci A, Gmachl C, Capasso F, Sivco DL, Hutchinson AL (1999) Long wavelength superlattice quantum cascade lasers at $\lambda \approx 17$ μm. J Appl Phys Lett 74:638–640
12. Kar A, Sain S, Rossouw D, Knappetta BR, Pradhanb SK, Botton GA, Wheatley AEH (2017) Targeting low-cost type-II heterostructures: synthesis, structure and photoreactivity. J Alloy Comp 698:944–956. https://doi.org/10.1016/j.jallcom.2016.12.167
13. Chui HC, Hammons BE, Harff NE, Simmons JA, Sherwin ME (1996) $2 \times 106\ cm^2$/Vs electron mobility by metalorganic chemical vapor deposition with tertiarybutylarsine. J Appl Phys Lett 68:208–210. https://doi.org/10.1063/1.116462
14. Feng J, Clement R, Raynor M (2008) Characterization of high-purity arsine and gallium arsenide epilayers grown by MOCVD. J Cryst Growt 310:4780–4785. https://doi.org/10.1016/j.jcrysgro.2008.08.023
15. Alferov Z (2013) Heterostructures for optoelectronics: history and modern trends. Proc IEEE 101(10):2176–2182. https://doi.org/10.1109/jproc.2013.2274912
16. Amann MC, Capasso F, Larsson A, Pessa M (2009) Focus on advanced semiconductor heterostructures for optoelectronics. New J Phys 11(12):125012–125015. https://doi.org/10.1088/1367-2630/11/12
17. Akura M, Dunn G, Missous M, Sexton J (2017) Potential well barrier diodes for submillimeter wave and high frequency applications. IEEE Electron Device Lett 38:1–4. https://doi.org/10.1109/LED.2017.2673662
18. Akura M, Dunn G, Missous M (2017) A hybrid planar-doped potential-well barrier diode for detector applications. IEEE Transctions Electron Devices 64:4031–4035. https://doi.org/10.1109/TED.2017.2733724
19. Harrison P, Valavanis A (2016) Quantum well, wires and dots: theoretical and computational physics of semiconductor nanostructure, 4th edn. Wiley NJ, West Sussex, United Kingdom, pp 64–65, 68–70
20. Flores YV, Albo A (2017) Impact of interface roughness scattering on the performance of GaAs/$Ga_{1-x}Al_x$As terahertz quantum cascade lasers. IEEE J Quantum Electron 53(3):1–8. https://doi.org/10.1109/JQE.2017.2689743
21. Ferry DK (1995) Quantum mechanics: an introduction for device physicists and electrical engineers. IOP Publishing, London

22. Mukherjee S, Karmakar R, Deyasi A (2011) Theoretical computation of transmission coefficient of double quantum well triple barrier structure in presence of electric field. Int J Soft Comput Eng (IJSCE) 1:41–44
23. Gain J, Sarkar MD, Kundu S (2010) Energy and effective mass dependence of electron tunnelling through multiple quantum barriers in different heterostructures. arXiv:1002.1931v1 [cond-mat.mes-hall], Mesoscale Nanoscale Phys 1–8
24. Yang L, Li Y, Wang Y, Xu S, Hao Y (2016) Asymmetric quantum-well structures for AlGaN/GaN/AlGaN resonant tunneling diodes. J Appl Phys 119:164501–164508. https://doi.org/10.1063/1.4948331
25. Jiang A, Matyas A, Vijayraghavan K, Jirauschek C, Wasilewski ZR, Belkin MA (2014) Experimental investigation of terahertz quantum cascade laser with variable barrier heights. J Appl Phys 115:163103–163105. https://doi.org/10.1063/1.4873461

Polarization Encoded Multi-logic Functions with Direct Detection

J. K. Saini, A. Saharia, T. Ismail, I. S. Fahim, M. Tiwari and G. Singh

Abstract In this paper, a new scheme for the realization of an optical logic circuit using Mach–Zehnder modulators (MZM) with direct detection has been proposed. Amplitude and phase information of the optical signals have been used for the differentiation of optical signals into four different states that can be represented using two binary inputs, while direct detection has been used for the effective mapping of these states with their respective binary outputs. The realization of seven logic gates, two reversible optical logic gates (Feynman and double Feynman gates) and half adder and half subtractor in a single optical circuit is achieved successfully. High extinction ratios (ERs) up to 50 dB are obtained while keeping the data rate constant at 10 Gbps.

Keywords All optical logic function · Mach–Zehnder modulator · Polarization · Vector addition

1 Introduction

Recently, it has been observed that high-speed performance can be achieved by reconfigurable computing. Next-generation computing systems and optical networks rely on using high-speed optical logic gates as key elements for the implementation of signal processing functions [1]. Optical functions like signal processing, data encoding, address recognition, parity checking, counters, etc., necessitates requirement of

J. K. Saini (✉) · A. Saharia · G. Singh
Department of ECE, Malaviya National Institute of Technology Jaipur (MNIT Jaipur), Jaipur, India
e-mail: 2017pec5485@mnit.ac.in

T. Ismail
Department of Engineering Applications of Laser (NILES), Cairo University, Giza, Egypt

I. S. Fahim
School of Engineering and Applied Science, Nile University, Giza, Egypt

M. Tiwari
Department of ECE, Manipal University Jaipur, Jaipur, India

V. Janyani et al. (eds.), *Optical and Wireless Technologies*, Lecture Notes in Electrical Engineering 648, https://doi.org/10.1007/978-981-15-2926-9_33

optical–electrical–optical conversions [2–7]. Two schemes based on nonlinear optics and modulators are of vital importance [8]. Where the first type is considered periodically poled lithium niobate (PPLN) [9], silicon-nanowire [10], nonlinear optical loop mirror (NOLM), highly nonlinear fiber (HNLF) [11], and semi-conductor optical amplifier (SOA) [12] are used. But this type suffers from the drawback of the requirement of high drain current for SOA and its poor speed limit [13, 14]. HNLF-based logic gates present very high dispersion and nonlinearly chirp noise signal when used with long fiber length [14]. The second type is Mach–Zehnder modulator (MZM) and Mach–Zehnder interferometer (MZI) that focused mainly on intensity information [8, 15].

In this paper, a new scheme for reconfigurable logic circuit has been proposed that is based on MZM with a polarization phase shifter. Amplitude, as well as phase polarization of optical signal, has been utilized here along with usage of direct detection [16] at the output port. The function is easily implemented by adjusting the biasing of MZM and the phase shift of the optical signal. The advantage of this methodology is that different optical logic functions are implemented with the same hardware that has high scalability and simple configuration. 3-input 3-output hardware circuit has been proposed with three MZMs, two polarization phase shifters and switches. Extinction ratio [17] of all the logic function is as high as 50 dB has been observed. Eleven logic functions including universal gates, other logical and optical gates like OR, AND, XOR, XNOR, NOT, Feynman, and Double Feynman, and logic functions like Half adder and Subtractor [18, 19] can be realized using three MZMs and varying their biasing and phase parameters involved at speed of 10 Gbps.

2 Operating Principle

The circuit schematic as shown in Fig. 1 comprising of the continuous wave laser (CW laser), three MZMs driven by three binary data input sequences which are connected in parallel, three photodetectors, two polarization phase shifters, and two switches. 3-input 3-output ports are designed for different optical logic functions, and adjustment of input signal amplitude and phase gets used for the selection of the logic function of interest. The basic formula for an output of MZM is shown below:

$$|E| = \frac{1}{10^{\frac{I}{20}}}\left\{\cos\left[\frac{\pi}{2V_\pi}(V_{\text{in}}(t) - V_{\text{bias}})\right]e^{j\frac{\pi V_{\text{bias}}}{2V_\pi}}\right\}\begin{pmatrix} a_x \\ b_y e^{j\theta} \end{pmatrix} e^{j\varphi} \tag{1}$$

where I is the insertion loss of MZM, V_π is the half-wave voltage, $V_{\text{in}}(t)$ shows input signal voltage, and V_{bias} shows biasing voltage of MZM. For a typical 3 × 3 logic circuit, we can arrange input and output ports according to the requirement of that particular logic circuit. The 2 × 1 logic gate performs mapping of all the four combinations of the two binary inputs [(0, 0), (0, 1) (1, 0), (1, 1)] to their desired/respective output state (0 or 1). The key factor behind this is vector addition.

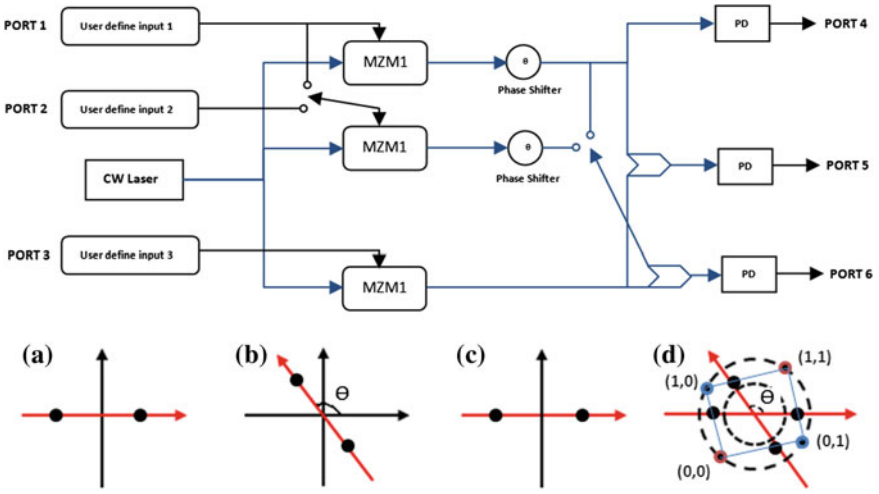

Fig. 1 Block diagram for logic gate implantation using MZMs describing operating principle of logical OR gate **a** constellation at MZM 1 output, **b** constellation at phase shifter output, **c** constellation at MZM 3 output, and **d** constellation after vector addition. Black dots denote '0' and '1' logic

For half adder, half subtractor, and Feynman gate, we need 2×2 logic circuit so two input ports and two output ports are used and the rest are open circuited. For double Feynman gate, all the three input ports and three output ports are used.

Taking OR Gate, for example, all MZMs are at the null point. Here, we use port-1 and port-3 for the input signal and port 5/6 for the output signal. So, MZM1 and MZM3 are driven by two different signals with the same voltages. As shown in Fig. 1a and c, after passing the two input signals through both the MZMs, they undergo same polarization phase, so the first signal is passed through the polarization phase shifter and it gets rotated by 120° (Fig. 1c). The purple and blue dots in Fig. 1d representing the constellation of combined signal denote all the four input combinations of the binary inputs. The two combinations of these four signals are detected in the electrical domain by photodetector thus OR gate is realized. For the NOT gate, port-1 is taken as the input port and port-4 as the output port. Similar to the realization of the OR gate discussed, all other logic gates can be configured by adjusting the amplitude and phase as stated in Table 1. Feynman gate uses port-1 and port-3 as input ports, and outputs are taken at port-4 and port-5, whereas for double Feynman gate, all input and output ports are taken. For double Feynman gate, the key is positioned to port-2. For half adder and half subtractor, 2 or 3 logic functions are needed to work simultaneously. Here, port-1 and port-3 are used as the input ports and port-5 and port-6 are used as output ports for both half adder and half subtractor.

For half adder, port-4 works as a sum port and port-6 as a carry port, and for half subtractor, port-5 works as a difference port and port-6 as a borrow port. For half subtractor key-1 is switched to position 1 so MZM-2 performs NOT operation,

Table 1 A configuration of eleven optical logic circuits

S. No.		Biasing			Polarization phase shift	
		MZM (1)	MZM (2)	MZM (3)	Phase shift (1)	Phase shift (2)
1	NOT	+Quad point	Zero point	Zero point	0	0
2	OR	Zero point	Zero point	Zero point	120	120
3	AND	Zero point	Zero point	Zero point	45	45
4	NOR	+Quad point	+Quad point	+Quad point	15	15
5	NAND	+Quad point	+Quad point	+Quad point	120	120
6	XOR	Zero point	Zero point	Zero point	180	180
7	XNOR	Zero point	Zero point	+Quad point	180	180
8	Feynman	Zero point	Zero point	Zero point	180	180
9	Double Feynman	Zero point	Zero point	Zero point	180	0
10	Half adder	Zero point	Zero point	Zero point	180	45
11	Half subtractor	Zero point	+Quad point	Zero point	180	45

now A and $\bar{A}$ both are present and XOR & AND operations are operated by shifting key-2 to position 2. Likewise, 11 logic circuits are realized by adjusting phase and amplitude of the signal in one circuit.

3 Results Analysis

As shown in Fig. 1a, CW laser with 10dBm power, 100 kHz line width, and 193.1 THz operating frequency has been employed. The three MZMs in parallel driven by input binary data of 2 V amplitude get biased and polarized accordingly based on the input binary data for the realization of different logic gates and functions, the details of which have been summarized in Table 1. The input signal of 10 Gbps is generated using the input bit sequence, and the eye diagram detection and waveform recording has been done by the use of an oscilloscope, the results of which are shown in Fig. 2. As shown in Fig. 3, ERs of different logic functions have been obtained by formula as shown below.

$$\mathrm{ER} = 10\log\left(\frac{P_{\mathrm{ON}}}{P_{\mathrm{OFF}}}\right)$$

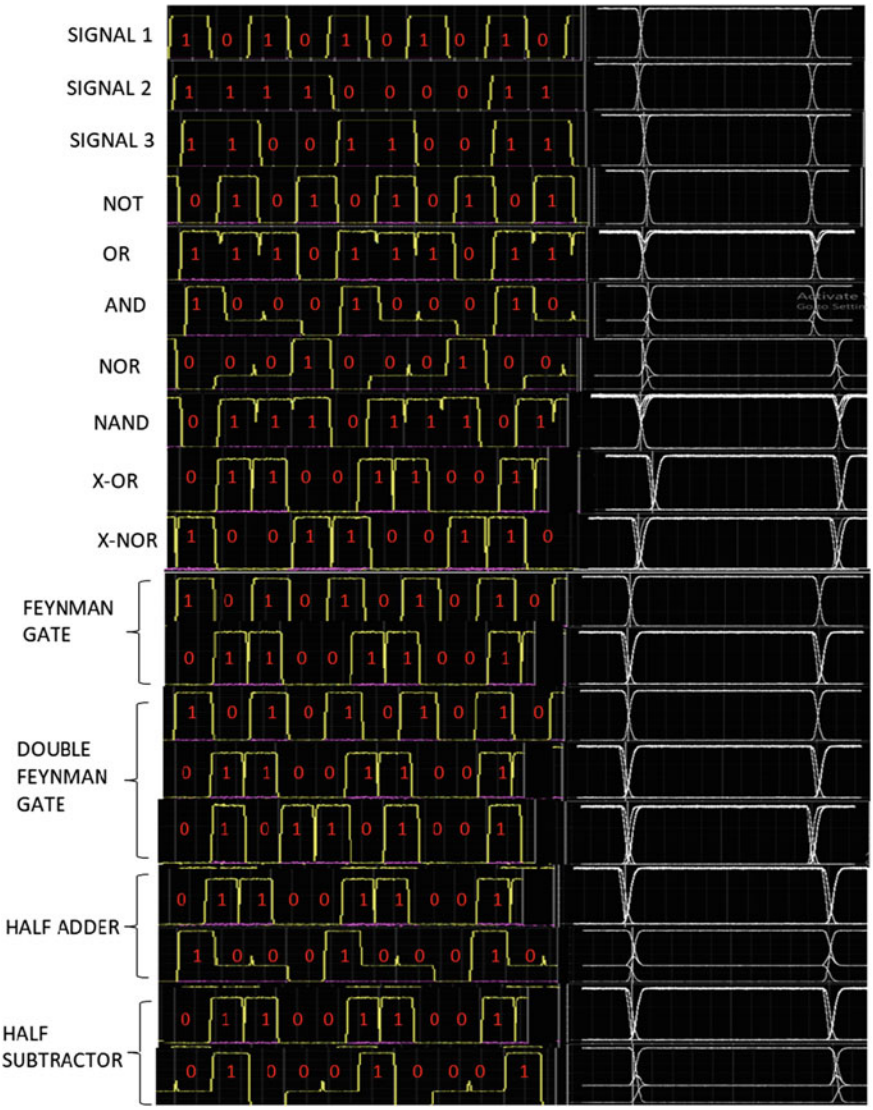

Fig. 2 Simulation results of all logic function

We consider 10 dBm for ON power and −100 dBm for OFF power of the laser. As the difference between P_{ON} and P_{OFF} widens, the receiver can easily distinguish between level '0' and level '1.' Thus, a high value of ER is always desirable. It is clear from Fig. 3 that there is a significant variation in ER value even at the same data rate which depends on the setting of parameters as mentioned in Table 1.

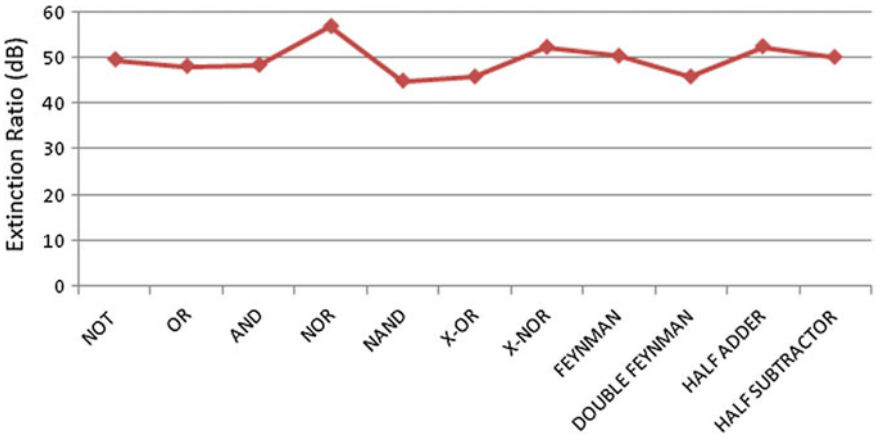

Fig. 3 Extinction ratio of all logic functions

4 Conclusions

This paper proposes a new scheme to realize different kinds of optical logic functions and combination circuits based on three MZM modulators. As a result of this circuit, complexity is reduced to the manifold. Both phase and intensity of the optical signal are employed to create the four combinations of the input signal. Pin diode photodetector is used to directly detect the output states of the circuit. Large ERs of the value 50 dB are calculated that is higher than reported in [4].

Acknowledgements The authors are grateful for the understanding of joint and coordinated research between the researchers from the Department of ECE of MNIT Jaipur, Manipal University, Jaipur, and partner Egyptian Universities (The Cairo University and The Nile University).

References

1. Pei-Li L, De-Xiu H, Xin-Liang Z, Yang W (2008) Single-SOA-based ultrahigh-speed all-optical half subtracter with polSK modulated signals. Chin Phys Lett 25(5):1705
2. Saruwatari M (2000) All-optical signal processing for terabit/second optical transmission. IEEE J Sel Top Quantum Electron 6(6):1363–1374
3. Bogoni A, Wu X, Bakhtiari Z, Nuccio S, Willner AE (2010) 640 Gbits/s photonic logic gates. Opt Lett 35(23):3955–3957
4. Kim JY, Kang JM, Kim TY, Han SK (2006) All-optical multiple logic gates with XOR, NOR, OR, and NAND functions using parallel SOA-MZI structures: theory and experiment. J Lightwave Technol 24(9):3392
5. Stubkjaer KE (2000) Semiconductor optical amplifier-based all-optical gates for high-speed optical processing. IEEE J Sel Top Quantum Electron 6(6):1428–1435
6. Zaghloul YA, Zaghloul ARM, Adibi A (2011) Passive all-optical polarization switch, binary logic gates, and digital processor. Opt Express 19(21):20332–20346

7. Qin J, Lu GW et al (2014) Simultaneous multichannel wavelength multicasting and XOR logic gate multicasting for three DPSK signals based on four-wave mixing in quantum-dot semiconductor optical amplifier. Opt Express 22(24):29413–29423
8. Tang X, Zhai Y et al (2016) Implementation of a reconfigurable optical logic gate using a single I/Q modulator with direct detection. IEEE Photon J 8(3):1–8
9. Lazzeri E, Malacarne A, Serafino G, Bogoni A (2012) Optical XOR for error detection and coding of QPSK I and Q components in PPLN waveguide. IEEE Photon Technol Lett 24(24):2258–2261
10. Yin Z, Wu J et al (2014) All-optical logic gate for XOR operation between 40-Gbaud QPSK tributaries in an ultra-short silicon nanowire. IEEE Photon J 6(3):1–7
11. Qin J, Lu GW, Sakamoto T et al (2014) Simultaneous multichannel wavelength multicasting and XOR logic gate multicasting for three DPSK signals based on four-wave mixing in quantum-dot semiconductor optical amplifier. Opt Express 22(24):29413–29423
12. Yu C, Christen L, Luo T, Wang Y, Pan Z, Yan LS, Willner AE (2005) All-optical XOR gate using polarization rotation in single highly nonlinear fiber. IEEE Photon Technol Lett 17(6):1232–1234
13. Kong D, Li Y et al (2013) All-optical XOR gates for QPSK signal based optical networks. Electron Lett 49(7):486–488
14. Fang Z, Tang X, Zhai Y, Zhang X, Xi L, Zhang W (2017) Reconfigurable optical logic gate of AND, OR, NAND and NOR based on polarization modulation with direct detection. In: Lasers and electro-optics pacific rim (CLEO-PR), pp 1–3
15. Reis C, Chattopadhyay T, André P, Teixeira A (2012) Single Mach–Zehnder interferometer based optical Boolean logic gates. Appl Opt 51(36):8693–8701
16. Green PE, Ramaswami R (1990) Direct detection lightwave systems: Why pay more? IEEE LCS 1(4):36–38
17. Packard H (1998) Measuring extinction ratio of optical transmitters. Appl Note 1550–8
18. Aditya M, Kumar YN, Vasantha MH (2016) Reversible full/half adder with optimum power dissipation. In: 10th international conference on in intelligent systems and control (ISCO), pp 1–4
19. Ghosh A, Jain A, Singh NB, Sarkar SK (2016) Single electron threshold logic based Feynman gate implementation. In: Research in computational intelligence and communication networks (ICRCICN), pp 266–268

Parametric Analysis of Optical Microring Resonator

A. Saharia, R. K. Maddila, T. Ismail, I. S. Fahim, M. Tiwari and G. Singh

Abstract This article presents the parametric analysis of the optical microring resonator. It includes the numerically simulated analysis. The mathematical formulation represents the several relations that could influence the performance of optical microring resonator. The simulations give the graphical representations of ring resonator performances by the alteration of various parameters. In this paper, we have analyzed the variations in quality factor, extinction ratio and the resonance peak of an optical microring resonator with changes in effective refractive index, length of the ring and the group index. The variation has been analyzed through numerical simulations and represented in the form of plots.

Keywords Microring resonator · Quality factor · Extinction ratio · Resonance peak

1 Introduction

Optical microring resonator is emerging as the most preferred device for optical circuit generation. In most of the applications of optical communication, the ring resonators are used as a basic element for complex circuit generation. The optical waveguides with nonlinear characteristics showed a vital role for various optical applications like switching, multiplexing, compression and logic operations [1]. With the always increasing scope for future optical circuits, the resonant structures are finding its application for various complex integrated optical circuits. Meanwhile, with the advantage of low power consumption and ultrahigh speed, it is also applied in

A. Saharia (✉) · R. K. Maddila · G. Singh
Department of ECE, Malaviya National Institute of Technology Jaipur (MNIT Jaipur), Jaipur, India

T. Ismail
Department of Engineering Applications of Laser (NILES), Cairo University, Giza, Egypt

I. S. Fahim
School of Engineering and Applied Science, Nile University, Giza, Egypt

M. Tiwari
Department of ECE, Manipal University Jaipur, Jaipur, India

V. Janyani et al. (eds.), *Optical and Wireless Technologies*, Lecture Notes in Electrical Engineering 648, https://doi.org/10.1007/978-981-15-2926-9_34

existing signal processing circuits for efficient working to achieve desirable transfer function [2], logic function [3] and time delay element [4] in a circuit. Along with this, an optical resonant structure finds lots of application in optical signal processing [5–7] by virtue of its various qualities like low loss, large free spectral range (FSR), signal generation and frequency conversion. The microring resonator performances are generally based on the resonance response of the device and the values of the parameters like quality factor, output gain and losses. Researchers have analyzed the variation in the parameters with different materials [5]. They have shown how different materials affect the resonance condition of the ring.

Along with this, the variation in the modulating voltage causes the change in the quality factor of the ring resonator, and due to this, it is difficult to stabilize the ring waveguide quality factor at a particular value when the modulating voltage is varying. With each shift in modulating voltage, the resonance peak of the ring also shifts to a new position. In this article, we have analyzed various other parameters which are varied to find variation in the values of quality factor, extinction ratio and output gain. The article has been structured in the following manner: Sect. 2 composed of mathematical relation associated with a ring resonator, Sects. 3 and 4 show the calculations for quality factor, output gain and extinction ratio, followed by conclusion and acknowledgment.

2 Mathematical Analysis

The mathematical relations for resonance condition for a ring resonator and shift in resonance are depicted through Eqs. (2) and (3), respectively. The quality factor (Q) of the ring and its relation with a full width half maximum (FWHM) can be given by [5]

$$\text{FWHM} = \lambda_{\text{res}}/Q \tag{1}$$

$$\lambda_{\text{res}} = \frac{n_{\text{eff}} L}{m} \tag{2}$$

$$\delta\lambda = \frac{\Delta n}{n_{\text{eff}}}\lambda_{\text{res}} \tag{3}$$

where "Δn" shows the change in refractive index, λ_{res} is the resonant wavelength, n_{eff} is the effective refractive index of the material, L is optical path length (ring circumference) and $\delta\lambda$ is the resonant shift. The coupling of the signal between ring and bus waveguide and vice versa is a function of the gap distance between the ring and the bus waveguide. The coupling efficiency between a ring and bus waveguide is given by [6, 7]

$$\kappa(s) = \frac{\omega\varepsilon_0 \cos\left(\frac{k_x w}{2}\right)}{2P\left(k_x^2 + \alpha^2\right)}\left(n^2 - n_0^2\right) \times \sqrt{\frac{\pi R}{\alpha}} \exp\left(-\alpha\left(s + \frac{w}{2}\right)\right) \times \left[\alpha \cos\left(\frac{k_x w}{2}\right) \sinh\left(\frac{\alpha w}{2}\right) + k_x \sin\left(\frac{k_x w}{2}\right) \cosh\left(\frac{\alpha w}{2}\right)\right] \tag{4}$$

where "s" is the gap distance ring and adjacent waveguide, k_x is the transverse propagation constant, α is energy loss rate in the cladding, R is the radius of the ring, w is the width of the waveguides and P is the mode power [6, 7]. The factors k_x, α and P are given as [6, 7]

$$k_x = \sqrt{n^2 k^2 - \beta^2} \tag{5}$$

$$\alpha = \sqrt{\beta^2 - n_0^2 k^2} \tag{6}$$

$$P = \frac{\beta}{2\omega\mu_0}\left(\frac{w}{2} + \frac{1}{\alpha}\right) \tag{7}$$

where n is the refractive index of the material and n_0 is the refractive index of the cladding. Considering air as cladding, so n_0 is 1 and β is the propagation constant which is assumed to be same in the bus and ring waveguide. In another relation, the quality factor is as given below [6, 7]

$$Q = \omega_{\text{res}}\tau = \frac{2\pi^2 Rn}{\lambda_{\text{res}}\kappa^2} \tag{8}$$

where Q is the loaded quality factor when the cavity is assumed to be lossless, τ is the energy decay time constant, R is the radius of the cavity, λ_{res} is the resonant wavelength and κ is the coupling efficiency. The quality factor is directly proportional to the radius of the ring waveguide or ring length; therefore, higher the ring radius, more is the quality factor of the ring resonator. The quality factor of the ring also depends on the effective refractive index, and the quality factor reduces when the effective refractive index increases.

3 Simulation and Analysis

The ring has been designed with ring length 80 μm and with adjacent waveguide gap of 0.003 μm; other design specifications of ring resonator are shown in Table 1.

In order to perform the parametric analysis of ring resonator, the ring has been connected with an optical source (Fig. 1) and its output spectrum has been analyzed through optical network analyzer. The modulation has been performed through the ring by connecting the ring to the optical modulator and a modulation voltage DC

Table 1 Properties of the ring resonator

Coupling coefficients 1 and 2	0.3 each
Effective index	2.29
Group index	4.42
Waveguide modes	TE
Ring length	80 μm

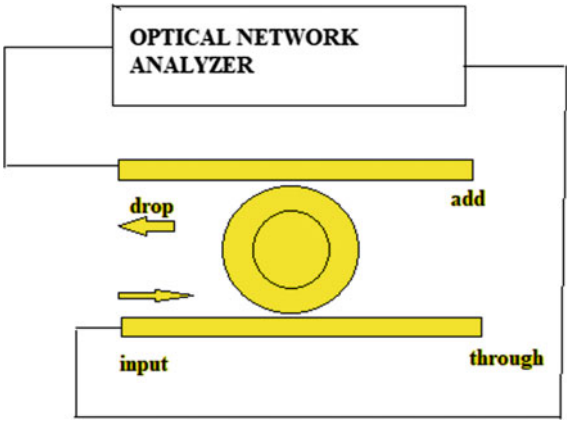

Fig. 1 Optical microring resonator analysis setup

source. The output resonance peak, *Q* factor and extinction ratio have been analyzed by varying effective index, length of the ring and group index.

3.1 Parameter Affecting the Resonance

Ring Length:

The ring length is the circumference of the ring; it is one of the parameters which affects the resonant condition of the resonator. Along with this, it also affects the quality factor and extinction ratio of the ring resonator. For the purpose of analysis, we have taken 4 ring lengths of 80, 100, 120 and 140 μm. The variation of length shows the variation in resonance peaks with the increasing ring length. We can also determine the change in quality factor and extinction ratio with the increasing ring length.

The variation in ring length from 80 μm to 140 μm shows the change in resonance peaks; also, the quality factor has been increased considerably from 1968 to 3444 as shown in Fig. 2a while increasing the ring length. The increase in ring circumference also increases the extinction ratio 17.27–65.66 as shown in Fig. 2b. With the above observations, we can find the behavior pattern of the ring resonator. The effective refractive index was kept at 2.29 and coupling coefficient at 0.3 for all calculations.

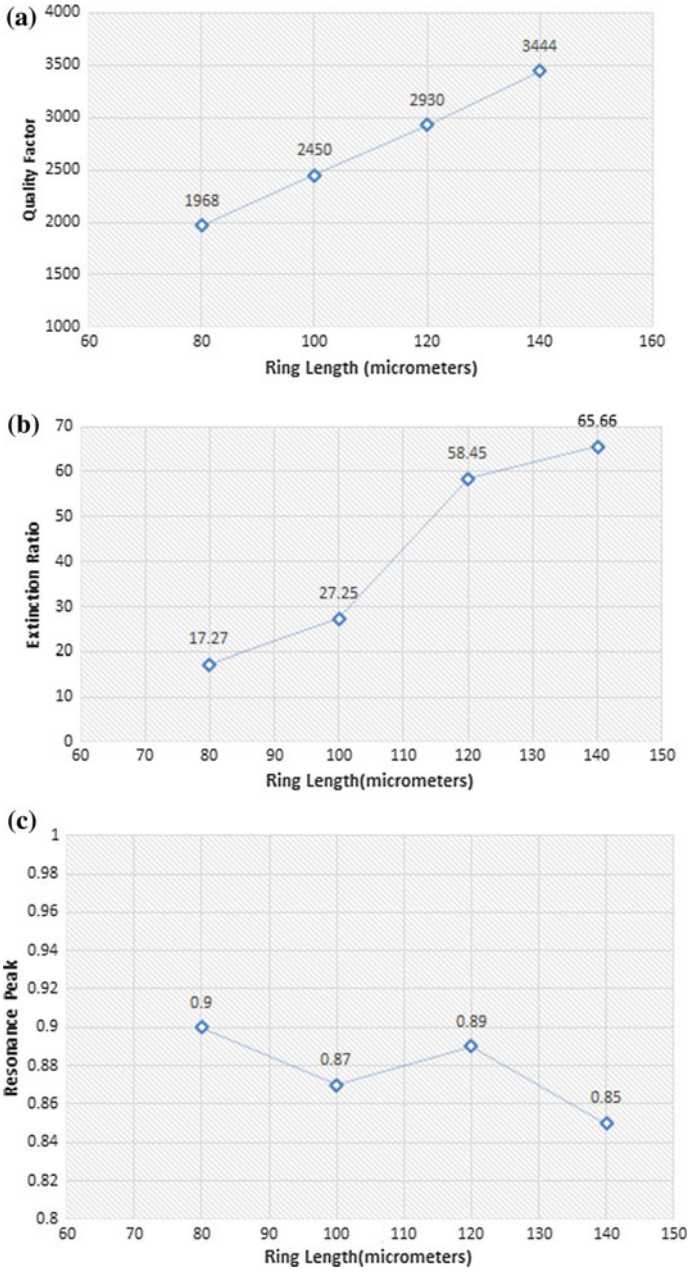

Fig. 2 Variation of parameters with ring length: **a** quality factor, **b** extinction ratio and **c** resonance peak

Effective Refractive Index:

The variation in resonant output, quality factor and extinction ratio with the variation in effective refractive index values is also analyzed. When we connect ring resonator with electric modulator, the change in modulating voltage would change the effective index of the ring; therefore, we have determined the ring response for effective index variation as well.

We have determined the response of ring resonator for three different effective refractive indexes as shown in Fig. 3a–c. The resonator has shown the nonlinear variation with extinction ratio, and resonator shows the highest quality factor of 2445 with the ring effective index of 2.25. The quality factor decreases when the effective index increases. We can also see the variation in resonance peaks with the increasing effective refractive index. The ring length is kept at 80 μm, and coupling coefficient is kept at 0.3 for all calculations.

Group Index:

The last parameter analyzed in this study is group index, and the resonance response, extinction ratio and quality factor have been calculated for the ring of radius 80 μm, effective index of 2.29 and coupling coefficient of 0.3. The calculation has been performed for 3 different group indexes of 2.0, 4.42 and 6.0.

The variation in the group index is shown in Fig. 4a–c explaining that an increase in group index also increased the quality factor of ring resonator as it shows 3345 for 6.0 from 1118 for group index 2.0. The three different group indexes show three different materials of the ring resonator. The extinction ratio, on the other hand, showed the highest value at 4.42. The resonance peaks show not so significant variation as it does not affect much by group index variation. The variations in all these parameters have a significant impact on ring resonator performance, especially when connected in cascade circuit.

4 Conclusion

This article demonstrated the analysis of ring resonator for different parametric variations. In this paper, we have proved the mathematical relation for the increase in a quality factor of the ring resonator with an increase in ring radius. We have also demonstrated the variation in the quality factor for different group indexes which showed that material with the highest group index will have the highest quality factor. Along with this, we have also shown the variation of quality factor with the increasing effective index, effective index of the ring changes when we apply external voltage for modulation, and we have shown the dependency of the quality factor over effective index too. All these parameters have a significant effect on the performance of ring resonator. The application of ring resonator in integrated optics [8–10] would need these parameters to be optimized at specific values; with this analysis, we can find the possible reasons for the variation in behavior pattern of ring resonator which would be very much required in complex optical circuits.

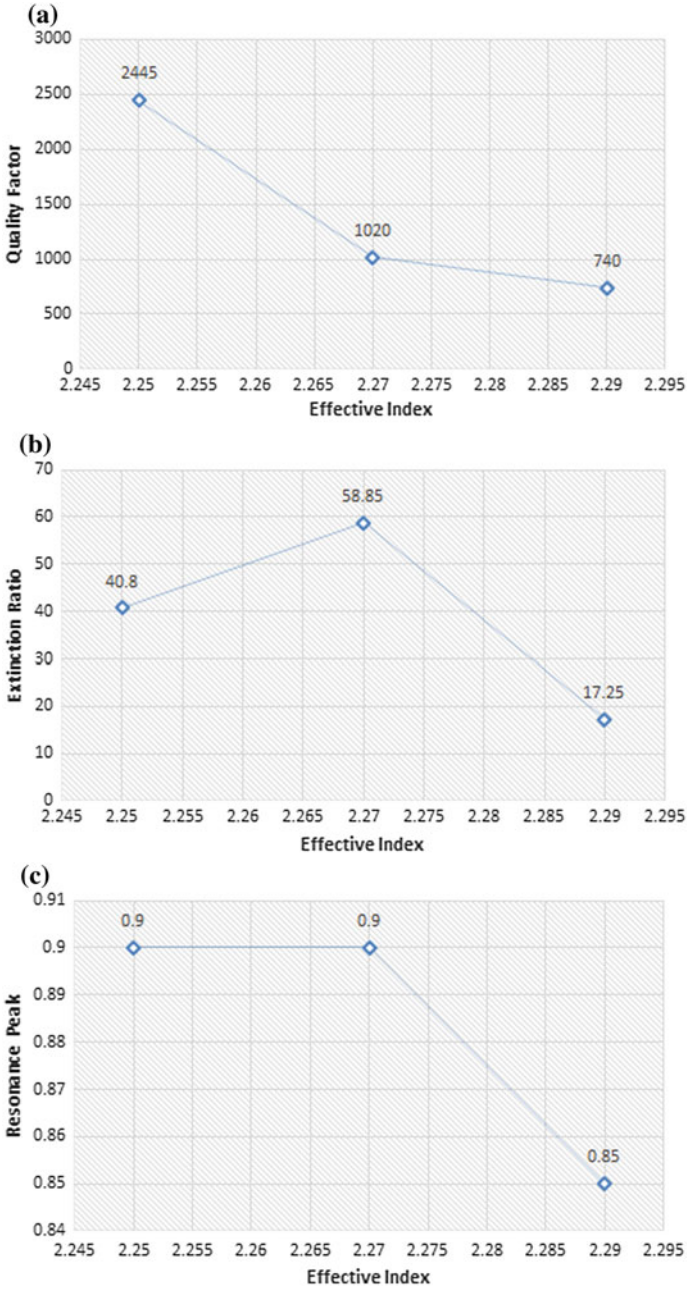

Fig. 3 Variation of parameters with effective index: **a** quality factor, **b** extinction ratio and **c** resonance peak

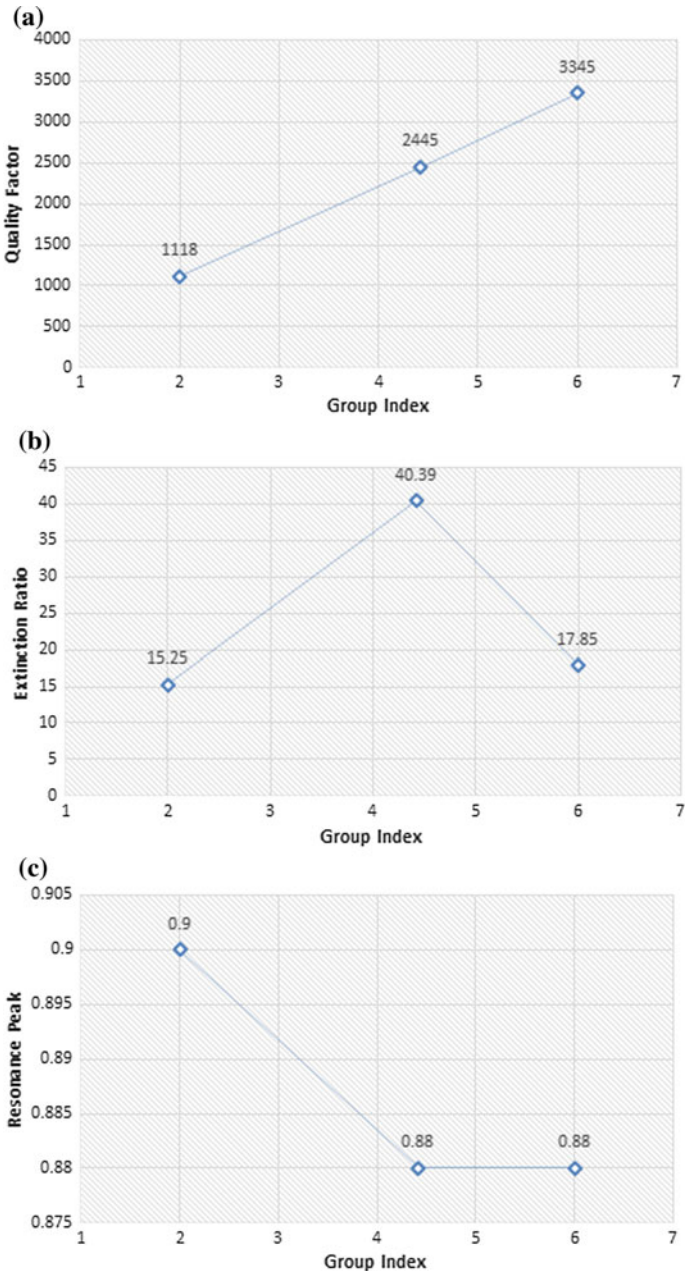

Fig. 4 Variation of parameters with group index: **a** quality factor, **b** extinction ratio and **c** resonance peak

Acknowledgements The authors are grateful for understanding of joint and coordinated research between the researchers from the Department of ECE of MNIT Jaipur, Manipal University Jaipur and partner Egyptian universities (the Cairo University and the Nile University).

References

1. Vahala K (2004) Optical microcavities, vol. 5. World Scientific Publishing Co. Pte. Ltd. ISBN 981-238-775-7
2. Little BE et al (1999) Vertically coupled glass microring resonator channel dropping filters. IEEE Photon Technol Lett 11(2):215–217
3. Van V et al (2002) Optical signal processing using nonlinear semiconductor microring resonators. IEEE J Sel Top Quant Electron 8(3):705–713
4. Heebner JE et al (2004) Optical transmission characteristics of fiber ring resonators. IEEE J Quant Electron 40(6):726–730
5. Kui LF, Uddin MR (2017) Photonic microring resonator modulated resonance response analysis. Opt Quant Electron 49:275. https://doi.org/10.1007/s11082-017-1113-5
6. Dali PP, Godbole A, Sahu S, Singh G, Tanabe T (2015) Microring resonator based NAND and NOT gate with higher output power. In: Proceedings of Asia communications and photonics conference
7. Godbole A, Dali PP, Janyani V, Tanabe T, Singh G (2016) All-optical scalable logic gates using Si_3N_4 microring resonators. IEEE J Sel Top Quant Electron 22(6):5900308
8. Bogaerts W et al (2012) Silicon microring resonators. Laser Photon Rev 6(1):47–73
9. Jalil MA, Amiri IS, Teeka C et al (2011) All-optical logic XOR/XNOR gate operation using microring and nano ring resonators. Phys Express 1(1):15–22
10. Rakshit JK, Chattopadhyay T, Roy JN (2013) Design of microring resonator based all-optical adder/subtractor. Prog Theor Appl Phys 1:32–43

Asymmetric CPW-Fed Multistubs Loaded Compact Printed Multiband Antenna for Wireless Applications

Ashok Kumar, Jitendra Kumar Deegwal, Arjun Kumar and Karan Verma

Abstract An asymmetric coplanar waveguide-fed branched multistubs resonators loaded printed antenna is presented for multiband operation. By incorporating an asymmetrical long and short L-shaped branched stubs, the lower resonances for 2.4 and 3.5 GHz bands are achieved while the higher resonance for 5.5 GHz band is achieved by embedding horizontal stub on asymmetric CPW-fed printed antenna. By placing multistubs resonators at suitable location on asymmetric CPW-fed printed antenna, it is likely to excite the triple resonances at 2.44/3.66/5.25 GHz frequencies and antenna exhibits the bandwidths of 5.73% (140 MHz, 2.36–2.50 GHz), 16.98% (630 MHz, 3.40–4.03 GHz), and 14.65% (800 MHz, 5.06–5.86 GHz), respectively. The design procedure and antenna characteristics of the proposed multistubs loaded multiband antenna are presented.

Keywords Multistubs resonators · Multiband antenna · Printed antenna

1 Introduction

Printed antennas are widely used in wireless communication systems owing to the essential characteristics such as lightweight, low cost, easy fabrication, and low profile. CPW-fed antennas can be easily integrated with the surface-mount devices as compared to microstrip-fed antennas owing to the presence of radiator and ground

A. Kumar (✉)
Department of Electronics and Communication Engineering, Govt. Mahila Engineering College, Ajmer, Rajasthan 305002, India

J. K. Deegwal
Department of Electronics Instrumentation and Control Engineering, Govt. Engineering College, Ajmer, Rajasthan 305025, India

A. Kumar
Department of Electronics and Communication Engineering, Bennett University, Greater Noida, Uttar Pradesh 201310, India

K. Verma
Department of Computer Science and Engineering, National Institute of Technology Delhi, New Delhi 110040, India

V. Janyani et al. (eds.), *Optical and Wireless Technologies*, Lecture Notes in Electrical Engineering 648, https://doi.org/10.1007/978-981-15-2926-9_35

in a solitary plane. Further, the wireless device that works at multiple frequencies has led to the design of diverse categories of antennas. Therefore, the CPW-fed printed antenna is a worthy solution for the reason that diverse resonance modes can be easily achieved. In the open literature, the various CPW-fed/microstrip-fed/ACS-fed printed/planar antenna structures have been investigated [1–9] to achieve the diverse design objectives. Numerous low profile printed multiband antennas have been realized by employing multiple radiating elements in the form of an inverted L-shaped and T-shaped strips/stubs [1–3], F-shaped slot [4], split-ring resonator (SRR) [5], stub-loaded rectangular patch [6, 7], vertex-fed pentagonal ring slot [8], and a meandered strips [9]. Unfortunately, the reported multiband antennas have been important shortcomings such as massive size and unusable bandwidths. In comparison, this work has small size ($14.5 \times 30 \times 1.6$ mm^3) and simple structure to realize the desired bands for wireless applications.

In this paper, a compact asymmetrical CPW-fed antenna loaded with two L-shaped branched stubs and a horizontal stub is proposed to achieve triple-band characteristics for 2.4/5.2/5.5 GHz WLAN and 3.5/5.5 GHz WiMAX applications. The reflection coefficient behavior of each configuration is compared to demonstrate the influence of distinct stubs on the antenna behavior, and also, the current distribution with radiation patterns at three resonant frequencies is discussed. Antenna design, configuration, and analysis of the proposed multistubs loaded printed antenna are described in Sect. 2. The conclusion is made in Sect. 3.

2 Design Procedure, Antenna Configuration, and Analysis

This section is describing the design procedure, antenna configuration, and analysis of the proposed antenna. The initial antenna design starts from an asymmetric CPW-fed printed antenna [i.e., Ant. 1]. The structure of the first stage of the proposed antenna is shown in Fig. 1 [see Ant. 1], is formed from an asymmetrical 50 Ω CPW-fed rectangular antenna, and is simulated on CST MWS simulation software. From the $|S_{11}|$ response of Ant. 1, shown in Fig. 2, it is noticeable that the antenna exhibits resonance at about 4.2 GHz. In the second stage, by integrating an asymmetrical long L-shaped stub in Ant. 1, Ant. 2 is formed and it creates the additional resonance at about 2.6 GHz. To shift the resonances in lower side to become usable bands of Ant. 2, an asymmetrical short L-shaped stub is integrated into Ant. 2 with a specific gap in the upper side to form Ant. 3. Further, by embedding a horizontal stub in Ant. 3 with a specific gap in the lower side, Ant. 4 [proposed antenna] is formed to create surplus resonance band at about 5 GHz in Ant. 3 without affecting the lower resonances.

These antennas are designed on a FR-4 dielectric substrate with $\varepsilon_r = 4.3$, thickness of 1.6 mm, and $\tan\delta = 0.025$. These are fed by an asymmetrical CPW feed with width $W_f = 2.5$ mm and identical gaps of 0.3 mm. $|S_{11}|$ comparison of the evolution stages [see Fig. 1] is shown in Fig. 2. The comparison of design stages and their respective impedance bandwidths (IBWs) and fractional bandwidths (FBWs) is summarized in Table 1. The geometry of the proposed antenna with labeled parameters is illustrated

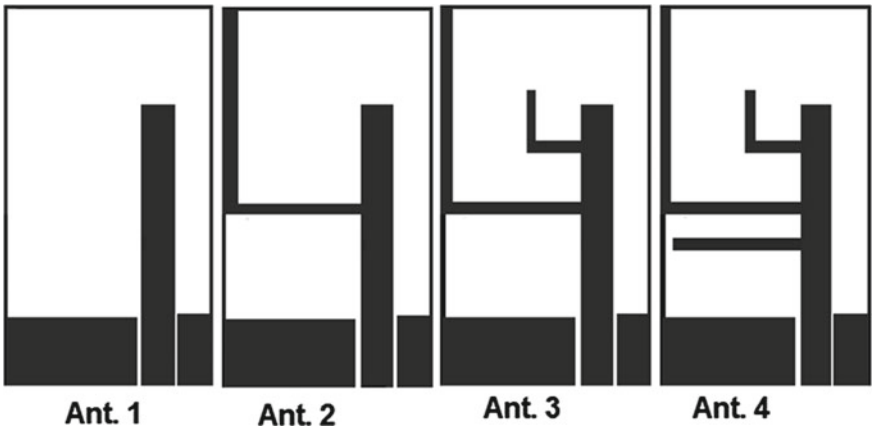

Fig. 1 Step-by-step evolution of the different antenna structures

Fig. 2 $|S_{11}|$ comparison of the evolution stages of the antenna structures

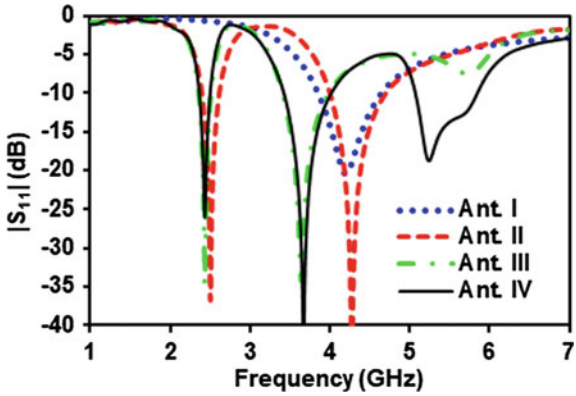

Table 1 Comparison of impedance and fractional bandwidth variations for evolution stages of the antenna structures

Antenna stages	Stub type	Bandwidths (GHz, f_r, %)	Antenna response
Ant. I	No stub	3.84–4.67, 4.19, 19.50	Single-band
Ant. II	Asymmetrical long L-shaped stub	2.39–2.61, 2.50, 8.80	Dual-band
		3.98–4.71, 4.20, 16.82	
Ant. III	Asymmetrical long L-shaped stub and short L-shaped stub	2.35–2.51, 2.44, 6.50	Dual-band
		3.39–4.00, 3.67, 16.53	
Ant. III	Asymmetrical long L-shaped stub, short L-shaped stub and horizontal stub	2.36–2.50, 2.44, 5.73	Triple-band
		3.40–4.03, 3.66, 16.98	
		5.06–5.86, 5.25, 14.65	

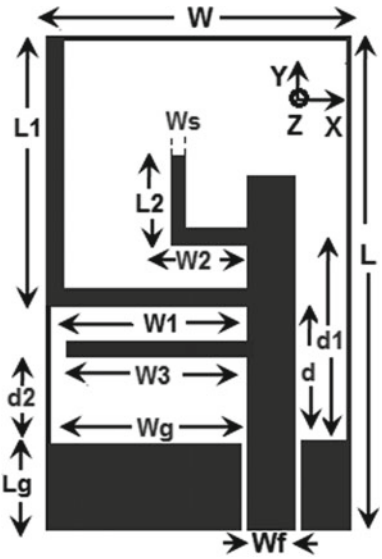

Fig. 3 Geometry of the proposed asymmetrical CPW-fed multistubs loaded printed antenna

in Fig. 3. The optimized dimensions of the proposed multiband antenna are as follows: $L = 30$ mm, $W = 14.5$ mm, $W_1 = 8.5$ mm, $W_2 = 2.9$ mm, $W_3 = 8$ mm, $W_f = 2.5$ mm, $W_g = 9.2$ mm, $W_s = 1$ mm, $L_1 = 18.2$ mm, $L_2 = 6.8$ mm, $L_f = 13.5$ mm, $L_g = 6.5$ mm, $d = 5.3$ mm, $d_1 = 8.5$ mm, and $d_2 = 3$ mm.

To elucidate the mechanism of resonances, the surface current vectors at three resonances at 2.44, 3.66, and 5.25 GHz are illustrated in Fig. 4a–c, respectively. It can be perceived from Fig. 4a, the current mainly on the asymmetrical long L-shaped stub (i.e., L_g, d, W_1, and L_1 pointed out in Fig. 3) in the forward direction which designates that the first resonance mode is excited at about 2.44 GHz.

Correspondingly, it can be observed from Fig. 4b that the current mainly on the asymmetrical short L-shaped stub (i.e., L_g, d_1, W_2, and L_2 pointed out in Fig. 3) in the forward direction which can lead to excite the second resonance mode at about 3.66 GHz. The third resonance mode is excited at about 5.25 GHz due to current flow in forward direction on horizontal stub (i.e., L_g, d_2, and W_3 pointed out in Fig. 3) as shown in Fig. 4c. So, it may be concluded that the respective resonances are mainly reliant on the total length of respective multistubs resonators.

Further, the design procedure for the excitation of resonances, the resonant frequency f_{ri}, and effective dielectric constant ε_{eff} can be calculated by Eqs. (1) and (2) as:

$$f_{ri} = \frac{c}{2L_{ti}\sqrt{\varepsilon_{\text{eff}}}}; \quad i = 1, 2, 3 \tag{1}$$

$$\varepsilon_{\text{eff}} \approx \frac{\varepsilon_r + 1}{2} \tag{2}$$

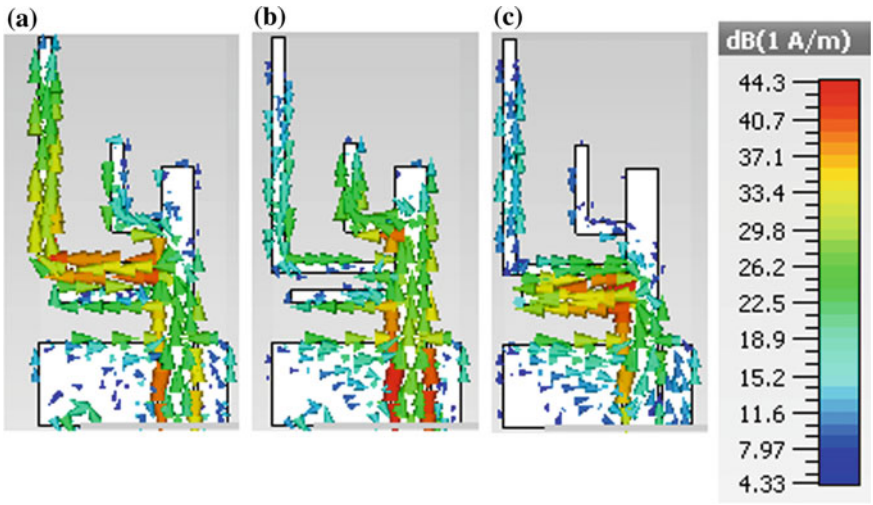

Fig. 4 Surface current distributions of the proposed multistubs loaded antenna at three resonance frequencies: **a** 2.44 GHz, **b** 3.66 GHz, and **c** 5.25 GHz

where c = speed of light in vacuum (3×10^8 m/s), ε_r = dielectric constant of the substrate, and L_{ti} = total length of the ith stub.

The total length of first ($i = 1$), second ($i = 2$), and third ($i = 3$) resonances can be calculated by Eqs. (3), (4), and (5) as:

$$L_{t1} = L_g + d + W_1 + L_1 = 38.5 \text{ mm} \tag{3}$$

$$L_{t2} = L_g + d_1 + W_2 + L_2 = 24.7 \text{ mm} \tag{4}$$

$$L_{t3} = L_g + d_2 + W_3 = 17.5 \text{ mm} \tag{5}$$

For first resonance, the simulated f_{r1} is 2.44 GHz while calculated by (1) is 2.39 GHz. Correspondingly, for second and third resonances, the simulated f_{r2} and f_{r3} are 3.66 and 5.25 GHz while calculated by (1) are 3.73 and 5.26 GHz, respectively, which is much close. Hence, the calculated resonances using design procedure are well agreeing full-wave simulation procedure.

Further, the effect of variation in length L_2 of asymmetrical short L-shaped stub and length W_3 of horizontal stub is studied while other parameters are kept constant as illustrated in Fig. 5a, b, respectively. When the length L_2 varied from 5.8 mm to 7.8 mm, it mainly affects second resonance and shifted toward lower frequency side from 3.78 GHz to 3.54 GHz, respectively, while first and third resonances are almost unaffected. Similarly, when length W_3 varied from 7 mm to 9 mm, it mainly affects third resonance and shifted toward lower frequency side from 5.79 GHz to 4.81 GHz, respectively, while first and second resonances are almost unaffected. From Fig. 5, it

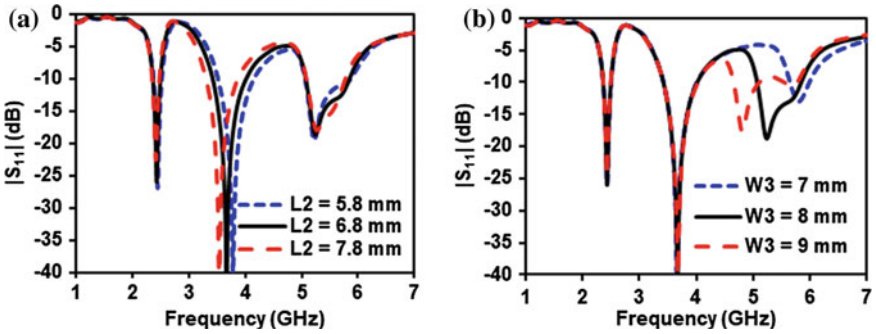

Fig. 5 Surface current distributions of the proposed multistubs loaded antenna at three resonance frequencies: **a** 2.44 GHz, **b** 3.66 GHz, and **c** 5.25 GHz

has been realized that $L_2 = 6.8$ mm and $W_3 = 8$ mm are taken for the desired band of operation.

The co- and cross-polarized components of the proposed antenna at three resonance frequencies 2.44, 3.66, and 5.25 GHz in *xz*- and *yz*-plane are shown in Fig. 6. Omnidirectional co-polarized patterns in *xz*-plane and bidirectional co-polarized patterns in *yz*-plane are observed. The gain at 2.44/3.66/5.25 GHz is 1.97/2.29/3.41 dBi, respectively, as displayed in Fig. 7.

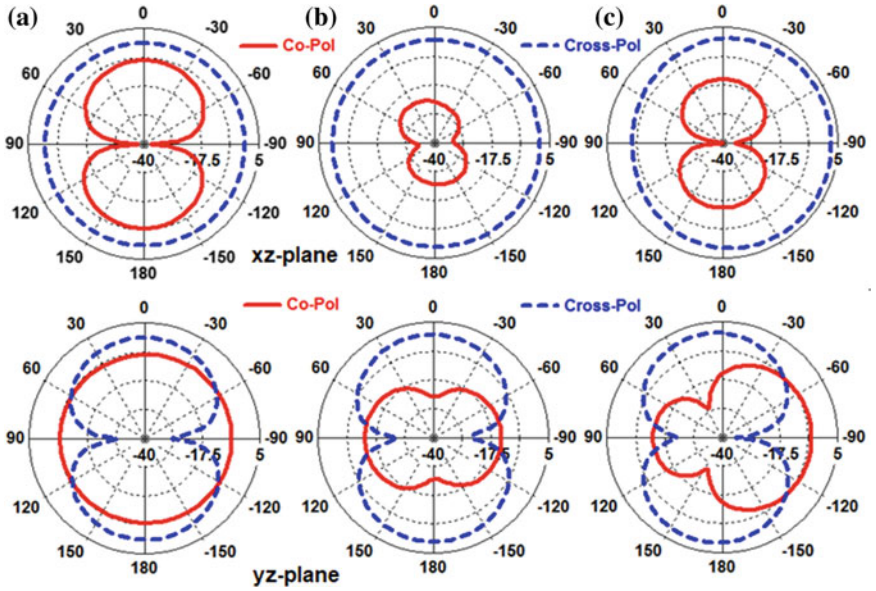

Fig. 6 Radiation patterns of the proposed multistubs loaded antenna at three resonant frequencies at **a** 2.44 GHz, **b** 3.66 GHz, and **c** 5.25 GHz

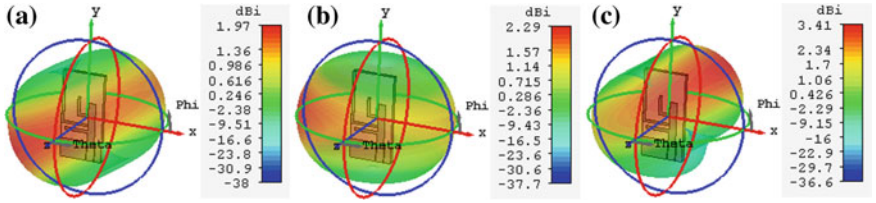

Fig. 7 3D patterns of the proposed multistubs loaded antenna at three resonant frequencies at **a** 2.44 GHz, **b** 3.66 GHz, and **c** 5.25 GHz

3 Conclusion

An asymmetrical CPW-fed compact printed multiband antenna with branched multistubs resonators is proposed. By incorporating two L-shaped branched stubs and a horizontal stub at a suitable position on asymmetric CPW-fed printed antenna, the triple resonances at 2.44/3.66/5.25 GHz are achieved. It provides bandwidths of 140 MHz (2.36–2.50 GHz), 630 MHz (3.40–4.03 GHz), and 800 MHz (5.06–5.86 GHz). The design procedure and analysis of the proposed multistubs resonator are presented. Owing to the small size, multiband functionality, very simple structure with good radiation patterns, the proposed antenna is suitable for WLAN and WiMAX applications.

References

1. Ellis MS, Zhao ZQ, Wu JN, Nie ZP, Liu Q-H (2014) A new compact microstrip-fed monopole antenna for triple band WLAN/WiMAX applications. Prog Electromagn Res Lett 48:129–135
2. Kumar A, Jhanwar D, Sharma MM (2017) A compact printed multistubs loaded resonator rectangular monopole antenna design for multiband wireless systems. Int J RF Microw Comput Aided Eng 27(9):e21147
3. Yadav M, Kumar A, Rathore KS, Sharma N, Mewara HS (2017) A compact ACS-fed triple-band dual-polarized stubs-loaded frequency reconfigurable printed antenna for WiMAX and WLAN applications. In: 2017 14th IEEE India council international conference (INDICON), Roorkee, India, pp 1–5
4. Gautam AK, Kumar L, Kanaujia BK, Rambabu K (2016) Design of compact F-shaped slot triple-band antenna for WLAN/WiMAX applications. IEEE Trans Antennas Prpoag 64(3):1101–1105
5. Naik KK (2018) Asymmetric CPW-fed SRR patch antenna for WLAN/WiMAX applications. Int J Electron Commun 93:103–108
6. Kumar A, Sharma MM (2018) Compact triple-band stubs-loaded rectangular monopole antenna for WiMAX/WLAN applications. In: Optical and wireless technologies. Lecture Notes in Electrical Engineering 472, pp 429–435
7. Kumar A, Sharma N, Yadav M, Sankhla V (2017) Compact offset CPW-fed inverted L-shaped dual-band dual-polarized reconfigurable printed antenna. In: 2017 IEEE applied electromagnetics conference (AEMC), Aurangabad, India, pp 1–2

8. Surendrakumar P, Mohan BC (2018) A triple-frequency, vertex-fed antenna for WLAN/WiMAX applications. IEEE Antennas Propag Mag 60(3):101–106
9. Liu G, Fang M, Zhi R, Bai J, Zeng Z (2017) Compact CPW-fed multiband antenna for TD-LTE/WLAN/WiMAX applications. Prog Electromagn Res Lett 65:9–14

Nanorod Dimer-Based Optical Fiber Plasmonic Sensor

Manoj Kumar Falaswal, Nitesh Mudgal and Ghanshyam Singh

Abstract A fiber optic localized surface plasmon resonance (LSPR)-based sensing is analyzed by determining the optical scattering cross section of gold nanorods using discrete dipole approximation method. This method is flexible and most powerful electrodynamic method to analyze the optical properties of particle having arbitrary geometry. To detect the shift in plasmonic resonance peak of gold nanorod on the tip of silica fiber, a finite difference time domain (FDTD) simulation is adopted. The proposed plasmonic sensor senses the change in the refractive index of the ambient.

Keywords Optical sensor · Localized surface plasmon resonance · Finite difference time domain

1 Introduction

The surface plasmon phenomenon was observed before a century in 1907 by Zenneck. He solved Maxwell's equations especially for surface wave. Further, he added that surface electromagnetic (EM) wave occur at the interface of two media provided that one medium should be lossy dielectric, e.g., metals (gold, silver, copper, aluminum), whereas another should be lossless medium, i.e., pure dielectric [1]. Furthermore, he presented that lossy part of dielectric function or extinction coefficient is accountable to bind the EM wave along the above said interface. Later, in 1909, Somerfield validated that electric field amplitude of the surface wave setup inverse relation with the square root of the horizontal distances measured from the source pole [2]. The phenomenon of SPR was flourished in 1957 by Ritche by exciting the surface plasmons on the metal surface [3]. Later, Otto arranged a configuration having prism-coupled attenuated total reflection which couples the bulk EM wave to surface wave [4]. Later, Kretschmann modified the Otto configuration by removing the thin air gap between substrate and plasmonic metal layer, and it is the best famous configuration till date [5].

M. K. Falaswal (✉) · N. Mudgal · G. Singh
Department of Electronics and Communication Engineering, Malviya National Institute of Technology, Jaipur 302017, Rajasthan, India
e-mail: manoj.falaswal@ecajmer.ac.in

V. Janyani et al. (eds.), *Optical and Wireless Technologies*, Lecture Notes in Electrical Engineering 648, https://doi.org/10.1007/978-981-15-2926-9_36

The confinement of surface plasmons in subwavelength nanoparticle generates localized surface plasmon (LSP) [6]. The surface plasmon resonance condition is achieved after the wave vector matching of incident light with the surface plasmon [7]. And, if the plasmonic material is subwavelength nanoparticle, it is known as localized surface plasmon resonance (LSPR) [7]. Optical sensors based on the excitation of LSPR have grate potential to sense the change in surrounding refractive index. Fiber-based LSPR sensing structures are being explored widely because optical fiber sensors offers has distinguish features, e.g., potential for remote sensing, small size, and robustness [8–10]. The laser is used to launch the light at one of the ends of the fiber. The entered light is guided by fiber as a result of total internal reflection. The sensing can be accomplished either outside or inside of the fiber. Here, the outside sensing is adopted. Sample which is to be detected is made in contact with the fiber core at the fiber cross section. The change in the concentration of sample changes the refractive index as a result of which property like transmission spectra, field intensity, phase, scattering cross section, wavelength, polarization, etc. of the guided light is changed. Conversely, the changes in these properties of the light can be measured to detect change in the refractive index of the sample.

Various techniques such as interferometer, evanescent wave absorption spectroscopy, photoluminescence, Doppler effect, surface plasmon resonance (SPR), and LSPR are being used for the sensing purposes [11]. Among all, the LSPR is the best choice because it can detect minute change in the refractive index of the sample. Generally used plasmonic materials are gold, silver, copper, and aluminum [12], out of which gold has highest stability against oxidation and corrosion [13]. The thin layers of these plasmonic metals exhibit near field optics of surface plasmon wave suitable for larger dimension molecules up to 200 nm [6]. In contrast to layered deposition, the discrete nanorod structure exhibits near field optics of surface plasmon wave suitable strong sensitivity for relatively smaller dimension molecules. Hence, gold nanorods are used to detect the change in the refractive index of sample.

LSPR-based sensing has vast application in the detection of chemical, biochemical, biomolecule, gas, etc. [14–16]. Because of the extraordinary detection property and performance, LSPR sensors are used in the study of interaction between different biomolecules, e.g., proteins, nucleic acids, peptides, receptors, antibodies, and lipids, in the investigation of viral binding for surface functionalization, in antiviral drug discovery tools, in food safety, in mines to sense the toxic and hazardous gas leakages, etc. [15]. Hence, in the proposed article, nanorod-based LSPR is used to detect the minute change in the refractive index of sample.

2 Principle of Operation

2.1 LSPR in Nanorods

Nanoparticles of noble metals, e.g., silver and gold, have strong optical excitation at near-infrared and visible wavelengths. These metals are capable of creating highly sensitive LSPR against surrounding. The longitudinal localized surface plasmon resonance of gold nanorods is greatly sensitive counter to the change in the concentration of ambient. Hence, gold nanorods are widely used for sensing against ambient refractive index change. From experimentation point of view, gold nanorods can be easily fabricated using the seeded growth method. One can tune proper resonant wavelength by changing the aspect ratio.

Localized surface plasmons (LSPs) are excited by conducting electrons of metallic nanostructures which are coupled to the electromagnetic field [6]. LSPs are non-propagating in nature. LSPs are excited in metallic nanorod dimer if it is placed in linearly polarized EM field whose direction is parallel to the axis of nanorods. And, the dimension of element should be in subwavelength region of incident light [17]. However, at optical frequencies, the precise EM response of the metal given by its complex dielectric constant must be accounted. The kinetic energy of the electrons replaces the magnetic energy of the inductance in EM response of the particle for small enough particles. This results in a size-independent LSPR which can be examined by shape and dielectric constant of the particle.

Since the resonance in nanorods depends on the aspect ratios of the rod geometry, regardless of size elongated rods resonates at longer wavelengths than spherical particles [18]. The crucial properties of nanorods can be defined in terms of shape-dependent depolarization factor N, their volume V, and the dielectric constant ε_r of the rod material ($\varepsilon_r = \varepsilon_{\text{rod}}/\varepsilon_{\text{med}}$), where ε_{med} is dielectric constant of surrounding medium. The polarizability α in the case of nanorods at operating wavelength λ can be given as [19];

$$\alpha = \frac{V}{(1/(\in_r - 1)) + N - i(4\pi^2 V/3\lambda^2)} \tag{1}$$

Much research attention is being given toward plasmonic coupling between a pair of metallic nanorods also called dimer. To understand the plasmonic coupling effect, these nanoparticle dimers or plasmonic "molecules" works as basic system which can be used to study the interactions between individual molecules. As shown in Fig. 1, plasmonic near-fields of two metallic nanorods approaching toward each other overlap which creates strong coupling between them. This strong coupling generates high electric field in between them and distance-dependent wavelength shift of the plasmon mode. This effect can be understood using the plasmon hybridization method [20–22]. In the plasmon hybridization, the coupled mode is assumed as antibonding and bonding combinations of the individual particle plasmon modes.

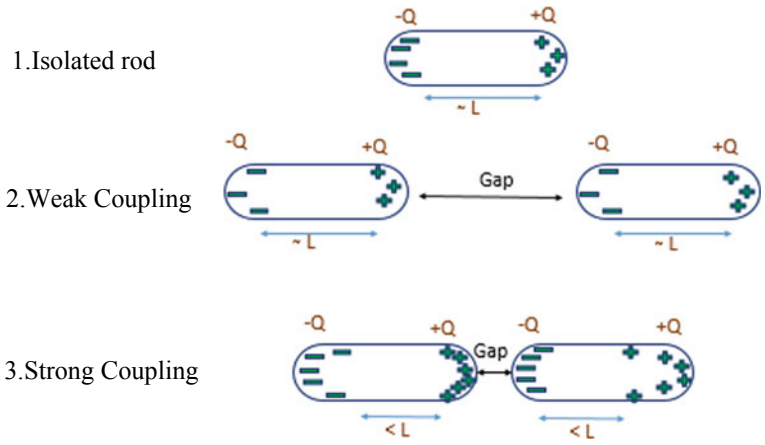

Fig. 1 Optical properties of coupled gold nanorods for field enhanced

In addition, the dependency on distance provides a useful parameter to measure the distance between two metallic particles in biological systems.

Figure 2 shows the schematic structure of gold nanorods dimer on the tip of single-mode silica fiber. In FDTD simulation, we employed one point time monitor to measure the field in between nanorods dimer and studied the effect of change in surrounding refractive index on the resonance peak. During simulations, rod radius is considered to be 12 nm, whereas length is varied in the range of 50–100 nm.

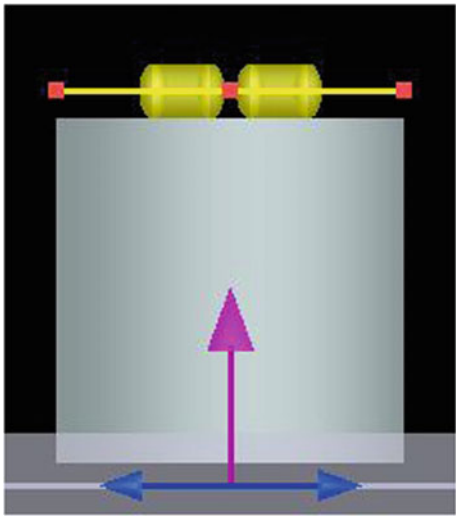

Fig. 2 Nanorod on the tip of a single-mode fiber

The distance between two consecutive rods is varied from 5 to 10 nm. In FDTD simulation, the light source was used plane light source, and all the boundaries were kept perfectly matched layer (PML) type.

3 Results and Discussion

From practical aspects, it is convenient to have nanorods with constant cross section and varying length. Thus, the relation between length of the nanorods and detuning looks similar to radio frequency regime, with longer (shorter) rods having longer (shorter) resonances wavelength. In order to observe the effects of coupling between two nanorods, two rods are placed on same axis having gap of 5 and 10 nm. For the FDTD simulation, grid size is considered to be 2 nm in *x*-, *y*- and *z*-directions. And FDTD time step is assumed to 0.57 nm. Figure 3a–c depicts the value for *Ex*, *Ey*, and *Ez* component of electric field, and Fig. 3d shows the square of normalized electric field value at resonance wavelength of 690 nm in between two gold nanorods.

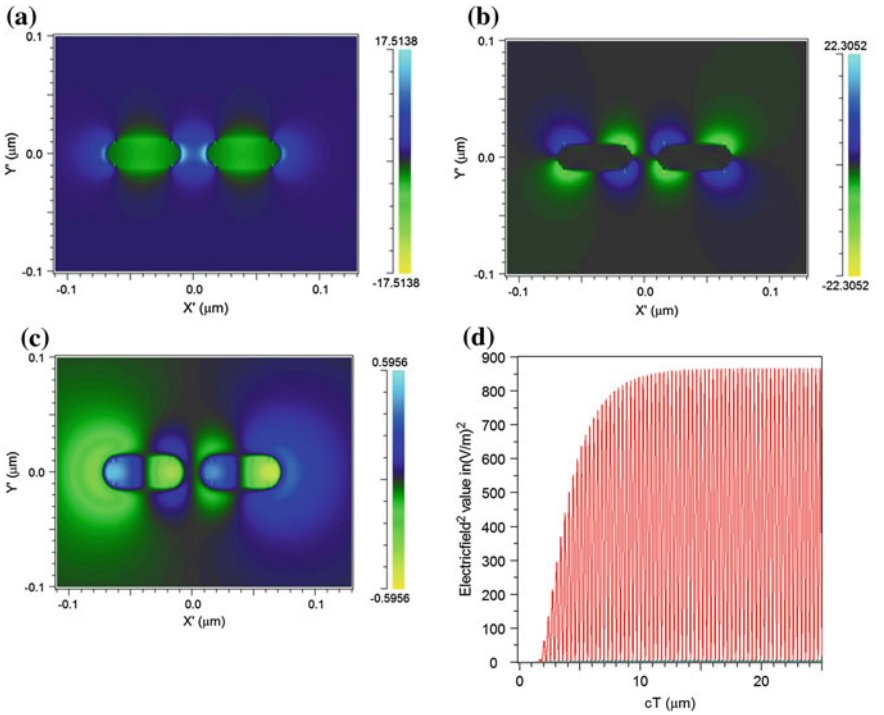

Fig. 3 Electric field distributions at cross section of two gold rod at steady-state value **a** Ex component, **b** Ey component, **c** Ez component, and **d** electric field square value at middle of two gold rod having length of 60 nm and cross section diameter 24 nm

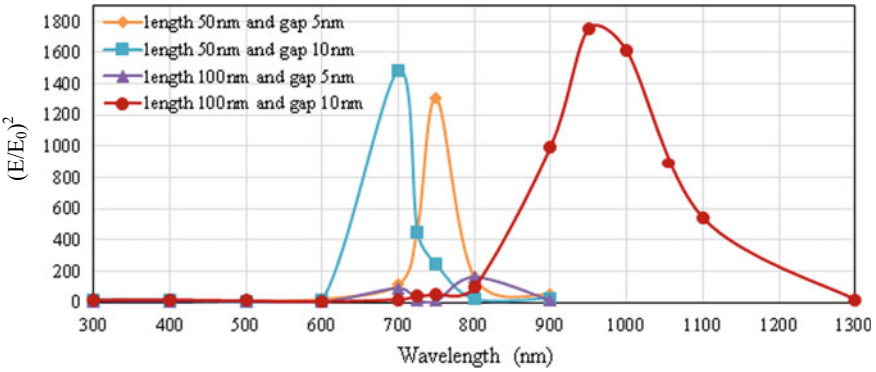

Fig. 4 Variation of normalized electric field along with incident wavelength for different combinations of length and gap between two nanorods

Figure 4 shows square of normalized electric field (*E*/*Eo*) value at the middle of two gold nanorods having particular diameter and different (length, gap) combinations: (50 nm, 5 nm), (50 nm, 10 nm), (100 nm, 5 nm) (100 nm, 10 nm). In case of two nanorods, enhancement is higher than single nanorod of same length due to coupling effect. We can also see from this figure that there is a shift in resonance wavelength. It can easily be observed in Fig. 4 that the resonance peak shifts toward higher wavelength (red shift) by increasing the length of the nanorod. In contrast, the resonance peak shifts toward lower wavelength (blue shift) by increasing the gap between two nanorods. This can be understood by simply approximating the array of interacting point dipoles. For in-phase illumination, the resonance shift direction can be determined by assuming the coulomb forces associated with the polarization of the particles. The charge distribution of neighboring particles either decreases or increases the restoring force acting on the oscillating electrons of each particle in the chain. Depending on direction of polarization of exciting light, this corresponds to red shift of the SPR for the excitation of longitude polarization of light.

The broader and shallower peak degrades the resolution and quality factor of the sensor [23, 24]. Although the resonance peak corresponding to length 100 nm and gap 10 nm is at highest wavelength and has highest peak, for the high resolution and quality factor the narrower peak should be preferred. But, here the beam width of the peak corresponding to length 100 nm and gap 10 nm is within limit, and hence, it can be considered for further detection of change in the refractive index of the sample.

In Fig. 5, the normalized electric field is varied corresponding to incident wavelength for different refractive index of sample at considered length (100 nm) and gap (10 nm) of nanorods. The considered samples are air, water, acetone, isopropanol which are arranged in increasing order of their refractive index, i.e., 1, 1.33, 1.3586, and 1.3776, respectively. It is seen that the resonance peak shift toward higher wavelength (red shift) as the sample‘s refractive index increases. This signifies the change in the refractive index of the sample. Consequently, in terms of biosensor or chemical sensor, it can be said that the red shift signifies the adsorbance or absorbance

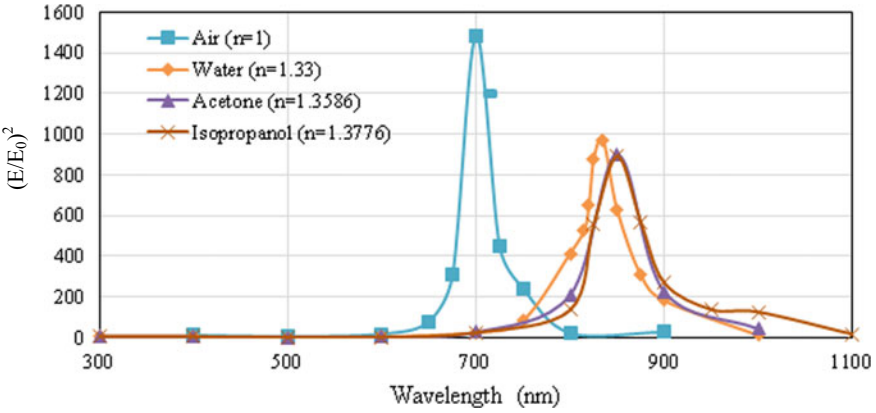

Fig. 5 Variation of normalized electric field along with incident wavelength for different refractive index of sample at considered length (100 nm) and gap (10 nm) of nanorods

of any molecule or biomolecule on the surface of nanorods because this absorbance increases the sample's refractive index in the vicinity of nanorod. It can also be observed from Fig. 5 that the resonance peak becomes broader and shallower as the refractive index of the sample increases which may degrade the resolution and quality of the sensor beyond a certain limit.

4 Conclusion

A fiber optic sensor based on localized surface plasmon resonance is presented. Its response to modifications in shape, size, and ambient refractive index is appraised. Plasmonic gold nanorods are used on SiO_2. FDTD method is used to obtain maximum field enhancement on the optimized dimension. The gap and the aspect ratio of the nanorods dimer structures are changed and concluded that gap of 10 nm and length of 100 nm gives the maximum enhancement in field. We observed red shift in LSPR peak by changing the ambient refractive index. It is believed that the proposed sensor can be used to sense a minute change in the refractive index of the sensor which can be fruitful in bio-sensing.

References

1. Zenneck J (1907) Uber die Fortpflanztmg ebner elektro-magnetischer Wellen langs einer ebenen Leiterflache and ihre Beziehung zur drahtlosen Telegraphie. Ann Phys 328:846–866
2. Sommerfeld A (1909) Propagation of waves in wireless telegraphy. Anals der Physik 28:665–736
3. Ritchie RH (1957) Plasma losses by fast electrons in thin films. Phys Rev 106(5):874

4. Otto Andreas (1968) Excitation of nonradiative surface plasma waves in silver by the method of frustrated total reflection. Zeitschrift für Physik A Hadrons and nuclei 216(4):398–410
5. Kretschmann E, Raether H (1968) Radiative decay of non radiative surface plasmons excited by light. Zeitschrift für Naturforschung A 23(12):2135–2136
6. Maier SA (2007) Localized surface plasmons in plasmonics; fundamentals and applications, 2nd edn. Spring Street, New York: Springer, pp 65–80
7. Mayer Kathryn M, Hafner Jason H (2011) Localized surface plasmon resonance sensors. Chem Rev 111(6):3828–3857
8. Chau L-K, Lin Y-F, Cheng S-F, Lin T-J (2006) Fiber-optic chemical and biochemical probes based on localized surface plasmon resonance. Sens Actuators B: Chem 113(1):100–105
9. Lin Yongbin, Zou Yang, Lindquist Robert G (2011) A reflection-based localized surface plasmon resonance fiber-optic probe for biochemical sensing. Biomed Opt Express 2(3):478–484
10. Chen Y, Ming H (2012) Review of surface plasmon resonance and localized surface plasmon resonance sensor. Photonic Sens 2(1):37–49
11. Bertolotti M, Sibilia C, Guzman AM (2017) Evanescent waves in optics: an introduction to plasmonics. https://doi.org/10.1007/978-3-319-61261-4
12. Maurya JB, Prajapati YK (2016) A comparative study of different metal and prism in the surface plasmon resonance biosensor having MoS2-graphene. Opt Quant Electron 48(5):280–291
13. Wu L, Chu HS, Koh WS, Li EP (2010) Highly sensitive graphene biosensors based on surface plasmon resonance. Opt Express 18(14):14395–14400
14. Dahlin A, Zäch M, Rindzevicius T, Käll M, Sutherland DS, Höök F (2005) Localized surface plasmon resonance sensing of lipid-membrane-mediated biorecognition events. J Am Chem Soc 127(14):5043–5048
15. Shpacovitch V (2012) Application of surface plasmon resonance (SPR) for the detection of single viruses and single biological nano-objects. J Bacteriol Parasitol 3(7):e110
16. Dmitriev A (ed) (2012) Performance of nanoplasmonic biosensors. In: Nanoplasmonic Sensor, Spring Street, New York: Springer, pp 232–240, 246-248
17. Mock JJ, Smith DR, Schultz S (2003) Local refractive index dependence of plasmon resonance spectra from individual nanoparticles. Nano Lett 3(4):485–491
18. Marinakos SM, Chen S, Chilkoti A (2007) Plasmonic detection of a model analytic in serum by a gold nanorod sensor. Anal Chem 79:5278–5283
19. Zhu J, Li F-K (2011) Effect of aspect ratio on the inter-surface plasmonic coupling of tubular gold nanoparticle. Eur Phys J B 80:83–87
20. Prodan Emil, Radloff Corey, Halas Naomi J, Nordlander Peter (2003) A hybridization model for the plasmon response of complex nanostructures. Science 302(5644):419–422
21. Nordlander P, Oubre C, Prodan E, Li K, Stockman MI (2004) Plasmon hybridization in nanoparticle dimers. Nano lett 4(5):899–903
22. Willingham B, Brandl DW, Nordlander P (2008) Plasmon hybridization in nanorod dimers. Appl Phys B 93(1):209–216
23. Pockrand I (1978) Surface plasma oscillations at silver surfaces with thin transparent and absorbing coatings. Surf Sci 72:577–588
24. Dahlin AB, Tegefeldt JO, Hook F (2006) Improving the instrumental resolution of sensor based on localized surface plasmon resonance. Anal Chem 78(13):4416–4423

Optimal Pricing for RAP in Heterogeneous Wireless Railway Networks

Vaishali and Sandeep Santosh

Abstract To facilitate the journey of passengers, the modern railway system should support a wide range of on-board high-speed Internet services. The Rail-track Access Points (RAPs) are an interesting idea to solve the increasing demands of passengers. These RAPs are deployed to support high-speed data rates. They are complementary to the cellular network base stations (BSs). In this paper, RAP and BS coexist in the network, and to utilize the RAP services, revenue model has been introduced. It also analyses the delay performance of the proposed user—RAP association scheme. Eventually, the passenger decides whether to associate with the RAP or not.

Keywords Payoff · Access points · Revenue · Arrival rate · Mean delay time

1 Introduction

The growth of wireless communication is at every corner of the world. It has now become the integrated part of human life. There is an increase in the use of personal wireless devices such as smart phones, tablets and laptops by the people. The transport industry in the past years has witnessed a high demand for Internet services to provide on-board passengers with Internet access on one hand and to ensure the safety of people and trains on the other hand [1]. As in case of high-speed trains, most of the journeys take a long duration; passengers may like to check their emails, surf a website or go for a real-time multimedia streaming by accessing Internet. To provide on-board Internet services, a heterogenous network architecture can be constructed that contains a series of RAPs. However, the RAP can only support intermittent wireless network coverage due to limited transmission power, and hence, the delay time experienced by the passenger is one of the most delicate issue in railway communication network. As heavy data traffic flushes data delivery, RAPs are used complement to the BSs.

This work focusses on the problems of service regulations faced by any RAP connection in a heterogeneous wireless railway network, where with the help of

Vaishali (✉) · S. Santosh
Department of Electronics and Communication Engineering, National Institute of Technology, Kurukshetra, India

V. Janyani et al. (eds.), *Optical and Wireless Technologies*, Lecture Notes in Electrical Engineering 648, https://doi.org/10.1007/978-981-15-2926-9_37

queueing game theoretic approach, a RAP and BS coexist together. It considers the revenue model and derives association delay time on RAPs connection behaviours, i.e. a condition where a passenger should join the RAP or not. The performance evaluation is provided for the heterogeneous wireless railway networks to elucidate the proposed passenger-RAP association scheme.

2 Related Works

Many researches have been conducted on modern railway system to vantage passenger's journey. An investigation on the optimal power allocation strategy via access points is studied for uplink transmission in high-speed trains [2]. In [3], the delay performance of the Internet multimedia streaming to satisfy passenger's demand in the railway network is discussed. A delay analysis model is proposed in high-speed train scenario through switch ports in carriages [4]. In recent literatures, the delay performance analysed on demand data delivery has sometimes came out to be inaccurate results [5]. In [6, 7] end-to-end delay bound is analysed for the data applications under the heterogeneous network for one server, but the cooperation between RAPs and BSs is not considered in both the works. Therefore, it is needed to focus on the delay performance in railway communication system.

Researchers have shown their interests in queueing theory. Now it is all passenger's choice whether to associate with a queue or not; this shows that passengers are ready to wait for the service in queue or to leave the queue in order to maximize their own profit [8]. Hence, a reward–cost framework is easy to construct which explicates the passenger's choice. Z. Han et al. studied the queueing control in cognitive radio networks with random service interruptions [9]. With an optimal threshold, an individual decides whether a data packet should associate with the queue or not [10]. Since the channel characteristics are unknown to the system, this kind of technique cannot be used everywhere, especially in heterogenous wireless railway network. Z. Chang et al. investigate a pricing strategy based on the queue length and the reward [11]. In [12], a social optimal strategy was developed from the view point of the customers that can be implemented on RAP. In [10], the channel ON-OFF process is discussed by using renewal theory. Here, the channel ON-OFF process is taken as the breakdown of the RAP. Hence, the first and the second moment of service time is required to do the analysis. Since it is inefficient to access the BSs for the railway networks, the much higher data transmission rate of RAP can complement the connectivity.

Motivated by the previous problems, our contribution to this paper is summarized below:

- To study a RAP heterogenous wireless railway network model, several Rail-track Access Points are widely deployed on a predefined railway line. It is assumed that passengers can decide whether to join the RAP service or to remain connected to the cellular network.

- A symmetric game is proposed to maximize the passenger's reward which is influenced by the delay time that they may face in the queue of the RAP. Hence, an optimal pricing is presented during the data transmission to facilitate the passenger in deciding whether to associate with the RAP or not.

The remaining of the manuscript covers the system model of the proposed scheme in Sect. 3, study of payoff model and queueing analysis in Sect. 4, Sect. 5 presents the simulation results followed by the conclusion in Sect. 6.

3 System Model

The system model of a railway communication network using RAP is shown in the Fig. 1. The RAPs are deployed along the railway track in such a manner that it gives intermittent coverage due to limited transmission power. Hence, passengers can only get connected to the services when they are in transmission range of RAPs. The packet delay and also the fast handover are neglected here. It is assumed that the allocation of network resources to the RAP and BS is handled by central controller. Therefore, the passenger's request can enter the queue and wait till they get served.

It is assumed that the train follows a straight path, and the information can be generated in advance regarding the speed and the location of the train. As shown in Fig. 1, the train can travel between source and destination stations in the time duration $[T_s, T_e]$. We consider a scenario in which three RAPs are deployed along the railway line, and hence for passengers, there exist three separated time durations

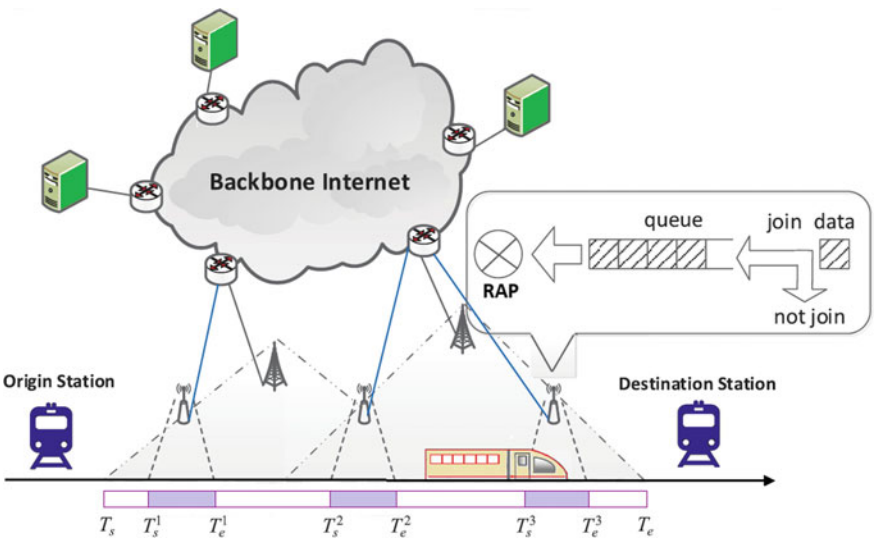

Fig. 1 System model

in which they can transfer the data packets. This can be represented by $\left[T_s^i, T_e^i\right]$ and $i \in [1, \ldots, I]$. Here, within the ith RAP, T_s^i represents the start time and T_e^i is the end time of the delivery. Assume that $T_s^i \leq T_e^i, T_s \leq T_s^1, T_e \geq T_e^1$ for $i \in [1, \ldots, I]$. These RAPs are working cooperative in nature.

3.1 Service Process and Data Arrival Process

By considering the proposed system model, the passengers will decide whether they will associate with the RAP or not. If the queue of the RAP is full and no more data can be taken from the passenger, we assume that it can be transferred to the cellular base station. The customer arrival rate λ follows the exponential process and is i.i.d. in nature. For the simplicity of model, consider an M/G/1 queuing system to analyse the average queueing delay T (waiting time + service time) with service rate μ_x assumed to follow exponential distribution and i.i.d. at the RAP. The service time of the customer is denoted by μ_y. The breakdown of RAP is given by the exponential rate β. In rural area, the service interruption is less, thus $\beta = 1$, whereas for urban area $\beta = 2$. To save the cost of deployment and to satisfy the customer's demand, in urban region more RAPs are deployed as compared to the rural region. Here assume that $T_s^{i+1} - T_e^i$ is distributed exponentially at rate ϵ which is the time taken by the train to cover two isolated RAPs, and the serving time $T_e^i - T_s^i$ of the RAP follows exponential process at a rate ϕ. The service order follows first come, first served (FCFS) rule, and also the queue information will be transferred to the next RAP when the train is not in the coverage range of the RAP.

During time duration *t,* the state of the queue is given by a pair $(N(t), I(t))$ at the RAP, which consists the status of the train position $I(t)$ and the number of customers in the system, i.e. length of the queue $N(t)$. $I(t) = 1$ when the train is in the transmission range, otherwise $I(t) = 0$.

4 Queueing Analysis on User Association

The data transmission rate of RAP wireless link is much higher as compared to the base station wireless link. It is assumed that the customer after getting served by RAP can get reward for the successful service, and also the cost of a customer that he is going to pay for the service will be the function of waiting time in the queue. Hence, considering the cost and reward a customer can get, he needs to make an irrevocable decision on whether to connect with the RAP as the customer after association cannot quite until being served. Since, the gap between two adjacent RAPs is very big, the customers will send create arriving requests by forming a queue before entering the covering range and will decide if they can wait in the queue until being served. This queue will get update each time a train passes the range. For the customers, we introduce one more term payoff that will be the difference between cost and reward.

This work considers the scenario where all the RAPs deployed are working in cooperative manner. Optimal pricing technique is shown on one RAP. Here the customers are aware of the status of the queue, and their aim is to maximize their payoffs. The revenue generated by the RAP is also formulated here.

4.1 Revenue Model

The customers of the train have the data packets to be transferred. They can obtain a reward ψ after they get served by the RAP which can be any form of benefit. For customer, we represent the cost by $\chi(T)$ which increases with T. Here we plead a linear example, and assume that $\chi(T) = CT$ where C is the value of unit cost. We assume that for $m = 0$, K is positive to avoid the trivial situation when $m = 0$ and $K = 0$, which leads to

$$\psi > \left(1 + \frac{\epsilon}{\phi}\right)\frac{C}{\mu_x} + \frac{C\epsilon}{\phi(\lambda + \phi + \epsilon)}. \tag{1}$$

For customers, we can make use a generic payoff model, commonly referred as queueing analysis [13, 14].

When the train is moving, the queue information is forwarded from one RAP to the next RAP, and accordingly, T is derived theoretically. For a customer, the payoff is given by

$$K = \psi - CT \tag{2}$$

This function is defined by T which includes service time and waiting time T that depends on the status of the queue and the decision of the customers regarding association with the RAP. If there is a positive payoff, the customers prefer to join the RAP but if there is a negative payoff, the customers choose not to connect with the RAP. If the payoff is 0, the customers take neutral decision. In this sense, the customers are said to be risk neutral in nature [15]. Using the parameter of waiting time in the queue denoted by W induced by the arrival rate λ, the average queueing delay T is obtained as,

$$T = W + \mu_E. \tag{3}$$

Using Pollaczek–Khinchin formula [17], the average waiting time is given by,

$$W = \frac{\lambda\mu_E^2}{2(1 - \lambda\mu_E)}. \tag{4}$$

When the service time of RAP μ_x and the service time of incoming customers μ_y both follow exponential distributions, then the first and second moments are obtained

as

$$\mu_E = \frac{1}{\mu_y}\left(1 + \frac{\beta}{\mu_x}\right) \tag{5}$$

$$\mu_E^2 = \frac{2}{\mu_y^2} + \frac{2\beta}{\mu_x^2\mu_y^2} + \frac{2\beta}{\mu_x^2\mu_y} + \frac{4\beta}{\mu_x\mu_y^2} \tag{6}$$

By using (3) and (4), obtain T as

$$T = \frac{\lambda\mu_E^2}{2(1-\lambda\mu_E)} + \mu_E. \tag{7}$$

To study the revenue model, analyse the probability q of the customers who decide to join the queue. Customers selfishly choose q to obtain non-negative reward and finish the service with arrival rate λ. Then, there exists a unique equilibrium arrival rate λ_e as follows

$$\lambda_e = \frac{2(\psi - K - C\mu_E)}{2\psi\mu_E - 2K\mu_E + C\mu_E^2 - 2C\mu_E^2}. \tag{8}$$

For a given effective rate λ_e

$$q(\psi - CT - K) = 0. \tag{9}$$

In particular, the customer decides whether to join or balk based on the revenue charged by the RAP. By considering the fact that the RAP's goal is to maximize the revenue by fixing an admission fee, the revenue model can be obtained as

$$\pi_K = \lambda_e K. \tag{10}$$

In order to make (10) into a convex form, replace π_K to π_{λ_e} and develop an equivalent form as given

$$\pi_{\lambda_e} = \lambda_e[\psi - CT]. \tag{11}$$

As T is convex and an increasingly continuous function, the π_{λ_e} in the interval $(0, 1/\mu_E)$ is strongly concave function. Here by the setting first derivative of π_{λ_e} to zero, it produces a unique optimal solution λ_e^o as follows

$$\lambda_e^o = \frac{1}{\mu_E} - \frac{\sqrt{C\mu_E^2\Omega}}{\mu_E\Omega} \tag{12}$$

where $\Omega = C\mu_E^2 + 2\psi\mu_E - 2C\mu_E^2$. To achieve the maximum revenue from customers, the RAP can adjust the arrival rate λ_e^o of the incoming customers in the queue.

4.2 Queuing Analysis When Both I(T) and N(T) Are Known

Here, for customers arriving with the data requests, both $N(t)$ and $I(t)$ can be generated [16]. A pure threshold strategy (PT1) is considered when the customers will be knowing the queue length and the train position, specified by the pair $(m_e(0), m_e(1))$. The customer decides according to the threshold $m_e(I(t))$ of the queue length whether to associate or not. We can define PT1 as at arriving time t, inspect $(N(t), I(t))$, and if $N(t) \leq m_e(I(t))$, then associate with RAP otherwise remain connected to cellular network by default. Hence, just before the arrival of customer, the expected waiting time is given as

$$T(m,i) = (m+1)\left(\frac{\epsilon}{\phi} + 1\right)\left(\frac{1}{\mu}\right) + (1-i)\left(\frac{1}{\epsilon}\right). \tag{13}$$

Accordingly, the thresholds $(m_e(0), m_e(1))$ where PT1 is a poorly dominant strategy can be presented as

$$((m_e(0), m_e(1)) = \left(\left\lfloor \frac{\psi\mu\phi - C\mu}{C(\epsilon+\phi)} \right\rfloor - 1, \left\lfloor \frac{\psi\mu\phi}{C(\epsilon+\phi)} \right\rfloor - 1\right). \tag{14}$$

Based on (13), the payoff of the customer who enters the queue with state (m,i) is given by

$$K(m,i) = \psi - CT(m,i). \tag{15}$$

It is observed from (15) that if $K(m,i) > 0$, a customer will join with the RAP. We assume that the connection between customer and BS is occurring in a natural way and if the customer finds it beneficial, they will connect to the RAP. The payoff is considered to be positive in this case. In the case when the customer decides to stay in the cellular network, the payoff is assumed to be less than 0. Hence, if $K(m,i) = 0$ for m, the customer will connect to the RAP if and only if the total customers in the queue $m = m_e(i), \forall \in \{0, 1\}$ and $(m_e(0), m_e(1))$ can be found in (14).

5 Numerical Results

Simulation results are obtained on the system model to explore the effect of several parameters on the behaviour of the passengers of the train. The equilibrium strategy

for arrival rate is satisfied by considering different situations. Figure 2 describes the relationship between the payoff K and customers' equilibrium arrival rate λ_e. With the increase in arrival rate, the price also increases. With the higher number of customers in queue of the RAP, the price charged is also increased.

Figure 3 shows the shape of revenue analysed for different values of channel availability β. For $\beta = 1$, there is higher number of passengers trying to associate with RAP, and hence, the revenue generated by the RAP is higher for lesser value of β.

For the case studied, it is assumed that the queue length and train position are known to the upcoming passengers. In Fig. 4, the expected mean time is plotted with the number of customers m in queue. It shows that when the greater number of customers chooses to wait for getting served in the queue, expected delay time

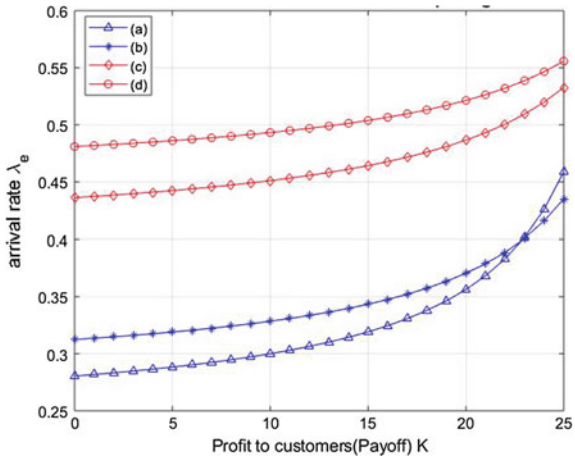

Fig. 2 Individual customer arrival rate λ_e versus payoff K with $\psi = 100$, $C = 1$ in four case: (a) $\beta = 2$, $\mu_y = 1.2$, $\mu_x = 0.5$; (b) $\beta = 2$, $\mu_y = 1.2$, $\mu_x = 0.6$; (c) $\beta = 1.5$, $\mu_y = 1.2$, $\mu_x = 0.5$; (d) $\beta = 1.5$, $\mu_y = 1.2$, $\mu_x = 0.6$

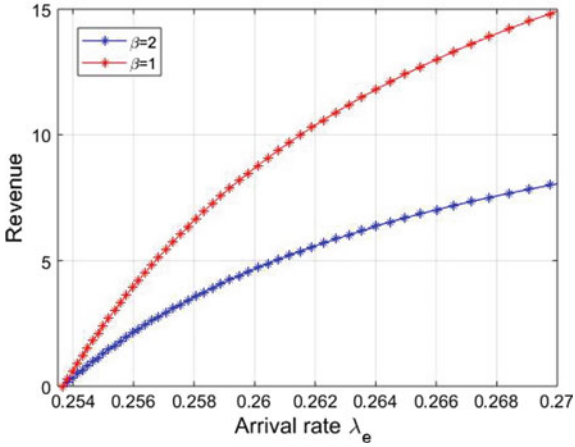

Fig. 3 Revenue versus equilibrium arrival rate with $R = 100$, $C = 1$, $\mu_y = 1.2$, $\mu_x = 0.5$ at $\beta = 1$ and $\beta = 2$

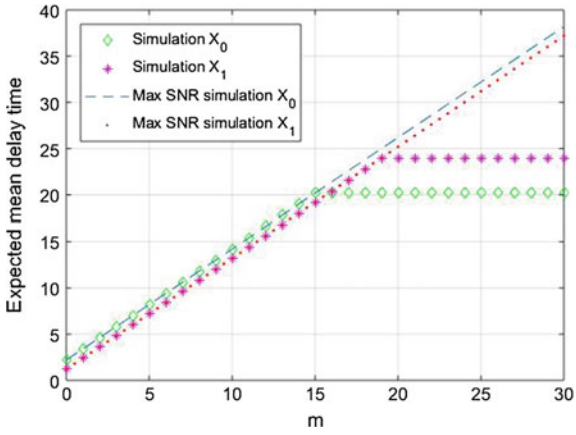

Fig. 4 Expected mean delay time versus m when $\mu_x = 5, \phi = 0.2, \epsilon = 1, \lambda = 0.5, \psi = 25, C = 1$.

increases. But after a certain extent, customers will avoid to join RAP and will remain in the cellular network.

From Fig. 5, we can find the thresholds; accordingly, the customer will choose to stay in the queue. We can see the monotonical decrease with the distance between two adjacent RAPs in the thresholds $m_e(I(t)), \forall I(t) \in \{0, 1\}$.

With the increase in ϵ, a greater number of data transmissions fail. It can be found that the threshold is higher for $I(t) = 1$, i.e. when the train is travelling in the coverage network of RAP. The customers prefer to join RAP and sustain a longer queue.

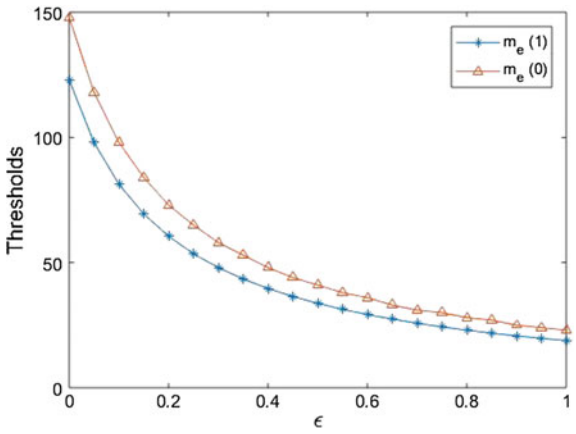

Fig. 5 Thresholds versus ϵ when $\mu_x = 5, \phi = 0.2, \psi = 25, C = 1, \lambda = 0.5$

6 Conclusion

In this chapter, a scenario of modern railway communication system is discussed where a series of Rail-track Access Points (RAPs) that are capable of providing high-speed Internet are deployed randomly across the railway lines. To satisfy the customer's demand, this system is adequate for providing a wide variety of on-board services. The problems faced by the customer in a heterogeneous wireless railway network while connecting to the RAPs are analysed here. We carried out the analysis on the expected mean delay time when the queue length and the status of the system are known to the arriving customers of the RAP. To decide whether to join the RAP or not, the revenue model is proposed. The proposed user RAP association scheme can help in providing data connectivity in heterogeneous wireless railway network.

References

1. Calle-Sánchez J, Molina-García M, Alonso JI, Duran AF (2013) Long term evolution in high speed railway environments: Feasibility and challenges. Bell Labs Tech J 18(2):237–253
2. Zhang C, Fan P, Xiong K, Fan P (2015) Optimal power allocation with delay constraint for signal transmission from a moving train to base stations in high-speed railway scenarios. IEEE Trans Veh Technol 62(12):5575–5588
3. Lei L et al (2016) Stochastic delay analysis for train control services in next generation high-speed railway communications system. IEEE Trans Intell Transp Syst 17(1):48–64
4. Jiang X, Guo L, Hong S, Zhou J (2015) Modelling delay propagation within a train communication network. In: Proceedings of IEEE annual reliability maintainability symposium (RAMS), Palm Harbor, FL, USA, pp 1–6
5. Xu S, Zhu G, Shen C, Li S, Zhong Z (2016) Delay-aware dynamic resource management for high-speed railway wireless communications. IEEE Veh Technol 83:1–5
6. Hu Y, Li H, Han Z (2015) Delay bound analysis using martingale for multimedia DTN under heterogeneous network for high-speed trains. In: Proceedings of IEEE global communications conference (GLOBECOM), San Diego, CA, USA, pp 1–6
7. Hu Y, Li H, Chang Z, Han Z (2017) Scheduling strategy for multimedia heterogeneous high-speed train networks. IEEE Trans Veh Technol 66(4)
8. Melnik AV (2014) Pricing in queueing systems M/M/m with delays. Contri Game Theory Manage 7:214–220
9. Zhou W, Huang W (2015) Two pricing mechanisms for a service provider when customers' delay costs are value-related. Comput Ind Eng 87:600–610
10. Li H, Han Z (2011) Socially optimal queuing control in cognitive radio networks subject to service interruptions: to queue or not to queue? IEEE Trans Wirel Commun 10(5):1656–1666
11. Chang Z, Ristaniemi T, Han Z (2015) Queueing game for spectrum access in cognitive radio networks. IEEE Commun Lett 19(11):2017–2020
12. Tran NH, Hong CS, Lee S, Han Z (2013) Optimal pricing effect on equilibrium behaviors of delay-sensitive users in cognitive radio networks. IEEE J Sel Areas Commun 31(11):2266–2579
13. Hassin R, Haviv M (2003) To queue or not to queue: equilibrium behavior in queueing systems, vol 59. Springer
14. Tran NH, Hong CS, Han Z, Lee S (2013) Optimal pricing effect on equilibrium behaviors of delay-sensitive users in cognitive radio networks. IEEE J Sel Areas Commun 31(11):2566–2579
15. Hu Y, Chang Z, Li H, Ristaniemi T, Han Z (2017) Service provisioning and user association for heterogeneous wireless railway networks. IEEE Trans Commun 65(7):3066–3078

16. Economou A, Kanta S (2008) Equilibrium balking strategies in the observable single-server queue with breakdowns and repairs. Oper Res Lett 36(6):696–699
17. Bertsekas DP, Gallager RG, Humblet P (1992) Data Networks. 2nd edn. Prentice-hall Englewood Cliffs

Novel Design of Compact Half Equilateral Triangular MSAs Gap-coupled with Sectoral Patches

Amit A. Deshmukh, Vivek Chaudhary, M. Shah, C. Kudoo and A. Mhatre

Abstract Multi-resonator gap-coupled design of compact half equilateral triangular microstrip antenna with another half equilateral triangular patch and smaller angle sectoral patches is proposed. The wideband response is the result of coupling between TM_{10} modes on fed and parasitic patches. The simulated and measured impedance bandwidth of more than 800 MHz (>56%) is obtained. Antenna exhibits pattern maxima in the direction perpendicular to the plane of antenna and exhibits linear polarization. Across the bandwidth, maximum peak broadside gain of 8.5 dBi has been realized. With the realized bandwidth and gain characteristics, proposed equivalent configuration can find applications in mobile communication designs; further, they also can be used in personal communication systems.

Keywords Half equilateral triangular microstrip antenna · Broadband microstrip antenna · Sectoral microstrip antenna · Multi-resonator configuration

1 Introduction

With the advent of personal and mobile communication systems, requirement of antennas which are low profile in design as well as which do not disturb the properties of hosting surface is needed, and here, microstrip antenna (MSA) finds application due to its above-required properties [1, 2]. Wideband equivalents of MSAs have been realized by using multi-resonator designs wherein second resonant mode is added either by using parasitic patch or by embedding slot inside the patch [3–12]. The slot cut technique was first introduced in 1995 and ever since it has been widely used for enhancing the antenna impedance BW [8]. Although slot cut antennas do not increase patch area but are relatively complex in design aspect. Against this, gap-coupled configurations are simpler to design [3]. The compact MSA has been realized either by cutting slot inside patch that only affects fundamental mode resonant length or by shorting the patch nearer to its fundamental mode [13, 14]. But these compact antenna techniques degrade antenna parameters like bandwidth (BW), radiation pattern and

A. A. Deshmukh · V. Chaudhary (✉) · M. Shah · C. Kudoo · A. Mhatre
EXTC, SVKM's DJ Sanghvi COE, Vile-Parle, Mumbai, India

V. Janyani et al. (eds.), *Optical and Wireless Technologies*, Lecture Notes in Electrical Engineering 648, https://doi.org/10.1007/978-981-15-2926-9_38

gain. By using the symmetry of field distribution at fundamental patch mode in circular MSA and equilateral triangular MSA (ETMSA), compact MSA has been realized and they are referred to as semi-circular MSA and half ETMSA (HETMSA). This compact MSA offers 50% reduction in patch size against their full equivalents. These compact designs offer similar pattern characteristics to that with full configuration but have smaller BW and gain. Present paper puts forward novel design of gap-coupled HETMSA with smaller dimensions parasitic HETMSA and narrow-angle sectoral MSAs. The BW enhancement is attributed to the coupling between TM_{10} modes on fed and parasitic patches. The proposed configuration yields simulated and measured impedance BW of larger than 800 MHz (>56%). This BW is larger than the BW obtained using gap-coupled design of ETMSA along with sectoral patches as reported in [15]. Also, the peak gain obtained here is larger than as realized in [15]. Therefore, a new contribution in present design is in simpler wide configuration with enhanced antenna characteristics. The IE3D simulations have been used in present paper first for analyzing and optimizing HETMSA variations, and N-type 50 Ω connector is used to feed antennas. The finite ground plane having side length of 35 cm is selected. Measurements have been carried out using ZVH–8, FSC 6 and SMB 100A inside antenna lab.

2 Wideband HETMSAs Gap-coupled with Sectoral Patches

The gap-coupled configurations of HETMSAs and that with parasitic sectoral patches are shown in Fig. 1a–f. Initially, gap-coupled configuration of two HETMSAs is studied. Further, its BW improvement is realized using two pairs of 30° sectoral patches.

The configurations are discussed in 1200 MHz frequency range. Thus, side length of equivalent ETMSA 'S' is selected for this TM_{10} mode frequency. MSA is fabricated on FR4 substrate ($h = 0.16$ cm, $\varepsilon_r = 4.3$ and $\tan\delta = 0.02$). Patch parameters are selected for total substrate thickness ($h + h_a$) of nearly $0.1\lambda_g$ (2.56 cm). For these parameters, equivalent ETMSA using proximity feeding yields BW of 500 MHz (~38%). An increment in its BW is realized by first splitting ETMSA into two HETMSA of unequal side length and further optimizing parasitic HETMSA side length 'S_1' and strip parameters. Impedance BW here depends upon spacing between TM_{10} mode frequencies on two HETMSAs as shown in Fig. 2a. For 'S_1' = 9 cm, multi-resonator design of two HETMSAs yields maximum simulated and measured BW's of around 677 MHz (48.86%), which is higher than the ETMSA BW.

Further, two sectoral patches of unequal radius 'r_1' and 'r_2' are gap-coupled to two HETMSAs design. Here, BW depends upon the spacing between TM_{10} mode frequencies on respective patches as shown in Fig. 2b. The position of sectoral patches 'x' that changes the coupling between various resonant modes governs the impedance BW. For 'x' = 3.3, 'r_1' = 6.5 and 'r_2' = 6 cm, optimum response is realized. Using simulation, this gap-coupled antenna yields BW of 750 MHz (53.19%). The

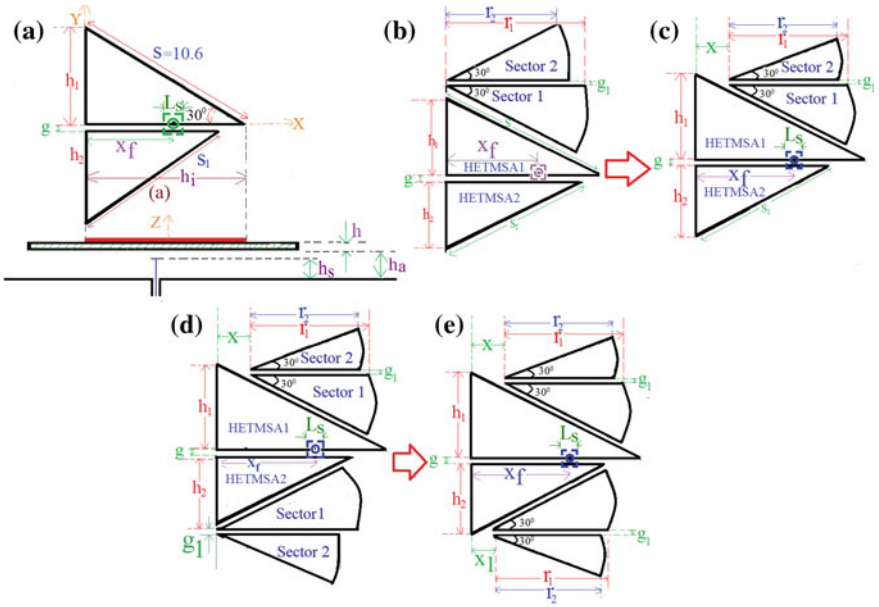

Fig. 1 **a**, **b** Gap-coupled HETMSAs fed using proximity coupling strip and its gap-coupled configurations with **c**, **d** two and **e**, **f** four sectoral patches

experimental BW is 763 MHz (54%). This BW is nearly 5% higher as compared with HETMSAs gap-coupled design. Multi-resonator design using only sectoral patch '1' has also been studied, which yields BW of 689 MHz (49.91%). To realize more symmetrical configuration with reference to proximity feed, sectoral patches were also gap-coupled along the side length of parasitic HETMSA of smaller side length as shown in Fig. 1(e, f). For symmetry, here dimensions of additional sectoral patches are taken to be the same. An optimum wider BW is obtained for 'x' = 3.3, 'x_1' = 2.5, 'r_1' = 6.5 and 'r_2' = 6 cm, as shown in Fig. 3a. Using simulation, impedance BW is 820 MHz (58.24%) and that using experiment, it is 829 MHz (59.58%). Co-polar broadside gain variation across the impedance BW and the radiation pattern nearer to band start and stop frequencies are provided in Figs. 3d and 4a–d, respectively.

The pattern across BW and at start and stop frequencies exhibits maxima in the bore-sight direction with cross polarization radiation component less than 10 dB as compared with co-polar component with E and H-planes along $\Phi = 0°$ and 90°, respectively. Thus, antenna exhibits linear polarization over the BW. Broadside antenna gain is larger than 6 dBi across most of impedance BW with peak gain of 8.5 dBi.

Thus in comparison, with respect to ETMSA design using proximity feed, presented configuration of HETMSAs with four sectoral patches yields 20% increment in VSWR BW. Although patch area has increased with addition of parasitic sectoral patches, since sectoral patches occupy the adjoining area of HETMSAs, overall increment in gap-coupled patch size is not significant. Proposed gap-coupled design

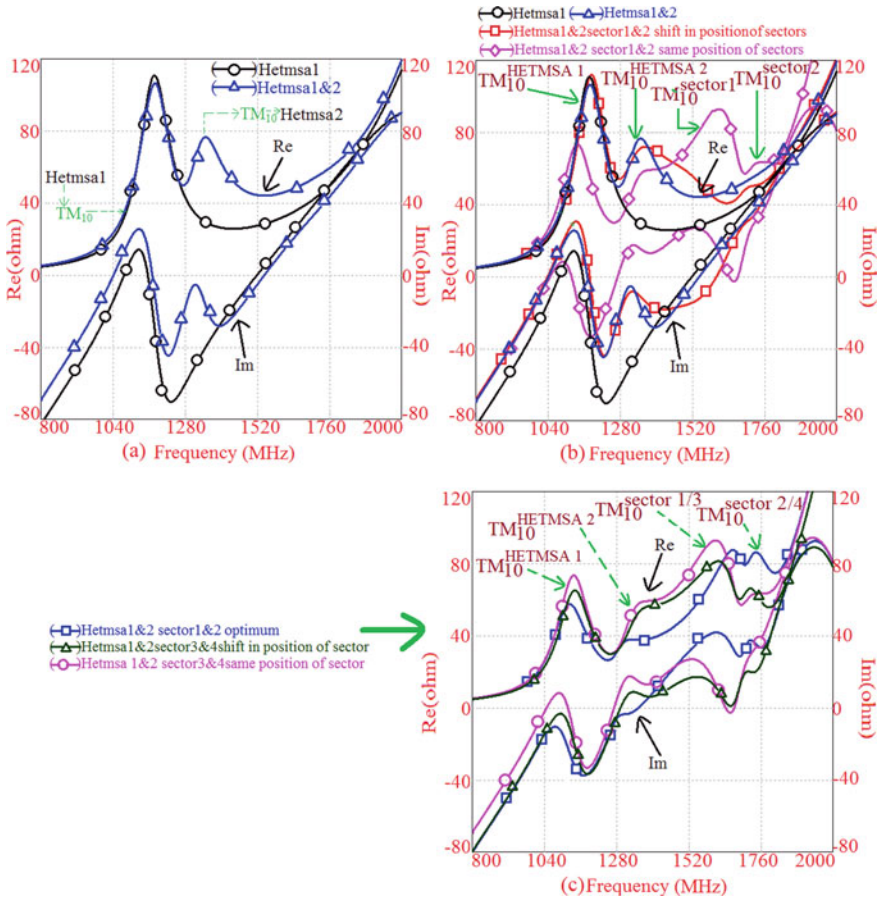

Fig. 2 Impedance graphs for gap-coupled design of **a** two HETMSAs, two HETMSAs gap-coupled to **b** two and **c** four sectoral patches

also yields higher peak gain against ETMSA. As compared with gap-coupled design reported in [15], proposed configuration yields 9% increment in BW. Against reported variations of slot cut antennas in the same frequency range, proposed design offers higher BW and is simpler in design. These are all the novelty in proposed design.

3 Conclusions

Novel gap-coupled design of compact HETMSA along with parasitic HETMSA and two pairs of 30° sectoral patches is presented. The wideband response is achieved due to coupling between TM_{10} modes frequencies of various patches. Proposed

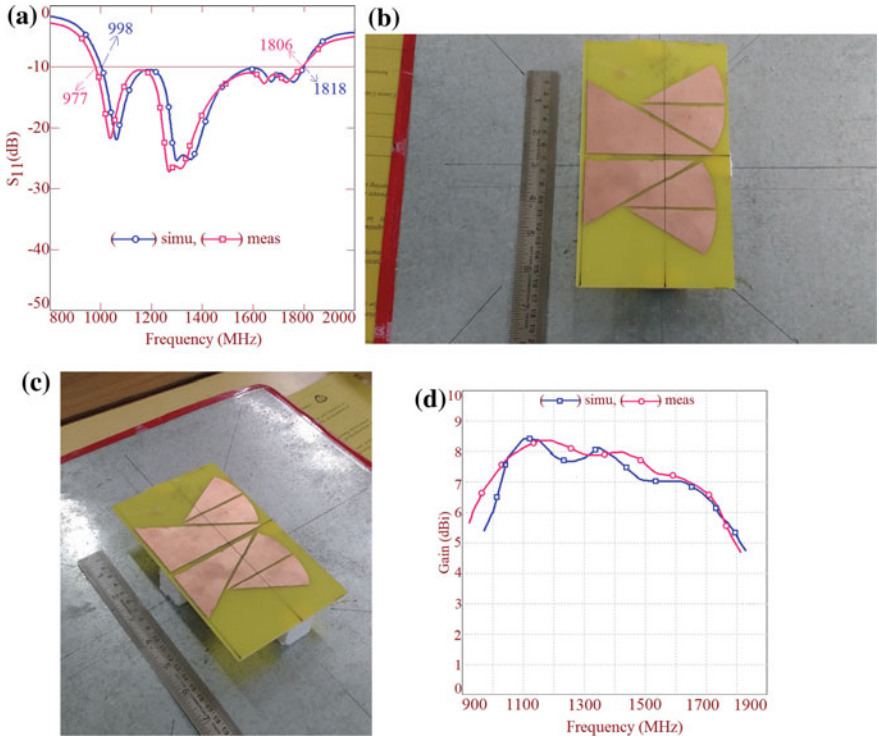

Fig. 3 **a** Optimum return loss (S_{11}) plots **b** top and **c** side views of fabricated antenna, and **d** gain variation across the BW for HETMSAs gap-coupled to four sectoral patches fed using proximity strip

antenna yields BW of more than 800 MHz (~58%). It exhibits pattern maximum in direction perpendicular to antenna plane and yields peak gain of above 8 dBi. With these antenna characteristics, equivalent designs of proposed configuration will find applications in mobile as well as personal communication systems.

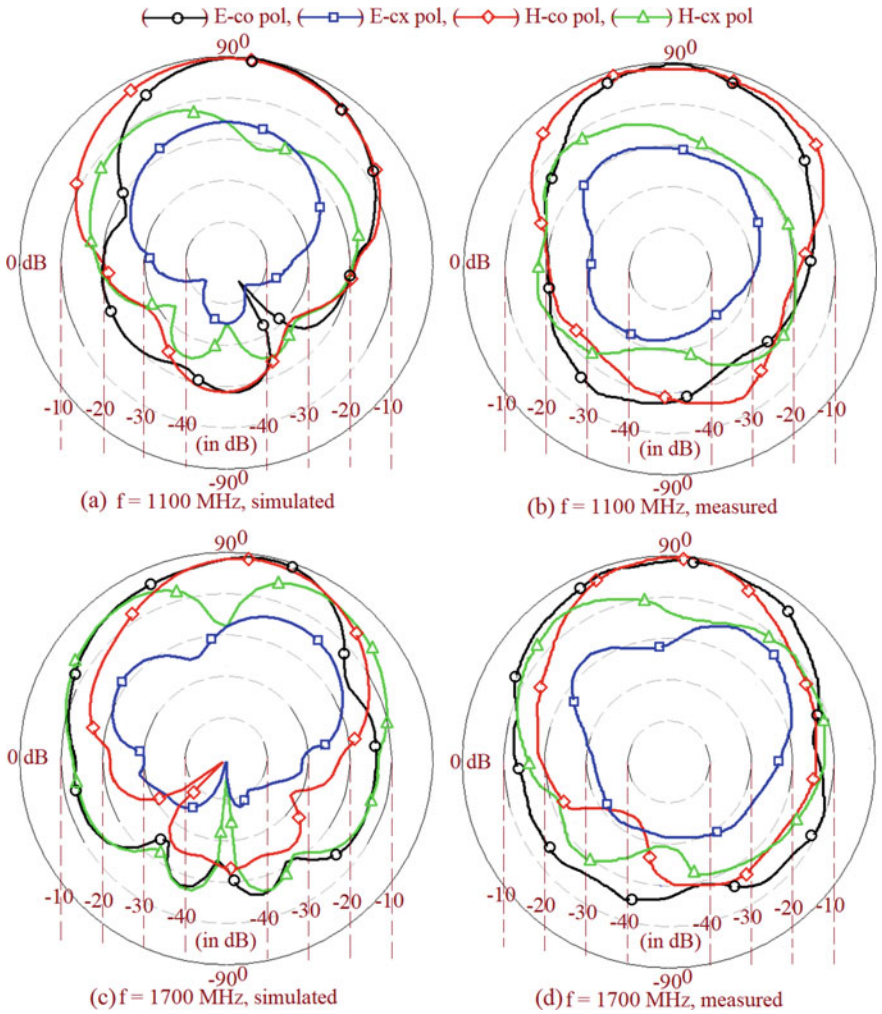

Fig. 4 Radiation pattern nearer to **a**, **b** band start and **c**, **d** band stop frequencies for HETMSAs gap-coupled with four sectoral patches fed using proximity strip

References

1. Carver KR, Mink JW (1981) Microstrip antenna technology. IEEE Trans Antennas Propag 29:2–24
2. Lee HF, Chen W (1997) Advances in microstrip and printed antennas. Wiley, New York
3. Kumar G, Ray KP (2003) Broadband microstrip antennas, 1st edn. Artech House, USA
4. James JR, Hall PS (1989) Handbook of microstrip antennas, vol 1. Peter Peregrinus Ltd., London
5. Chang E, Long SA, Richards WF (1986) An experimental investigations of electrically thick rectangular microstrip antennas. IEEE Trans Antennas Propag 34(6):767–772

6. Tiwari RN, Singh P, Kanaujia BK (2017) Butter fly shape compact microstrip antenna for wideband applications. Prog Electromagn Res Lett 69:45–50
7. Baudha S, Dinesh Kumar V (2015) Corner truncated broadband patch antenna with circular slots. Microw Opt Technol Lett 57(4):845–849
8. Wong KL (1997) Compact and broadband microstrip antenna. Wiley, New York
9. Rathi V, Kumar G, Ray KP (1996) Improved coupling for aperture coupled microstrip antennas. IEEE Trans Antennas Propag 44(8):1196–1198
10. Damiano JP, Bennegueouche J, Papiernik A (1990) Study of multilayer antennas with radiating elements of various geometry. IEE Proc Microw Antennas Propag 137(3):163–170
11. Clenet M, Shafai L (1999) Multiple resonances and polarization of U-Slot patch antenna. Electron Lett 35(2):101–103
12. Huynh T, Lee KF (1995) Single layer single patch wideband microstrip antenna. Electron Lett 31(16):1310–1312
13. Deshmukh AA, Kumar G (2007) Formulation of resonant frequency for compact rectangular microstrip antennas. Microw Opt Technol Lett 49(2):498–501
14. Deshmukh AA, Kumar G (2006) Compact broadband gap-coupled shorted square microstrip antennas. Microw Opt Technol Lett 48(7):1261–1265
15. Deshmukh AA, Chaudhary V, Shah M, Pawar S (2018) Wide band designs of equilateral triangular microstrip antenna with parasitic sectoral patches. In: Proceedings of ICACC–2018, 12th–15th Sept 2018, Kochi, India

Study of Approaches to Implement the Prism-Based Surface Plasmon Resonance Sensors

Nitesh Mudgal, Manoj Kumar Falaswal, T. Ismail, I. S. Fahim, Manish Tiwari and Ghanshyam Singh

Abstract Surface plasmon resonance (SPR) sensors are increasingly in demand due to their high sensitivity, better accuracy, and improved detection limit. Such performance parameters make these sensors suitable for biological and medical field's applications. During the last decade, prism coupling-based SPR sensors had been a preferred choice among the designer and developers across the globe. This article summarizes a review of prism coupling-based SPR photonic sensors. Important performance characteristics of such sensors have also been studied with respect to their detection accuracy, sensitivity, quality parameter, etc.

Keywords Refractive index · Optical prism · Diffraction grating · Optical waveguide-based biosensor

1 Introduction

The concept for research of SPR sensor began about a century ago when R.W. Wood found the first phenomena of light scattering by exciting surface plasmon waves [1]. Further attenuated total reflection (ATR) method was utilized by Otto and Kretschmann (1968) for excitation of the surface plasmon. Thereafter, SPR sensors have drawn attention for their use in the environment and biomedical science [2, 3]. SPR can be defined as an oscillation of charge density over the surface of an interface of two oppositely signed dielectric media, i.e. one metal and other one dielectric as shown in Fig. 1.

N. Mudgal (✉) · M. K. Falaswal · G. Singh
Department of Electronics and Communication Engineering, Malaviya National Institute of Technology Jaipur (MNIT Jaipur), Jaipur, Rajasthan 302017, India

T. Ismail
Department of Engineering Applications of Laser (NILES), Cairo University, Giza, Egypt

I. S. Fahim
School of Engineering and Applied Science, Nile University, Giza, Egypt

M. Tiwari
Department of ECE, Manipal University Jaipur, Jaipur, India

V. Janyani et al. (eds.), *Optical and Wireless Technologies*, Lecture Notes in Electrical Engineering 648, https://doi.org/10.1007/978-981-15-2926-9_39

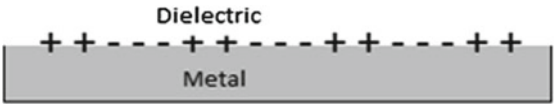

Fig. 1 Schematic representation of charge density at the interface of two different media metal and dielectric

These charge density oscillations are electromagnetic waves (transverse magnetic polarized wave) having a maximum value at the interface of two different media and evanescently propagating decay in both media. Wave vector of surface plasmon (β_{sp}) is given by

$$\beta_{sp} = \mathrm{Re}\{\frac{2\pi}{\lambda_{in}}\sqrt{\frac{\epsilon_{metal}\,\epsilon_{diele}}{\epsilon_{metal}+\epsilon_{diele}}}\} \tag{1}$$

where λ_{in} is incident light wavelength, and ϵ_{diele} and ϵ_{metal} are the dielectric constants of dielectric medium and metal, respectively [4].

2 Approaches for Surface Plasmon Resonance Sensors

It is clear from Eq. (1) that wave propagation in dielectric always has a smaller value than propagation constant of surface plasmon, so it is impossible to excite surface plasmon by incident light directly to the metal–dielectric surface interface. In order to match incident light momentum to surface plasmon wave (SPW), it is required to improve momentum of the incident light wave that can be attained by prism light coupling, grating, and optical waveguide light coupling approach [5]. A brief study of each light coupling approach for SPR sensor has been described in the below sections.

2.1 Prism Coupling Approach

Light coupling using prism configuration is a most common ATR method based on Kretschmann configuration due to its simplicity and variable parameters, where a prism having high refractive index (n_{pr}) is interfaced with metal–dielectric surface; here, refractive index of dielectric (n_{diele}) is less than prism refractive index ($n_{pr} > n_{diele}$) [6]. Kretschmann configuration for prism coupling in ATR method is shown in Fig. 2.

Resonance condition for prism coupling will be satisfied when an incident wave vector is equal to the wave vector of surface plasmon, i.e.

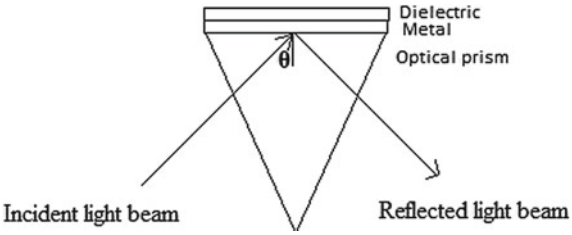

Fig. 2 Kretschmann configuration for prism coupling in the ATR method

$$\frac{2\pi}{\lambda_{in}} n_{pr} \sin\theta = \frac{2\pi}{\lambda_{in}} \mathrm{Re}\left\{\sqrt{\frac{\epsilon_{metal}\,\epsilon_{diele}}{\epsilon_{metal}+\epsilon_{diele}}}\right\} \tag{2}$$

From this equation, an incident angle can be calculated as:

$$\theta = \sin^{-1}\left[\left(\frac{1}{n_{pr}}\right)\mathrm{Re}\left\{\sqrt{\frac{\epsilon_{metal}\,\epsilon_{diele}}{\epsilon_{metal}+\epsilon_{diele}}}\right\}\right] \tag{3}$$

In a prism coupling approach, it is not necessary to have accurate control on plasmon metal layer thickness. The major disadvantage of this approach is high-cost set-up because prism is mounted on a goniometer which will increase the overall sensor set-up cost. Other cumbersome work is to make synchronization of rotation of prism table with the detector to acquire high-intense SPR light signal [6].

2.2 Grating Approach for Light Coupling

A diffraction grating is another approach for light coupling in SPR sensors based on diffraction of light. In 1902, Wood gives the concept of diffraction of light from diffraction grating for the surface plasmon excitation [1]. Schematic representation of grating is shown in Fig. 3. In this approach, light is made to an incident from a dielectric medium having refractive index n_{diele} on to the surface of the metal grating.

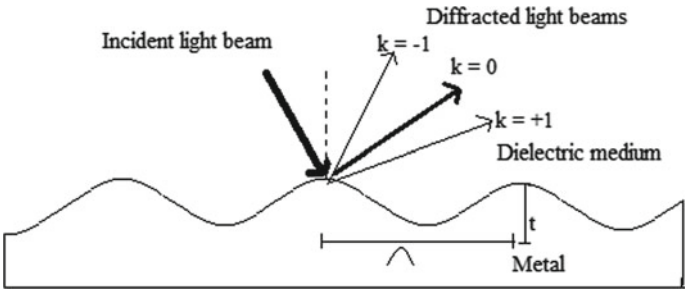

Fig. 3 Grating approach of light coupling in the SPR sensor

Later, the concept of diffraction angle was added in this grating approach of light coupling in the SPR sensor.

Diffraction angle for any order of diffracted light can be calculated from below equation [7, 8].

$$\sin\theta_k = \sin\theta + k\frac{\lambda_{in}}{\cap} \tag{4}$$

where θ_k is the angle of diffracted light of kth order, θ is the angle of incident light, is incident light wavelength and $\cap$ is the period of a groove for grating.

The condition for resonance in this grating configuration can be given by the following expression.

$$n_{diele}\sin\theta + k\frac{\lambda_{in}}{\cap} = \pm \mathrm{Re}\left\{\sqrt{\frac{\epsilon_{metal}\,\epsilon_{diele}}{\epsilon_{metal}+\epsilon_{diele}}}\right\} + \Delta n_{eff} \tag{5}$$

where and $\nabla\beta$ is shifting of the propagation constant due to the grating configuration. The mathematical modelling of the grating-based SPR sensor is more complicated than that for the prism-based SPR sensors. Therefore, data analysis for grating-based SPR sensor is more difficult. Limitation of grating-based SPR sensors for certain applications is that the flow cell and analyte should be optically transparent because the incident light beam is transmitted through sample [9].

2.3 Optical Waveguide Light Coupling Approach

Another approach for excitation of the surface plasmon is guided modes in dielectric planar waveguide where guided modes can be noticed as a strategy for improving sensor performance. Excitation phenomenon of SPW in waveguide SPR sensor is illustrated in Fig. 4.

When a guided mode is propagated in the waveguide, it enters and penetrates in the metal layer and then at outer surface of metal later it couples with surface plasmon. Coupling occurs when both propagation constant of guided mode (β_{mode}) and real part of surface plasmon propagation constant (β_{sp}) are equal;

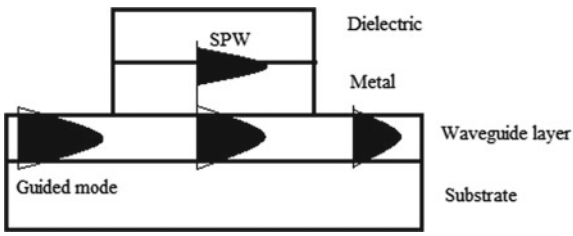

Fig. 4 Excitation of SPW in optical waveguide SPR sensor configuration

$$\beta_{\text{mode}} = \text{Re}\{\beta_{\text{sp}}\} \tag{6}$$

The advantages of waveguide-based SPR sensors include compactness, ruggedness, easiness in coupling, easier way to control the polarization light for triggering the surface plasmon excitation, small size, elimination of the effect of stray light, etc [10, 11].

3 Performance Parameters for SPR Sensor

Main performance parameters of an SPR sensor include accuracy, sensitivity, dynamic range, detection limit, and quality parameter. Detection accuracy of a sensor gives the degree of closeness for which sensor output reaches the true value of measurand (refractive index, the concentration of analyte, etc.). It is given in terms of signal-to-noise (SNR) ratio and should have high value. It can be calculated from the resonance curve of reflectivity and can be expressed as

$$\text{SNR} = \frac{\Delta\theta_{\text{resonance}}}{\Delta\theta_{0.5}} \tag{7}$$

Here, $\Delta\theta_{0.5}$ is half minima spectral width of the resonance curve. Sensitivity (S) of a sensor can be expressed as the ratio of change in the value of sensor output (angle, wavelength, polarization, intensity, phase, etc.) to the change on the value of measurand (refractive index, analyte concentration, etc.).

The sensitivity of a sensor, utilizing the angular modulation approach, depends on the value of the change in the resonance angle with a change in sensing layer refractive index. If the change in resonance angle increases with a refractive index change, then sensor sensitivity increases. The sensitivity of a sensor depends on the method of modulation approaches (angular modulation, intensity modulation, wavelength modulation method, etc.) and excitation approach of surface plasmon (prism-based coupling, grating coupling, optical waveguide coupling, etc.).

Dynamic range of SPR sensor is a span of measurand values that can be detected by using the sensor, whereas detection limit is the lowest value of analyte concentration that can be observed by using the sensor. Quality parameter (Q) of a sensor can be given in terms of sensor sensitivity and spectral width of half minima and can be represented as

$$Q = \frac{S}{\Delta\theta_{0.5}} \tag{8}$$

Sensor resolution describes the smallest change in measurand which gives a reasonable change in sensor output values. Resolution of a sensor depends on the level of noise at sensor output. The sources of sensor output noise are shot noise and fluctuations of intensity of emitted light [12, 13].

4 Sensing Structure Configurations for SPR Sensor

In this section, performance parameters like sensitivity, accuracy, detection limit, and a quality parameter of various prism coupling-based SPR sensors have been summarized and listed in Table 1.

4.1 Prism Coupling-Based SPR Sensors

High resistivity for oxidation and non-reactive property with other metals make gold more practical among all available metals [14]. In order to prove the performance of the sensor, the hybrid metal layer (gold–graphene) makes high adsorption of biomolecules due to a large surface area of the graphene layer [15]. In 2012, Maharana [16] reported a chalcogenide–graphene multilayer-based SPR affinity biosensor for refractive index having the range from 1.33 to 1.42. Schematic representation for this design is shown in Fig. 5.

The sensitivity and the detection accuracy were found to be 52 degree/RIU and 0.134/degree, respectively, for 632.8 nm wavelength. For 1000 nm wavelength, sensitivity and detection accuracy were found to be 36 degree/RIU and 2.320/degree, respectively [16]. Due to the excellent property of transparent metal oxide operating in infrared and visible spectrum region, indium tin oxide (ITO) is supportive composition without band to band transition forming no island in small thickness layer grown over dielectric layer [17]. In 2014, Sharma et al. [18] incorporated this transparent metal oxide material in designing SPR sensor with silica glass material prism and analysed this sensor using an angular interrogation method. Design structure for this sensor is shown in Fig. 6. For the optimum value of ITO layer thickness (50 nm) and incident light wavelength (1600 nm), the author found highest sensitivity of 164 degree/RIU for refractive index having a range from 1.30 to 1.35 [18].

Graphene is a single layer of carbon atoms arranged in hexagonal honeycomb lattice structure. The large surface area with excellent absorption properly make graphene as a choice of top layer in biosensors [19].

In 2016, Verma et al. [20] proposed a chalcogenide prism and graphene-based SPR biosensor for detection of bacteria with affinity layers of three different refractive indices such as 1.5265 for nicotine, 1.49268 for toluene, and 1.4370 for [poly (trifluoroethyl methacrylate)]. This structure comprises a gold layer (50 nm), graphene layer (0.34 nm), and affinity layer (3 nm) deposited on a chalcogenide prism surface. With affinity layer of refractive index (1.4370) for [poly (trifluoroethyl methacrylate)], detection accuracy, sensitivity, and value of quality parameter were obtained as 1.9960/degree, 38.4945 degree/RIU, and 28.51444/RIU, respectively.

Similarly, for the affinity layer of refractive index (1.4936) for toluene, detection accuracy, sensitivity, and value of quality parameter were obtained as 1.97984/degree, 38.74843 degree/RIU, and 28.283524/RIU, respectively. Similarly, for the affinity layer of refractive index (1.5265) for nicotine, detection accuracy, sensitivity,

Table 1 Summary of different structures of prism coupling-based SPR sensors

Type of simulating structure	Measurand	Simulation results			Year	References
		Sensitivity	Detection accuracy	Others		
Chalcogenide prism/gold/graphene/sensing medium	Refractive index (1.33-1.42)	52 degree/RIU	0.134 (632.8 nm)	–	2012	[16]
		36 degree/RIU	2.320 (1000 nm)			
Silica glass prism/indium tin oxide (ITO)/sensing medium	Refractive index (1.30-1.35)	164 degree/RIU	–	–	2014	[18]
Chalcogenide prism/gold (Au)/graphene/affinity layer	Refractive index (1.4370)—[poly (trifluoroethyl methacrylate)]	38.4945 degree/RIU	1.9960	Quality parameter (28.51444)	2016	[20]
	Refractive index (1.4936)—toluene	38.74843 degree/RIU	1.97984	Quality parameter (28.283524)	2016	[20]
	Refractive index (1.5265)—nicotine	38.88757 degree/RIU	1.97255	Quality parameter (28.179399)	2016	[20]
SF10 prism/gold (Au)/MoS2/graphene/sensing medium	DNA hybridization	87.8 degree/RIU	1.28	Quality parameter 17.56	2017	[21]
SF10 prism/ZnO/gold (Au)/MoS2/graphene/sensing medium	Refractive index (1.33–1.45)	101.58 degree/RIU	1.81	Quality parameter 15.11	2018	[25]

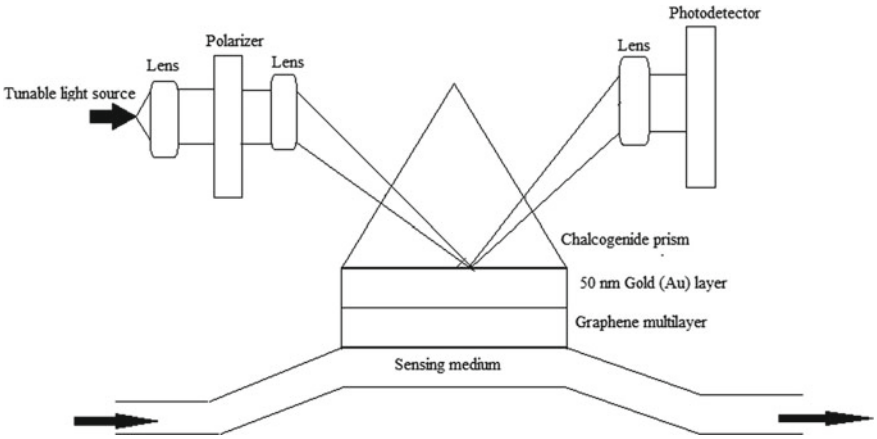

Fig. 5 Schematic representation of experimental set-up of chalcogenide-/gold-/graphene-based SPR sensor; reproduced from Ref. [16]

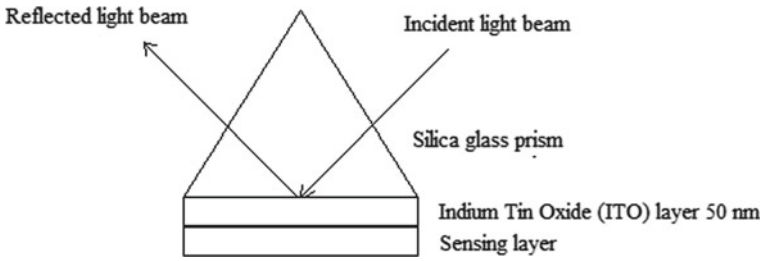

Fig. 6 Schematic representation of silica glass prism/ITO layer-based SPR sensor; reproduced from Ref. [18]

and quality parameter were obtained as 1.97255/degree, 38.88757 degree/RIU, and 28.179399/RIU, respectively. The author further compared this design with conventional chalcogenide SPR biosensor. This design was found 6.47 times more sensitive than the conventional design of chalcogenide SPR sensor [20].

In 2017, Saifur Rahman et al. [21] designed and numerically analysed a sensor with hybrid layer (gold–molybdenum disulphide (MOS_2)–graphene) for DNA hybridization detection. The author reported better sensitivity by adding monolayer of MOS_2 between graphene and gold layers. In this design, the author optimized the parameters of each layer and deposited over the surface of SF10 glass prism having the index of 1.732. Sensing medium for this proposed structure was phosphate-buffered saline. The optimum value of thickness and complex refractive index (n_g) of gold (Au) layer were considered as 50 nm and $n_g = 0.1726 + 3.4218i$, respectively [9].

For graphene layer, complex refractive index n_g and optimum thickness had been taken as $n_g = 3 + 1.1487i$ and 0.34 nm, respectively [22]. The optimum thickness and complex refractive index n_m for molybdenum disulphide (MOS_2) had been kept

as 0.65 nm and $n_m = 5.9 + 0.8i$, respectively [23, 24]. For the above considered optimum values of thickness and indices, the author found a high value of sensitivity (87.8 degree/RIU), better detection accuracy (1.28), and improved quality parameter (17.56) for this proposed sensor [21].

In 2018, Kushwaha et al. [25] proposed a sensor using a hybrid metal layer with improved sensitivity. Proposed sensing structure comprises zinc oxide (Z_nO) layer (40 nm) deposited over the SF10 prism surface. Further gold layer (42 nm), molybdenum disulphide (0.65 nm), and graphene layer (0.34 nm) were deposited over the Z_nO layer. The author considered a range of refractive index (1.33–1.45) for sensing medium. Angular interrogation technique had been used for analysis of the reflectance curve of this sensor. For optimum values of each layer thickness and 632.8 nm incident wavelength, the author reported a sensitivity of 101.58 degree/RIU, a quality parameter of 15.11/RIU, and detection accuracy of 1.81 [25].

5 Summary

This paper reviewed SPR technology and its application in sensing. Firstly, the concept of surface plasmon and condition for plasmonic resonance have been described. Secondly, different approaches, i.e. prism coupling, grating, and waveguide approach for light coupling, have been dentally explained and condition for light coupling for each approach has been discussed. Finally, work of previous years on prism coupling-based SPR sensors has been reviewed and has tabulated their performance characteristics in respect of detection accuracy, sensitivity, value of quality parameter, etc.

References

1. Wood RW (1902) on a remarkable case of uneven distribution of light in a diffraction grating spectrum. Philos Mag Ser 6(4):396–402
2. Otto A (1968) Excitation of Nonradiative surface plasma waves in silver by the method of frustrated total reflection. Z Physik 216:398–410
3. Kretschmann E, Raether H (1968) Radiative decay of non-radiative surface plasmons excited by light. Z Naturforsch 23A:2135–2136
4. Sambles JR, Bradbery GW, Yang F (1991) Optical excitation of surface plasmons: an introduction. Cont Phys 32:173–183
5. Liedberg B, Nylander C, Lundström I (1995) Biosensing with surface plasmon resonance–how it all started. Biosens Bioelectron 10
6. Wang Haiming (1995) Coupling to surface plasmon waves by the use of a birefringent prism coupler. Opt Commun 119:75–77
7. Homola J, Yee SS, Gauglitzand G (1999) Surface plasmon resonance sensors: review. Sens Actuators B 54:3–15
8. Sahu S, Ali J, Singh G (2017) Refractive index biosensor using sidewall gratings in dual-slot waveguide. Opt Commun 402:408–412

9. Homola J (2003) Present and future of surface plasmon resonance biosensors. Anal Bioanal Chem 377:528–539
10. Stöcker P, Menges B, Langbein U, Mittler S (2004) Multimode waveguide mode surface plasmon coupling: a sensitivity and device realizability study. Sens Actuators A 116:224–231
11. Sahu S, Ali J, Yupapinc PP, Singh G (2018) Optical biosensor based on a cladding modulated grating waveguide. Optik 166:103–109
12. Xinglong Y, Dingxin W, Zibo Y (2003) Simulation and analysis of surface plasmon resonance biosensor based on phase detection. Sens Actuators B 91:285–290
13. Homola J (ed) (2006) Surface plasmon resonance based sensors. Springer, Berlin/Heidelberg, Germany. ISBN 9783540339182
14. Raether H (1988) Surface plasmons on smooth and rough surfaces and on grating. Springer, Berlin Heidelberg
15. Soldano C, Mahmood A, Dujardin E (2010) Production, properties and potential of graphene. Carbon 48:2127–2150
16. Maharana PK, Jha R (2012) Chalcogenide prism and graphene multilayer based surface plasmon resonance affinity biosensor for high performance. Sens Actuators B 169:161–166
17. Verma RK, Gupta BD (2010) Surface plasmon resonance based fiber optic sensor for the IR region using a conducting metal oxide film. J Opt Soc Am A 27(4)
18. Sharma NK, Yadav S, Sajal V (2014) Theoretical analysis of highly sensitive prism based surface Plasmon resonance sensor with indium tin oxide. Opt Commun 318:74–78
19. Wu L, Chu HS, Koh WS, Li EP (2010) Highly sensitive graphene biosensors based on surface plasmon resonance. Opt Express 18:14395–14400
20. Verma Alka, Prakash Arun, Tripathi Rajeev (2016) Sensitivity improvement of graphene based surface plasmon resonance biosensors with chaclogenide prism. Optik 127:1787–1791
21. Saifur Rahman M, Shamim Anower Md, Rabiul Hasan Md, Biplob Hossain Md, Ismail Haque Md (2017) Design and numerical analysis of highly sensitive Au-MoS_2-graphene based hybrid surface plasmon resonance biosensor. Opt Commun 396:36–43
22. Tiwari JN, Tiwari RN, Kim KS (2012) Zero-dimensional, one-dimensional, two dimensional and three-dimensional nanostructured materials for advanced electrochemical energy devices. Prog Mater Sci 57:724–803
23. Rhodes C, Franzen S, Maria JP, Losego M, Leonard DN, Laughlin B, Duscher G, Weibel S (2006) SPR in conducting metal oxides. J Appl Phys 100:054905
24. Maurya JB, Prajapati YK, Singh V, Saini JP, Tripathi R (2015) Performance of graphene–MoS_2 based surface plasmon resonance sensor using silicon layer. Opt Quant Electron 47:3599–3611
25. Kushwaha AS, Kumar A, Kumar R, Srivastava SK (2018) A study of surface plasmon resonance (SPR) based biosensor with improved sensitivity. Photonics and Nanostructures Fundam Appl 31:99–106

Wideband Designs of Unequal Lengths Slot Cut Microstrip Antennas Backed by Slotted Ground Plane

Amit A. Deshmukh, Amita Mhatre, M. Shah, C. Kudoo and S. Pawar

Abstract Wideband designs of unequal lengths slot cut rectangular microstrip antennas backed by slots cut ground plane are proposed. The slots in ground plane (GP) alter TM_{02} and TM_{11} mode frequencies of equivalent GP, whereas additional slots on rectangular patch alter its TM_{11}, TM_{02} and TM_{12} mode frequencies, and an optimum spacing between them results in wider bandwidth. Maximum impedance bandwidth of 579 MHz (>50%) is obtained with unequal slot lengths on the GP as well as the radiating rectangular patch. All the slot cut designs yield broadside radiation across the impedance bandwidth and exhibit elliptical polarization. Peak broadside gain of larger than 7 dBi is obtained in the optimum configuration.

Keywords Broadband microstrip antenna · Defected ground plane microstrip antenna · Rectangular slot · Higher-order resonant mode

1 Introduction

Ever since the invention of microstrip antenna (MSA), also referred to as patch antennas in 1969, various methods have been adapted for enhancing its impedance bandwidth (BW) [1, 2]. The methods which have been commonly referred are use of multiple patches in planar gap-coupled or stacked configurations, use of modified feeding techniques like, and L-probe and widely referred technique of embedding slot in the patch [1–6]. Alternately by embedding slots in ground plane, enhancement in BW and realization of multi-band response has been reported [7]. These designs are referred to as defected ground plane structure (DGS) MSAs. When the dimensions of patch and ground plane are fixed, then with reference to the boundary condition applied to patch geometry, resonant modes in the structure are fixed [8]. Any modifications in patch with respect to slots will only alter the frequencies and impedance at respective modes to achieve wider BW as explained in [9]. A similar study to put forward the effects of slots on patch and ground plane together has not been discussed in literature. The present work addresses this research gap and novel wideband configurations using slots on patch, and the GP is presented in this paper.

A. A. Deshmukh · A. Mhatre (✉) · M. Shah · C. Kudoo · S. Pawar
EXTC, SVKM's DJ Sanghvi COE, Vile-Parle, Mumbai, India

V. Janyani et al. (eds.), *Optical and Wireless Technologies*, Lecture Notes in Electrical Engineering 648, https://doi.org/10.1007/978-981-15-2926-9_40

Initially, design of rectangular MSA (RMSA) backed by unequal lengths slot cut rectangular shape ground plane is discussed. Slots alter TM_{11} mode frequency of equivalent GP which along with TM_{10} mode in RMSA yields impedance BW of 165 MHz (17.81%). Further, three unequal length rectangular slots are embedded on RMSA. These slots modify patch TM_{11}, TM_{02} and TM_{12} mode frequencies that enhance the impedance BW further. With two equal lengths out of the three slots, antenna yields BW of 575 MHz (52.5) and with all three unequal length slots, antenna offers BW of 579 MHz (53.05%). Marginal increment in BW here is attributed to close spacing between modified patch resonant mode frequencies. All the proposed designs exhibit pattern maxima in the direction orthogonal to the plane of antenna. Designs with slots on the patch and the GP yield peak broadside gain of above 7 dBi. Proposed antennas in this paper were first optimized using IE3D simulations using N-type feed. Measurements have been carried out using ZVH–8, FSC 6 and SMB 100A. Although widely referred slot cut technique is used in present designs, an insight into functioning of antenna when multiple slots are present on patch and GP is presented here in terms of resonant modes. Similar kind of detailed study for DGS MSA is not available in literature, and thus, this is the novelty in proposed study.

2 RMSA Embedded with Slots Backed by DGS

Design of RMSA fed using proximity strip backed by unequal length slots cut DGS is shown in Fig. 1a, b. To maximize radiation efficiency, air substrate has been selected here. Here, three slots each have been embedded on the GP and the radiating patch. To optimize for wider BW, a detailed parametric study was carried out and impedance graphs for ground slots length variation are shown in Fig. 1c, d. The surface current distributions have been referred for different slots dimensions as present on the patch and ground plane. Based on resonant modes behaviour as observed in RMSA and GP, it was concluded that slots on ground modify equivalent ground rectangular patch's TM_{02g} and TM_{11g} ('g' for ground plane mode) modes. This mode identification was confirmed also by simulating ground plane as the patch and patch as the GP. The maximum BW with slots on ground plane is results of optimum spacing between TM_{11g} and patch's TM_{10} mode. For 'x_f' = 2.5, 'L_{g1}' = 6.5, 'L_{g2}' = 8.5 and 'L_{g3}' = 11 cm, respective simulated and measured BW's with only unequal lengths ground slots is 165 MHz (17.81%) and 174 MHz (18.2%). Here, the BW realized is smaller. The BW enhancement can be realized by modifying higher-order resonant modes and bringing them closer to TM_{10} mode on RMSA. With the placement of offset feed location (x_f = 3.0, y_f = 3.6 cm), BW seems to be increased. This increment is attributed to excitement of TM_{11} mode on the rectangular patch which yields simulated BW of 508 MHz (45.33%). However, radiation pattern variation across impedance BW was noticed because of orthogonal current components at TM_{11} mode. To minimize this, additional slots namely 'L_{p1}', 'L_{p2}' and 'L_{p3}' were introduced on RMSA as shown in Fig. 1a. Further parametric study was carried out and the impedance graph showing effects of these slots on various resonant modes is provided in Fig. 1e, f.

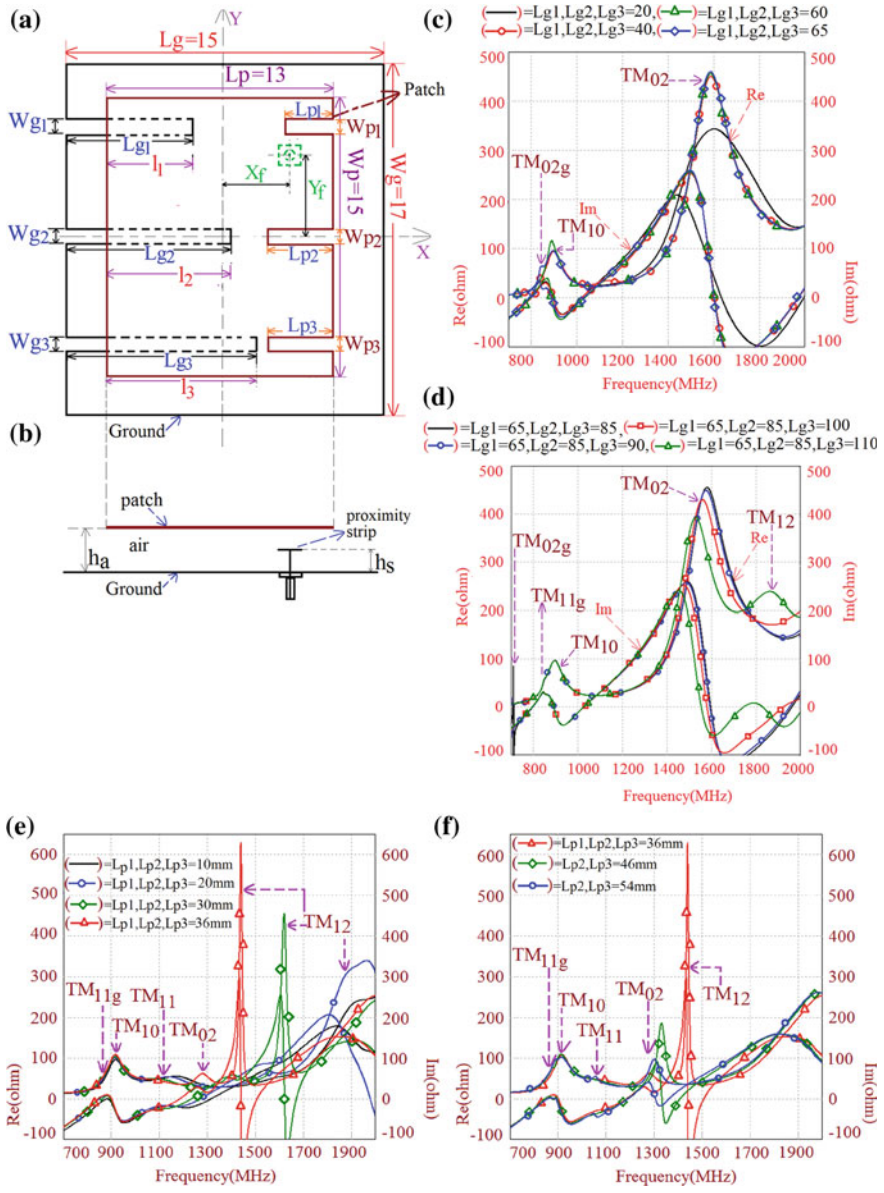

Fig. 1 **a**, **b** Slots cut RMSA backed by DGS fed using proximity strip and its impedance graphs for variation in **c**, **d** ground plane slot lengths, L_{g1}, L_{g2} and L_{g3} and **e**, **f** slot lengths on rectangular patch, 'L_{p1}', 'L_{p2}' and 'L_{p3}'

Here, initially, all three lengths (L_{p1}, L_{P2}, L_{P3}) were increased in equal steps. Further only middle (L_{P2}) and bottom (L_{P3}) horizontal lengths were increased, and later, the bottom horizontal length was increased. These lengths increment are orthogonal in direction to surface current at resonant TM_{02} and TM_{12} modes. Due to this, their frequencies reduce as observed from the impedance graphs. For the same ground slot and feed point parameters, with three equal length slots on the patch (L_{p1} = 3.6 cm), respective simulated and measured impedance BW of 524 MHz (48.93%) and 532 MHz (50.28%) is realized as shown in Fig. 2a.

The design with equal slots on RMSA yields broadside pattern across BW with cross-polar component of radiation less than 10 dB with reference to co-polar component. However, cross-polarization level increases towards higher frequencies of BW which is attributed to orthogonal components of surface current at TM_{02} and

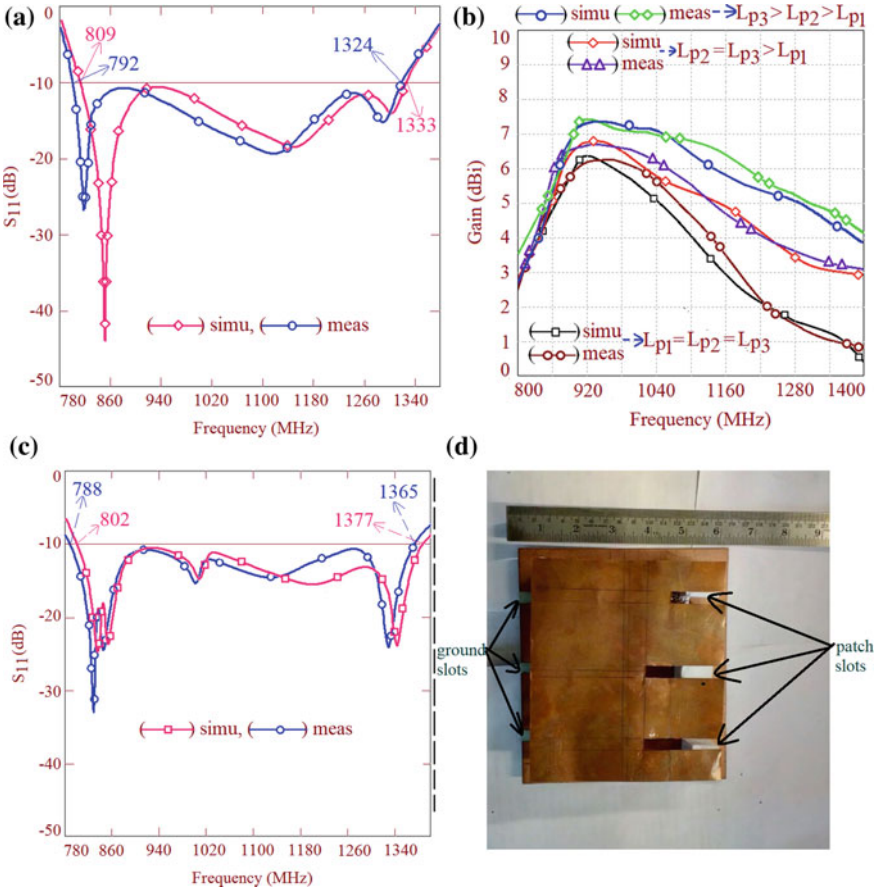

Fig. 2 **a** Return loss plots (S_{11}) for equal lengths slot cut RMSA backed by DGS, **b** gain variation across BW for wide band variations, **c** return loss plots and **d** fabricated antenna for slots cut RMSA backed by DGS for $L_{p2} = L_{p3}$

TM_{12} modes present towards higher frequencies. Due to this broadside antenna gain reduces towards higher frequencies as shown in Fig. 2b. To improve gain, variation effects of an increase in slot lengths were studied. Unequal increment in slot length is realized, and only lengths L_{p2} and L_{p3} were increased. This increment further reduces TM_{02} and TM_{12} mode frequencies as shown in Fig. 1f. A wider BW is obtained for $L_{p2} = L_{p3} = 5.4$ cm as shown in Fig. 2c.

Simulated BW is 575 MHz (52.78%), whereas measured BW is 577 MHz (53.6%). In this design also, antenna gain reduces towards higher frequencies of BW due to an increase in cross-polarization component as shown in Fig. 2b. But due to larger L_{p2} and L_{p3}, this reduction is smaller against equal slot length condition. The fabricated antenna for this variation is shown in Fig. 2d. To minimize gain variation, slot length L_{p3} is only increased. From impedance graph, it was noticed that modal frequencies marginally changes. An optimum response in terms of BW and gain variation is obtained for $L_{p3} = 6.9$ cm as shown in Figs. 2b and 3a.

Respective values of impedance BW using simulation and experiment are 579 MHz (53.05%) and 583 MHz (53.81%). The antenna with unequal slots length on patch yields peak gain of above 7 dBi and shows lesser reduction in gain towards higher frequencies of BW as observed from Fig. 2b. Polar pattern plots as shown in Fig. 3c–f shows maximum of radiation in a plane orthogonal to antenna plane and shows cross-polar component less than 8 dB throughout the BW, thereby realizing elliptical polarization. Thus, proposed study explains functioning of slot cut DGS wideband designs in terms of patch and GP modes. A similar study highlighting effects on patch modes in DGS structures is not explained in detail in the literature.

3 Conclusions

Wideband designs of unequal lengths slot cut RMSA backed by unequal lengths slot cut rectangular ground plane are presented. The optimum response in terms of BW, pattern and gain variation is obtained using three unequal length slots on patch and GP. It yields impedance BW of around 580 MHz (>50%) with peak gain of 7 dBi. The antenna exhibits broadside pattern and shows elliptical polarization across the BW. With the realized antenna characteristics, proposed design will be useful in application in various mobile and personal communication devices.

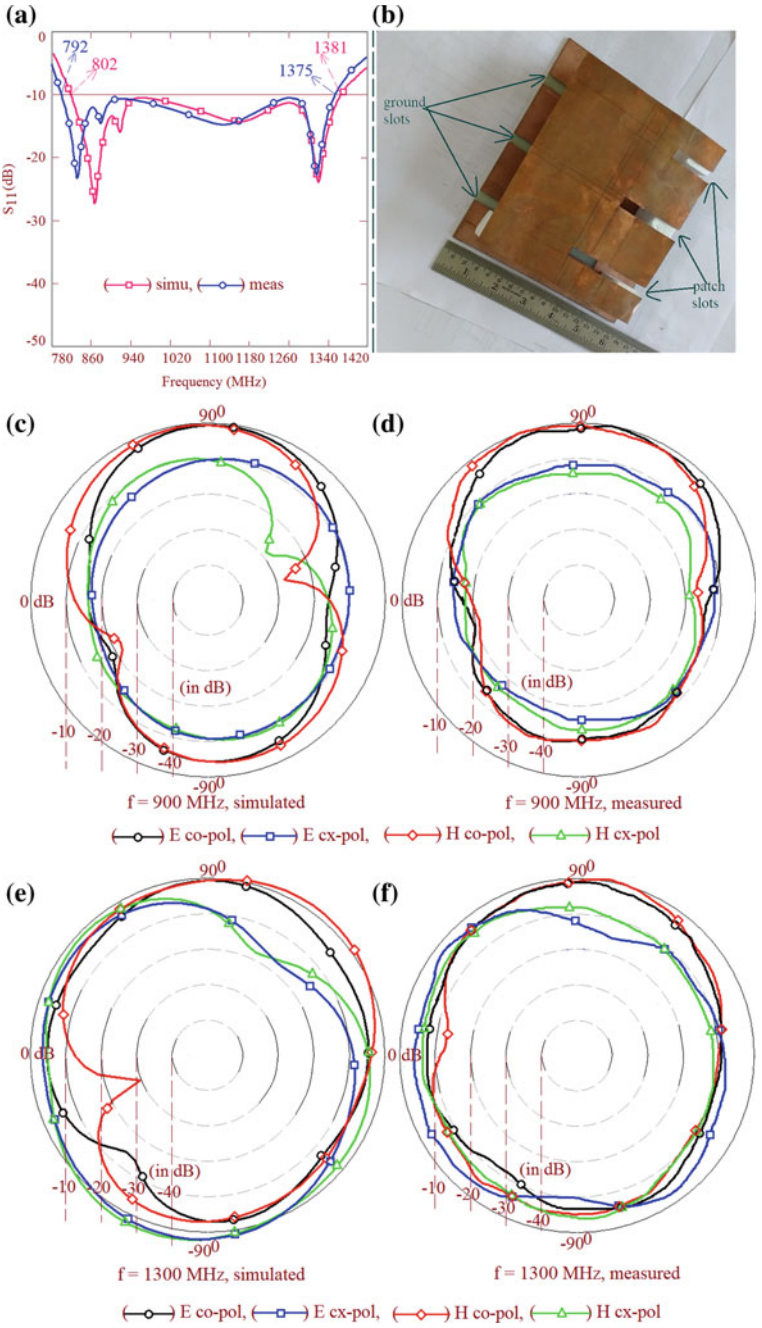

Fig. 3 **a** Return loss plots, **b** fabricated design and **c**–**f** pattern at two frequencies over impedance BW for RMSA with larger L_{p3} backed by DGS

References

1. Lee HF, Chen W (1997) Advances in microstrip and printed antennas. Wiley, New York
2. Kumar Girish (2003) Ray, Kamala Prasan: broadband microstrip antennas, 1st edn. Artech House, USA
3. Wong K-L, Tang C-L, Chiou J-Y (2002) Broad-band probe-fed patch antenna with a W-shaped ground plane. IEEE Trans Antennas Propag 50(6):827–831
4. Abbaspour M, Hassani HR (2008) Wideband star-shaped microstrip patch antenna. Prog Electromagn Res Lett 1:61–68
5. Mathur P, Chattopadhyay M, Kumar G (2014) Non-radiating edge gap coupled capsule-shaped and nose-shaped microstrip antennas for 3G applications. Int J Futur Comput Commun 3(2):80–83
6. Ray KP, Sevani V, Kakatkar S (2006) Compact broadband gap-coupled rectangular microstrip antennas. Microw Opt Technol Lett 48(12):2384–2389
7. Mandal K, Sarkar PP (2013) High gain wide-band U-shaped Patch antennas with modified ground planes. IEEE Trans Antennas Propag 61(4):2279–2282
8. James JR, Hall PS (1989) Handbook of microstrip antenna, vol II. Peter Peregrinus Ltd., London, UK
9. Deshmukh AA, Ray KP (2015) Analysis of broadband variations of U-slot cut rectangular microstrip antennas. IEEE Mag Antennas Propag 57(2):181–193

Single Feed Corner Trimmed Circularly Polarized Diagonal Patch Antenna

Shipra Bhatia and M. V. Deepak Nair

Abstract In this paper, a circularly polarized diagonal-shaped microstrip patch antenna for Wi-Fi and mobile applications is proposed. The radiating patch is diagonally trimmed from the opposite corners by length $L/2$ (i.e., 12 mm) and it resonates at 2.64 GHz with circular polarization. This is achieved using a simple structure of the microstrip antenna which consists of a single layer, single feed patch with smaller size as compared to conventional microstrip patch antenna. This paper presents a comparison of resonant frequency and a change in polarization from linear to circular by simply trimming the corners of the patch with different lengths. The proposed patch antenna is simulated in ANSYS HFSS and a prototype of antenna is fabricated and tested using Keysight Vector Network Analyzer N9925A. Experiments and simulations show that the proposed 12 mm trimmed antenna is capable of providing a gain of 2.17 dBi with an axial ratio of 4.05 dB.

Keywords Corner trimmed · Circular polarization · Microstrip antenna · Mobile applications · Single feed

1 Introduction

Since the last many years, microstrip patch antennas have been widely investigated, designed, and implemented in wireless communication systems such as remote sensing, satellite communication, mobile handsets, and many more [1]. This increasing demand of microstrip patch antenna is due to its light weight structure, small size, cost effectiveness, easy feeding techniques, multi-band and multi-polarization capability of a single antenna [2, 3]. Normally, patch antenna radiates linearly polarized waves and this happens when normal feed configuration is used with no further geometrical modifications in it [4, 5]. By changing feed arrangement or by modifying patch geometry, circular and elliptical polarizations can be obtained [6]. Circularly

S. Bhatia (✉) · M. V. Deepak Nair
Department of ECE, The LNM Institute of Information Technology, Jaipur, Rajasthan, India
e-mail: 17mec004@lnmiit.ac.in

M. V. Deepak Nair
e-mail: deepak.nair@lnmiit.ac.in

V. Janyani et al. (eds.), *Optical and Wireless Technologies*, Lecture Notes in Electrical Engineering 648, https://doi.org/10.1007/978-981-15-2926-9_41

polarized waves are generated when electric field with two orthogonal components have the same magnitude and 90 degree phase difference [7]. Circular polarization can also be obtained by changing the physical structure of the patch or by changing feed position in a patch or by using dual feeds in place of a single feed. One of the simplest ways to achieve circular polarization is by feeding the patch at two adjacent edges to excite two orthogonal modes [8]. Several antenna designs have been proposed in [7–11]. In [7] and [8], circular polarization has been achieved by introducing different shapes of slots in the patch. In [9], a hexagonal shape patch antenna has been designed for circular polarization. In [10], a circularly polarized patch antenna with dual slots is designed. In [11], the concept of introduction of slots and aperture-coupled feeding technique has been used to obtain circular polarization.

In the first subsection of following section, a simple square-shaped untrimmed patch antenna with a single feed has been proposed. In addition to that, geometry of the antenna in which two opposite corners of the radiating patch are trimmed to quarter length $L/4$ (i.e., 6 mm) is also shown. In the second subsection, the trimmed length is increased to half of the patch length $L/2$ (i.e., 12 mm). The dimension of the substrate is $36 \times 36 \times 1.58$ mm^3. The concept of trimming opposite corners of the patch with a single feed point at the same position as that of untrimmed square patch antenna has been used in this design.

2 Antenna Design and Geometry

2.1 Compact Linearly Polarized Untrimmed Patch Antenna and Elliptically Polarized 6 mm Trimmed Patch Antenna

Figure 1a shows the fabricated untrimmed square patch antenna with a single feed. The antenna is fabricated using a thin sheet of FR4 substrate with a dielectric constant

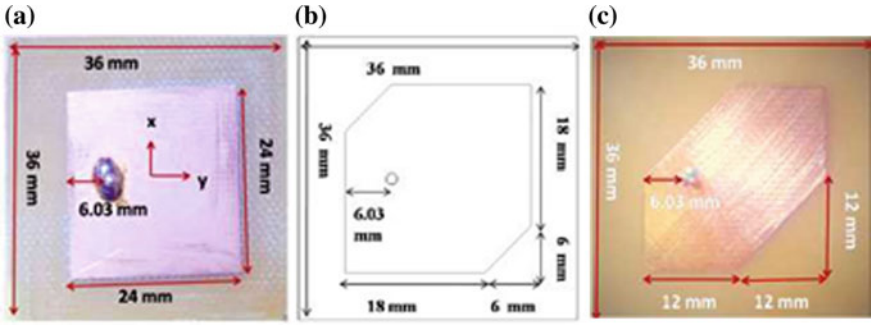

Fig. 1 **a** Fabricated untrimmed antenna **b** Geometry of 6 mm trimmed antenna **c** Fabricated 12 mm trimmed antenna

of 4.4 and loss tangent of 0.02. The square patch of dimension 24 × 24 mm^2 is co-axially fed to resonate at the frequency of 2.4 GHz. The feed point location is found to be best suited using ANSYS HFSS which comes out to be at the center along x-axis and 6.03 mm from edge of the patch along the y-axis [12]. Designed patch antenna with trimmed corners of length $L/4$ (i.e., 6 mm) is shown in Fig. 1b and change in frequency and polarization w.r.t. variation in length of the trimmed part are observed. The geometry of the patch antenna is same in all the three designs except the variation in length of trimmed corners.

2.2 Compact Circularly Polarized 12 mm Trimmed Patch Antenna

Figure 1c shows the fabricated prototype of patch antenna with corners trimmed by length $L/2$ (i.e., 12 mm). This antenna design overcomes the complexity of using multiple feeds or introduction of different slots to obtain circular polarization. Ideally, axial ratio for circularly polarized wave is 0 dB but practically, it is not possible to achieve pure circularly polarized wave. Therefore, range of acceptable axial ratio value is considered up to 6 dB for practical applications [13, 14].

3 Results and Observations

For experimental verification of the proposed designs, Keysight Microwave Vector Network Analyzer N9925A was used. All the following experimental results were obtained from the VNA. The results and observations from the proposed antenna prototype are shown in the subsections below.

3.1 Return Loss and Gain

Figure 2 depicts the reflection coefficient curves of all the three designs for VSWR < 2. It is found that the untrimmed patch antenna resonates at 2.744 GHz (−19.06 dB) with a gain of 3.30 dBi. The 6 mm trimmed antenna resonates at two frequencies, i.e., 2.776 GHz (−14.43 dB) and 3.096 GHz (−18.7 dB) with a gain of 3.11 and 3.19 dBi. This dual band resonance is due to automatic excitation of higher order modes because of larger aspect ratio as compared to 12 mm trimmed antenna. Larger aspect ratio will lead to orthogonal frequencies spaced closely. Antenna with 12 mm trimmed corners resonates at 2.648 GHz with the highest return loss of −22.5 dB and a gain of 2.14 dBi.

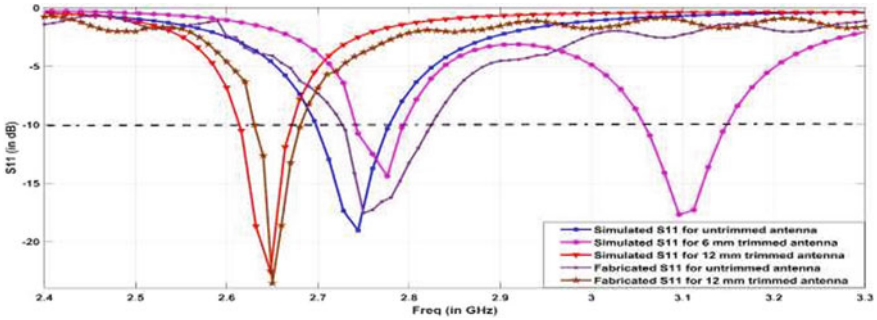

Fig. 2 Reflection coefficient curves of proposed antenna designs

3.2 Axial Ratio and Radiation Pattern

Figure 3a depicts E-plane (phi = 0 degree) polar plot for comparison of axial ratio value of proposed designs. This polar plot is drawn at different values of theta for a particular resonant frequency. The axial ratio is measured at 0 degree value of theta. From the obtained results, proposed untrimmed antenna has an axial ratio of 51.97 dB (linear polarization), whereas the antenna with 6 mm trimmed corners has an axial ratio of 7.452 and 15.78 dB (elliptical polarization) corresponding to two resonant frequencies. The antenna with 12 mm trimmed corners has an axial ratio of 4.05 dB (circular polarization). Figure 3b and c shows the E-H radiation pattern plot for proposed designs. It is observed from the figure that untrimmed antenna has highest radiation intensity, whereas the minimum radiation intensity is obtained from 6 mm trimmed patch antenna. The below plots are shown for only one resonant frequency (2.776 GHz) of 6 mm trimmed antenna.

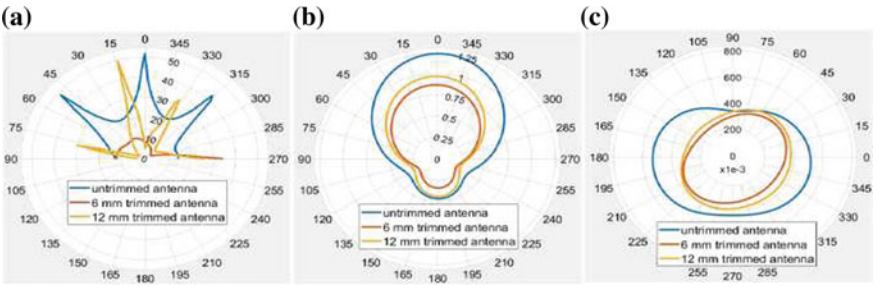

Fig. 3 **a** Axial ratio polar plot **b** E-plane radiation pattern polar plot **c** H-plane radiation pattern polar plot for proposed antenna designs

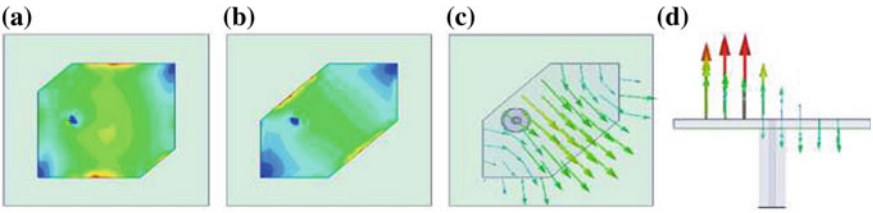

Fig. 4 Total surface current density in **a** 6 mm trimmed patch antenna **b** 12 mm trimmed patch antenna **c** H-field vectors in 12 mm trimmed patch **d** E-field vectors in 12 mm trimmed patch

3.3 Surface Current Density and Field Patterns

Figure 4a and b shows the surface current density for 6 and 12 mm trimmed patch antenna. Green and yellow colors in the patch depict high current density at that part of antenna. Figure 4c shows H-field vectors at the surface of the patch. The field vectors travel from feed point and cover whole area of patch. Figure 4d depicts E-field vectors which are perpendicular to the x-y plane. Red and green colored vectors show high field density at that part of patch.

4 Conclusions

Proposed three antenna designs are compared based on resonant frequency, gain, and axial ratio. Untrimmed linearly polarized antenna resonates at 2.744 GHz with a gain of 3.30 dBi, whereas antenna with 6 mm trimmed corners resonates at 2.776 and 3.096 GHz. This trimmed design provides a gain of 3.11 and 3.19 dBi with elliptical polarization. Antenna with 12 mm trimmed corners resonates at 2.648 GHz with an A.R. of 4.05 dB making it circularly polarized. These designs offer advantage of reducing complexity due to slots and multiple feeds. Thus, by increasing the length of trimmed corners and keeping all other parameters of the antenna same, the polarization can be moved from linear to circular.

References

1. Lo Y, Solomon D, Richards W (1979) Theory and experiment on microstrip antennas. IEEE Trans Antennas Propag 27(2):137–145
2. Kumar MP, Kumar S, Jyoti R, Reddy V, Rao P (2010) Novel structural design for compact and broadband patch antenna. In: 2010 International workshop on antenna technology (iWAT), Lisbon, Portugal, pp 14
3. Wong K-L, Sze J-Y (2000) Slotted rectangular microstrip antenna for bandwidth enhancement. IEEE Trans Antennas Propag 48(8):1149–1152

4. Kiruthika R, Shanmuganantham T (2016) Comparison of different shapes in microstrip patch antenna for X-band applications. In: 2016 International conference on emerging technological trends (ICETT), Kollam, India, pp 1–6
5. Derneryd A (1976) Linearly polarized microstrip antennas. IEEE Trans Antennas Propag 24(6):846–851
6. Khidre A, Lee K-F, Yang F, Elsherbeni AZ (2013) Circular polarization reconfigurable wideband E-shaped patch antenna for wireless applications. IEEE Trans Antennas Propag 61(2):960–964
7. Nasimuddin Z-NC, Qing X (2011) Circularly polarized slotted/slit-microstrip patch antennas. In: Nasimuddin N (ed) Microstrip antennas. InTech
8. Kumar S, Sharma A, Kanaujia BK, Khandelwal MK, Gautam AK (2016) Dual-band stacked circularly polarized microstrip antenna for S and C band applications. Int J Microw Wirel Technol 8(08):1215–1222
9. Saravanan M, Rangachar MJS (2016) Design of wide beam hexagonal shaped circularly polarized patch antenna for WLAN application. In: Proceedings of the eighth international conference on soft computing and pattern recognition (SoC-PaR 2016) 614
10. Hasan N, Gupta SC, A dual band microstrip patch antenna with circular polarization, p 6
11. Sharma AK, Mittal A, Diagonal slotted diamond shaped dual circularly polarized microstrip patch antenna with dumbbell aperture coupling, p 4
12. Jasim SE, Jusoh MA, Mazwir MH, Mahmud SNS (2015) Finding the best feeding point location of patch antenna using HFSS. ARPN J Eng Appl Sci 10(23):6
13. Kumar G, Ray KP (2003) Broadband microstrip antennas. Artech House, Boston, Mass
14. Long S, Shen L, Schaubert D, Farrar F (1981) An experimental study of the circular-polarized elliptical printed-circuit antenna. IEEE Trans Antennas Propag 29(1):95–99

UWB Antenna for Breast Cancer Detection Using Back Scattering

Praveen Kumar Rao and Rajan Mishra

Abstract Traditional medical imaging systems are not able to identify tumor in human fast and reliable way. Imaging systems as computed tomography scan, magnetic resonance imaging, etc., bring human health-related issues because of the ionization effect. In this study, the design and performance analysis of a 3D antenna has been done for microwave imaging application to diagnose cancer. A folded radiating structure, directive 3-D antenna has been used for the application of microwave imaging for clinical diagnosis. By optimizing the complete dimension, projected antenna is achieved with a reduced size of 20 × 20 mm^2. In addition, the antenna was modeled with four layers of woman breast phantom tissues. This shows that the projected antenna is an appropriate equipment which can be used to construct a microwave diagnostic procedure meter for early women breast cancer detection.

Keywords Ultra-wideband · Monopole antenna · Flexible antenna · Phantom model · Breast cancer detection · Scattering signal

1 Introduction

Breast cancer is the second leading cause of cancer in women today after lung cancer. In most of the cases, the method used for breast cancer diagnosis is MRI, but it is having hazardous health issues of x-ray wave interfacing directly to the human body. X-ray mammography is having more than 20% false detection rate and value is higher in breast cancer diagnosis in young girls [1, 2]. Ultrasound and MRI scans are alternatives but these techniques are expensive and high chances of wrong decision probability. Moreover, not safe to use regularly due to ionization effect and

P. K. Rao (✉) · R. Mishra
Department of Electronics and Communication Engineering, Madan Mohan Malaviya University of Technology, Gorakhpur, India

V. Janyani et al. (eds.), *Optical and Wireless Technologies*, Lecture Notes in Electrical Engineering 648, https://doi.org/10.1007/978-981-15-2926-9_42

Table 1 Imaging methods used for cancer detection

Modality	Complexity	Cast	Resolution
Gamma camera	High/moderate	Moderate	Moderate
X-ray	Moderate	Moderate	High
PET	High	High	High
Radiometry	Low	Low	Low
IR	Moderate	High/moderate	High
MRI	High	High	High
Ultrasound	Moderate	Moderate	Moderate

painfulness [3, 4]. This contrast is fundamental hypothesis for passive diagnostic technique, it helps in thermal mapping for breast tissues, and from that the presence of malignant cells is inferred. Microwave diagnostic technique has specific low cost of prices and less technological issues, conjointly low in comparison with the opposite method as shown in Table 1 [5, 6].

Microwave imaging is the most reliable method used to detect the breast cancer. It is able to detect breast cancer in early stage effectively. Other advantages are low cost, non-ionizing, secure and non-invasive. However, UWB technology is a safe breast screening tool, but accurate diagnosis is needed to be improved [7, 8]. It uses a low power and low wavelength wave for scanning, and the drawback of this method is that there is back reflection from breast [5, 6].

The above-mentioned antennas are not versatile instead have bulky structure, hence, flexible antennas are designed for the woman breast by taking into consideration the outcome of biological tissues for the economic radio bands except [9, 10]. So, during these antennas, we have tried to be a little flexible antenna exploiting RT/duraid 5880(tm) substrate. The simulation results of designed antenna show that it can be used for early breast tumors detection by constructing a microwave imaging instrument. Moreover, to point out its impact on the antenna S-parameter response, the projected antenna is employed in touch with biological woman breast tissue.

2 Flexible Antenna Design

The geometries of the designed UWB antenna are given in Fig. 1. 20×20 mm^2 Rogers RT/duraid 5880(tm) substrate with a thickness of 0.254 mm. The relative permittivity of Rogers RT/duraid 5880(tm) is 2.2. The feed circuit may be a coplanar waveguide cable having 50-Ω ohmic. All the numerical simulations are calculated with high-frequency structure simulator (HFSS) software to verify the effectiveness of the wideband (Table 2).

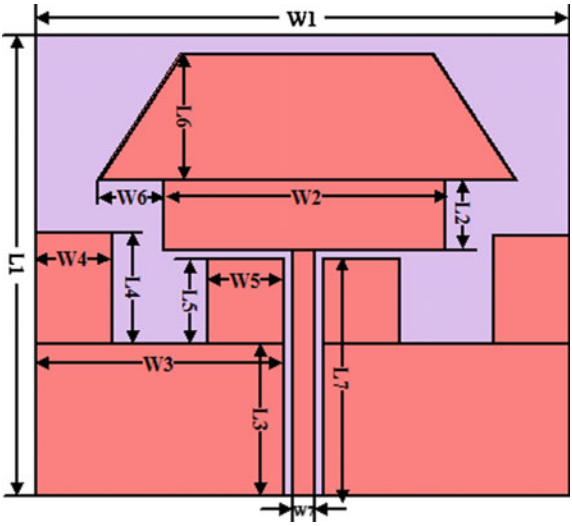

Fig. 1 Geometry of the flexible antenna

Table 2 Parameter of antenna

Parameter	Value (mm)	Parameter	Value (mm)	Parameter	Value (mm)	Parameter	Value (mm)
W1	20	W2	12	W3	9.3	W4	3
L1	20	L2	3	L3	6	L4	4
W5	3	W6	3	W	1	L5	2.8
L6	7.7	L7	8.8				

3 Microwave Imaging

In this, our aim is to find backscattering signal from the tumor which consists of dielectric inclusion, for this we used breast phantoms with single tumor which have very high dielectric consent [11]. Off the shelf, breast phantom is also used for microwave imaging. The size of phantom is 20 × 20 × 26.5 mm which is nearly equality dielectric property like human breast. These phantoms have four layers [12, 13], which are defined as skin layer, tissues layer, canoes barest tumor and air layers. The phantom dielectric is shown in Table 3. The tumor cell consists of water which has high dielectric constant as compared with low water tissues. Figure 2 shows the setup of microwave imaging system in which two antennas are studied face to face at distant 16 mm between these two antennas. The mechanical system is used to rotate the antennas 360° around the phantom. Step motor is used for the rotation of antennas at 360°. This rotation control by Arduino Uno control circuit. These two antennas also maintain 6.5 mm distant from breast phantom. To measure the antennas scattering signal, the antenna is connected to vector network analyzer (VNA). All these steps are controlled by the PC which is also connected to VNA. In microwave

Table 3 Breast layers properties [14]

Tissue	Permittivity	Conductivity	Thickness (mm)
Muscle	52.4	1.91	5
Glandular tissues	20.1	0.5	20
Fat	5.2	0.1	10
Skin	38	1.46	1.5

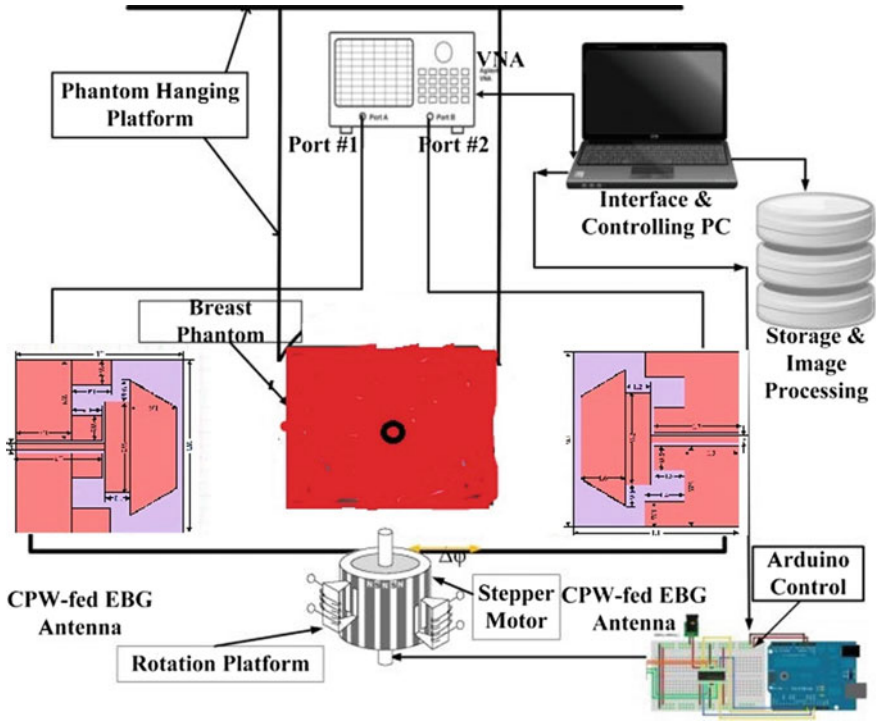

Fig. 2 Block diagram of breast cancer imaging system

imaging system, we are not using a human due to safety propose. To rotate the antennas around the phantom, and collect the data for localize the exact position of tumor.

4 Breast Phantom Model

Firstly, to design breast phantom model as shown in Fig. 3, simple four layers stabbed

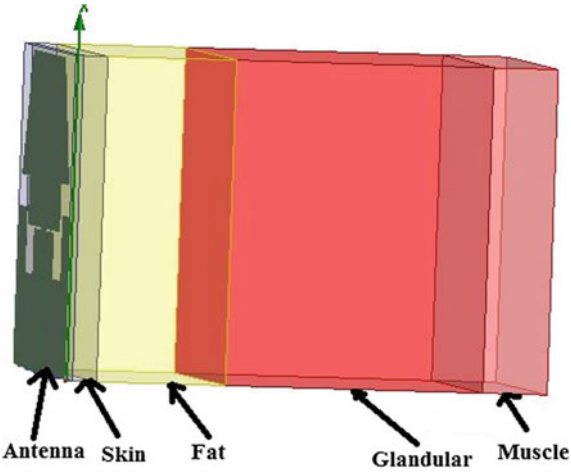

Fig. 3 Geometry of breast phantom model with antenna

model using different biological tissues is applied. Table 3 shows electrical and physical properties like electrical permittivity and conductivity at 6.4 GHz and thickness according to the average for each tissue layer.

5 Result and Discussion

Figure 4 shows that reflection cofficient of antenna for different steps. For step 1 the bandwidth is 2–4.5 GHz. For step 2 bandwidth is zero. For step 3 bandwidth is 3.2–6.5 GHz and step 4 gives maximum bandwidth as 3.5–7.5GHz.

The reflection coefficient of these antennas are shown in Fig. 5 which shows that step 4 antenna gives good radiation performance in band 3.5–7.5 GHz.

The current distributions of the simulated UWB antenna are shown in Fig. 4. The current distribution got in both the condition with and without phantom. Figure 6a shows the current distribution without phantom and Fig. 6b shows the current distribution with phantom. Without phantom current distribution higher with respect to with phantom so parameters like gain and radiation efficiency decrease with frequency.

At frequencies 5 GHz, the distributed radiation pattern with respect to gain (dBi) for E- and H-plane is shown in Fig. 7. According to radiation plot, the scheduled antenna shows nearly omnidirectional radiation pattern in H- and E-plane.

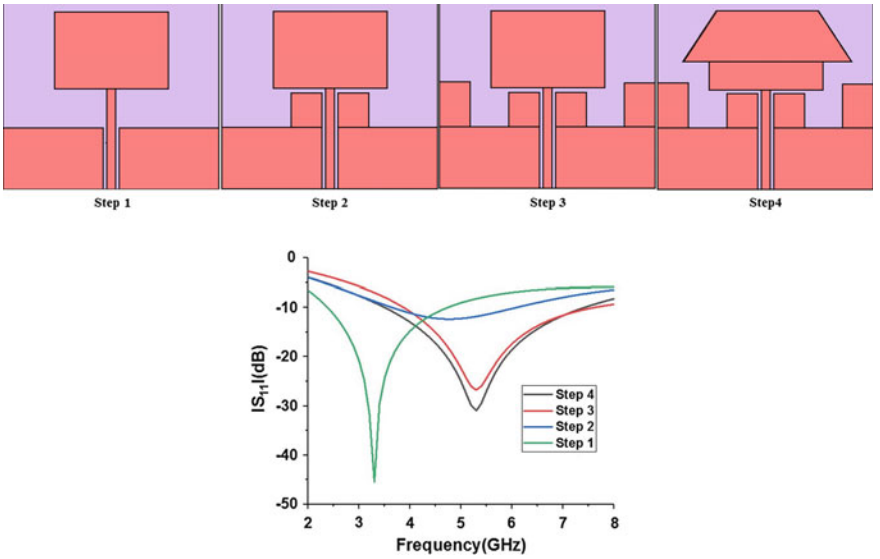

Fig. 4 Simulated reflection cofficient in different structures of step antenna

Fig. 5 Comparison between simulated $IS_{11}I$ (dB) with phantom and simulated $IS_{11}I$ (dB) without phantom of scheduled antenna

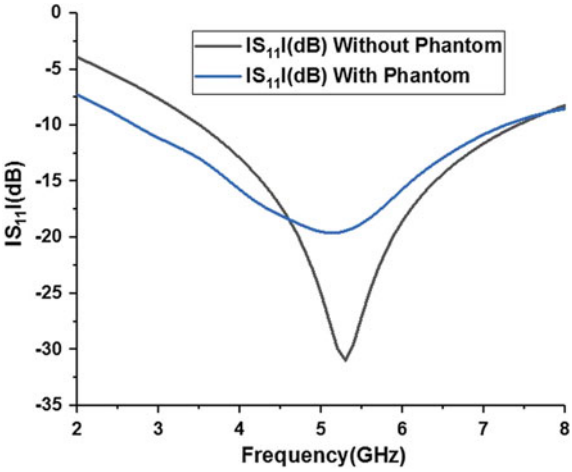

6 Conclusion

This research focuses on designing a cost-efficient 3D antenna for portable biomedical diagnosis using microwave imaging systems. The proposed structure of the folded 3D design gives the antenna compactness. The proposed CPW-fed antenna is used as a transceiver in breast tumor detection system based on automated PC controlled microcontroller. MATLAB programming has been used for transmitter, receiver, data

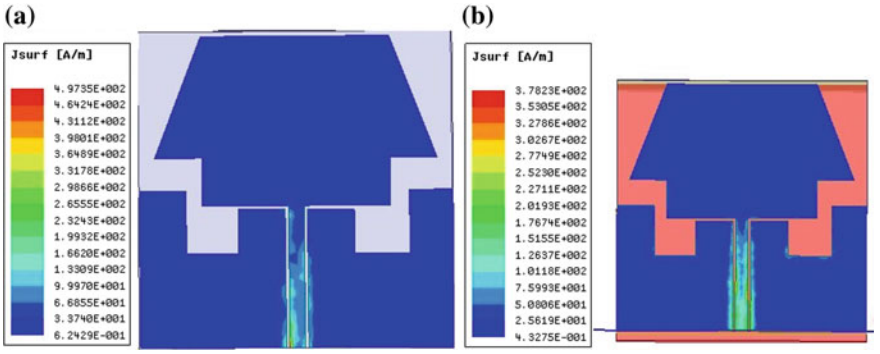

Fig. 6 Surface current distribution of antenna at frequencies **a** without phantom, 5 GHz, **b** with phantom 5 GHz

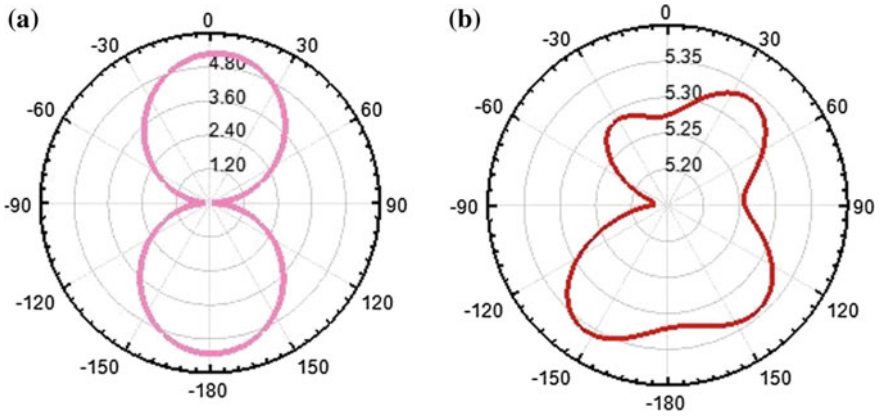

Fig. 7 Simulated radiation pattern of the scheduled antenna for E-plane and H-plane with respect to dBi, **a** E-plane 5 GHz, **b** H- plane 5 GHz

acquisition system and image processing. The dielectric properties variation of the phantom affects the variation of scattering signal. This system is easy to install, compact in size and of low cost. The system was analyzed using breast phantom. In conclusion, the obtained results of imaging system validate it for the earlier breast tumor detection.

Acknowledgements This work is part of UPCST sponsor project.

Reference

1. Kahar M, Ray A, Sarkar D, Sarkar P (2015) An UWB microstrip monopole antenna for breast tumor detection. Microw Opt Technol Lett 57:49–54
2. Zhang H (2015) Microwave imaging for ultra-wideband antenna based cancer detection
3. Mishra R, Pandey A (2016) Asymmetric crescent shaped dual band monopole antenna for UWB. IJOMAOT 11(5)
4. Rao PK, Mishra R (2018) A disc shape monopole antenna with Tri-Band-Notched 2.55/3.5/5.5 GHz characteristics. In: 2018 IEEE international students' conference on electrical, electronics and computer science (SCEECS)
5. https://www.aecc.es/SobreElCancer/elcancer/Paginas/Elcancer.aspx. Accessed Enero 2017
6. Fariñas-Coronado W, Paz Z, Orta GJ, Rodrìguez-Denis E (2002) Estudio del factor de disipación dieléctrica como herramienta diagnóstica. Rev Biomdica 13(4):249–255
7. Kuhl CK, Schrading S, Leutner CC, Morakkabati-Spitz N, Wardelmann E, Fimmers R et al (2005) Mammography, breast ultrasound, and magnetic resonance imaging for surveillance of women at high familial risk for breast cancer. J Clin Oncol 23:8469–8476
8. Elmore JG, Barton MB, Moceri VM, Polk S, Arena PJ, Fletcher SW (1998) Ten-year risk of false positive screening mammograms and clinical breast examinations. N Engl J Med 338:1089–1096
9. Rao PK, Mishra R (2018) Multi band antenna with multi band notch 2.5/3.7/6.4/8.1/12.4/14.4 GHz characteristics. In: 2018 5th IEEE Uttar Pradesh section international conference on electrical, electronics and computer engineering (UPCON)
10. Mishra R, Tripathi VS (2017) A compact circular disc shaped monopole antenna for UWB applications. Int J Appl Eng Res 12(12):3049–3053. ISBN 0973-4562
11. Berg WA, Gutierrez L, NessAiver MS, Carter WB, Bhargavan M, Lewis RS et al (2004) Diagnostic accuracy of mammography, clinical examination, US, and MR imaging in preoperative assessment of breast cancer. Radiology 233:830–849
12. Chen X, Zhang W, Ma R, Zhang J, Gao J (2007) Ultrawideband CPW-fed antenna with round corner rectangular slot and partial circular patch. IET Microwaves, Antennas and Propagation 1(4):847–851
13. Afyf A, Bellarbi L, Riouch F, Achour A, Errachid A, Sennouni MA (2015) Flexible miniaturized UWB CPW II-shaped slot antenna for wireless body area network WBAN) applications. In: Third international workshop on RFID and adaptive wireless sensor networks (RAWSN)
14. Mahmud MZ, Islam MT, Misran N, Kibria S, Samsuzzaman Md (2018) Microwave imaging for breast tumor detection using uniplanar AMC based CPW-fed microstrip antenna. https://doi.org/10.1109/access.2018.2859434. IEEE Access

Implementation of SAC-OCDMA System Using Generalized Codes Over FSO Channel

Sharwan Kumar Jangid and Ritu Sharma

Abstract In this paper, the spectral amplitude coding technique for optical code division multiple access (SAC-OCDMA) system is implemented over free space optic (FSO) channel using generalized codes. The generalized codes are constructed using a generalized code construction algorithm for the weight greater than 2. This algorithm provides the same code length increment for an additional user. The generalized code performance is analyzed for different transmission distance in FSO channel, BER, and different data rates using direct detection.

Keywords FSO · Generalized codes · Direct detection and SAC-OCDMA

1 Introduction

The optical code division multiple access (OCDMA) system assigns different codes to each user, and all the users can access same transmission medium asynchronously and simultaneously. Due to this property, OCDMA systems are more suitable for those networks, where traffic is asynchronous such as local area network.

The OCDMA system is affected by multiple access interference (MAI), which degrades the system performance, when a large no. of users are active in the system. There are many OCDMA techniques that have been developed to enhance the system performance, and one of them is spectral amplitude coding—optical code division multiple access technique (SAC-OCDMA). The multiple access interference (MAI) is completely removed in SAC-OCDMA systems by using ideal in-phase cross-correlation property of codes. SAC-OCDMA system provides codes in spectral domain [1–9]. For the SAC-OCDMA, many coding techniques have been developed such as modified quadratic congruence code for prime weights [1–9], Khazani–Syed (KS) code [2], modified double weight (MDW) code [1–9], enhanced double weight

S. K. Jangid (✉) · R. Sharma
Department of Electronics and Communication Engineering, Malaviya National Institute of Technology, Jaipur, India
e-mail: sharwanjangid.ece@mnit.ac.in

R. Sharma
e-mail: rsharma.ece@mnit.ac.in

V. Janyani et al. (eds.), *Optical and Wireless Technologies*, Lecture Notes in Electrical Engineering 648, https://doi.org/10.1007/978-981-15-2926-9_43

code (EDW) [9], and many others. The EDW and MDW code have odd weight and even weight greater than 2, respectively. These codes use mapping technique for a large no. of users.

A generalized algorithm for code construction is reported in [1], which can generate codes (generalized codes) like EDW and MDW for any weight greater than 2 without mapping. It maintain cross-correlation value almost one ($\lambda_C \leq 1$). Length and other properties are similar to MDW and EDW codes [1, 9].

Free space optic is a technology that can provide point-to-point communication with high speed. In many communication links, such as aircraft to ground, satellite to ground, building to building, and ship to ship, the FSO technology can be used [2–10]. FSO communication technology can be used as an alternative to optical fiber, where fiber laying is difficult [2, 8]. The FSO communication technology is highly susceptible to attenuation due to turbulence and weather conditions. The FSO link is generally affected by two types of losses, i.e., geometric losses and atmospheric losses. Geometric losses are due to misalignment of antennas and link distance, and atmospheric losses are mainly due to scattering, absorption, etc.

In this paper, SAC-OCDMA system is implemented over free space optic (FSO) channel using generalized codes.

The performance of the system is evaluated using FDTD-based simulation software for different data rates and transmission distance. Numerical results obtained are also compared.

2 Description of the SAC-OCDMA System Using Generalized Codes

The basic block diag. of the system (SAC-OCDMA) is shown in Fig. 1. It consists of a transmitter section for each user. Each user transmitter section consists of a light source (LED), encoder, user data, and modulator. The each user output is combined, encoded, and transmitted to FSO communication channel. The received signal is split and decoded at the receiver end. The received signal after decoding is sent to the detector of each user.

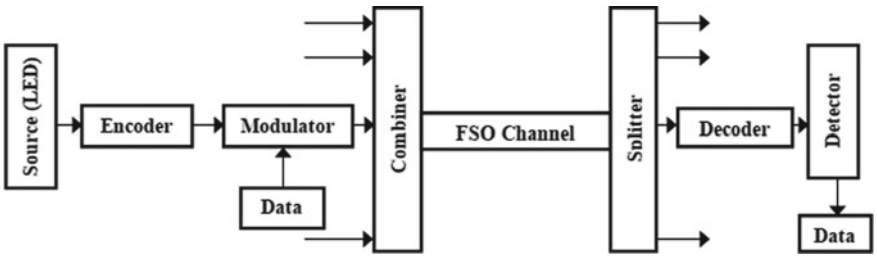

Fig. 1 Block diagram of SAC-OCDMA system

3 SAC-OCDMA System Implementation Using Generalized Code

Snapshot of the simulation setup in Optisystem is shown in Fig. 2. The generalized code construction algorithm for SAC–OCDMA system is stated below [1]:

- Choose W (weight of code) and N (no. of users),
- Calculate L (code length) using $L = N \times (W - 1)$
- Construct base matrix M per Eq. (1).
- Repeat base matrix (M) up to $(N - 1)$ times.
- In last column of matrix U, R1 is placed at last row and R2 is placed at first row.
- Fill empty places with zeros.

The generalized code for $W = 4$ and $N = 3$ is given in Eq. (3).

$$M = \begin{bmatrix} \mathrm{R1} \\ \hline \mathrm{R2} \end{bmatrix} = \begin{bmatrix} \left\lfloor \frac{W-2}{2} \right\rfloor 0\mathrm{s} & \left\lfloor \frac{W+1}{2} \right\rfloor 1\mathrm{s} \\ \left\lfloor \frac{W}{2} \right\rfloor 1\mathrm{s} & \left\lfloor \frac{W-1}{2} \right\rfloor 0\mathrm{s} \end{bmatrix} \tag{1}$$

$$M = \begin{bmatrix} 0\ 1\ 1 \\ 1\ 1\ 0 \end{bmatrix} \tag{2}$$

$$\lambda_1\ \lambda_2\ \lambda_3\ \lambda_4\ \lambda_5\ \lambda_6\ \lambda_7\ \lambda_8\ \lambda_9$$

$$U = \begin{bmatrix} 0\ 1\ 1\ 0\ 0\ 0\ 1\ 1\ 0 \\ 1\ 1\ 0\ 0\ 1\ 1\ 0\ 0\ 0 \\ 0\ 0\ 0\ 1\ 1\ 0\ 0\ 1\ 1 \end{bmatrix} \begin{matrix} \text{user1} \\ \text{user2} \\ \text{user3} \end{matrix}$$

$$\text{sum} = \overline{1\ 0\ 1\ 1\ 0\ 1\ 1\ 0\ 1} \tag{3}$$

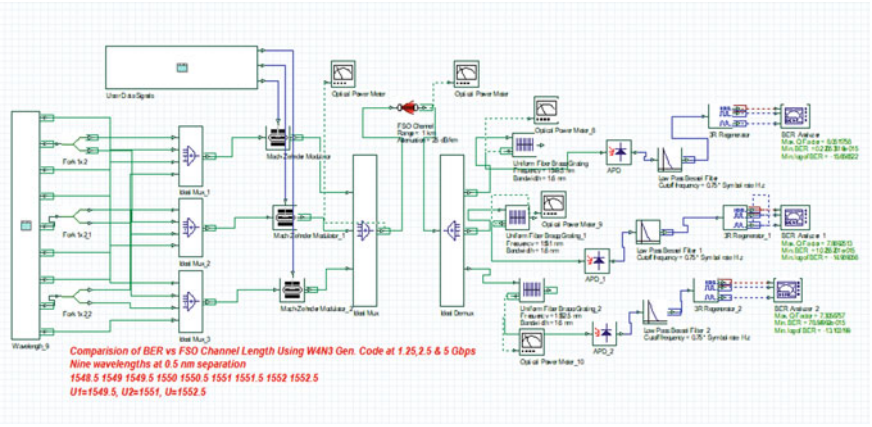

Fig. 2 Snapshot of simulation setup for SAC-OCDMA ($W = 4$, $N = 3$) using direct detection

Table 1 Simulation parameters [2, 11]

Parameter	Value
Source line width (Δv)	3.75 THz
Bit rate	1.25, 2.5 and 5 Gbps
Quantum efficiency (η)	0.6
Transmitted power (Pt)	10 dBm
Atmospheric attenuation (a)	8.68 dB/km
Transmission distance (S)	2 km, 4 km
Transmit aperture diameter (d_1)	0.05 m
Receive aperture diameter (d_2)	0.2 m
Beam divergence (D)	2 mrad

In matrix U, the sum of all unique codes provides $(W - 2)$ wavelengths for each user which is non-overlapping. These wavelengths are corresponding to 1's in binary sum. In detection process, the non-overlapping wavelengths are used.

4 Results and Discussion

4.1 Simulation Results and Discussion

FDTD-based simulation software is used for performance evaluation of the SAC-OCDMA system (Table 1).

Figure 3 shows the BER performance using direct detection technique at different transmission distance and data rates. In simulated result, only first user's BER values are considered and three data rates are used, i.e., 1.25, 2.5, and 5 Gbps. The graph shows that BER increases at higher data rates for the same transmission distance. At higher data rates, required bandwidth increases, and therefore, noise in the system increases [1]. Thus, the system performance degrades at higher data rates. The system BER increases with increasing transmission distance. This system can support up to 1.5, 1.3, and 0.8 km for data rates 1.25, 2.5, and 5 Gbps, respectively, when transmitted power is 10 dBm (Fig. 4).

4.2 Numerical Results and Discussion

To calculate the system BER performance, the Gaussian approximation is used [1, 7] Table 2:

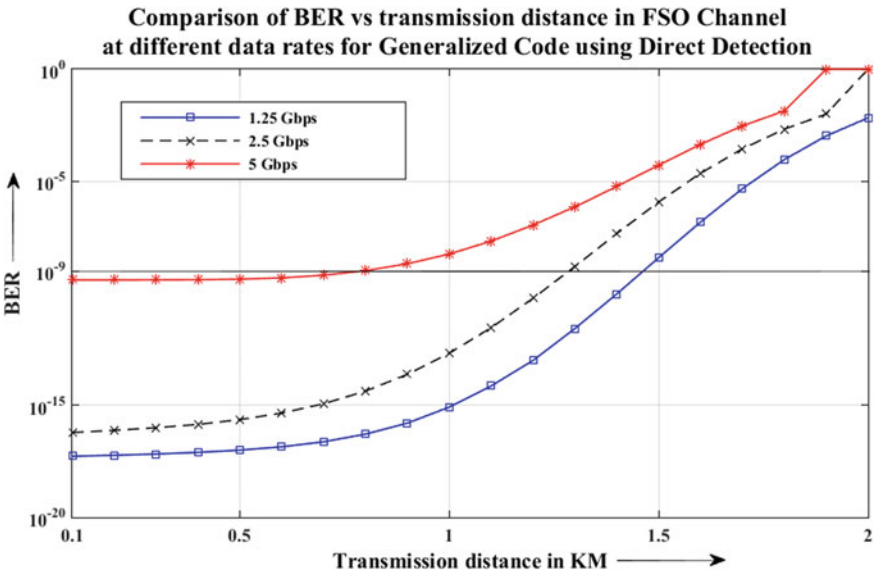

Fig. 3 Results of SAC-OCDMA system when transmitted power = 10 dBm at different data rates

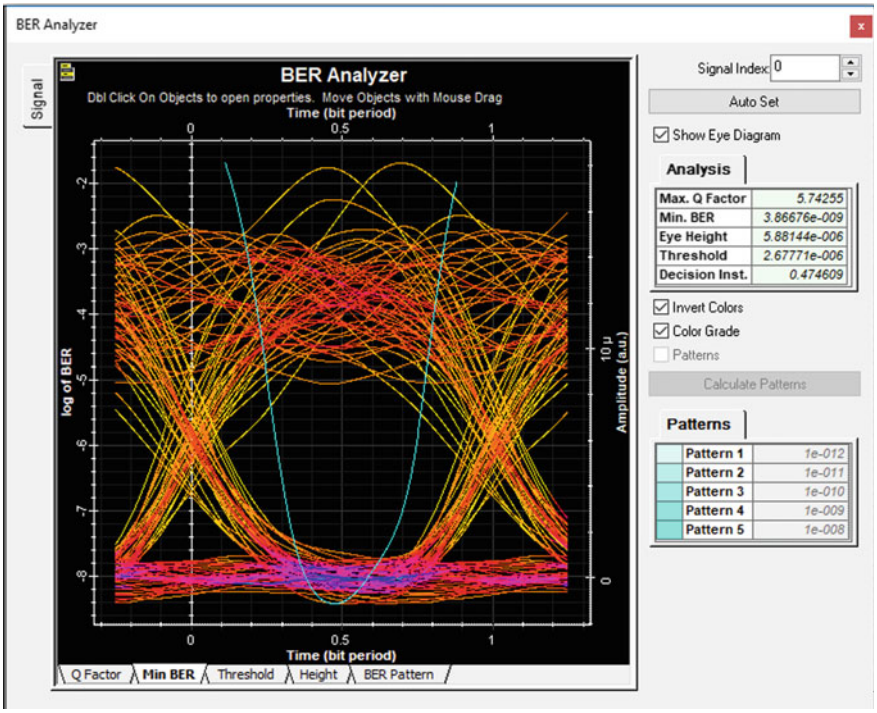

Fig. 4 Eye diagram for channel 1 at 1.25 Gbps, distance 1.5 km

Table 2 Parameters for numerical calculation

Parameter	Value
Electrical BW (B)	0.625, 1.25, 2.5 GHz
Bit rate	1.25, 2.5, 5 Gbps
Operating wavelength (λ_0)	1550 nm
Receiver noise temperature (T_n)	300 K
Receiver load resister (R_L)	1030 Ω
Electron charge (e)	1.6×10^{-19} C
Planck's constant (h)	6.66×10^{-34} J/S
Boltzmann's constant (K_b)	1.38×10^{-23} J/K

- All the light sources are ideally unpolarized and its spectrum is flat for given bandwidth [$v0 - \Delta v/2$, $v0 + \Delta v/2$], where $v0$ = central optical frequency and Δv = source bandwidth.
- For all users, each bit stream is synchronized.
- For all users, received power is equal.
- Spectral width of each frequency component is identical.

Following SNR and BER equations [1] used in calculations:
FSO channel link budget equation [11]

$$\text{Psr} = \text{Pt} \times \frac{(\text{d2})^2}{(\text{d1} + (D \times S))^2} \times (10)^{\left(-a \times \frac{S}{10}\right)} \tag{4}$$

SNR for generalized code using direct detection technique

$$\text{SNR} = \frac{\left(\frac{\text{RPsr}(W-2)}{L}\right)^2}{\text{eBR}\left[\frac{\text{Psr}(W-2)}{L}\right] + \frac{4K_b T_n B}{RL}} \tag{5}$$

BER for generalized code using direct detection technique

$$\text{BER} = \frac{1}{2}\text{erfc}\sqrt{(\text{SNR}/8)} \tag{6}$$

where $R = \eta \text{e}/h v_0$ is the responsivity and Psr = broadband effective power at receiver.

Figure 5 shows the numerical results based on Eqs. (4), (5), and (6). The BER is plotted against transmission distance for SAC-OCDMA system at different data rates, i.e. 1.25, 2.5, and 5 Gbps. According to numerical results, this system can support up to 1.3, 1.4, and 1.5 km at 10 dBm transmitted power for 5, 2.5 and 1.25 Gbps data rates, respectively. As the distance increases, channel loss also increases, which degrades the system BER performance.

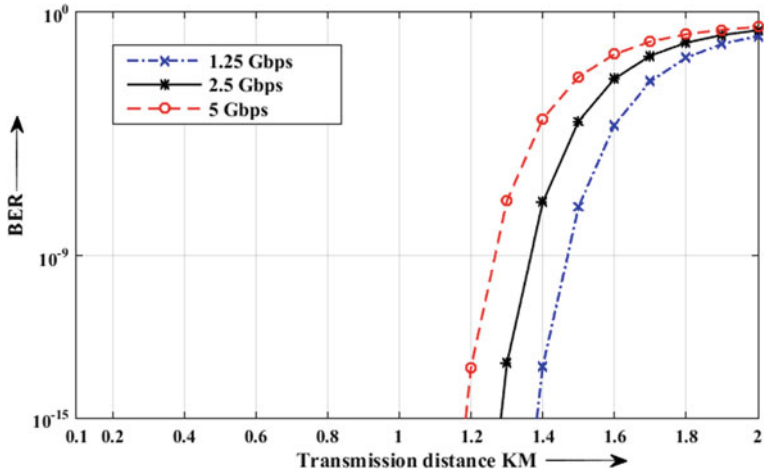

Fig. 5 Numerical results of SAC-OCDMA system for different data rates

5 Conclusion

In this paper, the three users SAC-OCDMA system is implemented and analyzed using generalized code over FSO channel at 8.68 dB/km atmospheric attenuation. This value of attenuation is generally considered for heavy rain environment. The simulation result shows that the system can support up to 1.5, 1.3, and 0.8 km under heavy rain condition for data rates 1.25, 2.5, and 5 Gbps, respectively, when transmitted power is 10 dBm.

The system has achieved acceptable BER (10^{-9}) at different data rates in numerical result as well as in simulation results. The numerical result shows better result due to some approximation used in calculation, and numerically, it can support up to 1.5, 1.4, and 1.3 km at 10 dBm transmitted power for 1.25, 2.5, and 5 Gbps data rates, respectively.

References

1. Kumawat S, Kumar MR (2016) Generalized optical code construction for enhanced and modified double weight like codes without mapping for SAC–OCDMA systems. Opt Fiber Technol 30:72–80. https://doi.org/10.1016/j.yofte.2016.03.004
2. Sahbuddin RKZ, Mazlin K, Hitam S, Mokhtar M, Anas SBA (2012) Performance of SAC-OCDMA—FSO communication Systems. Optik Int J Light Electron Opt. http://dx.doi.org/10.1016/j.ijleo.2012.08.067, https://optiwave.com/wp-content/uploads/2014/08/Performance-of-SAC-OCDMA-FSO-communication-systems2.pdf
3. Kwong WC, Prucnal PR, Perrier PA (1989) Synchronous versus asynchronous CDMA for fiber-optic LANs using optical signal processing. In: Global telecommunications conference

1989 and exhibition communications technology for the 1990s and beyond. https://doi.org/10.1109/glocom.1989.64112, https://ieeexplore.ieee.org/stamp/stamp.jsp?tp=&arnumber=64112
4. Abdullah MK, Aljunid SA, Anas SBA, Sahbudin RKZ (2007) A new optical spectral amplitude coding sequence: Khazani-Syed (KS) Code. In: 2007 International Conference on Information and Communication Technology 984-32-3394-8. IEEE. https://doi.org/10.1109/icict.2007.375391, https://ieeexplore.ieee.org/document/4261414
5. Abdullah MK, Hasoon FN, Aljunid SA, Shaari S (2008) Performance of OCDMA systems with new spectral direct detection (SDD) technique using enhanced double weight (EDW) code. Opt Commun 281:4658–4662
6. Ashour IAM, Shaari S, Menon PS, Bakarman HA (2012) Optical code-division multiple-access and wavelength division multiplexing: hybrid scheme review. J Comput Sci 8(10). https://doi.org/10.3844/jcssp.2012.1718.1729, https://www.researchgate.net/publication/273256955_Optical_CodeDivision_MultipleAccess_and_Wavelength_Division_Multiplexing_Hybrid_Scheme_Review
7. Wei Z, Shalaby H, Ghafouri-Shiraz H (2001) Modified quadratic congruence codes for fiber Bragg-grating-based spectral-amplitude-coding optical CDMA systems, J Light Technol 19(9). https://doi.org/10.1109/50.948274, https://ieeexplore.ieee.org/stamp/stamp.jsp?tp=&arnumber=948274
8. Arivazhagi K, Shanthi TK (2018) An effective 8 × 7.5 GBPS WDM free space optical communication system. Int J Eng Res Technol (IJERT). ISSN: 2278-0181 www.ijert.org. RTICCT—2018 Conference Proceedings. https://www.ijert.org/research/an-effective-87.5-gbps-wdm-free-space-optical-communication-system-IJERTCONV6IS08011.pdf
9. Kumawat S, Kumar MR (2017) Development of ZCCC for multimedia service using SAC-OCDMA systems. Opt Fiber Technol 39:12–20 10.1016/j.yofte.2017.09.015
10. Cvijetic N, Qian D, Yu J, Huang Y-K, Wang T (2009) 100 Gb/s per-channel free space optical transmission with coherent detection and MIMO processing. In: Proceedings of the european conference on optical communication (ECOC 2009), Vienna, Austria, Sept, pp 20–24
11. Bloom S, Korevaar E, Schuter J, Willebrand H (2003) Understanding the performance of free-space optics. J Opt Netw 2(6, 12):178–200

Design and Investigation of Octagonal Patch Antenna Using Artificial Magnetic Conductor for 5G Applications

Ashok Kumar, Arjun Kumar, Ashok Kumar and M. V. Karthikeyan

Abstract In this paper, the impact of artificial magnetic conductor (AMC) enabled octagonal patch antenna is presented for 5G applications. The different configurations of three AMC square cells and modified square unit cells supported octagonal patch antenna are analyzed. By using microstrip inset feed and quarter-wave transformer, it is feasible to provide better impedance matching. It is designed on Rogers RT/duroid 5880 substrate with $\varepsilon_r = 2.2$ and size of 10×10 mm^2. The simulated impedance bandwidth is 17.45 GHz, which is 57% more than the basic octagonal patch antenna.

Keywords Metamaterials · Artificial magnetic conductor (AMC) · Octagonal patch · Patch antenna · 5G frequencies

1 Introduction

In recent times, low data speed due to the shortage of bandwidth is the major drawback in wireless cellular networks. To resolve this problem, the fifth-generation communication system use millimeter-wave bands [1]. The current generation, i.e., fourth-generation (4G) unable to fulfill the consumer's requirements due to poor coverage, low data speeds, dropped connection and flexibility [2]. The 5G technology is the extended version of 4G technology, which provides large bandwidth, high gain, compact size and high data speed up to Gbps [3]. The antenna is a fundamental component of wireless systems that must be designed to fulfill customer demands such

A. Kumar (✉) · A. Kumar
School of Engineering and Applied Sciences, Bennett University, Greater Noida, India

A. Kumar
e-mail: arjun.kumar@bennett.edu.in

A. Kumar
Department of Electronics and Communication Engineering, Govt. Women Engineering College, Ajmer, Uttar Pradesh 201310, India

M. V. Karthikeyan
Department of Electronics and Communication Engineering, Indian Institute of Technology Roorkee, Roorkee, India
e-mail: kartik@ieee.org

V. Janyani et al. (eds.), *Optical and Wireless Technologies*, Lecture Notes in Electrical Engineering 648, https://doi.org/10.1007/978-981-15-2926-9_44

as large bandwidth, high gain and stable radiation patterns. The antenna for wireless communication system must be small size, lightweight, high gain, easy to manufacture, cost effective and easy to integrate with wireless communication devices [4, 5]. The patch antenna is appropriate for such applications and used for wide bandwidth, circular polarization and dual-band frequencies [6]. The metallodielectric EBG, electromagnetic bandgap and photonic bandgap-based structures and array are used for enhancing the performance of printed antennas and circuits [7, 8]. On the other hand, the AMC structures were also used to enhance the antenna performance because they are the metamaterials that exhibit a specific property such as reflection phase and amplitude [9–11]. A CPW-fed T-shaped antenna with frequency reconfigurability for millimeter-wave applications is proposed [12]. A microstrip patch antenna with parasitic element for 5G application with 4.28 GHz bandwidth is proposed [13]. Therefore, the octagonal patch is preferred in this paper due to having characteristics of low profile, easy to fabricate and simply structured. The AMC structure considered from [14] to analyze the octagonal patch antenna. The aim of various configurations based on design is to analyze how different configurations will affect the characteristics of an antenna. In this paper, the study of various configurations of octagonal patch antenna is integrated with two different designs of AMC unit cells. The simulated results are compared to octagonal patch antenna with patch AMC and without patch AMC.

2 Unit Cell AMC Geometry

The geometry of square AMC and modified AMC unit cell is shown in Fig. 1. Both AMC unit cells are designed on Rogers RT/duroid 5880 substrate material with dielectric constant (ε_r) = 2.2, thickness of substrate = 1.52 mm and loss tangent

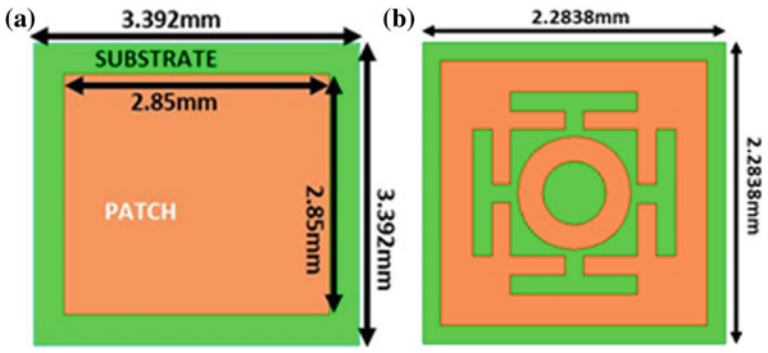

Fig. 1 **a** Square AMC, and **b** modified AMC unit cell [14]

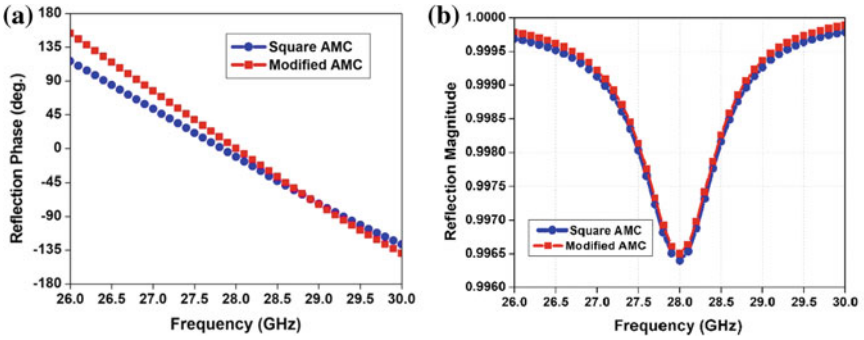

Fig. 2 **a** Reflection phase of square and modified unit AMC cells, **b** reflection magnitudes of square and modified unit AMC cells

(tan δ) = 0.0009. Initially, a square AMC of size 3.392 × 3.392 mm^2 is designed for 28 GHz frequency. Further, a square AMC is modified and analyzed for 28 GHz frequency. It is observed that the size of the modified AMC is reduced, and the overall size is 2.2838 × 2.2838 mm^2.

The reflection phase and magnitude behavior of unit AMC cells are depicted in Fig. 2a, b, respectively. In Fig. 2, 0° phase reflection value of unit square and modified AMC cell is about 27.9 and 28 GHz frequency indicates that the unit cell AMC structure has an operating band of 26.4–29.3 and 26.8–29.2 GHz in the range of ±90° phase, respectively. Hence, the square AMC unit cell has large bandwidth as compared to modified AMC unit cell so square AMC unit cell can be used for bandwidth enhancement. Consequently, the reflection magnitude of about 0.9968 and 0.9965 is observed from Fig. 2b for square and modified unit AMC cell, respectively. Hence, both AMC unit cells act as a good reflector as the reflection magnitude is about 1.00 and can be used for gain enhancement.

3 Antenna Design Configurations

3.1 Basic Octagonal Patch

The geometry of basic octagonal patch antenna with inset feed is shown in Fig. 3. By optimizing the length and width of the inset feed line, 50 Ω impedance is achieved for matching at operating frequency of antenna. The design parameters of the basic octagonal patch antenna are as follows: $L_s = 10$ mm, $W_s = 10$ mm, $W_f = 0.76$ mm and width of inset feed = 0.2 mm. To keep the resonance frequencies of 5G applications, three AMC cells are considered as a patch AMC unit cells and incorporated on the octagonal patch antenna to see their impact on basic octagonal patch antenna performance.

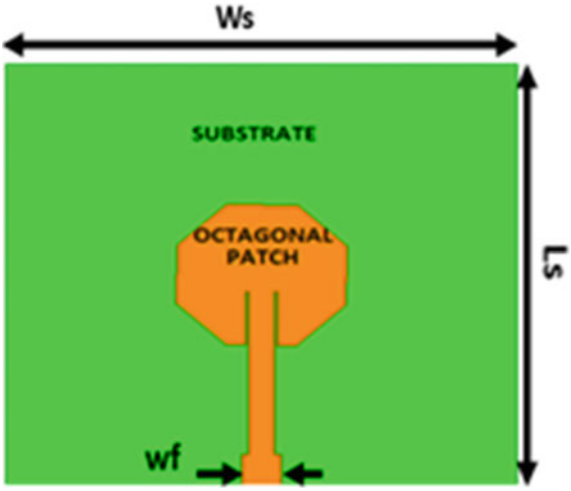

Fig. 3 Geometry of basic octagonal patch antenna

3.2 Different Configurations of Octagonal Patch Antenna with AMC

Initially, a basic octagonal patch antenna is integrated with three square patch AMC cells as shown in Fig. 4 (i.e., configuration 1) then bandwidth and gain of the antenna enhanced because of three square AMC cells act as a reflector.

Further, one square AMC is replaced through a modified AMC in the ratio of 1:2 as shown in configuration 2 of Fig. 4 then resonance frequencies are shifted toward lower side due to increase the electrical length of modified AMC cell. Hence, the bandwidth and gain of configuration 2 are slightly reduced. In configuration 3, the modified patch AMC is introduced as the ratio of 2:1 along with square patch AMC then bandwidth is slightly reduced, and gain is improved. In addition, the overall operating band shifted toward lower side in configuration 2 and 3. The aim of these different configurations is to see the impact on 5G resonance frequencies, bandwidth and gain of the basic octagonal patch antenna. To meet aforementioned requirement, the third square AMC is replaced through a modified patch AMC then the antenna performance is slightly improved due to three modified AMC unit cell behaves as a reflector.

4 Results and Discussion

The comparison of reflection coefficients for different configurations of Fig. 4 with basic octagonal patch antenna is depicted in Fig. 5. The comprehensive results are summarized in Table 1.

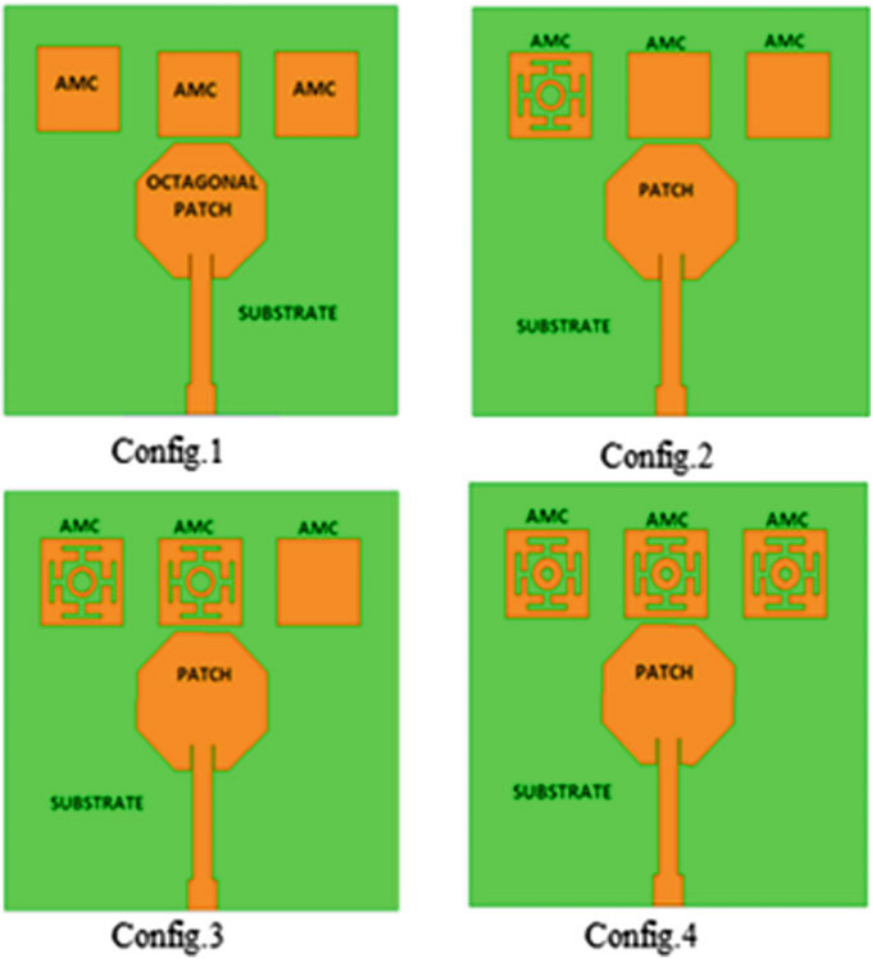

Fig. 4 Four different configurations of AMC cells enabled octagonal patch antenna

From Table 1, four different configurations with patch AMC unit cells offer large bandwidth and high gain as compared to octagonal patch antenna without patch AMC unit cell. The octagonal patch antenna with square patch AMC unit cells provides large bandwidth and gain due to increase patch area size and acted as good reflector. The simulated normalized radiation patterns at 28 GHz for different configurations of AMC cells in octagonal patch antenna in E-plane and H-plane are shown in Fig. 6a, b, respectively. It can be seen that the antenna can radiate directional patterns in both the planes.

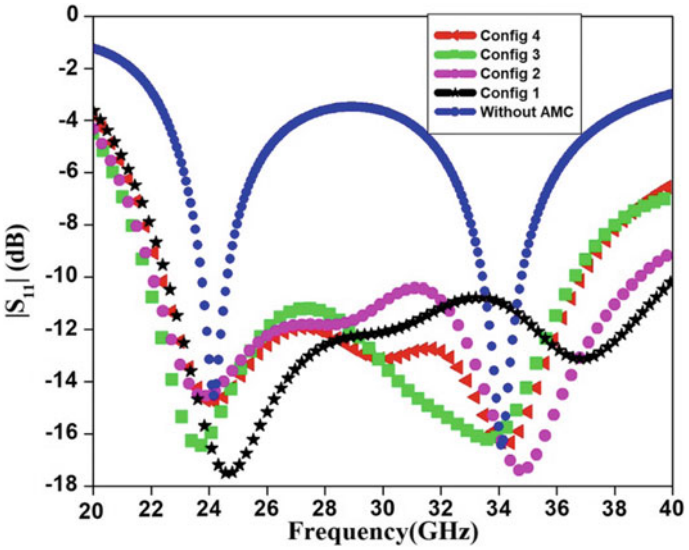

Fig. 5 Reflection coefficient for four different configurations of AMC cells enabled octagonal patch antenna

Table 1 Tabulated results of different configurations of octagonal antenna with AMC cells

Design pattern	IBW (GHz)	% Increment of BW	Gain (dB)
Antenna without AMC	23.10–25.62	–	6.48
	32.30–36.10		
Antenna with configuration 1	22.55–40	57	7.95
Antenna with configuration 2	22.08–38.66	54	6.28
Antenna with configuration 3	21.88–36.64	48	6.64
Antenna with configuration 4	22.38–36.85	47	6.72

The proposed antenna with different configurations has large bandwidth and large gain as compared to previous researches at 28 GHz frequency [2, 12, 13]. Table 2 is the summarized performance comparison of proposed work with previously published work on 5G antennas.

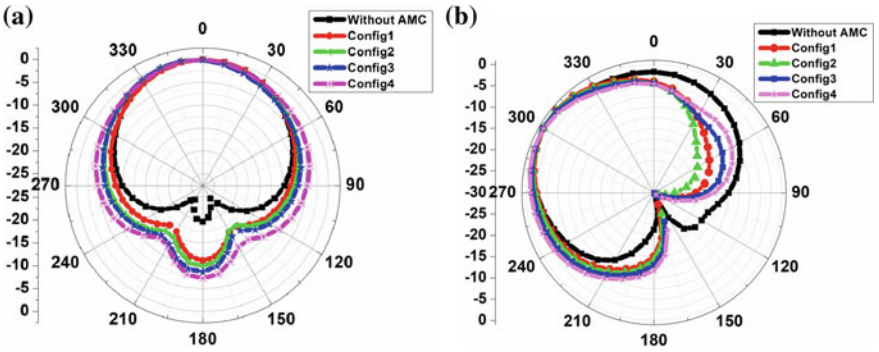

Fig. 6 **a** E-plane radiation patterns for different configurations of the octagonal antenna, **b** H-plane radiation patterns for different configurations of the octagonal antenna

Table 2 Tabulated results of different configurations of octagonal antenna with AMC cells

References	Size in terms of λ_g	BW (GHz)	Peak Gain (dB)
[2]	2.57 λ_g × 2.57 λ_g	1.5	6.60
[12]	1.54 λ_g × 1.54 λ_g	6	4.5
[13]	1.0 λ_g × 1.31 λ_g	4.26	6.72
Our work	1.35 λ_g × 1.35 λ_g (without AMC)	2.98 3.35	6.48
	1.35 λ_g × 1.35 λ_g (configuration 1)	17.45	7.95
	1.35 λ_g × 1.35 λ_g (configuration 2)	16.58	6.28
	1.35 λ_g × 1.35 λ_g (configuration 3)	14.76	6.64
	1.35 λ_g × 1.35 λ_g (configuration 4)	14.47	6.72

5 Conclusions

The small size octagonal patch antenna with two different AMC unit cells is proposed for 5G frequency band applications. Four configurations of octagonal patch antenna with combination of square and modified AMC unit cells are studied. The simulated result reveals that antenna has small size, wide impedance bandwidth, high gain and directive radiation patterns and makes it suitable for future 5G applications.

References

1. Rappaport TS, Sun S, Mayzus R, Zhao H, Azar Y, Wang K, Wong GN, Schulz JK, Samimi M, Gutierrez F (2013) Millimeter wave mobile communications for 5G cellular: it will work! IEEE Access 1:335–349

2. Jandi Y, Gharnati F, Said AO (2017) Design of a compact dual bands patch antenna for 5G applications. In: IEEE International conference on wireless technologies, embedded and intelligent systems (WITS), Fez, Morocco, pp 1–4
3. Goudos SK, Tsiflikiotis A, Babas D, Siakavara K, Kalialakis C, Karagiannidis GK (2017) Evolutionary design of a dual band E-shaped patch antenna for 5G mobile communications. In: 6th International conference on modern circuits and systems technologies, Thessaloniki, Greece, pp 1–4
4. Kamakshi, Ansari JA, Singh A, Aneesh M (2014) Desktop shaped broadband microstrip patch antennas for wireless communications. Prog Electromagn Res Lett 50:13–18
5. Jackson D, Alexopoulos N (1985) Gain enhancement methods for printed circuit antennas. IEEE Trans Antennas Propag 33(9):976–987
6. Eardprab S, Phongcharoenpanich C, Torrungrueng D (2013) Improvement of a circular microstrip antenna excited by four feeds and suspended with artificial magnetic conductors. Int J Antenna Propag. Article ID: 310686, 1–10
7. Gonzalo R, De Maagt P, Sorolla M (1999) Enhanced patch-antenna performance by suppressing surface waves using photonic-bandgap substrates. IEEE Trans Microw Theory Tech 47(11):2131–2138
8. Abhari R, Eleftheriades GV (2003) Metallo-dielectric electromagnetic bandgap structures for suppression and isolation of the parallel-plate noise in high-speed circuit. IEEE Trans Microw Theory Tech 51(6):1629–1639
9. Zhang Y, Hagen JV, Younis M, Fischer C, Wiesbeck W (2003) Planar artificial magnetic conductors and patch antennas. IEEE Trans Antennas Propag 51(10):2704–2712
10. Feresidis AP, Goussetis G, Wang S, Vardaxoglou JC (2005) Artificial magnetic conductor surfaces and their application to low-profile high-gain planar antennas. IEEE Trans Antennas Propag 53(1):209–215
11. Sohn JR, Kim KY, Tae H-S, Lee HJ (2006) Comparative study on various artificial magnetic conductors for low-profile antenna. Prog Electromagn Res 61:27–37
12. Jilani SF, Abbas SM, Esselle KP, Alomainy A (2015) Millimeter-wave frequency reconfigurable T-shaped antenna for 5G Networks. In: IEEE 11th International conference on wireless and mobile computing, networking and communications (WiMob), Abu Dhabi, United Arab Emirates, pp 100–102
13. EI Bakkali M, El Gholb Y, Tabakh I, Mounsef A, El Amrani El Idrissi N (2017) A 28 GHz rectangular patch antenna with parasitic element for small satellite applications. In: Proceedings of the 2nd international conference on computing and wireless communication systems, Larache, Morocco, pp 1–5
14. Muhamad M, Abu M, Zakaria Z, Hassan H (2017) Novel artificial magnetic conductor for 5G application. Indones J Electr Eng Comput Sci 5(3):636–642

Numerical Investigation of T-Shape Waveguide-Based Directional Coupler

S. Radhakrishnan, Ajit Kumawat, G. Thavasi Raja and D. Sriram Kumar

Abstract Silicon-on-Insulator (SOI)-based structure has a lot of advantages and overcomes the limitation of conventional copper- and fiber-based technologies. SOI waveguide-based directional coupler is broadly used in high-speed networks and hybrid interconnects due to its high index difference. The SOI directional coupler (DC) is designed with odd and even modes of TE and TM for symmetric and asymmetric structures. For symmetric structure, TM mode requires lower coupler length for the coupling power of cross-port and parallel port power, and for asymmetric structure, TE mode requires larger coupler length for the coupling power of cross-port and parallel port power. Coupler was designed using an effective index method with optimized structural parameter such as coupler length, polarization dependence, and wavelength. Finally, the proposed coupler and its performance were investigated in terms of coupling efficiency, cross-talk, and coupling length.

Keywords Directional coupler · Cross-talk · Coupling length · Coupling power · Coupling efficiency

1 Introduction

The Si-wire WG (SWG) is made up of Si core and Sio_2 or air cladding material. The SWG has several advantages and overcomes the boundary of conventional Si-rib WG [1]. At 1550 nm wavelength, SWG produced high index difference for symmetric ($\Delta \approx 2$) and for asymmetric ($\Delta \approx 2.4$). In SWG, power transmission is high, and bending loss is low when compared to the conventional rib WG [2, 3]. There are so many applications in SWG such as array-WG-grating (AWG) [4], wavelength converters [5], photonic crystal lens [6], and switches [7]. The waveguide-based directional coupler acts as a polarizer rotators [8], polarizer-dependent coupler [3],

S. Radhakrishnan (✉) · A. Kumawat · G. Thavasi Raja · D. Sriram Kumar
Department of Electronics and Communication Engineering, National Institute of Technology Tiruchirappalli, Tiruchirappalli 620015, India
e-mail: srk3mail@gmail.com

D. Sriram Kumar
e-mail: srk@nitt.edu

V. Janyani et al. (eds.), *Optical and Wireless Technologies*, Lecture Notes in Electrical Engineering 648, https://doi.org/10.1007/978-981-15-2926-9_45

multiplexer [9], etc. The micrometer range coupling of the SWG-based directional coupler (DC) characteristics, and its fabrication had studied [2]. Preserving the same polarization of DC is a major factor because of the small dimensions of the waveguide [3]. Multimode waveguide has several advantages such as low loss, fabrication simplicity, polarization independence and reduces the higher-order mode generation are also feasible [10]. Symmetric and asymmetric waveguide design and their performance analysis were studied and achieved the minimal cross-talk in the first window at 1.35 μm [11]. There was a study for lower-to-higher-order mode coupling in a forward direction and lower-to-lower-order mode coupling in a backward direction [12]. Phase-matching condition for TM mode is perfectly satisfied, while TE mode shows large phase mismatch [13]. In this letter, we propose a novel structure of passive directional coupler or mode converters using symmetric and asymmetric configurations.

The proposed numerical investigation has made with coupling length, coupling gap, coupler width, and coupler configuration using the effective index approach. There are various numeric steps followed to find out the cross-talk, cross-port power, parallel port power, and coupler length for symmetric and asymmetric configurations. This paper covers the novel structure of WG coupler for symmetric and asymmetric design and configurations with their performance analysis.

2 DC Design and Performance Analysis

The proposed symmetric waveguide structures are shown above, and their mode profile is also taken with a help of COMSOL tool. Even and odd modes are generated at the initial input wavelength of 1550 nm. The core region of the proposed structure is 800 nm × 500 nm with a refractive index of 3.47. The refractive index of upper cladding is one. The gap between the waveguide is 200 nm. The proper coupling of waveguide depends on various parameters such as the gap, width, coupling length, and operating wavelength. The perfect coupling is possible in the proposed structure with effective index (n_{eff}) 2.514594 (odd-TM), 2.515325 (even-TM), 2.846308 (odd-TE), and 2.846819 (even-TE) with the coupling gap of 200 nm. The coupling lengths (L_{C}) were calculated using numerical calculations. While calculating the coupling length, wavelength is also a major parameter. Using coupling length, the normalized distance (q_z) was calculated. Due to the higher effective index difference between the odd and even modes of TM, the TM mode requires a lower coupler length than TE in the symmetric configuration. Coupling lengths are dominated by WG distance, wavelength for effective mode coupling, and index difference (Fig. 1).

In Fig. 2(a1), the dimension of the left-hand side core region of the proposed structure is 400 nm × 500 nm, and the right-hand side of the core region is 800 nm × 500 nm with a refractive index of 3.47. As same as the symmetric structure, here also we can use input wavelength 1550 nm. Due to the structural dimension variation, the mode coupling appears in either right side or left side for the wavelength of 1550 nm. To achieve the effective coupling in asymmetric structure, the gap in WG, WG

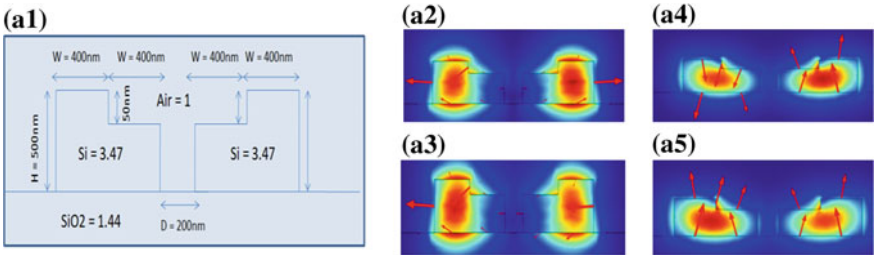

Fig. 1 **a1** Cross section of the proposed symmetric coupler structure, **a2**, **a3** TM mode profile of odd and even, respectively, **a4**, **a5** TE mode profile of odd and even, respectively

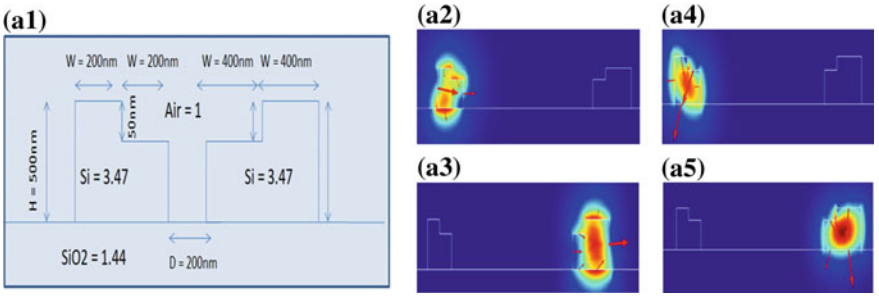

Fig. 2 **a1** Cross section of the proposed asymmetric coupler structure, **a2**, **a3** TM mode profile of odd and even, respectively, **a4**, **a5** TE mode profile of odd and even, respectively

width, coupling length, and operating wavelength are more important parameters. In this case, the mode confines at the effective index values of 2.437677 (even-TM), 2.039326 (odd-TM), 2.306696 (odd-TE), and 2.736455 (even-TE) at the coupling gap of 200 nm. The asymmetric effective index difference is contrast with symmetric structure. Due to the higher effective index difference of odd and even modes, the TE mode requires higher coupler length than TM. So the proper coupling depends on the coupling lengths which were dominated by normalized distance, width, effective index difference, and operating wavelengths.

The Fig. 3 describes that the transmission and coupling intensity with coupler length L. Here, as shown in Fig. 3a, c, parallel port and cross-port powers are coupled well in symmetric WG, but in asymmetric WG, it has not coupled properly as shown in Fig. 3b, d. The sin and cosine wave of transmitted power (P_a) and coupled power (P_b), respectively, for symmetric WG and asymmetric WG has been plotted in Fig. 3c, d. Optical power is calculated with parallel port power (P_a) and cross-port power (P_b). It can be expressed as [3, 14]

$$P_a(z) = P_{\text{parallal}}/P_{\text{in}} = 1 - F\sin^2(qz) \tag{1}$$

$$P_b(z) = P_{\text{cross}}/P_{\text{in}} = F\sin^2(qz) \tag{2}$$

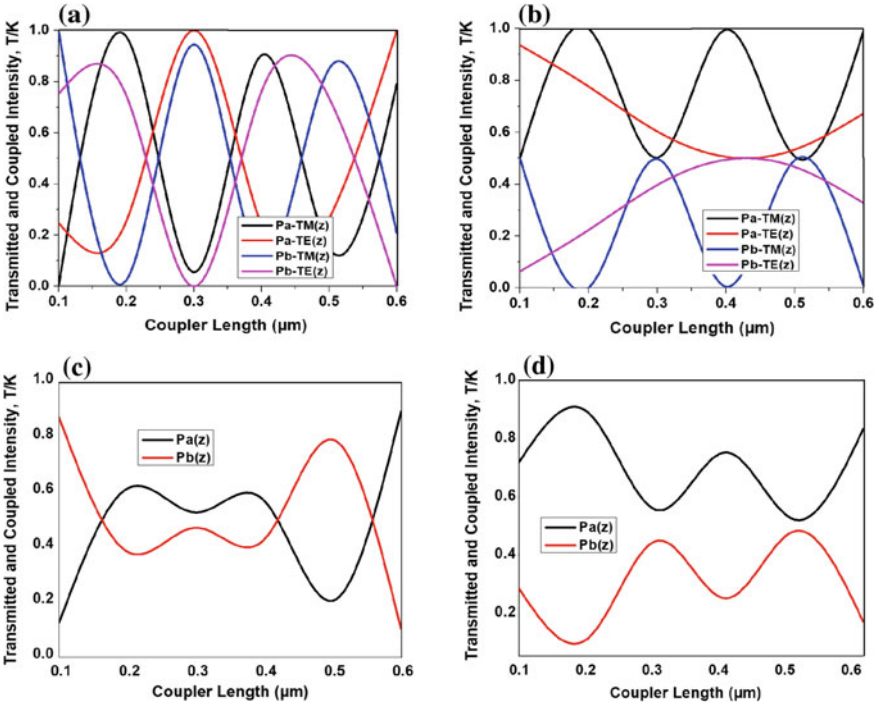

Fig. 3 **a** Transmitted/coupled power for TE and TM modes—symmetric, **b** asymmetric, **c** clear view of coupling between TE and TM—symmetric, and **d** asymmetric

By using the normalized distance $qz = \pi L/2L_c$ [3, 14], the coupling efficiency (F) of symmetric waveguide is unity. By observing the coupling of symmetric graph (Fig. 3a), the coupler length of TE is larger than TM which has been explained clearly; TE mode is coupled around 0.21 μm and TM is coupled around 0.15 μm. Coupling length (L_c) is nothing but the coupler length (L) that helps light coupling to transfer from one WG to another with the function of effective index difference between odd and even modes and wavelength $L_c = \frac{\lambda}{2} \times \Delta n_{\text{eff}}$ [3, 14]. In Fig. 3c, we can see that there is no coupling loss for symmetric WG, i.e., $P_a + P_b = 1$. Therefore, the coupling efficiency is $F = 1$. The asymmetric structure in Fig. 3b shows that the coupling Length of TE is larger than TM and it has been clearly explained that TM modes are coupled around 0.3 μm coupler length and TE modes are coupled around 0.42 μm coupler length. In Fig. 3d shown that there is some coupling loss in asymmetric WG, i.e., $P_a + P_b < 1$ [14] and obviously the coupling efficiency $F < 1$. Using the difference between the transmitted and coupled power $P_{a(z)} - P_{b(z)}$, we can calculate the coupling loss. Due to the greater difference in the dimension of WG and phase mismatch between the interference waves, the losses of asymmetric WG were found higher than the symmetric WG.

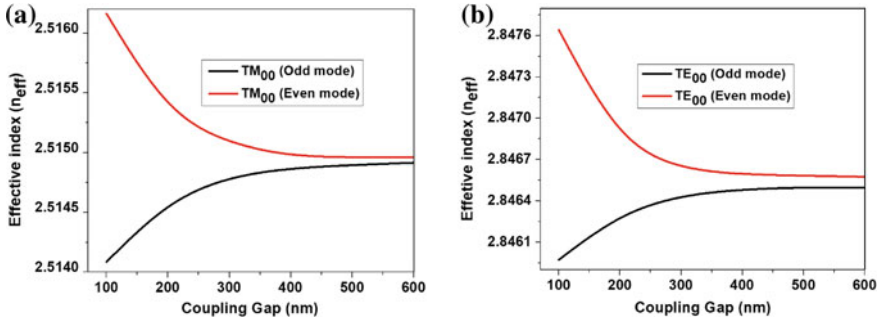

Fig. 4 Effective index versus coupling gap for **a** TM and **b** TE modes—Si-wire (800 × 500 nm^2)

In Fig. 4, the effective index n_{eff} of TE modes has higher values than TM modes. In TM, even and odd modes are merging when we increase the coupling gap with respect to effective index. The required coupling gap is more for merging the even and odd modes in TE than TM. If the waveguide width and wavelength are fixed, the TE_{mn} or TM_{mn} mode exists at the corresponding effective index. Therefore, the effective index of the WG is responsible for the particular mode generation. For example, the value of effective index for TM_{00} mode at 1550 nm is 2.51. Similarly, for 1450 nm with same waveguide width, the effective index value is 2.57.

In Fig. 5, the different coupled modes for different wavelength have been explained. It means that the effect of wavelength change will reflect in mode coupling. This is resultant of effective index of the odd and even modes as the function of wavelength and coupling length. Ultimately, wavelength is fixed for optimum coupling. But in all wavelengths, some undesired mode is coupled with the desired signal. This unwanted mode coupling is called cross-talk, and it can be expressed as a ratio of logarithmic function of undesired power to desired power.

$$\text{WGs Crosstalk(dB)} = 10\log[p_{\text{u}}/p_{\text{d}}] \approx 10\log\left[\cos^2(qz)\right] \tag{3}$$

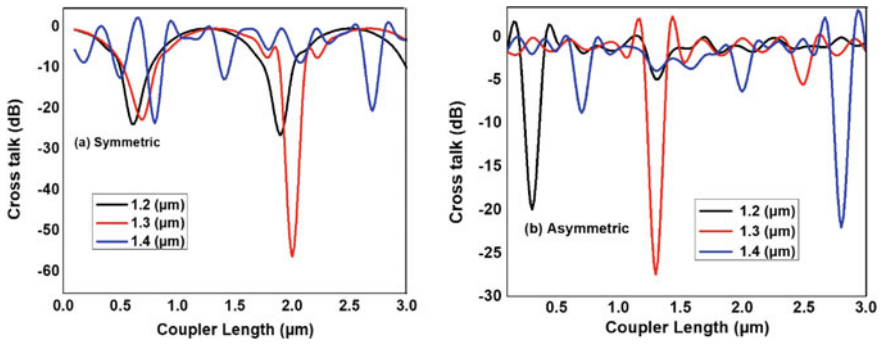

Fig. 5 Cross-talk versus coupler length for **a** symmetric and **b** asymmetric

Here p_u and p_d are unwanted and coupled power at the cross-port, and it will be approximately equal to the square of cosine value of normalized distance. As per reference [15], the TE and TM modes of cross-talk were found with similar results. In our proposed structure, cross-talk is a function of wavelength and coupler length. From the plot of symmetric structure of cross-talk, we have observed the increasing wavelength from 1.2 to 1.4 μm, and the curves are moved to the right for TE_{00} mode. In Fig. 5a, first shift describes about lower cross-talk −23 dB at the wavelength $\lambda = 1.3\,\mu m$ in 0.6 μm coupler length and higher cross-talk −55 dB at the same wavelength in 2 μm coupler length. Therefore, at some particular wavelength, the effect of increasing the coupling length will be the result of increasing the cross-talk. From the reference [11, 15], −20 dB is considered as an acceptable range of cross-talk. As same as symmetric WG, the curve of the asymmetric WG is shifted in the right side as shown in Fig. 5b. But in the first shift onward, there was a higher cross-talk −28 dB at the wavelength 1.3 μm in 1.25 μm coupler length. So there is no need of further shift analysis for asymmetric structure.

3 Conclusion

The observation of Si-wire WG and DC properties with their numerical analysis is considered for our proposed coupler design. The modes' confinement and polarization are to be influenced by WG width and effective index. From the design and result, we have investigated the transmitted and coupled power with the coupler dimension of 800 × 500 nm, and by this investigation, we come to know that in coupling TM modes are dominant over TE modes for symmetric structure and asymmetric structure. Symmetric and asymmetric passive couplers were designed using FEM tool with effective index and coupler length approach. The performance of the coupler is investigated with cross-talk, coupling length, normalized distance, and coupling efficiency. In our proposed structure, an enhanced coupling length is found for lower WG width and distance. The coupling efficiency depends on WG dimension and the smaller WG pair, and it is more efficient than larger WG pair. Therefore, the proposed coupler is suitable for small-scale integration and can be well and good platform of nano-optical devices. We have achieved the lower cross-talk about −23 dB as compared with the existing model cross-talk about −35 dB, and the required coupler length of our proposed system is lower than the existing system. From all these investigations, we found that symmetric coupler has lower cross-talk than asymmetric coupler and TM modes require short coupling length than TE for mode coupling of both couplers.

References

1. Yamada H, Chu T, Ishida S, Arakawa Y (2006) Si photonic wire waveguide devices. IEEE J Sel Top Quantum 12:1371–1379
2. Yamada H, Chu T, Ishida S, Arakawa Y (2005) Optical directional coupler based on Si-wire waveguides. IEEE Photon Technol Lett 17:585–587
3. Passaro VM, Dell'Olio F, Timotijevic B, Mashanovich GZ, Reed GT (2008) Polar-ization in sensitive directional couplers based on SOI wire waveguides. OpenOpt. J2
4. Fukazawa T, Ohno F, Baba T (2004) Very compact arrayed-waveguide-grating de-multiplexer using Si photonic wire waveguides. Jpn J Appl Phys 43:L673
5. Yamada K, Fukuda H, Tsuchizawa T, Watanabe T, Shoji T, Itabashi S (2006) All-optical efficient wavelength conversion using silicon photonic wire wave-guide. IEEE Photon Technol Lett 18:1046–1048
6. Ahmed R, Prodhan MH, Ahmmed R (2012) Design & analysis of optical lenses by using 2D photonic crystals for sub-wavelength focusing. Editor Pref 3
7. Liang L, Qv L, Zhang L, Zheng C, Sun X, Wang F, Zhang D (2014) Fabrication and characterization on an organic/inorganic 2 × 2 Mach–Zehnder interferometer thermo-optic switch. Photon Nanostruct 12:173–183
8. Wohlfeil B, Zimmermann L, Petermann K (2012) Asymmetric codirectional coupler between regular nano waveguide and slot-waveguide for polarization conversion. Integr Photon Res Silicon Nanophoton Opt Soc Am 5
9. Liang H, Soref R, Mu J, Li X, Huang W-P (2015) Electro-optical phase-change 2 × 2 switching using three-and four-waveguide directional couplers. Appl Opt 54:5897–5902
10. Chin M-K, Lee C-W, Lee S-Y, Darmawan S (2005) High-index-contrast waveguides and devices. Appl Opt 44:3077–3086
11. Ahmed R (2016) Multimode waveguide based directional coupler. Opt Commun 370:183–191
12. Wen K, Hu Y, Chen L, Zhou J, Lei L, Guo Z (2015) Theoretical analysis of plasmonic unidirectional propagation at visible frequency based on subwavelength waveguide. Opt Commun 336:243–247
13. Ni B, Xiao J (2017) A compact silicon-based TE-pass polarizer using three-guide directional couplers. IEEE Photon Technol Lett 29(19):1631–1634
14. Okamoto K (2010) Fundamentals of optical waveguides. Academic Press, Cambridge
15. Lee C-W (2011) Design of polarization-independent coarse wavelength splitters based on ridge-waveguide directional couplers. Int J Opt

Design and Analysis of Slot Coupled Antenna on Different Dielectric Materials

G. Anjaneyulu and J. Siddartha Varma

Abstract This work presents a slot coupled patch antenna with a square patch located on the top layer for the X- and Ku-band frequencies. The patch and feed are placed on two different dielectric substrates and separated with a gap between them, which is filled by foam having low dielectric constant. Two types of slots, H-shaped and unequal X-shaped, are etched on the ground plane, and the results are compared. Two different dielectric materials with different relative permittivity values are used in the simulation, and the results are compared. The simulated antenna has a wide bandwidth of 2.38 GHz from 11.62 to 14.00 GHz. These antennas have applications in satellite and wireless communications.

Keywords Slot coupled patch · Wide bandwidth · High gain · Circular polarization · Cross slot

1 Introduction

The rapid growth in society demands more advanced wireless communication devices with less radiating structures and more efficient systems. Microstrip patch antennas are one such best choice because of their low weight and many other advantages [1]. So many different techniques are available to design an efficient patch antenna, but a major disadvantage of microstrip antenna is its narrow bandwidth. Aperture coupling is one of the popular feeding mechanisms, and it allows separation between the feed and radiating element with a ground layer in the middle. This type of feeding is called non-contacting feed and helps as shielding from spurious radiation.

Aperture coupled feeding technique is presented by Pozar [2], and many researchers provided the design methods for designing slot coupled antennas [3, 4]. Antennas with U-shaped and E-shaped slots are etched on the ground plane to enhance the bandwidth and are presented in [5–8]. A F-shaped slot antenna for having a wide beam width and circular polarization is presented [9], and also, slot coupled antenna with corrugated ground plane [10] is also designed.

G. Anjaneyulu (✉) · J. Siddartha Varma
MVGR College of Engineering, Vizianagaram, India

V. Janyani et al. (eds.), *Optical and Wireless Technologies*, Lecture Notes in Electrical Engineering 648, https://doi.org/10.1007/978-981-15-2926-9_46

This aperture coupled antennas are designed for different applications. A loop-shaped slot [11] antenna for WLAN and WiMAX applications, simple line slot [12, 13] for wireless applications and branch-like feed line [14] is also used for ultra-wide band which is also presented. Apart for the wide bandwidth, slot coupled is also used to generate high-gain circularly polarized antenna and is presented in [15] and by placing an foam in between the two substrates to increase the bandwidth and using FSS layer [16] to increase gain and aperture coupled can also be used in the array configuration [17] also to enhance gain furthermore.

In this presented work, an aperture coupled antenna microstrip antenna is designed on two different dielectric substrates having different relative permittivity, and both the results are compared and analysed. Two different shaped slots are etched on the ground and Rohacell foam is also placed in between the two substrates to enhance the bandwidth. The design methodology and discussions on results are presented in the following sections.

2 Design Methodology

Figure 1 shows an antenna structure with a square patch on the top layer and two different slots on ground plane, which is on the second layer and feed placed on the third layer. The dielectric substrates used in the proposed antenna are RT duroid 5880 with a relative permittivity of 2.2 having a thickness of 1.6 mm and another

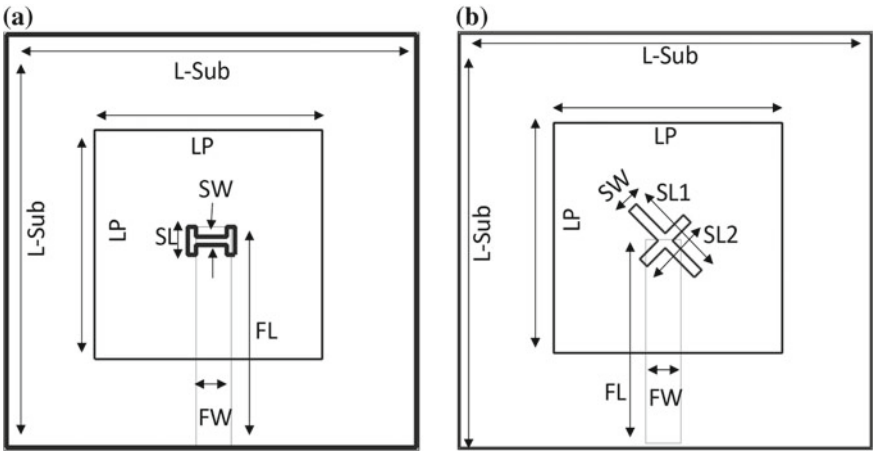

Fig. 1 Antenna geometry with **a** H-slot, **b** X-slot

Table 1 Optimized values of the proposed structure

Design variable	Value (mm)	Design variable	Value (mm)
Substrate length (L-sub)	40	H-slot length (SL)	3.3
Patch length (LP) for RO 4003C	6	H-slot width (SW)	1.2
Patch length (LP) for RT 5880	8	X-slot length (SL1)	9
Feed length (FL)	20.8	X-slot length (SL2)	6
Feed width (FW)	1.5	X-slot width (SW)	1
Foam thickness	3.2	Gap (g)	3.2

material is Rogers RO 4003C with a relative permittivity of 3.55 having a thickness of 0.508 mm. A Rohacell foam material with relative permittivity of 1.07 with a thickness of 3.2 mm is inserted between the two substrates. The proposed antenna is fed using a 50 Ω microstrip line feed. Complete list of dimensions is provided in Table 1.

The variation in the patch length between the two substrates is due to the difference in the relative permittivity. The H-shaped slot dimensions are fixed after the parametric study to have better impedance bandwidth, and X-type slot has an unequal slot length to achieve circular polarization. The typical aperture coupled patch antenna consists of two dielectric substrate layers, the patch is printed on the top layer of first substrate and ground plane is on the top layer of second substrate and feed is placed on the bottom layer. There is a gap between two substrates, and Rohacell foam of thickness g is used to fill the gap. In this design, a similar dielectric material is used on both layers.

3 Results and Discussion

The analysis of the proposed antenna has been carried out using the commercially available finite element-based ANSYS High Frequency Structure Simulator (HFSS). Several iterations of parametric analysis are done to have better performance of the antenna. Results of two different substrates are compared in this section, for convenience RO 4003C is referred to as sub-a and RT 5880 is referred to as sub-b in discussion.

The reflection coefficient versus frequency plot of different antennas is shown in Fig. 2, and here antenna with two different slots with and without foam is presented.

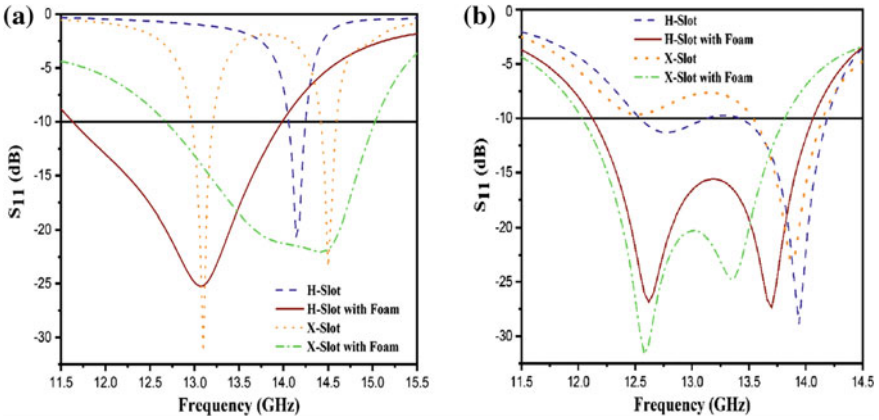

Fig. 2 S_{11} versus frequency for different dielectric materials, **a** RO 4003C, **b** RT 5880

As shown in Fig. 2, patch antenna with foam placed in between the two layers have wide bandwidth compared to the others. Patch antenna designed on the dielectric substrate RO 4003C has slightly more bandwidth than the other substrate, because of the higher relative permittivity of the substrate. From the above analysis, it is clearly proved that overall thickness of the antenna is directly proportional to the impedance bandwidth of patch antenna. It is observed that sub-a has dual band characteristics with X-slot. Comparison of antenna parameters of both dielectric materials is provided in Tables 2 and 3.

Gain versus frequency for the two dielectric materials is shown in Fig. 3, and it can be seen that sub-a has more gain close to 7 dBi with both the substrates along with the foam. Antenna variations without foam for sub-a also have a decent gain of 5.3 and 3.7 dBi. But in sub-b patch antenna without foam has high gain than with the antenna with foam, and reason for this is relative permittivity of the substrate.

Table 2 Comparison of antenna parameters for substrate RT 5880

Antenna parameter	RT 5880			
	H-slot	H-slot with foam	X-slot	X-slot with foam
Resonant frequency (GHz)	13.9	12.5	13.8	12.6
Impedance bandwidth (<−10 dB)	13.41–14.19 GHz (0.77 GHz)	12.12–14.07 GHz (1.95 GHz)	13.53–14.15 GHz (0.62 GHz)	12.03–13.82 GHz (1.79 GHz)
Gain (dBi)	6.5	5.04	5.2	3.88
Axial ratio bandwidth (<3 dB)	–	–	13.94–14.13 GHz (0.19 GHz)	12.74–13.29 GHz (0.55 GHz)

Table 3 Comparison of antenna parameters for substrate RO 4003C

Antenna parameter	RO 4003C			
	H-slot	H-slot with foam	X-slot	X-slot with foam
Resonant frequency (GHz)	14.2	13	13, 14.5	14.35
Impedance bandwidth (<−10 dB)	14.06–14.25 GHz (0.19 GHz)	11.62–14.00 GHz (2.38 GHz)	12.97–13.22 GHz 14.42–14.60 GHz	12.67–15.03 GHz (2.36 GHz)
Gain (dBi)	5.3	6.97	3.7, 3.6	6.75
Axial ratio bandwidth (<3 dB)	–	–	14.38–14.70 GHz (0.32 GHz)	13.30–14.20 GHz (0.90 GHz)

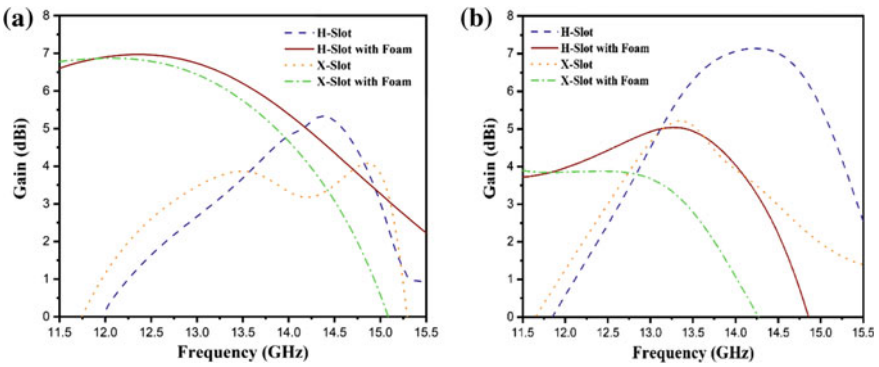

Fig. 3 Gain versus frequency for different dielectric materials, **a** RO 4003C, **b** RT 5880

Antenna with unequal X-slot has achieved circular polarization, and Fig. 4 shows axial ratio plot for both sub-a and sub-b. It is seen that sub-a with X-slot with foam has wider axial ratio bandwidth of about 0.90 GHz having minimum value of 0.3 dB. Radiation pattern of antenna at frequency of 13 GHz is shown in Fig. 5 for both substrates.

4 Conclusion

An aperture coupled antenna with two different dielectric materials is presented in the paper. A square patch with H-slot and unequal X-slot on the ground plane with and without foam placed between two substrates is compared in this work. Patch antenna which has foam placed between two substrates has more impedance bandwidth compared to antenna without foam. Patch antenna designed on RO 4003C

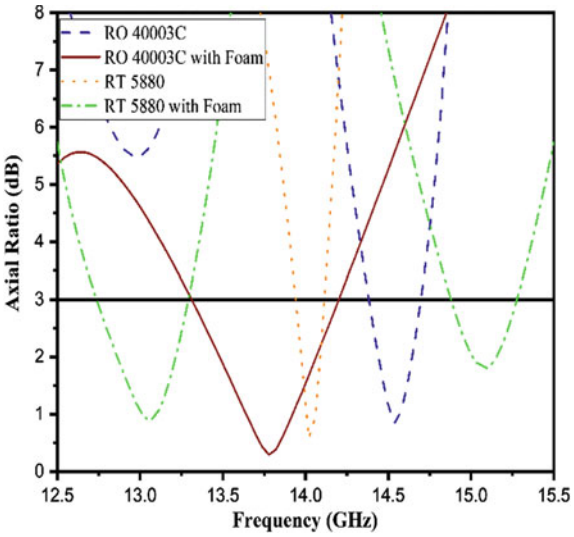

Fig. 4 Axial ratio versus frequency plot of antenna

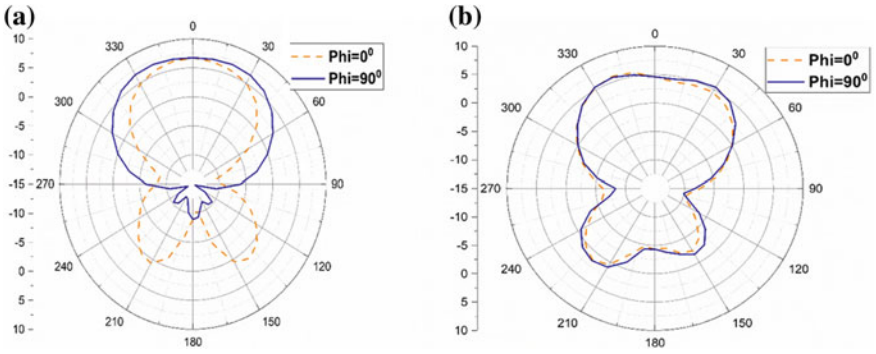

Fig. 5 Radiation pattern of antenna with foam at 13 GHz. **a** H-slot on RO 4003C, **b** X-slot on RT 5880

substrate has high gain of about 7 dBi compared to the RT 5880 material. Antenna having X-slot on the ground plane is having circular polarization characteristics with good axial ratio bandwidth of 0.90 GHz.

These simulated antennas are useful in the X- and Ku-band frequencies for wireless applications.

Acknowledgements This work (major project) was funded by Science and Engineering Research Broad, the Department of Science and Technology (DST), Government of India, Sanction No. EEQ/2016/000396 and Order No. SERB/F/8020/2017-18.

References

1. Garg R, Bhartia P, Bahl I, Ittipiboon A (2001) Microstrip antenna design handbook. Artech House antennas and propagation library
2. Pozar DM (1985) Microstrip antenna aperture-coupled to a microstripline. Electron Lett 21(2):49
3. Splitt G, Davidovitz M (1990) Guidelines for design of electromagnetically coupled microstrip patch antennas on two-layer substrates. IEEE Trans Antennas Propag 38(7):1136–1140
4. Civerolo M, Arakaki D (2011) Aperture coupled patch antenna design methods. In: IEEE international symposium on antennas and propagation, pp 876–879
5. Liu S, Wu W, Fang DG (2016) Single-feed dual-layer dual-band E-shaped and U-slot patch antenna for wireless communication application. IEEE Antennas Wirel Propag Lett 15(2):468–471
6. Khodae GF, Nourinia J, Ghobadi C (2008) A practical miniaturized U-slot patch antenna with enhanced bandwidth. Prog Electromagn Res B 3:47–62
7. Singh A, Singh S (2014) Antenna by using inverted U-slot, vol 2014
8. Hoseini Izadi O, Mehrparvar M (2010) A compact microstrip slot antenna with novel E-shaped coupling aperture. In: 2010 5th international symposium on telecommunications, IST 2010, pp 110–114
9. Nasimuddin, Yong Y, Chen ZN, Alphones A (2009) Circularly polarized F-shaped slot microstrip antenna with wide beamwidth. In: European microwave conference week 2009, EuMW 2009: science, progress and quality at radiofrequencies, conference proceedings—39th European microwave conference, EuMC 2009, vol 1, no Oct, pp 1531–1534
10. Qin Kun, Li Minquan, Xia Huimin, Wang Jun (2012) A new compact aperture-coupled microstrip antenna with corrugated ground plane. IEEE Antennas Wirel Propag Lett 11:807–810
11. Sharma AK, Reddy BVR, Mittal A (2015) Slot loaded microstrip patch antenna for WLAN and WiMax applications. In: Proceedings of 2015 IEEE international conference on computational intelligence & communication technology, CICT 2015, pp 597–599
12. Singh M, Basu A, Koul SK (2006) Design of aperture coupled fed micro-strip patch antenna for wireless communication. In: 2006 Annual India conference INDICON
13. Raina TK, Kaur A, Khanna R (2012) Design of aperture coupled micro-strip patch antenna for wireless communication applications at 10 Ghz (X BAND). Int J Electron Eng 4(1):25–28
14. Ghassemi N, Rashed-Mohassel J, Neshati MH, Ghassemi M (2008) Slot coupled microstrip antenna for ultra wideband applications in C and X bands. Prog Electromagn Res M 3:15–25
15. Yazdanpanah N, Zehforoosh Y (2017) High gain CP aperture-coupled antenna for X-band application. Aust J Electr Electron Eng 14(1–2):12–19
16. Ganaraj G, Kumar C, Kumar VS, Shankaraiah (2018) High gain circularly polarized resonance cavity antenna at X-band. In: IEEE international conference on antenna innovations & modern technologies for ground, aircraft and satellite applications (iAIM), pp 1–5
17. Poduval D, Ali M (2017) Wideband aperture coupled patch array antennas—high gain, low side lobe design. Prog Electromagn Res 160:71–87

The Effect of Atmosphere on FSO Communication at Two Optical Windows Under Weather Condition of Bhubaneswar City

Jagana Bihari Padhy, Adyasha Satarupa and Bijayananda Patnaik

Abstract Free-space optical (FSO) network is the optical wireless technology used for future ultra-high-speed communication applications. The quality of FSO links is highly affected by the surrounding atmospheric conditions such as haze, rain, and fog. The performance of FSO system is highly dependent on the visibility parameter. This paper proposes the effect of various weather conditions on FSO communication under the weather conditions in Bhubaneswar city. The analysis is done based on the measured real-time visibility data of the Indian Meteorological Department (IMD) for Bhubaneswar city. The predicted atmospheric attenuation found is then compared for the two wavelengths (850 and 1550 nm). Finally, the free-space optical link has been estimated from the measured visibility data and predicted attenuation data.

Keywords Scattering coefficient · Attenuation · Free-space optics · Link margin

1 Introduction

Free-space optical (FSO) communication is known as the optical wireless technology of future generation. FSO uses a narrow laser beam operating in the infrared region for data communication. It has significant importance because of its beneficial features such as unlicensed spectrum, high data rate, huge bandwidth, highly secure, less power consumption, and required less mass. Hence, it is a prime alternative to conventional radio frequency (RF) networks [1]. It uses optical laser carrier in the infrared frequency to establish terrestrial links, space links, etc. However, the quality of FSO links is highly affected by the surrounding atmospheric conditions such as haze, rain, and fog. The performance of FSO system highly depends on

J. B. Padhy (✉) · A. Satarupa · B. Patnaik
Department of Electronics and Telecommunication Engineering, IIIT Bhubaneswar, Bhubaneswar, India
e-mail: c116005@iiit-bh.ac.in

A. Satarupa
e-mail: b215006@iiit-bh.ac.in

B. Patnaik
e-mail: bijayananda@iiit-bh.ac.in

V. Janyani et al. (eds.), *Optical and Wireless Technologies*, Lecture Notes in Electrical Engineering 648, https://doi.org/10.1007/978-981-15-2926-9_47

the visibility parameter. In the past literature, various methods have been adopted to mitigate the effects of atmosphere and to increase the FSO link distance. Dabiri et al. [2] proposed an FSO model by considering the background noise, thermal, and amplified spontaneous emission noise and derived an closed-formed expression for ergodic capacity, outage capacity, and outage probability with the help of analytic and simulation results. Shumani et al. [3] analyzed and simulated the FSO-based system for a city of Malaysia, on haze weather under different optical wavelength and calculated the link distance for FSO system at different visibility conditions. Mansour Abadi et al. [4] proposed an FSO system and investigated the effects of various link parameters on the performance of the FSO system. Here, the authors use the measuring parameters such as detection threshold, Q-factor, and bit-error-rate (BER) for the evaluation of the system. The FSO network also greatly affected by the atmospheric turbulence and scintillation causes fluctuation in air refractive index, as a result there is loss due to beam spreading and image dancing. Generally, these effects are wavelength dependent of the optical signal.

In this paper, we analyze the effect of different atmospheric attenuation parameters from the real-time data collected from Indian Metrological Department (IMD) for the Bhubaneswar city (India) using two wavelengths that are 850 and 1550 nm [1]. Various atmospheric constraints such as air, haze, rain, fog, and snow are considered for the analysis. The effect of scattering loss and the attenuation to the system performance is investigated under different wavelength and by varying the transmission distance. This presented a simulation model for FSO system to be adopted by the Bhubaneswar city atmosphere based on the theoretical perspective. For the first time, this type of model has been proposed for Bhubaneswar city as an effective FSO system targeting the change in weather condition. This will be helpful to implement in the development of the smart city.

2 Concept and Principle

The performance degradation of FSO system has occurred due to the environmental constraints of the earth's atmosphere. The performance analysis of FSO-based systems is generally carried out by considering the following parameters.

2.1 Choice of Wavelengths for FSO

Selection of wavelength in FSO communication is a very important design parameter, as it affects the detector sensitivity and the link performance of the system. The wavelength selection for an optical system is carried out by considering the three main objectives (i) eye and skin safety (ii) low attenuation window, and (iii) the working range of optical components available in the market [5, 6]. Accordingly, the

Table 1 Specification for visibility equipment

Distance	10 m to 75 km
Tolerance	+2%
Laser source	850 and 1550 nm
Weight of sensor head	7 kg
Forward scatter meter angle	45°
Working temperature range (°C)	−50 to 60

optical radiations can be classified into two categories: (i) 780–850 nm wavelengths and (ii) 1520–1600 nm wavelengths.

2.2 Visibility Data

The maximum detection range of the propagated optical signal is known as visibility or meteorological visual range [7]. For human eyes, the visibility sensitivity is carried out at 550 nm wavelength. In technical point of view, visibility is the distance where light loses 2% of its original power. The data for visibility were taken from the Indian Meteorological Department (IMD). The data were recorded on hourly observation for three months period from August to October 2018. About 2300 data were collected for these three months.

The electronic sensor used to collect the visibility data is working in the principle of forward scattering meter technology. Here, the sensors calculated the amount of light scattered due to haze, fog, or smoke particles present in the atmosphere. The specification of visibility measuring equipment is given in Table 1.

Lower visibility occurs when the concentration and size of particles are higher compared to average visibility. It reduces the efficiency of FSO systems and causes increased scattering and attenuation.

2.3 Geometric Attenuation

Geometric attenuation is a loss factor which arises due to the beam divergence of an optical signal propagating through free space. It comprises three main parameters necessary for improving the performance of FSO link: minimizing the divergence angle, link distance, and increasing the receiver aperture area [8]. It causes the light beam to diverge from the propagating path. This loss is time invariant for a specific FSO system. Geometrical attenuation is directly proportional to the link distance [2].

Mathematically, geometric attenuation is expressed in dB as [2]

$$G_{\text{Att}}(\text{dB}) = 10\log(L.\theta/D)^2 \tag{1}$$

where θ is the beam divergence angle, D is the aperture diameter of the receiver, and L is the link distance.

2.4 Absorption and Scattering Loss

The laser beam is greatly affected by the smallest particles such as gas molecules and aerosol present in earth's atmosphere during propagation. Depending on the size of particles and wavelength of laser, scattering is classified into three types [1, 9]:

(i) $r \ll \lambda$ is Rayleigh scattering, (ii) $r \approx \lambda$ is Mie scattering, and (iii) $r \gg \lambda$ is non-selective scattering.

To determine the scattering coefficient in hazy days [2],

$$\sigma = \frac{3.91}{V}\left(\frac{\lambda}{550}\right)^{-q(\upsilon)} \tag{2}$$

where V is the visibility data (kilometers), λ is the wavelength (nm), and $q(\upsilon)$ is the size distribution of scattering particles.

$$q(\upsilon) = \begin{cases} 1.6 \text{ for } V > 50 \text{ km} \\ 1.3 \text{ for } 6 < V < 50 \text{ km} \\ 0.16\,V + 0.34 \text{ for } 1 < V < 6 \text{ km} \\ V - 0.5 \text{ for } 0.5 < V < 1 \text{ km} \\ 0 \text{ for } V < 0.5 \text{ km} \end{cases} \tag{3}$$

The visibility is influenced by three factors: coherence angle of the source, the difference between the propagation paths, and the detector location with respect to the source.

2.5 Atmospheric Attenuation

The losses due to the absorption and scattering of laser photons in the atmosphere are due to various aerosols and gaseous molecules existing in the air. It is calculated with the help of the scattering coefficient of free space. In this work, the laser source is operated at 850 nm and 1550 nm which lies within the low atmospheric absorption spectrum. Hence, the absorption effect to the performance analysis is neglected in this work. The total attenuation loss is mainly concentrated on scattering loss. The atmospheric particle size with respect to the transmission laser wavelength defines the type of scattering. Atmospheric attenuation is calculated using exponential Beer–Lambert law [4].

$$\tau_{\mathrm{R}}(\mathrm{dB}) = -10\log\left(\frac{P_{\mathrm{R}}}{P_O}\right) = -10\log\left(\mathrm{e}^{-\beta L}\right) \tag{4}$$

where τ_{R} is the attenuation coefficient, P_{R} is the received power, P_O is the source power, total extinction coefficient, and L is the link distance.

Based on the FSO parameters as shown in Table 1, we calculated the total attenuation as a combination of both scattering attenuation and geometric attenuation.

2.6 Link Margin

Link margin (dB) is the difference between received signal powers to the threshold signal power at the receiver. Link margin is calculated based on the meteorological data obtained at Bhubaneswar city under different climate conditions. The link margin is useful to predict the possibility of FSO link in an optical network to satisfy the quality of services for a web route for data transmission [5].

$$L_{\mathrm{marigin}} = P_{\mathrm{e}} - |S_{\mathrm{R}}| - A_{\mathrm{geo}} - A_{\mathrm{haze}} - A_{\mathrm{sci}} \tag{5}$$

where L_{marigin} is the link margin (dB), P_{e} is the total emitter power (dBm), $\mathrm{S_R}$ is the receiver sensitivity, A_{geo} is the geometrical attenuation, A_{haze} is haze attenuation, and A_{sci} is scintillation attenuation.

3 Results and Discussion

The above system has been simulated in MATLAB environment with the FSO system parameters taken as per the real scenario. The system parameters are laser source power, receiver sensitivity, transmitter and receiver aperture area, operating wavelength, and beam divergence. The values are 13.8 dBm, −65 dBm, 0.025 and 0.08, 850 nm and 1550 nm, and 2 mrad, respectively. Figure 1 shows the measured visibility data distribution for Bhubaneswar city from August 1, 2018, to October 31, 2018. The data are collected from Indian Metrological Department (IMD) for the Bhubaneswar city (India). The readings are taken on an hour basis for individual day. Then, the average value of each day has been considered for the analysis. About 2300 data were collected for these three months. Figure 2 shows the variation of the scattering coefficient with average visibility. The size distribution is considered for two different wavelengths to obtain the plot. The dimension of scattering particles is taken into consideration as $(0.585)^{1/3}$. It was observed that for 850 nm wavelength, the scattering coefficient showed a higher value under average visibility compared to 1550 nm wavelength in simulation result. Furthermore, the wavelength of 850 nm was much more scattered than 1550 nm wavelength. Figure 3 shows the plot between beam divergence angles to link distance at an operating wavelength of 1550 nm. It

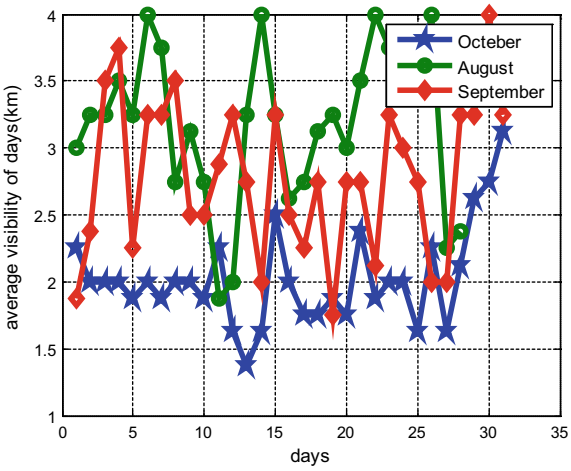

Fig. 1 Measured visibility data distribution for Bhubaneswar city from August 1, 2018, to October 31, 2018

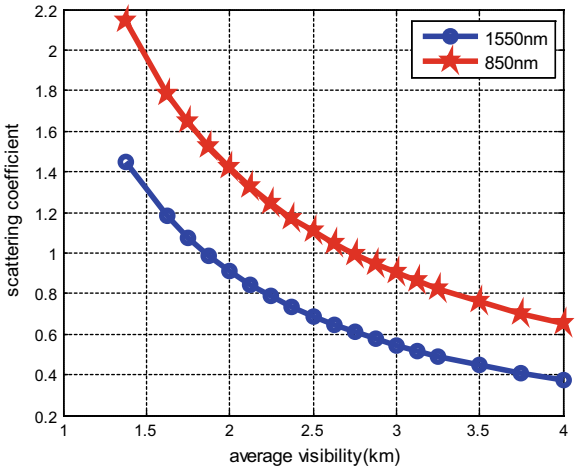

Fig. 2 Scattering coefficient versus average visibility for two different wavelengths of 850 and 1550 nm

is observed that for a minimum value of divergence angle of 2 mrad, the geometric loss is 5–40 dB for a link distance of 0.5–3 km with a receiver aperture of 0.08 m. This is best suitable for FSO system in the city. Whereas for divergence angle of 10 mrad, the geometric loss is 35–70 dB for a link distance of 0.5–3 km which is not at all suitable for the FSO system. Figure 4 shows the graph between attenuation loss versus the link distance between transmitter and receiver. It is observed from the plot that the third window of optical signal with frequency of operation of 1550 nm has very immune to first window optical signal with an operating frequency of 850 nm. The achieved link distance is a prime factor for the evaluation of a FSO system. From equation −2, it is clear that the attenuation directly depends on the operating wavelength. It is concluded that 1550 nm is useful.

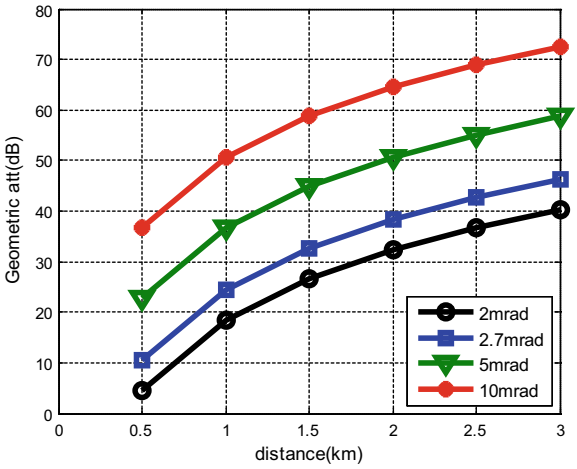

Fig. 3 Geometric loss versus distance (km) for different divergence angle

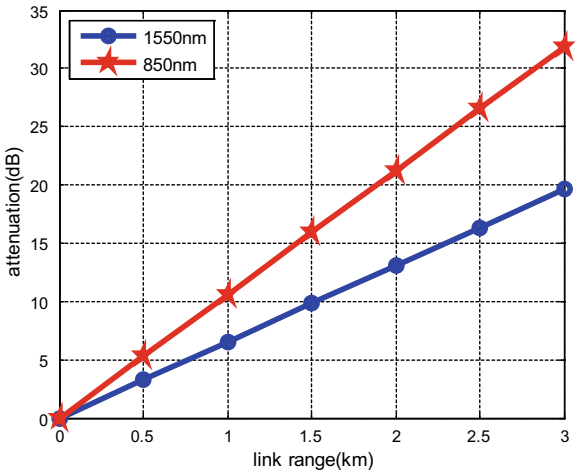

Fig. 4 Atmospheric attenuation versus transmission range of 0.5–3 km for wavelength of 850 and 1550 nm

Figure 5a, b shows the total attenuation at 1550 and 850 nm wavelength versus link distance for different visibility. At a lowest visible distance, the system with 1550 nm working wavelength shows a loss of 44 dB, whereas for the system with 850 nm the loss is 65 dB at a link distance of 3 km. Similarly, at the highest visible distance, the system with 1550 nm working wavelength shows a loss of 12 dB, whereas for the system with 850 nm the loss is 20 dB at a link distance of 3 km. It is found that the attenuation effects are lowest at 1550 nm compared to 850 nm for different visibility data.

Finally, the link margin of the FSO system has been calculated by varying the link distance from 0 to 3 km at visibility distance of 1.395, 2.95, and 4.00 km. To calculate the link margin, here we have considered the haze attenuation and the

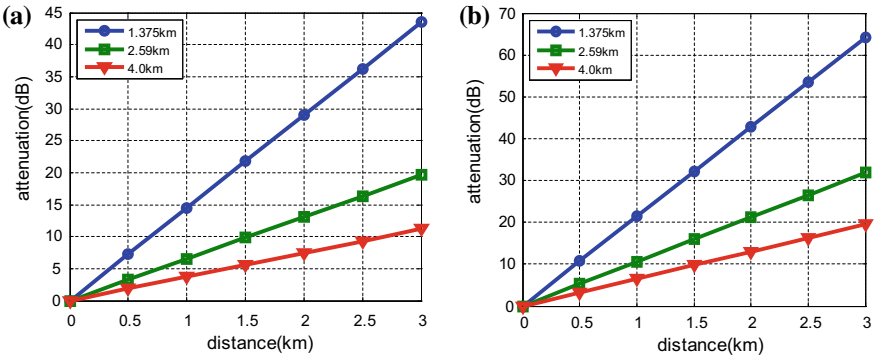

Fig. 5 **a** Total attenuation versus link distance (km) at different visibility levels for 1550 nm. **b** Total attenuation versus link distance (km) at different visibility levels for 850 nm

Table 2 Link margin at different visibility data for a link distance of 0–3 km of the FSO system

Link distance	Visibility = 1.395 km		Visibility = 2.957 km		Visibility = 4.0 km	
(km)	1550 nm	850 nm	1550 nm	850 nm	1550 nm	850 nm
0	Inf	Inf	Inf	Inf	Inf	Inf
0.5	79.39489	75.92968	83.3696	81.33737	84.77415	83.37918
1	58.28547	51.35505	66.23489	62.17044	69.04399	66.25406
1.5	42.92907	32.53407	54.85383	48.75715	59.06748	54.88259
2	29.92958	16.06874	45.82843	37.69952	51.44662	45.86677
2.5	18.22024	0.894188	38.09379	27.93267	45.11654	38.14172
3	7.327336	−13.4639	31.1756	18.98225	39.6029	31.23312

geometric attenuation. The emitted transmitter power is 13.8 dBm, and the receiver sensitivity is −65 dBm. It is found from the observed result as shown in Table 2. The link margin is highest for the system with a working wavelength of 1550 nm compared to its counterpart not only at lowest visibility but also at highest visibility.

4 Conclusion

In this paper, we analyzed the effect of different atmospheric attenuation parameters from the real-time data collected from the Indian Metrological Department (IMD) for the Bhubaneswar city (India). As we know, the link reliability is an important parameter for FSO-based network; hence, the adverse impact of climate change on FSO has been investigated for two wavelengths that are 850 and 1550 nm. It is found that the impact on FSO communication with 1550 nm wavelength is less, as signal

attenuation is greatly reduced. Therefore, the 1550 nm wavelength is more preferred for FSO communication. Also, the link margin for different visibility range obtained for 1550 nm wavelength was better than at 850 nm wavelength. It is concluded that 1550 nm wavelength is highest. The system analysis can further be analyzed for a different model of visible data distribution. The system may further be expanded by considering the turbulence effect and its impact to the performance of the system. Also, the analysis may be extended for complete year weather data exploration for different climate condition.

Acknowledgements The authors of the paper are very much thankful to the Indian Metrological Department (IMD) for providing real-time data for the analysis and performance measuring of FSO system. Also, the authors are very much thankful to Dr. Prasant Kumar Sahu, IIT Bhubaneswar, for his valuable support and guidance.

References

1. Seeds A, Shams H, Fice M, Renaud C (2015) TeraHertz photonics for wireless communications. J Lightwave Technol 33:579–587
2. Dabiri M, Sadough S (2018) Performance analysis of all-optical amplify and forward relaying over log-normal FSO channels. J Opt Commun Netw 10:79
3. Shumani M, Abdullah M, Suriza A (2016) The effect of haze attenuation on free space optics communication (FSO) at two wavelengths under Malaysia Weather. In: International conference on computer & communication engineering, pp 459–464
4. Mansour Abadi M, Ghassemlooy Z, Zvanovec S, Bhatnagar M, Khalighi M, Wu Y (2017) Impact of link parameters and channel correlation on the performance of FSO systems with the differential signaling technique: errata. J Opt Commun Netw 9:1062
5. Khalighi MA, Uysal M (2014) Survey on free space optical communication: a communication theory perspective. IEEE Commun Surv Tutor 16:2231–2258. https://doi.org/10.1109/COMST.2014.2329501
6. Wang Z, De Zhong W, Fu S, Lin C (2009) Performance comparison of different modulation formats over free-space optical (FSO) turbulence links with space diversity reception technique. IEEE Photonics J 1:277–285. https://doi.org/10.1109/JPHOT.2009.2039015
7. Popoola W, Ghassemlooy Z, Leitgeb E (2009) BER and outage probability of DPSK subcarrier intensity modulated free space optics in fully developed speckle. J Commun 4
8. Agrawal GP (2002) Fiber-optic communications systems, 3rd edn.
9. Majumdar AK (2005) Free-space laser communication performance in the atmospheric channel. J Opt Fiber Commun Rep 2:345–396. https://doi.org/10.1007/s10297-005-0054-0

Design and Analysis of SRR-Inspired Ultra Wideband Antenna

Ritesh Kumar Saraswat, Antriksh Raizada and Himanshu Garg

Abstract The paper presents a compact and low cost SRR-based ultra wideband (UWB) antenna for wireless communication. The proposed antenna has the operability to cover the UWB range from 3.1 to 10.6 GHz. It is design on Forgotten Realms 4 (FR-4) substrate having a thickness of $h = 1.6$ mm with a trapezoidal-shaped feedline as well as ground plane. Radiating patch consists of splits rings are utilized in the regular 8-sided polygon to get better results. The proposed antenna with compact size of $22 \times 32 \times 1.6$ mm^3 is analyzed with the help of simulated results. In overall, UWB band antenna has steady radiation characteristics.

Keywords Mictrostrip trapezoidal-shaped feedline · Octagonal polygon ring · Split-ring resonator · Ultra wideband

1 Introduction

In present scenario, UWB technology is emerging field for wireless communication system which is increasing rapidly. UWB system plays an important role in communication system such as pulse radar where UWB antenna is the key element for such systems. UWB technology has been proposed for various wireless applications as imaging radar, localization, and indoor communication [1].

The federal communication commission (FCC) allocated the frequency band from 3.1 to 10.6 GHz authorized for ultra wideband (UWB) range. Due to the UWB range, the field of broadband antenna design for wireless systems is emerging rapidly and new challenges are also arising in this research process [2]. The UWB antenna is operating over wider bandwidth for impedance matching with omnidirectional radiation

R. K. Saraswat · A. Raizada · H. Garg (✉)
Manikya Lal Verma Textile & Engineering Govt. College, Bhilwara, Rajasthan, India
e-mail: himanshugarg2989@gmail.com

R. K. Saraswat
e-mail: ritesh.saraswat9@gmail.com

A. Raizada
e-mail: antrikshraizada13@gmail.com

V. Janyani et al. (eds.), *Optical and Wireless Technologies*, Lecture Notes in Electrical Engineering 648, https://doi.org/10.1007/978-981-15-2926-9_48

characteristics. Due to wider bandwidth, it reduces fading and multipath effect with low-power requirements. UWB radio system is transmitting the short duration pulses with more effectively and accurately for small range. UWB applications are becoming very popular because of reliability, security, and high speed data transmission over smaller distances. For the UWB system implement a compact size microstrip patch antenna for transmitting as well as receiving purpose for wireless communication applications [3–6]. The designing of small-size microstrip patch antenna with good performance is quite a challenging task [7, 8].

In this article, a compact split-ring resonator (SRR)-based polygon ring is proposed covering the major UWB wireless applications. The proposed antenna comprises an 8-sided polygon structure followed by several iterations with slits for better results in the required operating frequency. The advantage of employing a polygon ring is that it provides more area to be covered with less amount of electrical contact or material and hence, it facilitates the antenna design to be small and compact with cost effectiveness. Thus, the designed antenna has a very compact size, low profile, and low cost. The design considerations and the most significant antenna characteristics are presented in the subsequent sections.

2 Proposed Antenna Configuration

The UWB antenna has a dimension of 22×32 mm^2 and is been fabricated on a 4.3 permittivity Forgotten Realms 4 (FR-4) substrate having a thickness of $h = 1.6$ mm, as shown in Fig. 1. The trapezoidal-shape microstrip line is used for supplying antenna having dimension $L_8 = 3.16$ mm, $L_7 = 2.2$ mm and $L_{11} = 11$ mm to provide better impedance match with the coaxial cable connector. It has a trapezoidal-shape

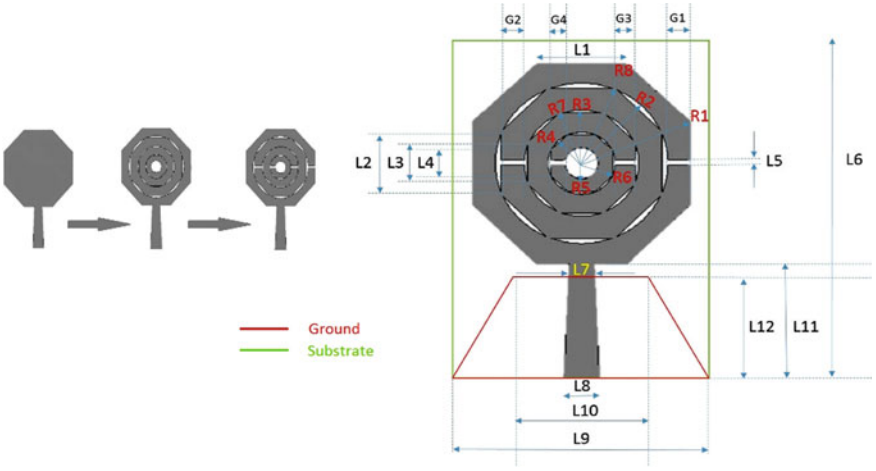

Fig. 1 Evolution of the proposed antenna

ground plane having dimension $L_9 = 22$ mm, $L_{10} = 10$ mm, and $L_{12} = 9.5$ mm which provides good radiation characteristics in the desired direction and also provides better gain and directivity. Firstly, an 8-sided polygon ring is designed having a radius of 10.5 mm and an edge length of 8 mm as the radiating patch. Then the radiating patch is modified by etching cylinder with radius 7.7 mm and drawing another polygon ring with radius of 7.8 mm and edges of length 6 mm. The etching of cylinder and drawing of polygon ring are continued for next three iterations with different radius and edge length. Then, the slots are etched with length equal to polygon ring and having similar width of 0.5 mm for each polygon ring.

The radiating patch consists of four different polygon rings having radius as follows $R_1 = 10.5$ mm, $R_8 = 7.8$ mm, $R_7 = 5.2$ mm, and $R_6 = 3.02$ mm and these have an edge length of $L_1 = 8$ mm, $L_2 = 6$ mm, $L_3 = 4$ mm, and $L_4 = 2.5$ mm, respectively. The final antenna dimensions after series of parametric studies are as follows, $L_5 = 0.5$ mm, $L_6 = 32$ mm, $G_1 = 2.1$ mm, $G_2 = 2.2$ mm, $G_3 = 2$ mm, $G_4 = 1.4$ mm, $R_2 = 7.7$ mm, $R_3 = 5.1$ mm, $R_4 = 3$ mm, and $R_5 = 1.5$ mm. The image of the proposed antenna is shown in Fig. 1. The structure of the radiating patch and its characteristics are modified to provide better performance in the operating UWB band [8–10].

3 Result and Discussion

Simulations of proposed octagonal ultra wideband monopole antenna are performed by using the appropriate simulator. The feedline width (L_7, L_8) and the shape (Trapezoidal) of the conventional octagonal ultra wideband monopole antenna play an important role in determining the range of frequencies upon which the antenna could function [8–10].

3.1 Return Loss Characteristics

As shown in Fig. 2, the impedance bandwidth after simulation for $|s11| < -10$ dB is found in the range from 3.0 to 14.1 GHz. This frequency band covers the UWB frequency band ranging from 3.1 to 10.6 GHz. The UWB band is observed below the -10 dB mark as represented by Fig. 2.

3.2 Gain of Antenna

Figure 3 represents the proposed antenna 3D gain plots which are observed and simulated for a number of resonant frequencies such as 2.4, 5.4, 7.5, and 10.0 GHz and also for distinct values of phi and theta in maximum radiation direction. It can

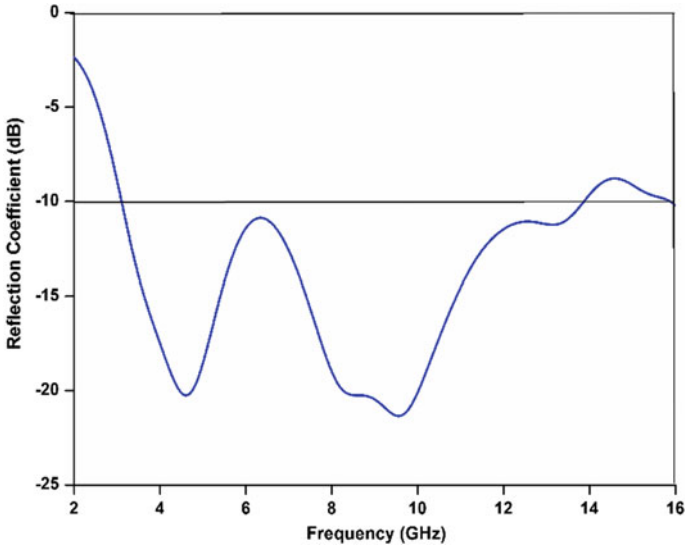

Fig. 2 Simulated return loss characteristics of the proposed antenna

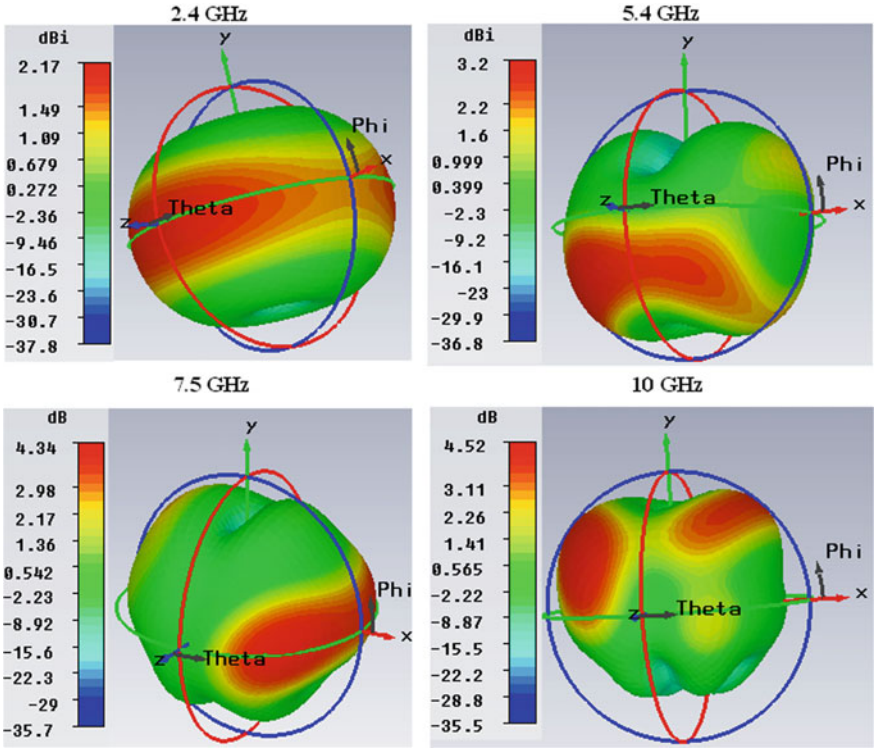

Fig. 3 Simulated gain (dB) of the proposed UWB antenna for different frequencies

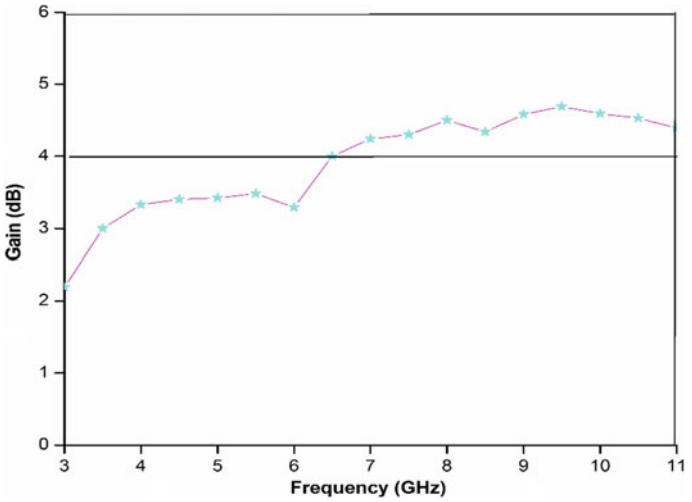

Fig. 4 Gain of the proposed design in UWB range for simulation mode

also be observed that at lower frequency levels (<6 GHz), the gain starts decreasing below the 4 dB reference level, whereas it starts improving for higher frequency levels (>6 GHz). Also with increasing frequency, the directivity increases, so that the gain is improved [11, 12]. The gain of UWB antenna design is shown in Fig. 4. It can be concluded that the antenna has an acceptable gain of 3.7 dB in UWB mode [11–14].

3.3 Radiation Efficiency

As shown in Fig. 5, the simulated radiation efficiency of the proposed antenna varies in the range of 98.9–78.5% in case of UWB mode. So, we can conclude that in all operating bands, the antenna maintains its efficiency above 70% and it starts decaying with increment of frequency [11–14].

3.4 E-Plane and H-Plane Radiation Patterns

The radiation patterns of the proposed design for principle E- and H-plane are indicated in Figs. 6 and 7, respectively. These radiation patterns are plotted for some selected frequencies such as 2.4, 5.4, 7.5, and 10 GHz. They are plotted for two

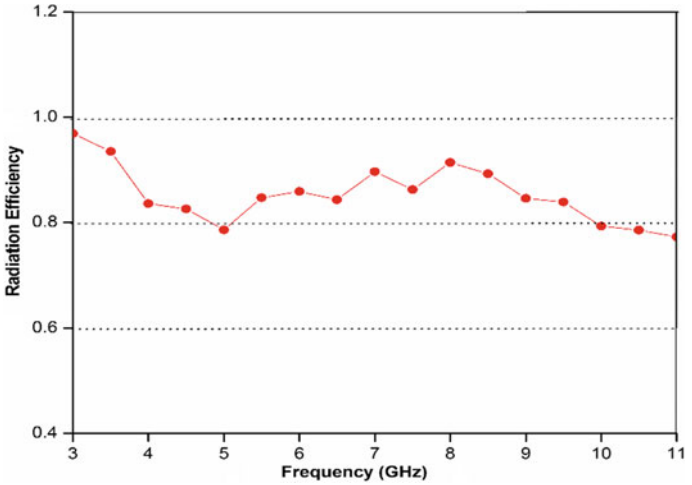

Fig. 5 Simulated radiation efficiency of the proposed UWB antenna

different planes (E-Plane and H-Plane). It can be observed from Fig. 6 that the E-Plane radiation pattern is quasi-omnidirectional in nature, whereas from Fig. 7 that H-Plane radiation pattern resembles dumb-bell shape [12–14]. It can be observed from the radiation patterns that they are stable with respect to frequency.

4 Conclusion

A UWB octagonal shape SRR-based antenna covering UWB band having frequencies from 3.1 to 10.6 GHz are evaluated with gain, efficiency, and radiation patterns presented in this paper. The radiating element consists of pairs of octagonal concentric split rings single-port antenna which can find wide applications in UWB band such as imaging radar, communication, and localized application.

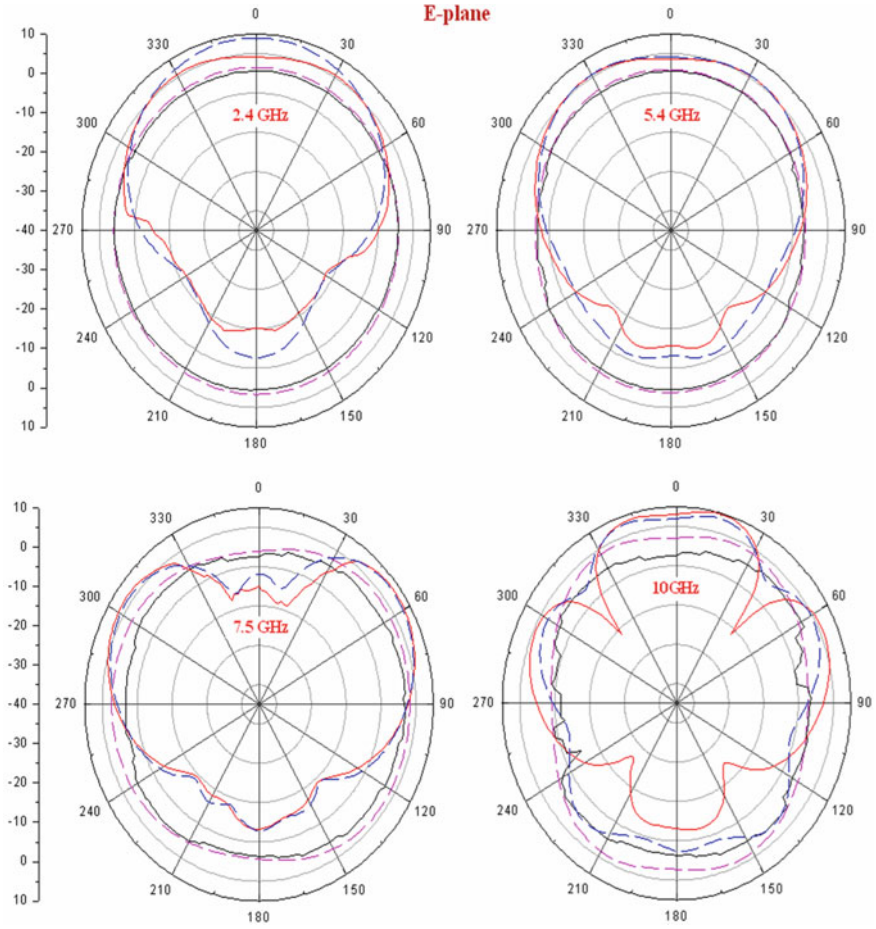

Fig. 6 E-plane radiation pattern at different frequencies for the proposed antenna

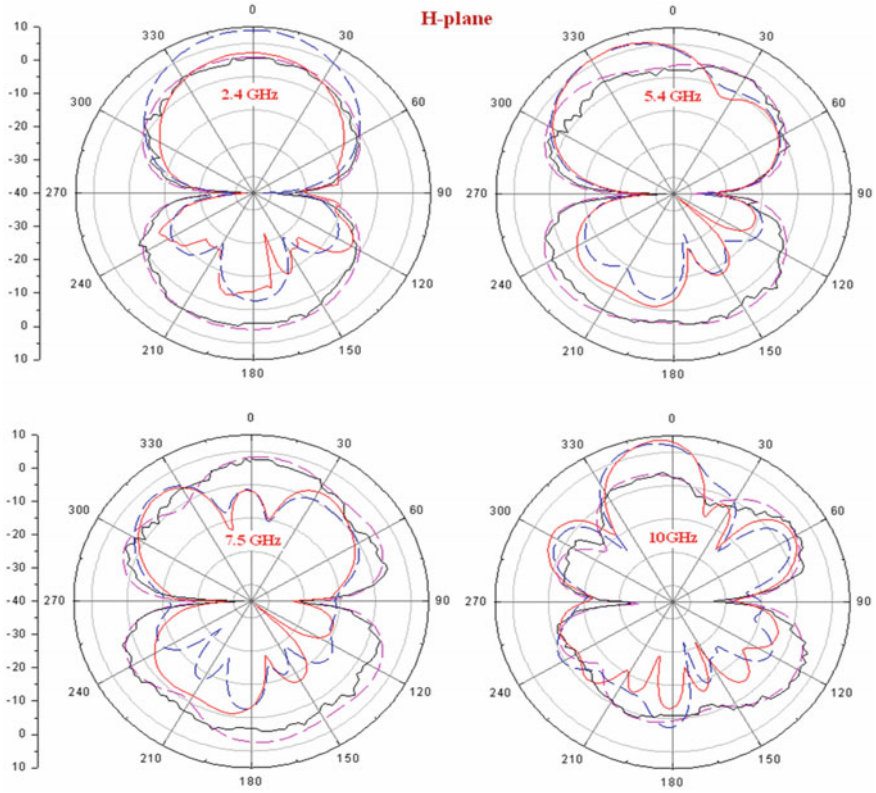

Fig. 7 H-plane radiation pattern at different frequencies for the proposed antenna

References

1. Aiello GR, Rogerson GD (2003) Ultra-wideband wireless systems. IEEE Microwave Mag 4(2):36–47
2. Breed G (2005) A summary of FCC rules for ultra wideband communications. High Frequency Electronics, 42–44 (2005)
3. Liang JX, Choo CC, Dong CX, Parini CG (2005) Study of a printed circular disc monopole antenna for UWB systems. IEEE Trans Antennas Propag 53(11):3500–3504
4. Aanandan CK (2007) Square monopole antenna for ultra wide band communication applications. J Electromagn Waves Appl 21(11):1525–1537
5. Geran F, Dadashzadeh G, Fardis M, Hojjat N, Ahmadi A (2007) Rectangular slot with a novel triangle ring microstrip feed for UWB applications. J Electromagn Waves Appl 21(3):387–396
6. Xiao JX, Yang XX, Gao GP, Zhang JS (2008) Double printed Ushape ultra-wideband dipole antenna. J Electromagn Waves Appl 22(8):1148–1154
7. Liu L, Xiong JP, Yin YZ, Zhao YL (2008) A novel dual F-shaped planar monopole antenna for ultra wideband communications. J Electromagn Waves Appl 22(9):1106–1114
8. Saraswat RK, Chaturvedi AK, Sharma V, Jagmohan (2016) Slotted ground miniaturized UWB antenna metamaterial inspired for WLAN and WiMAX applications. In: IEEE international conference on computational intelligence and communication networks (CICN), India, pp 213–216

9. Saraswat RK, Kumar M (2015) A frequency band reconfigurable UWB antenna for high gain applications. Prog Electromagn Res B 64:29–45
10. Saraswat RK, Kumar M (2016) Miniaturized slotted ground UWB antenna loaded with metamaterial for WLAN and WiMAX applications. Prog Electromagn Res B 65:65–80
11. Saraswat RK, Kumar M (2015) A reconfigurable patch antenna using switchable slotted structure for polarization diversity. In: IEEE international conference communication systems and network technologies (CSNT-2015), India, pp 11–14
12. Saraswat RK, Kumar M, Gurjar S, Singh CP (2015) A reconfigurable polarized antenna using switchable slotted ground structure. In: IEEE international conference communication systems and network technologies (CSNT-2015), India, pp 15–19
13. Saraswat RK, Kumar M (2016) Planar frequency-band reconfigurable switchable slotted ground UWB antenna. In: IEEE international conference communication systems and network technologies (CSNT-2016), 5–7 Mar 2016, India
14. Saraswat RK, Kumar M, Ram G, Singh A (2016) A reconfigurable microstrip bowtie patch antenna with pattern diversity. In: IEEE international conference communication systems and network technologies (CSNT-2016), 5–7 Mar 2016, India

Secrecy Performance Analysis for Multi-hop and Single-Hop Relaying Model

Shweta Pal and Poonam Jindal

Abstract Physical layer security is the foremost concept for providing security to a wireless communication network. Three-hop wireless relaying model consisting of single source and destination node, along with two relay nodes and an eavesdropper, is analysed in this paper. Performance analysis of this multi-hop network is done by comparing different parameters of it with a conventional single-hop wireless model. The results demonstrated that secrecy rate improves by increasing the distance between relay and eavesdropper (*R-E*) and distance d_{E} for all the cases. On the other hand, it is found that the increase in relay-to-destination distance d_{RD} and distance d_{EH} results in decreasing secrecy performance. Furthermore, an increase in value of path loss exponent degrades the system's performance. For all cases, AF protocol improves secrecy rate by 11.9% for single-hop while 42.86% for multi-hop scenario as compared to DF protocol.

Keywords Physical layer security · Amplify-and-forward · Decode-and-forward · Multi-hop network · Secrecy rate

1 Introduction

With the advent of growing advancement in wireless network, communication nowadays becomes more prone to various security breaches that make the network insecure. Physical layer security (PLS) has emerged as a new archetype which has gained a lot of importance among research areas for providing security to wireless communication network. It has been observed that in PLS, a secure communication without any key exchange is obtained, provided that channel capacity of main channel is better than that of channel capacity of wiretap channel. Gaussian wiretap channel expresses this conclusion in a more precise and illustrative way in [1], where positive secrecy rate is obtained using different cooperative schemes. The range of a

S. Pal (✉) · P. Jindal
Department of Electronics and Communication Engineering, National Institute of Technology Kurukshetra, Kurukshetra, Haryana, India

P. Jindal
e-mail: poonamjindal81@nitkkr.ac.in

V. Janyani et al. (eds.), *Optical and Wireless Technologies*, Lecture Notes in Electrical Engineering 648, https://doi.org/10.1007/978-981-15-2926-9_49

wireless network is generally large enough, so whenever two remotely nodes want to communicate with each other, a strong signal link between both of them is essential [2]. Cooperative communication, which was proposed earlier, is an effective way to achieve this for a basic single-hop conventional network. However, for better coverage extension, multiple relays are connected in series. Such network where communication from source end to destination end is carried out through a number of relay nodes is termed as multi-hop network (MHN). The concept of MHN involves reducing the transmission power of each participating node and thus apparently leads to shorter frequency reuse distance and lower interference level [3]. In comparison with single-hop network, multi-hop relaying network is a favourable solution for extending the coverage area of a single access point and thus enhances the system's performance for different wireless communication network especially for wireless sensor network (WSN), Internet of Things (IoT) and small-scale indoor networks.

Whenever the source-to-destination condition of the channel is poor as compared to the source-to-eavesdropper channel condition, positive secrecy rate is difficult to obtain. To countermeasure this situation, various node cooperation approaches were utilised [4], where in order to enhance the secrecy rate, multiple relay nodes are made to cooperatively work together. In order to improve secrecy rate further [5], relays are designed in such a fashion so as to choose one of the three different modes of operation: cooperative jamming (CJ), decode-and-forward (DF) and amplify-and-forward (AF). MHNs based on half-duplex amplify-and-forward protocol are presented in [6] to improve the network coverage of a region, and however, since multiple phases of time are deployed in it, it suffers loss in spectral efficiency. Recently, path combining and the path selection schemes are introduced in [7] for MHNs so that high-performance gain can be obtained. While the abovementioned work considered a relaying model with dual-hop, a secure communication via multi-hop relaying system is worth inspecting in which multiple hops are taken for transfer of information.

A three-hop wireless relaying system consisting of a single source node, single destination node along with two relay nodes and an eavesdropper is considered in this paper. A conventional multi-hop relaying model is considered in [8], whose secrecy performance is being compared with conventional single-hop wireless relaying model. Further, the manuscript is categorised as follows. The system model for multi-hop relaying network is introduced in Sect. 2. Achievable secrecy rate for both single- and multi-hop models is calculated in Sect. 3. Section 4 presents the performance analysis, followed by the conclusion in Sect. 5.

2 System Model

System model for single-hop relaying network is depicted in Fig. 1 [9], which employ a single source node point (S), single destination node point (D), a relay node (R), a passive eavesdropper (E) and a power beacon node (B). Noise present at each of the individual network node is assumed to be AWGN, i.e. additive white gaussian noise

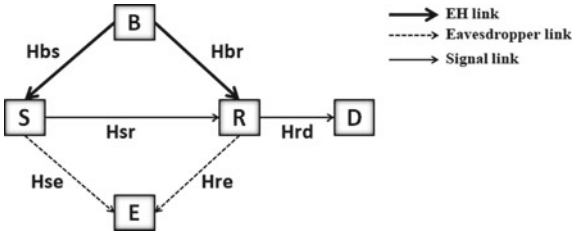

Fig. 1 System model for a single-hop relaying model

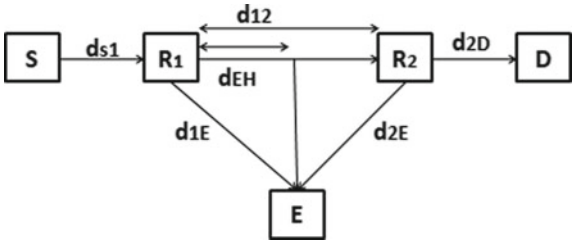

Fig. 2 System model for a multi-hop relaying network

with variance $= \sigma^2$ and mean $= 0$. Complex channel gains related from S to E, S to R, R to E, R to D, B to R and B to S are represented as H_{SE}, H_{SR}, H_{RE}, H_{RD}, H_{BR}, H_{BS} resp. and there is no self-interference found in the system.

Performance of this conventional single-hop network is compared with a 3-hop multi-relaying model [10] consisting of a single source and single destination node point, one eavesdropper node and two trusted relays R_1 and R_2 as depicted in Fig. 2.

During the first transmission phase, each of the relay nodes performs decode-and-forward technique by interpreting or decoding the message signal from the prior adjoining node. In the next transmission phase, it re-encodes and retransmits this message signal towards destination. In this paper, it has been considered that both destination and relay nodes suffer from propagation loss and receive signal from their prior adjoining node only, whereas eavesdropper may overhear source as well as relays message [11, 12]. The type of fading effect experienced by channels is flat fading. Complex channel gains from to S to R_1, R_1 to E, R_2 to E, R_1 to R_2 and from R_2 to D are denoted by H^*_{S1}, H^*_{1e} H^*_{2e} H^*_{12} and H^*_{2D}, respectively. Similar to single-hop, here also noise at each individual node is assumed to be complex AWGN, i.e. additive white gaussian noise with variance $= \sigma^2$ and mean $= 0$ and no direct link between S-E is possible. After receiving the desired signal from the prior adjoining node, each of the relay node transmit a jamming signal while operating in a full duplex mode. Self-interference signal at each of the FDR is perfectly cancelled.

2.1 DF Protocol

It is a decode-and-forward protocol involving 2-stage process. During first transmission stage, the information signal $w(N)$ is transmitted from S to R_1 and simultaneously jamming signal $j(2N)$ is transmitted from R_1 to E as described in Fig. 3. The signals received at relay and eavesdropper for $2N$th time slot is given [12] as:

$$Y_1(2N) = \sqrt{P_S} H_{s1} w(N) + n_1(2N) \tag{1}$$

$$Y_E(2N) = \sqrt{P_S} H_{se} w(N) + \sqrt{P_{1j}} H_{1e} j(2N) + n_E(2N) \tag{2}$$

where P_{1j} is jamming power of relay R_1 to E, $n_1(2N)$ is AWGN noise present at R_1, $n_E(2N)$ is AWGN noise present at E.

In the second stage, relay performs decoding followed by encoding of received signal. Finally, this re-encoded version is forwarded to destination and jamming signal $j(2N + 1)$ is simultaneously transmitted to eavesdropper by R_2 as depicted in Fig. 4. Received signals at E and D during $(2N + 1)$th time slot are given as:

$$y_E(2N + 1) = \sqrt{P_1} H_{1e} w(N) + \sqrt{P_{2j}} H_{2e} j(2N + 1) + n_E(2N + 1) \tag{3}$$

$$y_D(2N + 1) = \sqrt{P_2} H_{21} w(N) + n_2(2N + 1) \tag{4}$$

where P_{2j} is the jamming power present at R_2, and $n_2(2N + 1)$ is AWGN noise present at R_2.

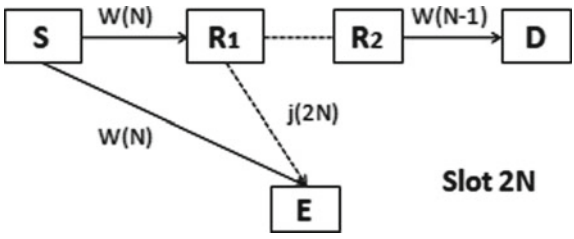

Fig. 3 Transmission of signal during $2N$th time slot

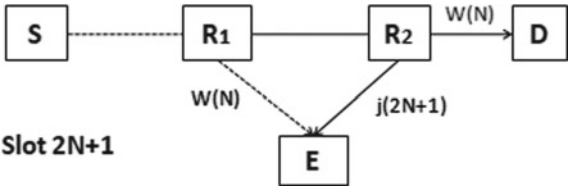

Fig. 4 Transmission of signal during $(2N + 1)$th time slot

2.2 AF Protocol

It is also a dual-stage process similar to DF scheme. In the first stage, S sends signal to R which is overheard by E simultaneously. Signal reached at both R and E is mathematically represented by Eqs. (5) and (6). Signals arrived at R and E during this stage are also same as represented in Eqs. (4) and (3). In the next stage, source S transmits a jamming signal $j(2N)$ towards E, whereas R forwards amplified version of the received signal towards D. Received signals at nodes D and E at $(2N + 1)$th time slot are given as [13].

$$y_D(2N+1) = G\sqrt{P_2}H_{21}y_R(2N) + n_2(2N+1) \tag{5}$$

$$y_E(2N+1) = G\sqrt{P_1}H_{1e}y_R(2N) + \sqrt{P_{2j}}H_{2e}j(2N+1) + n_E(2N+1) \tag{6}$$

where G is the scaling factor given as $G = \frac{1}{\sqrt{P_1.|H_{1e}|^2+N_0}}$, and N_0 is the AWGN noise variance.

3 Achievable Secrecy Rate

In this paper, secrecy rate has been evaluated as a performance metric. Achievable secrecy rate is characterised as the rate at which source transmits a message signal to a receiver through a secure and reliable link. It is generally evaluated in terms of secrecy capacity which is given by the following expression:

$$C_S = [C_T - C_E]^+ \tag{7}$$

where C_E and C_T are the eavesdropper channel and data transmission capacity, respectively, and $[X]^+ = \max(X, 0)$. Achievable secrecy rate for both single- and multi-hop with DF and AF cooperation protocols is given as:

3.1 Single-Hop Relay Network

3.1.1 DF Protocol

Using Eqs. (1), (2), (3) and (4), rate of signal transmission at D and E is given as [14]

$$R_D = 0.5\log_2(1 + P_r\gamma_{RD}) \tag{8}$$

$$R_E = 0.5\log_2\left(1 + \frac{P_s\gamma_{SE}}{1 + P_{rj}\gamma_{RE}} + \frac{P_r\gamma_{RE}}{1 + P_{sj}\gamma_{SE}}\right) \tag{9}$$

where $\gamma_{RD} = \frac{|H_{rd}|^2}{\sigma^2}$, $\gamma_{SE} = \frac{|H_{se}|^2}{\sigma^2}$, $\gamma_{RE} = \frac{|H_{re}|^2}{\sigma^2}$. Further, secrecy rate is calculated using Eqs. (8) and (9) as $R_s = \max\{R_D - R_E, 0\}$, where

$$R_D - R_E = 0.5\log_2\left(\frac{1 + P_r\gamma_{RD}}{1 + \frac{P_s\gamma_{SE}}{1+P_{rj}\gamma_{RE}} + \frac{P_r\gamma_{RE}}{1+P_{sj}\gamma_{SE}}}\right) \tag{10}$$

3.1.2 AF Protocol

Using (1), (2), (5) and (6), rate of transmission at D and E is given as [13]

$$R_D = 0.5\log_2\left(1 + G^2(P_s\gamma_{RD})\right) \tag{11}$$

$$R_E = 0.5\log_2\left(1 + \frac{P_s\gamma_{SE}}{1 + P_{rj}\gamma_{RE}} + \frac{G^2P_s\gamma_{RE}}{1 + P_{sj}\gamma_{SE}}\right) \tag{12}$$

where $\gamma_{RD} = \frac{|H_{rd}|^2}{\sigma^2}$, $\gamma_{SE} = \frac{|H_{se}|^2}{\sigma^2}$, $\gamma_{RE} = \frac{|H_{re}|^2}{\sigma^2}$. Secrecy rate is again calculated using Eqs. (11) and (12) as: $R_s = \max\{R_D - R_E, 0\}$, where

$$R_D - R_E = 0.5\log_2\left(\frac{1 + G^2P_r\gamma_{RD}}{1 + \frac{P_s\gamma_{SE}}{1+P_{rj}\gamma_{RE}} + \frac{G^2P_s\gamma_{RE}}{1+P_{sj}\gamma_{SE}}}\right) \tag{13}$$

3.2 Multi-hop Relay Network

3.2.1 DF Protocol

The transmission rates at D and E are given as:

$$R_D = 0.5\log_2(1 + P_2\gamma_{2D}) \tag{14}$$

$$R_E = 0.5\log_2\left(1 + \frac{P_1\gamma_{1E}}{1 + P_{2j}\gamma_{2E}} + \frac{P_2\gamma_{2E}}{1 + P_{1j}\gamma_{1E}}\right) \tag{15}$$

where $\gamma_{2D} = \frac{|H_{2d}|^2}{\sigma^2}$, $\gamma_{1E} = \frac{|H_{1e}|^2}{\sigma^2}$, $\gamma_{2E} = \frac{|H_{2e}|^2}{\sigma^2}$. We compute the achievable secrecy rate using Eqs. (14) and (15) as $R_s = \max\{R_D - R_E, 0\}$, where

$$R_D - R_E = 0.5 \log_2 \left(\frac{1 + P_2 \gamma_{2D}}{1 + \frac{P_1 \gamma_{1E}}{1 + P_{2j} \gamma_{2E}} + \frac{P_2 \gamma_{2E}}{1 + P_{1j} \gamma_{1E}}} \right) \tag{16}$$

3.2.2 AF Protocol

Using Eqs. (5), (6), (11) and (12), rate of transmission at node D and E is given as [14]

$$R_D = 0.5 \log_2 \left(1 + G^2 (P_1 \gamma_{2D})\right) \tag{17}$$

$$R_E = 0.5 \log_2 \left(1 + \frac{P_1 \gamma_{1E}}{1 + P_{2j} \gamma_{2E}} + \frac{G^2 P_2 \gamma_{2E}}{1 + P_{1j} \gamma_{1E}} \right) \tag{18}$$

where $\gamma_{RD} = \frac{|H_{rd}|^2}{\sigma^2}$, $\gamma_{SE} = \frac{|H_{se}|^2}{\sigma^2}$, $\gamma_{RE} = \frac{|H_{re}|^2}{\sigma^2}$. The achievable secrecy rate using Eqs. (17) and (18) is calculated as:

$\mathrm{R_s} = \max\{\mathrm{R_D} - R_\mathrm{E}, 0\}$, where

$$R_D - R_E = 0.5 \log_2 \left(\frac{1 + G^2 P_1 \gamma_{2D}}{1 + \frac{P_1 \gamma_{1E}}{1 + P_{2j} \gamma_{2E}} + \frac{G^2 P_2 \gamma_{2E}}{1 + P_{1j} \gamma_{1E}}} \right) \tag{19}$$

4 Performance Analysis

This section aims to present numerical results to investigate the secrecy performance of multi-hop relay system using both DF and AF techniques where level of security is improved with the help of relays operated in FDR mode. The performance of this system employing 3-hop multi-relaying network is evaluated in form of secrecy rate and is then compared with conventional single-hop wireless system. It is assumed that all the significant nodes including S, D, R_1 and R_2 are located in a LOS (line of sight) configuration as shown in Fig. 2, whereas E is located vertically away from the line. Also, all nodes are employed with equal power allocation (EPA) scheme. In Fig. 2, $d_{S1,}$ d_{12} and d_{2D} represent the distances from $S - R_1$, $R_1 - R_2$ and $R_2 - D$, respectively. Furthermore, the distance from relay R_1 to E (d_{1E}) and the distance from relay R_2 to eavesdropper $E(d_{2E})$ are computed with the help of $d_{1E} = \sqrt{d_E^2 + d_{EH}^2}$ and $d_{2E} = \sqrt{d_E^2 + (d_{12} - d_{EH})^2}$, respectively. In order to investigate effect of various distances on secrecy rate, we consider that the channel between any of the two nodes will follow a LOS model, i.e. $d^{-C/2} \mathrm{e}^{j\Phi}$, where '$d$' denotes distance between any two nodes, while 'Φ' is random phase distributed evenly within the range of

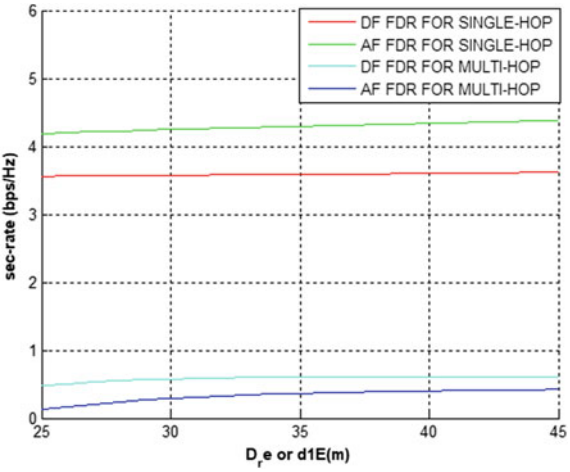

Fig. 5 Secrecy rate versus D_{re} or d_{1E}

$[0, 2\pi)$. All the simulation results are obtained using MATLAB R2014a software. In the following results, we assume noise power to be −30 dBm, total transmit power = 30 dBm [15], path loss exponent 'c' is 3.5 and conversion efficiency as unity.

Case 1: Secrecy rate versus relay-to-eavesdropper distance: Fig. 5 represents the plot of secrecy rate versus $\mathbf{D_{re}}$ or $d_{1E,}$ i.e. relay-to-eavesdropper distance using DF and AF schemes for both single-hop and multi-hop relay network. Parameters for conventional system are taken as: $D_{SR} = 10$ m, $D_{BR} = 7$ m, $D_{BS} = 7$ m and $D_{RD} = 15$ m, while for multi-hop network distance parameters are: $D_{S1} = 25$ m, $D_{12} = 25$ m, $D_{2D} = 30$ m and $D_e = 45$ m, $D_{eh} = 15$. Value of path loss exponent for both cases is 3.5. Results indicate that for both AF and DF techniques, there is a hike in secrecy rate with increase in D_{RE} (d_{1E}) for single- and multi-hop model.

Case 2: Secrecy rate versus relay-to-destination distance: Fig. 6 represents the plot of secrecy rate versus relay-to-destination distance, i.e. D_{RD} or d_{2D} for both single- and multi-hop model for DF and AF schemes with parameters for conventional system as: $D_{BR} = 7$ m, $D_{BS} = 7$ m $D_{SR} = 10$ m and $D_{RE} = 15$ m and for multi-hop model as: $D_{S1} = 25$ m, $D_{12} = 25$ m, $D_e = 45$ m, $D_{eh} = 15$ and $c = 3.5$. The plot illustrates that secrecy rate decreases as D_{RD} increases for both the cases.

Case 3: Secrecy rate Versus Path Loss Exponent (c): Fig. 7 shows the plot of secrecy rate w.r.t path loss exponent for both single- and multi-hop model. Parameters for conventional system are taken as: $D_{RD} = 15$ m, $D_{BR} = 7$ m, $D_{BS} = 7$ m and $D_{SR} = 10$ m and $D_{RE} = 15$ m, while for multi-hop network distance parameters are: $D_{S1} = 25$ m, $D_{12} = 25$ m, $D_{2D} = 30$ m, $D_e = 45$ m, $D_{eh} = 15$. It is indicated by the plot that transmission becomes less secure with increase in the value of path loss exponent as the channel performance degraded for both the cases.

Case 4: Secrecy Rate Versus $\mathbf{d_{EH}}$: Fig. 8 shows the plot of secrecy rate w.r.t. d_{EH} distance in the system for both single- and multi-hop system with conventional model parameters as: $D_{RD} = 15$ m, $D_{BR} = 7$ m, $D_{BS} = 7$ m and $D_{SR} = 10$ m and $D_e = 12$ m and multi-hop parameters as: $D_{S1} = 25$ m, $D_{12} = 25$ m, $D_{2D} = 30$ m and $D_e = 45$ m.

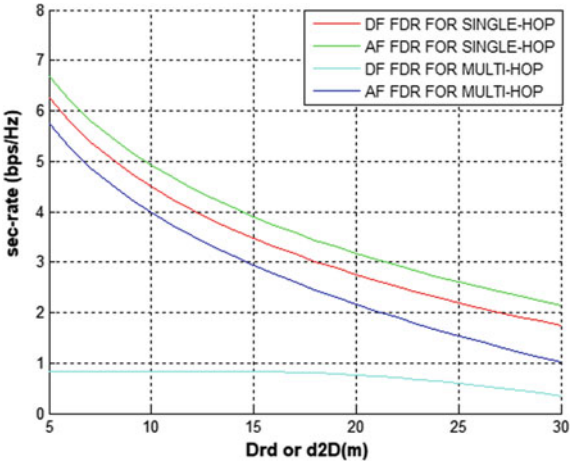

Fig. 6 Secrecy rate versus D_{RD} or D_{2D}

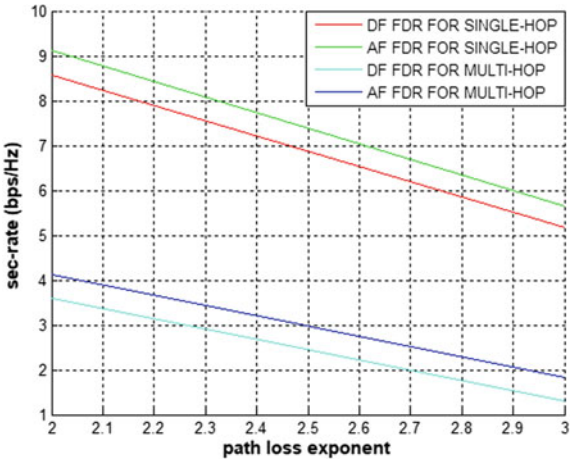

Fig. 7 Secrecy rate versus path loss exponent

Plot shows that when the distance between two relay nodes increases, secrecy rate decreases.

Case 5: Secrecy Rate Versus $\mathbf{d_E}$: Fig. 9 represents the plot of secrecy rate w.r.t d_E distance in the network model for both single- and multi-hop network using AF and DF schemes. Distance parameters for single-hop are: $D_{RD} = 15$ m, $D_{BR} = 7$ m, $D_{BS} = 7$ m and $D_{SR} = 10$ m and $D_{eh} = 8$ m and for multi-hop are: $D_{S1} = 25$ m, $D_{12} = 25$ m, $D_{2D} = 30$ m and $D_{eh} = 0$ m. It is shown that when the distance d_E increases, secrecy rate tends to decrease.

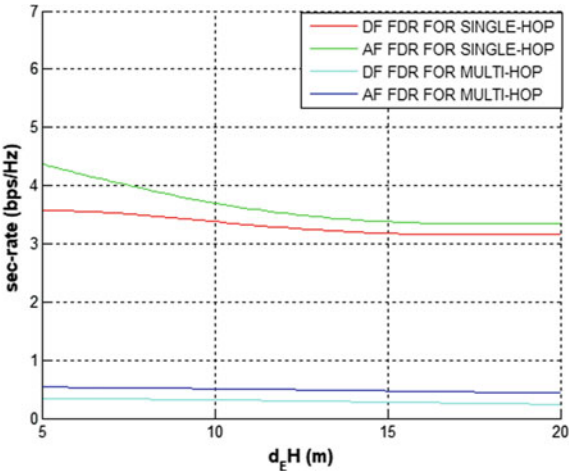

Fig. 8 Secrecy rate versus d_{EH}

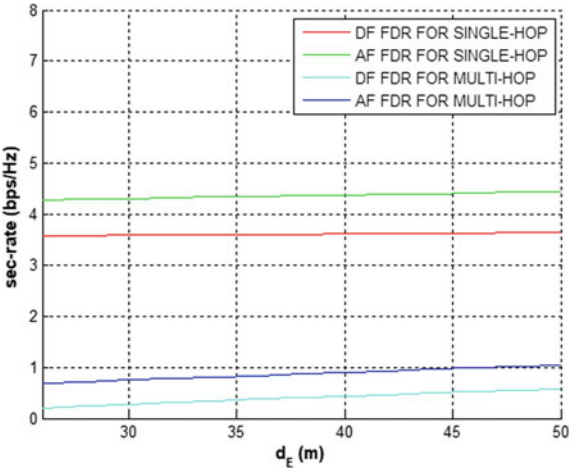

Fig. 9 Secrecy rate versus d_E

The results for the comparison between secrecy performance of both conventional and multi-hop network are illustrated in Table 1. AF performs better than DF for all the cases giving 11.87% better secrecy rate for single-hop and 42.86% for multi-hop network.

5 Conclusion

In this paper, we examine the secrecy performance of a 3-hop wireless relaying system model under total transmit power constraint of 30 dBm. A novel FDR approach for

Table 1 Performance comparison of single-hop and multi-hop network w.r.t their secrecy rate

Secrecy rate (bps/Hz)	Single-hop network		Multi-hop network	
	AF	DF	AF	DF
w.r.t d_E	3.78	3.42	0.6759	0.1735
w.r.t d_{EH}	4.36	3.56	0.5548	0.3632
w.r.t d_{rd}/d_{2D}	6.25	5.75	4.20	0.9967
w.r.t d_{re}/d_{1e}	3.89	3.47	0.3191	0.267
w.r.t path loss exponent	9.13	8.57	4.131	3.5995

multi-hop model has been implemented, where each FDR transmits jamming signal to E and simultaneously receives information signal from the prior node. Performance has been analysed for both DF and AF relaying techniques. Results demonstrated that secrecy rate improves by increasing D_{re} and d_E for all cases, while it tends to decrease for distance d_{RD} and d_{EH}. Furthermore, it has been observed that an increase in the value of path loss exponent degrades the system's performance. AF protocol improves secrecy rate by around 11.87% for single-hop while 42.86% for multi-hop network. Multi-hop wireless network is a favourable solution as compared to single-hop for extending the coverage area of a single access point and thus enhances the system's performance for wireless communication network but as far as secrecy performance is concerned, conventional system gives better results as compared to multi-hop model.

References

1. Xing C, Ma S, Fei Z, Wu Y, Poor HV (2013) A general robust linear transceiver design for multi-hop amplify-and-forward MIMO relaying systems. IEEE Trans Signal Process 61(5):1196–1209
2. Jain N, Dongariya A, Verma A (2017) Comparative study of different types of relay selection scheme for cooperative wireless communication. In: 2017 ICICIC, Aug 2017, pp 1–4
3. Gawtham KD, Jindal P (2017) Analysis of amplify and forward technique to improve secrecy rate in multi-hop relaying system. IEEE RTEICT, vol 6, Jan 2017, pp 2604–2614
4. Zheng G, Choo L, Wong K (2011) Optimal cooperative jamming to enhance physical layer security using relays. IEEE Trans Signal Process 59(3):1317–1322
5. Dong L, Han Z, Petropulu AP, Poor HV (2010) Improving wireless physical layer security via cooperating relays. IEEE Trans Signal Process 58(3):1875–1888
6. Farhadi G, Beaulieu NC (2009) Power-optimized amplify-and-forward multi-hop relaying systems. IEEE Trans Wireless Commun 8(9):4634–4643
7. Bhatnagar MR (2012) Performance analysis of a path selection scheme in multi-hop decode-and-forward protocol. IEEE Commun Lett 16(12):1980–1983
8. Nasir AA, Zhou X, Durrani S, Kennedy RA (2013) Relaying protocols for wireless energy harvesting and information processing. IEEE Trans Wireless Commun 12(7):3622–3636
9. Sinha R, Jindal P (2017) A study of physical layer security with energy harvesting in single hop relaying environment. In: 2017 SPIN, Feb 2017, pp 530–533
10. Sanguinetti L, DAmico AA, Rong Y (2012) A tutorial on the optimization of amplify-and-forward MIMO relay systems. IEEE J Sel Areas Commun 30(8):1331–1346

11. Li J, Petropulu AP, Weber S (2011) On cooperative relaying schemes for wireless physical layer security. IEEE Trans Signal Process 59(10):4985–4997
12. Long H, Xiang W, Zhang Y, Liu Y, Wang W (2013) Secrecy capacity enhancement with distributed precoding in multirelay wiretap systems. IEEE Trans Inf Forensics Secur 8(1):229–238
13. Kumar N, Bhatia V (2015) Performance analysis of amplify-and forward cooperative networks with best-relay selection over Weibull fading channels. Wireless Pers Commun 85(3):641–653
14. Lee JH (2015) Full-duplex relay for enhancing physical layer security in multi-hop relaying systems. IEEE Commun Lett 19(4):525–528
15. Lee J-H (2015) Full-duplex relay for enhancing physical layer security in multi-hop relaying systems. Access IEEE 19(4)

Investigation of Substrate Integrated Waveguide (SIW) Filter Using Defected Ground Structure (DGS)

Amrita Dixit, Ashok Kumar, Ashok Kumar and Arjun Kumar

Abstract In this paper, the behavior of substrate integrated waveguide (SIW) with conventional defected ground structures has been studied and compared their performance in terms of size reduction, quality factor, and filter selectivity. Various dumbbell-shaped defected ground structures (DB-DGS) have been investigated with SIW having filtering characteristics at 3-dB cutoff at 2 GHz by keeping the same dimension for all structures. This article holds good studies for beginners in filter designing. For comparative analysis, all the simulations have been carried out using HFSS 19.1.

Keywords Substrate integrated waveguide (SIW) filter · DB-DGS · *Q*-factor · High-frequency structure simulator (HFSS)

1 Introduction

In this modern era of mobile communication, the researchers are forced to take challenges for developing microwave and millimeter wave components with compact size, cost-effective, low profile, and enhanced performance. There are few popular technologies such as low-temperature co-fired ceramic (LTCC), low-temperature co-fired ferrite (LTCF) along with the structure such as photonic band gap (PBG), energy band gap (EBG), defected ground structure (DGS) that are available for improving the performance of the microwave components, and among all the above-mentioned techniques, DGS is very popular technique to reduce the component size with enhanced performance. In 2003, substrate integrated waveguide (SIW) filter

A. Dixit (✉) · A. Kumar · A. Kumar
School of Engineering and Applied Sciences, Bennett University,
Greater Noida, Uttar Pradesh 201310, India

A. Kumar
e-mail: arjun.kumar@bennett.edu.in

A. Kumar
Department of Electronics and Communication Engineering,
Govt. Women Engineering College, Ajmer, India

V. Janyani et al. (eds.), *Optical and Wireless Technologies*, Lecture Notes
in Electrical Engineering 648, https://doi.org/10.1007/978-981-15-2926-9_50

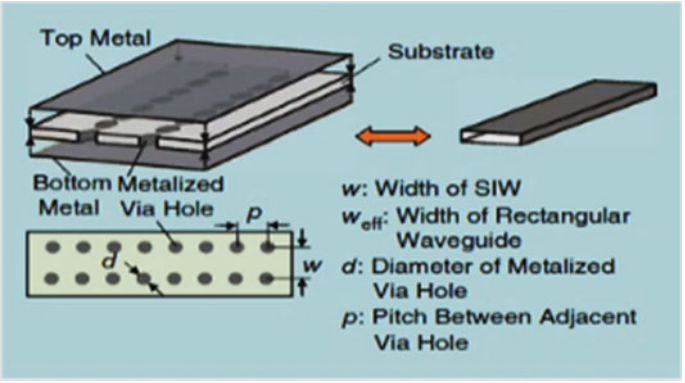

Fig. 1 An SIW and its equivalent rectangular waveguide [5]

was proposed which was having small size, low cost, and high Q-factor [1–4]. SIW is the best technique to convert non-planar structure to planar structure with high Q.

Low-temperature co-fired ceramic (LTCC) technology is used to synthesize SIW filter to convert a non-planar waveguide into planar form. The SIW is an artificial waveguide synthesized and constructed with rows of metalized via-holes embedded in the same substrate used for the planar circuit as shown in Fig. 1. In SIW, the side walls of rectangular waveguide are replaced by the rows of metallic via-holes which convert the conventional waveguide into planar structure. So, SIW has a property of high Q-factor and low radiation losses same as metallic waveguide with the advantage of compact size. SIW only supports the transverse electric modes. If TM mode generates it will create loss through unbounded via window along the transversal direction. Due to the absence of TM mode in SIW, leakage losses are low which create favorable condition for the bandpass filter design because certain mode problems due to out-of-band parasitic responses can be avoided. This gives a distinct feature to SIW technique for filter designing [6].

For reducing the size of the SIW filter, different techniques are used as SIW filter loaded with split ring resonator [7, 8], folded SIW filter [9, 10], combline SIW filter [11, 12], and half-mode SIW filter [13]. These applications have some drawbacks, such as low value of Q-factor and high insertion loss, so these methods have limited applications. Figure 2 shows the one example of conventional SIW filter with non-resonating node, CSRR DGS, and half mode.

2 Design Specifications/Goals

The design goals and the specification are shown in Table 1, and these specifications are used for designing various conventional DB-DGSs in this paper. In Table 1, the target resonance frequency is 2.5 GHz and the cutoff frequency is 2 GHz. For all

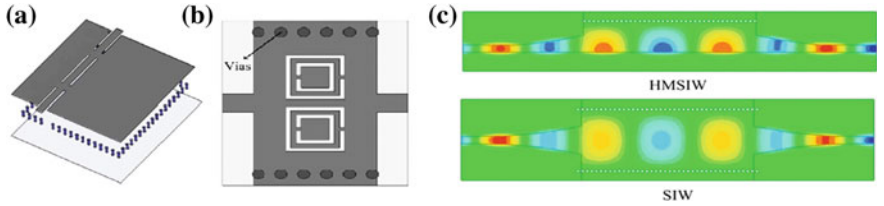

Fig. 2 **a** SIW filter with non-resonating node [7]. **b** SIW with square CSRR DGS [8]. **c** Field distribution in half-mode SIW filter (HMSIW) and SIW filter [13]

Table 1 Design goals and specifications

S. No.	Specification	Value
1	Cutoff frequency (f_c)	2 GHz
2	Insertion loss (S_{21})	<−0.8 dB
3	Reflection coefficient (S_{11})	>−15 dB
4	Neltec 9348(tm) dielectric constant (ε_r)	3.48
5	Loss tangent (δ)	0.003
6	Height of substrate	1.5 mm
7	Thickness of conducting plate	0.07 mm

DB-DGS, dimensions are kept constant for 2 GHz. The overall size of this SIW filter is 40 mm × 40 mm which is kept same for all the DB-DGS structures.

3 Design Configurations of Various DB-DGS

In this paper, the concept of defected ground structure (DGS) is introduced. DGS is most popular technique for the size reduction and bandwidth enhancement of the filter among the three basic techniques, i.e., photonic band gap (PBG), energy band gap (EBG), and DGS. In DGS, single or few geometrical slots are etched on the ground plane. This paper presents the performance of SIW filter with different DB-DGSs as shown in Fig. 3. In this paper, dumbbell-shaped pattern of DGS is used because it is simple and easy to design. Dumbbell-shaped DGS gives the slow wave effect in band gap and pass band. All dimensions are calculated for the SIW filter. In some research papers [14–16], different shapes of DGS structure are studied to achieve wide stopband, better selectivity, compact size, and lower insertion loss.

All different shapes of DGS are etched on the ground plane of SIW filter having the specification shown in Table 2.

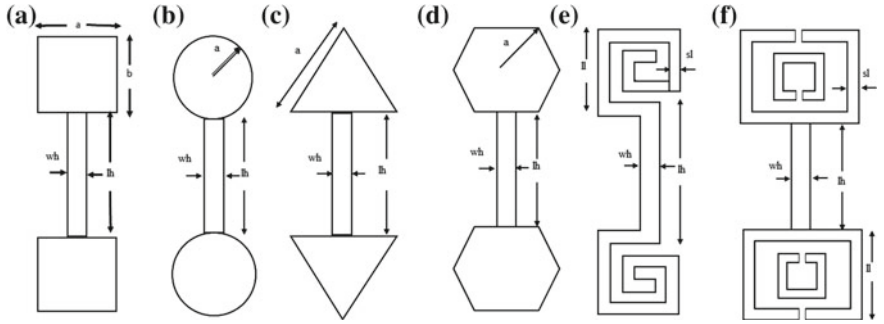

Fig. 3 Various shapes of DB-DGS, **a** square dumbbell, **b** circle-shaped dumbbell, **c** triangular-shaped dumbbell, **d** hexagonal-shaped dumbbell, **e** spiral dumbbell, and **f** CSRR DGS

Table 2 Dimensions of various DB-DGS structures at 2 GHz cutoff frequency

S. No.	Design configuration of DB-DGS	*a* (mm)	*b* (mm)	*lh* (mm)	*wh* (mm)	*sl* (mm)	*ll* (mm)
1	Square	4	4	6	1	–	–
2	Circle	3	–	6	0.5	–	–
3	Triangle	6	–	6.5	0.5	–	–
4	Hexagonal	5	–	10	3	–	–
5	Spiral	–	–	8	0.5	0.25	1
6	CSRR	–	–	8	0.5	0.5	0.5

4 *L-C* Equivalent Circuit Modeling of DB-DGS

The *L-C* equivalent of DB-DGS can be drawn in parallel combination as shown in Fig. 4. The value of effective capacitance (C), effective inductance (L), sharpness factor (SF), and quality factor (q-factor) can be computed using formulas [17–19].

Equivalent circuit of DB-DGS

$$C = \frac{5 f_C^2}{\pi \left[f_0^2 - f_C^2 \right]} \text{pF} \tag{1}$$

$$L = \frac{250}{C(\pi f_0)^2} \text{nH} \tag{2}$$

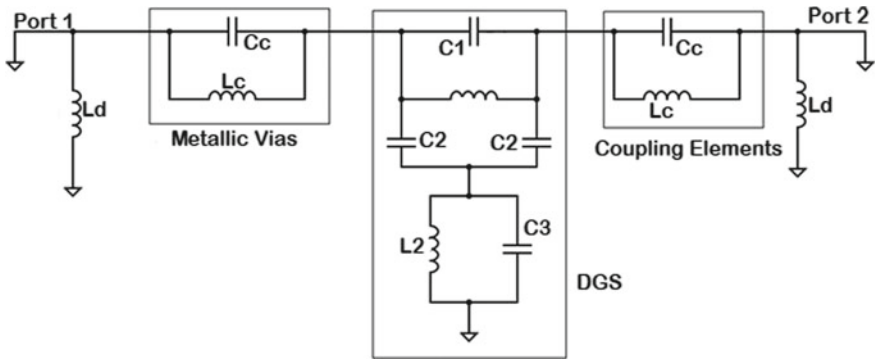

Fig. 4 Equivalent circuit of SIW with DGS [15]

$$\mathrm{SF} = \frac{f_\mathrm{c}}{f_0} \tag{3}$$

$$Q_\mathrm{L} = \frac{f_0}{\Delta f_3} \tag{4}$$

$$Q_\mathrm{e} = \frac{Q_\mathrm{L}}{10^{-IL/20}} \tag{5}$$

$$\frac{1}{Q_\mathrm{U}} = \frac{1}{Q_\mathrm{L}} - \frac{1}{Q_\mathrm{e}} \tag{6}$$

where f_c—cutoff frequency, f_0—resonant frequency, Δf_3—3-dB cutoff frequency, C—capacitance, L—inductance, SF—sharpness factor, Q_L—loaded Q-factor, Q_e—external Q-factor, Q_U—unloaded Q-factor

5 Study of Different Parameters of DB-DGS

Figure 5 shows the simulated S-parameter (S_{11}) of all DB-DGS structures. For all DB-DGS structures capacitance, inductance, Q-factor, and sharpness factor are calculated using the formula given in Eqs. (1)–(4). All calculated values are shown in Table 3. Filter dimensions are kept constant for all structures. The sharpness factor for all filters is approximately the same except the triangle-shaped DGS. For triangle-shaped DGS, the capacitance value is also small as compared to other structures. The capacitance and sharpness factor are related to each other . In all structures, CSRR

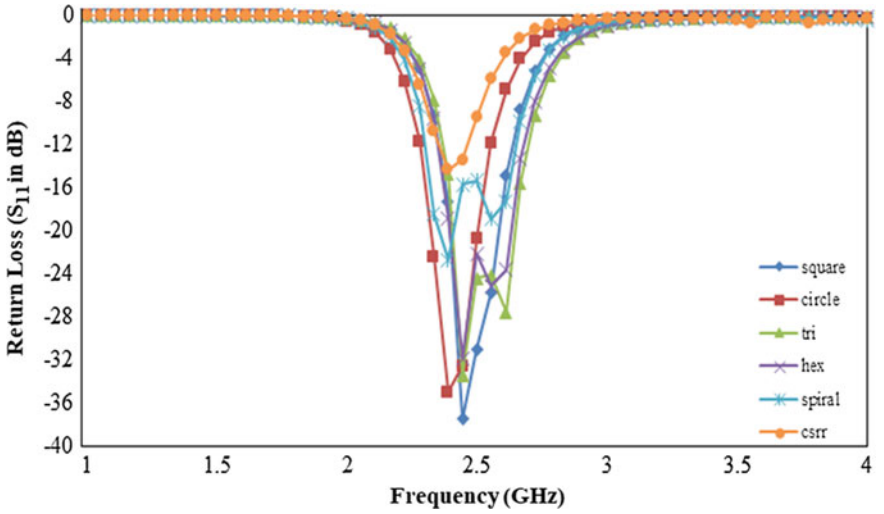

Fig. 5 *S*-parameters results of simulated proposed filter

has the highest capacitance and so its sharpness factor is also highest close to 0.933. For all DB-DGS structures, *Q*-factor is also calculated. Highest *Q*-factor is obtained in square- and circle-shaped DB-DGS. In Fig. 5, 3-dB cutoff frequency is almost the same for all DB-DGS structures and return loss graph shows that highest bandwidth is obtained in spiral-shaped DB-DGS structure. All structures have desired return loss greater than 10 dB.

6 Conclusions

In this paper, various topologies of DB-DGS are compared and analyzed. All DB-DGS configurations are simulated and compared with their return loss characteristics for the SIW filter. Highest quality factor is obtained 111.5 for square- and circle-shaped DGS while highest sharpness factor is obtained for CSRR structure. For the given structures, spiral-shaped DB-DGS has large bandwidth.

Table 3 Various parameters of different DB-DGS structures at 2 GHz cutoff frequency

S. No.	Design configuration of DB-DGS	Insertion loss (S_{21})	f_c 3-dB cutoff (GHz)	f_0 resonant frequency (GHz)	3-dB bandwidth (MHz)	Capacitance (C) in nF	Inductance (L) in nH	Q-factor	Sharpness factor
1	Square	0.369	2.24	2.44	540	3.81	1.12	111.56	0.918
2	Circle	0.369	2.22	2.44	540	3.44	1.23	111.56	0.909
3	Triangle	0.368	2.24	2.5	610	2.89	1.4	102.49	0.896
4	Hexagonal	0.394	2.23	2.45	600	3.45	1.22	96.56	0.91
5	Spiral	0.467	2.55	2.8	830	3.03	1.06	66.57	0.91
6	CSRR	0.755	2.22	2.38	330	4.8	0.93	87.23	0.933

References

1. Weng LH, Guo Y, Shi X, Chen X (2008) An overview on defected ground structure. Prog Electromagn Res 7:173–189
2. Hong JS, Karyamapudi BM (2005) A general circuit model for defected ground structures in planar transmission lines. IEEE Microw Wirel Compon Lett 15(10):706–708
3. Lim JS, Park JS, Lee YT, Ahn D, Nam S (2002) Application of defected ground structure in reducing the size of amplifiers. IEEE Microw Wirel Compon Lett 12(7):261–263
4. Dominic D, Wu K (2003) Single-substrate integration technique of planar circuits and waveguide filters. IEEE Trans Microw Theory Tech 51(2):593–596
5. Chen XP, Wu K (2014) Substrate integrated waveguide filter: basic design rules and fundamental structure features. IEEE Microw Mag 15(5):108–116
6. Wu K (2001) Integration and interconnect techniques of planar and nonplanar structures for microwave and millimeter-wave circuits status and future trend. In: Proceedings of Asia–Pacific microwave conference, Taipei, Taiwan, pp 411–416
7. Dong YD, Yang T, Itoh T (2009) Substrate integrated waveguide loaded by complementary split-ring resonators and its applications to miniaturized waveguide filters. IEEE Trans Microw Theory Tech 57(9):2211
8. Wei S, Sun XW, Yin WY, Mao JF, Wei QF (2009) A novel single-cavity dual mode substrate integrated waveguide filter with non-resonating node. IEEE Microw Wirel Compon Lett 19(6):368–370
9. Nikolaos G, Izquierdo BS, Young PR (2005) Substrate integrated folded waveguides (SIFW) and filters. IEEE Microw Wirel Compon Lett 15(12):829–831
10. Alotaibi SK, Hong JS (2008) Novel substrate integrated folded waveguide filter. Microw Opt Technol Lett 50(4):1111–1114
11. Barrera JD, Huff GH (2010) An adaptive SIW filter using vertically-orientated fluidic material perturbations. In: Adaptive hardware and systems (AHS), pp 205–208
12. Martinez JD, Sirci S, Taroncher M, Boria VE (2012) Compact CPW-fed combline filter in substrate integrated waveguide technology. IEEE Microw Wirel Compon Lett 22(1):7–9
13. Wang Y, Wei H, Dong Y, Liu B, Tang H, Chen J, Yin X, Wu K (2007) Half mode substrate integrated waveguide (HMSIW) bandpass filter. IEEE Microw Wirel Compon Lett 17(4):265–267
14. Shen W, Yin WY, Sun XW (2011) Compact substrate integrated waveguide (SIW) filter with defected ground structure. IEEE Microw Wirel Compon Lett 21(2):83–85
15. Liu C, An X (2017) A SIW-DGS wideband bandpass filter with a sharp roll-off at upper stopband. Microw Opt Technol Lett 59(4):789–792
16. Li W, Tang Z, Cao X (2017) Design of a SIW bandpass filter using defected ground structure with CSRRs. Act Passiv Electron Compon 2017
17. Rahman AB, Verma AK, Boutejdar A, Omar AS (2004) Control of bandstop response of Hi-Lo microstrip low-pass filter using slot in ground plane. IEEE Trans Microw Theory Tech 52(3):1008–1013
18. Kumar P, Mahmood R, Kishor J, Shrivastav AK (2009) Control of band stop responses of very compact size microstrip filter of improved Q factor & sharp transition by using hexagonal transmetal DGS. In: Emerging trends in electronic and photonic devices & systems, ELECTRO'09, pp 383–386
19. Papapolymerou J, Cheng JC, East J, Katehi LP (1997) A micromachined high-Q X-band resonator. IEEE Microw Guided wave Lett 7(6):168–170

Energy-Efficient MAC-ROUTE Cross-layer Optimal Distance Chain Protocol for Wireless Sensor Network

P. M. Prathibhavani and T. G. Basavaraju

Abstract Sensor nodes in wireless sensor networks (WSNs) are tiny devices with limited energy, computing ability, storage capacity, sensing capacity, and movement. The main issues accountable for energy expenditure in WSNs are numerous; among them, unnecessary high transmission range is the important issue to address. This chapter explores to optimize the energy consumption across MAC and network layers to prolong the lifetime of WSN. The energy efficiency must be supported across MAC, and network layers of protocol stack through a cross-layer design are highlighted in this work. In this context, designed MAC-ROUTE cross-layer technique for chain-based protocol addressed unnecessary high transmission range. The simulation is carried out using MATLAB, and it is observed that proposed protocol is efficient than existing chain-based routing protocols of WSN. The simulation result shows that proposed protocol accomplishes maximum network lifetime compared to existing chain-based routing protocols.

Keywords WSN · MAC-ROUTE · Network lifetime · Optimal distance · Chain based · Cross-layer

1 Introduction

Sensor nodes of WSNs are extensively used and are small in size, with special sensing capability and battery-powered with limited lifetime duration. The key purposes of WSN primarily consist of health monitoring, military, vehicles tracking, environmental monitoring (speed, temperature, pressure, and distance), home, and other commercial applications [1, 2]. Even though WSNs have extensive applications, limited transmission range and limited storage are some important demerits along with non-replenishable battery power [3–5]. By designing an energy-efficient and scalable routing algorithm, these limitations must be addressed [6–8].

P. M. Prathibhavani (✉)
Department of CSE, UVCE, Bangalore, India

T. G. Basavaraju
Department of CSE, Govt. S K S J T I, Bangalore, India

V. Janyani et al. (eds.), *Optical and Wireless Technologies*, Lecture Notes in Electrical Engineering 648, https://doi.org/10.1007/978-981-15-2926-9_51

Routing protocols' classification in WSN is divided into various categories based on flat, location, QoS, and hierarchical [9–11] deployment. In these available classifications, for network scalability and competent communication, hierarchical-based routing protocol is the most excellent choice in real-time application [12].

Clustering of nodes in large-scale WSN environments is required to achieve scalability and to prolong network lifetime [6–8, 13]. During clustering, entire network is divided into tiny groups called clusters; perhaps each group consists of number of group members and a cluster head. During data transmission, group member transmits their sensed data to their cluster head which aggregates in turn and transmits the same to sink using greedy algorithm [6, 7]. In small-scale cluster-based networks, the member nodes communicate to sink node with high power transmission when they are far away from the sink; this leads to less network lifetime [14].

Cluster-based protocols have disadvantage of dynamic cluster formation and communication with high power transmission which in turn directs to more energy expenditure. Chain-based routing protocol overcomes the disadvantages of dynamic cluster formation and high power transmission. Chain-based protocols are energy efficient by creating chain between cluster head and cluster member with possible short distance. In comparison with cluster-based protocol, the main drawback of chain-based protocol is high network delay [15]. Chain-based protocols address energy efficiency and delays to some extent with low load balance [16–19]. Sharing of information between MAC and network layer to schedule the optimal path improves the lifetime of network with less delay. Hence, it is required to design and implement chain-based cross-layer scheduling protocol called Energy-Efficient Cross-layer Optimal Distance Chain Protocol.

This research paper includes following sections. Section 2 includes literature survey, while Sect. 3 describes the analysis of existing protocols. Section 4 describes the operations of proposed protocol. Section 5 compares simulation outcomes of proposed and aforementioned methods. The last section concludes the paper with future scope.

2 Literature Survey

Lifetime maximization is considered as one of the key metrics to assess the accomplishment of WSN protocols, and the performance of WSN protocols is evaluated by one of the key metrics, Lifetime Maximization, tackled in the literature from various methods like data aggregation, energy-efficient routing, and radio optimization and sleep/wake-up schemes. In the WSN topology, low-energy adaptive clustering hierarchy (LEACH) [20] is one among the important clustering protocols. In LEACH, the entire network is partitioned into clusters, and each cluster will have an elected cluster head. Each cluster member node communicates to cluster head (CH), which in turn to base station (BS).

The hierarchical routing protocol, LEACH, reduces energy consumption with multi-hop communication than direct transmission protocols. Unfortunately, LEACH

suffers from many drawbacks such as LEACH is not suitable for dense network and adopts a randomized cluster head selection which leads to reduce the lifetime of network. To extend the lifetime of CH (ELCH) [21], the protocol is alienated into two phases, setup phase and steady-state phase. Neighbor selects the CH during setup phase based on the ratio of residual energy to distance. Sensed data gets collected at CH and transmits the same to BS through multi-hop transmission during steady-state phase. In EERA [22], forwarding node is selected as cluster head based on reliability and residual energy. Cluster head will have information of all its member nodes, and it stores the same in forwarding table [23]. CAMP divides the region into zones; each zone has some designated CH nodes. A non-cluster member transmits the data using intelligent routing process (IRP). Cluster not only performs routing but also involves in the overall routing process. This protocol is called cluster-aided multi-path routing.

Authors Khalid Haseeb et al. proposed [24] AECR protocol to improve energy conservation and data delivery performance, based on nodes' distribution and generate balanced-sized clusters to avoid random cluster formation. Protocol optimizes both intra- and inter-cluster routing paths for data delivery improvement and also reduces the excessive energy consumption with improving load distribution. Exploiting network conditions, CH shifted dynamically among nodes. In DCRR [25], CH selection is dynamic in the incident region according to residual energy. CH collects the data and sends the same to sink along the network backbone. Here CH can trace the changing period of incident and also nodes outside the cluster use this fluctuation to send data periodically.

In order to make chain-based hierarchical protocols compete with cluster-based routing protocols, some changes are necessary to incorporate in existing chain-based energy-efficient hierarchical routing protocols. PEGASIS [26] is one of the important energy efficient chain-based protocols in WSN. In this protocol, each member node communicates the sensed information with a neighbor node and conveys the same to BS through cluster head. In PEGASIS, chain formation and data communication method reduces the energy consumption and performs better in comparison with LEACH by about 100–300% for diverse network size and topologies. PEGASIS achieves better than LEACH in terms of scalability, robustness, and also lifetime by reducing the overhead of dynamic cluster formation.

Young-Long Chen et al. proposed phase-based coverage algorithm (PBCA) [27] with existing PEGASIS to find the redundant nodes and make them to sleep. PBCA simulation results perform better compared to LEACH and PEGASIS protocols. Authors Young-Long Chen et al. combine the PEGASIS with IBCA [28] to find surplus nodes and make them to sleep by means of IBCA. IBCA simulation results perform better compared to LEACH, PEGASIS, and PBCA protocols. MH-PEGASIS [29] is a variant of PEGASIS and is energy efficient than original PEGASIS [reference-EECBSIGIWSN]. Ideal PEGASIS is a variant of PEGASIS, where deployment is fixed and known locations are used to place nodes. Due to fixed placement location, the distance is same between each node that causes each node takes leadership position in turn. To extend network lifetime, authors [30] Young-Long Chen and Jia sheng Lin et al. proposed Intra-Grid PEGASIS. Grid PEGASIS

uses PEGASIS as base in association with grid. Compared to ideal PEGASIS and PEGASIS, network life time of Grid PEGASIS is better and energy consumption is similar to ideal PEGASIS with more delay.

This work deduced energy consumption of Grid PEGASIS and ideal PEGASIS is similar. Here design and implementation of novel MAC-ROUTE protocol is proposed called Energy-Efficient Cross-layer Optimal Distance Chain Protocol to address above-mentioned limitations.

3 Mathematical Energy Model of Ideal PEGASIS and Intra-Grid PEGASIS

To calculate total energy expenditure in each round, network uses data communication model to provide mathematical model. The transmission energy is $E_{\mathrm{Tx}}(l, d)$, where l bits of data packets transmit over distance d from transmission end to receiving end. Transmission energy $E_{\mathrm{Tx}}(l, d)$ is sum of transiting electron $E_{\mathrm{Tx\text{-}elec}}(l, d)$ circuitry energy and amplifier power $E_{\mathrm{Tx\text{-}amp}}(l, d)$ energy, shown in Eq. (1) [4].

$$\begin{aligned} E_{\mathrm{Tx}}(l, d) &= E_{\mathrm{Tx\ -\ elec}}(l, d) + E_{\mathrm{Tx\ -\ mp}}(l, d) \\ &= \begin{cases} E_{\mathrm{ele}} \times l + \varepsilon_{\mathrm{fs}} \times l \times d^2, d < d_0 \\ E_{\mathrm{ele}} \times l + \varepsilon_{\mathrm{mp}} \times k \times d^4, d \geq d_0 \end{cases} \end{aligned} \tag{1}$$

$$E_{\mathrm{Rx}}(l) = E_{\mathrm{ele}} \times l \tag{2}$$

where E_{elec} is electronic circuit's l bit of energy for transmission and $E_{\mathrm{Tx\text{-}amp}}(l, d)$ is the amplifier signal energy expenditure during communication process $l \times \varepsilon_{\mathrm{mp}} \times d^{\alpha}$. Based on threshold value $d_0 = \sqrt{\varepsilon_{\mathrm{fs}}/\varepsilon_{\mathrm{mp}}}$, data transmission will take place using multi-path or free space, where $\varepsilon_{\mathrm{fs}}$ is free space model, $\varepsilon_{\mathrm{mp}}$ is multi-path decay model, and α is attenuation exponent for wireless electromagnetic wave with value of 2 for free space and 4 for multi-path decay model. The energy consumption at the receiving end to receive l bits of information is $E_{\mathrm{Rx}}(l)$ shown in Eq. (2).

While in ideal PEGASIS, state is ideal that causes fixed placement and known location leads to leader position turn by each node. In this section, analysis of ideal PEGASIS and Intra-Grid PEGASIS energy consumption model is carried out. There are two types of nodes in ideal PEGASIS, mid-node and end node. To determine the energy required to complete one round based on two leader cases, i.e., end node and mid-node act as leaders.

In given network random deployment of N nodes in the region of $M \times M$ m^2, the spacing between each node d is the same, and then $d = \sqrt{E^2/N}$, where E is edge length. Energy consumption for electronic circuitry is E_{elec}, and energy consumption for data aggregation is E_{da}. Mid-node energy consumption is addition of received information from other sensor node, the aggregation of information, and final transmission of collected information to the next sensor node [4].

Mid-node energy consumption is given in Eq. (3)

$$E_{\text{mid}} = E_{\text{elec}} \times l + E_{\text{da}} \times l \times 2 + E_{\text{elec}} \times l + l \times E_{\text{fs}} \times d^2 \tag{3}$$

End node energy consumption is given in Eq. (4)

$$E_{\text{end}} = E_{\text{elec}} \times l + l \times E_{\text{fs}} \times d^2 \tag{4}$$

To determine the whole energy required in one round under ideal PEGASIS network architecture is given as shown in Eq. (5).

$$E_{\text{rnd\_existing}} = 2N \times E_{\text{ele}} \times 2N \times E_{\text{da}} \times l + M^2 \times l \times E_{\text{fs}} + l \times E_{\text{mp}} \times d^4 \tag{5}$$

In paper [30], deduced mathematical model for ideal PEGASIS and proposed Intra-Grid PEGASIS topology to overcome limitations of ideal PEGASIS and extended the lifetime of WSN. Simulation results showed lifetime of Intra-Grid PEGASIS longer than PEGASIS and originate that energy expenditure in each round of ideal PEGASIS and Intra-Grid PEGASIS topology is alike.

4 Energy-Efficient Cross-layer Optimal Distance Chain Protocol (EECLODC)

To design mathematical model for proposed protocol, consider first-order radio model [17]. To extend network lifetime, in this section proposed Energy-Efficient Cross-layer Optimal Distance Chain Protocol (Fig. 1). To design proposed protocol, the concept of Euclidean distance to find optimal distance (minimum distance) in association with MAC-ROUTE cross-layer communication (source_address, destimation_address, midnode_address, leadernode_address) is used.

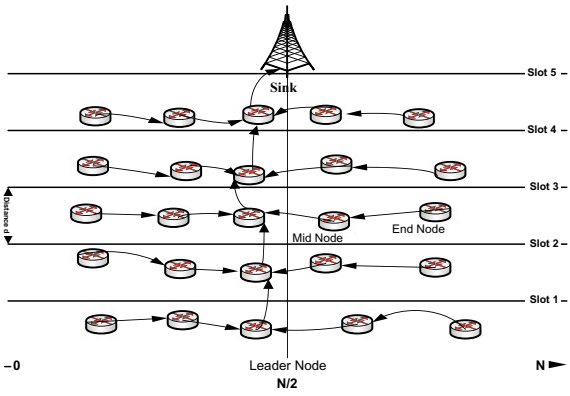

Fig. 1 Network architecture of EECLODC protocol

Proposed protocol is categorized into three stages, namely setup phase, chaining phase, and data communication phase, as discussed below.

A. **Setup phase**

Step 1. N number of sensors deployed randomly in an area 'A'.
Step 2. Divide an area 'A' vertically into two equal halves.
Step 3. Name two halves as left half ($A\_left = A/2$) and right half ($A\_right = A/2$).
Step 4. Find optimal distance 'dl' among left half using Euclidean.
Step 5. Repeat Step 4 to find optimal distance 'dr' among right half using Euclidean.
Step 6. Find minimum distance among '*dl*' and *'dr* and assign to 'd', where d = min(dl, dr).
Step 7. With distance 'd', divide the entire area horizontally into 'S_n' number of slots ($S_n = A/d$, where $n = 1, 2, 3, 4, \ldots$).

B. **Chaining phase**

Step 1. Among each slot, far node of *A_left* and *A_right* from mid of network elected as end node.
Step 2. Start chaining from end node simultaneously in both left half and right half.
Step 3. Elect leader node near to mid of network with high residual energy.

C. **Data communication phase**

Step 1. Initiate data communication from end node.
Step 2. Neighbor node fuses its data with end node and repeats till it reaches leader node.
Step 3. With multi-hops or single hop, leader node transmits data to sink node.
Step 4. Above steps repeat for all S_n slots.

In this research work, random deployment of N nodes in an area of $A = M \times M$ m^2. Divide an area 'A' vertically into two equal halves (*A_left*, *A_right*) and find optimal distance (dl, dr) among both the halves using Euclidean. Find minimum among these optimal distances using min(dl, dr) and assign to d. With distance d, divide the area A into S_n number of slots, i.e., $S_n = A/d$, where $n = 1, 2, 3, 4, \ldots$. Deployed sensor nodes will be dividing into three types of nodes—end nodes, mid-nodes, and leader nodes.

Energy consumed in mid-sensor (E_{mid}) is shown in Eq. (6)

$$E_{\text{mid}} = E_{\text{elec}} \times l + E_{\text{da}} \times l + l \times E_{\text{fs}} \times d^2 \tag{6}$$

Energy consumed in end sensor (E_{end}) is shown in Eq. (7)

$$E_{\text{end}} = E_{\text{elec}} \times l + l \times E_{\text{fs}} \times d^2 \tag{7}$$

Table 1 Simulation parameters

Parameter	Value
Network size	100 m × 100 m
E_{int}	0.25 J
Nodes	100
Location of BS	(50, 100)
E_{fs}	10 pJ/bit/m^2
E_{mp}	0.0013 pJ/bit/m^4
E_{da}	5 nJ/bit/signal
E_{ele}	50 nJ/bit
Radio attenuation exponent	Free space $\propto = 2$

Energy consumed in leader sensor (E_{leader}) is shown in Eq. (8)

$$E_{\text{leader}} = E_{\text{elec}} \times l + l \times E_{\text{mp}} \times d^4 \tag{8}$$

From above Eqs. (7), (8), and (9), the total energy consumption for one round of proposed protocol is shown in Eq. (10).

$$E_{\text{rnd\_proposed}} = E_{\text{end}} + n(E_{\text{mid}}) + E_{\text{leader}} \tag{9}$$

$$E_{\text{rnd\_existing}} > E_{\text{rnd\_ proposed}} \tag{10}$$

where n is number of hops between mid-node and leader node. Substituting the values of parameter shown in Table 1 into Eqs. (5) and (9) comes to the conclusion that proposed protocol is more energy efficient than ideal PEGASIS and Intra-Grid PEGASIS.

5 Results and Discussion

MATLAB simulation is used to validate mathematical Eq. (10) and to simulate network lifetime of proposed and existing protocols. Simulation is carried out for random deployment of 100 sensor nodes (Fig. 2) in the sensing area 100 m × 1 m, BS location is (50, 100) with energy of E_{ele} is 50 nJ/bit, E_{da} for each data is 5 nJ/bit/signal, and parameters are given in Table 1.

This section compares the network lifetime of proposed protocol (EECLODC protocol) with existing protocols, PEGASIS, Intra-Grid PEGASIS, and ideal PEGASIS. Figure 3 shows the network lifetime of PEGASIS, Intra-Grid PEGASIS, ideal PEGASIS, and proposed protocol, where the sensor area is divided randomly in an area of 100 m × 1 m with initial energy of E_{int} = 0.25 J. From Fig. 3 found that in PEGASIS, first node dies in round 270, in ideal PEGASIS, first node dies in round

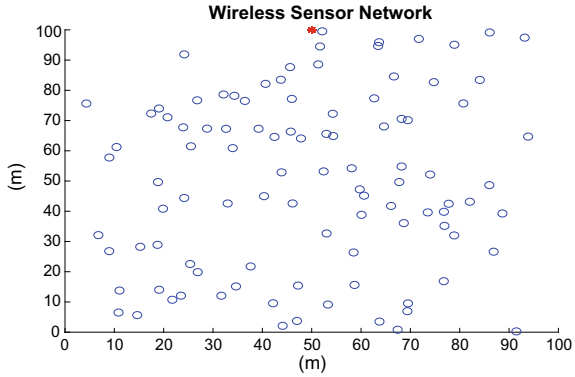

Fig. 2 100 m × 100 m node deployment

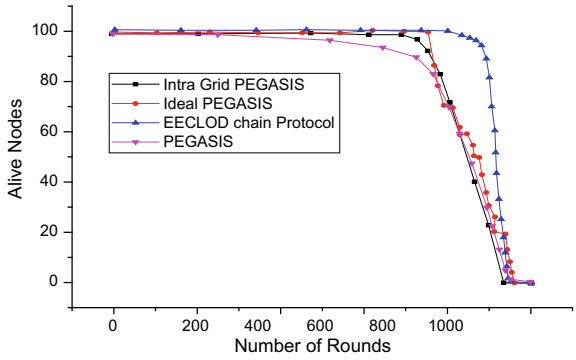

Fig. 3 Number of nodes alive versus number of rounds

601, in Intra-Grid PEGASIS, first node dies in round 562, and in proposed protocol first node dies in round 870, so stability period of proposed protocol is 35.40% more than existing protocol Intra-Grid PEGASIS. Figure 3 shows that the network lifetime of proposed protocol is better than the existing protocols.

Figure 4 shows energy consumed per transmission, and Fig. 5 depicts average consumption of energy by a node per transmission for proposed protocol. Above simulation results prove that the proposed protocol is better in terms of network lifetime, energy consumption, and average energy consumption than existing protocols.

6 Conclusion

This chapter explores to optimize the energy consumption across MAC and network layers to prolong the lifetime of WSN. The energy efficiency must be supported across MAC and network layers of protocol stack through a cross-layer design which is validated. In this context, designed MAC-ROUTE cross-layer technique for chain-based protocol addressed unnecessary high transmission range through optimal distance

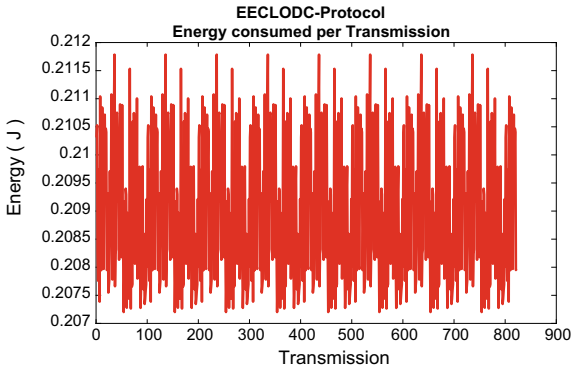

Fig. 4 Energy consumed per transmission

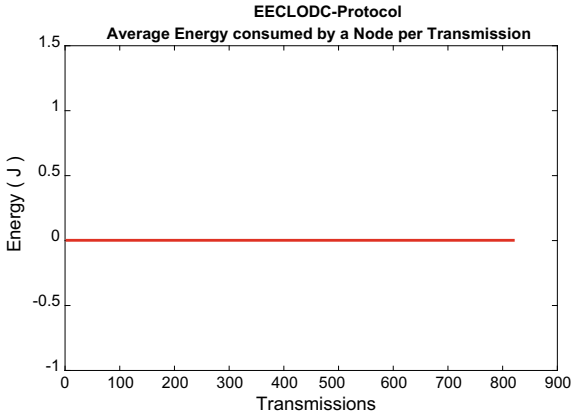

Fig. 5 Average energy consumed by a node per transmission

selection. The simulation is carried out using MATLAB, and it is observed that proposed protocol is efficient than existing chain-based routing protocols of WSN. The simulation result shows that proposed protocol accomplishes maximum network lifetime compared to existing chain-based routing protocols. As a future enhancement, optimize the proposed protocol using real-time testbed.

References

1. Tyagi S, Kumar N (2013) A systematic review on clustering and routing techniques based upon LEACH protocol for wireless sensor networks. J Netw Comput Appl 36(2):623–645
2. Guleria K, Verma AK (2018) Comprehensive review for energy efficient hierarchical routing protocols on wireless sensor networks. Wirel Netw 1–25
3. Shurman M, Al-Mistarihi M, Darabkh K (2013) Merging dynamic address auto configuration and security key protocols in mobile Ad hoc networks. In: Proceedings of 36th IEEE international convention on information and communication technology, electronics and microelectronics (MIPRO 2013), May 2013, pp 441–445

4. Shurman MM, Al-Mistarihi MF, Darabkh KA, Dynamic distribution of security keys and IP addresses coalition protocol for mobile Ad hoc networks. Automatika—J Control, Education and Sports of the Republic of Croatia
5. Khalifeh AF, AlQudah M, Darabkh KA (2017) Optimizing the beacon and superframe orders in IEEE 802.15.4 for real-time notification in wireless sensor networks. In: Proceedings of 2017 international conference on wireless communications, signal processing and networking (WiSPNET 2017), March, Chennai, India
6. Darabkh KA, Albtoush WY, Jafar IF (2017) Improved clustering algorithms for target tracking in wireless sensor networks. J Supercomput
7. Darabkh KA, Al-Rawashdeh Wala'a S, Al-Zubi RT, Alnabelsi SH (2017) C-DTB-CHR: centralized density- and threshold-based cluster head replacement protocols for wireless sensor networks. J Supercomput
8. Darabkh KA, Al-Rawashdeh Wala'a S, Hawa M, Saifan R, Ala'F K (2017) A novel clustering protocol for wireless sensor networks. In: Proceedings of 2017 international conference on wireless communications, signal processing and networking (WiSPNET 2017), March, Chennai, India
9. Bazzi HS, Haidar AM, Bilal A (2015) Classification of routing protocols in wireless sensor network. In: 2015 International conference on computer vision and image analysis applications (ICCVIA). IEEE, 18–20 Jan 2015, pp 1–5
10. Aaasser ME, Ashour M (2013) Energy aware classification for wireless sensor networks routing. In: Advanced communication technology (ICACT), pp 66–71
11. Dai S, Jing X, Li L (2005) Research and analysis on routing protocols for wireless sensor networks. In: Proceedings of international conference on communications, circuits and systems, vol 1, 27–30, pp 407–411
12. Xu DW, Gao J (2011) Comparison study to hierarchical routing protocols in wireless sensor networks. In: 3rd International conference on environmental science and information application technology (ESIAT 2011). Elsevier, Amsterdam, pp 595–600
13. Yadav S, Yadav RS (2016) A review on energy efficient protocols in wireless sensor networks. Wirel Netw 22(1):335–350
14. Tyagi S, Kumar N (2013) A systematic review on clustering and routing techniques based upon LEACH protocol for wireless sensor networks. J Netw Comput Appl 623–645
15. Darabkh KA, Al-Maaitah NJ, Jafar IF, Ala' FK (2017) EA-CRP: a novel energy-aware clustering and routing protocol in wireless sensor networks. Comput Electr Eng 1–17
16. Sen F, Bing Q, Liangrui T (2011) An improved energy-efficient PEGASIS based protocol in wireless sensor networks. In: Eighth international conference on fuzzy systems and knowledge discovery (FSKD), vol 4, pp 2230–2233
17. Salim A, Osamy W (2015) Distributed multi chain compressive sensing based routing algorithm for wireless sensor networks. Wirel Netw 21(4):1379–1390
18. Yueyang L, Hong J, Guangxin Y (2006) An energy-efficient PEGASIS based enhanced algorithm in wireless sensor networks. China Commun 91
19. Feng Sen, Qi Bing, Tang Liangrui (2011) An improved energy-efficient PEGASIS based protocol in wireless sensor networks. IEEE Conf 4:2230–2233
20. Heinzelman WR, Chandrakasan A, Balakrishnan H (2000) Energy-efficient communication protocol for wireless microsensor networks. In: Proceedings of the Hawaii international conference on system sciences, 4–7 Jan 2000. IEEE, pp 1–10
21. Lotf JJ, Bonab MN, Khorsandi S (2008) A novel cluster-based routing protocol with extending lifetime for wireless sensor networks. In: 5th IFIP international conference on WOCN'08. IEEE, pp 1–5
22. Shah NF, Gautam S, Gosain D et al (2016) EERA: energy efficient reliable routing algorithm for WSN. In: 2016 1st India international conference on information processing (IICIP). IEEE, pp 1–5
23. Sajwan M, Gosain D, Sharma AK (2018) CAMP: cluster aided multi-path routing protocol for wireless sensor networks. Wirel Netw 1–18

24. Haseeb K, Bakar KA, Abdullah AH, Darwish T (2017) Adaptive energy aware cluster-based routing protocol for wireless sensor networks. Wirel Netw 23(6):1953–1966
25. Guo B, Li Z (2009) A dynamic-clustering reactive routing algorithm for wireless sensor networks. Wirel Netw 15(4):423–430
26. Lindsey S, Raghavendra CS (2002) PEGASIS: power efficient gathering in sensor information systems. In: Proceedings, IEEE aerospace conference, vol 3, pp 3–1125
27. Chen Y-L, Wang N-C, Chen C-L, Lin Y-C (2011) A coverage algorithm to improve the performance of PEGASIS in wireless sensor networks. In: IEEE conferences, pp 123–127
28. Chen Y-L, Lin Y-C, Wang N-C (2012) An intersection based coverage algorithm for PEGASIS architecture in wireless sensor networks, vol 5, pp 1727–1731. IEEE
29. Aliouat Z, Aliouat M (2012) Efficient management of energy budget for PEGASIS routing protocol. In: IEEE conferences, pp 516–521
30. Chen Y-L, Lin J-S, Huang Y-F et al (2010) Energy efficiency of a chain-based scheme with intra-grid in wireless sensor networks. In: International symposium on computer control and automation, IEEE, pp 484–487

Baud Rate-Based Hierarchical Multihop Routing Protocol for WSNs

G. V. Sowmya and M. Kiran

Abstract In wireless sensor networks (WSNs), the data sensed by the sensor node are forwarded to the sink node either by direct communication or by multihop communication. The disadvantage of direct communication is that the sensor nodes consume more energy to reach the sink node as each sensor node has to work alone to reach the sink node, and if the sink node is too far, condition gets worsens. Contrary to direct communication, the multihop communication saves energy as it forwards the data to the nearest neighbor node which in turn forwards the data toward the sink node. In multihop communication, choosing the best neighbor node for forwarding the data is the most challenging task. Hence, in this article, a novel hierarchical multihop routing protocol for WSNs referred to as "*Baud Rate-Based Hierarchical Multihop Routing Protocol for WSNs*" has been proposed which uses Shannon channel capacity model 'C' and neighbor node distance to choose the best neighbor node; the chosen neighbor node will be capable of transmitting data with high baud rate, thereby increasing the throughput of the network. Further, the proposed model also increases the lifetime of the network as the nearest neighbor node will be chosen for the data transfer which saves the energy of the sensor node. The proposed algorithm is compared against the LEACH routing protocol and multihop LEACH protocol and is implemented in MATLAB. The quantitative and qualitative analysis of the simulation results depicts that the proposed algorithm performs better against the parameters *remaining energy of the sensor nodes, network lifetime,* and *data throughput* when compared to LEACH and multihop LEACH protocols.

Keywords Wireless sensor networks · Multihop routing · LEACH · Shannon channel capacity · Data collection

G. V. Sowmya (✉)
Jawaharlal Nehru National College of Engineering, Shimoga, Karnataka, India
e-mail: gvsowmya@jnnce.ac.in

M. Kiran
National Institute of Technology Karnataka, Suratkal, Mangalore, India

V. Janyani et al. (eds.), *Optical and Wireless Technologies*, Lecture Notes in Electrical Engineering 648, https://doi.org/10.1007/978-981-15-2926-9_52

1 Introduction

Wireless sensor networks (WSNs) contain large set of sensor nodes, randomly deployed in the environment for monitoring environment parameters such as temperature, pressure, and humidity. The data from environment are sensed by the sensor node and then delivered to the base station for further processing [1]. This method is called data collection, which is the basic function of WSNs. In data collection mechanism, each sensor node sends the data to the sink either by *direct communication* or by *multihop communication*. In direct communication, the sensor node depletes more energy as it has to reach the base station all alone, and the condition worsens when the sink node is too far. Thus, direct communication reduces the network lifetime. In multihop communication [2], all sensor nodes forward the data to its nearest neighbor node toward the base station using multihop path, and hence, it saves energy, thereby increasing the lifetime of the network. In multihop communication, selection of neighbor node along the path to the sink node is very important and is very challenging task. In the literature, many parameters are considered for selecting the best neighbor node for forwarding data to the sink node, namely hop count value and residual energy of node [3], weight of the node [4], etc. Through theoretical and simulation study, these parameters have been proven to be the good parameters for neighbor node selection.

As sensor nodes have limited resources, different parameters hinder its data transmitting capability such as low power, limited energy, limited buffer size, and limited bandwidth. Data rate of sensor node can be considered as an important parameter for neighbor node selection, as it contributes to the network throughput. Thus, in the proposed model among the pool of neighbor nodes, the node having the high data transmitting rate and nearest neighbor node will be selected for data forwarding. Using Shannon channel capacity model, the data rate 'C' of each neighbor node and its distance will be calculated and will be used to choose the best neighbor node. In the proposed model, the neighbor node having high data transfer rate is selected. Hence, the proposed model increases the throughput of the network, and nearest neighbor node will be selected for data transfer; the proposed model also increases the lifetime of the network.

The rest of the paper is organized as follows: in Sect. 2, related work and the identified research gap are discussed; in Sect. 3, the proposed model is discussed in detail; the simulation results and its analysis is given in Sect. 4. Section 5 concludes the paper with future work.

2 Related Work

The literature finds many protocols which use distance as the parameter for neighbor node selection in WSNs. Also, very limited articles have used Shannon channel capacity model for neighbor node selection in WSNs. In this section, the most important articles which use multihop concept are discussed.

Heinzelman et al. [5] proposed low-energy adaptive clustering hierarchy (LEACH) routing protocol for WSNs; the protocol works in two phases, setup phase and steady phase. In setup phase, among the randomly deployed nodes, one of the node will be chosen as cluster head (CH) which receives the messages from base station (BS) and forwards the same message to other nodes. In steady-state phase, non-CH nodes send data to CH, CH aggregates the received data, and then, the aggregated date will be sent to BS. The simulation results show that the LEACH gives good results against the parameters, energy dissipation, and alive nodes when compared to direct transmission and minimum transmit protocol

Sawant et al. [6] have studied the affect of changing the transmission power and baud rate on transmission distance. The authors have shown that the transmit power and baud rate are related to transmission distance in WSNs by Shannon channel capacity formula and log-distance path loss model.

A weighted and intra-cluster multihop (LEACH-WM) routing protocol for WSNs was proposed by Zhang et al. [4]. LEACH-WM has two phases similar to LEACH, i.e., setup phase and steady-state phase. During the steady-state phase, data are forwarded to BS from CH, through weight relay node. Depending on neighbor node's residual energy and its distance from the BS, relay node is elected. LEACH-WM is simulated in OPNET and metrics such as lifetime, dead nodes, and alive nodes are evaluated.

Xingguo et al. [7] have proposed a LEACH-based algorithm for WSN which uses optimized threshold formula for selecting the CH. Optimized threshold is a function of remaining energy, the average energy of the rest of the nodes, and the total residual energy of rest of the nodes. The proposed algorithm is implemented in ns-2 and is compared with LEACH for its performance evaluation. The proposed algorithm is superior to LEACH protocol in terms of amount of data packet sent by the nodes and network lifetime, and energy utilization is shown by simulation results.

The network lifetime and throughput were improved by adapting dual transmitting power levels and CH replacement technique in MODLEACH protocol proposed by Mahmood et al. [8]. MODLEACH's simulation results show improvement in throughput and network lifetime when compared to LEACH. In MODLEACH, due to dynamic cluster formation, the distance between BS and the CH may be too far, and some of the cluster node might also be far away from its CHs. Hence, more energy is consumed.

Xianing [9] has proposed energy LEACH and multihop LEACH protocols for WSNs where CH uses multiple hops instead of single hop to reach BS. In the proposed algorithm, the CH will forward the data to its neighbor CH, which in turn forwards the data to its neighbor CH so as to reach the BS. Thus, an optimal path among the CHs is

selected to reach the BS. Multihop LEACH protocol is implemented in MATLAB and is compared with LEACH and energy LEACH protocol for performance evaluation. It is observed from the simulation result that multihop LEACH has more residual energy and survived longer than both energy LEACH and LEACH protocol.

River formation dynamics-based multihop routing protocol (RFDMRP) proposed by Guravaiah and Leela Veluswamy [3] is based on river formation dynamics mechanism for the selection of best neighbor node in multihop communication. RFDMRP uses two parameters, namely hop count and residual energy, for selecting the best neighbor node to forward data. RFDMRP has better results than the LEACH and MODLEACH protocol.

The survey reveals that there are less articles in the literature which have used multihop communication to reach the BS. Further, the parameters used for selecting the neighbor nodes in multihop routing algorithm are very limited, perhaps only energy and distance. Hence, this article concentrates on multihop communication for WSNs which uses Shannon channel capacity 'C' along with the distance to find the optimal neighbor node for the data transfer

3 Proposed Methodology

Shannon channel capacity is the maximum rate at which information can be transmitted over communication channel of a specified bandwidth in the presence of noise and then formulated a complete theory of information and its transmission [10]. The study of smooth surface is considered, and two-ray ground path loss model is used.

The proposed algorithm uses the same approach used in the LEACH protocol for creating cluster and for selecting CH. Further, like LEACH protocol, the proposed algorithm will also have several rounds in which each round involves CH selection and cluster member selection. The selection of the CH is completely stochastic, and CH has to be chosen in the beginning of each round. A node which is a CH in the current node cannot become CH in the consecutive rounds; it has to wait till all the nodes in the clusters play the role of CH. Once the CH and cluster members are chosen, using time-division multiple access (TDMA) channel access scheme, CH assigns each member a time slot for transmitting the data. The nodes are allowed to send the data only during its time slot.

The second phase of each round involves selection of the best neighbor CH for forwarding the data. For this, Shannon channel capacity 'C' for each neighbor CH is found using Eq. (1).

$$\mathrm{C} = \mathrm{BW}\ \log_2(1 + \mathrm{Pr}\,/(\mathrm{No} * \mathrm{BW})) \tag{1}$$

where BW is channel bandwidth in Hz, Pr is received power in watts, and No is noise power (k * T, where k is Boltzmann constant, $1.3806503 \times 10^{-23}$ m^2 kg s^{-2} K^{-1}, and T is temperature in degree Kelvin). In order to find Pr in Eq. (1), Eq. (2) will be used;

$$\mathrm{Pr}(d)[\mathrm{dB}] = \mathrm{Pt}[\mathrm{dB}] - \mathrm{Pl}(d)[\mathrm{dB}] \tag{2}$$

where Pr(d)[dB] is power received in dB at a distance 'd' from transmitter, Pt[dB] is power transmitted in dB, and Pl(d)[dB] is path loss in dB at a distance 'd' from transmitter. For finding Pl(d)[dB] in Eq. (2), two-ray ground path loss model is used which is shown in (3);

$$\mathrm{Pl}(d) = 40\log d - 10(\log \mathrm{Gt} + \log \mathrm{Gr} + 2\log \mathrm{hr} + 2\log \mathrm{ht}) \tag{3}$$

where d is distance between transmitter and receiver, Gt and Gr are gain of transmitting and receiving antenna, and ht and hr are height of transmitting and receiving antennas. Now, by substituting Eq. (2) in Eq. (1),

$$\mathrm{C} = \mathrm{BW}\log_2(1 + (\mathrm{Pt}[\mathrm{dB}] - \mathrm{Pl}(d)[\mathrm{dB}])/(\mathrm{k} * \mathrm{T} * \mathrm{BW})) \tag{4}$$

Equation (3) is substituted in Eq. (4) to get bit rate 'C';

$$\mathrm{C} = \mathrm{BW}\log_2(1 + (\mathrm{Pt}[\mathrm{dB}] + 40\log \mathrm{d} - 20\log \mathrm{hr} - 20\log \mathrm{ht})/(\mathrm{k} * \mathrm{T} * \mathrm{BW})) \tag{5}$$

Thus, using Eq. (5), 'C' for each neighbor CH will be calculated.

Before forwarding, data received from non-cluster nodes will be aggregated at the CH and then will be forwarded to the neighbor CH. The complete algorithm is given in Fig. 1.

```
1.    if the node is non CH then
2.    Sense the data.
3.    Wait for its turn for transmission.
4.    When its turn comes, forward the data to CH
5.    end if.

1.  if the node is CH then
2.      Aggregate the collected data from non CH
3.      Calculate the 'C ' for each neighbor CH using eqn. (5)
4.      Chose the highest 'C' of neighbor CH and forward the aggregated data.
5.  end if.

1.   if the node is BS
2.   Receive the data from CH and process it.
3.   end if.
```

Fig. 1 BRM algorithm

4 Simulation Result and Analysis

The proposed algorithm is developed and tested using MATLAB and is compared against classical LEACH [5] protocol and the latest multihop LEACH [9] protocol for its qualitative and quantitative analysis against the performance parameters such as number of nodes alive and total number of data packets reaching the BS; the remaining energy and energy consumed were considered. Several simulations were carried out and the average of these simulation results is discussed in this section. The proposed model is tested for different node densities with 100, 200, and 300 nodes randomly deployed in the 200 m × 200 m area to check its scalability factor. The sensor node's initial energy was set at 0.5 J, and transmitting energy (Et) was set as 50 J. The energy consumption of a sensor node for transmitting data using space model (εfs) and multipath fading (εmp) was set as 10 pJ/bit/m^2 and 0.0013 pJ/bit/m^4, respectively. Power transmitted (Pt) was set as 50 db, bandwidth (BW) was set as 900 MHz, and temperature was set to 1000 K.

Figure 2a–c shows the number of alive nodes over simulation rounds for 100, 200, and 300 nodes, respectively. In LEACH, all the nodes expire very soon as each node directly communicates with the BS, thereby depleting more energy for data transfer. In multihop LEACH, though each CH node uses multiple hops to reach the BS, it may choose neighbor node which may not be resource rich, hence ending up with more energy depletion. On the other hand, the proposed model gives better results when compared to LEACH and multihop LEACH for two reasons; firstly, it uses multihop to reach BS, and secondly, it will choose the resource-rich neighbor node for data forwarding in terms of high baud rate. Hence, the lifetime of the nodes is extended in the proposed model when compared to LEACH and multihop LEACH protocol.

Figure 3a–c shows the total data packets received at the BS successfully for 100, 200, and 300 nodes, respectively. In LEACH, total data packets received at the BS will be less as all the non-CH nodes expire very soon due to direct communication with the BS. And in muiltihop LEACH, since the path loss is not considered while choosing the neighbor CH node for data transfer, the chosen neighbor node may not forward the data efficiently. Whereas in the proposed model, as the neighbor node will be chosen which has less path loss, more data packets will be relayed to the BS.

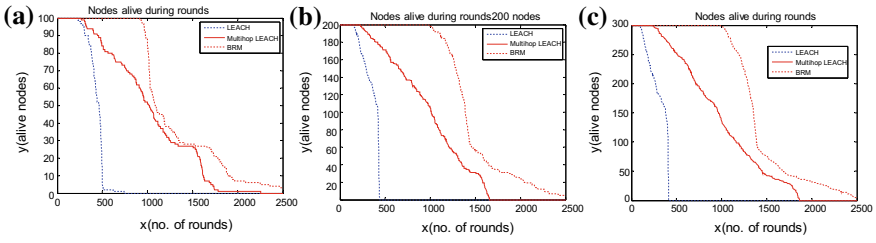

Fig. 2 Total number of alive nodes (all nodes)

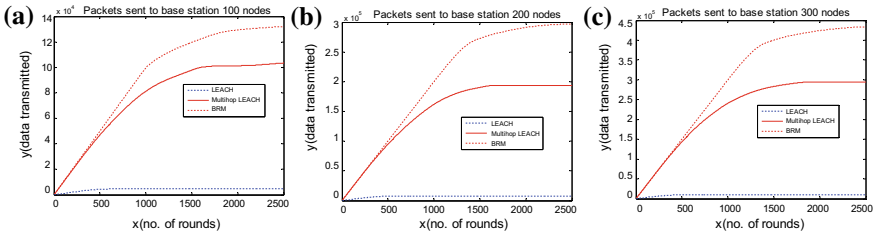

Fig. 3 Packet sent to base station

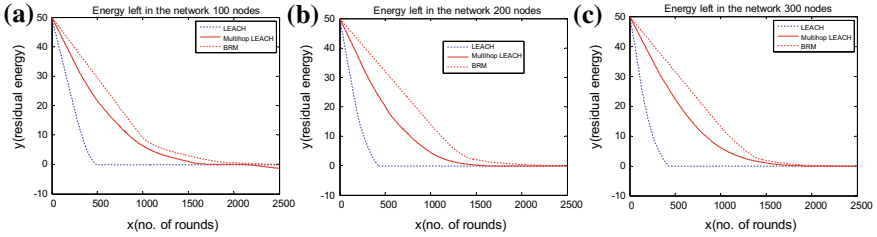

Fig. 4 Remaining energy in the network

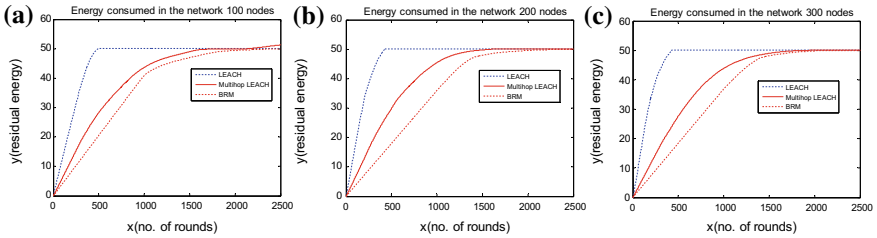

Fig. 5 Energy consumption in the network

Figure 4a–c shows the remaining energy in the network for 100, 200, and 300 nodes, respectively. The proposed model consumes less energy compared to multihop LEACH and LEACH algorithm as the nearest neighbor node will be chosen for data transfer. Since neighbor node will be nearer, each node depletes less energy for data transfer. Similarly, the graph plotted for energy consumption of each round is shown in Fig. 5a–c for 100 nodes, 200 nodes, and 300 nodes, respectively.

5 Conclusion

In this article, an efficient multiphop communication model is proposed for WSNs. The proposed model uses Shannon channel capacity model ‘C’ and the distance to

find the best neighbor node for relaying the data. Since the high baud rate neighbor node will be chosen, the proposed model shows good improvement in the packet transfer. And since nearest neighbor node is chosen for relaying data, the network lifetime is also increased.

A study is also made about the total number of alive nodes for the proposed model. Using MATLAB, the proposed model is studied for its efficiency, and the results are compared with LEACH and multihop LEACH protocol. The proposed model has shown good results against the parameters *network lifetime, number of packets delivered to BS,* and *energy consumption* when compared the LEACH and multihop LEACH.

References

1. Wang F, Liu J (2011) Networked wireless sensor data collection: issues, challenges and approaches. IEEE Commun Surv Tutorials 13(4):673–687
2. Al-Karaki JN, Kamal AE (2004) Routing techniques in wireless sensor networks: a survey. IEEE Wirel Commun 11(6):6–28
3. Guravaiah K, Leela Veluswamy R (2015) RFDP: River Formation Dynamics based Multihop routing Protocol for data collection in Wireless Sensor Network. Procedia Comput Sci 54:31–36 (Elsevier)
4. Zhang J, Chen J, Xu Z, Liu Y (2016) LEACH-WM: weighted and intra-cluster multi-hop energy-efficient algorithm for wireless sensor networks. In: 2016 35th Chinese control conference (CCC), pp 8325–8328
5. Heinzelman W, Chandrakasan A, Balakrishna H (2000) LEACH: energy efficient communication protocol for Wireless Micro sensor Networks. IEEE Trans Wirel Commun 660–670
6. Sawant RP, Liang Q, Popa DO, Lewis FL (2007) Experimental path loss models for wireless sensor networks. IEEE
7. Xingguo L, Junfeng W, Linlin B (2016) LEACH protocol and its improved algorithm in wireless sensor network. In: 2016 international conference on cyber-enabled distributed computing and knowledge discovery (CyberC), pp 418–422
8. Mahmood D, Javaid N, Mahmood S, Qureshi S, Memon AM, Zaman T (2013) MODLEACH: a variant of LEACH for WSNs. In: Eighth international conference on broadband and wireless computing, communication and applications (BWCCA). IEEE, pp 158–163
9. Xianing F (2007) Improved on LEACH protocol of wireless sensor network. In: 2007 International conference on sensor technologies and applications
10. Taub H, Schilling DL (1986) Principles of communication systems. McGraw-Hill, New York

Performance Analysis of Underwater 2D OCDMA System

Ajay Yadav and Ashok Kumar

Abstract The performance of two-dimensional optical code-division multiple access system is analyzed in the presence of weak turbulence and different water types. For weak turbulence, lognormal probability density function is used in the performance analysis. The different water types are pure sea, clear ocean, and coastal water. The error probability of 10^{-9} is achievable for all the water types with four-user OCDMA system. Also, error probability is very high ($>10^{-3}$) in the presence of coastal water as compared to pure sea and clear ocean.

Keywords UWOC · 2D · OCDMA · OCFHC/QCC · HL

1 Introduction

In underwater wireless optical communication (UWOC), high data rate can be achieved as compared to acoustic communication which has been used for several decades. UWOC systems offer larger bandwidth, high security, and low latency as compared to acoustic communication systems [1]. For a multi-user UWOC system, optical code-division multiple access (OCDMA) can play an important role as it provides secure communication as well as large bandwidth. In OCDMA-based UWOC system, optical codes are used where each user is assigned an optical codeword. The optical codes are divided into one-dimensional (1D), two-dimensional (2D), and three-dimensional (3D) codes depending upon whether time, time, and wavelength or space, and time, wavelength, and space or polarization, respectively, are used as dimensions in the code design. In this research work, a 2D one-coincidence frequency hopping code/quadratic congruence code (OCFHC/QCC) is used for the performance evaluation of UWOC OCDMA system [2].

A. Yadav (✉)
Department of Electronics and Communication Engineering, Bennett University, Greater Noida, Uttar Pradesh 201310, India
e-mail: ajayyadavbsz@gmail.com; ajay@gweca.ac.in

A. Kumar
Department of Electronics and Communication Engineering, Government Mahila Engineering College, Ajmer, Rajasthan 305002, India

V. Janyani et al. (eds.), *Optical and Wireless Technologies*, Lecture Notes in Electrical Engineering 648, https://doi.org/10.1007/978-981-15-2926-9_53

UWOC systems are generally used for short-distance communication due to absorption, scattering, and turbulence effects in the underwater channel. Absorption and scattering cause attenuation of the optical signal. The turbulence is due to random fluctuations in refractive index of the water which results in fading of the optical signal [3]. In addition, beam divergence also affects the performance of UWOC OCDMA system by decreasing power density at the receiver. The effect of absorption and scattering on the path loss is studied using Beer–Lambert's law. The different water types which have been considered are pure sea, clear ocean, and coastal water. Pure sea is water from sea or ocean with salinity of 3.5%. Pure seawater is denser than fresh water (naturally occurring water) and pure water (water without impurities). The other water type, i.e., clear ocean water, consists of very clear water like in the Tongue of the Ocean (TOTO), Bahamas islands. TOTO is a deep oceanic trench separating the islands of Andros and New Providence. Coastal water is the third water type which is the near-shore coastal water like in San Pedro Channel, California, USA. Further, lognormal fading is used for modeling turbulence in the underwater optical channel [4]. In underwater optical channel with OCDMA system, multiple access interference (MAI) also affects the performance of OCDMA system. MAI can be mitigated to a large extent by using double hard limiters (HLs). HL decreases the effect of MAI by removing interference pulses from the undesired users in the system. The rest of the paper is organized as follows: Sect. 2 describes the UWOC OCDMA system. The underwater channel is modeled in Sect. 3 which considers the effect of beam divergence, turbulence, and different water types. The performance analysis and its results are discussed in Sects. 4 and 5, respectively.

2 Underwater Wireless Optical Communication OCDMA System

The information bits from the N users are intensity modulated using on–off keying (OOK) as shown in Fig. 1. The modulated bits are assigned optical codeword using encoder. The encoder consists of wavelength division multiplexer, fiber-optic delay lines, and wavelength division demultiplexer. The encoder output is combined using $N \times 1$ coupler and transmitted through the optical antenna. The transmitted optical signal is attenuated by absorption and scattering of different water types: pure sea, clear ocean, and coastal water. The salinity and different temperatures of underwater cause fading of the optical signal. In receiver, the attenuated and faded optical signal is received by the optical receiver antenna. Further, the optical signal is split with $1 \times N$ coupler. Two HLs are used to remove the interference patterns in the OCDMA system. The decoder between the HLs correlates with the received optical signal and generates autocorrelation peak and cross-correlation values. The second HL is followed by photo-detector and threshold detector to recover the transmitted information bits at the receiver.

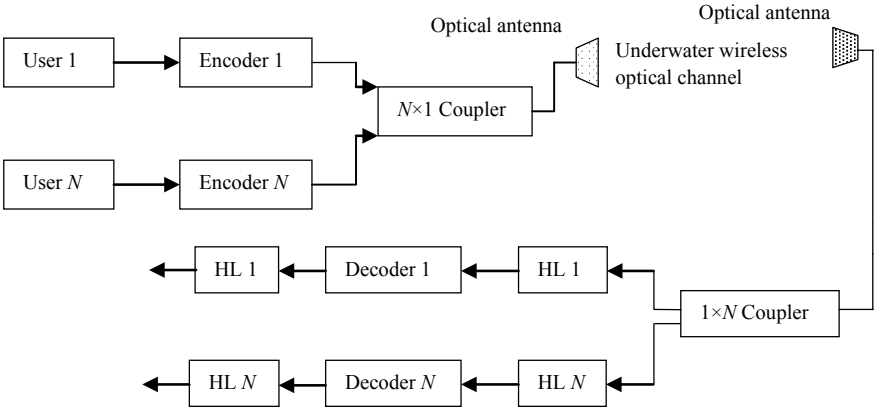

Fig. 1 2D OCDMA system for underwater wireless optical channel

3 Channel Modeling

In UWOC, the optical signal spreads out due to beam divergence and attenuated by absorption and scattering. Using Beer–Lambert's law, the path loss factor γ is given by [2]

$$\gamma = \frac{A_{\mathrm{r}}}{\pi\left(\frac{\phi_{\mathrm{s}} L}{2}\right)^2} \mathrm{e}^{-\sigma L} \tag{1}$$

where A_{r} is the area of optical antenna at the receiver, ϕ_{s} the beam divergence angle (radian), L the link length (meters), and σ the attenuation coefficient (m^{-1}), respectively. The value of σ for different water types is shown in Table 1.

The optical signal is also affected by underwater turbulence. For a random process which represents received optical signal, the weak underwater turbulence is characterized by lognormal probability density function (pdf). Lognormal pdf is used for weak turbulence since it resembles well with the actual atmospheric turbulence. Lognormal pdf is defined as [2]

$$f_X(x) = \frac{1}{\sqrt{2\pi\sigma_X^2 x}} \exp\left(-\frac{\left(\ln x + \sigma_X^2/2\right)^2}{2\sigma_X^2}\right) \tag{2}$$

Table 1 Water type and attenuation coefficient in underwater wireless optical communication

Water type	Attenuation coefficient (m^{-1}) [3]
Pure sea	0.056
Clear ocean	0.150
Coastal water	0.305

Here, X represents the random variable, x is the real number which corresponds to this random variable values, i.e., $f_X(x) = \mathrm{d}/\mathrm{d}x(P(X \leq x))$ where $P(X \leq x)$ is the probability that $X \leq x$. σ_X^2 is the log-amplitude variance. For weak turbulence, $\sigma_X^2 =$ 0.16 [1].

4 Performance Analysis

The performance is analyzed in the presence of MAI, turbulence, and different water types. The 2D UWOC OCDMA system is assumed chip synchronous and slot asynchronous. Avalanche photo-detector (APD) with photon count approach is used for detection of optical signal at the receiver. The received power P_{R} after the beam divergence, attenuation in the underwater channel, and coupling loss due to receiver coupler is given by

$$P_{\mathrm{R}} = \gamma \frac{P_{\mathrm{T}}}{N} \tag{3}$$

where P_{T} is the transmitted power from the transmitter antenna and N is the number of users in the OCDMA system. The photon absorption rate α_{s} for photons which fall on the APD considering the effect of fading on the optical signal is given as [2]

$$\alpha_{\mathrm{s}}(x) = \frac{\eta x P_{\mathrm{R}}}{hf} \tag{4}$$

Here, η is the quantum efficiency, f the average optical frequency which is obtained from the average optical wavelength λ, i.e., $f = c\lambda$, c the speed of light, and h the Planck's constant.

In the receiver, the first HL removes the interference patterns from the received optical signal. The interference patterns which could not be removed with the first HL are eliminated with the second HL. HL snips the pulses which are above threshold Th to a fixed value and below Th to zero. The APD output for data bit '1' is given by

$$p_{Y1}(y|i, x, b = 1) = \frac{1}{\sqrt{2\pi\sigma_1^2(x)}} \exp\left(-\frac{(y - \mu_1(x))^2}{2\sigma_1^2(x)}\right) \tag{5}$$

where i denotes the number of pulses of the intended user which are interfered, $\mu_1(x)$ is the mean, and $\sigma_1^2(x)$ is the variance. Similarly, the APD output for '0' data bit is

$$p_{Y0}(y|i, x, b = 0) = \frac{1}{\sqrt{2\pi\sigma_0^2(I, x)}} \exp\left(-\frac{(y - \mu_0(I, x))^2}{2\sigma_0^2(I, x)}\right) \tag{6}$$

Here, $I = (I_1, I_2, \ldots, I_w)$ denotes the interference vector where total marks are equal to weight of the code (w). $\mu_0(I, x)$ is the mean and $\sigma_0^2(I, x)$ the variance. The second HL would clip the intensity above Th to $w\alpha_s i_m(|I|)$. $|I|$ denotes the number of nonzero elements of the code.

The 2D OCDMA system uses OCFHC/QCC for time and wavelength assignment in two dimensions. The probability of hits between two codewords of OCFHC/QCC is given by

$$h_{1,2} = \frac{n_{1,2}}{2\big((m-1)\big(m_1^{k1}-1\big)m_1^{k1}-1\big)} \tag{7}$$

$$h_{2,2} = \frac{n_{2,2}}{2\big((m-1)\big(m_1^{k1}-1\big)m_1^{k1}-1\big)} \tag{8}$$

where $n_{1,2}$ and $n_{2,2}$ are the number of one hit and two hits, respectively. $n_{1,2}$ and $n_{2,2}$ are counted in MATLAB using cross-correlation function. m, m_1, and k_1 are the prime numbers. OCFHC/QCC construction method is given in [5]. The pdf of MAI $P_I(i, t)$ is given by

$$P_I(i,t) = \binom{w}{i}\binom{i}{t}(-1)^{i-t}\left(h_{0,2} + h_{1,2}\frac{t}{w} + h_{2,2}\frac{t(t-1)}{w(w-1)}\right)^{N-1} \tag{9}$$

In this expression, $h_{0,2}$ denotes the probability of zero hits out of maximum value of 2 which is given by

$$h_{0,2} = 1 - h_{1,2} - h_{2,2} \tag{10}$$

The probability of error P_e for intensity modulation, i.e., OOK, in the presence of $|I|$ interfering users is [6]

$$P_e(|I|, x) = \frac{1}{2}\left[Q\left(\frac{\mu_1(x) - \mathrm{Th}}{\sigma_1(x)}\right) + Q\left(\frac{\mathrm{Th} - \mu_0(|I|, x)}{\sigma_0(|I|, x)}\right)\right] \tag{11}$$

The total probability of error P_E in the presence of MAI, turbulence, and different water types can be evaluated as

$$P_E = P_{e1} + P_{e2} \tag{12}$$

where P_{e1} and P_{e2} are expressed as

$$P_{e1} = \underset{\mathrm{Th}}{\mathrm{Min}} \int_0^{\infty} \sum_{i=0}^{w-1} \sum_{t=0}^{i} P_I(i,t) P_e(|I|, x) f_X(x) \mathrm{d}x \tag{13}$$

and

$$P_{e2} = \underset{\text{Th}}{\text{Min}} \int_0^{\infty} \sum_{i=0}^{w} P_I(w,t) P_e(|I|, x) f_X(x) \mathrm{d}x \tag{14}$$

Thus, the performance of double hard-limited OCDMA system considering the effect of MAI, turbulence, and different water types is evaluated using (12).

5 Results and Discussion

The variation in P_E of OCFHC/QCC-based 2D UWOC OCDMA system with variation in P_T and N is discussed in this section. The various parameters which have been used for the performance evaluation are shown in Table 2. The different water types which have been considered are pure sea, clear ocean, and coastal water. The weak turbulence is characterized by lognormal pdf in the analysis. The performance of 2D OCDMA system is better than 1D OCDMA system as demonstrated in [7]. Thus, we have used 2D OCDMA system for performance evaluation in the underwater channel.

For $N = 4$, $L = 20$ m, and receiver aperture $D_r = 5$ cm, P_E decreases with an increase in P_T as shown in Fig. 2 for different water types in the presence of weak turbulence. The decrement in P_E is due to an increase in the number of photons which are falling on the APD with an increase in P_T. $P_E = 10^{-9}$ when P_T is 3.78, 11.96, and 25 dBm for pure sea, clear ocean, and coastal water, respectively.

P_E increases with an increase in N for all the water types as shown in Fig. 3. The increment in P_E is due to an increase in MAI with increment in N. When $P_T = 15$ dBm, $P_E = 10^{-6}$ if N equals 16 and 15 for pure sea and clear ocean, respectively. P_E is very high for coastal water due to very high attenuation (absorption and scattering) from the organic and inorganic matter in the coastal water as compared to pure sea and clear ocean.

The 2D OCDMA system provides secure communication in the underwater channel. The effect of turbulence, attenuation from different water types, noise, beam divergence, and MAI from the interfering users degrades the performance of the 2D OCDMA system. The OCDMA-based secure communication can be used between submarines, warships, and ships.

Table 2 Various parameters of 2D UWOC OCDMA system

Symbol	Quantity	Value
η	APD quantum efficiency	0.8
L	Propagation length	20 m
w	Code weight	7
n	Code length	49
R	Data rate	1 Gbps

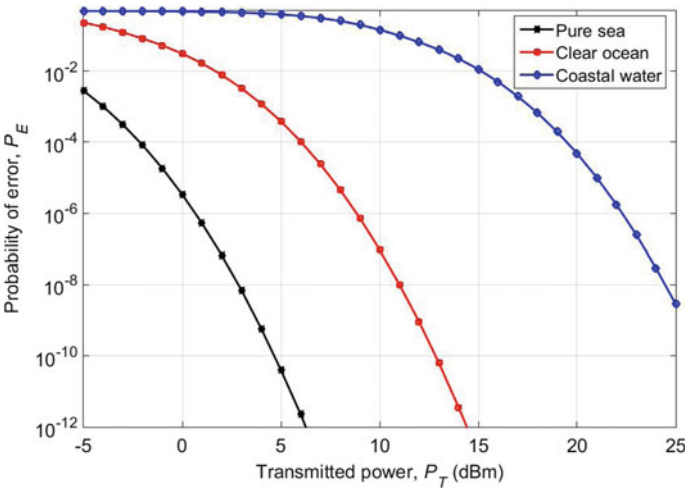

Fig. 2 Probability of error versus transmitted power in the presence of different water types

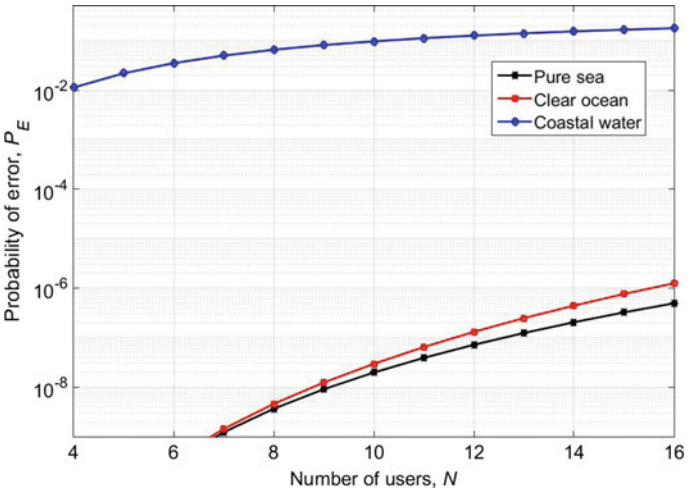

Fig. 3 Probability of error versus number of users for the different water types

6 Conclusion

The performance of 2D OCFHC/QCC-based OCDMA system is analyzed in the underwater channel. The different water types which have been considered are pure sea, clear ocean, and coastal water. With four-user OCDMA system, error probability of 10^{-9} is achievable irrespective of the water type in the underwater channel. Error probability of OCDMA system is more with coastal water as compared to pure sea

and clear ocean. 2D OCFHC/OOC-based OCDMA system can be used for secure communication between submarines, naval warships, boats, and ships.

References

1. Jamali VH, Salehi JA (2015) On the BER of multiple-input multiple-output underwater wireless optical communication systems. In: 4th international workshop on wireless optical communications, Istanbul, pp 26–30
2. Yadav A, Kar S, Jain VK (2017) Performance analysis of wireless OCDMA multi-user system based on new 2-D code in presence of atmospheric turbulence and various weather conditions. In: 9th international conference on communication systems and networks (COMSNETS), Bengaluru, pp 109–115. https://doi.org/10.1109/comsnets.2017.7945365
3. Elamassie M, Miramirkhani F, Uysal M (2019) Performance characterization of underwater visible light communications. IEEE Trans Commun 67(1):543–552. https://doi.org/10.1109/TCOMM.2018.2867498
4. Jamali MV, Nabavi P, Salehi JA (2018) MIMO underwater visible light communications: comprehensive channel study, performance analysis, and multiple-symbol detection. IEEE Trans Veh Technol 67(9):8223–8237. https://doi.org/10.1109/TVT.2018.2840505
5. Yadav A, Kar S, Jain VK (2018) Performance analysis of a new OCFHC/QCC vis-a-vis synchronous PC/OOC code using photon count approach. IET Optoelectron. https://doi.org/10.1049/iet-opt.2018.5090
6. Yadav A, Kar S, Jain VK (2018) Performance enhancement of double hard-limited 2D OCDMA system using aperture averaging and spatial diversity. IET Commun. https://doi.org/10.1049/iet-com.2018.5787
7. Yadav A, Kar S, Jain VK (2017) Performance of 1-D and 2-D OCDMA systems in presence of atmospheric turbulence and various weather conditions. IET Commun 11(9):1416–1422. https://doi.org/10.1049/iet-com.2016.1008

Next-Generation PON with Enhanced Spectral Efficiency: Analysis and Design

Mukesh Kumar Gupta, Ambrish and Ghanshyam Singh

Abstract This model depicts a detailed analysis of spectral efficiency and reach enhancement in next-generation passive optical network (NG-PON). The DPSK modulation format mitigates stimulated Raman scattering (SRS) effects in the fiber and boosts channel capacity with the multi-gigabit transmission rate. At 20 km fiber length, a power loss of 8 dB was observed that is compensated to 7 dB with a pump power of 180 mW. A system is analyzed at 10 Gbps data rate to 128, 32 users for 20 km and 55 km, respectively, in permissible BER. The DPSK modulation with interferometry detection technique provides 0.3 (bits/s)/Hz higher spectral efficiency in comparison with other modulation formats.

Keywords Wavelength-/time-division multiplexing (WDM/TDM) · Distributed Raman amplification (DRA) · Differential phase shift keying (DPSK) · Stimulated Raman scattering (SRS) · Passive optical network (PON) · Subcarrier multiplexing (SCM)

1 Introduction

In the optical communication system, the wavelength-division multiplexing passive optical network (WDM-PON) technique is one of the most promising technologies for the broadband access network [1–3]. For long reach, optically amplified hybrid WDM-TDM-PONs are in huge demand due to its low cost and high bandwidth [4–6]. A basic PON system uses a 1490 and 1550 nm wavelength for downstream transmission for combined data/voice and video traffic distribution [7, 8]. A data and video

M. K. Gupta (✉)
Department of Electronics and Communication Engineering, MBM Engineering College, Jodhpur, India

Ambrish
Department of Electronics and Communication Engineering, Netaji Subhas Institute of Technology, New Delhi, India

G. Singh
Department of Electronics and Communication Engineering, Malaviya National Institute of Technology, Jaipur 302017, Rajasthan, India

V. Janyani et al. (eds.), *Optical and Wireless Technologies*, Lecture Notes in Electrical Engineering 648, https://doi.org/10.1007/978-981-15-2926-9_54

signal together in WDM-TDM system at short distance degrade the performance of data signal significantly due to Raman cross talk [9]. The Raman amplification used in optical fiber communication system has attracted a lot of attention as they have broad amplification bandwidth and flexible central wavelength [10, 11]. The discrete Raman amplification and distributed Raman amplification are two main categories used in Raman amplification [12]. The gain and typical transmission length for distributed Raman amplification are larger and improve system performance too. The transmission rate of the WDM system can be enhanced by increasing either spectral efficiency or a wider optical bandwidth or both. The spectral efficiency limit is determined by the information-theoretic capacity per unit bandwidth. The DPSK modulation technique allows information to encode in two degrees of freedom per polarization, and its spectral efficiency limits are much higher in typical terrestrial systems [12–16]. The constant intensity-modulated systems have only one degree of freedom, which reduces spectral efficiency [15]. We can also do some other modulations like QPSK and DQPSK as they have high OSNR sensitivity, but they are more complex in design and their implementation cost is very high [17–19].

In practice, most of the PON systems have 20 km physical reach with 32 splits and 28 dB of link budget [20]. An FTTH with GEPON system operating at 2 Gbps is proposed by Kochar et al. [21]; the system was simulated for different users like 32, 48 and 64 at 20 km fiber length with booster amplifier. The complete setup depicts better performance for 56 users. Hesham et al. [22] observe the effect of power for a GPON system. They propose 9 dBm power is suitable to achieve 128 users for 20 km fiber length. This methodology is implemented for the WDM systems, where more than one wavelength is multiplexed and the average power is increased which results in the increase in nonlinearity and degrading the system performance. Kaler et al. [23] propose a Gigabit Ethernet Passive Optical Network (GEPON) for 0–20 km optical fiber length for the different numbers of user and achieve that 15 km is a suitable length for the 10 Gbps data rate system. Cheng et al. [24] demonstrate a 20 km TWDM-PON system for dual-rate transmitter, delay modulation using DML for 10 Gbps transmission. Power over fiber technique is proposed by Penze et al. [25] to achieve the 10 Gbps data rate system for 32 users at 50 km. This technique can be a deployed to amplify entire optical band but fails to amplify individual selective wavelength. Acharya et al. [11] demonstrated a system with a remote Raman amplification where a continuous wave counter-propagating pump is injected from one of the optical network units. The setup was tested for 1.25 Gbps data rate for 32 or 64 users for 40 km and 25 km length, respectively. As per our knowledge in video overlay PON network, the remote Raman pump is the best choice.

In this paper, we discuss effective distributed Raman amplification in WDM-PON using DPSK modulation for enhancement of reach and system capacity. The benefit of using DPSK modulation along with Raman amplification results in enhanced spectral efficiency of the signal due to DPSK and increased transmission length by Raman amplification; hence, the signal can be transmitted for long distance with the higher transmission rate. The spectral efficiency is directly proportional to system capacity which is also a most economical mean to increase DWDM system capacity.

It has also been stated in previous work that the spectral efficiency is also reduced in constant intensity or direct detection.

2 Modeling and Equation Analysis

2.1 Effective Raman Gain

The larger effective area A_{eff} of the fiber is beneficial for optical amplification as it reduces nonlinear effects when we launch high signal power. Moreover, in Raman pumping the gain increases when effective area of the fiber decreases. The effective Raman gain (G_{e}) is the ratio of Raman gain coefficient over an effective area of the fiber. Mathematically, it can be defined as $\frac{g_{\text{R}}}{A_{\text{eff}}}$, which is more practical parameter than Raman gain coefficient in Raman amplifier. We can determine the effective area for Raman gain as $A_{\text{eff}} = a_{\text{Eff}}\pi\left(\frac{\text{Diameter}}{2}\right)^2$; here, a_{Eff} is a dimensionless number, which is related to actual effective area of the mode to the core diameter. Similarly, the Raman gain coefficient g_{R} describes how Stokes power raises as pump power is transferred to it through stimulated Raman scattering (SRS). The Raman gain in terms of power can be described as

$$\frac{\mathrm{d}P_{\text{s}}}{\mathrm{d}z} = \frac{\gamma_{\text{R}}}{A_{\text{eff}}} P_{\text{p}} P_{\text{s}} \equiv g_{\text{R}} P_{\text{p}} P_{\text{s}} \tag{1}$$

Here, γ_{R} is the nonlinear strength $\gamma_{\text{R}} = 2\pi n_2/(\lambda A_{\text{eff}})$, n_2 is nonlinear refractive index and λ is the signal wavelength. The power evolutions for signal and pump waves along an optical fiber can be described by using different equations called propagation equations. The signal and pump equation can be expressed as

$$\frac{\mathrm{d}P_{\text{s}}}{\mathrm{d}z} = g_{\text{R}} P_{\text{s}} P_{\text{p}} - \alpha_{\text{s}} P_{\text{s}} \tag{2}$$

$$\frac{\mathrm{d}P_{\text{p}}}{\mathrm{d}z} = -\frac{\omega_{\text{s}}}{\omega_{\text{p}}} g_{\text{R}} P_{\text{s}} P_{\text{p}} - \alpha_{\text{p}} P_{\text{p}} \tag{3}$$

where P_{s} and P_{p} are signal and pump powers, respectively, g_{R} is the Raman gain efficiency for the wavelength of signal and pump, ω_{s} and ω_{p} are the frequencies of signal and pump waves and α_{s} and α_{p} are attenuation coefficients of optical fiber at signal and pump wavelength. If we consider the signal power low enough as compared to pump power, then pump depletion is negligible. After solving Eq. (2), when pump is off the obtained output power is attenuated due to fiber loss only.

$$P_{\text{s-off}}(L) = P_{\text{s}}(0)\exp(-\alpha_{\text{s}} L) \tag{4}$$

When the pump power is high enough to stimulate the Raman effects than its power is transferred to high wavelength week signal, and signal gets amplified. The amplification of the signal can be described from the following equations

$$P_{\mathrm{s-on}}(L) = P_{\mathrm{s}}(0)\exp\left(\frac{g_{\mathrm{R}}P_0L_{\mathrm{eff}}}{KA_{\mathrm{eff}}} - \alpha_{\mathrm{s}}L\right) \equiv G(L) \tag{5}$$

where the P_0, $P_{\mathrm{s}}(0)$ are input pump power and stock power at zero fiber length, $G(L)$ is the net signal gain and $G(L)$ in dB is given by $G(L) = 4.34\left[\frac{g_{\mathrm{R}}P_0L_{\mathrm{eff}}}{A_{\mathrm{eff}}} - \alpha_{\mathrm{s}}L\right]$, where L is the amplifier length and $L_{\mathrm{eff}} = \frac{1-\exp(-\alpha_{\mathrm{p}}L)}{\alpha_{\mathrm{p}}}$ is effective length of the fiber. The net signal gain $G(L)$ can be less than 1 (net loss) if the Raman gain is not sufficient to overcome the fiber loss. Then, the Raman on–off gain G_{A} in dB can be defined as

$$G_{\mathrm{A}} = 10\log_{10}\left(\frac{P_{\mathrm{s-on}}(L)\text{ with pump on}}{P_{\mathrm{s-off}}(L)\text{ with pump off}}\right) \tag{6}$$

where L is the length of the fiber and $P_{\mathrm{s-on}}(L)$ with pump on is considered without amplified spontaneous emission (ASE) noise and thermal noise. After substituting the value of Eqs. (3) and (4), the effective Raman gain can be obtained as

$$G_{\mathrm{e}} = \frac{g_{\mathrm{R}}}{A_{\mathrm{eff}}} = \frac{2\pi n_2}{\lambda A_{\mathrm{eff}}^2} = \frac{G_A}{4.343L_{\mathrm{eff}}P_{\mathrm{pump}}} \tag{7}$$

Here, P_{pump} is the pump power launched into the fiber and $\frac{g_{\mathrm{R}}}{A_{\mathrm{eff}}}$ is the depolarized effective Raman gain.

2.2 *Spectral Efficiency Limit*

The performance analysis of broadband Raman amplifiers is affected by several factors which should be controlled. The Raman spontaneous scattering in Raman amplifiers appears as a noise signal as a random phase associated with spontaneously generated photons. The spectral efficiency in DWDM can be defined as the ratio of channel capacity to the channel spacing. The channel capacity in communication is the maximum number of bits that can be transmitted through a channel without any error. This is common to all modulation formats because it does not depend upon encoding or decoding schemes. Hence, this can also be defined as the optimal probability density of the transmitted signal. If we consider S as spectral efficiency, C as capacity per channel, B as occupied bandwidth per channel and Δf as the channel spacing, then $S = C/\Delta f$ denotes spectral efficiency limit.

The ASE spectral density is defined as

$$S_{\mathrm{ASE}} = n_{\mathrm{sp}} h \nu_0 g_{\mathrm{R}} G(L) \int_0^L \frac{P_{\mathrm{p}}(z)}{G(z)} \mathrm{d}z \tag{8}$$

The parameter n_{sp} is defined as $n_{\mathrm{sp}}(\Omega) = 1/\left[1 - \exp(-h\Omega/\kappa_{\mathrm{B}} T)\right]$, where $\Omega = |\mu - \nu|$ is the Raman shift and T denotes absolute temperature of the amplifier. The spectral density is constant and presents at all frequencies (white noise). In practice, the noise exists only over the amplifier bandwidth and will further be reduced by placing an optical filter at the amplifier output. According to this consideration, we can calculate the total ASE power after the amplifier

$$P_{\mathrm{ASE}} = 2 S_{\mathrm{ASE}} B_{\mathrm{opt}} = 1.4 S_{\mathrm{ASE}} R_{\mathrm{b}} \tag{9}$$

Here, B_{opt} is the bandwidth of optical filter and R_{b} is the bit rate for signal transmission. The factor of 2 indicates two polarization modes of the fiber span. ASE can be reduced by 50% if a polarizer is used after the amplifier. In our consideration, if we are not using any polarizer the signal-to-noise ratio of the amplified signal is given by

$$\mathrm{SNR}_{\mathrm{o}} = \frac{P_{\mathrm{s-on}}(L)}{P_{\mathrm{ASE}}} = \frac{G(L) P_{\mathrm{s}}(0)}{P_{\mathrm{ASE}}} \tag{10}$$

In DPSK modulation technique, the information is encoded in an optical signal having a nominally constant intensity. Now at high SNR, the capacity can be defined as [9]

$$C = B_{\mathrm{opt}} \left[\frac{1}{2} \log_2(\mathrm{SNR}_{\mathrm{o}}) + 1.10 \right] \tag{11}$$

Hence, spectral efficiency is [9]

$$S = \frac{B_{\mathrm{opt}}}{\Delta f} \left[\frac{1}{2} \log_2(\mathrm{SNR}_{\mathrm{o}}) + 1.10 \right] \tag{12}$$

The unit of spectral density is b/s/Hz. It is necessary to consider a heterodyne or phase diversity homodyne with differentially coherent (one-bit delay) demodulation of DPSK signal. This is only applicable to coherent detection because for non-coherent it never offers high spectral efficiency. Homodyne receiver requires bandwidth approximately equal to the symbol rate R_{s} which is just half of the heterodyne receiver bandwidth. Hence, we prefer homodyne receiver which requires a pair of balance receiver for detection. The optical DWDM demultiplexer is used that provides narrowband filtering of the received signal and ASE. In the absence of fiber nonlinearities, with proper dispersion compensation and matched filtering, all formats of DPSK should provide the same SNR and spectral efficiency. Under interferometric detection of DPSK, a Mach–Zehnder interferometric detector is used

with a path difference of one-symbol duration that compares phase transmitted in successive symbols which provides intensity-modulated output that is detected by using a balanced receiver.

3 Simulation Model of Hybrid WDM-/TDM-PON Architecture

The general features of the proposed topology are illustrated in Fig. 1. The highlighted segments for WDM-PON are optical line terminal (OLT) and optical network unit (ONU). The triple play (i.e., voice, video and data) services are considered, with data/voice signal transmission range from 1450 to 1500 nm and video signals within 1550–1560 nm range. The radio frequency (RF) video signals are having wavelength 1542, 1550 and 1558 nm, and data/voice signals are having wavelength 1482 and 1490 nm. All signals are exhibited with pseudorandom bit sequence (PRBS) generator (bit rate 10 Gbps), non-return to zero (NRZ) modulator and phase-modulated (PM) continuous wave (CW) lasers. The subcarrier multiplexing (SCM) is the method of combining (or multiplexing) many different communication signals so that they can be transmitted along the optical fiber. The video transmitter consists of a summer to combine two electrical signals and a CW laser modeled with a phase modulator. Each SCM signal is using two channels from the standard National Television System Committee (NTSC) and cable television (CATV) frequency plan. The channel number (2, 78), (3, 79) and (4, 80) combinations for each 1542 nm, 1550 nm and 1558 nm

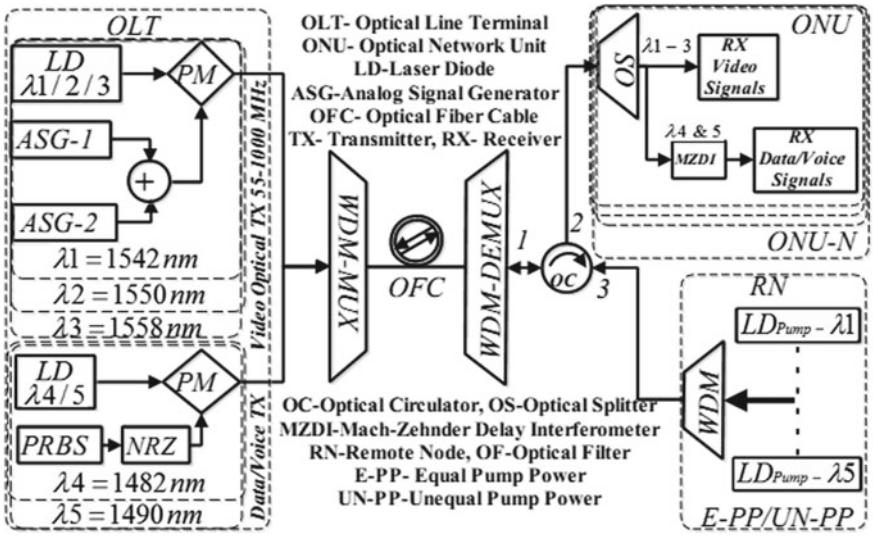

Fig. 1 Simulation model of proposed distributed Raman amplified WDM-PON architecture

video signal are taken, respectively. Each channel is transmitting separate frequency as shown in Fig. 1 within the frequency range 55–1000 MHz. The multiplexed output of all input signals is transmitted via forward input of the bidirectional single-mode fiber (SMF), and other backward input is reserved for Raman pumping to achieve Raman amplification. A bidirectional single-mode fiber (SMF) with core diameter 8.2 μm is used for data transmission. An average fiber attenuation of ~0.25-dB/km is taken into consideration. The nominal channel spacing and Raman gain coefficient are 100 GHz and 9.8E−14 m/W, respectively. Raman amplification also depends on two equal and unequal pump power (i.e., E-PP and UE-PP) configurations. In both configuration processes, lower wavelength data signals transfer their energy to higher wavelength signals due to stimulated Raman scattering (SRS) property of the fiber. A splitter/WDM de-mux is used to transmit these services to different, e.g., 32, 64, 128, etc., users/splits. The video and data/voice signals are Raman amplified using pump of wavelengths 1481 nm, 1497 nm, 1513 nm, 1405 nm and 1415 nm, respectively. A WDM-mux is used to combine all these pump wavelengths, and the multiplexed output is applied via a remote optical node unit to the bidirectional fiber. The backward pumping configuration is preferred for Raman amplification as nonlinear effects are least in this case and the signal power is smallest throughout the link length. Raman gain is calculated and analyzed per signal before service distribution to the subscribers.

At optical network unit (ONU), the received signals are separated into video and data signals using a suitable filter because the phase deviation in the modulator has been identified as a parameter that can affect the transmission.

It has already been reported in previous research work that the DPSK modulated signal gets more power (approximately >3 dB) at optical network unit (ONU) terminal when using suitable demodulation techniques [16]. It is also to be noticed that in this technique there is no extra component introduced, such as an SOA or highly nonlinear fiber or EDFA, besides remote Raman pumps.

4 Results and Discussion

The launching powers, with and without Raman pump powers, are shown in Fig. 2. It was observed that half power (approximately) of the signal is reduced just after 20 km fiber span. If we again increase the transmission length, the complete signal loss can be observed beyond the 40–50 km fiber length. At receiver, the eye diagrams of the pump signal can be observed by using electrical BER visualizer. The increased number of users also reduces the received power for each individual user. Hence if Raman pump is in the offstage (i.e., without pump), the received power with an increased number of users will also reduce the transmission length. Thus, the amplification of signals is required to achieve the desired reach and the number of users. The higher wavelength signals have higher gain in comparison with lower wavelength data/voice signals as defined in past research work. It is also essential that each signal must have at least 7 dB gain enhancement for both pump power

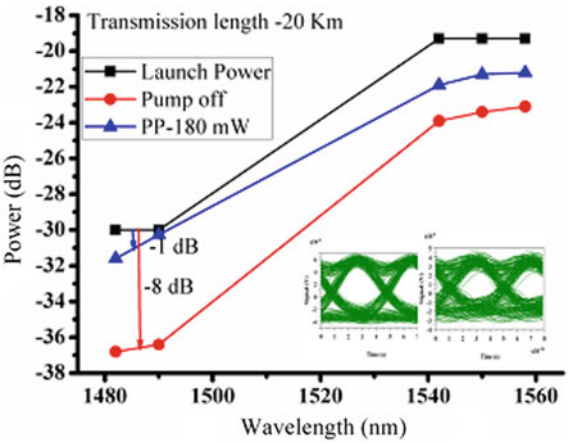

Fig. 2 Received power and eye diagram analysis with and without Raman pump at 20 km fiber length before ONU

configurations to achieve the desired transmission length or a number of users or both. If we compare eye height and signal quality of all signals, the higher wavelength signals will always have wider eye-opening and better signal quality in comparison with lower wavelength signals.

In equal pump power (E-PP) configuration, the 100 mW pump power is taken for each pump wavelength whereas for unequal pump power (UE-PP) configuration, the pump power decreases with increasing pump wavelength. It can be observed from the plot of Fig. 3a that the Raman gain at any fiber length is higher for E-PP than in the UE-PP pumping mode. Raman gain is dominant for shorter fiber length, and Raman on–off gain always increases with increasing transmission distance. Raman gain increases up to the effective length of the fiber and decreases beyond it due to nonlinear effects. The Raman on–off gain is calculated (see Eq. 6) after observing the received power at fiber end for both on and off stages of Raman pumps. Effective Raman gain is observable from the plot that initially this gain increases and after some fiber length it becomes saturated due to constant Raman gain coefficient and effective area of the fiber. The resulting analysis for both OSNR and spectral efficiency parameters behaves in the same way as Raman gain with respect to each fiber span. The only difference is that they are oppositely related to the Raman gain at each pump power configuration. This signifies that OSNR, as well as spectral efficiency, is higher and Raman gain is lesser for E-PP case at any fiber span or vice versa.

In each configuration, reach and data transmission rate are dependent on the effective Raman gain and spectral efficiency parameters. The maximum 55 km reach is achieved for 32 users, and beyond this length, the received power at the photodetector is below its acceptable level; hence, no communication can be achieved.

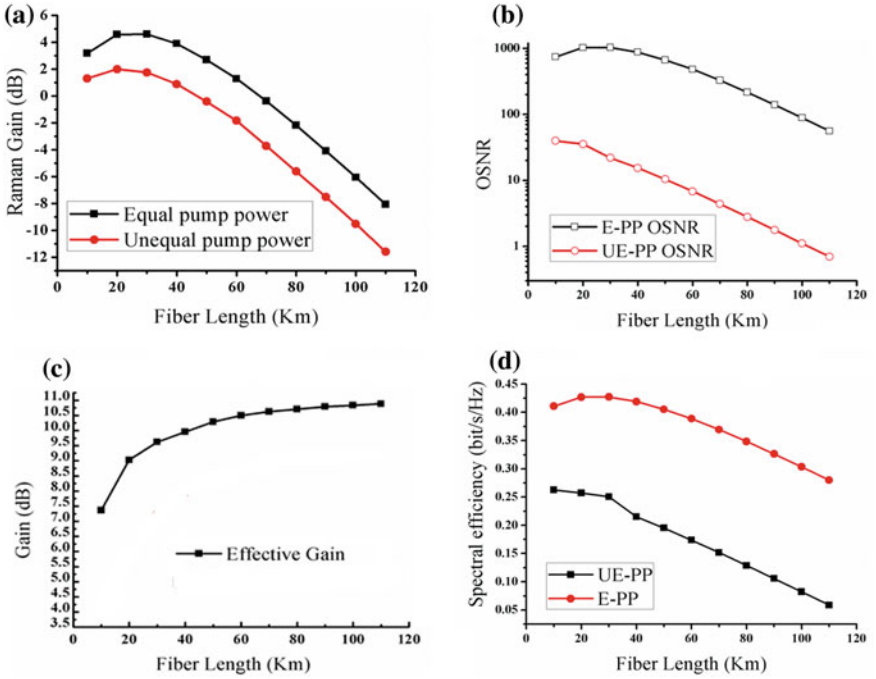

Fig. 3 Raman gain, optical signal-to-noise ratio, effective Raman gain and spectral efficiency analysis with increasing fiber length

5 Conclusion

The DPSK modulated distributed Raman amplifier in a WDM passive optical network system is designed and analyzed parametrically. The numerical data of system model design is employed to obtain the best performance characteristics of optical fiber Raman amplifiers in an optical communication system. The result analysis of the WDM-PON system provides 55 km transmission reach for 32 users and 0.3 bits/s/Hz higher spectral efficiency with 10 Gbps transmission speed. The network system efficiency is upgraded by increasing the transmission bit rate, distance and capacity of the system to support the maximum number of users or subscribers. There are many more interesting challenges that remain for future work. One can use bidirectional Raman pumping configuration for Raman amplification under the effect of temperature variation along the fiber cable. This yields the highest system capacity per channel and ultra-long-haul transmission distance for advanced optical communication system. Further investigations of nonlinear effects, including nonlinear phase noise on DPSK systems, are also feasible for longer transmission distance.

References

1. Park S, Lee C-H, Jeong K-T, Park H-J, Ahn J-G, Song K-H (2004) Fiber-to-the-home services based on wavelength-division-multiplexing passive optical network. J Lightwave Technol 20(11):2582–2591
2. Gupta MK, Dali PP, Singh G (2014) A novel approach to enhance the performance of ring based WDM PON. In: 2014 International conference on signal propagation and computer technology (ICSPCT), Ajmer, pp 329–331
3. Kachhatiya V, Shanthi P (2018) Downstream performance analysis and optimization of the next generation passive optical network stage 2 (NG-PON2). Opt Laser Technol 104:90–102
4. Breuer D et al (2011) Opportunities for next generation optical access. IEEE Commun Mag 49:16–24
5. Mahloo M et al (2014) Toward reliable hybrid WDM/TDM passive optical networks. IEEE Commun Mag 52:S14–S23
6. Gupta MK, Agarwal J, Dhingra A, Singh G (2016) Performance analysis and optimization of 40 Gbps transmission system over 4000 km with FBG. In: Proceedings of the international conference on recent cognizance in wireless communication & image processing, Jaipur, April, pp 759–765
7. Kaiser G (2013) Optical fiber communication, 5th edn. Tata McGraw-Hill Education, pp 545–546. ISBN 13: 9781259006876
8. Tian F, Hui R, Colella B, Bowler D (2004) Raman crosstalk in fiber-optic hybrid CATV systems with wide channel separations. IEEE Photonics Technol Lett 16(1):344–346
9. Kim H et al (2001) Performance limitations of hybrid WDM systems due to stimulated Raman scattering. IEEE Photonics Technol Lett 13(10):1118–1120
10. Fevrier HA, Chbat MW (2001) Raman amplification technology for bandwidth extension. In: Proceedings in the IEEE LEOS, San Diego, pp 344–345
11. Acharya K, Raja MYA (2010) Cross-talk penalty compensation and reach extension in wavelength division multiplexed passive optical network using remote Raman pump. Opt Eng 49(8):085002
12. Lu Y, Liu J, Hong X, Zeng D (2009) A novel evolution method for hybrid WDM/TDM-PON based on DPSK/NRZ orthogonal modulation. In: Asia communications and photonics conference and exhibition (ACP), Nov, pp 1–6
13. Rodríguez CC, Fernández FA et al (2015) Linewidth penalty on optical access networks using DPSK modulation format. Ingenius Sci Pap. https://doi.org/10.17163/ings.n13.2015.05
14. Chenyang H, Wei H (2011) Simulation and comparison of advanced modulation formats for wavelength reuse in High-Speed WDM-PON system. J Phys Conf Ser 276(1):9
15. Kahn JM, Ho K-P (2004) Spectral efficiency limits and modulation/detection techniques for DWDM systems. IEEE J Sel Top Quant Electron 10(2):259–272
16. Lu GW, Miyazaki T (2008) Spectrum efficient 80-Gb/s DPSK transmitter using phase interleaving technology without optical time or polarization division multiplexing. Opt Eng 47(5):050501. https://doi.org/10.1117/1.2931597
17. Winzer PJ, Essiambre RJ (2006) Advanced modulation formats for high-capacity optical transport networks. J Lightwave Technol 24(12):4711–4728
18. Proakis JG (2000) Digital communications, 4th edn. McGraw-Hill, New York
19. Headley C, Agrawal GP (2005) Raman amplification in fiber optical communication systems. Elsevier, San Diego
20. Gigabit-capable Passive Optical Networks (GPON), ITU-T, G.984 Series Recommendations
21. Kochera D, Kalera RS, Randhawa R (2013) Simulation of fiber to the home triple play services at 2 Gbit/s using GE-PON architecture for 56 ONUs. Opt Int J Light Electron Opt 124(21):5007–5010
22. Bakarman HA, Shaari S, Ismail M (2010) Simulation of 1.25 Gb/s downstream transmission performance of GPON-FTTx. In: International conference on photonics 2010, Langkawi, Kedah, July, pp 1–5

23. Kalera R, Kaler RS (2011) Simulation of fiber to the home at 10 Gbit/s using GE-PON architecture. Opt Int J Light Electron Opt 122(15):1362–1366
24. Cheng N, Zhou M, Effenberger FJ (2015) 10 Gbit/s delay modulation using a directly modulated DFB laser for a TWDM PON with converged services [invited]. IEEE/OSA J Opt Commun Networking 7(1):A87–A96
25. Penze RS, Rosolem JB, Duarte UR, Paiva GER, Filho RB (2014) Fiber powered extender for XG-PON/G-PON applications. IEEE/OSA J Opt Commun Networking 6(3):250–258

Comparative Analysis of a Novel Shape Patch Antenna for Wi-Max Band with Genetic Algorithm Optimization

Priyanka Jain, Raghavendra Sharma and Vandana Vikas Thakare

Abstract The size reduction of microstrip patch antenna is an important design consideration for the communication development in practical aspects. Here, a microstrip patch antenna is designed with different slits of L and parallel shape with a substrate of FR-4 ($\varepsilon_r = 4.4$) in order to decrease the antenna size and improved its gain. Genetic algorithm optimization is used to optimize the antenna structure. In this paper, three different antennas are designed with same structure but having different size of patch. The optimization with genetic algorithm is corporate with high-frequency structure simulator (HFSS) to obtain the optimal values of patch antenna. The simulation results give the reduction in size 18% than 44% and the increase in gain 5.3 and 8.6 db in the optimized design.

Keywords Rectangular Patch antenna · High-frequency structured simulator · Optimization · Genetic algorithm · Gain · Directivity

1 Introduction

Microstrip antennas have developed for microwave and millimeter wave application, for this reason they put forward a number of divergent rewards in excess of conservative microwave antennas [1–3]. These advantages consist of miniature size, simple fabrication, light mass, and uniformity by the present surface of vehicle, aeroplane, artillery, and straight incorporation through the developing electronics [4, 5]. Microstrip patch antennas (MSA) are known with many names, for example, imprint antennas (be capable of in print straight on top of a circuit panel), planar antenna, microstrip patch antenna or else basically microstrip antennas (MSA) [6].

P. Jain (✉) · R. Sharma
Department of ECE, Amity School of Engineering & Technology, Amity University Madhya-Pradesh, Gwalior, Madhya Pradesh, India

R. Sharma
e-mail: rsharma3@gwa.amity.edu

V. V. Thakare
Department of ECE, Madhav Institute of Technology and Science, Gwalior, Madhya Pradesh, India

V. Janyani et al. (eds.), *Optical and Wireless Technologies*, Lecture Notes in Electrical Engineering 648, https://doi.org/10.1007/978-981-15-2926-9_55

MSA commonly consists of a conducting patch, a conducting ground flat surface, a dielectric substrate sandwich in the middle of two, in addition to a feed coupled to the patch all the way through the substrate [7–10].

In recent years, there is a requirement for additional compact antennas as a result of fast reduce in the dimension of individual communication devices [11–13]. As communication devices develop into lesser because of better incorporation of electronics, the antenna becomes an appreciably big fraction in generally enclose capacity [14–16]. These grades a command for reductions in antenna dimension. In totaling, small shape antenna designs are also significant for the permanent wireless request. The microstrip antennas used in an extensive range of applications as of message systems to satellite and biomedical applications.

2 Microstrip Patch Antenna Design

The MSA used the material "FR4_EPOXY" for the dielectric substrate which has dielectric constant of 4.4 and height of dielectric substrate is 1.6 mm. The dimension of antenna is given in Table 1. The patch is fed with coaxial probe (50 Ω) which is easy to formulate and have simulated radiation. In proposed feeding method, the coaxial connector applies as of ground from end to end of the substrate and is joined to the radiating patch, whereas the external conductor extends from ground up toward substrate.

Here, Fig. 1 shows the image of patch antenna in dimension. Figure 2 shows the return loss of antenna which is −22.71 at 2 GHz frequency and −13.82 at 1.5 GHz frequency. There is a band of frequency from 1.5 GHz to 2 GHz, and VSWR of the

Table 1 Dimension of antenna

Resonance frequency (fr)	2.4 GHz
Dielectric constant (ε_r)	4.4
Height of the substrate (h)	0.5 mm
Length of patch (L)	38.5 mm
Width of patch (W)	28 mm
Dimension of L_a	21 × 1 mm
Dimension of L_b	21 × 1 mm
Dimension of L_c	11.5 × 1 mm
Dimension of L_d	11.5 × 1 mm
Dimension of L_e	11.5 × 1 mm
Dimension of L_f	11.5 × 1 mm
Dimension of L_g	3 × 1 mm
Dimension of L_h	3 × 1 mm
Radius of circular slot R	3 mm

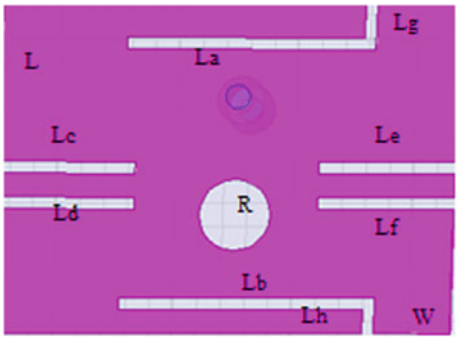

Fig. 1 Image of patch antenna

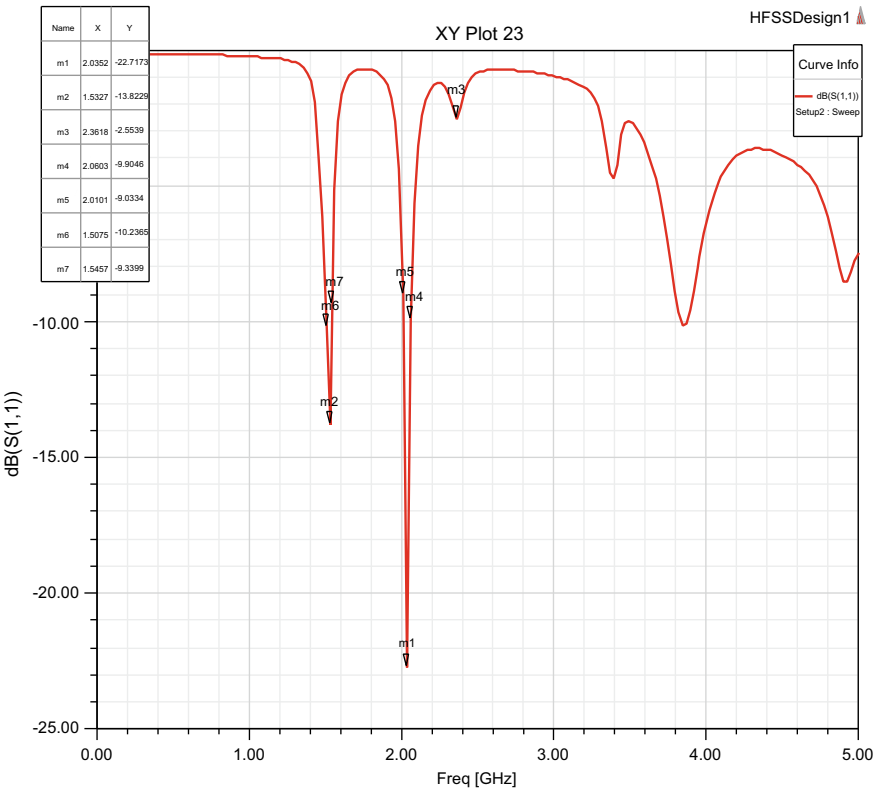

Fig. 2 Return loss of antenna

antenna is also below 2 which is 1.95 and 1.75 at these frequencies. Figures 3 and 4 show the gain and radiation pattern of antenna, which is 2.4 db.

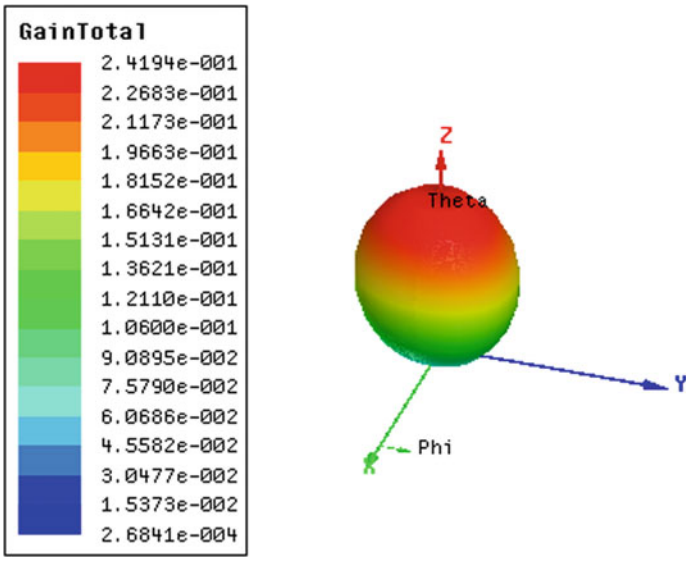

Fig. 3 Gain of antenna

3 Optimization of Patch Antenna

To get the finest probable result, the antenna has been optimized in a numeral behavior. Here, the optimization of patch antenna is done by the HFSS software. For this optimization procedure, genetic algorithm is used. The algorithms proceed through the subsequent input. The Maximum no. of generations is 20, the no. of parents is 10, and no. of individuals in the mating pool is 10. The individual crossover probability is 1 and variable crossover probability is 1, uniform mutation probability is 0.05, individual mutation probability is 1, and Pareto front value is 10. The next-generation parameters are, i.e., the no. of individuals—5. Here, the length (L) and width (W) of the microstrip patch antenna have been optimized; the bandwidth and return loss also have been simultaneously optimized. The result of the optimization is shown in Table 2.

After the optimization in all the possible ways the best results as shown in Table 2 and from this table, a best result will be designed practically which is highlighted. In Table 3, the dimension of re-designed optimized antenna is given, and software implementation of the design is shown in Fig. 5.

In Fig. 6, the return loss of optimized antenna is shown which is −14.42 at 1.783 GHz and −29.21 at 4.32 GHz and the VSWR of the antenna is also below 2 which is 1.52 and 1.71 at these frequencies. It shows the effectiveness of optimization by which we get the better result with reduced size of antenna. Figures 7 and 8 show the gain and radiation pattern of antenna which is 5.3 db.

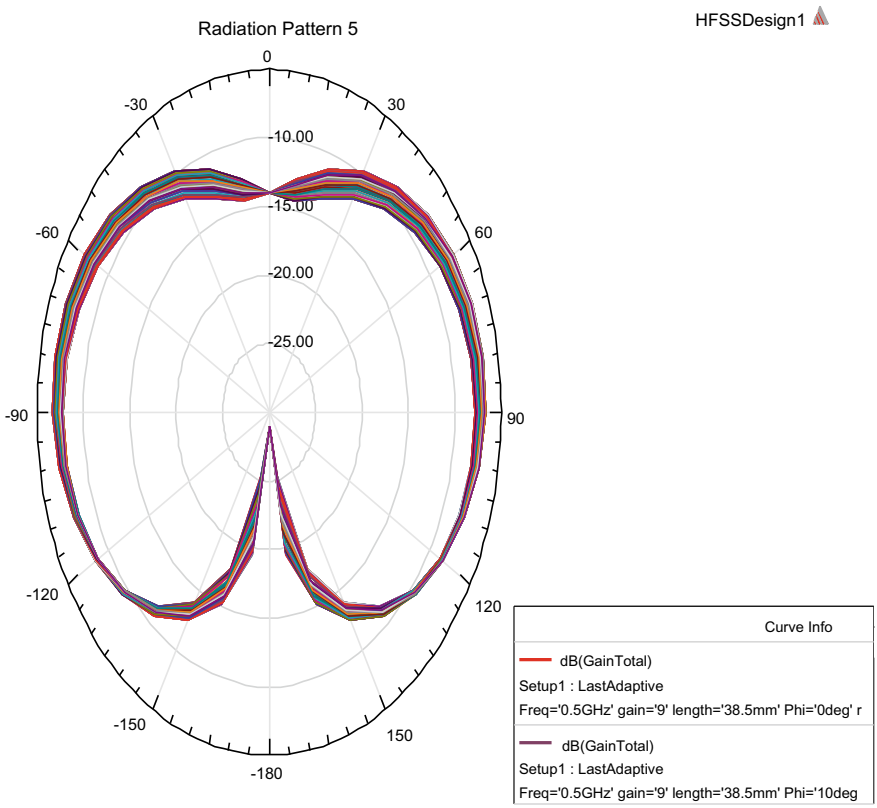

Fig. 4 Radiation pattern of antenna

Table 2 Optimization result of the microstrip patch antenna

Variation	Gain	Length	Return loss	Width
1	6.430357	56.2060991241188 mm	29.73830378	25.940183721427 mm
2	**9.43878**	**32.7655949583422 mm**	**28.83861812**	**19.8243964964751 mm**
3	5.017197	49.0552766502884 mm	14.61552782	38.2700277718436 mm
4	5.936506	39.4088335825678 mm	30.25663015	27.3022858363598 mm
5	6.782479	21.4424802392651 mm	13.47547838	25.2548600726341 mm

4 Double Optimization of Patch Antenna

For a personalized device, we required more small size antenna, and for this, we again do the optimization with the same parameter of this small size antenna. Table 4 shows the best possible optimization result. The optimization of the patch antenna is

Table 3 Dimensions of the optimized microstrip patch antenna

Resonance frequency (fr)	2.4 GHz
Dielectric constant (ε_r)	4.4
height of the substrate (h)	0.5 mm
Length of patch (L)	32 mm
Width of patch (W)	19 mm
Dimension of L_a	18 × 1 mm
Dimension of L_b	18 × 1 mm
Dimension of L_c	11.5 × 1 mm
Dimension of L_d	11.5 × 1 mm
Dimension of L_e	11.5 × 1 mm
Dimension of L_f	11.5 × 1 mm
Dimension of L_g	3 × 1 mm
Dimension of L_h	3 × 1 mm
Radius of circular slot R	2 mm

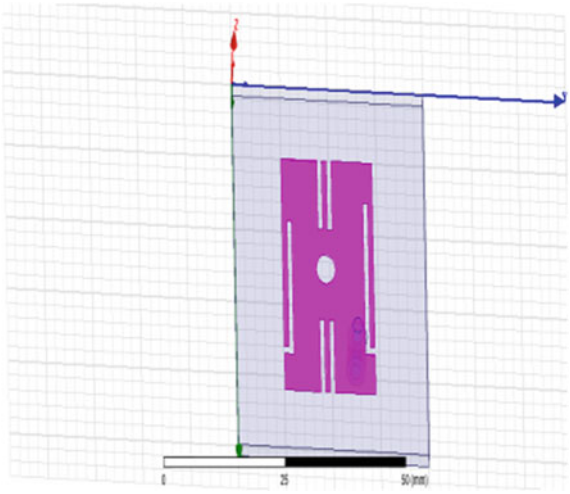

Fig. 5 Image of patch antenna

done by genetic algorithm procedure, and it proceeds with the same input parameters again.

After the optimization, we get the best probable results as shown in Table 4, and the best result from this table will be designed practically which is bold. In Table 5, the dimension of re-designed optimized antenna is given, and software implementation of the design is shown in Fig. 9.

In Fig. 10, the return loss of optimized antenna is shown which is −16.67 at 2.51 GHz and −30.90 at 4.44 GHz, and the VSWR of the antenna is also below than 2 as 1.12 and 1.27 at these frequencies. The gain and radiation pattern of antenna is

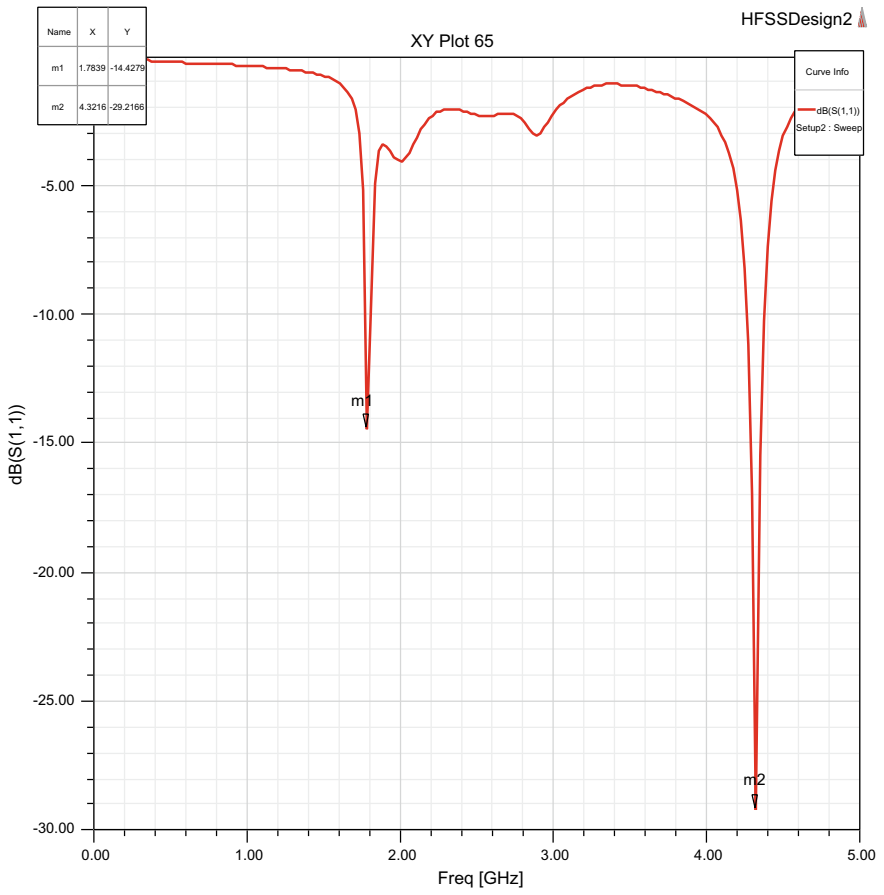

Fig. 6 Return loss of antenna

given in Figs. 11 and 12 which is 8.6 db. It shows the effectiveness of optimization by which we get the better result with reduced size of antenna.

5 Conclusion

In this paper, the result shows that genetic algorithms are extremely valuable for optimization of antenna, and also, these algorithms are designed for diverse RF optimization problem. The result shows, three microstrip patch antennas at 2.4 GHz are developed with the same design, but their dimension depends on their optimization result based on GA implanted in HFSS tool. Different parameter of antenna is optimized such as operating frequency, bandwidth, and radiation pattern through this tool. Primary parameters of antenna are set up as well as run the model of antenna

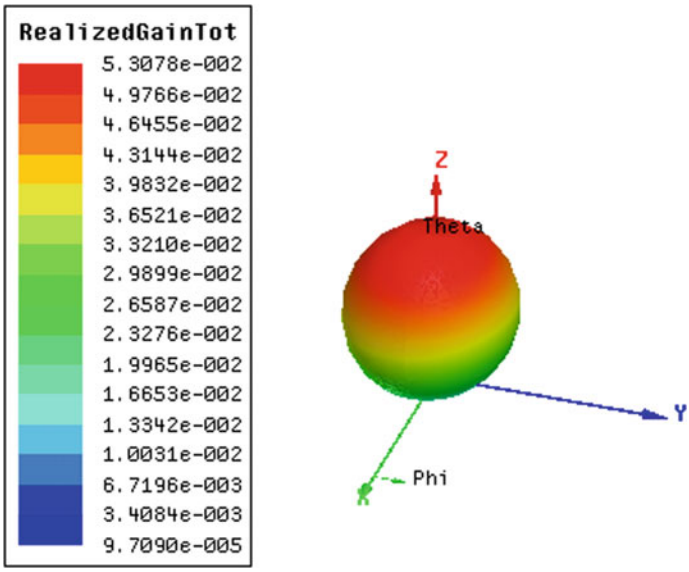

Fig. 7 Gain of antenna

in HFSS atmosphere, and after that, the fitness function is estimated. We select the first optimal entity according to the frequency in addition to the antenna reflection coefficient. The procedure is repeated until the optimal composition is originated for creating the new design. The comparative analysis of these three antennas is shown in Tables 6 and 7. Here, two types of comparison are done for this antenna which is dimension based and performance based. In dimension-based comparison (Table 6), the size is analyzed, and in performance based (Table 7), the result of antenna is analyzed based on different parameters like return loss, VSWR, etc. We also investigate a double-optimized antenna at 2.4 GHz. The antenna parameters are compared in Tables 6 and 7 and from these comparison tabs show that we get very good result after optimization and also achieve the new design with the 44% reduction in size and gain 6 dB which is also very good for antenna performance and practically implantation.

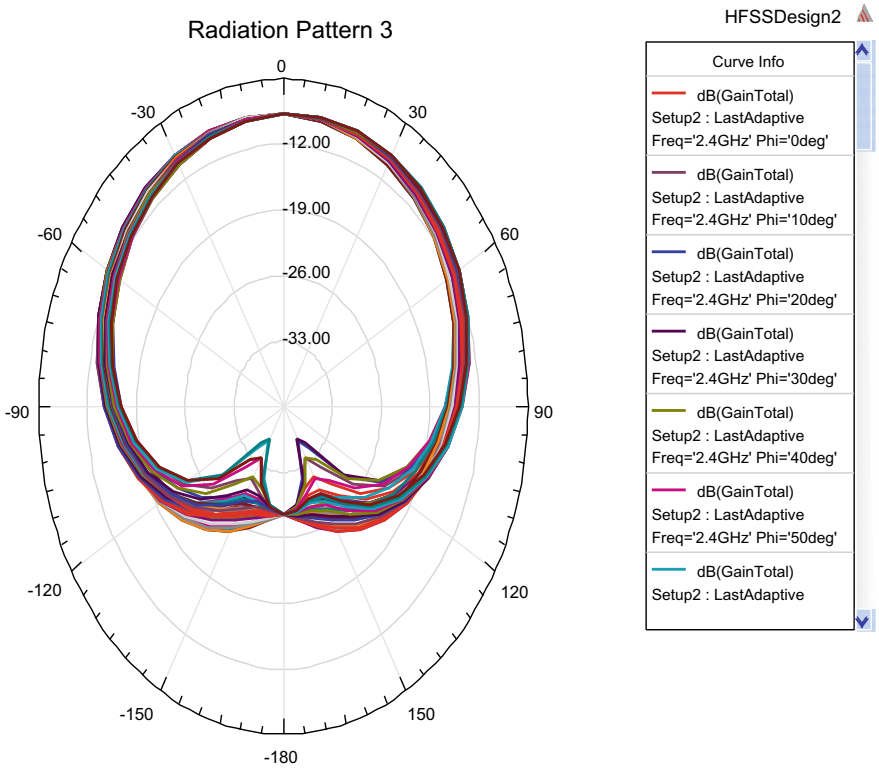

Fig. 8 Radiation pattern of antenna

Table 4 Optimization result of the microstrip patch antenna

Variation	Gain	Length	Return loss	Width
1	6.430356761	56.2060991241188 mm	29.73830378	25.940183721427 mm
2	9.43877987	32.7655949583422 mm	28.83861812	19.8243964964751 mm
3	5.01719718	49.0552766502884 mm	14.61552782	38.2700277718436 mm
4	5.936506241	39.4088335825678 mm	30.25663015	27.3022858363598 mm
5	6.782479324	21.4424802392651 mm	13.47547838	25.2548600726341 mm
6	5.455015717	55.961706900235 mm	32.99798578	19.3304849391156 mm
7	**12.10029908**	**21.6551484725486 mm**	**28.53379925**	**17.9239478743858 mm**
8	12.00141911	57.6207541123691 mm	11.94332713	14.0452894680624 mm
9	6.469634083	43.4307306131169 mm	26.26779992	33.2522965178381 mm
10	8.256065554	47.8250907925657 mm	28.31559191	25.4308908352916 mm

Table 5 Dimensions of the optimized microstrip patch antenna

Resonance frequency (fr)	2.4 GHz
Dielectric constant (ε_r)	4.4
Height of the substrate (h)	0.5 mm
Length of patch (L)	21 mm
Width of patch (W)	17 mm
Dimension of L_a	12 × 1 mm
Dimension of L_b	12 × 1 mm
Dimension of L_c	11.5 × 1 mm
Dimension of L_d	11.5 × 1 mm
Dimension of L_e	11.5 × 1 mm
Dimension of L_f	11.5 × 1 mm
Dimension of L_g	2 × 1 mm
Dimension of L_h	2 × 1 mm
Radius of circular slot R	4 mm

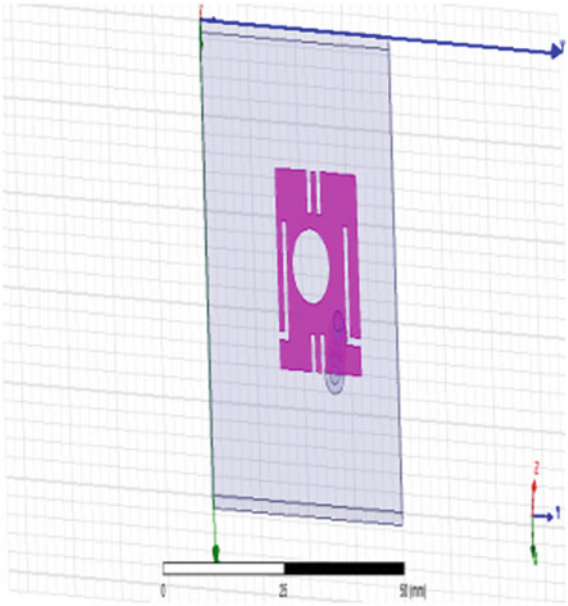

Fig. 9 Image of patch antenna

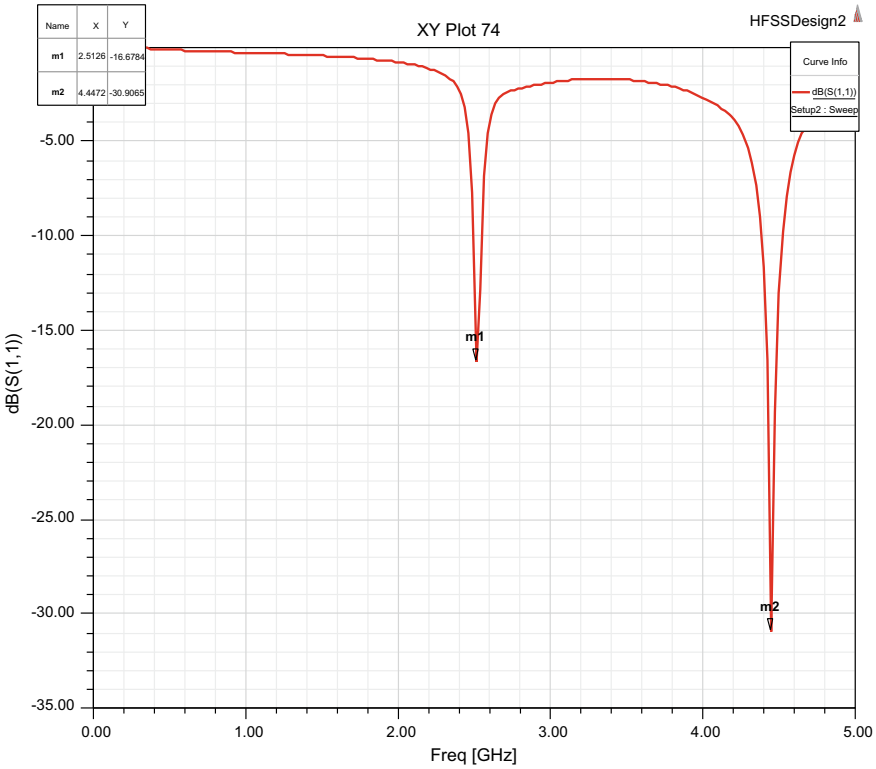

Fig. 10 Return loss of antenna

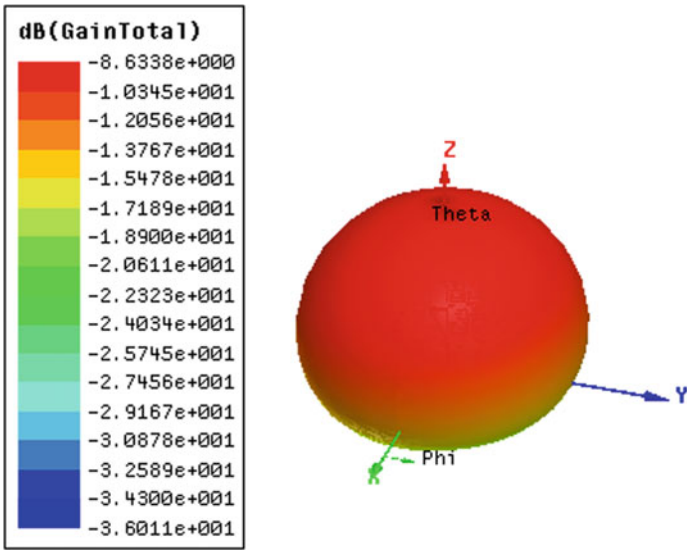

Fig. 11 Gain of antenna

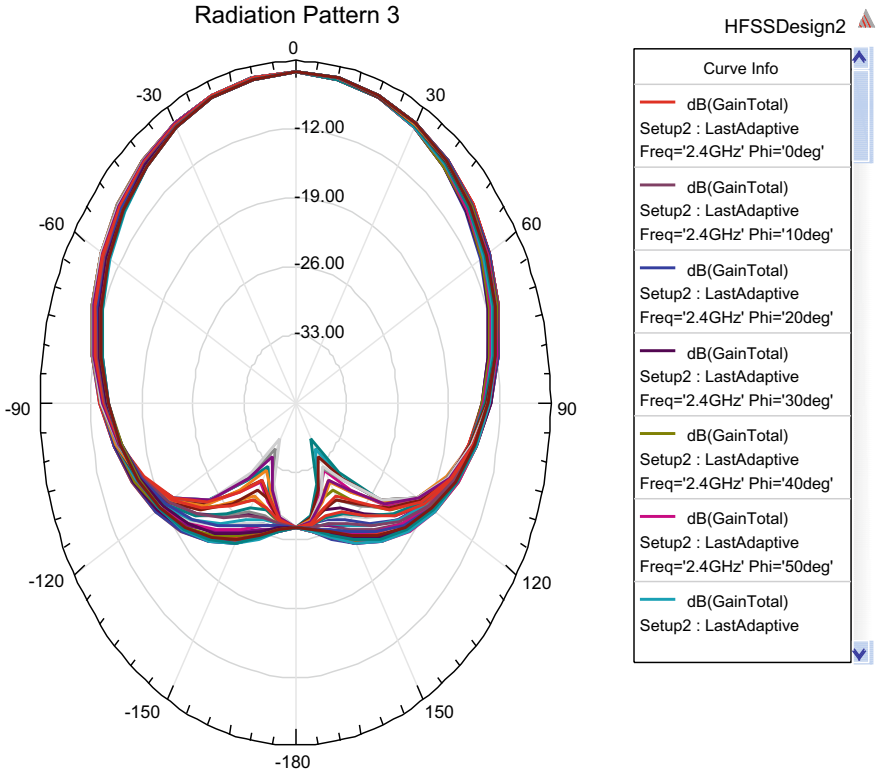

Fig. 12 Radiation pattern of antenna

Table 6 Comparison of antennas on dimension based

Dimension	Antenna	Optimized antenna	Double-optimized antenna
Resonance frequency (fr)	2.4 GHz	2.4 GHz	2.4 GHz
Dielectric constant (ε_r)	4.4	4.4	4.4
Thickness of the substrate (h)	0.5 mm	0.5 mm	0.5 mm
Length of patch (L)	38.5 mm	32 mm	21 mm
Width of patch (W)	28 mm	19 mm	17 mm
Dimension of L_a	21 × 1 mm	18 × 1 mm	12 × 1 mm
Dimension of L_b	21 × 1 mm	18 × 1 mm	12 × 1 mm
Dimension of L_c	11.5 × 1 mm	11.5 × 1 mm	11.5 × 1 mm
Dimension of L_d	11.5 × 1 mm	11.5 × 1 mm	11.5 × 1 mm
Dimension of L_e	11.5 × 1 mm	11.5 × 1 mm	11.5 × 1 mm
Dimension of L_f	11.5 × 1 mm	11.5 × 1 mm	11.5 × 1 mm
Dimension of L_g	3 × 1 mm	3 × 1 mm	2 × 1 mm
Dimension of L_h	3 × 1 mm	3 × 1 mm	2 × 1 mm
Radius of circular slot R	3 mm	2 mm	4 mm

Table 7 Comparison of antennas on result parameter based

Parameters	Antenna	Optimized antenna	Double-optimized antenna
Bandwidth (MHz)	203	210, 250	230, 280
Return loss	13.82, 22.71	14.42, 29.21	16.67, 30.90
VSWR	1.95,1.75	1.52, 1.71	1.12, 1.27
Frequency range (GHz)	1.5–2	1.783–4.32	2.54–4.44

References

1. Garg R, Bhartia P, Bahl IJ, Ittipiboon P (2001) Microstrip antenna design handbook. Artech House, Boston
2. Olaimat MM, Dib NI (2011) A study of 15°–75°-90° angles triangular patch antenna. Prog Electromagnet Res (PIER) 21:1–9
3. Olaimat MM, Dib NI (2011) Improved formulae for the resonant frequencies of triangular microstrip patch antennas. Int J Electron 98(3):407–424
4. Karaboga D, Guney K, Kaplan A, Akdagli A (1998) A new effective side length expression obtained using a modified tabu search algorithm for the resonant frequency of a triangular microstrip antenna. Int J RF Microwave CAE 8(1):4–10
5. Chen W, Lee KF, Dahele JS (1992) Theoretical and experimental studies of the resonant frequencies of the equilateral triangular microstrip antenna. IEEE Trans Antennas Propag Ap-40(10):1253–1256
6. Nasimuddin, Esselle K, Verma AK (2005) Resonant frequency of an equilateral triangular microstrip antenna. Microwave Opt Technol 47(5):485–489
7. Guha D, Siddiqui JY (2004) Resonant frequency of equilateral triangular microstrip patch antenna with and without air gaps. IEEE Trans Antennas Propag 52(8):2174–2177

8. Wong K (2002) Compact and broadband microstrip antennas. Wiley, New York
9. Kin-Lu W, Wen-Hsiu H (1997) Broadband triangular microstrip antenna with U-shaped slot. Electron Lett 33:2085–2087
10. Mudgal R, Shrivastava L (2014) Study of compact and wideband microstrip U-slot patch antenna with DGS for satellite applications. Int J Adv Innov Res 3:54–56
11. Ali MT, Aizat A, Pasya I, Zaharuddin MMH, Ya'acob N (2011) E-shape microstrip patch antenna for wideband applications. In: IEEE international conference on RF and microwave, pp 439–443
12. Wong H, Luk K-M, Chan CH, Xue Q, So KK, Lai HW (2012) Small antennas in wireless communications. Proc IEEE 100(7):2109–2121
13. Mazhar W, Tararm A, Tahir FA, Ullah S, Bhatti FA (2013) Compact microstrip patch antenna for ultra-wideband applications. In: PIERS proceedings, Stockholm, Sweden, 12–15 Aug 2013
14. Rajaraman G, Anitha M, Mukerjee A, Sood K, Jyoti R (2015) Dual-band, miniaturized, enhanced-gain patch antennas using differentially-loaded metastructures. Indian J Sci Technol 8(1):11
15. Madhav BTP, Khan H, Kotamraju SK (2016) Circularly polarized slotted aperture antenna with coplanar waveguide fed for broadband applications. J Eng Sci Technol 11(2):267–277
16. Ramna ASS (2013) Design of rectangular microstrip patch antenna using particle swarm optimization. Int J Adv Res Comput Commun Eng 2(7)

Analysis of Transmission Spectra of a Metal–Liquid Crystal–Metal Waveguide Structure with Different Metallic Layers

Ronak Dadhich and Ritu Sharma

Abstract In this paper, the transmission spectrum of liquid crystal waveguide between two metallic layers is studied and evaluated with finite difference time-domain (FDTD) technique. By putting a consistent electric field to the structure, the transmission range can be regulated effectively. The physical standard of this phenomenon is considered from the electro-optic effect of liquid crystals and the phase of surface plasmon polaritons (SPPs) in the waveguide. The numerical analysis has explained that an extensive tuning scope of the transmission range is achievable. For the switching purpose, the interaction of the optical properties and electrical switching of the proposed structure are utilized. In this paper, a correlation of transmission range of nematic liquid crystal E7-based waveguide with various metals (Cu, Ag, and Au) is effectively accomplished. For miniaturization and tuning purpose, this proposed structure can be proved as a proficient component in ultrahigh nanoscale coordinated photonic circuits.

Keywords Nematic liquid crystal · Optical waveguide · FDTD · Electro-optic effect

1 Introduction

Liquid crystals (LCs) have proved useful material in free-space and waveguide structure-based optical switches. In the near-infrared spectrum, LCs are transparent to any data format. A small quantity of material is useful to process a large number of devices, and therefore, it is cost-effective. As other materials (such as in polymers, silica on silicon, and glass) are based on optical fibers and optical waveguides, LC has a range of refractive index between 1.4 and 1.6. It provides a large electro-optic effect due to the high susceptibility of LCs molecular reorientation to the external electric field. It is related to high birefringence along with low scattering losses scales

R. Dadhich (✉) · R. Sharma
Department of Electronics and Communication Engineering, Malaviya National Institute of Technology, Jaipur, India
e-mail: 2017PWC5472@mnit.ac.in

V. Janyani et al. (eds.), *Optical and Wireless Technologies*, Lecture Notes in Electrical Engineering 648, https://doi.org/10.1007/978-981-15-2926-9_56

at a usable range of wavelength in the fiber optic systems. In the view of electro-optic effect in inorganic materials, for example, $LiNbo_3$ cannot be utilized for the manufacturing of large-dimensional switching matrices in the waveguide geometries because of less unwavering quality and reproducibility over vast regions [1].

The LC waveguide appears to be brilliant for future millimeter wave (MMW)-based advances. It is preferred because of its small size along with lightweight and can work productively beneath 30 GHz. The reorientation of LC's director changes the permittivity of LC with respect to the polarized wave with a magnetostatic or electrostatic field. Along these features, LC will turn into an interesting material for the application based on MMW devices. LC can be utilized as a tunable dielectric material, for example, the substrate for microstrip in the waveguide [2]. LC waveguide-based devices attain a speed in the microsecond range [3]. Nowadays, in meta-material research, optical waveguides based on SPP become an area of interest. One of the special features of these dielectric waveguides is the possibility to beat the diffraction limit for acknowledging high integrated nanoscale photonic devices [4, 5]. Waveguides based on an insulator between metallic layers become popular due to their solid optical subwavelength control of electromagnetic energy coupled with SPPs propagating in a profound dielectric core among plasmonic conducting structures [6–8]. Ongoing exploration in the plasmonic region has prompted vital advances being developed of different metal–insulator–metal (MIM) plasmonic devices, for example, wavelength sorters [9], bends and splitters [10, 11], Mach–Zehnder interferometers [12], and Y-shaped combiners [13]. SPP filters are one of the main parts in the SPP mix stage. Distinctive SPP channel structures based on the MIM waveguides have been proposed to include tooth-shaped channels [14], ring resonator channels [15, 16], and Bragg-grating filters. There are few techniques to actualize tunable plasmonic structures such as excitation in terms of temperature [17], optical control, mechanical control, and voltage control [18] provide effective regulation in the device's optical properties. Conceivable uses of the devices based on LCs can be found in, however, are not limited to, optical correspondence frameworks and lighting applications [19]. The transmission spectrum can be managed by utilizing liquid crystal in the structure's insulator area and presenting this structure to a consistent remotely connected electric field region. Henceforth, there is no need to change in the geometrical parameters of the channel. The inspiration for considering LC is the probability of utilizing the guidelines in controlling the plasmonic signals [20].

This paper is composed of pursues. Subsequently, after the introduction, a concise survey of the 2D structure of M-LC-M waveguide is reported in Sect. 2. In Sect. 3, the dispersion relations of different metals by Lorentz-Drude model are expressed. At that point, the results of this design with variations in the molecular director's angle are presented and explained in Sect. 4. The explanation of fundamental physical standard of the procedure of dynamic transmission reaction control based on the dependency of effective refractive index on misalignments of LC molecules is investigated. At last, the paper is completed with the conclusion in Sect. 5.

2 2D Structure of M-LC-M Waveguide

Under this investigation, the proposed structure containing a waveguide section of 2L width with its interfaces normal to the x-axis, which is loaded up with nematic liquid crystals (NLC) is shown in Fig. 1 and comprises two metallic layers at both sides. It behaves as a waveguide for the propagation of SPP as a waveguide mode for TM-polarized waves along the z-direction (Fig. 2).

LC layer's width (2L) is selected too small as compared to incident light's wavelength for excitation of fundamental SPP mode only. Here, the LC layer's width is kept 100 nm.

Effective refractive index depends on different alignments of the LC molecular director. In the representation of the molecular director's orientation, θ shows a

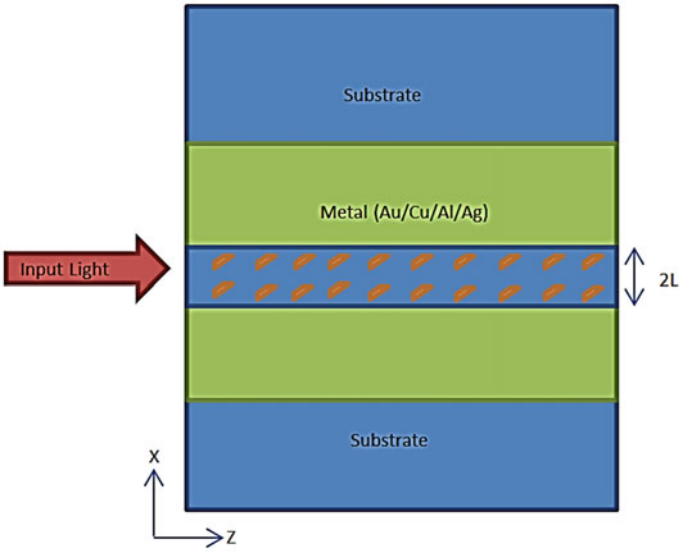

Fig. 1 Structure of M-LC-M waveguide

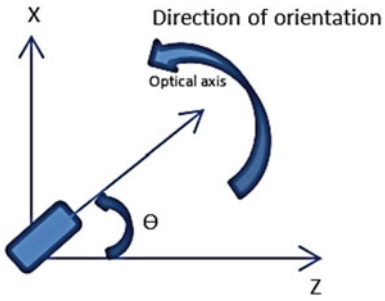

Fig. 2 Molecular director's orientation

twist angle between *Z*-axis and an optical axis of the molecular director which can be altered by applying voltage, so that active transmission response control can be easily achieved.

3 Numerical Analysis

The dispersion behavior of different metals which are used in M-LC-M waveguide has been evaluated by Lorentz-Drude model. For dispersive behavior of metals, Lorentz model cannot be used. However, Drude model can be used to describe dispersive behavior of metals but not for bounded electrons in the material. It has also a limitation when the dielectric constant depends on the wave vector. To overcome these limitations, the Lorentz-Drude model can be used efficiently. It also increases the accuracy compared to the other two models because it contains numerous Sellmeier coefficient. The summation of numerous resonance Lorentzian functions and the frequency-dependent dielectric permittivity can be depicted as [21]:

$$\varepsilon_r(\omega) = \breve{\varepsilon}_{r,\infty} + \sum_{m=0}^{M} \frac{A_m \acute{\Omega}_m^2}{\omega_m^2 - \breve{\omega}^2 + j\breve{\omega}\Upsilon_m} \tag{1}$$

where $\breve{\varepsilon}_{r,\infty}$ denotes the relative permittivity at the infinite frequency, m indicates the number of oscillators, A_m implies oscillator strength, Ω_m stands for plasma frequency, ω_m denotes resonant frequency, $\acute{\omega}$ indicates incident ray's angular frequency, and Υ denotes factor of damping or collision frequency.

Different metals like Cu, Au, and Ag are considered for metallic layers in M-LC-M waveguide and their dispersive behavior is tabulated in Tables 1, 2 and 3.

Here, metals such as Cu, Au, and Ag have unit relative permittivity at an infinite frequency, whereas R' denotes resonance, S represents the strength of the corresponding resonance terms, P denotes plasma frequency, R denotes frequency at resonant condition, and D indicates collision frequency. The values of S, P, R, and D are calculated by Lorentz-Drude model by Eq. 1.

Table 1 Estimation of dispersion behavior of copper (Cu) using the Lorentz-Drude model at $R' = 5$

R'	S	P (rad/s)	R (rad/s)	D (rad/s)
1	5.75e−1	1.645350e16	0.00e00	4.55e13
2	6.10e−2	1.645350e16	4.42e14	5.74e14
3	1.04e−1	1.645350e16	4.49e15	1.60e15
4	7.23e−1	1.645350e16	8.05e15	4.88e15
5	6.38e−1	1.645350e16	1.69e16	6.54e15

Table 2 Estimation of dispersion behavior of gold (Au) using the Lorentz-Drude model at $R' = 6$

R'	S	P (rad/s)	R (rad/s)	D (rad/s)
1	7.60e−1	1.371880e16	0.00e00	8.05e13
2	2.40e−1	1.371880e16	6.30e14	3.66e14
3	1.00e−2	1.371880e16	1.26e15	5.24e14
4	7.10e−1	1.371880e16	4.51e15	1.32e15
5	6.01e−2	1.371880e16	6.53e15	3.78e15
6	4.38e−2	1.371880e16	2.02e15	3.36e15

Table 3 Estimation of dispersion behavior of silver (Ag) using the Lorentz-Drude model at $(R') = 6$

R'	S	P (rad/s)	R (rad/s)	D (rad/s)
1	8.45e−1	1.3690e16	0.00e00	7.29e13
2	6.50e−2	1.3690e16	1.24e15	5.90e14
3	1.24e−1	1.3690e16	6.80e15	6.86e15
4	1.10e−2	1.3690e16	1.24e16	9.87e15
5	8.40e−1	1.3690e16	1.38e16	1.39e15
6	5.64e00	1.3690e16	3.08e16	3.67e15

In general, the anisotropic LC director's optic axis is arranged in the x–z plane and then corresponding dielectric tensor for the permittivity of LCs director is shown as [22]:

$$\overline{\overline{\varepsilon}} = \begin{bmatrix} n_e^2 \cos^2\theta + n_o^2 \sin^2\theta & 0 & \left(n_e^2 - n_o^2\right) \sin\theta \cos\theta \\ 0 & n_e^2 & 0 \\ \left(n_e^2 - n_o^2\right) \sin\theta \cos\theta & 0 & n_o^2 \cos^2\theta + n_e^2 \sin^2\theta \end{bmatrix}$$

In the above equation, n_e and n_o stand for the extraordinary and ordinary refractive indices, respectively. Here, θ represents the tilt angle between z-axis and the optical axis of the LC director. At room temperature, parameters of nematic liquid crystal, such as n_e and n_o are chosen to be 1.737 and 1.518. The measure of voltage expected to switch a modulator based on the nematic liquid crystal is an element of the particular material utilized, alignment, and cell thickness variation (Figs. 3 and 4).

At $\theta = 0$, the LC particles are adjusted parallel to the rectangular strip with a little pretwist angle. In this way, the optical tensor basically reduces to the ordinary index for any of the input light polarization. So, the guided mode cannot be energized. Henceforth, the waveguide is switched to the cutoff state. As θ expands, the optical tensor detects extraordinary refractive index, and therefore, guided mode can be effectively energized and the waveguide is turned into the energized state.

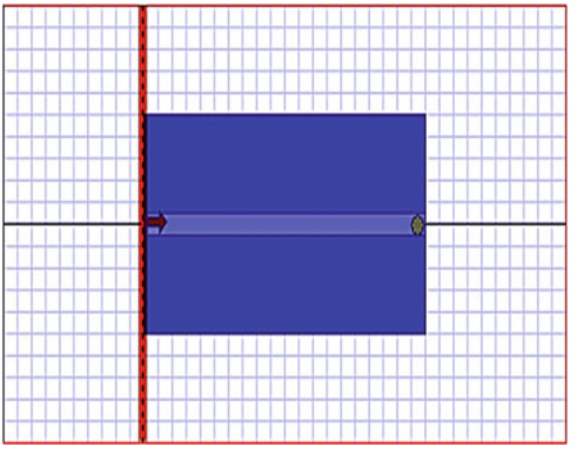

Fig. 3 Design of M-LC-M waveguide on optiFDTD [22]

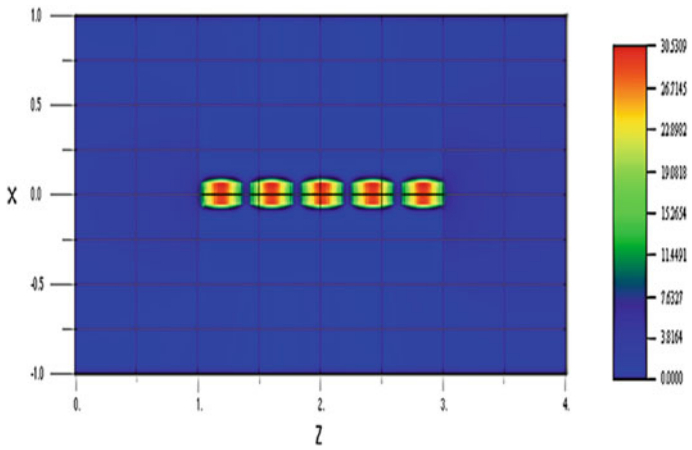

Fig. 4 Magnetic field distribution (Hy) of the waveguide

4 Result and Discussion

It can be easily observed that high light restriction has accomplished for little LC director tilt angles for the given waveguide structure. By increasing the tilt angle, effective permittivity alters and as a result transmittance increases. It is also demonstrated that the degree of this light confinement or transmission spectrum can be varied by varying the tilt angle of the LC molecules, which can be most conveniently accomplished through an externally applied voltage.

In Fig. 5, the transmittance of M-LC-M waveguide at different molecular director's angle is shown using different metal layers.

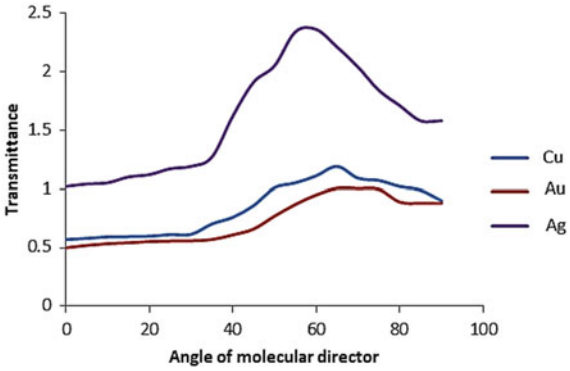

Fig. 5 Transmittance of M-LC-M waveguide versus angle of molecular director

From the graph, it can be observed that transmittance increases with the increment in the angle of molecular director up to 55° angle. At 60°, highest transmission spectrum is demonstrated after that it declines gradually. The transmission response of metals increases in the following manner:

$$\text{Ag} > \text{Cu} > \text{Au}$$

The normalized transmittance is defined as $P_{\text{out}}/P_{\text{in}}$. The transmission spectra are evaluated and depicted in Fig. 6 for three cases such as the metallic layer of silver, copper, and gold, respectively. Among these metals, silver provides the highest transmission spectra. It is also estimated from the graph that flat spectra or wide tuning wavelength range from 1.45 to 1.7 μm is obtained for the designed M-LC-M waveguide. These three metals increase the electro-optic effect in liquid crystal waveguide at the dielectric–metal interface compared to other metals.

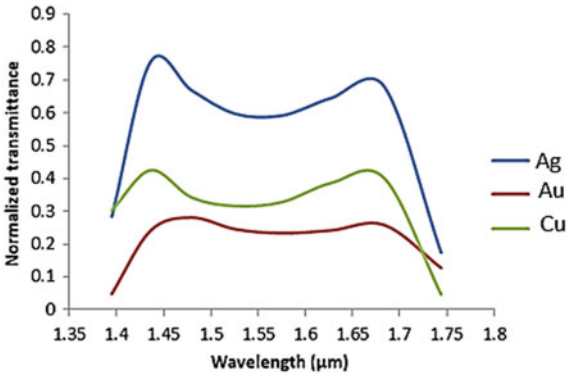

Fig. 6 Optical power transmission characteristics of M-LC-M waveguide in a specific wavelength range

5 Conclusion

The transmission spectra of a metal–liquid crystal–metal waveguide structure with different metallic layers like Ag, Au, Al, and Cu with respect to variations in angle is analyzed in this paper. Point-by-point qualities of this structure are examined by numerical recreations to exhibit the practicality of this idea by utilizing the Lorentz-Drude model of various metals. The orientations of LC particles can be regulated by applying a low external voltage, thus inducing a variation in the refractive index of LC by the guided SP mode field can be easily observed. The highest transmission response at 60° angle of LC molecular director with flat spectra in 1.45–1.7 μm wavelength range is achieved. It is clearly shown that the transmission response can be controlled easily without changing the geometrical parameters of structure from the simulated results.

References

1. D'Alessandro A, Asquini R (2003) Liquid crystal devices for photonic switching applications: state of the art and future developments. Mol Cryst Liq Cryst 398(1):207–221
2. Wang H, Zheng L, Chen J, Wu TX, Wu S-T (2004) Smart millimeter-wave devices using liquid crystal. In: Smart structures and materials 2004: smart electronics, MEMS, BioMEMS, and nanotechnology, vol 5389. International Society for Optics and Photonics, pp 476–486
3. Davis SR, Farca G, Rommel SD, Johnson S, Anderson MH (2010) Liquid crystal waveguides: new devices enabled by >1000 waves of optical phase control. In: Emerging liquid crystal technologies V, vol 7618. International Society for Optics and Photonics, p 76180E
4. Barnes WL, Dereux A, Ebbesen TW (2003) Surface plasmon subwavelength optics. Nature 424(6950):824–830
5. Ebbesen TW, Lezec HJ, Ghaemi HF, Thio T, Wolff PA (1998) Extraordinary optical transmission through sub-wavelength hole arrays. Nature 391(6668):667–669
6. Economou EN (1969) Surface plasmons in thin films. Phys Rev 182(2):539–554
7. Prade B, Vinet JY, Mysyrowicz A (1991) Guided optical waves in planar heterostructures with negative dielectric constant. Phys Rev B 44(24):13556–13572
8. Burke JJ, Stegeman GI (1986) Surface-polariton-like waves guided by thin, lossy metal films. Phys Rev B 33(8):5186–5201
9. Kang Z, Wang GP (2008) Coupled metal gap waveguides as plasmonic wavelength sorters. Opt Express 16(11):7680–7685
10. Veronis G, Fana S (2005) Bends and splitters in metal-dielectric-metal subwavelength plasmonic waveguides. Appl Phys Lett 87:(131102) 1–3
11. Lee TW, Gray SK (2005) Subwavelength light bending by metal slit structures. Opt Express 13(24):9652–9659
12. Han Z, Liu L, Forsberg E (2006) Ultracompact directional couplers and Mach-Zehnder interferometers employing surface plasmon polaritons. Opt Commun 259(2):690–695
13. Gao H, Shi H, Wang C, Du C, Luo X, Deng Q, Lv Y, Lin X, Yao H (2005) Surface plasmon polariton propagation and combination in Y-shaped metallic channels. Opt Express 13(26):10795–10800
14. Lin XS, Huang XG (2008) Tooth-shaped plasmonic waveguide filters with nanometric sizes. Opt Express 33(23):2874–2876
15. Tao J, Huang XG, Lin X, Chen J, Zhang Q, Jin X (2010) Systematical research on characteristics of double-sided teeth-shaped nanoplasmonic waveguide filters. JOSA B 27(2):323–327

16. Wang TB, Wen XW, Yin CP, Wang HZ (2009) The transmission characteristics of surface plasmon polaritons in ring resonator. Opt Express 17(26):24096–24101
17. Chen MK, Chang YC, Yang CE, Guo Y, Mazurowski J, Yin S, Ruffin P, Brantley C, Edwards E, Luo C (2010) Tunable terahertz plasmonic lenses based on semiconductor microslits. Microwave Opt Technol Lett 52(4):979–981
18. Vincenti MA, D'Orazio A, Buncick M, Akozbek N, Bloemer MJ, Scalora M (2009) Beam steering from resonant subwavelength slits filled with a nonlinear material. JOSA B 26(2):301–307
19. Li P, Sasaki T, Pan LF, Hane K (2012) Combdrive tracking and focusing lens actuators integrated on a silicon-on-insulator wafer. Opt Express 20(1):627–634
20. Wang X, Wang B, Bos PJ, McManamon PF, Pouch JJ, Miranda FA, Anderson JE (2005) Modeling and design of an optimized liquid-crystal optical phased array. J Appl Phys 98(7):(073101) 1–8
21. Eldlio M, Che F, Cada M (2014) Drude-Lorentz model of semiconductor optical plasmons. In: IAENG transactions on engineering technologies. Springer, Dordrecht, pp 41–49
22. Alavi SM, Armand H (2015) Liquid crystal-based dielectric-loaded plasmonic ring resonator filter. ACES 30(2):245–254

Studies of Various Artificial Magnetic Conductor for 5G Applications

Ashok Kumar, Amrita Dixit, Ashok Kumar and Arjun Kumar

Abstract In this paper, the characteristics of numerous types of artificial magnetic conductor (AMC) surface structures are investigated on high-frequency structure simulator (HFSS) and presented. These AMC surface structures are presented with zero-degree reflection phase property for a plane wave at 28 GHz frequency band. The ±90° in-phase reflection bandwidth, magnitude, and surface impedance of all AMC structures are simulated and compared with others. The simulated results show that all AMC surfaces act as a high impedance surface and good reflector. The simulated fractional bandwidth of proposed AMC type I, II, III, and IV structures are 4.68%, 7.12%, 9.03%, and 20.64%, respectively. The better performance of the proposed AMC type IV makes it as useful to improve the antenna's characteristics.

Keywords Metamaterials · Artificial magnetic conductor (AMC) · Reflection phase · Bandwidth · HFSS

1 Introduction

The metamaterials are the artificial structures, which have a unique characteristic such as both permittivity and permeability are negative. It is not found in nature and plays a vital role in the field of optical and microwave engineering [1]. The numerous metamaterial structures such as photonic band-gap (PBG) [2], complementary split-ring resonator (CSRR) [3, 4], defected ground structure (DGS) [5], frequency selective surfaces (FSS) [6], high impedance surface (HIS) [7], electromagnetic band-gap (EBG) [8], and artificial magnetic conductor (AMC) [9] are considered to enhance the radiation characteristics of microwave components. The great interest of researchers about AMCs is due to their two interesting properties that are in-phase reflection and high impedance surface [10]. The first AMC structure was proposed by Walser in 1993 [11]. In 1999, mushroom-like AMC structure is proposed by Dan Sievenpiper,

A. Kumar (✉) · A. Dixit · A. Kumar
School of Engineering and Applied Sciences, Bennett University, Greater Noida, India

A. Kumar
Department of Electronics and Communication Engineering, Government Women Engineering College, Ajmer, India

V. Janyani et al. (eds.), *Optical and Wireless Technologies*, Lecture Notes in Electrical Engineering 648, https://doi.org/10.1007/978-981-15-2926-9_57

with the substrate material TMM6 that mimic the behavior like perfect magnetic conductor (PMC) over the specific frequency band [12]. AMC is analogous to PMC surface in specific frequency range, and PMC introduces the zero-degree reflection phase to the incident waves [13, 14]. The reflection phase of the AMC unit cell is explained as the phase of reflected electric field component which is normal to the phase of the incident electric field at reflecting surface. If the reflection phase is zero degree, then it is called in-phase reflection. The reflection phase of AMC varies $+180°$ to $-180°$ and crosses the zero degree at its resonant frequency. The practical bandwidth of an AMC is the frequency range from $+90°$ to $-90°$ on both sides of resonant frequency in reflection phase graph relative to frequency [9], since in this range no destructive interference would occur between incident and reflected waves. AMC is an arrangement of infinitely periodic structure and unit cell is similar to waveguide. The key difference between AMC and waveguide model is four sides of boundary conditions. The two walls of PEC boundary are set orthogonally to electric field and another two walls to magnetic field [15]. The periodic arrangement of the AMC unit cells acts as high impedance reflector surface and have capacity to suppress the surface waves. In the antenna array system, when metal patches are placed at a distance less than $\lambda/4$ at the same plane cause the mutual coupling [16]. The mutual coupling is the interaction of electromagnetic field between the antenna elements. AMC's structures are used to minimize the mutual coupling between metal plates. Various AMC's structures are presented in the literature, which are helpful to enhance the radiation characteristics of antenna element. Some published AMCs are summarized as in Table 1. The mushroom-like EBG has drawback due to via as the integration of vias are difficult in design [9]. After that, uniplanar UC-EBG structure is proposed without vias. The focus of this paper is the comparative study of AMC unit cell based on reflection phase (degree), reflection magnitude, and surface impedance.

The outline of this paper is as follows: In Sect. 2, equivalent circuit of AMC unit cell is presented. Section 3 describes the various proposed AMC unit cell for 28 GHz frequency. Section 4 explains the results' analysis of AMC unit cell. Finally, Sect. 5 concludes the broad finding of the study.

2 Equivalent Circuit of AMC Unit Cell

As the wavelength is much smaller than a unit cell (single period), the effective surface impedance can be explained in terms of lumped components (i.e., inductors and capacitors). The equivalent circuit of AMC has a parallel capacitor (C) and inductor (L) with their impedances Z_1 and Z_2, respectively, as depicted in Fig. 1.

At resonance, the surface impedance of parallel LC circuit is [9]

$$Z_{\text{HIS}} = \frac{Z_1 Z_2}{Z_1 + Z_2} = \frac{1/j\omega C * j\omega L}{1/j\omega C + j\omega L} \tag{1}$$

Table 1 Published AMCs' unit cell

Reference	Unit cell type	f_r (GHz)	AMC BW (GHz, %)	Substrate used	ε_r	Overall size of AMC cell $W \times L \times h$ (mm^3)
[9]	Mushroom-like EBG	2.45	2.28–2.60, 12.08	TMM 6	6.0	18.2 × 18.2 × 2.54
	Uniplanar UC-EBG	2.45	2.38–2.49, 4.88	TMM 6	6.0	20 × 20 × 2.54
[17]	Novel SHF-band uniplanar AMC	5.7	5.52–5.95, 7.3	Arlon 25 N	3.28	11.52 × 11.52 × 0.762
[18]	JC-based AMC	2.45	4.40–4.90, 10.75	Vinyl	2.5	65.7 × 65.7 × 1.5
[19]	Square patch	28.0	26.24–29.79, 12.7	RT/Duroid 5880	2.2	3.392 × 3.392 × 0.254
	Modified AMC	28.0	27.24–28.60, 4.88	RT/Duroid 5880	2.2	2.2738 × 2.2738 × 0.254
[20]	Square Patch AMC	0.90	0.88–0.92, 4.4	FR-4	4.4	69 × 69 × 3.2

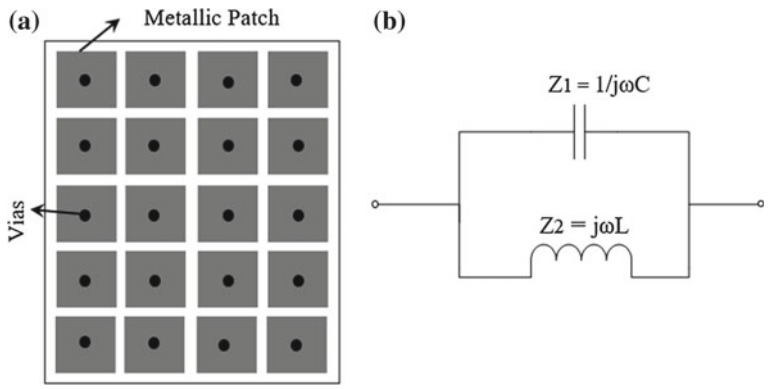

Fig. 1 AMC/HIS surface **a** top view and **b** equivalent circuit [9]

$$Z_{\text{HIS}} = \frac{j\omega L}{1 + j^2\omega^2 LC} = \frac{j\omega L}{1 - \omega^2 LC} \tag{2}$$

At resonance condition, the frequency of AMC/HIS can be calculated as:

$$f_r = \frac{1}{2\pi\sqrt{LC}} \tag{3}$$

By putting $\omega^2 LC = 1$ in Eq. (2), then the Z_{HIS} becomes infinite which shows the high impedance surface. It means that the surface impedance of AMC/HIS is infinite at its resonant frequency.

3 Various Types of AMC Unit Cell

The schematic diagrams of four different types of AMC unit cell structures are depicted in Fig. 2.

These structures are designed on low-loss RT/Duroid 5880 substrate with dielectric permittivity ε_r of 2.2, substrate thickness of 0.254 mm, and loss tangent 0.0009. The AMC unit cell type I is designed with center square ring of length $L_C = 0.3$ mm. It has four arms of length $k = 0.7$ mm and slots are of length $d = 0.25$ mm to achieve better performance. In AMC type II, the stub of length $L_a = 0.3$ mm. The

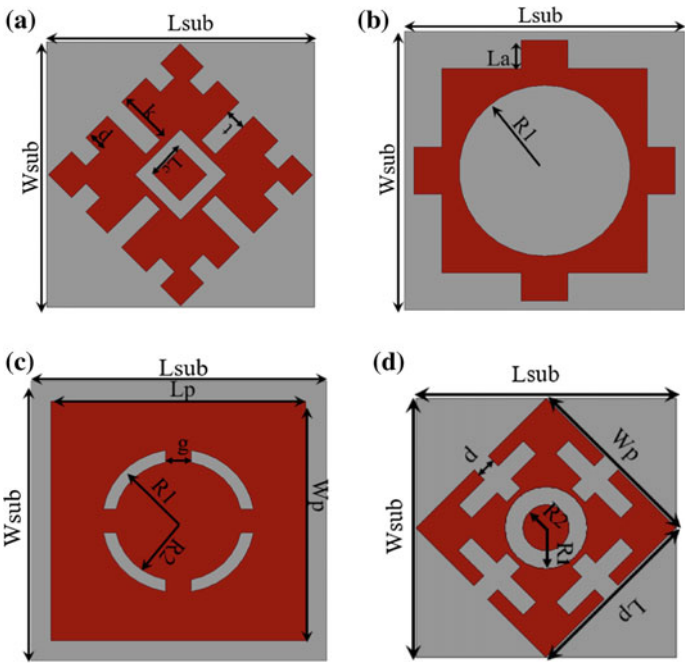

Fig. 2 Schematic diagrams of the proposed AMC surfaces: **a** AMC type I, **b** AMC type II, **c** AMC type III, and **d** AMC type IV

Table 2 Design parameters of various unit cells

S. No.	Unit cell type	Lsub (mm)	Wsub (mm)	Lp (mm)	Wp (mm)	R_1 (mm)	R_2 (mm)
1	AMC type I	3.3	3.3	2.3	2.3	–	–
2	AMC type II	3	3	2.2	2.2	0.91	–
3	AMC type III	3.5	3.5	3	3	0.90	0.75
4	AMC type IV	2.84	2.84	2.0	2.0	0.45	0.25

gap $g = 0.3$ mm is considered for designing the AMC type III. The AMC type IV is a rhombic-shaped AMC with slot arms and etched slot dimension d is 0.215 mm. The design dimensions' parameters of aforementioned AMC unit cells are given in Table 2.

4 Comparative Results Analysis of Various Unit Cells

Using full-wave simulation tool HFSS (ver. 19.1), the simulated reflection magnitude versus frequency of proposed unit cells is depicted in Fig. 3. Reflection magnitude can be calculated from the reflection phase of the AMC structure. As depicted in Fig. 3, all the proposed structures have reflection magnitude of 0.975, 0.977, 0.979, and 0.987, respectively. Hence, all the unit cells can be considered as a good reflector due to the reflection magnitude for all the unit cells is nearly equal to 1.

The surface impedance of various unit cells is depicted in Fig. 4.

The surface impedance for AMC type IV is very high within a specific frequency range compared to other proposed unit cells because the reflection magnitude of this unit cell is 0.987, which is almost equal to 1. The reflection phase (degree) diagrams of all the four proposed AMC unit cells are depicted as in Fig. 5.

The comparison results of proposed unit cells are depicted in Table 3.

5 Conclusions

The four types of AMC structures including different patterns are comparatively studied using full-wave simulation. The AMC structures are designed with in-phase property in the vicinity of 28 GHz frequency band. The simulated bandwidth of the reflection phase for proposed AMC unit cell IV is broader than the other proposed structures. By using RT/Duroid 5880 substrate, the four-unit cells are proposed. The

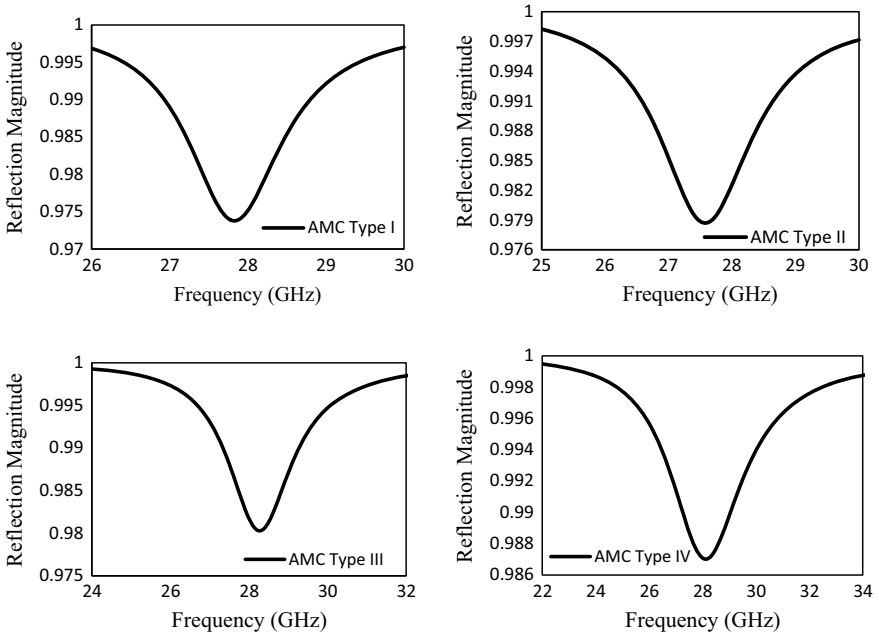

Fig. 3 Reflection magnitude of unit cells: **a** AMC type I, **b** AMC type II, **c** AMC type III, and **d** AMC type IV

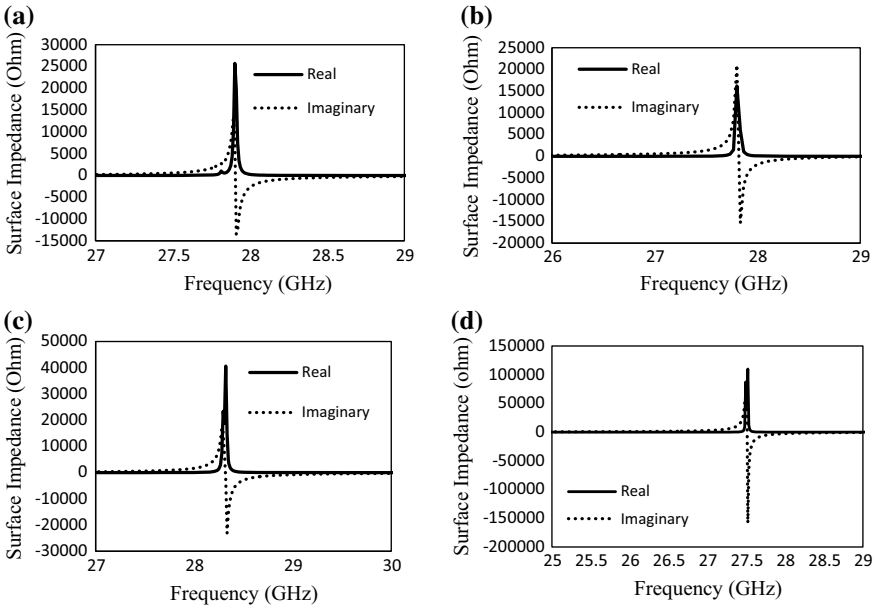

Fig. 4 Surface impedance of unit cells: **a** AMC type I, **b** AMC type II, **c** AMC type III, and **d** AMC type IV

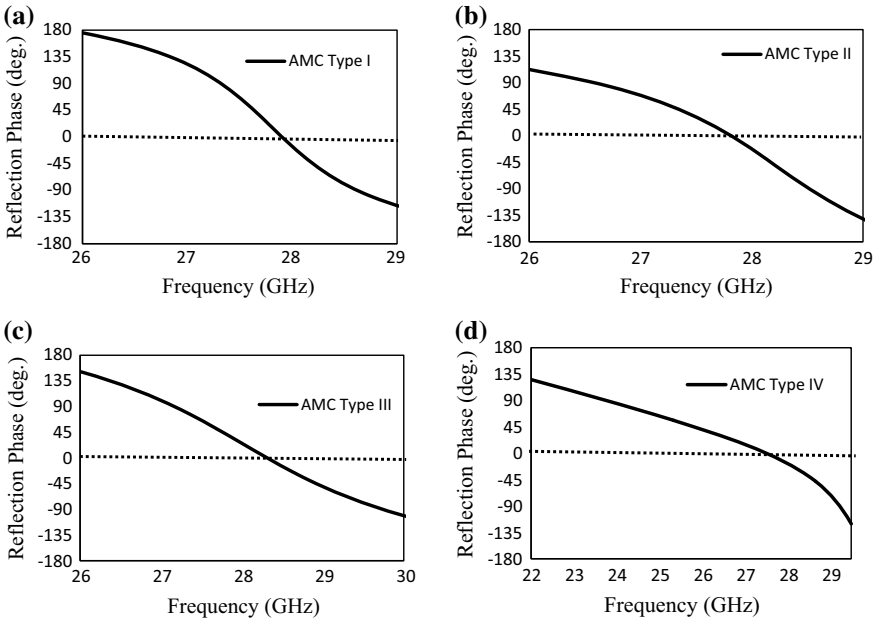

Fig. 5 Reflection phase of unit cells: **a** AMC type I, **b** AMC type II, **c** AMC type III, and **d** AMC type IV

Table 3 Results' analysis of various unit cells

S. No.	Proposed AMC pattern	AMC bandwidth (GHz)	Bandwidth (%)	Reflection magnitude	Overall size of AMC cell $W \times L \times h$ (mm^3)
1	AMC type I	27.30–28.61	4.68	0.975	3.3 × 3.3 × 0.254
2	AMC type II	26.56–28.52	7.12	0.976	3 × 3 × 0.254
3	AMC type III	27.16–29.73	9.03	0.98	3.5 × 3.5 × 0.254
4	AMC type IV	23.75–29.22	20.64	0.987	2.84 × 2.84 × 0.254

better performance of the AMC unit cell makes it useful for 5G applications to enhance the antenna's performance.

References

1. Fiddy MA, Tsu RX (2010) Understanding metamaterials. Waves Random Complex Media 20(2):202–222
2. Jose J (2014) Frequency selective bistable switching in metamaterial based photonic bandgap medium. Opt Commun 328:116–120
3. Xu Y, Alphones A (2010) Novel DGS-CSRR-based microstrip low pass filter with ultra-wide suppression. Int J Ultra-Wideband Commun Syst 1(3):169–172
4. Martin F, Falcone F, Bonache J, Marques R, Sorolla M (2003) Miniaturized coplanar waveguide stop band filters based on multiple tuned split ring resonators. IEEE Microwave Wirel Compon Lett 13(12):511–513
5. Mendez T, Alfredo J, Aguilar HJ, Flores-Leal R, Gonzalez EAA, Sanchez FI (2010) Improving frequency response of microstrip filters using defected ground and defected microstrip structures. Prog Electromagnet Res 13:77–90
6. Costa F, Simone G, Agostino M (2009) On the bandwidth of high-impedance frequency selective surfaces. IEEE Antennas Wirel Propag Lett 8:1341–1344
7. Li L, Wu Z, Li K, Yu S, Wang X, Li T, Li G, Chen X, Zhai H (2014) Frequency-reconfigurable quasi-Sierpinski antenna integrating with dual-band high-impedance surface. IEEE Trans Antennas Propag 62(9):4459–4467
8. Yang F, Samii YR (2009) Electromagnetic band gap structures in antenna engineering. Cambridge University Press, Cambridge, UK, pp 156–201
9. Sohn JR, Kim KY, Tae H-S, Lee HJ (2006) Comparative study on various artificial magnetic conductors for low-profile antenna. Prog Electromagnet Res 61:27–37
10. Capet N, Martel C, Sokoloff J, Pascal O (2011) Optimum high impedance surface configuration for mutual coupling reduction in small antenna arrays. Prog Electromagnet Res 32:283–297
11. Walser RM, Valanju AP, Winston W, Becker MF, Bene RW, Bruce Buckman A (1993) New smart materials for adaptive microwave signature control. In: Smart structures and materials 1993: smart materials. International Society for Optics and Photonics, 1916, pp 128–140
12. Sievenpiper D (1999) High-impedance electromagnetic surfaces. Ph.D. dissertation, Electrical Engineering Department University of California, Los Angeles, Los Angeles, CA, USA, (1999)
13. Yousefi L, Mohajer-Iravani B, Ramahi OM (2007) Enhanced bandwidth artificial magnetic ground plane for low-profile antennas. IEEE Antennas Wirel Propag Lett 6:289–292
14. Dewan R, Rahim MKA, Hamid MR, Yusoff MFM (2015) Analysis of wideband antenna performance over dual band artificial magnetic conductor (AMC) ground plane. In: Applied mechanics and materials, vol 735. Trans Tech Publications, pp 273–277 (2015)
15. Mosallaei H, Sarabandi K (2004) Antenna miniaturization and bandwidth enhancement using a reactive impedance substrate. IEEE Trans Antennas Propag 52(9):2403–2414
16. Jalali M, Naser-Moghadasi M, Sadeghzadeh RA (2017) Dual circularly polarized multilayer MIMO antenna array with an enhanced SR-feeding network for C-band application. Int J Microwave Wirel Technol 9(8):1741–1748
17. de Cos ME, Alvarez Y, Hadarig RC, Las-Heras F (2010) Novel SHF-band uniplanar artificial magnetic conductor. IEEE Antennas Wirel Propag Lett 9:44–47
18. Raad HR, Abbosh AI, Al-Rizzo HM, Rucker DG (2013) Flexible and compact AMC based antenna for telemedicine applications. IEEE Trans Antennas Propag 61(2):524–531
19. Muhamad M, Abu M, Zakaria Z, Hassan H (2017) Novel artificial magnetic conductor for 5G application. Indonesian J Electr Eng Comput Sci 5(3):636–642
20. Hong JH, Chiu CW, Wang HC (2018) Design of circularly polarized tag antenna with artificial magnetic conductor for on-body applications. Prog Electromagnet Res 81:89–99

A Triple Band-Reject Frequency Selective Surface with Dodecagon Patch Element

Jaiverdhan, Dharmveer Yadav, Sanjeev Yadav, M. M. Sharma and R. P. Yadav

Abstract This paper, proposed a frequency selective surface (FSS) with triple band-stop characteristics. The structure demonstrated can be effectively used to shield different scientific and technical applications from unwanted electromagnetic radiation. The compact unit cell consists of a cross-loop surrounded by a dodecagon. The overall dimensions of unit cell are 22 mm × 22 mm. The substrate material is RO-3003 with a dielectric constant (ε_r) 3 and thickness 60 mil. The dimensions of each unit cell have computed by the lowest cutoff frequency. This FSS structure is designed for the rejection of three frequency bands, 5.5 GHz, 3.5 GHz and 2.4 GHz, respectively. The proposed FSS structure provides preeminent electromagnetic shielding because of its polarization insensitivity and triple-band absorption.

Keywords EMI shielding · Frequency selective surface (FSS) · Wi-Fi/WiMAX · Electromagnetic radiation · Dodecagon · Polarization independent

1 Introduction

Nowadays, the requirement of wireless devices is increasing rapidly in wireless communication. This increment in wireless technology needs a security feature. Also, the transmission of wireless signals from source to destination without any

Jaiverdhan (✉) · D. Yadav · M. M. Sharma · R. P. Yadav
Department of ECE, Malaviya National Institute of Technology, Jaipur, India
e-mail: 2016rec9051@mnit.ac.in

D. Yadav
e-mail: 2016pwc5353@mnit.ac.in

M. M. Sharma
e-mail: mmsharma.ece@mnit.ac.in

R. P. Yadav
e-mail: rpyadav.ece@mnit.ac.in

S. Yadav
Department of ECE, Government Women Engineering College, Ajmer, India
e-mail: sanjeev.mnit@gmail.com

V. Janyani et al. (eds.), *Optical and Wireless Technologies*, Lecture Notes in Electrical Engineering 648, https://doi.org/10.1007/978-981-15-2926-9_58

attenuation or interference is an important concern [1, 2]. Currently, many researchers are working on these interference issues to resolve them. There are serval approaches reported in the literature to stop or reject unwanted EM radiation [3]. FSS has gained a considerable focus of research attention recently, and it comprises of periodic structures with identical elements, having periodicity in one or many dimensions. FSS has generally used as reflector antenna applications [4]. FSS with the aid of a spatial filter, performs EM wave filtering efficiently using intrusions of periodic as well as periodic arrays of dielectric and metallic materials or a combination of both on the plane of incidence. The inherent advantage of this device is that it provides angular freedom regarding the angle of incidence, thereby making feasible angular spectrum filtering as well [1, 3]. FSS is regarded as a superstrate that can be explained using its three critical characteristics, namely absorption, reflection and transmission. The frequency-dependent behavior of the systems also leads to the wide classification of these magnetic filters as, low-pass filter, high-pass filter, band-pass and band-stop filter. Transmission and reflection characteristics are based on the geometry of patch and designing parameters [6–10]. The FSS can characterize in two types first one is active FSS and second one passive FSS. Based on EM wave filtration, FSS is divided into two types: band-reject FSS and band-pass FSS. FSS work as a band-reject filter if the periodic element is patch type and work as a band-pass filter if it is used as an aperture type element. The frequency response of FSS can be controlled by the geometry of elements used or the spacing between them, patch material used as well as its lengths and widths used along with the type of substrate used. The dimensions of FSS elements are also a major designing parameter to provide the desired frequency response. A stable frequency response achieved if resonance frequencies do not change with incident EM waves orientation at different angles. An approach used to protect electronic devices from EM interference is called EM shielding. These EM radiations are very harmful to the human body [2]. When a building wall get covered by the FSS wall, these radiations can be effectively blocked as the system is aimed to block specific predefined frequencies and let other frequencies pass or vice versa [5]. There are several ways to analyze frequency selective surface as the equivalent circuit method, finite element method, mode matching, etc. [4]. Application fields of FSS are wireless security, interference mitigation, radome, filters, dichroic sub reflectors and artificial magnetic conductor.

In this paper, the triple band-reject FSS is designed and analyzed, which acts as a reflector for Wi-Fi, WLAN and WiMAX applications. The resonating elements designed such that FSS structure provides desired frequency response. The proposed FSS unit cell has been constructed using RO-3003 substrate material on which three patch elements of different shape has placed. By adjusting the size of these patch elements, the desired frequency response has achieved. For the simulation of the unit cell, periodic boundary conditions applied in computer simulation tool (CST) microwave studio v.17. For the simulation of the unit cell, frequency-domain solver has been used which is based on the FDTD method with tetrahedral meshing, and it is excited by Floquet wave-port technique, which does not need any external excitation source. The proposed design having features of polarization insensitivity, thin and compact design makes it a suitable candidate for various applications.

2 FSS Design

2.1 Design of FSS Unit Cell

Figure 1 shows the schematic representation of the proposed FSS unit cell with triple band-stop capability and optimized dimensions. The construction included the usage of Rogers RO-3003 substrate material which provides good frequency response and low losses. Rogers RO-3003 has dielectric constant ($\varepsilon_r = 3$), loss tangent 0.001 and thickness 60 mil. The overall dimensions of the unit cell are W (mm) $\times$ W (mm). To get desired frequency response, three different shape elements have etched out over the metallic surface of the substrate material. Vast simulations have taken place to get optimized parameters of proposed FSS unit cell structure. The list of optimized parameters has shown in Table 1. To optimize the FSS unit cell, vast parametric analysis using CST MW studio simulation software has been done. The unit cell structure is designed to stop three discrete frequencies, i.e., 2.4, 3.5 and 5.5 GHz. These frequencies are used for WLAN, WiMAX and Bluetooth/Wi-Fi applications. Hence, to design 2.4 GHz frequency band, a square loop of proper dimension is etched over the substrate material. This is lowest resonance frequency of over proposed FSS structure. The dimension of this outer square loop is computed by the following Eq. (1). The 3.5 and 5.5 GHz frequency bands are obtained by proper arrangement of dodecagon and cross-loop, respectively, as shown in Fig. 1. The optimized dimension of these elements is computed by parametric analysis of structure.

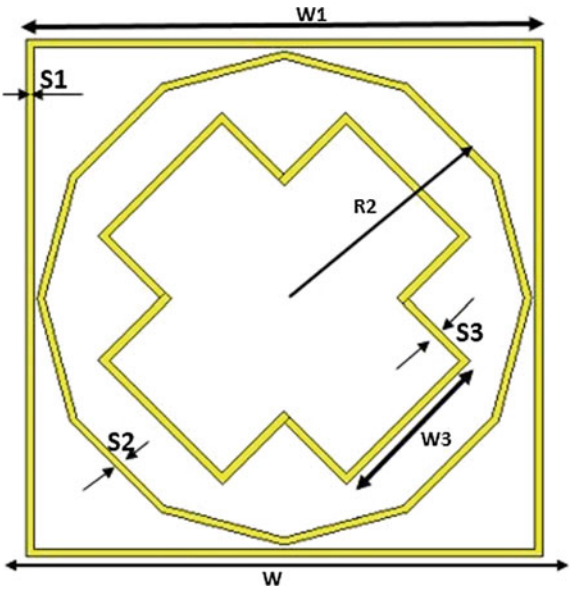

Fig. 1 Geometry of the proposed FSS unit cell with optimized dimensions

Table 1 Optimized designing parameters for unit cell

Parameter	Symbol	Values (mm)
Substrate width	W	22
Outer square loop width	W1	20.45
Outer square loop length	L1	20.45
Radius of dodecagon (middle)	R2	9.78
Width of cross-loop (inner)	W3	6.6
Length of the cross-loop (inner)	L3	13.86
Patch width	S	0.3
Substrate thickness	Ts	1.52
Thickness of copper	Tc	0.03

$$L = W = \frac{1}{4 f_{\mathrm{r}} \sqrt{\mu_0 \varepsilon_0} \sqrt{\frac{\varepsilon_{\mathrm{r}}+1}{2}}} \tag{1}$$

where W is the outer square loop width (in mm) and L is length (in mm) of the outer square loop. ε_{r} is the substrate dielectric constant and f_{r}, the lowest resonant frequency in GHz for which we want to design unit cell.

2.2 Finite Array Design

FSS unit cells have been organized in a periodic manner to attain desired frequency response that used for specific application. A constant periodicity for this array structure is P mm in both X and Y direction. For an array of 8 × 8 with dimensions, Wa × Wa (mm^2) has designed. The optimized parameters of array structure are given in Table 2. The array and its enlarged view are shown in Fig. 2. The remaining parameter of array structure used is similar to FSS unit cell (given in Table 1) in order to obtain required stopband characteristics.

Table 2 Dimension of 8 × 8 array

Name	Symbol	Value in (mm)
Periodicity	P	22
Substrate thickness	Ts	60 mil
Substrate width	Wa	176

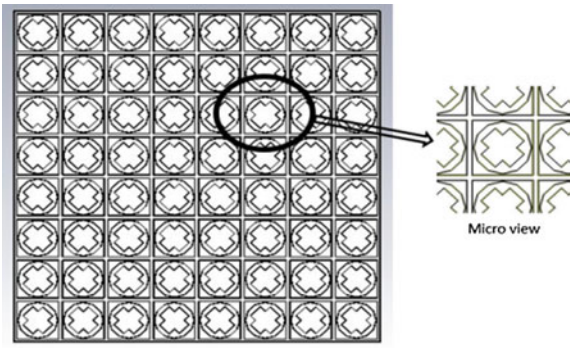

Fig. 2 Design of proposed 8 × 8 FSS array and its enlarged view

3 Simulation Results and Discussion

3.1 Insertion Loss for the Proposed Unit Cell

Insertion loss shows how much power can be reflected or transmitted by the proposed structure. The performance of the FSS array structure is evaluated by applying periodic boundary conditions to the FSS unit cell. These unit cell elements need proper alignment and geometry to achieve the desired stopband characteristics. The proposed design works as a band-reject filter at three frequency bands, viz. 5.5 GHz, 3.5 GHz and 2.4 GHz to effectively model for the WLAN, WiMax and Wi-Fi applications, respectively. The simulation result of insertion loss shows how much power has returned due to a reflection of EM waves from the surface as well as the transmission coefficient obtained when TE and TM modes of wave propagation are considered. The value of insertion loss in the form of transmission coefficient at frequencies 5.5 GHz, 3.5 GHz and 2.4 GHz were found to be −60.07 dB, −53.93 dB and −51.8 dB, respectively, for both modes of wave propagations considered.

- ***Transmission and reflection***

Transmission and reflection are important parameters in the wireless signal transmission mechanism. Transmission parameter shows how much power reached destination. Reflection shows how much power returned back during the transmission process and the signal neither gets transmitted nor reflected which is shown by the absorption. Figures 3 and 4 depict the return losses incurred in a FSS unit cell when TE and TM propagation modes are considered, and Figs. 5 and 6 show the reflection coefficient in TE mode of proposed frequency selective surface unit cell.

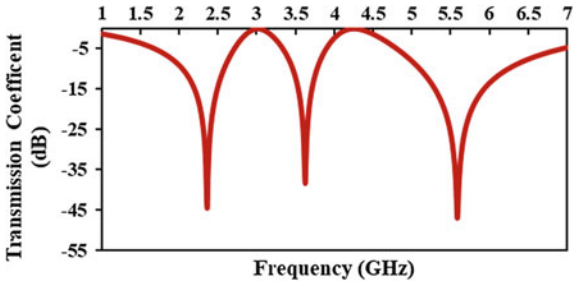

Fig. 3 Transmission coefficient of the unit cell in TE mode

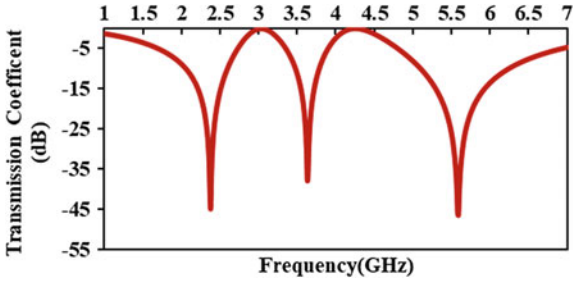

Fig. 4 Transmission coefficient of the unit cell in TM mode

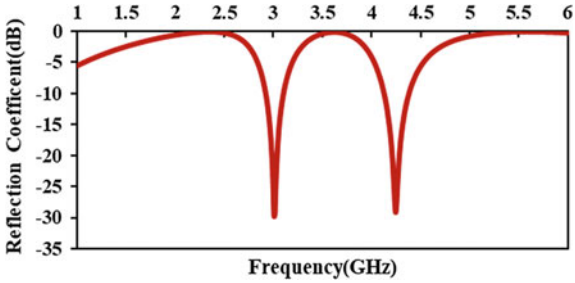

Fig. 5 Return loss of the unit cell in TE mode

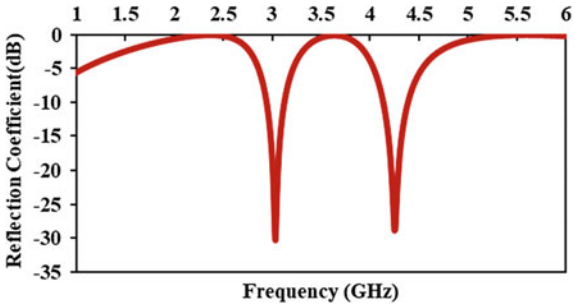

Fig. 6 Return loss of the unit cell in TM mode

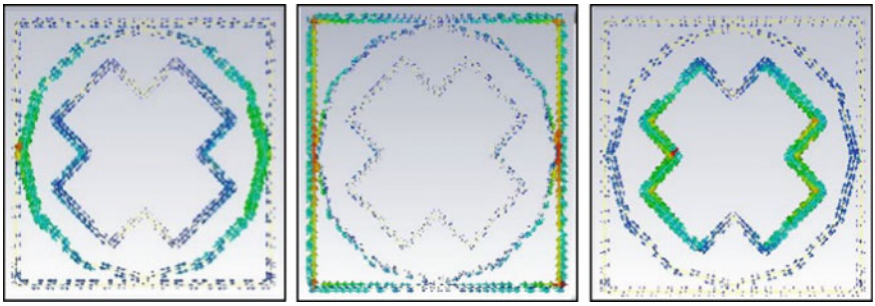

Fig. 7 Surface current of proposed FSS for TE mode at 2.4, 3.5 and 5.5 GHz

3.2 Surface Current

The surface current shows the effect of all patch elements of the unit cell. From the following figure, it is clear that each patch element has been designed to stop a particular frequency band. This parameter shows that only that element is responsible for stopping particular frequency which has a maximum intensity of surface current at the edges of all patch elements. Figure 7 shows the surface current effect of the unit cell at three specified frequency band-stop characteristics.

4 Effect of Incidence Angle Variations

Figure 8 shows that the transmission coefficient parameter has negligible changes with an increase in incidence angle (phi) from 0° and 90°. These minor changes that are observed reflect the stability of the system frequency response when angular variations are considered.

Figure 9 shows that the transmission coefficient parameter has negligible changes throughout the frequency range with an increase in incidence angle (theta) from

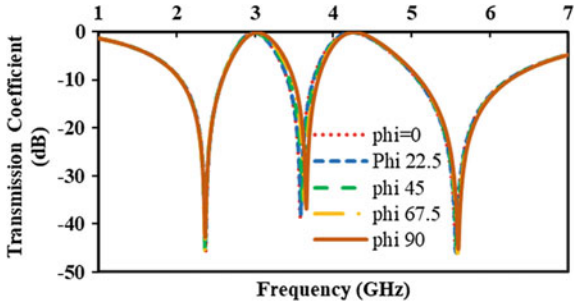

Fig. 8 Transmission coefficient for incident angle variation for phi = 0° and 90°

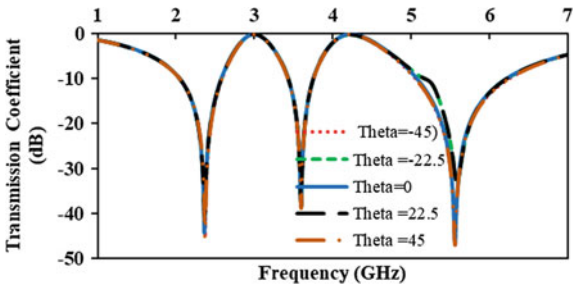

Fig. 9 Transmission coefficient for incident angle variation (theta) from −45° to 45°

–45° to 45°. Therefore, it has proved that the proposed FSS structure is polarization independent for both TE and TM modes with stable band-stop frequency response.

5 Conclusion

The proposed FSS structure has been designed to stop three bands of frequency, viz. 2.4, 3.5 and 5.5 GHz to remove electromagnetic (EM) radiation interference. This proposed structure is designed and optimized in such a way to reject these frequencies which can use for different scientific and technical applications. The frequency response is quite stable by the angle of incidence, when normal and oblique incidences have been considered in both TE and TM mode. Proposed FSS structure provides stopband characteristics so it can be used for both security and health applications at airport, school and hospitals to stop unwanted radiation and it can also use in smartphone covers to remove unwanted radiation during a voice call. In the future, this work can extend for broadband frequency range or multiple frequency bands.

References

1. Munk B (2005) Frequency selective surfaces: theory and design. Wiley, New York
2. Larik RSA, Mallah GA, Talpur MMA, Suhag AK, Larik FA (2016) Effects of wireless devices on human body. J Comput Sci Syst Biol 9(6):119–124
3. Munk BA (2003) Finite antenna arrays and FSS. Wiley, Hoboken, NJ, USA
4. Langley RJ, Parker EA (1982) Equivalent circuit model for arrays of square loops. Electron Lett 18(7):294–296
5. Wu T-K (1994) Four-band frequency selective surface with double-square-loop patch elements. IEEE Trans Antennas Propag 42(12):1659–1663
6. Sung GHH, Sowerby KW, Neve MJ, Williamson AG (2006) A frequency-selective wall for interference reduction in wireless indoor environments. IEEE Antennas Propag Mag 48(5):29–37
7. Kiermeier W, Biebl E (2007) New dual-band frequency selective surfaces for GSM frequency shielding. In: 2007 European microwave conference, Munich, pp 222–225

8. Chatterjee A, Biswas S, Chanda D, Sarkar PP (2011) A polarization independent compact multi-band frequency selective surface. In: 2011 Nirma University international conference on engineering, Ahmedabad, Gujarat, pp 1–4
9. Noor D, Yadav SK, Yadav S (2017) An ultra large polarisation independent bandstop frequency selective surface for the security of WiMAX and WLAN application. In: 2017 International conference on information, communication, instrumentation and control (ICICIC), Indore, pp 1–5
10. Yadav S, Jain CP, Sharma MM (2018) Smartphone frequency shielding with penta-bandstop FSS for security and electromagnetic health applications. IEEE Trans Electromagn Compat 99:1–6

Numerical Investigation of Nonlinear Parameters of Chalcogenide-Based Holey Fiber for Supercontinuum Generation in Mid-infrared Region

Shruti Kalra, Sandeep Vyas, Manish Tiwari and Ghanshyam Singh

Abstract The presented paper demonstrates the generation of supercontinuum spanning from 2000 nm to over 6000 nm by pumping pulse of peak power 1 kW in a highly nonlinear $As_{38.8}Se_{61.2}$ chalcogenide holey fiber. The conventional cladding region of a microstructured fiber consists of conventional circular-shaped air holes. In the proposed design of holey fiber, the shape of air holes was modified as elliptical air holes. The geometrical parameters of the modeled design of the fiber are selected to acquire a flat and broad dispersion profile in the anomalous region. The modeled fiber was numerically simulated to investigate the parameters—nonlinear coefficient and effective mode area portraying vital role to achieve the generation of supercontinuum. The observations of the investigations demonstrate that the modeled holey fiber is a suitable design for generating supercontinuum. Additionally, simulations performed to investigate generation of supercontinuum resulted in spectra spreading in mid-infrared region. The applications of the supercontinuum generated are also discussed.

Keywords Holey fiber · Chalcogenide glass · Dispersion profile · Effective mode area · Nonlinear coefficient · Supercontinuum generation

S. Kalra (✉) · S. Vyas
Department of ECE, Jaipur Engineering College and Research Centre, Jaipur, India
e-mail: shrutikalra.ece@jecrc.ac.in

S. Vyas
e-mail: vyas.sandeep@vitej.ac.in

M. Tiwari
Department of ECE, Manipal University Jaipur, Jaipur, India
e-mail: manishtiwari@ieee.org

G. Singh
Department of ECE, Malaviya National Institute of Technology, Jaipur, Rajasthan 302017, India
e-mail: gsingh.ece@mnit.ac.in

V. Janyani et al. (eds.), *Optical and Wireless Technologies*, Lecture Notes in Electrical Engineering 648, https://doi.org/10.1007/978-981-15-2926-9_59

1 Introduction

Supercontinuum generation (SCG) has attained stupendous interest of all researchers across the globe since last few decades due to their enormous applications in nonlinear optics fields like spectroscopy, defense, metrology, biomedical imaging, biomedicine, sensing, interferometry and various others [1–6]. As fundamental vibrational absorptions of most of the vital molecules, used in diagnosis of cancer at early stage, chemical-specific imaging of biological samples and optical sensing falls in the region spanning from ultraviolet to mid-infrared which results in significant role of supercontinuum in the region [7–12]. The fibers made up of chalcogenide, fluoride, tellurite glasses and waveguides designed with highly nonlinear materials have been studied and investigated for supercontinuum generation, due to the broad transmission windows offered in the desired range.

The chalcogenide-based microstructured fibers have emerged as one of the most suitable and favorable for generation of supercontinuum (SC) due to broad transmission window extending from 2 μm up to 15 μm and higher, the high nonlinear refractive index of chalcogenide glass and flexibilities in geometry design to tailor properties of the microstructured fiber [12].

In last few decades, considerable study and investigations have been reported by numerous various research groups with different chalcogenide glasses. The chalcogenide glasses with different compositions can be explored, among the group arsenic based chalcogenides mainly As_2S_3 and As_2Se_3 are widely used [13, 14]. It has been reported by Oh et al. that the $As_{38.8}Se_{61.2}$ chalcogenide material depicts much flatter and broader transparency than As_2Se_3 in the window ranging from 2 to 12 μm [15]. In 2016, Diouf et al. reported generation of supercontinuum in mid-IR region spanning from 2900 to 4575 nm, by pumping 0.88 kW peak power optical pulses in 5 cm long holey fiber at 3.7 μm wavelength [16]. Here, in this paper, we designed the photonic crystal fiber (PCF) to obtain the anomalous dispersion profile. The designed PCF was further optimized and then numerically simulated to find its suitability to generate supercontinuum. The designed PCF was pumped with 1 kW power at 3700 nm, and spectra spanning from 2000 to 6000 nm was obtained.

In the presented paper, a design of a solid-core chalcogenide-based holey fiber with elliptical-shaped air holes cladding is engineered to obtain broad dispersion profile in the anomalous region suitable to generate SC in mid-infrared region. The paper is organized in five different sections in sequence. The description of modeling linear, nonlinear parameters and SC generation is discussed in Sect. 2 of the paper. Section 3 presents the structure of PCF designed with $As_{38.8}Se_{61.2}$ chalcogenide glass. The numerical simulations and plots of anomalous dispersion profile, effective mode area and nonlinear coefficients are discussed in the section. Sect. 4 presents the generation of supercontinuum with the engineered photonic crystal fiber. The analysis of supercontinuum generation using generalized nonlinear Schrödinger equation is also presented in the section. The last section concludes the paper.

2 Modeling Linear, Nonlinear Parameters and SC Generation

Mathematical modeling of supercontinuum generation in a single-mode holey fiber design can be represented using generalized nonlinear Schrödinger equation (GNLSE). The linear loss, both linear and nonlinear effects, higher-order dispersion, Raman scattering and nonlinear response dependence on frequency are considered in the GNLSE used. The generation of the optical pulse in a nonlinear single-mode PCF can be modeled as equation below [17, 18]

$$\frac{\partial A}{\partial z} + \frac{\alpha}{2}A - \left(\sum_{n\geq 2}\beta_n \frac{i^{n+1}}{n!}\frac{\partial^n A}{\partial t^n}\right) = i\gamma\left(1 + \frac{i}{\omega_o}\frac{\partial}{\partial t}\right)A(z,t)\int_{-\infty}^{\infty} R(t')\left|A(z,t-t')\right|^2 \mathrm{d}t' \tag{1}$$

where $A(z, t)$ is the envelope function of slowly varying electric field amplitude, calculated by employing split-step Fourier method, α is the linear loss, time is represented by t, ω_0 is the carrier frequency, the nth derivative of the propagation constant, z denotes distance and τ is the retarded time traveling at the envelope group velocity. The nonlinear coefficient represented as γ *is* expressed as [17]

$$\gamma = \frac{n_2\omega_0}{c\,A_{\text{eff}}} \tag{2}$$

In Eq. 2, n_2 is the Kerr-nonlinear refractive index of the fiber, c is the speed of light travelling in the vacuum, and A_{eff} is the effective fundamental mode area of the designed holey fiber. The reported value of the Kerr-nonlinear refractive index of chalcogenide $As_{38.8}Se_{61.2}$ is 4.89×10^{-18} (m^2 W^{-1}) [16]. The expression of A_{eff} relates the effective cross-sectional area of the fundamental mode in the microstructured fiber as:

$$A_{\text{eff}}(\lambda) = \frac{\left(\iint_{-\infty}^{\infty}|E|^2\mathrm{d}x\mathrm{d}y\right)^2}{\iint_{-\infty}^{\infty}|E|^4\mathrm{d}x\mathrm{d}y} \tag{3}$$

In equation above, the electric field distribution of the optical fundamental mode of the chalcogenide $As_{38.8}Se_{61.2}$ fiber cross section is represented by (E) [17]. Raman contributions of instantaneous electronic vibrations $\delta(t)$ and Kerr nonlinearities are represented as the delayed Raman response function $R(t)$, which is modelled as equation below [17]

$$R(t) = (1 - f_r)\delta(t) + f_r\frac{\tau_1^2 + \tau_2^2}{\tau_1\tau_2^2}\exp\left(-\frac{t}{\tau_2}\right)\sin\left(\frac{t}{\tau_1}\right) \tag{4}$$

Parameters τ_1 and τ_2 relate the inverse of the phonon oscillation frequency and Raman gain spectrum bandwidth of the fiber material, respectively. The values of the parameters used in our research work for $As_{38.8}Se_{61.2}$ chalcogenide glass: τ_1= 23.38 fs, τ_2 = 60.31 fs and f_r = 0.031, representing fractional contribution of the delayed Raman response [16].

3 Structure Design of the Photonic Crystal Fiber

We present a solid-core $As_{38.8}Se_{61.2}$ chalcogenide PCF design with three rings in the cladding as depicted in Fig. 1. The shape of the air-holes of the conventional PCF cladding is circular. The air-holes of the inner two rings were deformed to elliptical shape keeping the outer ring of the cladding intact as circular air holes. To develop a clear understanding of the design, we use the nomenclature of minor and major radius of elliptical- shaped air holes in ring 1 and ring 2 of the PCF cladding. The pitch value (Λ) between the rings changes due to change of shape of air-holes, which at initial design step was kept identical as 2 μm. The air-holes of the outermost ring of the holey fiber cladding were kept circular in shape of 0.66 radius. The notation d_3 in the figure denotes diameter of the circular air holes. Similarly, we have designated the geometrical dimensions of elliptical air holes as d_{1a} and d_{1b} for inner ring 1 and d_{2a} and d_{2b} for ring 2 of PCF cladding. The geometrical design values of the air holes in cladding are mentioned in Table 1.

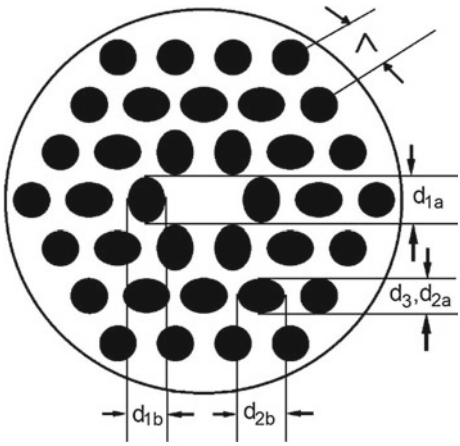

Fig. 1 Pictorial representation of the designed holey fiber

Table 1 Diameters of air-holes of ring 1 and 2 of cladding

Ring	Diameters of elliptical air holes	
Ring 1	d_{1a} = 1.4 μm	d_{1b} = 1.32 μm
Ring 2	d_{2a} = 1.3 μm	d_{2b} = 1.44 μm

The geometrical parameters were optimized to achieve dispersion in anomalous region and the zero-dispersion wavelengths (ZDW) in proximity of the available pump wavelength in the mid-infrared (MIR) region. The Sellmeier equation is used to compute the refractive index as function of wavelength of the PCF. In our work, we have used the Cauchy equations for the transparent region which is illustrated as [16]

$$n(\lambda) = \sqrt{7.65 + \frac{0.73}{\lambda^2} + \frac{0.87}{\lambda^4}} \tag{5}$$

The chromatic dispersion is related to material and waveguide dispersion and can be numerically expressed as below [17]

$$D_C(\lambda) = D_M(\lambda) + D_W(\lambda) \tag{6}$$

$$D(\lambda) = -\frac{\lambda}{c}\frac{\mathrm{d}^2}{\mathrm{d}\lambda^2}\mathrm{Re}[n_{\mathrm{eff}}(\lambda)] = -\frac{2\pi c}{\lambda^2}\beta_2(\lambda) \tag{7}$$

To achieve the dispersion in the anomalous region, the geometrical design parameters of the holey fiber were tailored and further optimized. The broad dispersion profile in anomalous region obtained with numerical simulation of the optimized PCF is depicted in Fig. 2. The dispersion obtained in anomalous region resulted in ZDW at 2.7 and 6 μm. The ZDW 2.7 μm was suitable to pump the PCF with peak pulse at pump wavelength 3.7 μm.

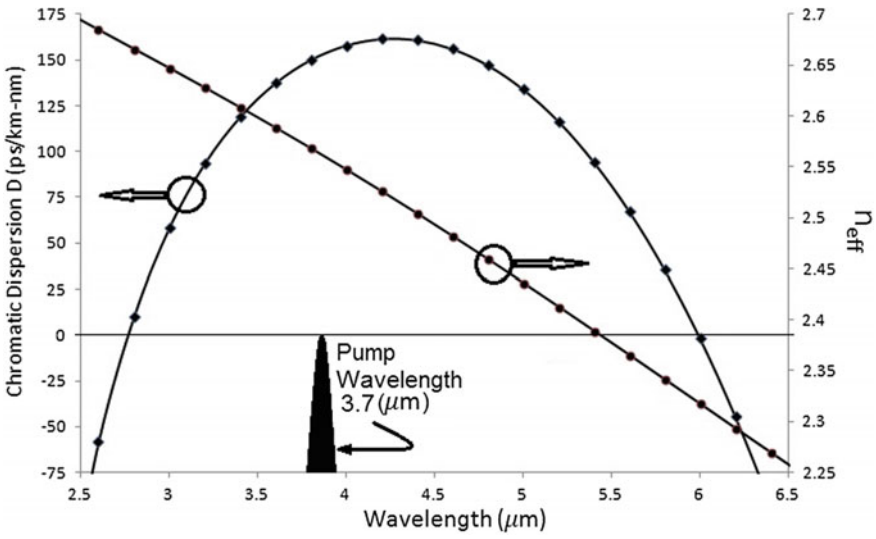

Fig. 2 Dispersion profile plot of the PCF versus wavelength

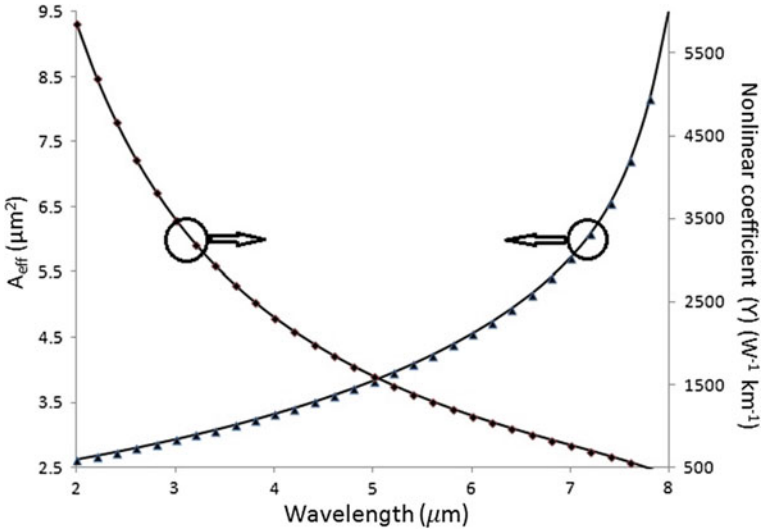

Fig. 3 Plot of (A_{eff}) and (γ) of designed holey fiber versus wavelength

Nonlinear coefficient and effective area of the fundamental mode of the fiber are the two essential parameters to obtain supercontinuum generation along with other nonlinear effects. The simulation of the optimized fiber design resulted in the numerical values of parameters—effective area and nonlinear coefficient—as plotted in Fig. 3 for wavelength ranging from 2 to 8 μm. The numerical values of effective fundamental mode area (A_{eff}) and nonlinear coefficient (γ) at pump wavelength 3.7 μm were as recorded as 3.1976 μm^2 and 2602 W^{-1} km^{-1}.

4 Supercontinuum Generation with the $As_{38.8}Se_{61.2}$ PCF

The formation of supercontinuum is a complex process constituting a specific "mixture" of various nonlinear effects occurring during interaction of intense pumped pulse traveling in nonlinear medium, resulting in significant spectral broadening with intense spectral density and spatial coherence [1, 19]. In the presented section, we examine the generation of broad supercontinuum in MIR region. The linear and nonlinear parameters of the designed PCF were evaluated along with the chromatic dispersion profile of the designed PCF to simulate the SCG by pumping at wavelength 3.7 μm close to one of the ZDWs. The solutions of GNLSE in both frequency and time domain were obtained by using the split-step Fourier method input pulses [17]. Figure 4 depicts spectral evolution in 100-mm-long fiber for a secant hyperbolic input pulse with power of 1 kW and 80 fs. The mathematical expression for secant hyperbolic input pulse can be expressed as

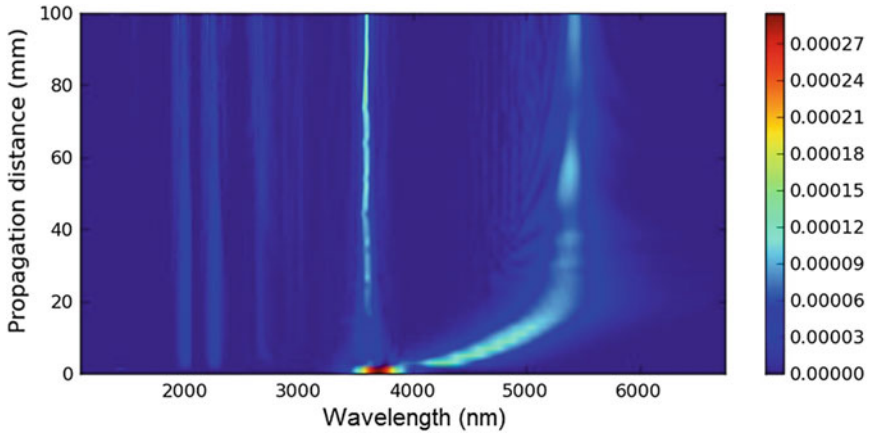

Fig. 4 Supercontinuum spectral evolution in the designed PCF

$$A(z=0,t)=\sqrt{P_0 \text{sech}\frac{t}{t_0}}\exp\left(-i\frac{c}{2}\frac{t^2}{t_0^2}\right) \tag{8}$$

In the equation above, P_0 represents the peak power of the launched input pulse and T_0 is the input soliton duration. The broadband SC obtained extended from 2000 to 6000 nm by pumping the pulse at 3.7 pump wavelength in the 100-mm-long PCF.

In the anomalous dispersion regime, the formation of supercontinuum is primarily governed by the nonlinear effects like self-phase modulation (SPM), dispersive wave, soliton dynamics and stimulated Raman scattering (SRS). The initial pulse broadening in the fiber length is predominantly due to self-phase modulation (SPM). After traversing in the fiber length, the later broadening of the spectrum is governed by the nonlinear processes like four-wave mixing (FWM), stimulated Raman scattering (SRS) and dispersion, thus forming a broadband supercontinuum. The center wavelengths of the solitons split from initial input pump pulses, due to soliton self-frequency shifting, and move outwards. The number of sub-peaks keeps on increasing continuously between two major peaks resulting in generation of spectra [20].

5 Conclusion

The paper numerically demonstrated the broadband supercontinuum generation in mid-infrared region with $As_{38.8}Se_{61.2}$ chalcogenide-based 100-mm-long PCF with elliptical shaped air-hole in cladding. The spectra spanned from 2000 to 6000 nm. The design was engineered to obtain two ZDW in anomalous regime wide enough to result in broad dispersion profile. The numerically calculated values of essential

nonlinear parameters, effective area and nonlinear coefficients, at the pump wavelengths of 3.7 μm were 3.1976 μm^2 and 2602 W^{-1} km^{-1}, respectively, suitable to generate broad supercontinuum. This work is improved results of our previous design with conventional air holes, where the spanning extended from 2000 to 5800 nm. The proposed design is a promising PCF design to be used to generate broadband efficient coherent supercontinuum in MIR region. The generated SC is suitable for innumerable desirable applications, such as biomedical sensing, optical imaging, gas sensing, food quality control, diagnosis of several diseases and many more.

References

1. Dudley JM, Genty G, Coen S (2006) Supercontinuum generation in photonic crystal fiber. Rev Mod Phys 78:1135–1184
2. Labruyère A, Tonello A, Couderc V, Huss G, Leproux P (2012) Compact supercontinuum sources and their biomedical applications. Opt Fiber Technol 18:375–378
3. Smirnov SV, Ania-Castanon JD, Kobtsev S, Turitsyn SK (2016) Supercontinuum in telecom applications. In: Alfano RR (ed) Supercontinuum laser source. Springer, Berlin, pp 371–403
4. Stingel AM, Vanselous H, Petersen PB (2017) Covering the vibrational spectrum with microjoule mid-infrared supercontinuum pulses in nonlinear optical applications. J Opt Soc Am B 34:1163–1169
5. Petersen CR, Moselung PM, Huot L, Hooper L, Bang O (2018) Towards a table–top synchrotron based on supercontinuum generation. Infrared Phys Technol 91:182–186
6. Petersen CR, Prtljaga N, Farries M, Ward J, Napier B, Lloyd GR, Nallala J, Stone N, Bang O (2018) Mid-infrared multispectral tissue imaging using a chalcogenide fiber supercontinuum source. Opt Lett 43:999–1002
7. Seddon AB (2011) A prospective for new mid-infrared medical endoscopy using chalcogenide glasses. Int J Appl Glass Sci 2:177–191
8. Xu HL, Chin SL (2011) Femtosecond laser filamentation for atmospheric sensing. Sensors 11:32–53
9. Tu H, Boppart SA (2013) Coherent fiber supercontinuum for biophotonics. Laser Photonics Rev 7:628–645
10. Du Q, Luo Z, Zhong H, Zhang Y, Huang Y, Du T, Zhang W, Gu T, Hu J (2018) Chip-scale broadband spectroscopic chemical sensing using an integrated supercontinuum source in a chalcogenide glass waveguide. Photonics Res 6:506–510
11. Kaneshima K, Takeuchi K, Ishii N, Itatani J (2016) Generation of spectrally stable 6.5-fs visible pulses via filamentation in krypton. High Power Laser Sci Eng 4:e17
12. Ung B, Skorobogatiy M (2010) Chalcogenide microporous fibers for linear and nonlinear applications in the mid-infrared. Opt Express 18:8647–8659
13. Vyas S, Tanabe T, Singh G, Tiwari M (2016) Broadband supercontinuum generation and Raman response in $Ge_{11.5}As_{24}Se_{64.5}$ based chalcogenide photonic crystal fiber. In: IEEE international conference on computational techniques in information and communication technologies (ICCTICT), pp 607–611. https://doi.org/10.1109/ICCTICT.2016.7514651
14. Vyas S, Tanabe T, Tiwari M, Singh G (2016) Mid-infrared supercontinuum generation in $Ge_{11.5}As_{24}Se_{64.5}$ based chalcogenide photonic crystal fiber. In: IEEE international conference advances in computing, communications and informatics (ICACCI), pp 2547–2552. https://doi.org/10.1109/icacci.2016.7732436
15. Oh M-S, Seo I (2015) Preparation and characterization of As40Se60 and $As_{38.8}Se_{61.2}$ glasses with high quality for single mode IR glass fiber. Opt Fiber Technol 21:176–179

16. Diouf M, Salem AB, Cherif R, Saghaei H, Wague A (2017) Super-flat coherent supercontinuum source in $As_{38.8}Se_{61.2}$ chalcogenide photonic crystal fiber with all-normal dispersion engineering at a very low input energy. Appl Opt 56(2):163–169
17. Agrawal GP (2007) Nonlinear fiber optics, 4th edn. Academic, New York
18. Lægsgaard J (2007) Mode profile dispersion in the generalized nonlinear Schrödinger equation. Opt Express 15:16110–16123
19. Jain D, Sidharthan R, Moselund PM, Yoo S, Ho D, Bang O (2016) Record power, ultra-broadband supercontinuum source based on highly GeO2 doped silica fiber. Opt Express 24:26667–26677
20. Vyas S, Tanabe T, Tiwari M, Singh G (2016) Chalcogenide photonic crystal fiber for ultraflat mid-infrared supercontinuum generation. Chin Opt Lett 14:123201

Characterization of Crosstalk Under Bending and Twisting Condition in Homogeneous Multicore Fiber

Piyush Ranjan, Dablu Kumar and Rakesh Ranjan

Abstract For the characterization of crosstalk in multicore fiber, the discrete changes model for real homogeneous cores and conventional coupled mode theory/coupled power theory-based model for perfectly homogeneous cores have been overviewed in terms of some significant fiber parameters, such as fiber bending radius, fiber length and twist rate of fiber. The simulated results from both the models have been compared with each other to determine the crosstalk behavior. It has been observed that once the various design parameters have been fixed for the multicore fiber, the DCM model is more effective for the crosstalk estimation than the conventional models. There is nearly 4 dB difference in estimated crosstalk power level due to the DCM model in comparison with the conventional model. The numerical results state that the crosstalk level increases with increase in the bending radius and the fiber length and decreases with increase in twist rate.

Keywords Multicore fiber · Crosstalk · Discrete changes model · Bending and twisting

1 Introduction

High capacity of optical transmission system is becoming crucial in the time of gradual increasing demand for the optical transmission data. To meet this future demand, space division multiplexing (SDM)-based multicore fiber (MCF) [1] is one of the appropriate solution. The main concern of MCF is to reduce inter-core crosstalk (ICXT) due to the presence of the multicores in a single cladding region. The ICXT increases, when coupling effect between two cores increases. In the recent years,

P. Ranjan (✉) · D. Kumar · R. Ranjan
Department of Electronics and Communication Engineering, National Institute of Technology Patna, Patna, Bihar 800005, India
e-mail: piyush.ece17@nitp.ac.in

D. Kumar
e-mail: dablu.ece15@nitp.ac.in

R. Ranjan
e-mail: rr@nitp.ac.in

V. Janyani et al. (eds.), *Optical and Wireless Technologies*, Lecture Notes in Electrical Engineering 648, https://doi.org/10.1007/978-981-15-2926-9_60

the crosstalk (XT) suppression is becoming primary involvement in MCF research [2, 3] for high-traffic long-distance optical data transmissions. The XT behavior in perfect homogeneous MCF can be estimated using the coupled power/coupled mode theory-based approaches [4]. Evidently, the crosstalk level changes with the change in bending radius of the MCF [5]. In this paper, the impact of fiber bending with twisting effect have been investigated on the crosstalk behavior. Crosstalk is calculated using the conventional method, i.e., CMT/CPT, and the method of discrete changes model (DCM) [6], in the terms of fiber bending. The numerical outcomes of coupled mode equation in uncoupled step-index MCF have been compared with crosstalk estimations from the DCM technique. On comparing DCM model with the conventional model, nearly 4 dB difference in ICXT power level has been observed for the real homogeneous uncoupled MCF, which is mainly due to the fact that for real homogeneous fiber, the difference in mode propagation constants between the neighboring cores can never be zero (i.e., $\Delta\beta \neq 0$). Therefore, the results obtained using the DCM approach can be anticipated as more accurate than the conventional approach.

2 Crosstalk Estimation

2.1 Coupled Mode Theory (CMT) and Coupled Power Theory (CPT) Based Analytical Model for Crosstalk Estimation

Coupled mode theory (CMT) and coupled power theory (CPT) [4] are used for the estimation of crosstalk under the perfectly homogeneous condition. The XT, involving the adjacent cores, is illustrated in terms of the optical power signal, as some amount of the optical power signal propagated in one of the core is coupled to other neighboring cores during the signal propagation. The expression of ICXT for two adjacent cores can be written as, XT (dB) = $10\log_{10}(P_2/P_1)$, where P_1 and P_2 is the output power from the *core n* and power coupled from adjacent *core m* [7], respectively. The coupled mode equation describing the crosstalk behavior in a particular core, let *core n*, of MCF, can be expressed as [6],

$$\frac{\mathrm{d}A_n(z)}{\mathrm{d}z} = \sum_{\substack{m=1 \\ m\neq n}}^{N_c} (-j)k_{nm}(z)\exp[-j(\Phi_m(z) - \Phi_n(z))]A_m(z), \quad 1 \leq n \leq N_c \quad (1)$$

where, $\Phi(z) = \int_0^z \beta_{eq}(z')\mathrm{d}z'$, '$z$' represents the longitudinal axis coordinate in MCF, 'A' is the slowly varying complex amplitude of the electric field, N_c is the total number of cores of the MCF, 'k_{nm}' is the mode-coupling coefficient from *core m* to *core n* and β_{eq} is the equivalent propagation constant of core n, which is based on the equivalent index model. Similarly, the coupled power equation (CPE) in homogeneous MCF based on CPT [3] can be given as,

$$\frac{\mathrm{d}P_n}{\mathrm{d}z} = \sum_{n \neq m} h_{nm}(z)[P_m(z) - P_n(z)] \tag{2}$$

where, P_n and P_m is average power in cores n and m, respectively, and h_{nm} is power-coupling coefficient (PCC) between cores n and m. On solving, the CPE in its simplest form, the expression for PCC is given by,

$$h_{nm} \cong \frac{2k_{nm}^2 R_b}{\beta \Lambda} \tag{3}$$

Hence, the average crosstalk (XT_μ) between two neighboring cores in MCF can be given as [7]

$$\mathrm{XT}_\mu \cong h_{nm} L \cong \frac{2k_{nm}^2 R_b}{\beta \Lambda} L \tag{4}$$

where k_{nm} is mode-coupling coefficient between the cores n and m, R_b is bending radius, L is length of fiber and β is mode propagation constant. Here, Eq. (4) illustrates that the average XT level is directly depending on various fiber parameters, such as core pitch, length and bending radius of fiber along with the mode-coupling coefficient, whereas it has indirect dependence on the wavelength of propagation and core effective refractive index.

2.2 *Discrete Changes Model Approach for Crosstalk Estimation*

In discrete changes model approach, the influence of bending and twisting is deliberated in the propagation constant of the cores, while the impact of bending and twisting on the mode-coupling coefficient has not been considered [6]. The optical field in *core n* can be represented as [6],

$$A_n(z) = A_n(0) - j \sum_{\substack{m=1 \\ m \neq n}}^{N_c} \int_0^z k_{nm}(z') \exp\left[-j\left(\theta_m(z') - \theta_n(z')\right)\right] A_m(z') \mathrm{d}z' \tag{5}$$

Equation (1) may be assumed as the initial step for the derivation of the discrete changes model for the perfectly homogeneous MCF, where the major crosstalk impact takes place at every phase-matching point (PMP) along the length of the fiber. This results in evolution of discrete random changes-based estimation of crosstalk, as the phase-offsets between fiber cores are different at each PMPs. These phase-offsets can be modeled as the 'random phase shifts (RPSs)' between the successive PMPs [8]. Moreover, to implement the discrete changes model for real homogeneous MCF,

the random phase shift has been applied between two successive PMPs, and the MCF of length L has been segmented into $N + 1$ segments [6], where N = number of RPSs. For a large number of RPSs (N), the coupled optical field in *core n* at the fiber output is the discrete sum of field contributions from all the N segments and can be expressed as,

$$A_n(L) \cong A_n(0) - j * \sum_{k=1}^{N} K_{nm,k} \exp\left[-j\Phi_{nm,k}\right] A_m(z_{k-1}) \tag{6}$$

where, $\Phi_{nm,k}$ represents the RPSs, which is considered as a random variable, distributed uniformly between 0 and 2π and $K_{nm,k} = \int_{z_{k-1}}^{z_k} k_{nm}(z) \exp -j[(\theta_m(z) - \theta_n(z))]\mathrm{d}z$ = Discrete changes coefficient. Further, the average ICXT power level can be estimated as follows,

$$\mathrm{XT} = \frac{|A_n(L)|^2}{|A_m(0)|^2} \cong \sum_{k=1}^{N} \left|K_{nm,k}\right|^2 \tag{7}$$

In order to visualize the impact of field propagation in $K_{nm,k}$, the impact of phase propagation difference may be separated and a new normalized discrete changes coefficient ($K'_{nm,k}$) can be expresses as [6],

$$\begin{aligned} K'_{nm,k} \cong\ & \mathrm{e}^{j\Delta\beta_{mn}\frac{\pi}{(2\gamma)}} \mathrm{e}^{-jx_{nm}sin(\varphi)} \\ & * \left\{ \frac{k_{nm}}{\gamma} \left[\pi J_0(x_{nm}) + j \sum_{\substack{v=-\infty \\ v\neq 0}}^{\infty} J_v(x_{nm}).\frac{(-1)^v - 1}{v} \right] \right. \\ & \left. - \frac{k_{nm}}{\gamma^3}(\Delta\beta_{mn})^2.\left[\frac{\pi^3}{24} J_0(x_{nm}) - 2j\left(\frac{\pi^2}{4} - 2\right) J_1(x_{nm}) \right] \right\} \end{aligned} \tag{8}$$

where, $x_{nm} = \beta_n \Lambda_{nm}/R\ \gamma$, $y_{nm} = \Delta\beta_{mn}/\gamma$ and for very large twist rates ($x_{nm} \ll 1$ and $|y_{nm}| \ll 1$, i.e., $\gamma \gg \beta_n \Lambda_{nm}/R$ and $\gamma \gg |\Delta\beta_{mn}|$, respectively), the lower order value has been considered for ($v = 0$, 1 and -1) Bessel functions when $|\Delta\beta_{mn}| \neq 0$. From Eq. (8), it has been observed that, for exceedingly high value of twist rates, the normalized discrete changes coefficient and the crosstalk power level reduce as the mismatch between the effective index of core m and n increases.

$$\langle \mathrm{XT} \rangle = \sum_{\substack{m=1 \\ m\neq n}}^{N_c} N \left|K'_{nm}\right|^2 * L \tag{9}$$

Equation (9) has been used to determine the XT behavior for DCM model as demonstrated in Sect. 3.

3 Results and Discussion

Here, the considered fiber design parameters for MCF have been illustrated in Table 1. The simulation results based on discrete changes model for real homogeneous multicore fiber have been compared with the results based on conventional CMT/CPT approach for perfectly homogeneous MCFs. The effective refractive index parameter has been obtained through the finite element method (FEM) simulation based on COMSOL Multiphysics software, and which is further used for analytical numerical computation for estimation of ICXT.

Figure 1 shows the influence of fiber bending radius on mean ICXT power level in the terms twisting rates of $y = \pi, 2\pi$ and 4π rad/m, with fiber length and wavelength of 250 m and 1550 nm, respectively. The simulation results exhibit that the ICXT level increases with the increase in bending radius. The XT level also decreases as twist rate increases. It also compares both the methodologies for XT estimation, in which, XT behavior due to DCM model is more effective for real homogeneous cores, because two cores cannot be similar after the fabrication. There is a difference of nearly 4 dB in XT power level in comparison with conventional CMT/CMT model. The bending radius cannot be exceeded from 250 mm, because the DCM model is only valid under peak bending radius (R_{pk}), which is obtained as 250 mm during calculation with the help of mode effective index difference value ($\Delta n_{\text{eff}} = 0.012\%$).

The ICXT performance with respect to the fiber length in terms of twisting rates of $\gamma = y = \pi$, 2π and 4π rad/m, with fiber bending radius and wavelength of 140 mm and 1550 nm, respectively, has been demonstrated in Fig. 2. This kind of result is beneficial to use the MCFs under near end applications, for example, optical interconnects, etc. Effect of twist rate illustrates that the ICXT level decreases as the rate of twisting increases.

Figure 3 illustrates the impact of twisting rate [9] on ICXT performance, with different bending radius values. Here, it has been recognized again that the ICXT

Table 1 Considered parameters for the step-index multicore fiber

Parameter	Symbol	Value	Parameter	Symbol	Value
Radius of core	a	4 μm	Mode-coupling coefficient	k_{pq}	0.1283
Core pitch between two cores	Λ_{nm}	30 μm	Effective refractive index of core n	n_{eff}	1.4537
Cladding refractive index	n_0	1.45	Fiber bending radius	R	Variable
Core refractive index	n_1	1.4573	Twist rate	γ	Variable
Core–cladding relative refractive index difference	Δ_1	0.5%	Length of fiber	L	Variable
Twist offset of core n $(2 \leq n \leq 7)$	φ	$(n-2)\,\pi/3$	Operating wavelength	λ	1550 nm

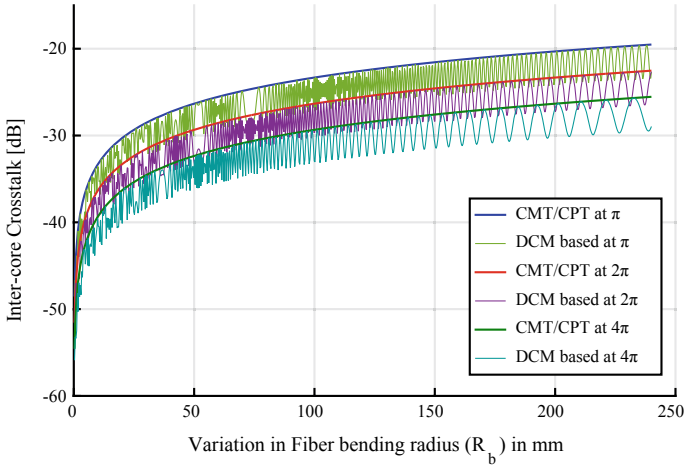

Fig. 1 Crosstalk versus bending radius for both the models at different twist rate, i.e., π, 2π and 4π

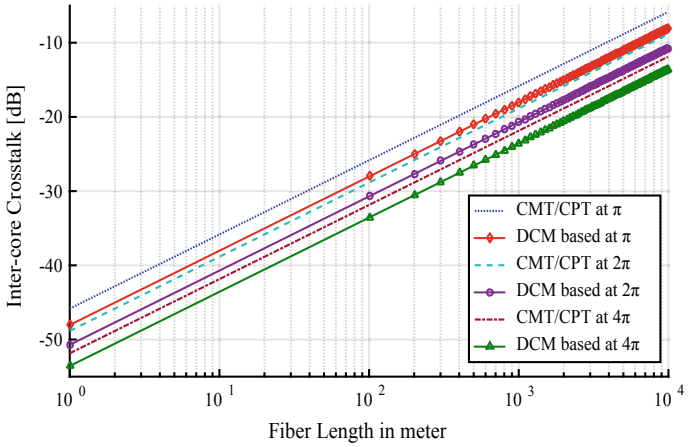

Fig. 2 Crosstalk versus fiber length for both the models at different twist rate, i.e., π, 2π and 4π

level reduces with increase in twist rate. This is because of dissimilarity of mode effective index (n_{eff}) between two adjacent cores, which make Δn_{eff} value large for real homogeneous cores in MCF. It leads to lessening the coupling between the adjacent cores, which further help to decrease the ICXT level in MCF.

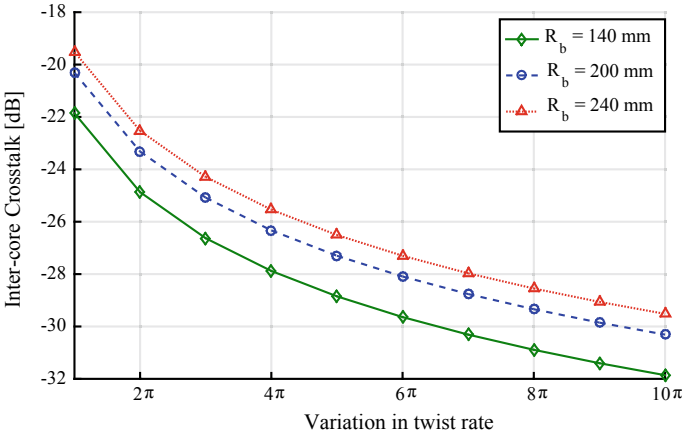

Fig. 3 Crosstalk versus twist rate for the different bending radius values

4 Conclusion

The discrete changes model for real homogeneous multicore fiber and conventional CMP/CPT model for perfectly homogeneous MCF have been overviewed to characterize crosstalk in terms of some significant fiber parameters, such as fiber length, bending radius and twist rate. The simulated results from both the models have been compared, and it has been observed that the DCM approach is more effective than CMT/CPT model approach for average ICXT estimation. This is because, in real scenario, the two adjacent cores in homogeneous MCF do not have same mode effective index after the fabrication. Hence, nearly 4 dB reduction in ICXT power level with DCM approach has been achieved in comparison with CMT/CPT-based model. The numerical results state that the ICXT increases with increase in bending radius and fiber length. Significant impact of twist rate has also been observed over the ICXT performance, as the XT level reduces with increase of twist rate. This kind of analysis may be beneficial to characterize average ICXT behavior before fabrication because once the MCF is fabricated the XT performance cannot be altered; therefore, it is essential to do the analysis and appropriate design of MCF, so that the XT performance can be improved, for the short-reach applications, like optical interconnects, etc.

Acknowledgements This research work is part of Early Career Research Award project sponsored by Science and Engineering Research Board, Department of Science and Technology, Government of India.

References

1. Saitoh K, Matsuo S (2016) Multicore fiber technology. J Lightwave Technol 34:55–66
2. Desurvire EB (2006) Capacity demand and technology challenges for lightwave systems in the next two decades. J Lightwave Technol 24:4697–4710
3. Hayashi T, Taru T, Shimakawa O, Sasaki T, Sasaoka E (2011) Design and fabrication of ultralow crosstalk and low-loss multi-core fiber. Opt Express 19:16576–16592
4. Koshiba M, Saitoh K, Takenaga K, Matsuo S (2011) Multi-core fiber design and analysis: coupled-mode theory and coupled-power theory. Opt Express 19:B102–B111
5. Fini JM, Zhu B, Taunay TF, Yan MF (2010) Statistics of crosstalk in bent multicore fibers. Opt Express 18:15122–15129
6. Adolfo V, Cartaxo T, Alves TMF (2017) Discrete changes model of inter-core crosstalk of real homogeneous multi-core fibers. J Lightwave Technol 35:2398–2408
7. Kumar D, Ranjan R (2018) Optimal design for crosstalk analysis in 12-core 5-LP mode homogeneous multicore fiber for different lattice structure. Opt Fiber Technol 41:95–103
8. Hayashi T, Nagashima T, Shimakawa O, Sasaki T, Sasaoka E (2010) Crosstalk variation of multi-core fibre due to fibre bend. In: 36th European conference and exhibition on optical communication, Torino, Italy, pp 19–23
9. Aozasa S, Tsujikawa K, Sakamoto T, Nozoe S, Nakajima K (2018) Crosstalk reduction in multi-core fiber using uniform twist. In: European conference on optical communication (ECOC), Roma, Italy

Design and Crosstalk Analysis in Homogeneous Trench-Assisted Multicore Fiber under Single-Mode Condition

Dablu Kumar and Rakesh Ranjan

Abstract The design of five different core structures (Str.1–Str.5) has been proposed by varying the core radius from 3 to 5 μm, with the optimally corresponding variations in relative refractive index difference of core–clad, under the single-mode propagation condition, in order to optimize the crosstalk level in seven-core trench-assisted multicore fiber. The crosstalk performance has been analyzed with respect to variations in fiber operational parameters, like fiber-bending radius, operating wavelength, and fiber length. The motivation of this work is to design the appropriate core structure model for multicore fiber, under low crosstalk, low dispersion, and acceptable mode effective area, which follows the standard rule to be used in telecom services.

Keywords Multicore fiber · Refractive index profile · Trench-assisted core · Crosstalk

1 Introduction

The space division multiplexing (SDM)-based multicore fiber (MCF) is an applicable and encouraging technology to overcome the limitations of transmission capacity (100 Tbit/s) [1] for a conventional single-mode single-core fiber (SM-SCF), where the increase in the core diameter may allow to pass more number of modes, which simultaneously causes the interference of modes with each other. Researchers, all over the world, are trying to enhance the information-carrying capacity by using the concept of multicore fiber, which not only improves the capacity/bandwidth, but also reduces the mode interference significantly [2–4]. In order to achieve the enhanced

D. Kumar (✉) · R. Ranjan
Optical Fiber Communication and Photonics Laboratory, Department of Electronics and Communication Engineering, National Institute of Technology (NIT) Patna, Patna, Bihar 800005, India
e-mail: dablu.ece15@nitp.ac.in

R. Ranjan
e-mail: rr@nitp.ac.in

V. Janyani et al. (eds.), *Optical and Wireless Technologies*, Lecture Notes in Electrical Engineering 648, https://doi.org/10.1007/978-981-15-2926-9_61

capacity, the specific design of MCF must be taken into consideration before the fabrication, because the presence of more than one core in single-clad region may cause the phenomena of crosstalk (XT) between the cores [5–9]. For the weakly coupled MCF design, the inter-core crosstalk (ICXT) is one of the substantial issues for transmission of signal. Nevertheless, ICXT can be restrained within a certain limit (i.e., less than −30 dB/100 Km) [5]. In the last few years, the XT reduction in MCF has been one of the main concerns for long-distance high-capacity optical fiber communication. There are some methodologies for XT reduction such as trench-assisted technique, heterogeneous core method, and propagation direction interleaving approach [5]. The reported work [9, 10] for XT reduction amount in homogeneous MCF has been done through approximate method, and an analytical expression is derived for TA-MCF structure with respect to the normal step-index core. The results provided in [10] have been re-simulated and validated using the approximate method as well as the semi-analytical method, which is consisting of finite element method (FEM) simulation and analytical computations. In this paper, crosstalk behavior for seven-core homogeneous trench-assisted (TA) MCF has been analyzed using the semi-analytical method, consisting of finite element method (FEM) simulation and analytical computations. The coupled mode theory and coupled power theory (CMT/CPT) [6, 7] have been used to evaluate the average XT in MCFs, and also included the bending effects [8]. In the current paper, the work of paper [10] has been extended and compared to examine the behavior of crosstalk in terms of various fiber operational parameters, such as wavelength, transmission distance, and bending radius by using the semi-analytical approach for the five newly proposed core structures.

2 Multicore Fiber Design and Crosstalk Analysis

A seven-core uncoupled homogeneous step-index MCF and its corresponding trench-assisted (TA) structure have been shown in Fig. 1, with six cores in the outer ring of the radius of 40 μm and one core at the center. The five different MCF structure designs along with its corresponding TA structures have been proposed for single-mode propagation by varying the core radius from 3 to 5 μm, with the corresponding

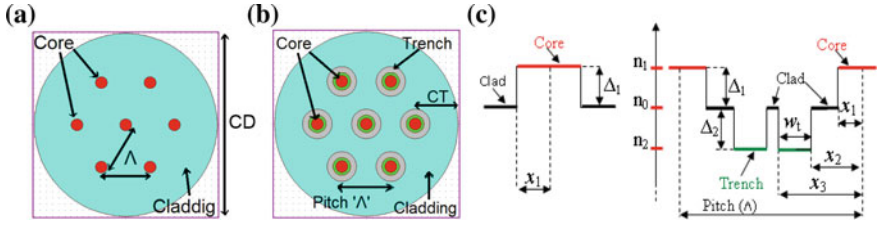

Fig. 1 **a** Seven-core uncoupled homogeneous MCF with core pitch 'Λ' of 40 μm, **b** its corresponding TA-MCF structure, and **c** refractive index profile of step-index core (left) and TA step-index core (right) [13]

Table 1 Design parameters of homogeneous multicore fiber

Parameters	Str.0 [11]	Str.1	Str.2	Str.3	Str.4	Str.5	Units
Core radius—x_1	4.5	5.0	4.5	4.0	3.5	3.0	μm
Clad diameter (CD)	125	125	125	125	125	125	μm
Core refractive index—n_1	1.4551	1.4548	1.4559	1.4575	1.4598	1.4632	–
Clad refractive index—n_o	1.45	1.45	1.45	1.45	1.45	1.45	–
Relative refractive index of core–clad—Δ_1 (%)	0.35	0.33	0.40	0.51	0.67	0.90	%
Effective refractive index—n_{eff}	1.452454	1.452541	1.453126	1.453921	1.455188	1.456957	–
Effective mode area—A_{eff}	–	93.6	75.8	59.7	45.6	34	μm^2

variations in Δ_1 as given in Table 1. These Δ_1 values have been chosen optimally corresponding to each of core radius values after simulating these core structures several times under the constraints of single-mode propagation through the fiber cores, whereas the authors in [10] have considered the generalized value of Δ_1 (=0.35%), instead of its optimal value. The main motivation for the current work is to search for the optimum core structure for the ultra-low crosstalk behaviors with single-mode operation. The TA approach [5, 11, 12] is one of the important methods to reduce the coupling and hence, the ICXT between two adjacent cores to a significantly low level by incorporating trench around the cores in MCF structures. Trench is a boundary structure having refractive index profile lower than that of the core and cladding. The refractive index profiles for a step-index core and TA step-index cores MCF have been shown in Fig. 1c [13], where x_1 is core radius, x_2 and x_3 are, respectively, the distance from the center of core to the inner, and outer border of the trench with $x_2 = 2x_1$. W_t is the width of trench, which is assumed as 5 μm for all five proposed core structures, while it is 4.5 μm for Str.0 [11]. The refractive index of core region is considered as n_1 for both normal and TA step-index cores, n_2 is the refractive index of the trench, and $n_0 = 1.45$, for the cladding region. The relative refractive index difference of core–clad is Δ_1, and of clad–trench is Δ_2, and mode effective area [14] is A_{eff}. The distance between any two neighboring cores (i.e., core pitch, 'Λ') should be such that each core in MCF behaves as a separate spatial channel. The length of fiber (L), core pitch (Λ), and operating wavelength (λ) are considered as 100 km, 40 μm, and 1550 nm, respectively. The detailed design specifications and mode effective parameters are provided below in Table 1.

Due to the presence of multiple numbers of closely packaged cores in the same cladding region, the crosstalk between the neighboring cores is a crucial factor. The

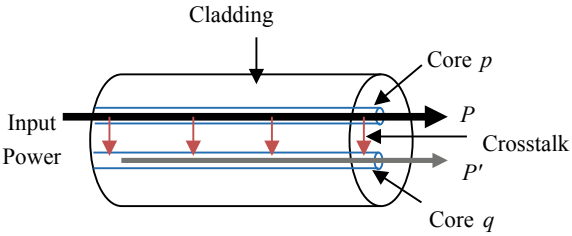

Fig. 2 Power coupling from input core to the neighboring core [11]

XT between the adjacent cores can be quantified in terms of optical signal power, as some amount of optical power propagating through the one of the core is coupled with its neighboring cores during its transmission, as shown in Fig. 2. The ICXT between two adjacent cores can be stated as, XT (dB) $= 10\log_{10}\left(\frac{P'}{P}\right)$, where the P and P' are the output optical power from the input core p and the neighboring core q, respectively [11].

For the analysis of crosstalk behavior, the semi-analytical method has been adopted. In this methodology, first the value of mode propagation constant (β) in a particular core has been obtained using the FEM-based simulation analysis, and then, this 'β' value is used in the implementation of CMT/CPT method for XT estimations.

Therefore, the final expression for average crosstalk (XT_μ) between two adjacent cores in MCF can be written as [6, 11],

$$XT_\mu \cong h_{pq} L \cong \frac{2k_{pq}^2 R_b}{\beta \Lambda} L \tag{1}$$

where R_b is bending radius, L is fiber length, k_{pq} is mode coupling coefficient [15] between the two adjacent step-index core, and $\beta = k \times n_{eff}$ = mode propagation constant, k is wave number $= 2\pi/\lambda$, λ is the light wavelength in vacuum. Equation (1) describes the direct dependency of average crosstalk on mode coupling coefficient, fiber-bending radius, fiber length, and core pitch along with its indirect dependency on wavelength and effective refractive index. In the trench-assisted MCFs, the mode coupling coefficient ($k_{pq}^{'}$) for two adjacent cores can be expressed as [9, 10],

$$k_{pq}^{'} = \frac{\sqrt{\Gamma}\sqrt{\Delta_1}}{x_1} \frac{U_1^2}{V_1^3 K_1^2(W_1)} \sqrt{\frac{\pi x_1}{W_1 \Lambda}} \exp\left(-\frac{W_1 \Lambda + 2(W_2 - W_1) W_t}{x_1}\right) \tag{2}$$

where $W_1 = x_1\left(\beta^2 - k^2 n_0^2\right)^{1/2}$ and $U_1 = x_1\left(k^2 n_1^2 - \beta^2\right)^{1/2}$, V_1 = normalized frequency $= 2\pi x_1 n_1 (2|\Delta_1|)^{1/2}/\lambda$, and $K_1(W_1)$ is the first order with second kind modified Bessel function. $V_2 = 2\pi x_1 n_0 (2|\Delta_2|)^{1/2}/\lambda$, $W_2 = \left(V_2^2 + W_1^2\right)^{1/2}$, and $\Gamma = W_1/\left[W_1 + (W_2 - W_1)\frac{W_t}{\Lambda}\right]$, respectively. In presence of more than one surrounding cores, the average crosstalk has been estimated numerically as the total sum of ICXT on a specific core by its all-neighboring cores [11, 16].

3 Result and Discussion

3.1 Crosstalk Versus Bending Radius

The influence of fiber bending on crosstalk behavior has been studied and demonstrated in Figs. 3 and 4 for the trench depths of -0.70% and -1.40%, respectively, for all the proposed core structures. The XT deteriorates slowly with increase in bending radius of the fiber. The improvements in XT level have been observed with deeper trench depth value of -1.40%. From the fiber-bending point of view, all the core structures have substantially improved XT performance as compared to the

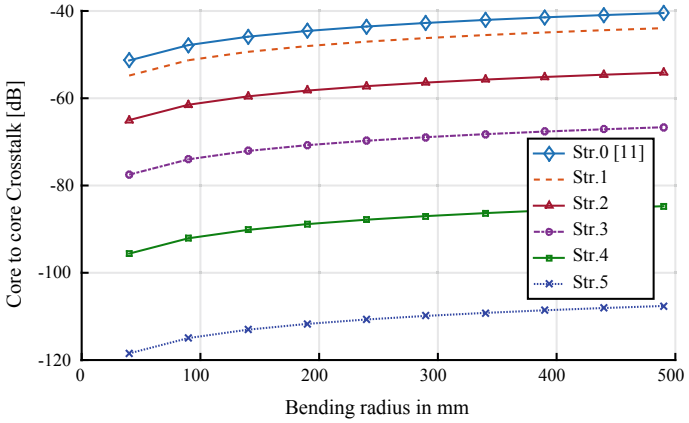

Fig. 3 Crosstalk versus fiber-bending radius at $\Delta_2 = -0.70\%$ value and core pitch 'Λ' of 40 μm

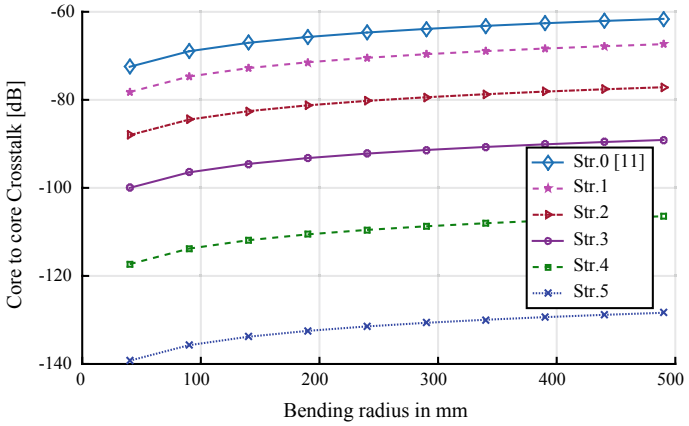

Fig. 4 Crosstalk versus fiber-bending radius at $\Delta_2 = -1.40\%$ value and core pitch 'Λ' of 40 μm

core structure-based 'Str.0 [11].' The figures are clearly demonstrating that for the fiber-bending radius of 140 mm, Str.3 to Str.5 have ultra-low XT levels, less than −70 dB, which is mainly because of strong mode confinement and hence, less coupling between the adjacent cores as high Δ_1 value and low core radius have been chosen for these structures.

3.2 Crosstalk Versus Wavelength

The wavelength-dependent XT analysis is very important from the propagation point of view, especially in wavelength division multiplexing-based optical systems and networks [17]. For the wavelength-dependent XT analysis, a wide range of operational wavelength from 1530 to 1620 nm has been considered, as the attenuation loss over this range of wavelength is ≤0.2 dB/km. The XT performance for all the respective core structures with different wavelengths has been depicted in Figs. 5 and 6, respectively, for the trench depth values of −0.70 and −1.40%. Again, for a wide range of wavelengths, the suppression of the crosstalk level can be recognized in Fig. 6 for deeper trench depth. During the simulation analysis, it has been realized that with the increase in wavelengths, the real part of n_{eff} values decreases slightly that was also dependent on Δ_1 values. This decrement in n_{eff} values results in deterioration of crosstalk performance, as depicted in Figs. 5 and 6. Once again, the improved XT performance has been observed for all the five core structures with respect to the core structure 'Str.0 [11].'

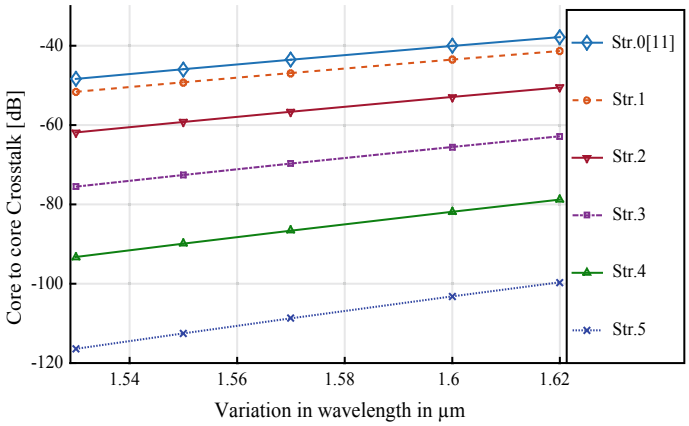

Fig. 5 Crosstalk versus wavelength at $\Delta_2 = -0.70\%$ value and core pitch 'Λ' of 40 μm

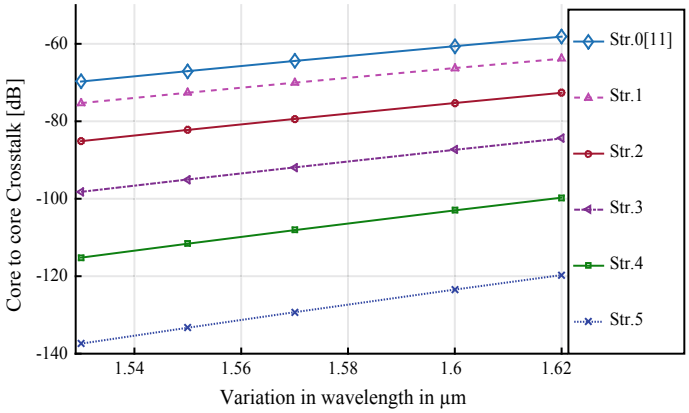

Fig. 6 Crosstalk versus wavelength at $\Delta_2 = -1.40\%$ value and core pitch 'Λ' of 40 μm

3.3 Crosstalk Versus Transmission Distance

For long-distance high-capacity communication, the optical fiber cables are more preferable than the metallic wire cables. As demonstrated in Eq. (1), the crosstalk in MCF is directly dependent on fiber length. The crosstalk performance with respect to transmission distance up to 10,000 km [6, 11] for all the five proposed core structures with fundamental (LP_{01}) mode propagation has been demonstrated in Figs. 7 and 8, respectively, for the trench depths (Δ_2) of -0.70 and -1.40%. Here, the operating wavelength, core pitch, and fiber-bending radius are assumed as 1550 nm, 40 μm, and 140 mm, respectively. The FEM-based semi-analytical results show that the core-to-core crosstalk level declines up to 10 dB/decade for all the respective

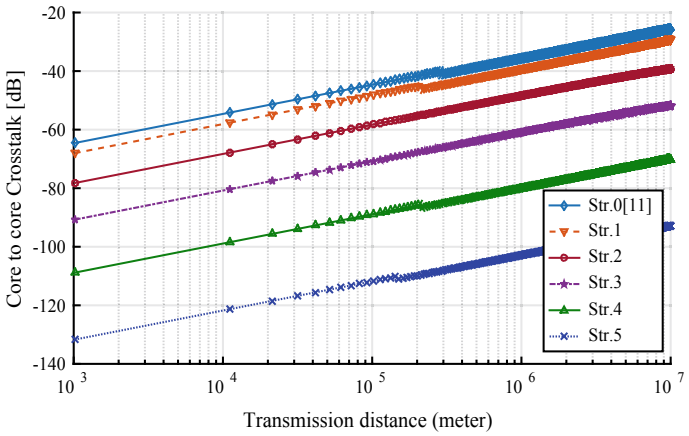

Fig. 7 Crosstalk versus fiber length at $\Delta_2 = -0.70\%$ value and core pitch 'Λ' of 40 μm

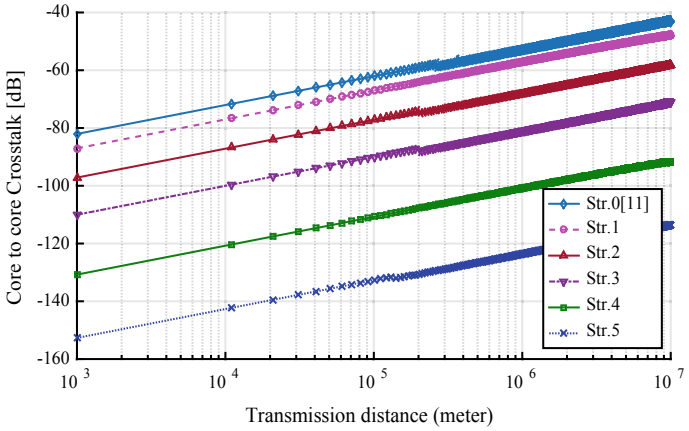

Fig. 8 Crosstalk versus fiber length at $\Delta_2 = -1.40\%$ value and core pitch 'Λ' of 40 μm

five different core structures. All the proposed core structures have better crosstalk performance than the core structure 'Str.0 [11]' over the same transmission lengths. For the transmission length of 100 km, the ultra-low crosstalk performance ≤ -70 dB can be achieved with the Str.3 to Str.5.

The mean ICXT power level with multiple interfering adjacent cores with equal core pitch is $10 \log_{10} N_i$ dB higher than the one interfering core, where N_i is the number of interfering cores. In seven-core MCF structure having hexagonal closed packing (HCP) arrangement, the center and outer cores are interfered by 6 and 3 adjacent cores, respectively, which results in corresponding increase in the mean XT value nearly by 7.8 and 4.8 dB in comparison with the case of only one interfering core.

4 Conclusion

In order to achieve the ultra-low crosstalk performance of MCF, the designs of five different core structures have been proposed by varying the core diameter from 6 to 10 μm with optimally corresponding variations in relative refractive index difference of core–clad (Δ_1) values, for the single-mode propagation condition with a cutoff wavelength of nearly 1515 nm. The crosstalk estimations have been done by using the semi-analytical method for the seven-core homogeneous trench-assisted multi-core fiber. The crosstalk performance has been examined with some fiber operational parameters, such as fiber-bending radius, operating wavelength, and fiber length. The ultra-low crosstalk levels can be achieved by optimally choosing the higher values of Δ_1 and Δ_2 with significantly smaller core radius value. For all the proposed core structures, the simulation results have demonstrated the significantly lower dispersion characteristics, nearly as -5 ps/nm-km at 1550 nm. But, simultaneously it has

been recorded that Str.4 and Str.5 have low mode effective area, which is not using in telecom services, and therefore these structures can be used for short-reach applications like optical interconnects and MCF sensors. The Str.2 and Str.3 are quite acceptable for long-distance telecom communications, because of low core-to-core crosstalk (less than −30 dB/100 km) and effective mode area (nearly 60–80 μm^2), which follows the standard rules for telecom services.

Acknowledgements This research work is part of Early Career Research Award project sponsored by Science and Engineering Research Board, Department of Science and Technology, Government of India.

References

1. Desurvire EB (2006) Capacity demand and technology challenges for lightwave systems in the next two decades. J Lightwave Technol 24:4697–4710
2. Essiambre RJ, Ryf R, Fontaine NK, Randel S (2013) Breakthroughs in photonics 2012: space-division multiplexing in multimode and multicore fibers for high-capacity optical communication. IEEE Photonics J 5:0701307
3. Richardson DJ, Fini JM, Nelson LE (2013) Space-division multiplexing in optical fibres. Nat Photonics 7:354–362
4. Puttnam BJ, Luís RS, Sakaguchi J, Klaus W, Mendinueta JMD, Awaji Y, Wada N (2016) High capacity multi-core fiber systems. In: European conference on networks and optical communications (NOC), Lisbon, Portugal, pp 1–3
5. Saitoh K, Matsuo S (2016) Multicore fiber technology. J Lightwave Technol 34:55–66
6. Hayashi T, Taru T, Shimakawa O, Sasaki T, Sasaoka E (2011) Design and fabrication of ultralow crosstalk and low-loss multi-core fiber. Opt Express 19:16576–16592
7. Koshiba M, Saitoh K, Takenaga K, Matsuo S (2011) Multi-core fiber design and analysis: coupled-mode theory and coupled-power theory. Opt Express 19:B102–B111
8. Fini JM, Zhu B, Taunay TF, Yan MF (2010) Statistics of crosstalk in bent multicore fibers. Opt Express 18:15122–15129
9. Kumar D, Ranjan R (2018) Optimal design for crosstalk analysis in 12-Core 5-LP mode homogeneous multicore fiber for different lattice structure. Opt Fiber Technol 41:95–103
10. Ye F, Tu J, Saitoh K, Morioka T (2014) Simple analytical expression for crosstalk estimation in homogeneous trench-assisted multi-core fibers. Opt Express 22:23007–23018
11. Ye F, Tu J, Saitoh K, Takenaga K, Matsuo S, Takara H, Morioka T (2016) Design of homogeneous trench-assisted multi-core fibers based on analytical model. J Lightwave Technol 34:4406–4416
12. Kumar D, Ranjan R (2017) Crosstalk suppression using trench-assisted technique in 9-core homogeneous multi core fiber. In: 2017 14th IEEE India council international conference (INDICON), Roorkee, India
13. Kumar D, Ranjan R (2017) Crosstalk analysis in homogeneous 12-core multicore fiber with different core layouts for LP_{01} and LP_{02} modes. In: Region 10 conference, IEEE TENCON 2017, Malaysia, pp 2405–2408
14. Matsuo S, Takenaga K, Arakawa Y, Sasaki Y, Taniagwa S, Saitoh K, Koshiba M (2011) Large-effective-area ten-core fiber with cladding diameter of about 200 μm. Opt Lett 36:4626–4628
15. Okamoto K (2006) Fundamentals of optical waveguides, 2nd edn. Academic Press, San Diego, USA, pp 183–187

16. Kumar D, Ranjan R (2017) Estimation of crosstalk in homogeneous multicore fiber for high core count under limited cladding diameter. In: IEEE conference on information and communication technology (CICT), Gwalior, India, pp 1–4
17. Ye F, Tu J, Saitoh K, Takenaga K, Matsuo S, Takara H, Morioka T (2016) Wavelength-dependence of inter core crosstalk in homogeneous multi-core fibers. IEEE Photonics Technol Lett 28:27–30

A Cavity-Backed Dual-Band SIW Antenna with Enhanced Gain and Harmonic Suppression

Ramesh Kumar, Chenchani Vasanthi, D. S. Chandu and Pachipala Sreekar

Abstract In this paper, a cavity-backed substrate integrated waveguide (SIW) antenna is proposed for dual-band applications. The antenna is excited using coaxial feed, and a cavity is designed at a fixed position from the open-circuit end to suppress the TE_{20} harmonic mode. The proposed antenna resonates in the TE_{10} mode due to SIW, and the TE_{12} mode is excited due to the cavity structure. Therefore, two distinct resonances are observed within the X-band at 8.7 GHz (f_l, due to the SIW mode) and 12.1 GHz (f_h, due to the cavity mode) with an impedance bandwidth ($S_{11} \leq -10$ dB) of 3.91% and 3.4%, respectively. The antenna occupies a compact area of 0.28 $\lambda_g \times 0.19\ \lambda_g$ and offers 4 dBi and 6.75 dBi gain at lower and upper frequency bands, respectively. A prototype of the antenna is manufactured, and the experimental results agree well with the simulations.

Keywords Cavity-backed · Dual-band · Harmonics · Substrate integrated waveguide (SIW)

1 Introduction

In the recent days, the demand for low cost, low profile, high gain planar multi-band antennas has increased with the latest inventions in modern day-to-day wireless communication systems. Especially, dual-band antennas were extensively investigated for wireless local area network (WLAN) and satellite applications using microstrip technology [1, 2]. However, due to their inherent limitations in power handling capability and efficiency, it is not suggestible to use microstrip technology at frequencies beyond X-band for practical applications. On the other hand, substrate integrated waveguide (SIW) was proposed as a promising technology which has high quality factor and power handling capability for high-frequency applications [3, 4].

A dual-frequency SIW cavity antenna with a circular ring slot was proposed in [5] for X-band satellite applications. There is almost 5 dB difference in gain between the TE10 and TE12 operating modes of the antenna. In [6], a cavity-backed SIW antenna was designed with a triangular ring slot to achieve dual-band operation, but

R. Kumar (✉) · C. Vasanthi · D. S. Chandu · P. Sreekar
National Institute of Technology Andhra Pradesh, Tadepalligudem 531402, India

V. Janyani et al. (eds.), *Optical and Wireless Technologies*, Lecture Notes in Electrical Engineering 648, https://doi.org/10.1007/978-981-15-2926-9_62

the frequency ratio (FR) was greater than 1.5. Two sharp resonances were obtained from a half-mode SIW antenna in [7], which occupies a large area of 0.32 λ_g^2 at the lowest operating frequency. Several cavity-backed slotted SIW antennas were proposed in [8–12]. At higher operating frequencies, slotted designs can lead to zero electric field inside the structure and cause a non-uniform current distribution in all directions around the slot. This may lead to the cancelation of current and results in decrease in the gain of the antenna. This work presents a simple cavity-backed SIW antenna which overcomes the above limitations of existing dual-band SIW antennas. The proposed dual-band antenna does not have any slots, and it is compact with stable gains in the operating bands. The low FR (1.37) makes the antenna extremely useful for satellite applications. The design, operating principle and experimental results of the proposed antenna are presented in the following sections.

2 Antenna Design and Working Principle

Initially, a probe-fed conventional SIW antenna without cavity is designed on FR4 substrate ($\varepsilon_r = 4.4$, height = 1.6 mm, and $\delta = 0.02$) as shown in Fig. 1a. The dimensions of effective width W_{eff}, length L, pitch p and diameter of the vias d are obtained from the literature for a frequency of 8 GHz [4]. The reflection coefficient plot of the antenna is plotted in Fig. 2, and it is observed that some of the modes in SIW coincide with the modes of conventional waveguide. A fundamental mode TE_{10} is observed at 8 GHz, whereas a strong TE_{20} mode at 15.96 GHz is also generated due to the printed microstrip behavior of the SIW. This mode is called as the harmonic mode, and it has to be suppressed. In conventional SIW, it is observed that standard FR

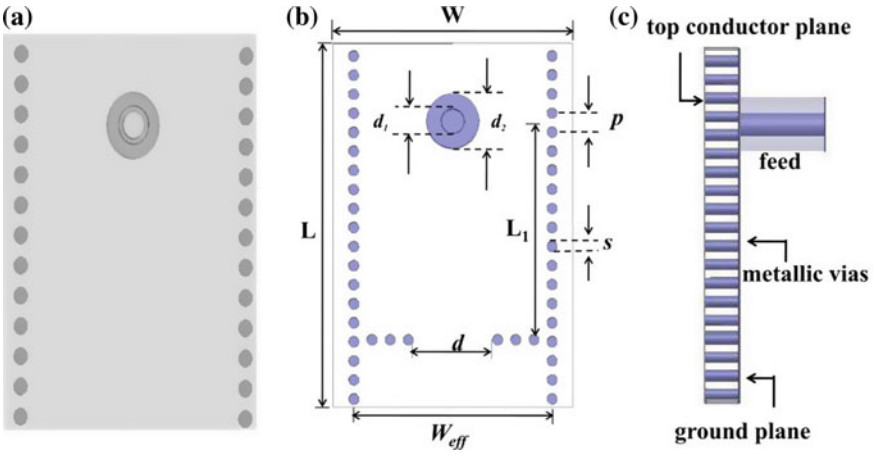

Fig. 1 Geometry of the SIW antennas. **a** conventional SIW antenna with co-axial feed, **b** proposed cavity-backed SIW antenna and **c** side view

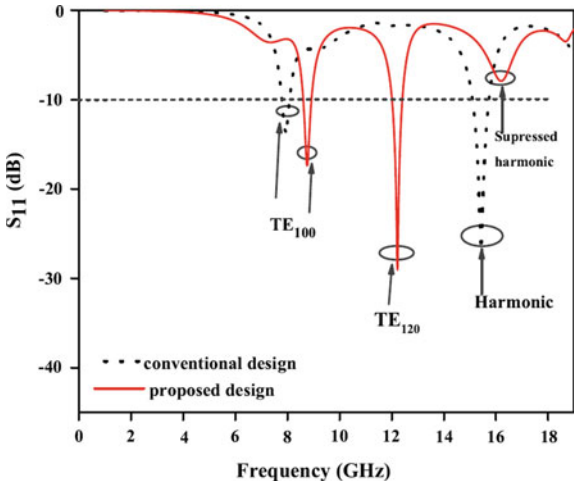

Fig. 2 Comparison of reflection coefficient for conventional and proposed SIW antennas

is 2. In order to reduce FR and to achieve dual-band operation, a cavity using metallic vias is introduced as shown in Fig. 1b. It is important to note that the dimensions of the antenna in Fig. 1a are not varied except that a cavity is introduced using metallic vias at exactly at a distance of half wavelength from the feed at the highest frequency of operation. Figure 1c shows the side view of the cavity-backed SIW antenna.

From Fig. 2, it can be observed that the proposed antenna resonates at 8.7 GHz (f_1) and 12.1 GHz (f_2). In order to have better understanding of the resonances and working principle, the electric field distribution is plotted in Fig. 3, and it can be confirmed that f_1 and f_2 correspond to TE_{10} and TE_{12} modes, thereby signifying the

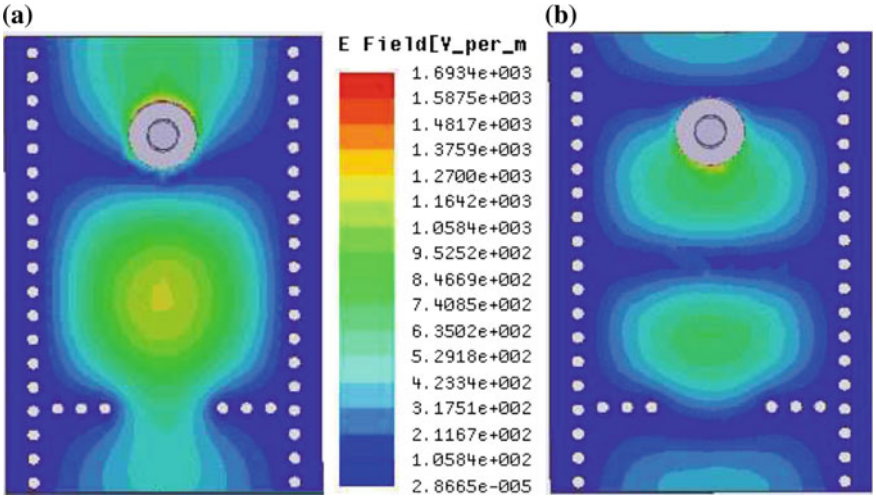

Fig. 3 Simulated electric field distributions at **a** 8.7 GHz and **b** 12.1 GHz

suppression of the TE_{20} harmonic mode. The lower operating frequency f_1 is due to the SIW mode that creates a path for the current from the patch to ground through smaller diameter vias instead of canceling the currents which results in increase in gain. The higher frequency f_2 is due to cavity which is exactly half wavelength at f_2, and it stores the energy which results in high quality factor and power handling capacity which in turn leads to high gain of 6.75 dBi. At 15.96 GHz TE_{20}, the cavity acts as a mismatched line and provides reflections. The suppressed harmonic can be clearly seen in Fig. 2. To investigate the effects of various parameters on the resonant frequencies, a parametric study is executed using a full-wave simulator. The variations of resonant frequencies with the cavity length (L_1) and number of metallic vias in cavity (n) are shown in Fig. 4. The resonant frequencies decrease with increase in parameter L_1. Hence, the lower resonant frequency and higher resonant frequency can be tuned from 8.46 to 8.78 GHz and 12.1–12.59 GHz, respectively, by changing L_1 in the range of 11.6125 to 13.6125 mm. Also, from Fig. 4b, it is observed that the

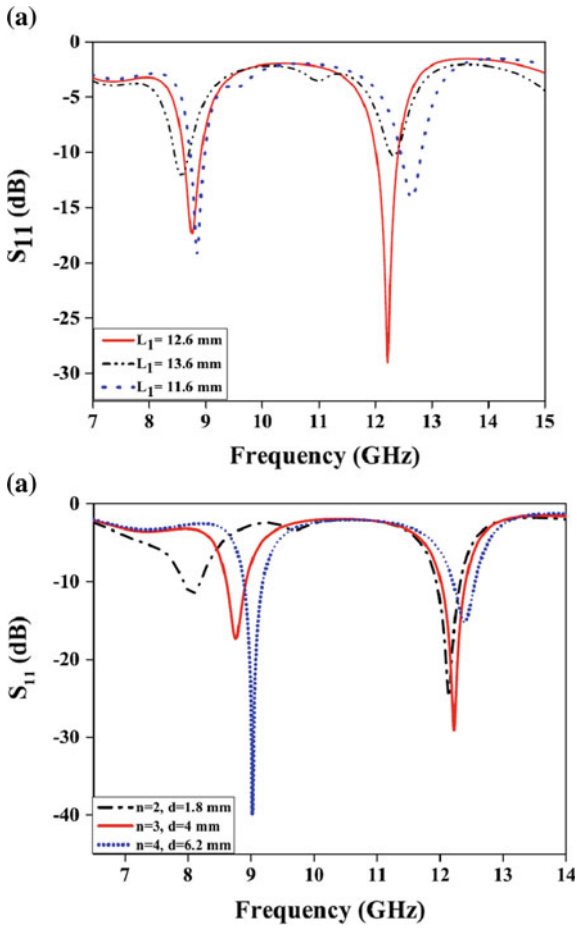

Fig. 4 Variation of reflection coefficients **a** with L_1 and **b** with n

resonating frequencies increase with increase in n. Therefore, f_1 and f_2 can be tuned from 8.03 to 9 GHz and 12.1–12.37 GHz, respectively, by changing the parameter n in the range of 2–4.

3 Results and Discussion

The manufactured antenna is shown in Fig. 5, and it is measured for reflection coefficient using Rohde and Schwarz vector network analyzer. The reflection coefficient of the proposed design is −17.89 dB and −29.8 dB at the lowest resonant frequency 8.72 GHz and the highest resonant frequency 12.1 GHz, respectively, which can be seen in Fig. 6. Minor discrepancies in the measured results may be attributed to the fabrication tolerances. Far-field measurements are carried out in an anechoic

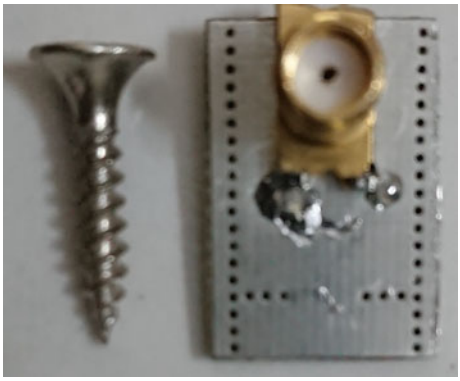

Fig. 5 Photograph of the manufactured antenna

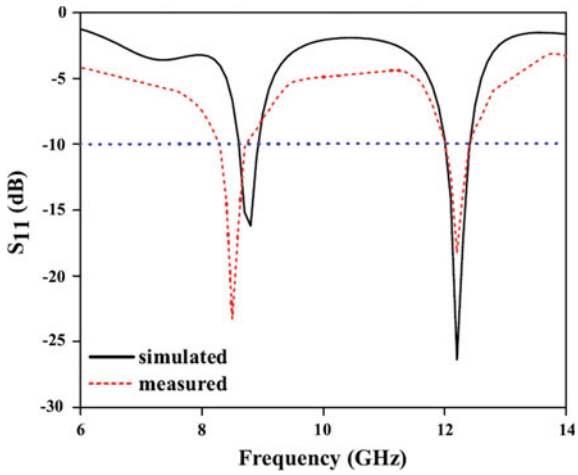

Fig. 6 Simulated and measured plot of the reflection coefficient

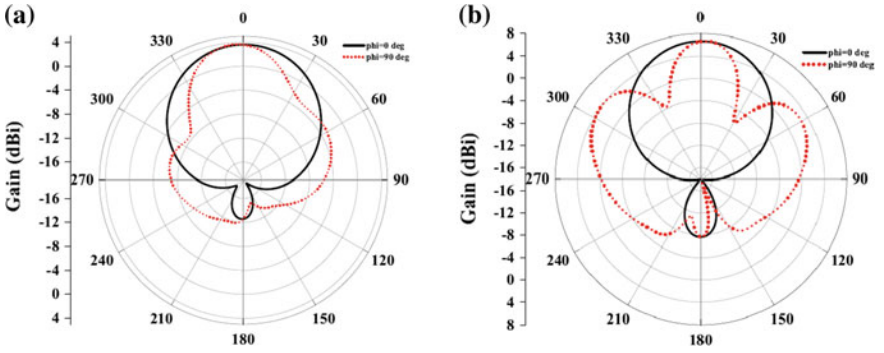

Fig. 7 Radiation patterns of the antenna at **a** 8.7 GHz and **b** 12.1 GHz

Table 1 Performance comparison of the proposed antenna with the existing dual-band SIW antennas

Ref.	IBW (%)	Freq Ratio	Antenna Size $(\lambda_g \times \lambda_g)$	Gain (dBi)
[6]	1.4,5.9	1.26	0.26x0.28	4.86,6.15
[9]	2.2,2.4	1.7	0.73x0.15	5.9,5.1
[11]	0.24,0.18	1.78	0.33x0.33	2.84,5.62
Proposed	3.9,3.4	1.37	0.28x0.19	4,6.75

chamber using a pre-calibrated wideband horn test antenna. The radiation patterns in the principle planes shown in Fig. 7 are plotted at two operating frequencies. The radiation gains at f_1 and f_2 are 4.0 and 6.75 dBi, respectively. Table 1 summarizes the performance of the proposed antenna with the state-of-the-art dual-band SIW antennas. The dual-band antenna presented in this work is better in terms of size, radiation gain and with a very small FR.

4 Conclusion

A dual-band substrate integrated waveguide antenna with a cavity-backed architecture was proposed. The TE20 mode was suppressed up to 20 dB using cylindrical metallic vias placed at $\lambda_0/2$ from the feed at the highest operating frequency. In addition, the gain of the antenna at the frequency due to the cavity mode was enhanced by 68.75% compared to the conventional SIW antenna. The narrow impedance bandwidth, high gain and compact size make the proposed antenna a suitable candidate for dual-band satellite applications.

References

1. Chen ZN, Qing X (2010) Dual-band circularly polarized S-shaped slotted patch antenna with a small frequency-ratio. IEEE Trans Antennas Propag 58(6):2112–2115
2. Luo GQ, Hu ZF, Liang Y, Yu LY, Sun LL (2009) Development of low-profile cavity backed crossed slot antenna for planar integration. IEEE Trans Antennas Propag 57(10):2972–2979
3. Bozzi M, Georgiadis A, Wu K (2011) Review of substrate-integrated waveguide circuits and antennas. IET Microwaves Antennas Propag 5(8):909–920
4. Deslandes D (2010) Design equations for tapered microstrip-to-substrate integrated waveguide transitions. In: International microwave symposium, USA
5. Wu CTM, Itoh T (2014) An X-band dual mode antenna using substrate integrated waveguide cavity for simultaneous satellite and terrestrial links. In: Asia Pacific microwave conference
6. Zhang T, Hong W, Zhang Y, Wu K (2014) Design and analysis of SIW cavity backed dual-band antennas with a dual-mode triangular-ring slot. IEEE Trans Antennas Propag 62(10):5007–5016
7. Banerjee S, Chatterjee S, Mohanty T, Ray S, Sarkar TS, Gangopadhyaya M (2016) A compact dual-band half-mode SIW based semicircular antenna. In: IEEE annual ubiquitous computing, electronics & mobile communication conference
8. Xu K-D, Li W, Liu Y (2017) Dual-frequency SIW cavity-backed slot antenna using two high-order modes. In: IEEE Asia-Pacific conference on antennas and propagation, Xi'an, China
9. Jiang S, Wang Z, Tong H (2018) Design of dual band SIW and HMSIW cavity backed U-shaped slot antennas. In: IEEE international conference on communication software and networks, China
10. Niu B-J, Tan J-H, He C-L (2018) SIW cavity-blocked dual-band antenna with good stop band characteristics. IEEE
11. Banerjee S, Rana B, Parui SK (2016) SIW based compact and dual-band equilateral triangular antennas. J Electromagn Waves Appl 1–15
12. Bao XL, Ammann MJ (2007) Dual-frequency circularly-polarized patch antenna with compact size and small frequency ratio. IEEE Trans Antennas Propag 55(7):2104–2107

Multiband Antenna for Wireless Applications

Sachin S. Khade, Samiksha Fulzele, Akanksha Sancheti, Samiksha Gawali and Divyani Rane

Abstract A small multiband antenna with step geometry is proposed. The proposed fork like antenna structure with partial ground plane is designed on FR4 substrate having dimensions 20 × 30 mm^2. The proposed antenna is designed such that it operates at three different bands. The multiband operations are obtained by adding split ring resonator on the back side of patch which is useful for Mobile and Wi-Fi/Wi-Max applications. The proposed antenna achieves impedance bandwidth from 1.89 to 1.91 GHz, from 3.16 to 3.91 GHz, from 3.914 to 4.28 GHz and from 5.693 to 6.323 GHz. The antenna achieved a maximum gain of 3.09 dB with efficiency more than 90%.

Keywords Multiband · Patch · Gain · Efficiency · Wi-Fi · Wi-Max

1 Introduction

Nowadays, microstrip patch antennas are used for various communication systems due to their light weight, compact in size, low cost, low profile and planar configuration. Currently, these antennas are desirable to meet some properties like multi-frequency/multiband operations [1, 2]. With the rapid development in technology of wireless communication, frequency resources are facing a serious problem of shortage. Various techniques have been investigated to achieve multiband operations for compact antennas using planar technology. These techniques include different patch dimensions, tapering, partial ground, split ring resonator (SRR), etc [3–6]. Rectangular patch source by microstrip feed line is to be placed at the top of the substrate material and partial ground plane at the bottom of substrate material. The height of ground plane affects the return loss with increase or decrease in length which also affects the reflection coefficient, hence partial ground technique is used [2].

S. S. Khade (✉) · S. Fulzele · A. Sancheti · S. Gawali · D. Rane
Department of Electronic and Telecommunication, YCCE, Nagpur, India
e-mail: sac_mob@rediffmail.com

V. Janyani et al. (eds.), *Optical and Wireless Technologies*, Lecture Notes in Electrical Engineering 648, https://doi.org/10.1007/978-981-15-2926-9_63

The operating frequency of an antenna is adjusted by varying the length of the patch; smaller dimension of the patch resulted in higher resonating frequency and vice versa. Patch antenna is usually known for antennas with smaller bandwidth, but with these of different techniques like partial ground and addition of split ring resonator (SRR) have been developed and studied, resulting in multiple frequency bands of antenna [2, 3, 9]. One of the most important elements is the SRR which is proposed to design small antennas for RF and wireless communication systems. The individual split ring resonator is added consisting of two rings with reduced diameter [3].

The basic structure of microstrip antenna consists of a dielectric substrate sandwiched between metal patch on one side and ground plane on the other side. Due to its small size, low profile configuration, low fabrication cost and capability to integrate with microwave circuits, the microstrip patch antenna is very well suited for wireless communication system applications like- cellular phones, radar system and satellite communication system, etc. [2, 6, 7].

The range of ultra wideband is 3.1 to 10.6 GHz, used for Wi-Fi and Wi-Max applications. For achieving multiple frequency ranges, usually multiple antennas are used but instead we altered the geometry of our single antenna by creating a small slot in the ground. The main goal of the research is to design an antenna which can operate at multibands and provide large bandwidth to wireless users [4, 5].

The design of multiband antenna with slots has been studied experimentally by many researchers. The proposed antenna is designed and simulated to operate in multiple frequency bands using three patches with different dimensions and a feed line.

2 Antenna Design

The proposed antenna consists of step geometry with three layers which includes ground plane at bottom, substrate in the mid followed by copper patch at the top. The substrate we have used is FR-4 lossy having a dielectric constant of 4.3 and height of 1.6 mm. Upper layer consists of a step-shaped patch with a tapered feedline with a minimum frequency of 3.5 GHz.

2.1 Design A

Initially, the design of antenna consists of three rectangular patches and a feed line having a fork like structure using FR4 lossy material as substrate. The overall size of antenna is 50 mm × 39 mm × 1.6 mm. The radiating element of antenna is composed of the patches with dimensions as ($g \times W_1$), ($L_2 \times W_2$), ($L_3 \times W_3$), and a 50 Ω feedline of dimenssions ($L_f \times W_f$) is used (Fig. 1). The proposed dimenssions of of antenna is given in Table 1.

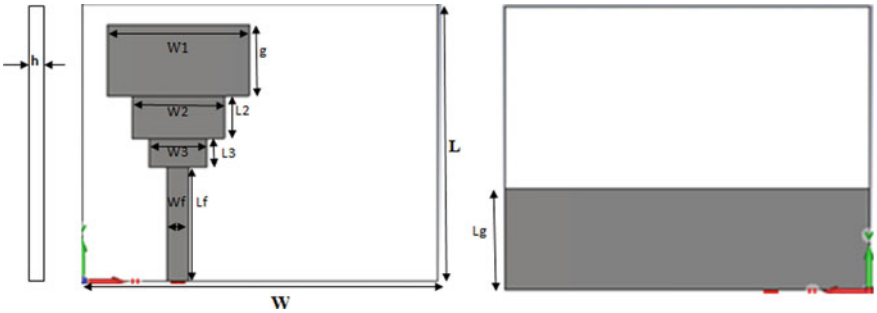

Fig. 1 Basic design representing fork like structure

Table 1 Dimensions of the proposed antenna (in mm)

Parameter	Dimension (mm)	Parameter	Dimension (mm)	Parameter	Dimension (mm)	Parameter	Dimension (mm)
L	39	W	50	L_2	6	W_2	13
g	10	W_1	20	L_3	4	W_3	8
h	1.6	L_g	14	L_f	16	W_f	3

The obtained frequency bands for initial design are from 1.85 GHz to 3.089 GHz and from 5.329 GHz to 7.029 GHz, with resonating frequency of 2.093 GHz and 5.9618 GHz, respectively, having reflection coefficient (S_{11}) −19.70 Ω for first band and −25.60 Ω for second band (Fig. 2). For the resonating frequency of 2.093 GHz, the obtained value of VSWR is 1.2314 and for resonating frequency of 5.9618 GHz,

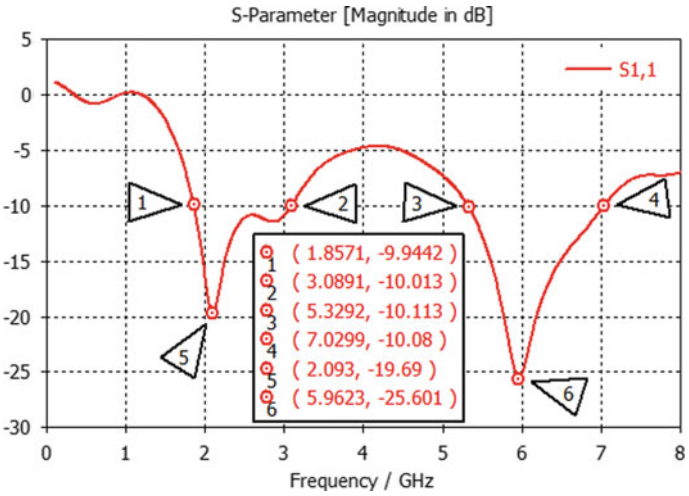

Fig. 2 Simulated s-parameter for design A

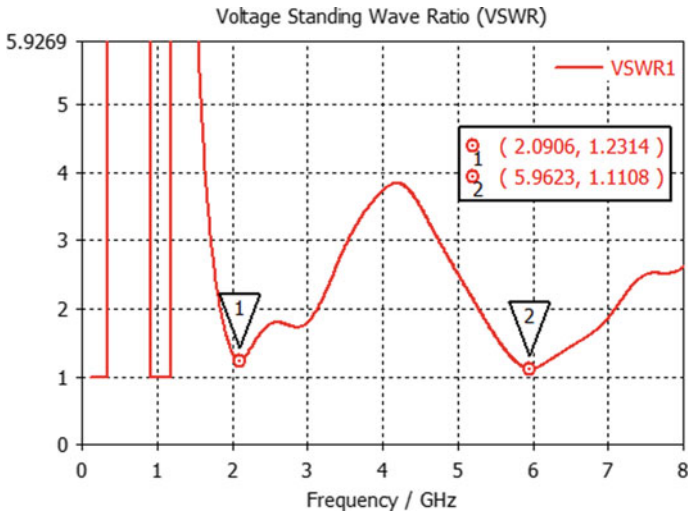

Fig. 3 Simulated VSWR for design A

the obtained value of voltage standing wave ratio (VSWR) is 1.1107 (Fig. 3). The impedance is acquired by using partial ground technique having the value of 45.028 Ω for resonating frequency 2.093 GHz and impedance 45.91 Ω for resonating frequency 5.9618 GHz. The maximum gain of proposed antenna is 3.74 dB at frequency of 5.96 GHz (Figs. 4 and 5).

2.2 Design B

In design B, modifications are done with respect to size reduction. The 50 Ω microstrip line of width 3 mm is then tapered from 3 to 1.8 mm to feed patch antenna with SMA connector. The tapered section of microstrip feed line is used to match the characteristics impedance over the frequency band (Fig. 6).

The optimized shape parameter of the proposed antenna is given in Table 2. The antenna is optimized by almost 63% as compared to previous geometry. The simulated results are displayed in Figs. 7 to 11, which includes all the results like-S-parameters, VSWR, Impedanceand Gain respectively.

With the change in dimensions, the results of antenna also deviate. The obtained frequency bands for design B are from 3.22 to 4.32 GHz, with resonating frequency of 3.6866 GHz having reflection coefficient (S_{11}) −20.86 Ω (Fig. 7). For the resonating frequency 3.6866 GHz, the value of VSWR is 1.1989 (Fig. 8). The impedance is acquired by partial ground technique, and the impedance of antenna at resonance is 49.39 Ω (Fig. 9). The gain of antenna in design B at resonance is 2.39 dB (Figs. 10 and 11).

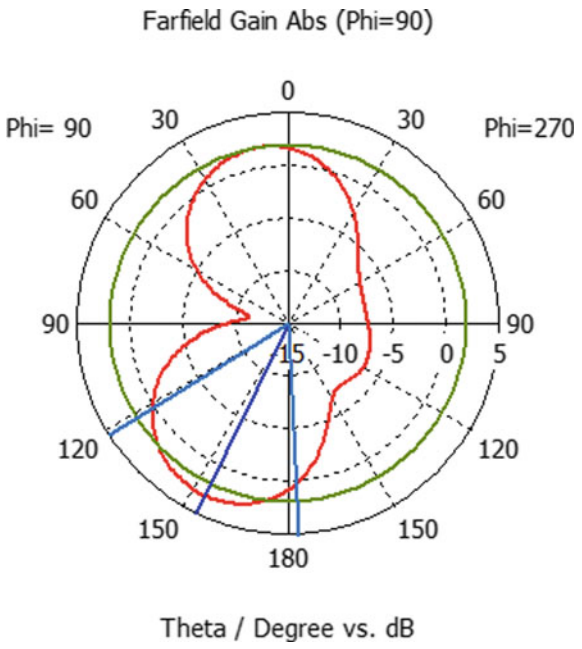

Fig. 4 2D far field plot for design A

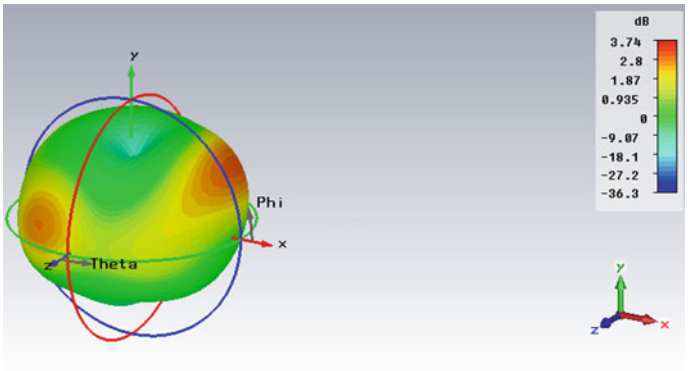

Fig. 5 3D far field plot for design A

2.3 Design C

In design C, split ring resonator is added. It consists of a pair of concentric metallic rings, and modifications are done in ring resonator to get the desired frequency band for various applications by adjusting the radius of inner and outer cylinders, hence achieving the desired impedance (~50 Ω). The inner and outer rings are spaced from

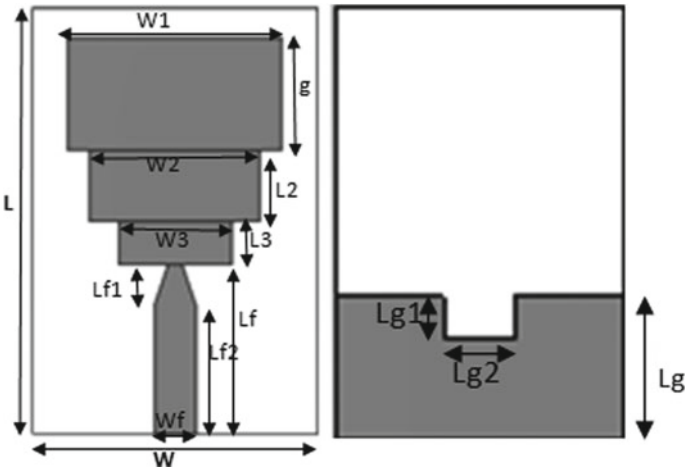

Fig. 6 Design of antenna with tapered feedline

Table 2 Dimensions of the proposed antenna for design B

Parameter	Dimension (mm)	Parameter	Dimension (mm)	Parameter (mm)	Dimension (mm)	Parameter	Dimension (mm)
L	30	W	20	L_2	5	W_2	12
g	8	W_1	15	L_3	3	W_3	8
L_f	12	W_f	3	L_{f1}	3	L_{f2}	9
h	1.6	L_g	10	L_{g1}	3	L_{g2}	5

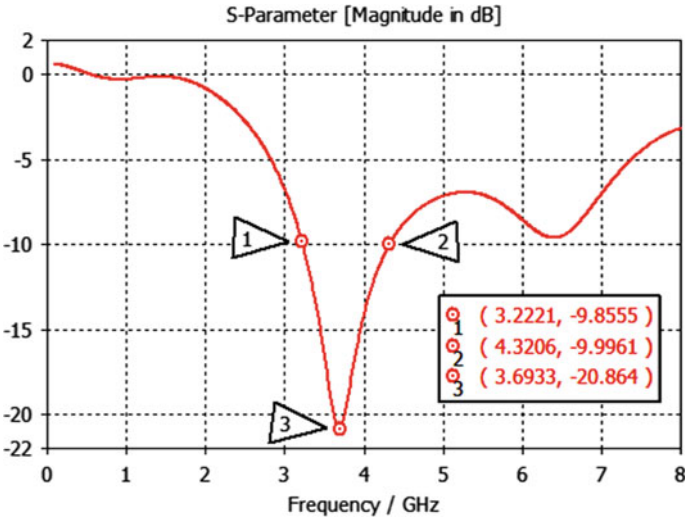

Fig. 7 Simulated s-parameter for tapered design B

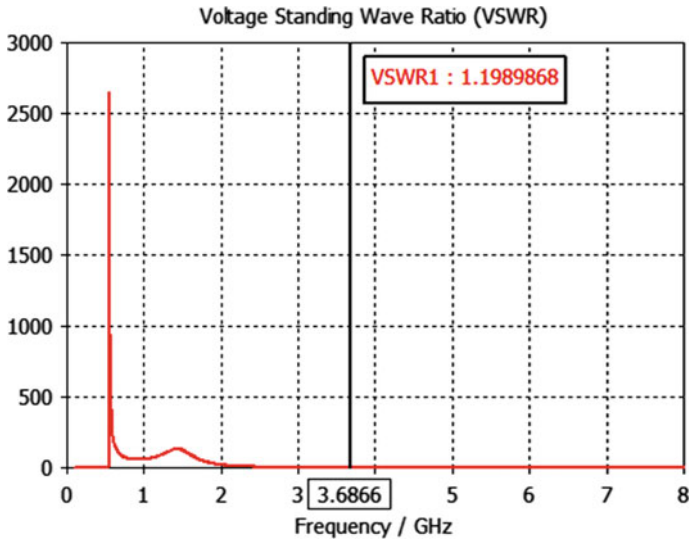

Fig. 8 VSWR for design B

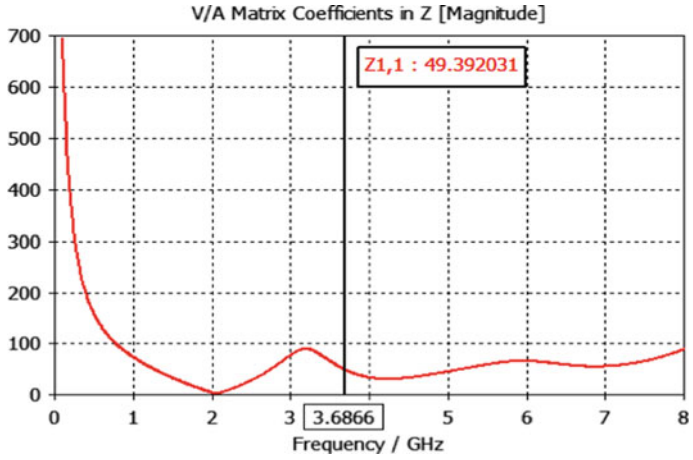

Fig. 9 Impedance of design B

each other by a distance of 2.5 mm. Modification in the size of patch ($g = 9$ mm) leads to better results for the frequency bands. The capacitance value changed with the increase in spacing between rings.

The obtained frequency bands are from 1.8944 GHz to 1.9128 GHz, from 3.1646 GHz to 3.9142 GHz, from 3.9142 GHz to 4.2847 GHz and from 5.6936 GHz to 6.3231 GHz, with resonating frequency of 1.90 GHz, 3.58 GHz, 4.01 GHz and 5.82 GHz, respectively (Fig. 13). The respective reflection coefficients are −

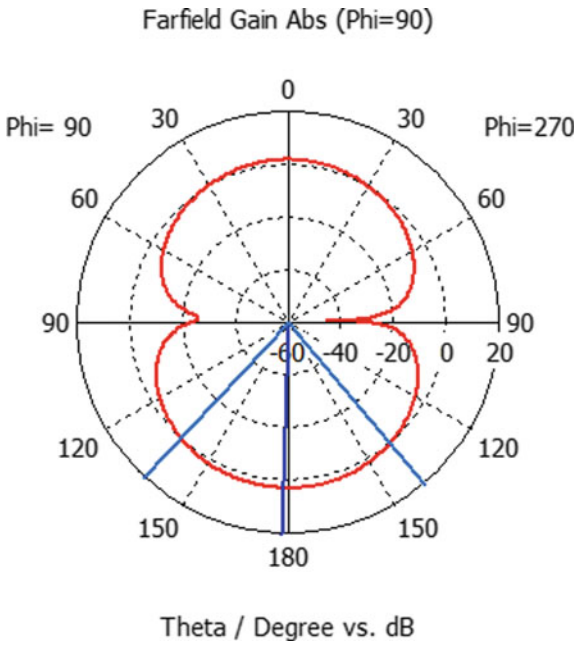

Fig. 10 2D far field plot for design B

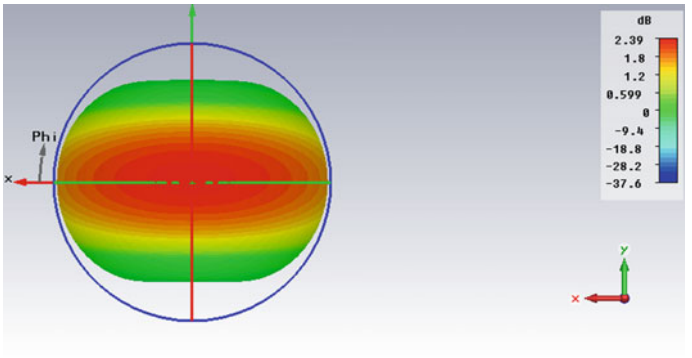

Fig. 11 3D far field plot for design B

11.366 dB, −20.088 dB, −15.123 dB and −19.746 dB, and the voltage standing wave ratios (VSWR) are 1.7444, 1.2197, 1.4253 and 1.2296, respectively (Fig. 14).

The simulated result of 2D and 3D radiation pattern for design C is presented in Figs. 17 and 18. The value of antenna gain is 2.36 dB for $f = 3.5839$ GHz and 3.09 dB for $f = 5.8214$ GHz. The power pattern of the antenna is shown in Fig. 17. The constant power is applied to the monopole antenna during the simulation. The antenna starts accepting the power from 2 GHz on words, out of which some of the

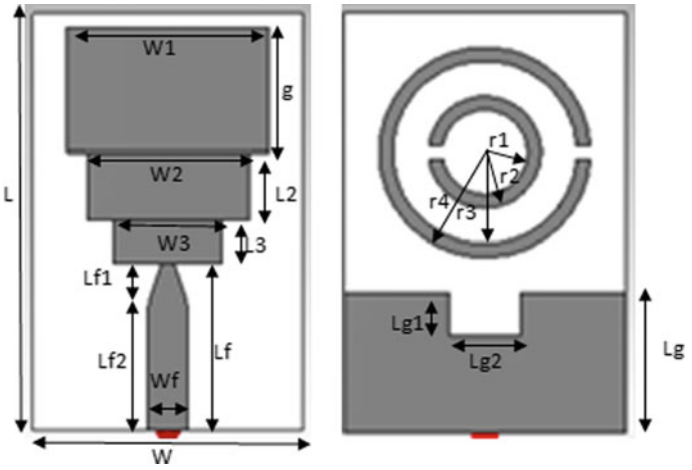

Fig. 12 Optimized design of antenna with split ring resonator

Table 3 Dimensions of the SRR

Parameter	Dimension (mm)	Parameter	Dimension (mm)	Parameter	Dimension (mm)
W_1	15	g	9	r_1	3
r_2	4	r_3	6.5	r_4	7.5

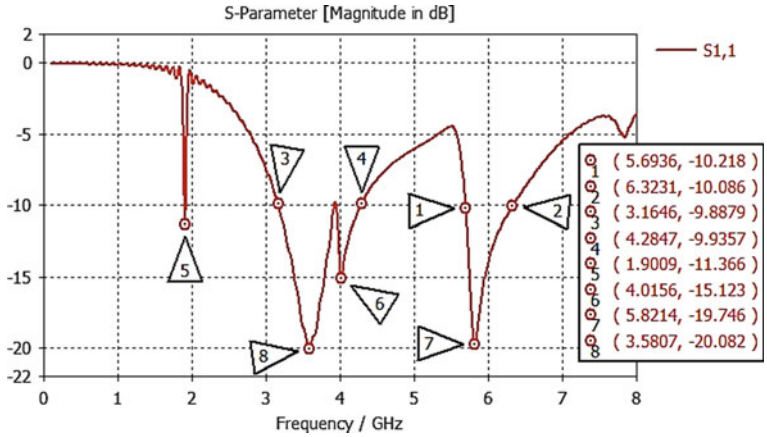

Fig. 13 Simulated s-parameter for design C

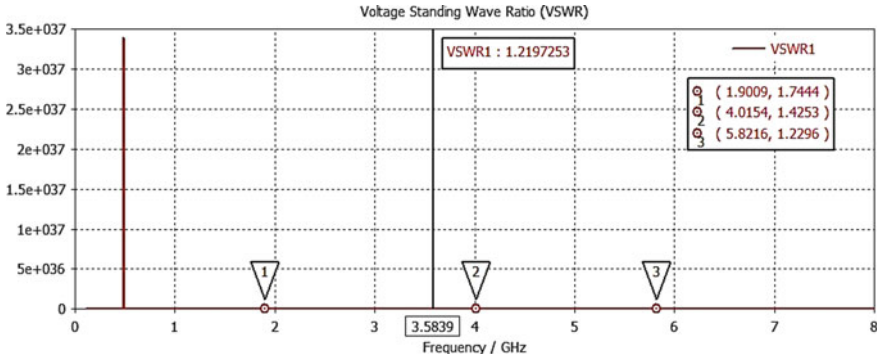

Fig. 14 VSWR for design C

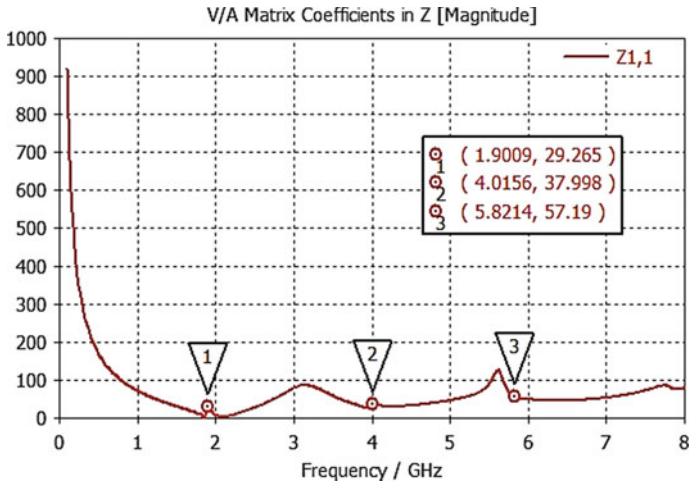

Fig. 15 Impedance of design C

power is radiated and remaining power is lost. The radiation of antenna is affected by losses across the FR4 material. The power accepted by an antenna is continuously varying with respect to frequency.

3 Fabricated Antenna and Results

The prototype is fabricated using milling machine as per the design specifications (Fig. 19). The measured reflection coefficient and VSWR are found very close to the simulated one (Figs. 20 and 21). These results confirm the usability of the antenna in wireless applications.

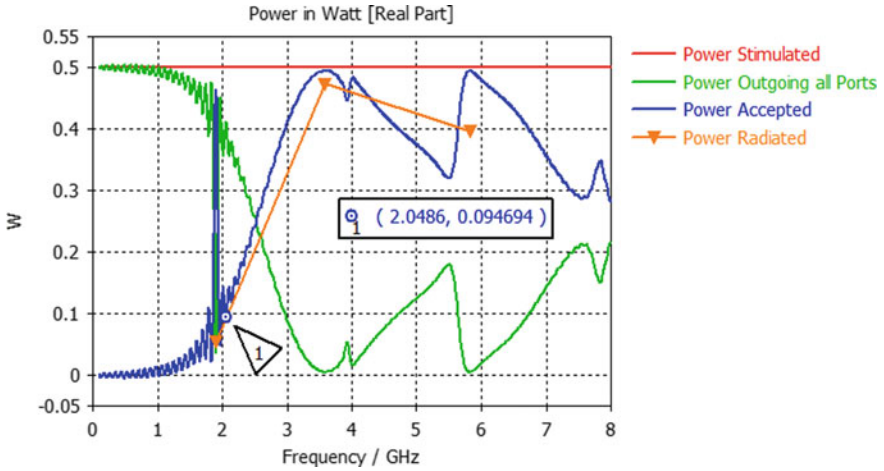

Fig. 16 Power pattern of antenna

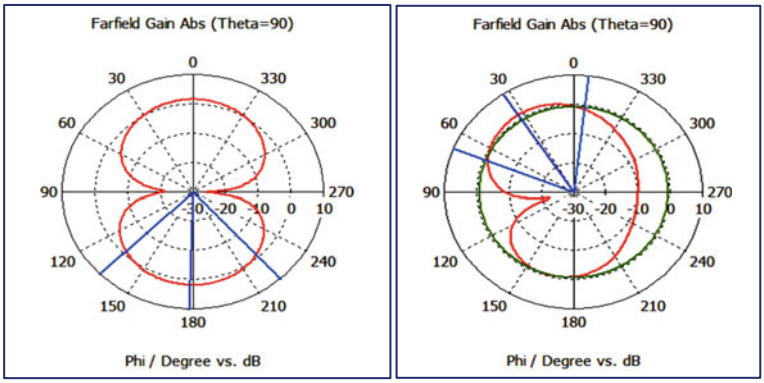

(a) for f=3.5839 GHz (b) for f=5.2814 GHz

Fig. 17 2D radiation pattern of design C

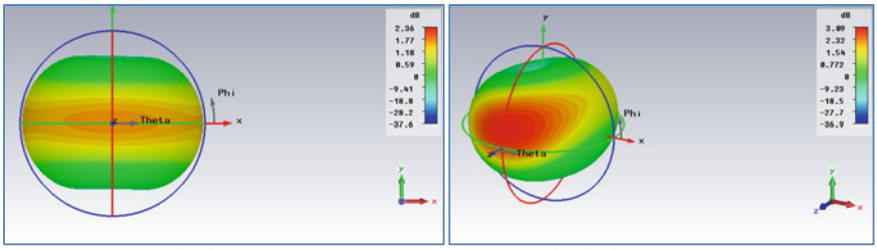

(a) for f=3.5839 GHz (b) for f=5.8214 GHz

Fig. 18 3D radiation pattern of design C

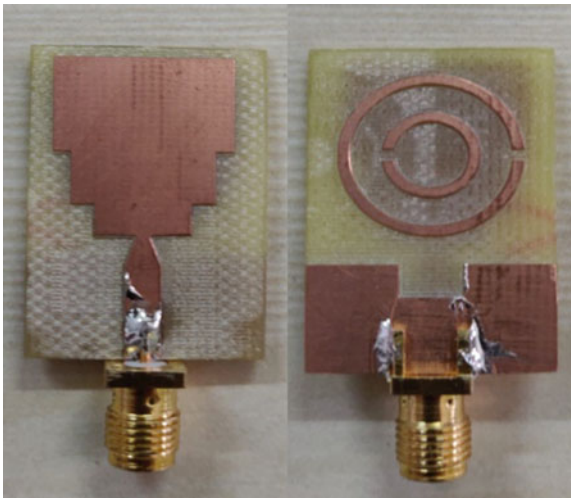

Fig. 19 Fabricated structure of antenna

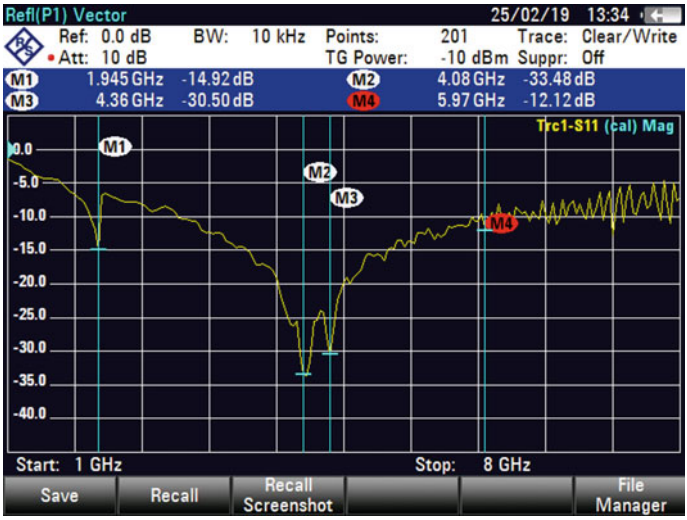

Fig. 20 Measured reflection coefficient

4 Conclusion

Thus, the design of patch antenna with multiple frequencies is proposed which can be used for wireless applications. Accordingly, we have evolved the geometry of the antenna for better results, and hence, we achieved the required output at lower frequencies. The final result provides a maximum gain of 3.09 dB with efficiency

Fig. 21 Measured VSWR

more than 90%. The antenna operates over four bands with frequency ranges of 1.89–1.91 GHz, 3.16–3.91 GHz, 3.914–4.284 GHz and 5.693–6.323 GHz which can be used for Mobile communication, Wi-Fi and Wi-Max applications.

References

1. Singh R (2017) High gain ultra wide band MIMO antenna. In: IEEE conference for convergence in technology. 978-1-5090-4307
2. Pradeep Kumar (2011) Multiband patch antenna for wireless communication. In: National conference on converging technologies beyond 2020, (CTB-2020), April 6, 7, 2011. Int J Appl Eng Res 6(5). ISSN 0973-4562
3. El Mrabet Otman (2013) A compact split ring resonator antenna for wireless communication systems. Prog Electromagn Res Lett 36:201–207
4. Pujitha P (2017) Design of multiband antenna for wireless communications. Int J Sci Eng Res 8(6). ISSN 2229-5518
5. Kshetrimayum RS (2008) Printed monopole antennas for multiband applications. Int J Microw Opt Technol 3(4)
6. Agrawall N, Kumar G, Ray K (1998) Wide-band planar monopole antennas. IEEE Trans Antennas Propag 46(2):294–295
7. Yazdi M, Komjani N (2011) Design of band-notched UWB monopole antenna by means of an EBG structure. IEEE Antennas Wirel Propag Lett 10:170–173
8. Arapoglou P-D, Bertinelli M, Cottis P (2011) MIMO over satellite: a review. IEEE Commun Surv Tutorials 13(1):27–51
9. Garg MK Partial ground microstrip patch antenna for ultrawide band applications. AKGEC Int J Technol 6(2)

Broadband Circularly Polarized CPW-Fed Inverted-L Grounded Strips and SRR Loaded Square Slot Antenna for Wi-Fi/WiMAX/5G Applications

Rashmi, Ashok Kumar, Jitendra Kumar Deegwal and Hari Shankar Mewara

Abstract A coplanar waveguide-fed inverted-L grounded strips and a square split-ring resonator (SRR) loaded circularly polarized square slot antenna is presented. The broadband circular polarization is achieved mainly by incorporating asymmetrical square SRR parasitically and a pair of inverted-L grounded strips on square slot antenna due to excitation of equal field components and 90° phase difference between them. The embedded strips and a square SRR on square slot antenna is also supported to enhance the impedance bandwidth. The antenna exhibits a wide 3-dB axial ratio bandwidth (ARBW) of 42.62% (1.3 GHz, 2.40–3.70 GHz) and impedance bandwidth ($|S_{11}| \leq -10$ dB) of 127.08% (7.46 GHz, 2.14–9.60 GHz), yielding this antenna can be used for Wi-Fi, WiMAX, and 5G applications.

Keywords Circular polarization · Inverted-L grounded strips · Slot antenna

1 Introduction

Circularly polarized (CP) antennas have been received wide consideration in many wireless communication system applications because of their capacity to lessen polarization mismatch and suppress multipath interference. Wireless systems can be operated at multiple frequency bands and required wideband and multiband antennas which can work on them [1, 2]. Some studies are found to propose antennas using multiple radiating elements with properties of broadband CP radiation [3–7]. These structures can be redistributed the current on the slot/strips in such a manner that two equal orthogonal field components and a 90° phase difference (PD) is generated to excite circular polarization. In [3], an asymmetrical rectangular slotted patch with T-shaped metallic stub and two inverted-L grounded strips are used to generate the broadband CP. In [4], a square slot antenna with a pair of inverted-L grounded strips

Rashmi · A. Kumar (✉)
Department of Electronics and Communication Engineering, Government Mahila Engineering College, Ajmer, Rajasthan 305002, India

J. K. Deegwal · H. S. Mewara
Department of Electronics Instrumentation and Control Engineering, Government Engineering College, Ajmer, Rajasthan 305025, India

V. Janyani et al. (eds.), *Optical and Wireless Technologies*, Lecture Notes in Electrical Engineering 648, https://doi.org/10.1007/978-981-15-2926-9_64

is used to enhance the axial ratio (AR) bandwidth. In [5], an L-shaped and inverted C-shaped monopoles loaded square slot antenna with G-shaped feed line is reported to produce circular polarization. In [6], a tapered L-shaped microstrip line and a square slot ground plane with stubs and slot loaded antenna are presented to achieve circular polarization. In [7], a parasitic inverted-L strip and engraved slots loaded orthogonal feed lines with L-shaped square slot antenna are reported for wideband circular polarization.

In this paper, a CPW-fed broadband CP square slot antenna (SSA) with a pair of inverted-L grounded strips and a square SRR (SSRR) is presented. A broadband 3-dB ARBW and impedance bandwidth are achieved by utilizing an asymmetrically SSRR and a pair of inverted-L grounded strips on the square slot antenna. In addition, it is possible to tune the CP band by adjusting the dimensions of the SSRR and strips. It has been designed to cover 3-dB ARBW of 2.40–3.70 GHz, and for this reason that it can be used for WLAN 2.4 GHz (2.4–2.7 GHz), WiMAX 2.5/3.5 GHz (2.5–2.69/3.4–3.69 GHz), and 5G 2.6/3.6 GHz (2.55–2.65/3.55–3.7 GHz) applications. Antenna design and analysis of the proposed square slot antenna are described in Sect. 2. The broad finding of the present study is presented in Sect. 3.

2 Antenna Design and Analysis

This section is describing the design process, CP mechanism, antenna configuration, and analysis of the proposed square slot antenna. Initially, the antenna design starts from a CPW-fed modified rectangular patch square slot antenna [i.e., Ant. 1]. The structure of the first stage of the proposed SSA is shown in Fig. 1 [see Ant. 1] and is formed from an 50 Ω CPW-fed rectangular SSA etched opposite corners of rectangular patch to the pair of symmetrical square slots and simulated on CST MWS simulation software. From the reflection coefficient ($|S_{11}|$) and axial ratio (AR) response of Ant. 1, shown in Fig. 2, it is clear that the antenna exhibits dual resonances at about 3 GHz and 8 GHz but no CP is attained. In the second stage, a square SRR (SSRR) is considered as a loading element, which is asymmetrically

Fig. 1 Step-by-step evolution of the different slot antenna structures

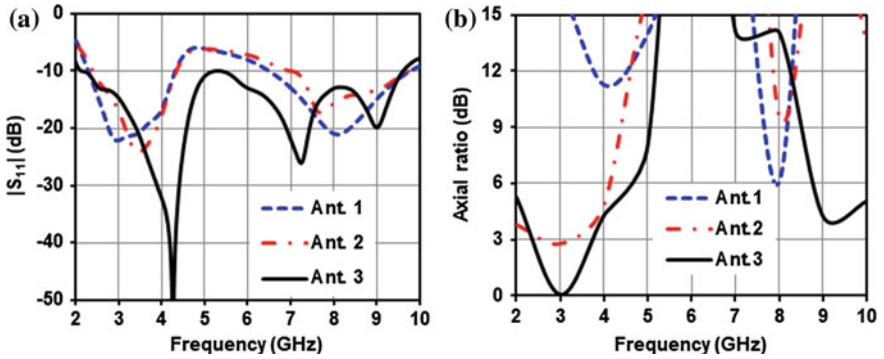

Fig. 2 Simulated results of evolution stages slot antenna structures: **a** $|S_{11}|$ and **b** AR

placed on backside of Ant. 1, and Ant. 2 is formed to create the CP band around 3 GHz in Ant. 1 but impedance bandwidth (IBW) of upper band is reduced. To improve the dual-band IBW and 3-dB ARBW of Ant. 2, an asymmetrical pair of inverted-L grounded strips in opposite corners of Ant. 2 is placed to form Ant. 3 [proposed antenna]. Ant. 3 is provided wide impedance bandwidth and broadband 3-dB ARBW. These slot antennas are designed on FR-4 dielectric substrate with $\varepsilon_r = 4.3$, the thickness of 1 mm, and $\tan\delta = 0.025$. These are fed by a CPW feed with width W_f and identical gaps g between them.

The simulated $|S_{11}|$ and AR result of the evolution stages of Fig. 1 is shown in Fig. 2. The comparison of design steps and their respective impedance bandwidths (IBWs), fractional bandwidths (FBWs) and 3-dB ARBW are summarized in Table 1. The front and back view geometry with labeled parameters of the proposed SSA is displayed in Fig. 3. The optimized dimensions of the proposed SSA are as follows: $L = 40$ mm, $L_{x1} = 9$ mm, $L_{x2} = 5$ mm, $W = 5$ mm, $W_1 = 9$ mm, $W_f = 2.4$ mm, $W_{g1} = 18.5$ mm, $g = 0.3$ mm, $k_1 = 1$ mm, $k_2 = 1$ mm, $s = 5$ mm, $W_2 = 8$ mm, $W_3 = 1$ mm, $W_4 = 5$ mm, $W_5 = 1.2$ mm, $d = 0.6$ mm, $L_x = 8.5$ mm, and $L_y = 23$ mm.

To elucidate the CP mechanism, the surface current vectors at 3 GHz CP frequency is illustrated in Fig. 4 for different time instants 0°, 90°, 180°, and 270°. It can be

Table 1 Comparison of impedance and 3-dB AR bandwidths of the Ants. 1-3

Antenna stages	Antenna type	IBWs (GHz, f_c, %)	3-dB ARBW (GHz, f_{cp}, %)
Ant. 1	Square slot antenna	2.29–4.31, 3.3, 61.21 6.49–9.77, 8.13, 40.34	–
Ant. 2	Square slot antenna with SSRR	2.40–4.34, 3.37, 56.57 7.02–9.74, 8.38, 32.46	2.73–3.15, 2.94, 14.29
Ant. 3 (This work)	Square slot antenna, SSRR and pair of inverted-L grounded strips	2.14–9.60, 5.87, 127.08	2.40–3.70, 3.05, 42.62

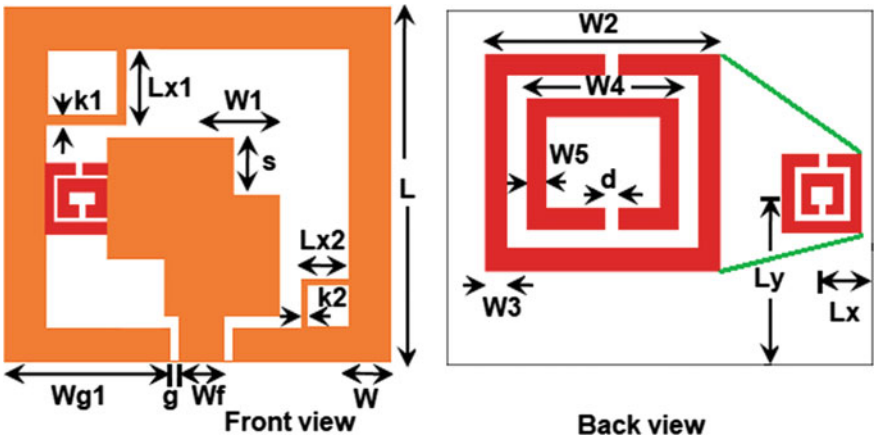

Fig. 3 Geometry of the proposed CPW-fed strips and SSRR loaded square slot antenna

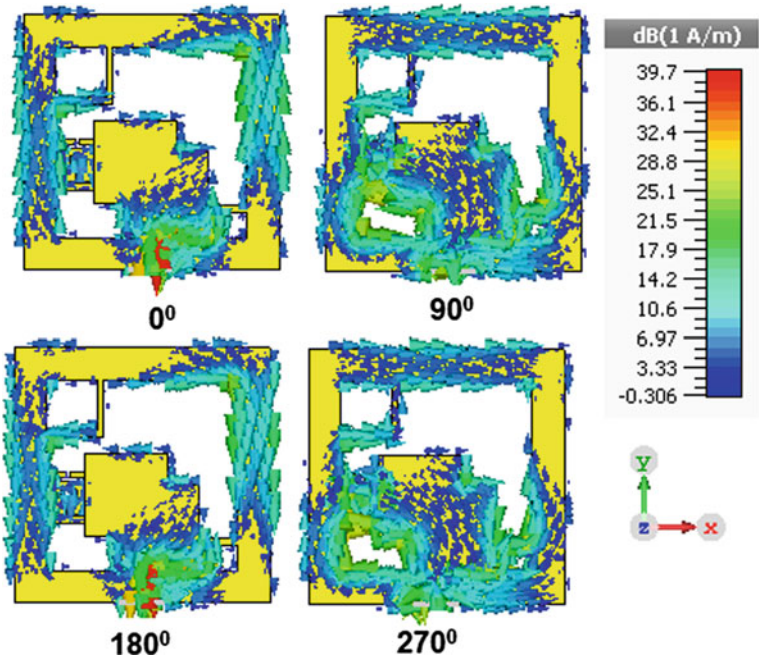

Fig. 4 Surface current vectors of the proposed CPW-fed strips and SSRR loaded square slot antenna at 3 GHz CP frequency

perceived that the surface current predominately altered on the modified rectangular patch, inverted-L grounded strips, and SSRR having almost equal amplitudes and 90° PD leading to produce CP in a broadband range. In addition, it can be observed from Fig. 4 that at different time instants from 0° to 270°, the resultant current vector rotates in the anticlockwise direction which infer the sense of polarization as right-handed circular polarization (RHCP) in $+z$ direction.

The normalized radiation patterns at 3 GHz CP frequency in xz-plane ($\phi = 0°$) and yz-plane ($\phi = 90°$) are shown in Fig. 5a, b, respectively. It can be seen that the antenna radiates RHCP wave in $+z$ direction, whereas left-handed circular polarization (LHCP) wave is in the $-z$ direction in both planes. In addition, the cross-polarization level >30 dB at $\theta = 0°$ is observed in both planes which exhibits excellent circular polarization radiation.

Table 2 summarizes the performance comparison of the proposed CPW-fed strips and SSRR loaded square slot antenna with recently published CP slot antennas. The antennas reported in [3–7] are limited to impedance bandwidth and 3-dB ARBW except [3, 6] but the proposed antenna is having widest impedance bandwidth, broadband 3-dB ARBW, simple structure, excellent circular polarization purity, and broadside RHCP radiation.

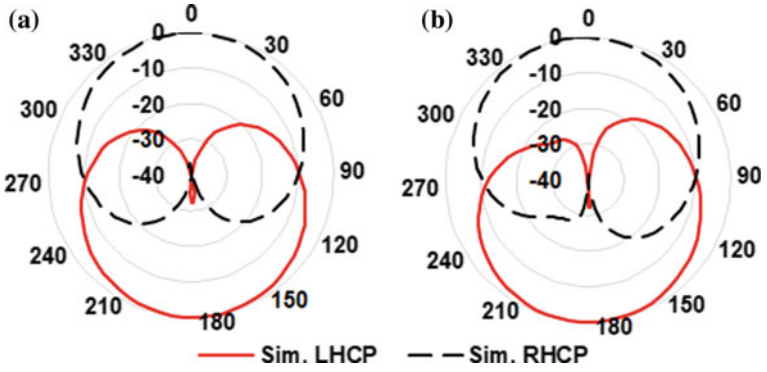

Fig. 5 Radiation patterns of the proposed SSA at 3 GHz **a** yz-plane and **b** xz-plane

Table 2 Comparison of proposed antenna with recently published CP slot antennas

Refs.	Antenna size	IBW (GHz, f_c, %)	3-dB ARBW (GHz, f_{cp}, %)	Polarization
[3]	40 × 40	5.02–10.84,7.93,73.39	5.07–9.22, 7.14, 58.08	LHCP
[4]	60 × 60	1.60–3.05, 2.33, 62.5	2.30–3.03, 2.66, 27.4	RHCP
[5]	30 × 30	3.32–6.95, 5.135, 70.1	4.5–6.55,5.525, 37.1	RHCP
[6]	40 × 40	5.15–14.05, 9.6, 92.7	5.65–9.85, 7.75, 54.19	RHCP
[7]	25 × 25	3.15–7.75, 5.45, 84.4	5.12–7.15, 6.14, 33.08	RHCP
Prop. work	40 × 40	2.14–9.60, 5.87, 127.08	2.40–3.70, 3.05, 42.62	RHCP

3 Conclusion

In this paper, a CPW-fed strips and SSRR loaded square slot antenna for broadband circular polarization is proposed. By placing a pair of inverted-L grounded strips and SSRR on the SSA, the broadband 3-dB ARBW and widest impedance bandwidth is achieved. The reflection coefficient bandwidth ($|S_{11}| \leq -10$ dB) is 127.08% (2.14–9.60 GHz) and 3-dB ARBW is 42.62% (2.40–3.70 GHz). Owing to the broadband ARBW, wide bandwidth, very simple structure, greater than 30 dB cross-polarization with RHCP radiation patterns, it is suitable mainly for Wi-Fi, WiMAX, and 5G applications.

References

1. Saraswat K, Harish AR (2018) Dual-band CP coplanar waveguide-fed split-ring resonator-loaded G-shaped slot antenna with wide-frequency ratio. IET Microw Antennas Propag 12(12):1920–1925
2. Sankhla V, Kumar A (2019) An offset CPW-fed dual-band circularly polarized printed antenna for multiband wireless applications. In: Optical and wireless technologies, Lecture notes in electrical engineering, vol 546. https://doi.org/10.1007/978-981-13-6159-3_43
3. Midya M, Bhattacharjee S, Mitra M (2018) Pair of grounded L strips loaded broadband circularly polarised square slot antenna with enhanced axial ratio bandwidth. Electron Lett 54(15):917–918
4. Sze JY, Chang CC (2008) Circularly polarized square slot antenna with a pair of inverted-L grounded strips. Antennas Wirel Propag Lett 7:149–151
5. Gyasi OK, Li J, Huang Y, Guangjun W (2017) Broadband circularly polarized square slot antenna with a G-shaped feedline. Microw Opt Technol Lett 59:3055–3063
6. Wang L, Fang W, En Y, Huang Y, Shao W, Yao B (2019) A new broadband circularly polarized square-slot antenna with low axial ratios. Int J RF Microw Comput Aided Eng 29(1):e21502. https://doi.org/10.1002/mmce.21502
7. Kumar A, Deegwal JK, Sharma MM (2018) Miniaturized wideband dual linearly and circularly polarized printed square slot antenna for multiradio wireless systems. Int J Electron Commun 88:44–51

Realization of Inter-satellite Optical Wireless Wavelength Division Multiplexed System with Polarization Interleaving for LEO, MEO, and GEO Satellites

Ruchi Sharma, Chetan Selwal and Ashish Kumar Ghunawat

Abstract In the realm of increasing demand for stable and excellent connectivity around the world, researches are done heavily to boost up the connectivity and transmission distance. Therefore, in this research work, we have made the realization of an inter-satellite optical wireless channel, wavelength division multiplexed system implemented with polarization interleaving technique in order to realize an 8-channel system capable of transmitting data rate of 20 Gbps per channel for the transmission distance of LEO, MEO, and GEO satellite orbits. The designed system is capable of data transmission with mitigated channel non linearities and acceptable SNR, BER, and Q-factor for the transmission distance of 40,000 km, 10,000 km, and 5000 km covered under the geostationary equatorial orbit, medium earth orbit, and low earth orbit, respectively. The system realized here is also considered to work efficiently under 1 μ radian to 3 μ radian transmitter and receiver pointing error losses. Optimal results can be observed on the basis of transmitted and received optical power spectrum, SNR values, total power received, eye-opening diagrams, BER, and Q-factor.

Keywords IS-OWC · WDM · Polarization interleaving · BER · SNR · Q-factor · LEO · MEO · GEO satellites

1 Introduction

In the era of increasing demands and requirements for high-speed communication, optical wireless communication has gained momentum due to its efficiency and robust qualities. We use different technologies and their combination to realize a beneficiary communication system as a whole in order to accomplish the results we desire. Similarly, to realize a high speed, long-haul optical communication system with minimum transmission error, and larger channel capacity, the idea of realizing

R. Sharma (✉) · C. Selwal
Electronics and Communication Engineering, Government Women Engineering College, Ajmer, India

A. K. Ghunawat
Electronics and Communication Engineering, MNIT, Jaipur, India

V. Janyani et al. (eds.), *Optical and Wireless Technologies*, Lecture Notes in Electrical Engineering 648, https://doi.org/10.1007/978-981-15-2926-9_65

an IS-OWC WDM system was arrived. OWC has been presently applied in quantity of applications, due to the reason that it has many advantages over traditional radio frequency signal. LASER is used to transmit data in space to communicate between satellites orbiting in same or different orbits. This technology is termed as inter-satellite optical wireless communication (IS-OWC). Along with the various properties like high speed, large capacity, this system empowers more active, competent, and constant operation of satellite system in the future. Therefore, by the use of IS-OWC, an evolutionary space network can be formed. For realizing a high capacity carrying optical communication system, WDM that is, wavelength division multiplexing is the most broadly used technology today. The research has been carried out for the realization of an efficient IS-OWC WDM system for LEO, MEO, and GEO satellites to attain acceptable and sufficient values of Q-factor and bit-error rate (BER) by the implementation of polarization interleaving technique responsible for the mitigation of channel nonlinearities and enhancement of the system performance to a great extent. The systems proposed in this paper for three satellite orbits are realized by optimizing the IS-OWC WDM-PI communication system for various needs of system parameters adequate enough in order to deliver the required output signal for various link distances included under LEO, MEO, and GEO satellite orbits. The proposed system in this paper is designed using the software Optisystem version 15 and the observations are recorded on the basis of the received results after the successful calculations of the simulations performed.

We have also studied and observed the effects on system performance due to misalignment losses or pointing errors included in the system parameters. When there is a misalignment in the transmitter and receiver of the system, power reduction in signal takes place at the receiver. The error caused due to this misalignment is called as pointing error.

The received signal power at the receiver side can be given as:

$$P_{\mathrm{r}} = P_{\mathrm{t}} G_{\mathrm{t}} \eta_{\mathrm{t}} \eta_{\mathrm{r}} G_{\mathrm{r}} L_{\mathrm{t}} L_{\mathrm{r}} (\lambda / 4\pi Z)^2 \tag{1}$$

where, P_{t} is the transmitter optical power, G_{t}, G_{r} is the transmitter and receiver telescope gain, η_{t}, η_{r} are the optical efficiency of the transmitter and receiver, L_{t} and L_{r} are the transmitting and receiving pointing error losses, λ is the operational wavelength, and Z is the distance between the transmitter and receiver of the system. It is very important for line of sight communication that there should be negligible misalignment of the transmitter and receiver in order to achieve a reliable communication because even a small divergence in the beam of signal can cause severe penalties in the communication link. The transmitter and receiver pointing error losses are given in the form as,

$$L_{\mathrm{t}} = \exp\left(-G_{\mathrm{t}} \theta_{\mathrm{t}}^2\right) \tag{2}$$

$$L_{\mathrm{r}} = \exp\left(-G_{\mathrm{r}} \theta_{\mathrm{r}}^2\right) \tag{3}$$

Here, L_t and L_r are the transmitter and receiver pointing error loss factors, G_t and G_r are the transmitter and receiver gains, θ_t and θ_r are the pointing error angles for transmitter and receiver antennas, respectively [2].

1.1 Polarization Interleaving

When we use the technology of incorporating expanded channel capacity WDM or DWDM technique in a system, nonlinear effects in the channel arises. As the channel spacing between the WDM channels are decreased and the data rates are increased, nonlinear impacts emerge out in a system. Polarization interleaving is a technique used to combat and reduce these nonlinearities to a great extent and is greatly reliable to double the transmission capacity.

In this method, channels are separately categorized as even and odd channels and multiplexed together being two even and odd branches. The states of polarization (SOPs) of each optical signal in consecutive channels are kept orthogonal to each other. These SOPs are adjusted with the help of polarization controllers such that they are orthogonal. The signal at both the branches is combined with the help of a device called as polarization combiner or polarization interleaver. This device is used to create a WDM signal having orthogonally polarized channels mutually. At the receiver end, polarization splitter device is used to regain the message signal employed before the WDM de-mux.

The remaining part of the paper is structured as follows, Sect. 2 contains the proposed system's design and description, Sect. 3 contains the results obtained from the empirical evaluation of the simulation followed by conclusion.

2 Proposed System Design

The schematic diagram of the proposed system design is shown in Fig. 1, in which the 8-channel IS-OWC WDM system is implemented with polarization interleaving scheme. Channels are categorized into separate odd and even branches of 4 channels each capable of transmitting the data rate of 20 Gbps, realizing an overall transmission of $8 \times 20 = 160$ Gbps for the distance covering under the GEO, MEO, and LEO orbits. Both the branches of channels are multiplexed separately with the help of a 4×1 WDM multiplexer. The signal out of the multiplexers is fed to the polarization controller at both the sides in which the states of polarization of odd and even channels are kept orthogonal to each other so that they tend to interfere less and creates negligible nonlinear effects.

The signal from both the polarization controllers are given with the values of their azimuth angles as 0° and 90° for odd and even branches, respectively, after which, the signal is passed on to the polarization combiner device which is responsible to combine both the orthogonal signal channels into a single ready for transmission. The

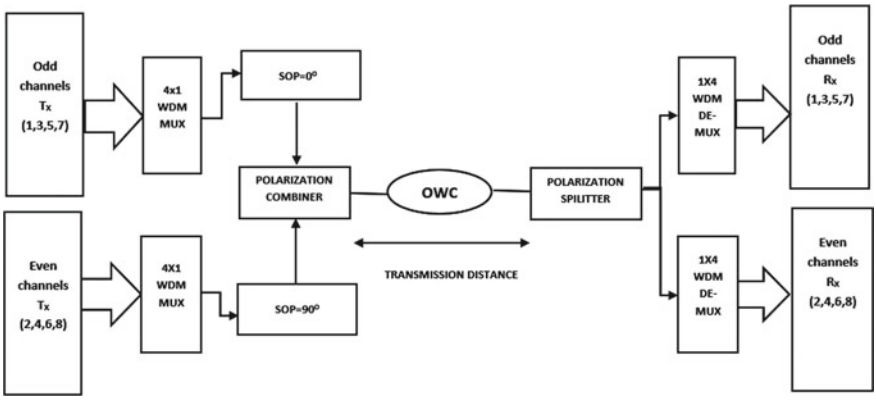

Fig. 1 Schematic block diagram of an IS-OWC WDM-PI system

combined signal is passed through an OWC channel which has the antenna aperture as 15 cm and 20 cm for transmitter and receiver, respectively. Transmitting and receiving errors are considered in this work, which is kept variable from 1 μ radian to 3 μ radian for each different value of transmission distance of 40,000, 10,000, and 5000 km. Optical amplifiers for preamplification and postamplification of the signal are used significantly in the system with parameters suiting best to the WDM and long-haul transmission of the optical signal. At the receiving end, polarization splitter acts as the signal reformer which divides the received signal according to its states of polarization into even and odd signals and fed to the WDM demultiplexer followed by the detection of signal with the help of avalanche photo diode (APD). The signal detected is then passed through a low-pass Bessel filter with a cut-off frequency of 15 GHz. The signal quality analysis is then done with the help of 3R generator and BER analyzer.

System parameters

See Table 1.

3 Results and Discussion

On the basis of the experimental simulations performed using Optisystem version 15 software, observations are made with the help of electrical power meter, electrical carrier analyzer, and bit-error rate analyzer. Eye-opening diagrams depicting BER and Q-factor of the corresponding channel and graphical representations of the performance analyzation of each IS-OWC WDM-PI system on the basis of SNR, received signal power, and Q-factor along with the pointing error variations for each satellite orbit considered are shown below (Fig. 2).

Table 1 System design and channel parameters for GEO, MEO, and LEO satellites

S. no.	System parameters	GEO	MEO	LEO
1	CW Laser input parameter (dBm)	30	30	15
2	Bit rate (Gbps)	20	20	20
3	Modulation	NRZ	NRZ	NRZ
4	Resolution bandwidth (nm)	0.1	0.1	0.1
5	Channel capacity (channels)	8	8	8
6	Channel spacing (GHz)	100	100	100
7	Amplifier gain (dB)	20	20	20
8	Filter cut-off frequency (GHz)	15	15	15
9	Operational frequency (nm)	1550	1550	1550
10	T_X and R_x efficiency	1	1	1
11	T_X antenna aperture (cm)	15	15	15
12	R_x antenna aperture (cm)	20	20	20
13	T_X pointing error (μrad)	1, 2 and 3	1, 2 and 3	1, 2 and 3
14	R_x pointing error	1, 2 and 3	1,2 and 3	1, 2 and 3
15	Transmission distance (km)	40,000	10,000	5000
16	Laser line width (MHz)	0.1	0.1	0.1
17	Dark current (nA)	10	10	10
18	Responsivity (A/W)	1	1	1

Eye diagrams for GEO satellite
See Fig. 3.
Eye diagrams for MEO satellite
See Fig. 4.
Eye diagrams for LEO satellite
See Fig. 5; Table 2.

4 Conclusion

In this research work, we have successfully realized an IS-OWC WDM-PI system capable of transmitting a total transmission of $8 \times 20 = 160$ Gbps for the transmission distance of 40,000 km, 10,000 km, and 5000 km covered under the GEO, MEO, and LEO satellite orbits, respectively. On the basis of the obtained results, we can conclude that the system performance of MEO satellite is better than LEO satellite as LEO orbital distance is subjected to greater atmospheric turbulences as compared to MEO orbital link distance hence affects the performance of the system designed for

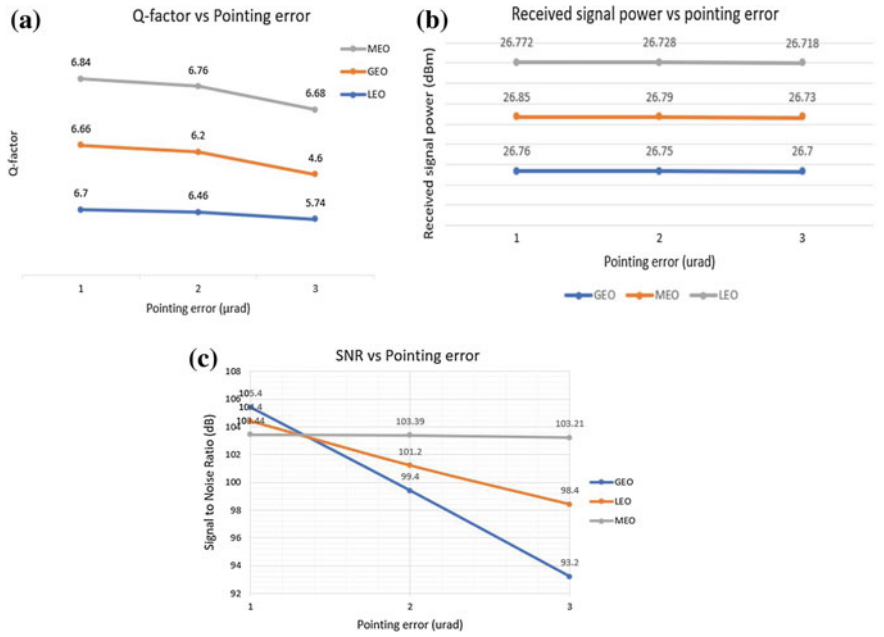

Fig. 2 **a** Performance analysis of Q-factor versus pointing error for GEO, MEO, and LEO satellites. **b** Performance analysis of received signal power versus pointing error for GEO, MEO, and LEO satellites. **c** Performance analysis of signal to noise ratio versus pointing error for GEO, MEO, and LEO satellites

LEO satellite. The system is also analyzed for withstanding the pointing error losses at the extent of 3 μ radian, after increasing the pointing error above 3 μ radian, the system performance degrades below the acceptable results. Therefore, the system is capable of withstanding pointing errors ranging from 1 μ radian to 3 μ radian for each GEO, MEO, and LEO satellite significantly.

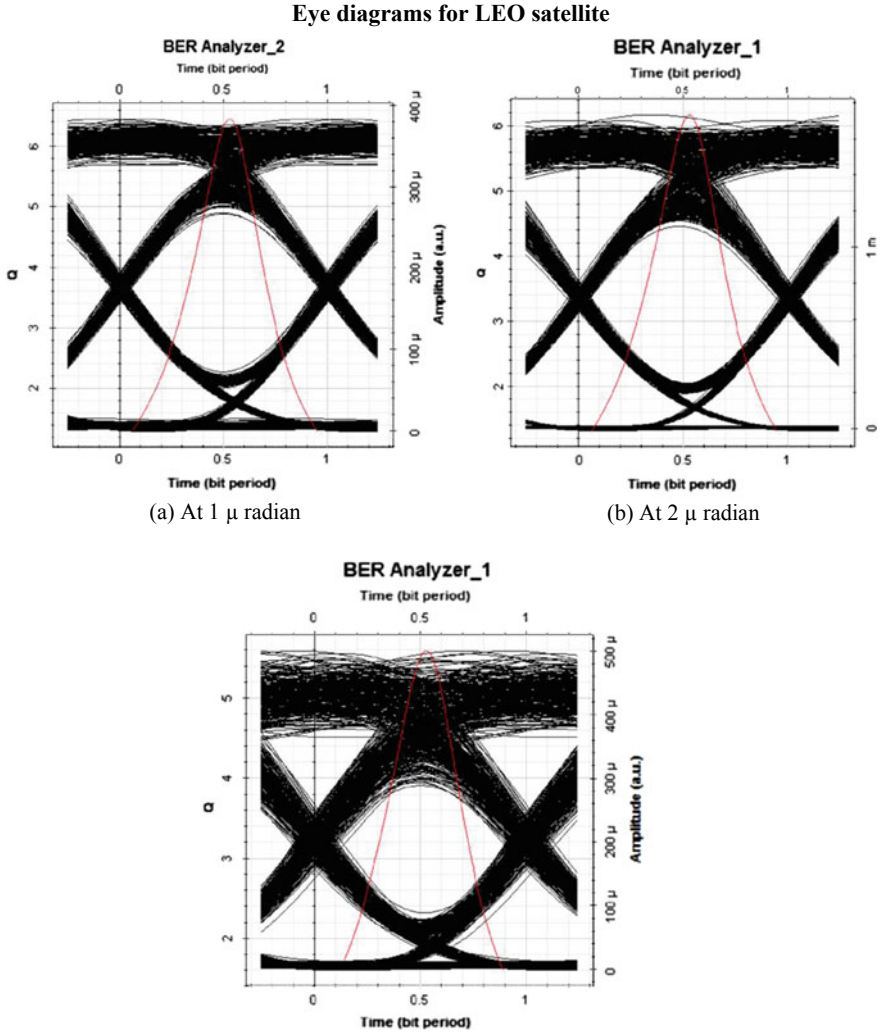

(a) At 1 μ radian

(b) At 2 μ radian

(c) At 3 μ radian

Fig. 3 BER and Q-factor of the proposed system at pointing error of 1, 2 and 3 μ radian for GEO satellite

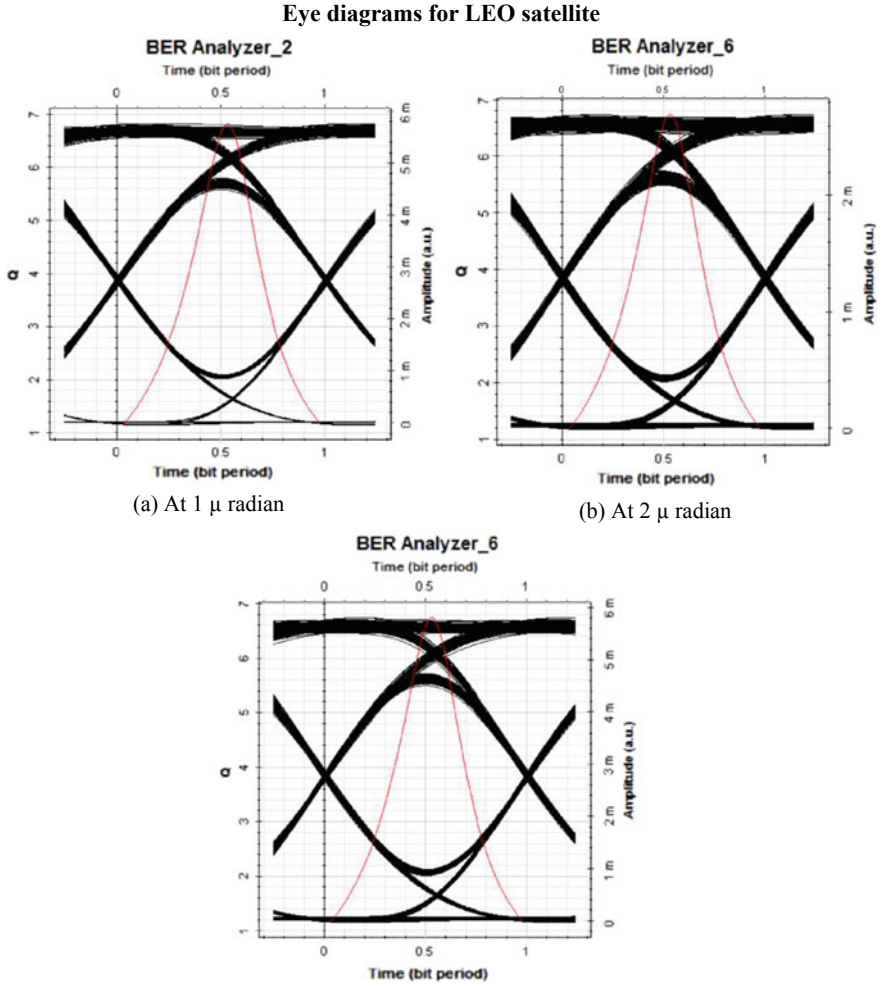

(a) At 1 μ radian

(b) At 2 μ radian

(c) At 3 μ radian

Fig. 4 BER and Q-factor of the proposed system at pointing error of 1, 2, and 3 μ radian for MEO satellite

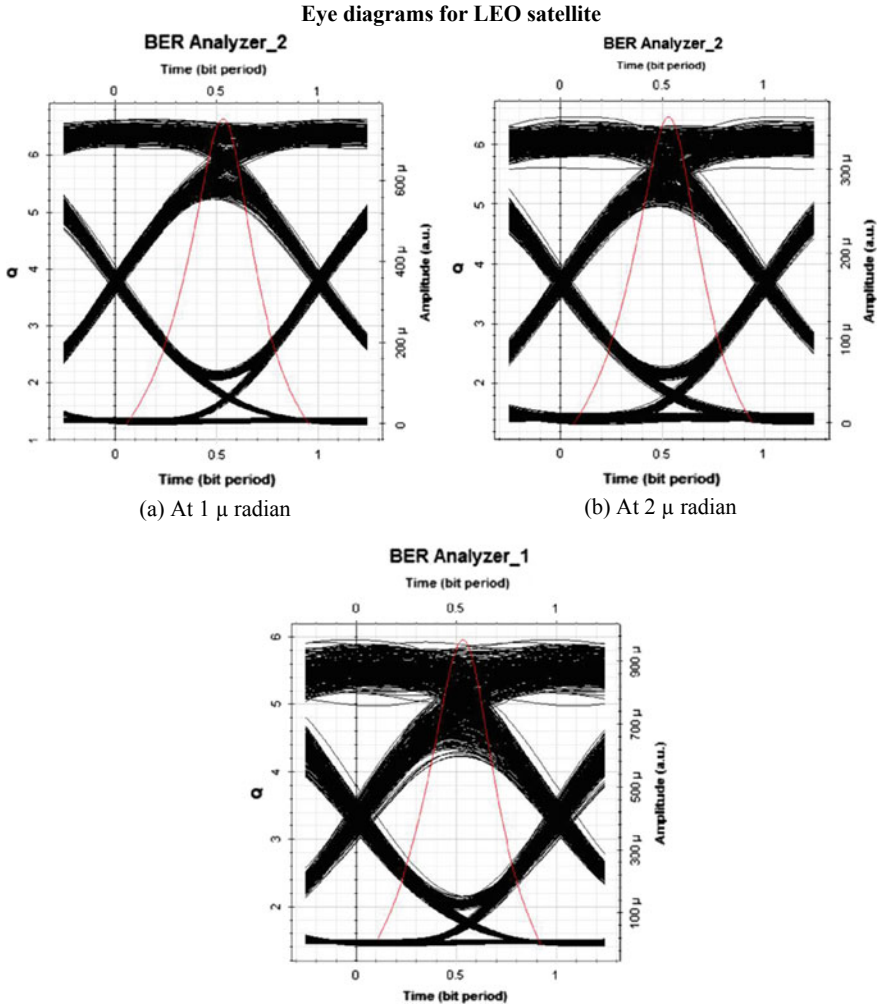

(a) At 1 μ radian

(b) At 2 μ radian

(c) At 3 μ radian

Fig. 5 BER and Q-factor of the proposed system at pointing error of 1, 2, and 3 μ radian for LEO satellite

Table 2 Results in Q-factor values and BER for GEO, MEO and LEO satellites at pointing er,rors of 1, 2, and 3 μ radian

Pointing error (μ radian)	GEO		MEO		LEO	
	Q-factor	BER	Q-factor	BER	Q-factor	BER
1	6.45111	$5.49516e^{-011}$	6.82509	$4.37877e^{-012}$	6.6389	$1.56778e^{-011}$
2	6.17083	$3.26474e^{-010}$	6.73745	$8.01465e^{-012}$	6.45946	$5.19775e^{-011}$
3	5.58586	$1.09351e^{-008}$	6.74164	$7.80457e^{-012}$	5.95735	$1.22407e^{-009}$

References

1. Kaur H, Kaur H (2017) Enhanced performance analysis of polarization interleaved advanced modulation scheme based 128 User Is-OWC DWDM system. Int J Adv Res Comput Sci 8(5)
2. Chaudhary S, Sharma A, Neetu (2015) 6 × 20 Gbps long reach WDM-PI based high altitude platform inter-satellite communication system article. Int J Comput Appl
3. Chaudhary S, Sharma S, Parveen (2014) Role of turbulences in WDM-polarization interleaving scheme based inter-satellite communication system. Int J Comput Appl
4. Kumari G (2016) Performance optimization for high speed WDM based inter-satellite optical wireless communication. In: SCOPES
5. Sharma A (2017) Study of various challenges in Is-OWC. https://doi.org/10.22214/ijraset.2017.8112
6. Uysal M, Nouri H (2014) Optical wireless communications—an emerging technology. In: ICTON 2014
7. Meenakshi (2017) Ultra high capacity wavelength division multiplexed optical wireless communication system. IJCRT 5(3). ISSN: 2320-2882
8. Sharma A, Kumar V, Gupta V (2018) A review on inter-satellite optical wireless communication. Int J Comput Appl (0975 – 8887) 180(12)
9. Sharma A, Kapoor R (2017) Study of various challenges in IS-OWC—a review. Int J Res Appl Sci Eng Technol (IJRASET)

M-Way Balanced Tree Data Aggregation Approach for Clustered Wireless Sensor Networks

Ikkurthi Bhanu Prasad, Biswajit Rout, Vipin Pal and Yogita

Abstract Energy efficiency has been the prime design issue for wireless sensor networks as sensor nodes are embedded with limited energy. Clustering algorithms are considered as energy-efficient approach for wireless sensor network. Cluster head nodes have been overburdened in most of clustering algorithms that result in load unbalanced network. Work of this paper presents a layout of work in progress of proposed m-way balanced tree data aggregation approach for clustered wireless sensor networks that aggregates the data at each level of m-way balanced tree instead of performed by the cluster head solely and also reduces the wake-up time period of cluster head.

Keywords Clustering · m-way balanced tree · Data aggregation · Wireless sensor networks

1 Introduction

Wireless sensor network [2, 6], an infrastructure-less network, consists of a large number of sensor nodes deployed over a region of interest. The sensor nodes carry limited battery power, limited memory and slow processing speed. Sensor nodes sense the defined phenomenon and with the help of radio transceivers transmit the data to the base station (BS) for further processing. The base station or sink acts as an interface between users and network. All the nodes work together in-collaboration

I. Bhanu Prasad · B. Rout · V. Pal (✉) · Yogita
Department of Computer Science and Engineering, National Institute of Technology Meghalaya, Shillong, India
e-mail: vipinrwr@gmail.com

I. Bhanu Prasad
e-mail: t17cs008@nitm.ac.in

B. Rout
e-mail: t17cs003@nitm.ac.in

Yogita
e-mail: thakranyogita@gmail.com

V. Janyani et al. (eds.), *Optical and Wireless Technologies*, Lecture Notes in Electrical Engineering 648, https://doi.org/10.1007/978-981-15-2926-9_66

to accomplish the defined task, which a single node cannot be able to do. The battery power constraint sensor nodes work in an inaccessible region of interest where recharge or replacement of battery unit is quite difficult as well as costly. In the deployed region, nodes exhaust battery power in every point of processing, so energy-efficient processing by sensor nodes is necessarily needed to be addressed [13].

Clustering approach [1, 13] has been considered as energy-efficient approach for wireless sensor networks in which all nodes are grouped in independent clusters with one representative of each cluster termed as cluster head. Clustering algorithm provides the characteristics of energy efficiency, fault tolerance, scalability to the wireless sensor network. The much-needed energy efficiency has been achieved by aggregating the data of member nodes at cluster head and by avoiding the long distance communication, only cluster head node is communicated over long distance as the representative of cluster, TDMA schedule avoids the collision, idle listening and others related issues of MAC [3]. Literature [1, 3] suggests that clustering algorithm attains the load balancing in the network, but most of clustering algorithms assign an array of work to the cluster head to perform consequently, cluster head consumes much higher energy as compared to member nodes. The resulted load unbalancing deteriorates the performance of clustering algorithm.

Work of this paper proposed an m-way balanced tree data aggregation and communication scenario for intra-cluster communication in clustered WSN in which member nodes of a cluster are organized in an m-way balanced tree with cluster head node as root of the tree. In the proposed approach, node sends data to parent node, and data of all child node has been aggregated by parent node. Further, cluster heads will be active for less number of time slots in data communication phase of clustering algorithm. Consequently, the network is well load balanced. Rest of the paper is organized as follows: Section 2 demonstrates the proposed approach with working example. Section 3 shows cluster structure in proposed approach. Section 4 concludes the work of paper.

2 Proposed Solution

2.1 Problem Statement

Clustering algorithm provides the required cost-effective energy consumption of sensor nodes with add-on features of scalability and fault tolerance [1]. Role of cluster head is rotated among all the nodes to distribute the load and for well load-balanced network in clustering protocols [5, 8, 12]. The cluster head nodes are active for the entire clustering round, as an representative of cluster, only cluster head nodes communicate to long distance placed base station, and hence, the cluster head nodes consume much higher amount of energy as compared to member nodes [11]. Member nodes within a cluster disseminate different amount of energy because of their distance to cluster heads. As a result, the load balancing of network gets affected due to uneven energy consumption between cluster head nodes and member nodes. To solve the problem, [7, 10] provides the solution by constructing tree with cluster head

as root and member nodes as the successor of root for intra-cluster communication. Member nodes rather sending the data to cluster head directly send the data to parent, parent sends the aggregated data to respective parent, and eventually, data has been received at the cluster head node. This multi-hop communication of data within the cluster reduces the energy consumption of cluster head node as compared to direct intra-cluster communication, but the tree formation is not structured, and the nodes in between the root and leaf do not have much data to aggregate. Therefore, there is a need of clustering solutions that can have structured tree formation for intra-cluster communication and to have better data aggregation for in between nodes to achieve a well load-balanced network.

2.2 Proposed M-Way Tree Data Aggregation Approach

In this paper, a distributed clustering approach has been proposed to do well load balancing in the network. For the network model, the proposed approach considers that (i) there are N number of sensor nodes are deployed over the square region and there is only one base station located outside the region of deployment, (ii) each sensor node knows respective location in the region by means of positioning algorithm [9] as the part of network set-up, (iii) nodes are stationary after deployment, and (iv) each node has been assigned unique local ID for identification.

The operation of proposed approach has been shown in Fig. 1. Operation of proposed approach has been carried in rounds and each round has two phases (i) Set-up phase and (ii) Steady phase. In set-up phase, cluster formation is performed locally by the nodes, and the data transmission from member nodes to base station has been performed in steady phase with in-network data collection and aggregation by cluster head node. Set-up phase starts with the selection of cluster heads by means of probabilistic approach [8]. The selected cluster head nodes broadcast the status message to the network, and the nodes select the nearest cluster head node based on received signal strength (RSS) of broadcast message and replies to the preferred cluster head node with location information. Then, the proposed approach performs the m-way balanced tree set-up operation for intra-cluster communication. Each cluster head node knows about the location of all member nodes of respective cluster. Cluster head node constructs an m-way balanced tree (with predefined value of m) with self as root of the tree and member nodes as descendant. The characteristic of m-way balanced tree makes the cluster well load balanced as the distance of data prorogation is almost similar for each branch of tree. After the m-way tree set-up operation, cluster

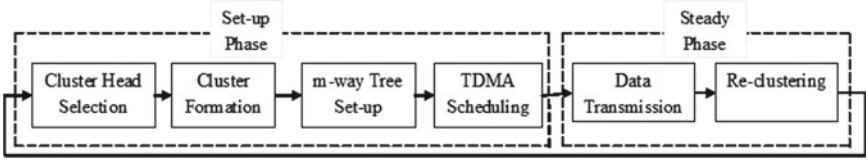

Fig. 1 Operation of proposed approach

head node constitutes the TDMA schedule for respective cluster and broadcasts the TDMA schedule to the all member nodes.

In the steady phase, data of the cluster has been collected at cluster head node. The parent node gathers data from the child nodes and aggregates the collected data with own data and forwards the locally aggregated data to respective parents. The nodes wake-up to send the data to parent with TDMA schedule, otherwise remains in sleep state. The proposed approach allows parents node to aggregate more data as compared to other tree-based approach and hence reduced the work of data aggregation over the cluster head node. The data has been eventually received by cluster head node. Cluster head node sends the data to base station. After completion of current round, re-clustering is performed again for next round.

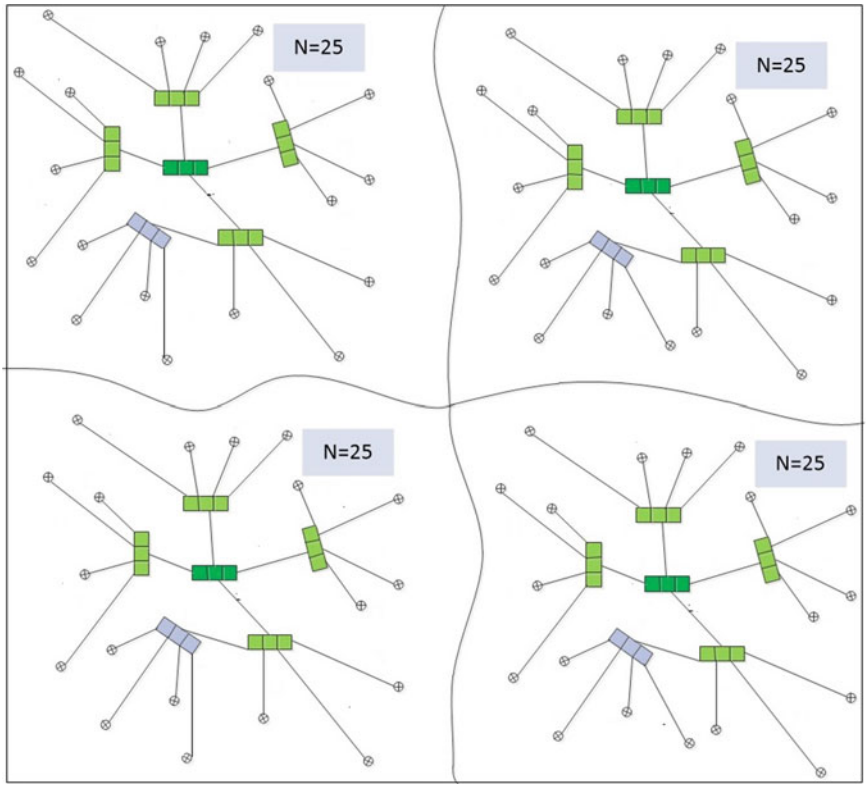

Fig. 2 Equal size clusters

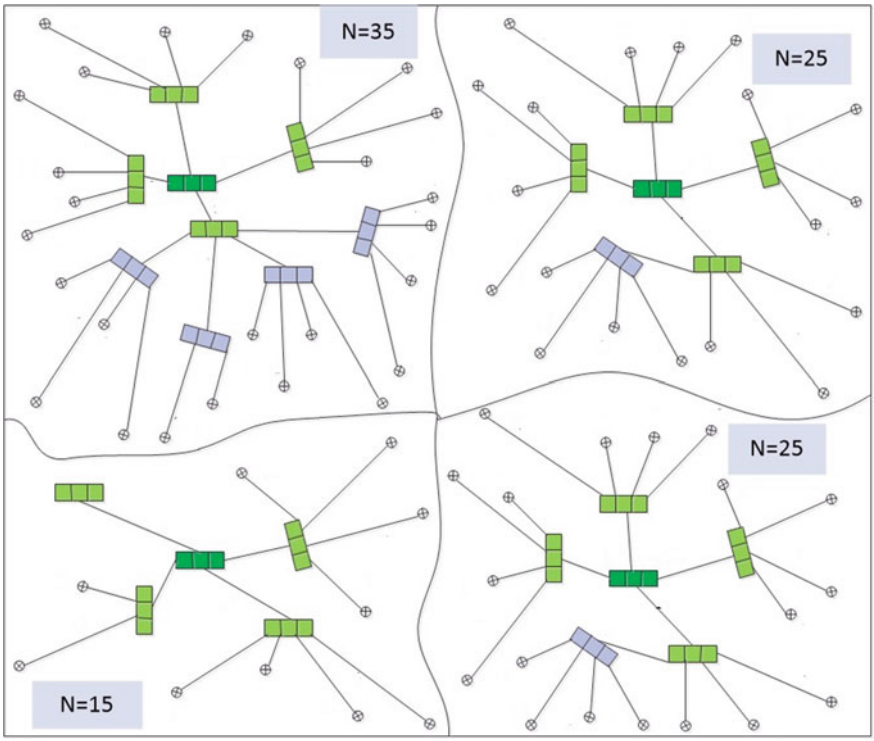

Fig. 3 Unequal size clusters

3 Cluster Structure in Proposed Approach

The proposed approach constructs m-way balanced tree for intra-cluster communication. A network of 100 nodes is considered for cluster structure demonstration. Literature suggests that clustering approach can be of either equal size or unequal cluster size [4]. The cluster structure of proposed approach is shown for both equal and unequal cluster size. Figure 2 shows the cluster formation for equal size clusters, while Fig. 3 shows the cluster formation for unequal cluster sizes. Value of m is 4 (that is also the degree of tree) for the cluster structure. Different levels are demonstrated in different colors.

The levels of tree depend on the value of m. Table 1 shows the level of tree with number of nodes at the level corresponding $m = 4$ and $m = 5$ for intra-cluster communication. As can be analyzed from Table 1 and cluster structure shown in Figs. 2 and 3 that cluster head receive data from only immediate child and aggregate the data and then send the aggregated data to the base station.

Table 1 Number of nodes at different levels of tree for proposed approach

Cluster size	$m = 4$	$m = 5$
5	Level 0 =1	Level 0 =1
	Level 1 = 4	Level 1 = 4
15	Level 0 =1	Level 0 =1
	Level 1 = 4	Level 1 = 5
	Level 2 = 10	Level 2 = 9
20	Level 0 =1	Level 0 =1
	Level 1 = 4	Level 1 = 5
	Level 2 = 15	Level 2 = 14
25	Level 0 =1	Level 0 =1
	Level 1 = 4	Level 1 = 5
	Level 2 = 16	Level 2 = 19
	Level 3 = 4	
30	Level 0 =1	Level 0 =1
	Level 1 = 4	Level 1 = 5
	Level 2 = 16	Level 2 = 24
	Level 3 = 9	
35	Level 0 =1	Level 0 =1
	Level 1 = 4	Level 1 = 5
	Level 2 = 16	Level 2 = 25
	Level 3 = 14	Level 3 = 4
40	Level 0 =1	Level 0 =1
	Level 1 = 4	Level 1 = 5
	Level 2 = 16	Level 2 = 25
	Level 3 = 19	Level 3 = 9
100	Level 0 =1	Level 0 =1
	Level 1 = 4	Level 1 = 5
	Level 2 = 16	Level 2 = 25
	Level 3 = 64	Level 3 = 69
	Level 4 = 15	

4 Conclusion and Future Work

The work of this paper presented an initial framework of m-way balanced tree data aggregation clustering for wireless sensor networks that reduced the overhead of cluster head. In future, we will analyze the performance of the proposed approach over network metrics such as network lifetime and throughput. We will also analyze the effect of m on network metrics.

Acknowledgements The work of the paper has been supported by National Mission On Himalayan Studies (NMHS) by the Ministry of Environment, Forest & Climate Change (MoEF&CC) sanc-

tioned project titled "Cloud-assisted Data Analytics based Real-Time Monitoring and Detection of Water Leakage in Transmission Pipelines using Wireless Sensor Network for Hilly Region" (Ref. No.: GBPNI/NMHS-2017-18/SG21).

References

1. Afsar MM, Tayarani-N MH (2014) Clustering in sensor networks: a literature survey. J Netw Comput Appl 46:198–226
2. Akyildiz I, Su W, Sankarasubramaniam Y, Cayirci E (2002) Wireless sensor networks: a survey. Comput Netw 38(4):393–422
3. Anastasi G, Conti M, Di Francesco M, Passarella A (2009) Energy conservation in wireless sensor networks: a survey. Ad Hoc Netw 7(3):537–568
4. Arjunan S, Pothula S (2017) A survey on unequal clustering protocols in wireless sensor networks. J King Saud Univ Comput Inf Sci
5. Arora VK, Sharma V, Sachdeva M (2016) A survey on leach and othes routing protocols in wireless sensor network. Optik Int J Light Electron Opt 127(16):6590–6600
6. Dargie W, Poellabauer C (2018) Fundamentals of wireless sensor networks: theory and practice. Wiley Publishing (Reprint)
7. Han Z, Wu J, Zhang J, Liu L, Tian K (2014) A general self-organized tree-based energy-balance routing protocol for wireless sensor network. IEEE Trans Nucl Sci 61(2):732–740
8. Heinzelman W, Chandrakasan A, Balakrishnan H (2002) An application-specific protocol architecture for wireless microsensor networks. IEEE Trans Wirel Commun 1(4):660–670
9. Karl H, Willig A (2007) Protocols and architectures for wireless sensor networks. Wiley
10. Kim KT, Lyu CH, Moon SS, Youn HY (2010) Tree-based clustering(tbc) for energy efficient wireless sensor networks. In: 2010 IEEE 24th international conference on advanced information networking and applications workshops, pp 680–685
11. Pal V, Singh G, Yadav RP (2015) Balanced cluster size solution to extend lifetime of wireless sensor networks. IEEE Internet Things J 2(5):399–401
12. Singh SK, Kumar P, Singh JP (2017) A survey on successors of leach protocol. IEEE Access 5:4298–4328
13. Yan J, Zhou M, Ding Z (2016) Recent advances in energy-efficient routing protocols for wireless sensor networks: a review. IEEE Access 4:5673–5686

Modified Gbest-Guided ABC Algorithm Approach Applied to Various Nonlinear Problems

Himani and S. K. Agrawal

Abstract A mathematical process which is used to search the maxima or minima of an objective function in the valid search space is known as the optimization. A wide range of nature-inspired optimization tactics such as spider monkey optimization, ant colony optimization and particle swarm optimization are used to find the most desirable solution and one of them is artificial bee colony (ABC) algorithm which is a population-based metaheuristic optimization approach. In the proposed work, a modification in gbest-guided ABC (GABC) algorithm is introduced by integrating some properties of Gaussian ABC algorithm. The aim of this paper is to overcome certain impediments of original ABC algorithm such as low speed of convergence, weak exploitation capability and solutions easily trapped by local optima. Experimental results by proposed algorithm are tested on several benchmark functions that show the modified GABC can improve upon ABC and GABC algorithms in most of the experiments.

Keywords Particle swarm optimization · Genetic algorithm · Artificial bee colony algorithm · Gaussian ABC · Gbest-guided ABC

1 Introduction

Swarm intelligence deals with natural and artificial structures composed of many individual groups that counterpart using decentralized control and self-organization. In particular, it focuses on the collective or cumulative behaviors that result from the local communication of the individuals with each other and with their environment. Some of the obvious swarm systems are clumping, flocking and schooling of ants, birds and fishes, respectively, and also the nest structuring behavior of wasps and termites [1–3]. ABC algorithm was discovered by Karaboga in 2005 which is the most popular research field based on stochastic population intelligence that resembles the collaborative foraging performance of bee colony. After its initiation, ABC algorithm has acknowledged eminent concern from researchers surveying in various fields and

Himani (✉) · S. K. Agrawal
Department of Electronics and Communication Engineering, Government Women Engineering College, Ajmer, India

V. Janyani et al. (eds.), *Optical and Wireless Technologies*, Lecture Notes in Electrical Engineering 648, https://doi.org/10.1007/978-981-15-2926-9_67

has been successfully applied to solve several practical problems due to its simplicity, ease of execution, adequacy and effectiveness. Relative studies have indicated that ABC algorithm is a competitive optimization approach compared to other algorithms such as GA and PSO [3, 4].

Analogous to other population-based swarm intelligence algorithms such as PSO and GA, the attainment of ABC algorithm is resolved by its exploration and exploitation capabilities. The exploitation process makes the use of prevailing information, but the exploration corresponds to an autonomous search operation. The exploration mechanism of standard ABC algorithm is suitable for many optimization problems, but the exploitation operation of this algorithm is not adequate for some complex optimization problems, many times the solution trapped into local optima and the speed of convergence may be affected. To settle this dispute, a number of differing ABC algorithms have been recommended by researchers [5]. Zhu and Kwong introduced an advanced ABC algorithm named gbest-guided ABC algorithm, consolidating the knowledge of global best solution into the solution search equation to elevate the exploitation. In this paper, a novel GABC algorithm is presented by adding some attributes such as the inertial weight of the Gaussian ABC algorithm to the existing GABC iteration equation to balance global and local searching techniques. The modified-GABC algorithm is tested on various benchmark functions and the experimental results show that the proposed mechanism can improve upon the existing GABC algorithm [4–6].

The rest of this paper is organized as follows. Section 2 describes ABC algorithm briefly. Both GABC and modified-GABC algorithms are presented in Sect. 3. Section 4 presents experimental results obtained and discussion. Finally, the conclusion is drawn in Sect. 5.

2 Artificial Bee Colony Algorithm

2.1 Fundamental ABC Algorithm

The ABC scheme is introduced by D. Karaboga which is relatively a simple and fast population-based optimization algorithm which attempts on fitness estimation and hence, the population of potential solutions is likely to proceed toward the better fitness areas of the search space [1]. It searches for near optimal solutions to the complex optimization problems through instigation from nature and is arrived from collaborative, trial and error behavior of honey bees. In this method, all the members are considered to be interactive, active, diligent and with very small inherent intelligence [6]. Exploration and exploitation are two significant concerns for designing a robust search procedure. The exploration means the ability of analyzing various unknown areas in solution search space to obtain the global optimum, while the exploitation refers to the ability of estimating improved optimum using the information of previous valuable solutions [7, 8].

Employed, onlookers and scouts are the three classes of bees, foraging for food sources, and this classification is based on the different food selection processes. Employed bees are answerable for searching nectar around food sources and also for circulating the knowledge of these food sources by performing waggle dance. Onlookers are bees at the beehive waiting to make a preference on the selection of the food source. Employed bees go to the food source inspected earlier and bees those are conducting a random search around their nest are scouts or in other words an employed bee whose food source has been depleted by other bees will turn into a scout. The scout bee searches at random to catch a new food source. Thus, employed bees and onlooker bees will control the exploitation process, and scout bees will do the same for exploration process. For each of the food source, single employed bee is there in essence number of food sources and employed bees are equal [8–11].

ABC algorithm needs chain of four phases: initialization stage, employed bees stage, onlooker bees stage and scout bees stage, each stage is explained below:

Initialization of population—The ABC algorithm randomly generates initial population M (size of solution population) where each solution $s_i (i = 1, 2, 3, \ldots, M)$ is a N-dimensional vector, where N is the number of optimization parameters.

Employed bees phase—After initialization, the population of the positions (solutions) is imposed to reiterative cycles. At each repeated cycle, employed and onlooker bees generate further solutions from the old one using (1).

$$u_{ij} = s_{ij} + \delta_{ij}(s_{ij} - s_{kj}) \tag{1}$$

where $k \neq i, k \in (1, 2 \ldots, M)$ and $j \in (1, 2 \ldots, N)$ are indexes chosen at random. s_{ij} (or u_{ij}) indicates the jth element of s_i (or u_i), and δ_{ij} is a uniform random number in $[-1, 1]$.

Onlooker bees phase—Sharing of information is a significant stage of the ABC algorithm, from which the collective intelligence arises. This is accomplished by prompting the behavior of onlookers which will choose their food source corresponding to following probability:

$$P_i = \frac{F_i}{\sum_{i=1}^{M} F_i} \tag{2}$$

where F_i is the fitness value of the ith solution. After receiving the information, onlooker bees analyze the fitness of the candidate source by improving the location in her memory. Now, greedy selection process is applied according to which if the fitness of the food source is higher than that of the preceding one the bee acquires the new position and neglects the past one.

Scout bees phase—For scheduled number of cycles (limit), if the position of a food source is not modified, then the food source is supposed to be dropped and scout bees phase is initiated. In this phase, the bee associated with the dumped food source becomes scout bee, and then, this scout bee generates a new nectar source at random within the given value bound using (3)

$$s_i^j = s_{\min}^j + \text{rand}[0, 1]\left(s_{\max}^j - s_{\min}^j\right) \tag{3}$$

Here, s_i denotes the abandoned solution, and $j \in (1, 2 \ldots, N)$ is a randomly produced index which denotes updated dimension. $s_{\max}^j$ and $s_{\min}^j$ are jth dimension's upper boundary and lower boundary, accordingly. Again, greedy selection process is applied, at each stage, every updated candidate solution is estimated by artificial bees, and the fitness (performance) of the new solution is compared with the fitness of the previous solution. Now, greedy selection process is applied [4, 12–14].

2.2 Pseudocode for ABC Algorithm

The pseudocode of the ABC algorithm is shown below:

Initialize the population of solutions, $s_i (i = 1, 2, 3, \ldots, M)$ using (1);
Cycle = 1;
While cycle $\leq$ MIter do (maximum number of cycles)

1. Generate new solution u_i for the employed bees using (1) and analyze them
2. Apply the greedy selection process for the employed bees
3. Do the calculation of probability values P_i for the solutions s_i using (2).
4. By making use of elected solutions s_i, establish the new solutions u_i for the onlooker bees depending on P_i and analyze them
5. Now, use the greedy selection process for the onlooker bees.
6. Replace the abandoned solution with newly generated random solution s_i using (3)
7. Memorize the best solution obtained so far
8. Cycle = Cycle + 1

End while.

3 Modified-GABC Algorithm

3.1 Gbest-Guided ABC Algorithm

As discussed in Sect. 1, even though ABC algorithm performs great in solving optimization problem, there is still a deficiency in ABC algorithm respecting its solution search equation. Equation (1) used to generate new solutions at both employed and onlooker bee stages is acceptable at exploration but insignificant at exploitation. In order to achieve prime optimization performance, there should be balance between these two abilities [2–5].

Zhu and Kwong proposed an algorithm termed as GABC algorithm to acknowledge the above problems. The algorithm assumes Eq. (4) to replace the Formula (1) in the original ABC algorithm.

$$u_{ij} = s_{ij} + \delta_{ij}\left(s_{ij} - s_{kj}\right) + \gamma_{ij}(t_j - s_{ij}) \tag{4}$$

In the above equation, the first two terms are exact to those of (1). Symbol t_j is the jth element of the global best solution, and γ_{ij} is a uniform random number in [0, L], where L is a positive constant. The constant L plays an essential role in balancing the exploration and the exploitation of the candidate's solution searching. According to their estimation, the desirable value of L is 1.5.

3.2 Gaussian ABC Algorithm

A regular distribution is used in the standard ABC to generate a candidate's food position from the previous one in memory. According to Gaussian ABC algorithm, next position is updated by following equation

$$u_{ij} = \begin{cases} t_j + \delta_{ij}\left(s_{ij} - s_{kj}\right)2T & \text{if rand}(0, 1) \le r \\ t_j + \delta_{ij}\left(s_{ij} - s_{kj}\right)mT & \text{else} \end{cases} \tag{5}$$

Here, r is a real number in the interval (0, 1) that should be trained from numerical experiments. T and m are calculated as $T = 0.5 - 0.25\left(\frac{\text{iteration}}{\text{MIter}}\right)$; $m = |l|$, where iteration represents the current iteration and MIter denotes the maximum iteration number. $|l|$ is a real number obtained by a Gaussian distribution [6].

3.3 Proposed Modified-GABC Algorithm

In order to increase the performance and to balance the exploration and exploitation process, we have proposed a modified-GABC algorithm by introducing some features of Gaussian ABC scheme. Modified GABC efficiently combines exploitative local search and explorative global search processes by adding Gaussian uniform distributions and GABC algorithm. The solution search equation that we have used to generate new solutions at employed bee and onlooker bee stages is defined as follows:

$$u_{ij} = \begin{cases} t_j + \delta_{ij}\left(s_{ij} - s_{kj}\right)2T + \gamma_{ij}\left(t_j - s_{ij}\right)2T & \text{if rand}(0, 1) \le r \\ t_j + \delta_{ij}\left(s_{ij} - s_{kj}\right)mT + \gamma_{ij}\left(t_j - s_{ij}\right)mT & \text{else} \end{cases} \tag{6}$$

where $T = 0.5 - 0.25\left(\frac{\text{iteration}}{\text{MIter}}\right)$; $r \in [0, 1]$; and all the parameters are same as explained above. Thus, exploitation capability in ABC algorithm can be increased, and more accurate optimum can be achieved with the counseling of the Gaussian distribution and global best information [3–6].

4 Simulation Results

In order to demonstrate the effectiveness and optimization performance of the three algorithms, original ABC algorithm, GABC algorithm and modified-GABC algorithm, we have selected several standard objective functions. The basic expressions of the three algorithms are given in Table 1. For comparison with the modified-GABC optimization algorithm, we have also selected four benchmark functions that have been used to analyze the performance of GABC algorithm. Comparison of optimal values for these algorithms is shown in Figs. 1 and 2.

The first standard objective function is Zakharov function which has no local minima except the local one, and global minimum is zero. Function is given by:

Table 1 Core expressions of three algorithms

Algorithm	Frame expressions
ABC algorithm	$u_{ij} = s_{ij} + \delta_{ij}(s_{ij} - s_{kj})$
GABC algorithm	$u_{ij} = s_{ij} + \delta_{ij}\left(s_{ij} - s_{kj}\right) + \gamma_{ij}(t_j - s_{ij})$
Modified-GABC algorithm (Proposed)	$u_{ij} =$ $\begin{cases} t_j + \delta_{ij}\left(s_{ij} - s_{kj}\right)2T + \gamma_{ij}\left(t_j - s_{ij}\right)2T & \text{if rand}(0, 1) \le r \\ t_j + \delta_{ij}\left(s_{ij} - s_{kj}\right)mT + \gamma_{ij}\left(t_j - s_{ij}\right)mT & \text{else} \end{cases}$

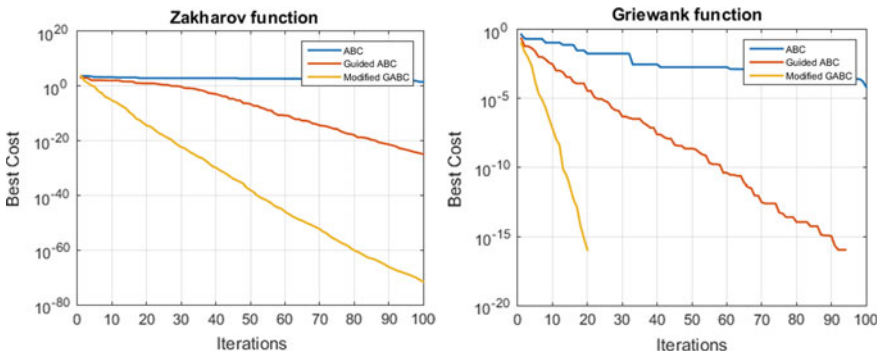

Fig. 1 Comparison of optimal values of Zakharov and Griewank function for ABC, GABC and modified-GABC algorithms

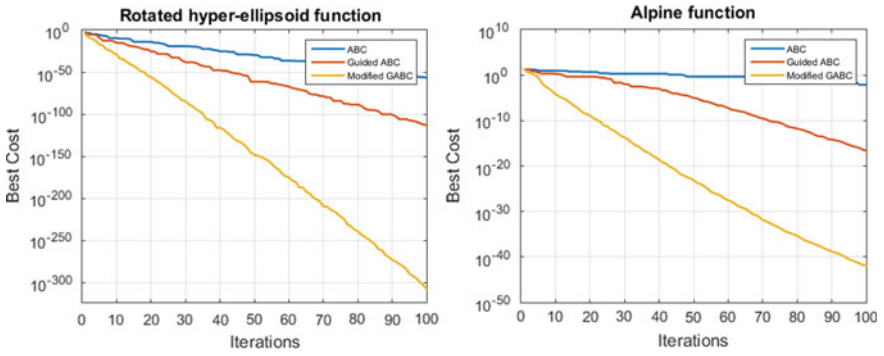

Fig. 2 Comparison of optimal values of Rotated Hyper-Ellipsoid and Alpine function for ABC, GABC and modified-GABC algorithms

$$f_1(y) = \sum_{i=1}^{D} y_i^2 + \left(\sum_{i=1}^{D} 0.5 i y_i\right)^2 + \left(\sum_{i=1}^{D} 0.5 i y_i\right)^4$$

Here, $y_i \in [-5, 10]$, for all $i = 1, 2, \ldots, D$ where D is dimension.

The second function is Griewank that has many widespread local minima, which are regularly distributed. Function is represented as follows:

$$f_2(y) = \sum_{i=1}^{D} \frac{y_i^2}{4000} - \prod_{i=1}^{D} \cos\left(\frac{y_i}{\sqrt{i}}\right) + 1$$

Here, $y_i \in [-600, 600]$, for all $i = 1, 2, \ldots, D$. For this function, global minimum is zero.

The third objective function is Rotated Hyper-Ellipsoid that is continuous convex and unimodal, and global minimum is zero. Function is represented as follows:

$$f_3(y) = \sum_{i=1}^{D} y_i^2$$

where $y_i \in [-65.536, 65.536]$, for all $i = 1, 2, \ldots, D$.

The fourth function is Alpine, and this is a multimodal minimization problem defined as follows:

$$f_4(y) = \sum_{i=1}^{D} [|y_i \sin(y_i) - 0.1(y_i)|]$$

Here, D represents the number of dimensions and $y_i \in [-10, 10]$ for $i = 1, 2, \ldots, D$ and global optimum is zero [6–8].

Table 2 Optimization results for various benchmark functions

Algorithms	ABC	GABC	Modified GABC
Best cost for Zakharov's function	29.899	7.4285e−27	4.1983e−75
Best cost for Griewank function	0.00019776	0	0
Best cost for Rotated Hyper-Ellipsoid function	5.3774e−59	2.439e−113	1.0771e−308
Best cost for Alpine function	0.0064265	7.9313e−16	4.7311e−42

The optimization results for objective functions the Zakharov, the Griewank, the Rotated Hyper-Ellipsoid and the Alpine are optimized by the ABC algorithm, the GABC algorithm and the modified-GABC algorithm which are given in Table 2. The optimization experiments have been run 100 times independently as shown in Figs. 1 and 2. In the comparison results, the D represents the dimension of the optimized problem, and best cost represents the best solution.

5 Conclusion

This paper first analyzes the pre-eminent ABC algorithm and addresses their known complications of consistency in solution and of primitive phenomenon. An extended optimization algorithm, modified GABC, has been proposed and narrated with the goal of advancing its performance through a better adjustment between exploration and exploitation of the search space. As correlated to its counterparts, the proposed algorithm can generate better optimal solutions which is the culmination point of this algorithm. The comparison results of the ABC algorithm, the GABC algorithm and the modified-GABC algorithm demonstrated that the modified-GABC algorithm could get better performance and has the benefit to be used for solving more complex optimization problems of more complex function.

References

1. Zhang Y, Zeng P, Wang Y, Zhu B, Kuang F (2012) Linear weighted gbest-guided artificial bee colony algorithm. In: Fifth international symposium on computational intelligence and design, IEEE Computer Society, pp 155–159; Clerk Maxwell J (1892) A treatise on electricity and magnetism, 3rd edn, vol 2. Oxford, Clarendon, pp 68–73
2. Tang KS, Man KF, Kwong S, He Q (1996) Genetic algorithms and their applications. IEEE Signal Process Mag 13:22–37
3. Kennedy J, Eberhart R (1995) Particle swarm optimization. In: Proceedings of IEEE international conference on neural networks, vol 4, pp 1942–1948
4. Huo J, Meng F (2016) An improved gbest-guided artificial bee colony algorithm based on dynamic regulatory factor. In: 8th International conference on advanced computational intelligence, pp 265–269

5. Kumar R (2014) Directed bee colony optimization algorithm. Swarm Evol Comput 17:60–73
6. dos Santos Coelho L, Alotto P (2011) Gaussian artificial bee colony algorithm approach applied to Loney's solenoid benchmark problem. IEEE Trans Magn 47:1326–1329
7. Karaboga D (2005) An idea based on honey bee swarm for numerical optimization. Technical Report-TR06, Kayseri, Turkey Erciyes University
8. Karaboga D, Akay B (2009) A comparative study of artificial bee colony algorithm. Appl Math Comput 214(1):108–132
9. Karaboga D, Gorkemli B, Ozturk C, Karaboga N (2012) A comprehensive survey: artificial bee colony (ABC) algorithm and applications. Artif Intell Rev. https://doi.org/10.1007/s10462-012-9328-0
10. Karaboga D, Ozturk C (2009) Neural networks training by artificial bee colony algorithm on pattern classification. Neural Netw World 19(3):279–292
11. Cobanli S, Ozturk A, Guvenc U, Tosun S (2010) Active power loss minimization in electric power systems through artificial bee colony algorithm. Int Rev Electr Eng-IREE 5(5, Part b):2217–2223
12. Sun L, Chen T, Zhang Q (2018) An artificial bee colony algorithm with random location updating. Hindawi, Scientific Programming. https://doi.org/10.1155/2018/2767546
13. Zhu G, Kwong S (2010) Gbest-guided artificial bee colony algorithm for numerical function optimization. Appl Math Comput, pp 3166–3173
14. Hoa SL, Yang S (2009) An artificial bee colony algorithm for inverse problems. Int J Appl Electromagn Mech 31:181–192
15. Panniem Amnat, Puphasuk Pikul (2018) A modified artificial bee colony algorithm with firefly algorithm strategy for continous optimization problems. J Appl Math. https://doi.org/10.1155/2018/1237823
16. Banharnsakun A, Achalakul T, Sirinaovakul B (2011) The best-so-far selection in Artificial Bee Colony algorithm. Appl Soft Comput 11:2888–2901
17. Agrawal SK, Sahu OP (2015) Artificial bee colony algorithm to design two-channel qaudrature mirror filter banks. Swarm Evol Comput, pp 24–31

An UWB Antenna with Dual Notched Band Characteristics at WLAN Band and X-Band Application

Disha Singh, B. K. Mishra and Sanjeev Yadav

Abstract A novel designed compact SRR slotted ultra-wideband antenna showing dual band-notched characteristics is designed and simulated. The antenna consists of an inverted rectangular split ring resonator slot on the radiation patch and inverted U-shaped slot etched on the 50 Ω microstrip line. By etching two slots on the radiation patch and microstrip fed line, two band notches are achieved in the WLAN band and X-band. The proposed antenna is a simple compact size of 21 × 30 mm^2 and operates from 3.89 to 11.58 GHz.

Keywords Ultra-wideband (UWB) · Slot antennas · Dual band-notched

1 Introduction

Ultra-wideband (UWB) utilizes the radio spectrum from 3.1 to 10.6 GHz. This technology provides high data rate and short-range wireless communication, and this technology is allocated by the Federal Communication Commission (FCC) in the year of 2002 [1]. UWB has the inherent features like compact size, high data transmission within short-range, wider bandwidth, easy hardware configuration and many more which makes viable for short distance communication [2, 3]. The interference is occurred due to the overlapping of many narrow bands in UWB band. These narrow band systems are WiMAX band (3.3–3.6 GHz), IEEE 802.11a wireless local area network (WLAN) in the frequency band of 5.15–5.35 GHz and 5.725–5.825 GHz, 5.45–5.725 GHz band and many other unlicensed bands. To overcome the electromagnetic interference between the bands, several approaches have been introduced such as different size and shapes, notches, slots in the patch and ground, and different type of components is used with simple planar structure to provide the optimum solutions [3, 4]. Therefore, UWB antennas with dual band-notched characteristics should not operate in desired frequency bands to discard interference.

D. Singh · B. K. Mishra
Thakur College of Engineering and Technology, Mumbai, India

S. Yadav (✉)
Government Women Engineering College, Ajmer, India

V. Janyani et al. (eds.), *Optical and Wireless Technologies*, Lecture Notes in Electrical Engineering 648, https://doi.org/10.1007/978-981-15-2926-9_68

Several UWB antenna with notched band characteristic has been reported recently. Monopole printed antenna by inserting the slots on the patch or on the ground are used to achieve a band-notched characteristic, plane such as inserting U-shaped slot, cutting a fractal slot are also used to achieve band notch in the complete band. Split ring resonators (SRRs) and complementary split ring resonator (CSRR) techniques are etched in the patch to achieve the band notches [5–11].

In this paper, an UWB antenna with dual band-notched characteristics is designed. This antenna is designed over FR4 dielectric substrate and is based on truncated square patch with rectangular split ring resonator (SRR) etched on radiation patch and by extruding an inverted U slot in microstrip line. These SRR and inverted U slot are responsible for achieving two notches, i.e. 5.5 GHz and X-Band. This antenna is simulated using simulation tool CST Microwave Studio. Designing of the proposed antenna is discussed in Sect. 2, and simulated results are discussed in Sect. 3.

2 Antenna Design and Analysis

The structure of the proposed antenna is depicted in Fig. 1. Proposed structure is designed on FR4 substrate having dielectric constant 4.4 and loss tangent 0.002 with height 1.6 mm. The radiating patch consists of a truncated rectangular patch with two SRR etched over the patch. This patch is fed by 50 Ω microstrip line having a inverted U slot in it. All the dimensions of this UWB antenna are illustrated in Fig. 1. The overall size of the compact antenna is 32 mm × 30 mm.

The proposed antenna covers the band from 3.89 GHz to 11.58 GHz with two band notches at 5.1 GHz and 8.8 GHz. The first band notch is centred at 5.1 GHz, and this band is obtained by etching SRR on the truncated patch. The length of the SRR slot is about λ/2 of the centre frequency of the band notch, which could be found out

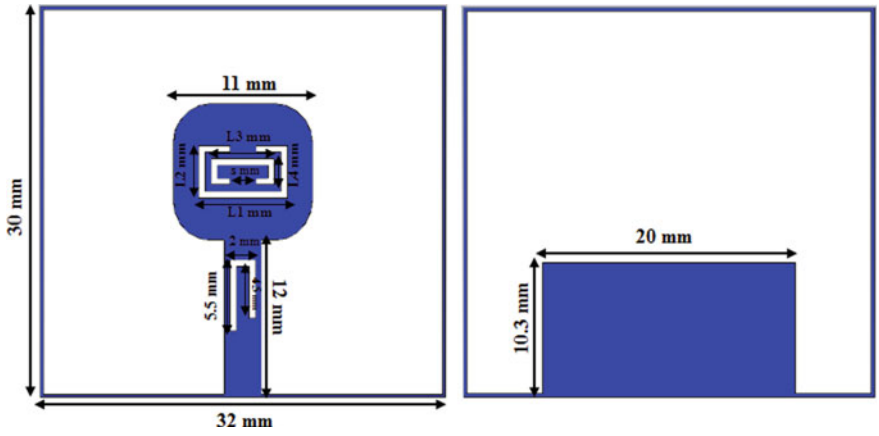

Fig. 1 Proposed antenna with all dimensions

through (1),

$$L = \frac{c}{2f\sqrt{\frac{\in_r+1}{2}}} \tag{1}$$

where L ($L = 2 * (L_1 + L_2) - s_1$) is the length of the slot where $L_1 = 6$ mm, $L_2 = 4$ mm and $s_1 = 2$ mm. Similarly, inner slot dimensions are $L_3 = 4$ mm, $L_4 = 2$ mm and $s_2 = 2$ mm.

3 Results and Discussions

The UWB antenna with dual band notch characteristics is analysed using the CST Microwave Studio simulation tool. Return loss versus frequency graph shown in Fig. 2 shows that the antenna radiates from 3.89 to 11.58 GHz with band notches at 5.1 GHz band and 8.8 GHz band. At 5.1 and 8.8 GHz frequency, return loss is −1.87 dB and −0.54 dB, respectively.

The VSWR versus frequency graph illustrated in Fig. 3 shows that VSWR value is less that 2 over the operating range except the notched frequency bands, i.e. 5.1 and 8.3 GHz of the proposed antenna.

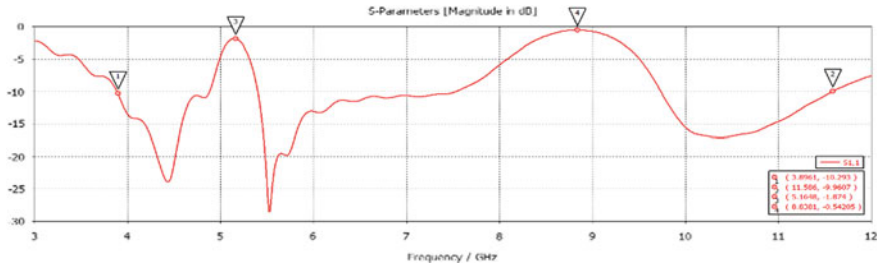

Fig. 2 Simulated return loss of proposed UWB dual notched antenna using CST Microwave Studio

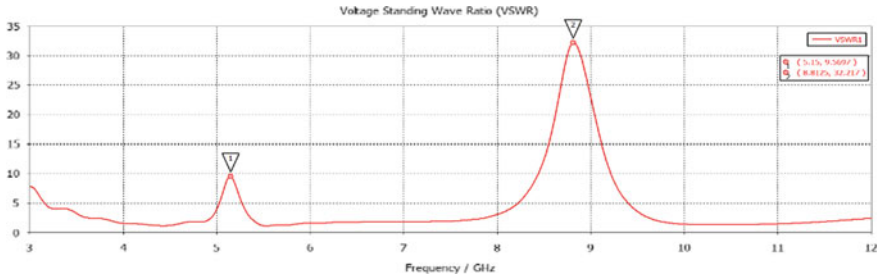

Fig. 3 Simulated VSWR of proposed dual notched UWB antenna using CST Microwave Studio

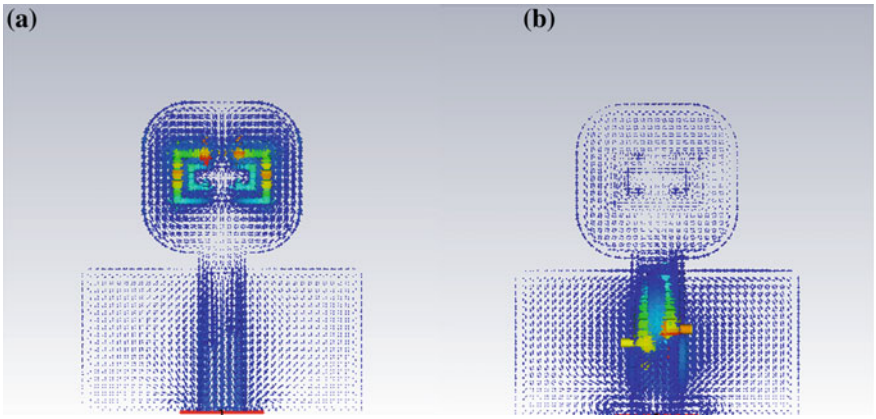

Fig. 4 Surface current at **a** 5.1 GHz, **b** 8.8 GHz

Surface current at 5.1 and 8.8 GHz is shown in Fig. 4, which represents the maximum effect of electric and magnetic field generation on the surface of the planar UWB antenna at notched frequencies.

The radiation pattern of the proposed antenna for the resonant frequencies at 4.44, 5.5 and 10.3 GHz is shown in Fig. 5. The pattern for 4.44 and 5.5 GHz is good, for 10.3 Ghz, it is little bit distorted, and it is due to the end point of the resonating band.

The gain versus frequency graph is shown in Fig. 6, which illustrates that the gain varies from 2 to 4 dBi in the complete band. This shows that the proposed antenna is better than the conventional UWB microstrip antennas as they have very less gain.

4 Conclusion

In this paper, a compact dual band-notched UWB antenna has been proposed and designed. The overall size of this compact antenna is 30 mm × 32 mm with high gain. This antenna covers the complete band from 3.89 to 11.58 GHz with band notches in WLAN (5.15–5.825 GHz) bands and X-band (8.831 GHz) to prevent interference from these two bands. This antenna can be used for indoor communications in offices buildings for short distance communication with high data rate.

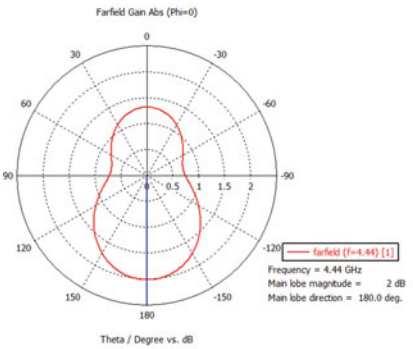

E-plane

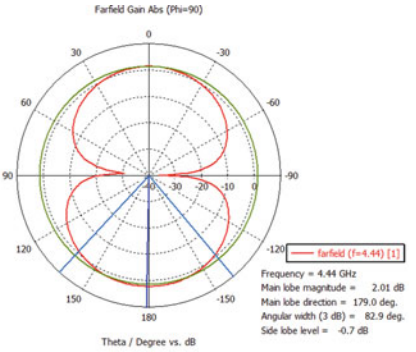

H-plane

(a) 4.44 GHz

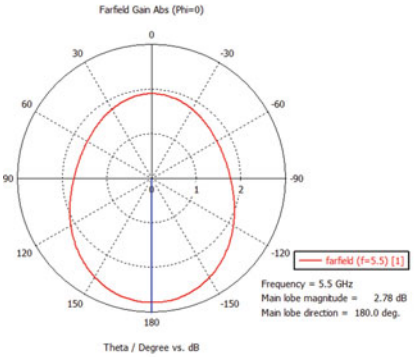

E-plane

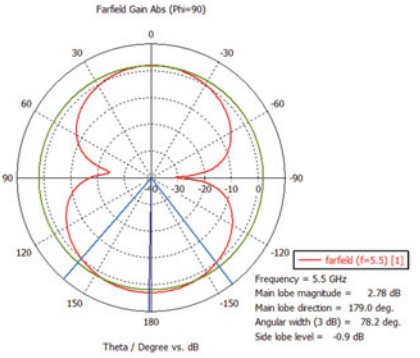

H-plane

(b) 5.5 GHz

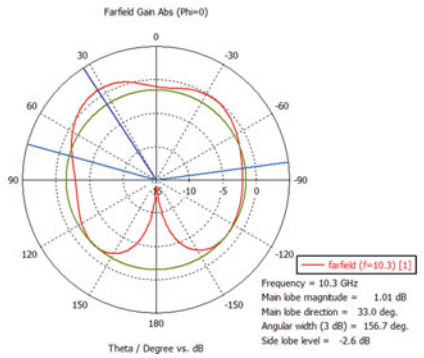

E-plane

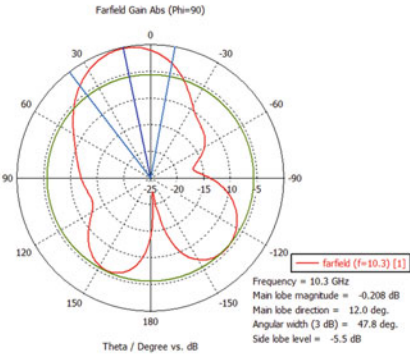

H-plane

(c) 10.3 GHz

Fig. 5 Measured radiation patterns of the dual band-notched antenna at the resonant frequencies at **a** 4.44 GHz, **b** 5.5 GHz and **c** 10.3 GHz

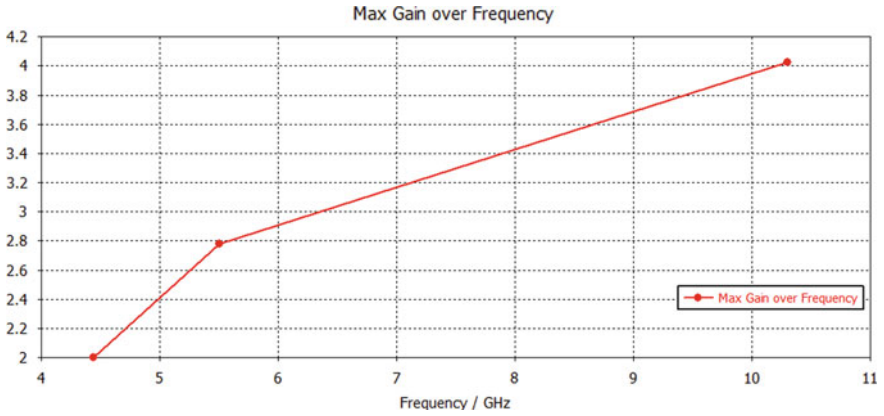

Fig. 6 Simulated gain versus frequency graph of proposed UWB antenna

References

1. First Report and Order, Revision of part 15 of the Commissions Rule Regarding Ultra-wideband Transmission systems FCC 02-48 (2002) Federal Communication Commission
2. Li Y, Liu Q, Chen Y, Li C, Mo Z, Li F (2018) A compact triple wideband-notched UWB antenna. In: 2018 International workshop on antenna technology (iWAT), Nanjing, pp 1–4
3. Suo Y, Li W, Wang H (2017) A dual-band notched ultra-wideband microstrip antenna. In: 2017 IEEE international symposium on antennas and propagation & USNC/URSI national radio science meeting, San Diego, CA, pp 1787–1788
4. Sharma MM, Yadav S, Kumar A, Bhatnagar D, Yadav RP (2010) Design of broadband multi-layered circular microstrip antenna for modern communication systems. In: 2010 Asia-Pacific microwave conference proceedings (APMC), pp 742–745, 7–10 Dec 2010
5. Chu Qing-Xin, Yang Ying-Ying (2008) A compact ultrawideband antenna with 3.4/5.5 GHz dual band-notched characteristics. IEEE Trans Antennas Propag 56(12):3637–3644
6. Jain P, Singh B, Yadav S, Verma A, Zayed M (2015) A novel compact circular slotted microstrip-fed antenna for UWB application. In: 2015 Communication, control and intelligent systems (CCIS), Mathura, pp 22–24
7. Shi-Wei Qu, Li Jia-Lin, Xue Quan (2006) A band-notched ultrawideband printed monopole antenna. IEEE Antennas Wirel Propag Lett 5(1):495–498
8. Sung Y (2012) UWB monopole antenna with two notched bands based on the folded stepped impedance resonator. IEEE Antennas Wirel Propag Lett 11:500–502
9. Lin CC, Jin P, Ziolkowski RW (2012) Single, dual and tri-band-notched ultra-wideband (UWB) antennas using capacitively loaded loop (CLL) resonators. IEEE Trans Antennas Propag 60(1):102–109
10. Ye LH, Chu QX (2009) Improved band-notched UWB slot antenna. Electron Lett 45(25):817–819
11. Mohammadi S, Nourinia J, Ghobadi C, Majidzadeh M (2011) Compact CPW-fed rotated square-shaped patch slot antenna with band-notched function for UWB applications. Electron Lett 47(24):817–819

Design and Simulink Implementation of Electrical Vehicle Charging Using Wireless Power Transfer Technology

Manish Kumar Thukral

Abstract In present era, wireless power transfer system is gaining popularity owing to its application in wide areas like wireless charging of devices such as cell phones, laptops, electric vehicles, underwater vehicles and implants. Inductive power transfer (IPT) is a type of wireless power transfer technology. It is emerging as a modern power distribution system even in harsh environment. This paper focuses on designing a IPT-based wireless power transfer charger for electric vehicle. For this, series–series (SS) compensated IPT system is designed. First, the designing formulas are derived for SS compensated IPT system. The designing procedure takes care of bifurcation phenomenon which is one of a vital issue in implementation of an efficient IPT system. Based on the designing formulas derived, electrical parameters are calculated for designing a 7.7 KW wireless power charger meeting SAEJ2954 standards which have not been met in previously published work. Finally, the proposed IPT system is implemented on Simulink platform.

Keywords Inductive power transfer · Single-phase inverter · Wireless charging · Coupled circuits · Stationary charging

1 Introduction

Wireless power transfer (WPT) is one of the emerging technologies where electric power is transferred from transmitter coil to receiver coil without any physical contact. IPT is a type of wireless power transfer technology and is based on Faraday's law of electromagnetic induction [1]. IPT technology is finding its numerous applications like wireless charging of biomedical implants, electrical vehicles, electronics gadgets [2]. Figure 1 shows basic block diagram of an IPT system.

In IPT system, a high frequency AC supply of range in Kilo Hertz is given as an input to the primary coil. The secondary coil uses a resonant tank so as to tune to the frequency of transmission. Since secondary coil uses resonance phenomenon to be tuned to transmitter frequency, therefore IPT is also known as resonant IPT. By using resonance phenomenon, the power transferred to receiving coil, and hence, the

M. K. Thukral (✉)
Electrical Engineering Department, Manipal University Jaipur, Jaipur, India

V. Janyani et al. (eds.), *Optical and Wireless Technologies*, Lecture Notes in Electrical Engineering 648, https://doi.org/10.1007/978-981-15-2926-9_69

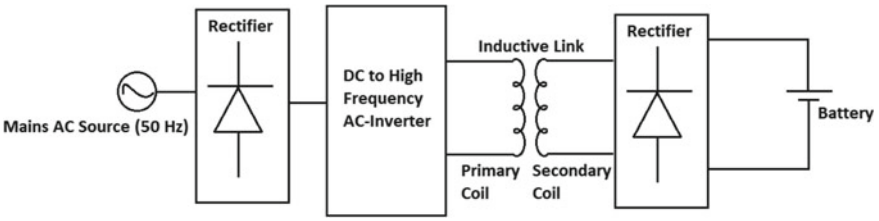

Fig. 1 Block diagram of inductive power transfer system

efficiency is increased [3]. This makes the electrical power transfer more efficient. In order to convert AC supply from mains 50 Hz to high frequency AC, the supply is first rectified, and then, power electronics-based inverter circuit is used.

The transmitter and receiver coil in IPT system have poor coupling because of presence of air gap, and hence, it is a loosely coupled transformer. Because of this reason, there is leakage flux which ultimately results in increased reactive power input requirement The increased reactive power requirement has direct effect in decreasing of power transfer capability, and not only that, the rating of devices in converter circuit also increases. This is a serious hindrance to efficient implementation of IPT technology. But with the advancement of time, researchers have developed compensation circuits so as to achieve near zero input reactive power [4]. In this technique, capacitor is added in both sides of the IPT circuit to compensate for the leakage flux and hence reduce the reactive power input [3]. This technique of compensation is named as capacitive compensation [5]. There are four basic capacitive compensation topologies that are used which are named as series–series (SS), series–parallel (SP), parallel–series (PS) and parallel–parallel (PP) compensation. The best part of the compensation technique is that with near zero input reactive power, the input impedance will be almost resistive which will result in zero phase angle between input voltage and current. This will result in transfer of more real power to the receiver coil, and hence, efficiency of IPT system increases. Also, besides having reduced converter components rating requirement, the zero voltage or zero current switching mechanism can also be implemented to further enhance the efficiency of the system. SS compensation topology is mostly because it has characteristics similar to a voltage source [6].

In the presented paper, using IPT technology, a wireless charger is 7.7 KW rating wireless charger is designed using SAEJ2954 standards which have not been considered in [7]. Society of Automotive Engineers (SAE) is an international committee which defines the standards for light-duty electrical vehicles. In the design, SS-IPT topology is used. In most of the IPT system designed, bifurcation phenomenon is avoided which is a serious issue as it degrades the performance of an IPT system. In designing, bifurcation phenomenon is taken into account. The paper is divided into various sections as follows. In Sect. 2, the electrical parameters designing formulas have been derived first. In Sect. 3, the electrical parameters calculations have been

done using these formulas. In Sect. 4, the series–series topology has been implemented on Simulink platform with the electrical parameter values as calculated in Sect. 3.

2 Derivation of Design Parameters

Figure 2 shows the circuit diagram of a basic SS-IPT system. The simplified equivalent circuit diagram of SS-IPT system is shown in Fig. 3. In this section, the formulas for electrical parameters designing used in [8] for SS-IPT topology are revisited and derived using equivalent circuit shown in Fig. 3.

By applying Kirchhoff's voltage law in equivalent circuit in primary and secondary side, one can write

$$Z_1 i_p - j\omega M i_s = V_P \tag{1}$$

$$Z_2 i_s = j\omega M i_p \tag{2}$$

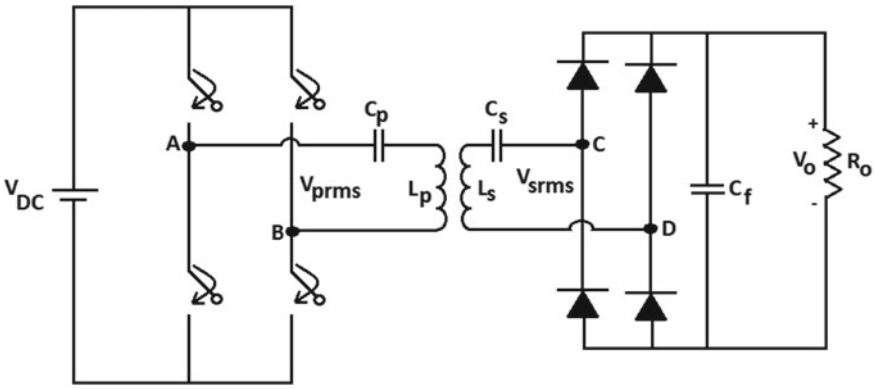

Fig. 2 Circuit diagram of SS-IPT system

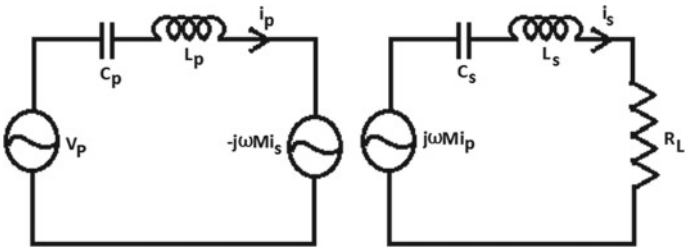

Fig. 3 Equivalent circuit diagram of SS-IPT system

where

$$Z_1 = j\omega L_p - 1/j\omega C_p$$

$$Z_2 = j\omega L_s - \frac{1}{j\omega C_s} + R_L$$

$R_L =$ Equivalent resistance viewed from terminals CD.
Multiplying Eq. (1) with Z_2 and Eq. (2) with $j\omega M$, one can write

$$Z_1 Z_2 i_p - j\omega M Z_2 i_s = V_P Z_2 \tag{3}$$

$$j\omega M Z_2 i_s + \omega^2 M^2 i_p = 0 \tag{4}$$

Adding Eq. (3) from Eq. (4), one can obtain

$$Z_1 Z_2 i_p + \omega^2 M^2 i_p = V_P Z_2 \tag{5}$$

Dividing Eq. (5) by Z_2, one can write

$$Z_1 i_p + \omega^2 M^2 i_p / Z_2 = V_P \tag{6}$$

$$Z_1 + \omega^2 M^2 / Z_2 = V_P / i_p \tag{7}$$

In Eq. (7), V_P / i_p is the impedance as viewed from primary side or it can be called as input impedance (Z_{in}) also, and $Z_r = \omega^2 M^2 / Z_2$ is the reflected impedance of secondary to primary side. Reflected impedance Z_r can be expressed as

$$Z_r = Z_r = \omega^2 M^2 / \left(j\omega L_s - \frac{1}{j\omega C_s} + R_L \right) \tag{8}$$

Reflected impedance Z_r at resonant frequency ω_o is given as

$$Z_r = \omega_0^2 M^2 / \left(j\omega_0 L_s - \frac{1}{j\omega_0 C_s} + R_L \right) \tag{9}$$

At resonant frequency, term $j\omega_0 L_s - \frac{1}{j\omega_0 C_s} = 0$, and therefore, we have, therefore, the expression of secondary compensation capacitor is given as

$$C_s = 1/L_s \omega_0^2 \tag{10}$$

$$Z_r(\omega = \omega_o) = \omega_0^2 M^2 / R_L \tag{11}$$

The input impedance at resonant frequency is given as

$$Z_{\text{in}} = j\omega_o L_p + \frac{j}{\omega_o C_p} + \omega_0^2 M^2 / R_L \tag{12}$$

Also, at resonance, the imaginary part of input impedance becomes zero, and from this fact, we get the value of the primary side compensation capacitor as

$$C_p = 1/L_p \omega_0^2 \tag{13}$$

In resonance condition, the secondary side circuit becomes pure resistive, reactance parameters cancel each other, and therefore, one can obtain

$$\left| j\omega_o M i_{\text{prms}} \right| = i_{\text{srms}} * R_L \tag{14}$$

From Eq. (14), the expression for mutual inductance can be written as

$$M = i_{\text{srms}} * \frac{R_L}{i_{\text{prms}} * \omega_o} \tag{15}$$

Now, quality factor of secondary side can be expressed as

$$Q_s = \omega_0 * L_s / R_L \tag{16}$$

From Eq. (16), one can write design expression for secondary coil inductance as

$$L_s = Q_s * R_L / \omega_0. \tag{17}$$

Also, coefficient of coupling k is expressed as

$$k = \frac{M}{\sqrt{L_p L_s}} \tag{18}$$

From Eq. (18), primary coil inductance expression can be written as

$$L_p = \frac{M^2}{k^2 * L_s} \tag{19}$$

When resonance takes place, the angle between input voltage and current is zero and the particular frequency which causes this condition is called resonant frequency or zero power angle (ZPA) frequency [8]. Doubly tuned circuits like IPT experience a phenomenon called bifurcation in which the circuit instead of being tuned at particular ZPA frequency starts operating at multiple ZPA frequencies. This happens when some of the parameter of the circuit is changed like coupling coefficient [7]. Bifurcation phenomenon is not desirable since, at bifurcation condition, the efficiency of the IPT

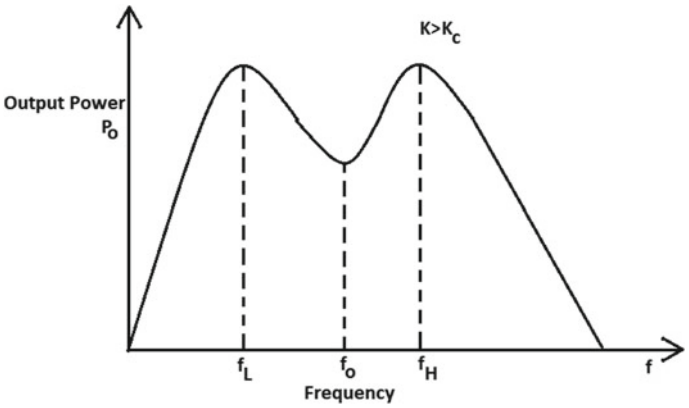

Fig. 4 Output power graph versus supply frequency

system deteriorates. This is so because at bifurcation, some output quantities like load power are not peak at ZPA frequency but at other two ZPA frequencies which appear at bifurcation condition as shown in Fig. 4.

In Fig. 4, it can be observed that as coefficient of coupling k is above a critical value, k_c then there exist three ZPA frequencies f_L, f_H and f_o. An important observation can be made from the graph that where the peak of output power was at resonant frequency f_o now at bifurcation condition the peak of output power is at two other ZPA frequencies. It can be easily understood from the graph that the ZPA frequency to which the circuit was tuned now the circuit does not have peak output power on it. So, care must be taken while designing the IPT system that the circuit does not go into bifurcation condition. In [7], the expression for critical value of coefficient of coupling k_c above which the circuit goes into bifurcation is given as

$$k_c = \left(\frac{1}{Q_s}\right) * \sqrt{1 - (1/(4 * Q_s^2)} \tag{20}$$

As derived in [7], the condition to be met to avoid bifurcation phenomenon is $k < k_c$. By satisfying this condition although there exist three ZPA frequencies f_L, f_H and f_o but out of these f_L and f_H are complex and only f_o is real.

3 Calculation of Design Parameters

As per the wireless charging standards of Society of Automotive Engineers technical information report J2954, the resonant frequency should be in between the range 81.39–90 kHz [9]. Also, the power levels as per SAEJ2954 standards allow four levels of power output for a wireless power transfer system, i.e., 3.7, 7.7, 11 and 22 KW.

Table 1 Desired Specifications as per SAEJ2954 standards

Power output level	7.7 KW
Output voltage	400 V (Compatible with available lithium-ion battery available)
Resonant frequency	85 kHz
Supply voltage	240 V

In electrical vehicles, lithium-ion battery is used which is available in the range of 300–600 V [10]. The advantage of lithium-ion battery is that it has good power density.

Following the SAEJ2954 WPT standards and available lithium-ion battery voltage range for electrical vehicles, here we calculate the electrical parameter with the following specification.

Now, using the derived formulas in Sect. 2 and meeting the desired specifications as shown in Table 1, the electrical parameter values are calculated as follows

$$R_0 = \frac{V_o^2}{P_0} = \frac{400 * 400}{7700} = 20.77\ \Omega$$

$$R_L = \left(\frac{8}{\pi^2}\right) * \frac{V_o^2}{P_o} = \left(\frac{8}{\pi^2}\right) * \frac{400 * 400}{7700} = 16.84\ \Omega$$

$$V_{\text{srms}} = \frac{2\sqrt{2}V_o}{\pi} = 2\sqrt{2} * \frac{400}{\pi} = 360.12\ \text{V}$$

The expressions for R_L and V_{srms} are taken from [8].

$$L_s = Q_s * \frac{R_L}{\omega_0} = 4 * \frac{16.84}{2 * \pi * 85{,}000} = 1.261 \times 10^{-4}\ \text{H}$$

$$I_{\text{srms}} = \frac{V_{\text{srms}}}{R_L} = \frac{360.12}{16.84} = 21.38\ \text{A}$$

$$I_{\text{prms}} = \frac{P_o}{V_{\text{prms}}} = \frac{7700}{240} = 32\ \text{A}$$

$$M = i_{\text{srms}} * \frac{R_L}{i_{\text{prms}} * \omega_o} = 21.38 * \frac{16.84}{32 * 2 * \pi * 85{,}000} = 2.106 \times 10^{-5}\ \text{H}$$

Now, for bifurcation free operation considering quality factor $Q_s = 4$, we get the value of critical coupling coefficient from Eq. (20) as follows

$$k_c = \left(\frac{1}{Q_s}\right) * \sqrt{1 - (1/(4 * Q_s^2))} = (1/4) * \sqrt{1 - (1/(4 * 4^2))} = 0.248$$

So, in order to have bifurcation free operation, the condition to be satisfied is $k < k_c$, and for this, the value of coefficient of coupling is taken 0.2.

$$L_p = \frac{M^2}{L_s * k^2} = \frac{2.106 * 10^{-5} * 2.106 * 10^{-5}}{1.261 * 10^{-4} * 0.2 * 0.2} = 8.793 \times 10^{-5} \text{ H}$$

$$C_p = 1/L_p\omega_0^2 = \frac{1}{8.793 * 10^{-5} * 2 * \pi * 85{,}000 * 2 * \pi * 85{,}000} = 3.98 \times 10^{-8} \text{ F}$$

$$C_s = 1/L_s\omega_0^2 = \frac{1}{1.261 * 10^{-4} * 2 * \pi * 85{,}000} = 2.78 \times 10^{-8} \text{ F}$$

4 Simulink Implementation of SS-IPT Model

The SS-IPT model is implemented on the Simulink platform as shown in Fig. 5. The values of the electrical parameters calculated in Sect. 3 are inserted in the Simulink model. The waveforms of the output voltage V_o, primary side current and secondary side current as obtained through Simulink model are shown in Figs. 6, 7 and 8, respectively.

The graphs obtained from Simulink platform can easily infer that the theoretical values calculated for output voltage V_o, primary current RMS value I_{prms}, secondary current RMS value I_{srms} match almost.

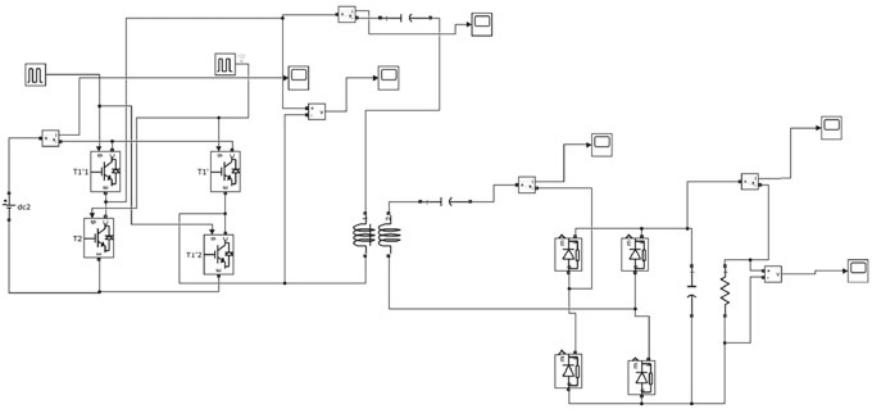

Fig. 5 Simulink model of SS-IPT system

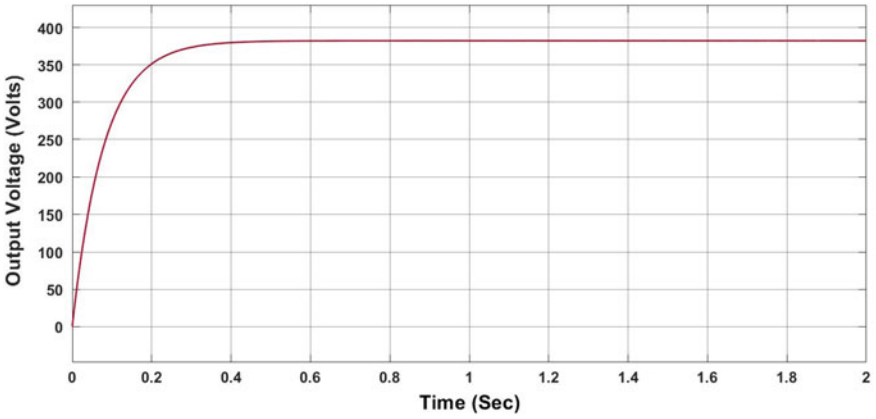

Fig. 6 Output voltage

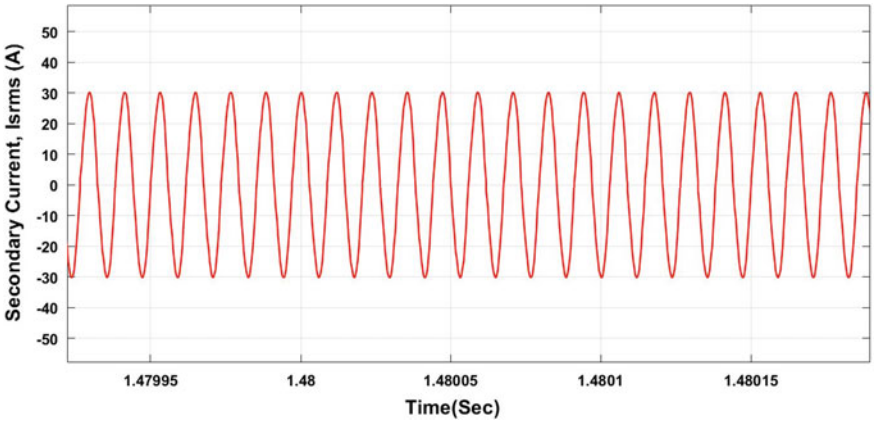

Fig. 7 Primary side current

5 Conclusion

In this paper, using SS-IPT topology, a WPT-based charger is designed for electrical vehicle charging. In designing procedure, SAEJ2954 standards have been followed which meet the latest charging requirements. Another important consideration in designing that has been taken is bifurcation phenomenon which most of the IPT charging designs have avoided. The Simulink results match the theoretical calculation which prove that designing methodology is correct.

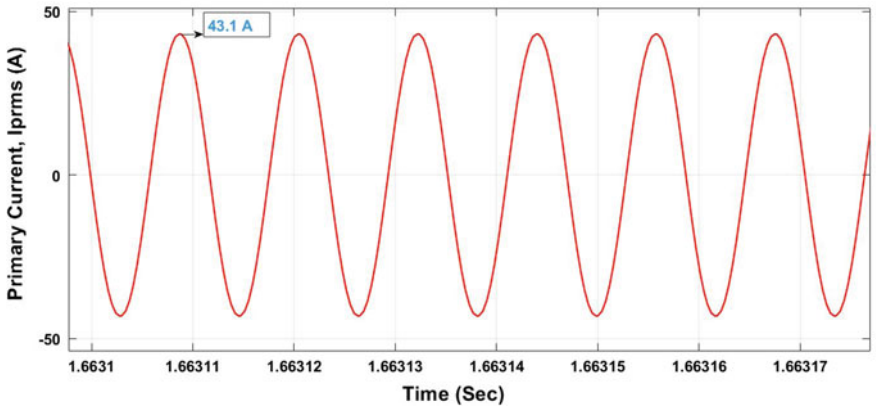

Fig. 8 Secondary side current

References

1. Huang Z, Wong SC, Chi KT (2019) An inductive power transfer converter with high efficiency throughout battery charging process. IEEE Trans Power Electron (2019)
2. Miller JM, Daga A (2015) Elements of wireless power transfer essential to high power charging of heavy duty vehicles. IEEE Trans Transp Electrification 1(1):26–39
3. Li S, Mi CC (2015) Wireless power transfer for electric vehicle applications. IEEE J Emerg Sel Top Power Electron 3(1):4–17
4. Qu X, Jing Y, Han H, Wong S-C, Chi KT (2017) Higher order compensation for inductive-power-transfer converters with constant-voltage or constant-current output combating transformer parameter constraints. IEEE Trans Power Electron 32(1):394–405
5. Zhang Z, Pang H, Georgiadis A, Cecati C (2019) Wireless power transfer—an overview. IEEE Trans Industr Electron 66(2):1044–1058
6. Gati E, Kampitsis G, Manias S (2017) Variable frequency controller for inductive power transfer in dynamic conditions. IEEE Trans Power Electron 32(2):1684–1696
7. Aditya K, Williamson SS (2019) Design guidelines to avoid bifurcation in a series-series compensated inductive power transfer system. IEEE Trans Industr Electron 66(5):3973–3982
8. Košík M, Fajtl R, Lettl J (2017) Analysis of bifurcation in two-coil inductive power transfer. In: 2017 IEEE 18th workshop on control and modeling for power electronics (COMPEL). IEEE, pp 1–8
9. Cell, Module, and Pack for EV application. [Online]. Available http://www.eco-aesc-lb.com/en/product/liion_ev/
10. Miller P (2015) State of the art and future developments in lithium-ion battery pack for passenger car application. Johnson Matthey Technology Review, p. 59

Hybrid Chaining Security Approach in Cloud Computing

Vartika Kulshrestha, Seema Verma and R. K. Challa

Abstract In the innovative world, the advance progression of information in cloud computing has become the concern since information is the most significant asset which needs to be secure. Several encryption techniques are broadly available and used in information security across all platforms. Encryption algorithms are arranged into two major groups: symmetric key and asymmetric key. Asymmetric-key encryption is utilized close by symmetric-key encryption to develop the best execution of information exchange. Numerous analysts have proposed different encryption calculations, for example, AES, DES, Blowfish, and so forth. However, as security level is expanding, the time and multifaceted nature of calculation are additionally expanding. This is the significant reason for diminishing the speed and proficiency of the encryption framework, and cloud computing is growing expertise that is vague to several security issues. The proposed scheme is based on hybridization of RSA and AES, encryption algorithm, i.e., "Hybrid Chaining Algorithm (HCA)" which upgrades the security execution. The HCA is a blend of open private (AES and RSA) key encryption algorithm that utilizes 128–1024 bits key size and also uses MD5 hashing procedure to expand the security. This calculation utilizes MD5 hashing procedure to expand the security. The fundamental focal point of this framework is to hinder data access from cloud information stockpiling centers by unapproved clients. This superbly put away data at cloud information stockpiling centers and recovers information from it once it is required. This gives the highly secured state of information security for online virtual framework and spares the misrepresentation clients to utilize your insight.

Keywords AES · RSA · Hybrid chaining algorithm (HCA) · MD5 · Cloud computing

V. Kulshrestha (✉) · S. Verma
Department of Electronics, Banasthali Vidyapith, Banasthali, Rajasthan 304022, India

R. K. Challa
NITTTR, Chandigarh 160019, India

V. Janyani et al. (eds.), *Optical and Wireless Technologies*, Lecture Notes in Electrical Engineering 648, https://doi.org/10.1007/978-981-15-2926-9_70

1 Introduction

Online cloud computing portals/services are being extensively used to provide a large volume of storage space and high-end computing platforms. Hence, there is an essential requirement for providing security and veracity in cloud resources [1]. In general, cloud foundations are much dependable and groundbreaking than conventional figuring stages. However, unapproved access and noxious clients have observed to be a huge issue in verifying the cloud frameworks. These unwanted clients may adjust or erase the meaning data being put away in the cloud computing infrastructure [2]. The distributed computing model incorporates a few innovative progressions, for example, virtualization, Web administrations, and service-level agreement (SLA) to execute the big business application. Because of fast improvement in advances in technologies, more and more specialist organizations and clients are moving toward cloud condition. Currently, armed forces, administration, and business endeavor frameworks are utilizing distinctive cloud administrations to provide an arrange network and high administration accessibility to the end clients. Cloud suppliers offer their administrations in three crucial models [2]: Infrastructure as a Service (IaaS), Platform as a Service (PaaS), and Software as a Service (SaaS). Despite the fact that distributed computing has numerous focal points when contrasted and the customary information stockpiling instruments, security concern is an obstruction for picking distributed computing from the consumers' perspective. The researchers/specialists have completed several investigations identified with security issues in cloud [2]. The infrastructure is accessible out in unrestricted and private mode. Private cloud is committed to a solitary client or organization. Nowadays, a wide scope of accessibility and unwavering quality instruments are fused into the online cloud administrations for giving the veracity and security in cloud assets. Cloud facilities are provided for consumers over the Internet on a demand basis. Thus, the undesirable cloud administrations can be expelled by the clients that would reduce the absolute expense. These days, numerous cloud co-ops are delivering a various cloud facilities like online storage, computing procedures, grid substructures, etc. With the development in advancements, the accompanying cloud specialist organizations are in particular, CenturyLink, Yahoo, Oracle Corporation, Google, IBM, eBay, Microsoft, Amazon and Apple [3–5] have just put resources into distributed computing.

The execution of these cloud specialist co-ops can be delineated with the assistance of different execution assessment parameters, in particular, the response and waiting time of the virtual machine to access the cloud, the expense of each cloud benefits, etc. Cloud specialist organizations have built up various conventions for getting to the cloud assets. However, they give less security administrations to the end clients. Encryption technique is a vital cryptographic contrivance for secure data communication over the years [6–9]. This technique is utilized in defense and government systems to upgrade the security for classified information [10]. The facilitated administrations are offered to predetermined number of people groups; this limits the security concern, but in case of public cloud, the network infrastructure is claimed and overseen by cloud supplier itself. Thus, security and privacy of information are

essential concerns [2, 10], but to maintain the quality of service (QoS) of cloud is another important issue to look after as the numbers of virtual users are increasing. A huge number of clients share enormous amount of information at high speeds from all over the world including the scattered areas. But, in real time, distributed computing environment, information security, performance, and reliability are still major issues [10]. The proposed approach delivers a reasonable and brief perspective to secure the information within the cloud environment and also in the transmission.

2 Motivation

Over 70% of organizations have adopted the encryption-based frameworks to ensure their correspondence channel [11]. What is more interesting is more than 53% of the industry people are utilizing an encryption module in the information storage framework. Encryption is utilized to secure the information as well as to resist the changes in information [12]. There are reports claiming that information is seized or changed during the transit time [13]. Consequently, information ought to be shielded from interloper or unapproved clients. In this way, encryption is generally utilized in the space of Internet business, mobile correspondence, remote correspondence, cloud-fiasco arrangement, virtual, organize, robotized teller machine, IoT-condition, and smart home framework [14]. The most famous verified encryption techniques are hash functions, constructed cipher functions, small domain encryption algorithms, and tree-based algorithms, etc. [3, 9]. There are many studies that prove the work on small domain encryption techniques [4]. However, the exploration on this area is still insufficient. This technique is mostly used to encode the short messages, but the uses are expanding like individual identification, Visa and platinum card [5].

3 Related Research Review

In today's era, every field of business environment and our life is impacted by cloud computing. Cloud computing has become one of the major planned and premeditated directions for several organizations. However, as more sensitive private facts and figures are relocated to the cloud, into social media sites, DropBox, Baidu WangPan, etc., data security and privacy issues are questioned [15]. Various security approaches and encryption techniques have been implemented in the cloud by using AES and RSA [15, 16]. In an article [17], Patil et al. discuss the importance of cryptography in cloud computing environment to improve the data security. They have applied and examined the AES and RSA along with the DES and Blowfish in a cloud environment. In an article [18], Shimbre et al. investigate the data storage security difficulty for cloud computing and discuss the AES and hashcode techniques to deliver the data security. In an article [19], Usman et al. implement the AES to improve the data security for Global Software Development in cloud computing environment. Raphael

et al. [15] discuss the data security threats in cloud computing and apply the AES with a secure hash algorithm to deliver the data security. In article [20], authors propose the AES implementation on data classification to improve the cloud security. In an article [21], Kaur and Singh implement RSA at windows azure cloud to improve the data storage security. Authors propose fast RSA to improve the information confidentiality in the cloud [22]. Amit Asthana et al. propose three-step security model based on RSA and steganography to improve the data security, and they also state that RSA is more secure [20]. In article [23], authors implement RSA and MD5 to deliver the data security and integrity. In article [16], authors discuss the factorization method of RSA to improve the data security.

The paper [24] contemplated diverse security issues in administration conveyance models of distributed computing. They additionally propose an incorporated security display for giving distinctive dimensions of security to information in cloud foundation. The dangers and assaults that are conceivable to propelling cloud computing information stockpiling are considered in [25] and after that proposed another security instrument. Information integrity amid the transmission can be ensured by the SSL convention connected. In file transferring and downloading session, MD5 checksum is utilized for giving confirmation and approval. The consistency and security challenges of a large-scale cloud computing have been discussed in paper [26]. Authors have broken down two major highlights of virtual storage: ability of cloud storage and data security that is stored in cloud using CAP theorem. In paper [27], characteristic-based encryption with the key administration has been discussed for information security. To ensure the veracity of information, third party auditor scheme has been proposed which also improves the information retrieval [28, 29]. The comparative analysis of AES, DES, and RSA has been discussed in the paper [30, 31] on the basis of execution time of encryption and decryption time.

4 Proposed Work

This proposed model is also based on the hybridization of symmetric and asymmetric cryptography, where public key and symmetric key both are used. But, in the encryption process, after the randomly generated first set of public key and private key of RSA algorithm, AES key is used followed by the second set of public key and private key of RSA algorithm to the intermediate cipher. The decryption process starts in a reverse way. The key generation method has already been explained. Then, all the five keys are being hashed by the salted MD5 as shown in Fig. 1. The AES and RSA cryptosystem is implemented in JDK 1.8.0_121 using javac compiler over Eclipse Compiler for Java (ECJ). Furthermore, compilation and running of the program have been done using command-line interface rather than GUI to enhance the performance of program.

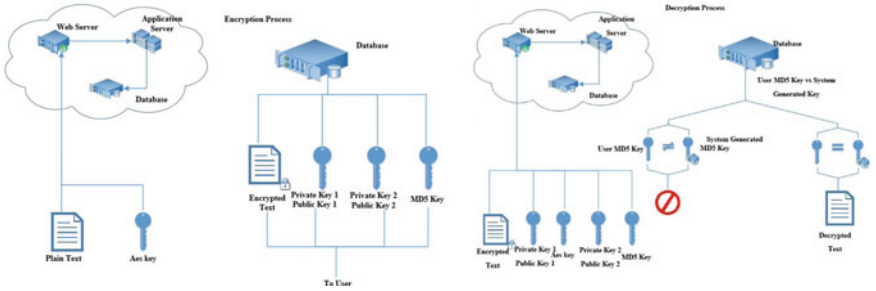

Fig. 1 Proposed algorithm framework

5 Result and Discussion

To maintain the essential security, 128 bits key size of an integer is required to perform the operation on mathematical functions used in symmetric-key cryptography and 128–1024 bits of RSA key size in public key cryptography systems and a message to encrypt. The library provisions diverse processor families and delivers optimizations in the procedure of assembly code for specific families of cryptographic processes and all the required primitives for executing novel approaches. Intel I5 5200 U (power saving mode) machine at 2.20 GHz, under both Windows 10 and Ubuntu LTS 16.04, is used to run the codes.

The proposed algorithm has been tested for the 128–1024 RSA key bit variations on both Ubuntu and Windows operating system as shown in Figs. 2, 3, 4, and 5. HCA is more secure than the normal RSA and double RSA since this algorithm is using the AES encryption techniques. Table 1 illustrates the throughput of the proposed hybrid cryptography algorithm compared with the existing algorithms for different sizes of file sizes.

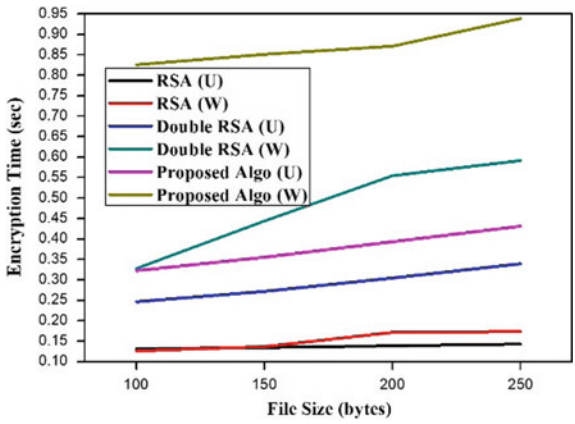

Fig. 2 Encryption time analysis performed on both Windows and Ubuntu operating system (128-bit)

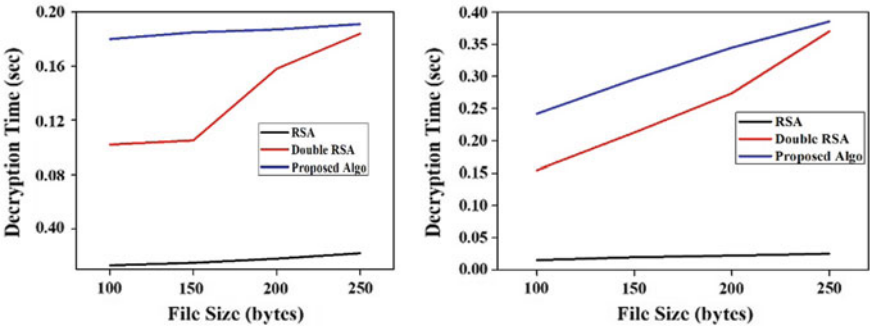

(a) Ubuntu operating system (128 – bit) (b) Windows operating system (128 – bit)

Fig. 3 Decryption time analysis

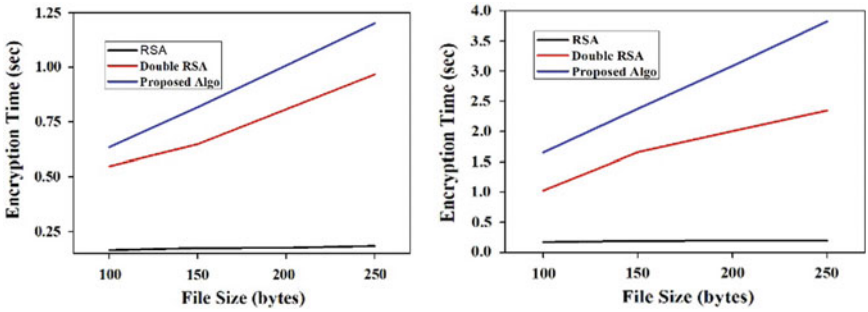

(a) Ubuntu operating system (256 – bit) (b) Windows operating system (256 – bit)

Fig. 4 Encryption time analysis

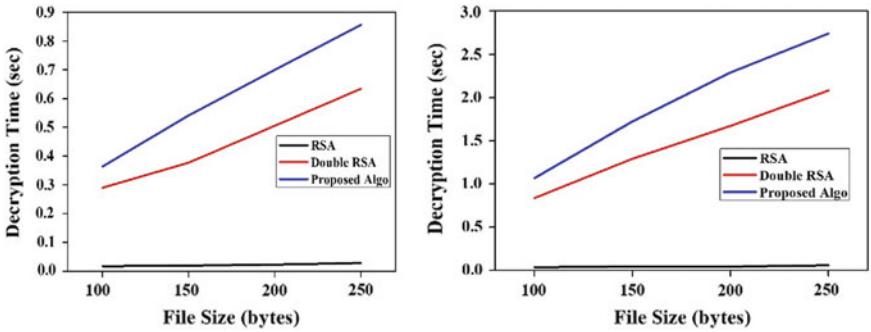

(a) Ubuntu operating system (256 – bit) (b) Windows operating system (256 – bit)

Fig. 5 Decryption time analysis

Table 1 Comparative analysis of throughput of HCA with existing algorithms

Algorithms	128-bit key	256-bit key	512-bit key	1024-bit key
AES	491.2	–	–	–
RSA	1151.3	912.6	545.1	161.06
Double RSA	365.3	99.4	12.51	1.01
HCA	281.4	63.97	8.731	0.7705

6 Conclusion and Future Work

To deliver a safe and effective arrangement for keeping up information classification, a hybrid encryption algorithm has been proposed that is intended to keep away from the security issues existed in single-hash figures. The security issues of the proposed plan are examined and contrasted with the security of some single-hash figures. The twofold cryptographic technique makes it more secure than the other existing hash-based figures. HCA permits two methods of encryption. The encryption key can be taken care of as either symmetric or deviated key without a lot of changes in the encryption conspire itself. In addition, HCA makes it less demanding to change from symmetric to unbalanced key and the other way around without changing the encoded information itself. With respect to future work, HCA can be used in cloud applications all around successfully. The ciphertext makes the plan appropriate for scrambling and sharing enormous information on the cloud with its basic and exquisite key taking care of instrument.

References

1. Su Q, Pan Z, Lin K (2016) A new approach with combination of fitting and encryption for transmission. IEEE, pp 446–449
2. Bennasar H, Essaaidi M, Bendahmane A, Ben-othman J (2016) State-of-the-art of the cloud computing cyber-security. IEEE
3. Zhou Z, Tsang KF, Zhao Z, Gaalou W (2016) Data intelligence on the Internet of Things. Springer, Pers Ubiquit Comput. https://doi.org/10.1007/s00779-016-0912-1
4. Ristenpart T, Yilek S (2013) The mix-and-cut shuffle: small-domain encryption secure against N queries. In: Canetti R, Garay JA (eds) CRYPTO, Part I. LNCS, vol 8042. Springer, pp 392–409
5. Hoang VT, Morris B, Rogaway P (2012) An enciphering scheme based on a card shuffle In: Safavi-Naini R, Canetti R (eds) CRYPTO, LNCS, vol 7417. Springer, pp 1–13
6. Fleischmann E, Forler C, Lucks S, Wenzel J (2012) Weimar-DM: a highly secure double-length compression function. LNCS, ACISP 7372:152–165
7. Lee J, Kapitanova K, Son SH (2010) The price of security in wireless sensor networks. Elsevier Comput Netw 54(17):2967–2978
8. Lee JY, Huang YH (2014) A lightweight authentication protocol for Internet of Things. IEEE Explore, ISNE, pp 1–2
9. Fleischmann E, Forler C, Lucks S (2012) McOE: a family of almost foolproof on-line authenticated encryption schemes. LNCS, FSE 7549:196–215

10. Chen Y, Yao W, Luo J (2016) Research on the active defence security system based on cloud computing of wisdom campus network. In: 28th Chinese control and decision conference (CCDC). IEEE, pp 1292–1297
11. Mazumder R, Miyaji A, Su C (2017) A simple construction of encryption for a tiny domain message. IEEE
12. Rogaway P (2004) Efficient instantiations of Tweakable Blockciphers and refinements to modes OCB. PMAC, Asiacrypt 3329:16–31
13. Yasuda K (2011) A new variant of PMAC: beyond the birthday bound. Crypto 6841:596–609
14. Atzori L, Iera A, Morabito G (2010) The internet of things: a survey. Elsevier Comput Netw 54(15):27872805
15. Erbes J, Motahari-nezhad HR, Graupner S (2012) The future of enterprise IT in the cloud. Computer 45(5):66–72
16. Motahari Nezhad HR, Stephenson B, Singhal S (2009) Outsourcing business to cloud computing services: opportunities and challenges. HP Laboratories
17. Elson J, Howell J (2009) Refactoring human roles solves systems problems. In: Proceeding of conference on hot topics in cloud computing (HotCloud'09), Article no 6
18. Khajeh-Hosseini A, Greenwood D, Sommerville I (2010) Cloud migration: a case study of migrating an enterprise IT system to IaaS. In: IEEE 3rd international conference on cloud computing, pp 450–457
19. Saripalli P, Walters B (2010) QUIRC: a quantitative impact and risk assessment framework for cloud security. In: 2010 IEEE 3rd international conference on cloud computing, pp 280–288
20. Yu S, Wang C, Ren K, Lou W (2010) Achieving secure, scalable, and fine-grained data access control in cloud computing. In: Proceedings of IEEE INFOCOM, pp 1–9
21. Saripalli P, Pingali G (2011) MADMAC: multiple attribute decision methodology for adoption of clouds. In: 2011 IEEE 4th international conference on cloud computing, pp 316–323
22. Misra SC, Mondal A (2010) Identification of a company's suitability for the adoption of cloud computing and modelling its corresponding return on investment. Math Comput Model 53(3–4):504–521.https://www.sciencedirect.com/science/article/pii/S089571771000155X
23. Mollah MB, Islam KR, Islam SS (2012) Next generation of computing through cloud computing technology. In: 2012 25th IEEE Canadian conference on electrical computer engineering (CCECE), pp 1–6
24. Wilson Piers (2011) Positive perspectives on cloud security. J Inf Secur Tech Rep 16(3–4):97–101
25. Gebremeskel GB, Wang C, He Z (2012) The paradigm integration of computational intelligence performance in cloud computing towards data security. In:5th International conference on information and computing science (ICIC), pp 19–22
26. Subashini S, Kavitha V (2011) A survey on security issues in service delivery models of cloud computing. J Netw Comput Appl 34(1):1–11
27. Yu H-S, Gelogo YE, Kim KJ (2012) Securing data storage in cloud computing. J Secur Eng, pp 252–259
28. Hsu CW, Wang CW, Shieh S (2010) Reliability and security of large scale data storage in cloud computing, part of the Reliability Society Annual Technical Report
29. Mahajan P, Sachdeva A (2013) A study of encryption algorithms AES, DES and RSA for security. Glob J Comput Sci Technol Netw Web Secur 13(15):15
30. Babitha MP, Ramesh Babu KR (2016) Secure cloud storage using AES encryption. In: International conference on automatic control and dynamic optimization techniques (ICACDOT), International Institute of Information Technology (I^2IT), Pune, pp 859–864
31. Wang Q, Wang C, Li J, Ren K, Lou W (2015) Enabling public verifiability and data dynamics for storage security in cloud computing. IEEE Syst J 9(1)